
COPY
FUN
SOFT

Contractile and elastic behaviour of human muscle-tendon complexes with inertial loading

Apostolos Galantis

This thesis is submitted to the University of London in partial fulfilment for the degree of Doctor of Philosophy

U.C.L. Institute of Human Performance
Department of Physiology
R.N.O.H.T.
Brockley Hill
Stanmore
HA7 4LP

2002

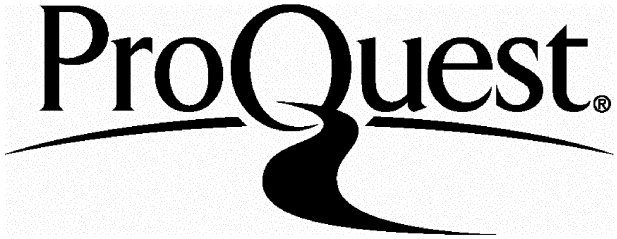

Abstract

Voluntary movement requires that inertial and gravitational forces acting on the limbs be overcome by active muscle-tendon complexes (MTCs). A lot of information exists about the mechanical properties of tendon and the mechanical behaviour of active muscle preparations shortening against constant loads or at constant speeds. During limb movement however, muscles are not expected to shorten at a constant speed or under a constant load as contractions are performed against the series elasticity of the MTC and the inertia of the limbs. This thesis investigates the relationship between the kinetics of inertial and inertial/gravitational loads external to shortening MTCs and the mechanical behaviour of the components of these MTCs. Mathematical modelling revealed the fundamental principles governing the behaviour of MTC-inertial/gravitational load systems. MTC-load model systems behave in a manner, which is largely predictable from the load that is 'sensed' by the MTC. Other factors and their effects have also been identified. It was found that there is an upper limit on the extent to which muscle generated power can be amplified by the elastic properties of tendon. Experimental observations were made of human volunteers performing index finger abduction against purely inertial loads and standing ankle plantar-flexions against inertial/gravitational loads. A method was developed which allows the kinetic behaviour of the components of shortening MTCs to be determined from simple, non-invasive measurements of torque and angular displacement of the moving limbs around their joints. Theoretical and experimental results are compared and critically discussed.

Table of contents

List of tables

List of figures

List of abbreviations and symbols

A	CC activation parameter for the contractile component (and occasionally correlation coefficient)
CR	Centre of rotation
CV	Coefficient of variation
d.p.	Decimal places
$\frac{d}{dx}(y)$	Symbol for the derivative of a function y with respect to x.
$\frac{d^2}{dx^2}(y)$	Second derivative of y with respect to x
E	Energy
e	2.718 (3 d.p.) or energy normalising factor
ε	Dimensionless energy
F	Force
f	Force normalising factor
φ	Dimensionless force
FDI	First dorsal interosseus
g	Acceleration due to gravity
K	Stiffness
k	Stiffness normalising factor
κ	Dimensionless stiffness
K_{rot}	Rotational stiffness
L	Load

l	Length of long lever
LR	Lever ratio
M	Mass. Also normalised force or velocity at which peak muscle power can be generated, expressed relative to the curvature G of the force-velocity relationship (pp. 76)
m	Mass normalising factor
MTC	Muscle-tendon complex
MTI	Muscle-tendon-inertial load system
P	Power
p	Power normalising factor
ρ	Dimensionless power
R	Power ratio
r	Correlation coefficient
R_{CC}	Peak muscle power expressed as a fraction of the maximal power it can generate
RS	Right side (of an equation)
S	Length of short lever
s	Lever length normalising factor
SEC	Series elastic component
SSE	Sum of the squares of errors
T	Time
t	Time normalising factor
τ	Dimensionless time

T_{LAT}	Latent period between delivery of an electrical stimulus to the CC and the onset development of activation (as defined in this thesis)
TC	CC exponential time constant
τc	Dimensionless CC exponential time constant
Tq	Torque
tq	Torque normalising factor
τq	Dimensionless torque
Tq_N	Normalised torque output, i.e. torque output in which the effects of CC activation, torque-angle relation and of preceding contractions have been accounted for
tq_P	Static torque potential
$Tq_{\max}$	Maximal static torque
TS	Triceps surae
υ	Dimensionless velocity
v	Velocity normalising factor
X	Displacement
x	Length normalising factor
χ	Dimensionless displacement
γ	Dimensionless gravitational force
Θ	Angular displacement
θ	Angle normalising factor
ϑ	Dimensionless angular displacement
Z	Stiffness ratio at equal torque (or force) values

Ξ	Dimensionless mass
ξ	Dimensionless moment of inertia
Ω	Angular velocity
$\Omega_{CC_{max}}$	Maximal CC shortening velocity expressed in rotational terms

Acknowledgements

During the last four years I have worked under the guidance of Professor Roger Woledge. It is difficult to express my gratitude to this unique individual in just a few words but I can honestly say that I could not have had a better guide than Roger. I am lucky and privileged to have worked with him.

Special thanks go to Dr. Stephen Harridge and Mr. Anthony Christopher. Steve has provided me with scientific and financial support as well as with encouragement to keep up the effort while progress appeared to be slow. He has done an excellent job as a second supervisor. Tony, our technician, has been of great help throughout this project and has taught me a great deal of laboratory skills. Together with my two supervisors he has been a brilliant educator.

I would also like to thank my colleagues at the Institute of Human Performance and other U.C.L. staff: Dawn, Dee, Don, Effie, Fang, Gladys, Martin, Steve P. (list is in alphabetical order). I would also like to thank the UCL Department of Physiology and especially Dr. Sally Page, for all their assistance. Special thanks to the M.R.C. for funding this research.

Last but not least I would like to thank my family both in Greece and in England for the huge support, especially my mother (Zoe), father (Alexandros), grandparents (Apostolis, Sofia, Kostas and Tonya), uncle John and my wife Sus. What they have all given me I do not know whether I will ever be able to return. A last word for Sus: Many thanks and love for the dedication and effort you have put into our relationship while I have been working on this project.

This work is dedicated to Our Father

General introduction

1. Introduction

Over the last century a considerable amount of knowledge has been produced on the mechanical properties of actively shortening skeletal muscle and of the elastic tissues associated with it. Some of the major advances in understanding the behaviour of contracting muscle may include the characterisation of the relationship between muscle force and its shortening velocity (Hill A.V., 1938), and the development of the sliding filament (Huxley and Hanson, 1954; Huxley and Niedergerke, 1954) and the cross-bridge (Huxley, 1957) theories of muscle contraction. The load-elongation properties of tendinous tissue have also been studied in detail (e.g. Rigby *et al*, 1959; Diamant *et al*, 1972; Zuurbier *et al*, 1994). Most of this information comes from *in vitro* experiments using various isolated muscle and tendinous tissue preparations obtained from small experimental animals. Such experiments have the advantage of direct measurement of force and movement and of controlled experimental conditions.

The mechanical properties of isolated human muscle and tendinous tissue preparations have also been studied. Small human muscle samples are commonly obtained using the needle biopsy technique (Bergström, 1962). Such samples can be further processed to obtain demembranated ('skinned') muscle fibre segments, which can then be used in physiological experiments (e.g. Harridge *et al*, 1996; Widrick *et al*, 1996, 1999). In the past, human muscle fibre bundles have also been obtained from open biopsies and used to study human muscle properties (Faulkner *et al*, 1980). Human tendon load-elongation properties have also been studied *in vitro* using cadaveric

specimens (e.g. Loren and Lieber, 1995), but storage of collagenous material has been shown to alter its mechanical properties (Silver *et al*, 2000). The information obtained on human muscle and tendinous tissue specimens is limited as many of the experimental procedures used in animals are ethically unacceptable in human subjects.

Many studies on human muscle function are mainly focused on examining the *in vivo* performance of the musculoskeletal system during a particular task (e.g. Wilkie, 1950; Komi, 1990; Cook and McDonagh, 1996a). Muscles inside the body have a considerable amount of tendinous tissue associated with them. This association is not only structural but also functional, as the mechanical properties of the tendinous tissue and those of active muscle interact such that the instantaneous mechanical output delivered to the skeleton may be different to that of the muscle. This is why a muscle and its tendons are collectively termed a muscle-tendon complex (MTC). Recent studies using ultrasound imaging have determined the *in vivo* load-elongation properties of the tendinous structures of human MTCs (e.g. Kubo *et al*, 2000; Maganaris and Paul, 2000a,b). Such studies have also shown that despite a constant MTC length, muscle fascicles may be actively shortening and thus stretching the tendinous tissue (e.g. Ichinose *et al*, 1997; Maganaris and Paul 2000a and b; Kurokawa *et al*, 2001). Because of the well documented relationship between the force that a muscle is generating and the velocity at which it shortens (e.g. Hill, 1938; also see Woledge *et al*, 1985), most *in vivo* experiments on humans have studied the mechanical output during movements at constant external loads ('isotonic') (e.g. Wilkie, 1950; Chow and Darling, 1999) or constant

rotational joint velocity ('isokinetic' or 'isovelocity') (e.g. Cook and McDonagh, 1996a; Ichinose *et al*, 2000). Wilkie (1950) was able to predict with good accuracy the time course of the load velocity that was measured experimentaly during 'isotonic' elbow flexion using a model consisting of: (a) a contractile component (muscle) obeying an experimentally determined hyperbolic force-velocity relationship, (b) an elastic element in series with the muscle (tendinous tissue) whose compliance was also determined experimentally, and (c) a load (inertial-gravitational). When the compliance of the series elastic component was not accounted for, the prediction was not as successful. It has also been shown (Ichinose *et al*, 2000), using ultrasound imaging, that muscle fascicle shortening velocity of the vastus lateralis muscle changed throughout the entire range of movement during 'isokinetic' knee extension. Moreover, the difference in the average muscle fascicle shortening velocity showed a fourfold increase as a result a fivefold increase in the angular velocity of knee extension ($30^0 sec^{-1}$ *versus* $150^0 sec^{-1}$). These observations were attributed mainly to the properties of elastic tissue in series with the fascicles.

Pure 'isotonic' or 'isokinetic' shortening contractions at the level of the muscle fascicles are even less likely during natural movements performed *in vivo* against loads with inertial properties. As inertia is a fundamental property of matter, body parts and objects external to the body have inertia that needs to be overcome during a movement. However, not much is known about how a MTC and its components will behave during shortening contractions against inertial loads, probably because it would not be possible to maintain the

velocity of the movement or the force constant. For example, application of a constant force on an inertial load will cause it to continuously accelerate in proportion to that force, for as long as the force is being applied.

The aim of this study is to obtain an understanding of the mechanical behaviour of human muscle and its series elasticity during shortening contractions performed *in vivo* against inertial loads in the absence or presence of a gravitational force. The theoretical behaviour of MTC-inertial load systems is first investigated on the basis of simple models. Then a method is developed by which kinetic data obtained from maximal efforts against inertial loads can be processed to obtain a possible solution for the elastic and contractile properties of two human MTCs: the first dorsal interosseus (FDI) and the triceps surae (TS). Contractions of the FDI MTC are electrically evoked and are performed against purely inertial loads. Contractions of the TS MTC are voluntary and performed against inertial-gravitational loads. These properties can then be used to obtain the time course of the mechanical output of both the muscle and its series elasticity. The relationship between muscle generated and externally recorded power receives particular attention in this study. Thus, this thesis begins with a review of the literature aiming to provide a comprehensive background of the physiological and mechanical properties of muscle, tendon and MTC that are relevant to the theoretical and experimental work undertaken. In order to avoid repetition, some of the material on the *in vivo* mechanical properties of human muscle and tendinous structures covered in later sections of the thesis has either not been included in this introduction,

or is only briefly discussed. More information can be found in the relevant sections.

2. Mechanics of skeletal muscle contraction

2.1. Force-length relation

The term 'isometric' derives from the Greek words 'iso' meaning equal and 'metro' which is referring to length. During an isometric contraction the total length of a whole muscle or muscle group, fibre bundle, fibre or fibre segment is constant. Real isometricity at the sarcomere level is difficult to achieve during contraction and therefore the term 'fixed end' rather than isometric contraction would be more appropriate. For the sake of simplicity however, the term isometric will be used in this section. For a given fully active, fresh (unfatigued) muscle preparation and under same experimental conditions (e.g. temperature, bathing solution etc.), the amount of isometric force that can be developed depends on the preparation's length. This relationship is called the force-length relation. Factors affecting isometric force production at a given muscle length in a given preparation or between different preparations will be mentioned in later sections.

2.1.1. Force-length relationship in single fibres

The observation that there is an optimal muscle length (L_0) for maximal isometric force production below or beyond which force declines, has been made more than a hundred years ago (Heidenhain, 1864; Blix, 1985). In 1940, Ramsey and Street observed that the maximal isometric force (F_0 when measured; F_{max} when read off from force-velocity plots) of intact

semitendinosus frog fibres occurred at the fibre's resting length. Calculations based on the lengths of the myofilaments in frog muscle show a resting sarcomere length of 2μm. At shorter or longer lengths F_0 declined. There was a nearly linear drop in F_0 with increasing fibre length beyond L_0 and a nearly exponential drop with reducing the length below L_0. Force development dropped to zero when the fibre was stretched to twice its L_0.

In 1954 the sliding filament theory was proposed, based on the observation that the length of the myofilaments did not change appreciably during muscle shortening (Huxley and Hanson, 1954; Huxley and Niedergerke, 1954). According to the sliding filament theory, changes in sarcomere or muscle (fibre) length are due to sliding of the thin and thick filaments relative to each other and not due to changes in the lengths of these filaments. Huxley and Niedergerke (1954), trying to provide a possible explanation to Ramsey and Street's observations, suggested that the linear drop in F_0 at lengths greater than L_0 could be explained, if F_0 was proportional to the amount of overlap between thin and thick filaments within each half-sarcomere. This would require that the force generated by active sites, acting independently of one another, be uniformly distributed along the zone of overlap of the thin and thick filaments. It would therefore be expected that isometric force would drop down to zero, at preparation lengths where there is no overlap between the myofilaments. According to this explanation, the sarcomere length at which isometric force would be expected to drop to zero with extension beyond L_0, (i.e. the length at which the filaments would not overlap any more), could be calculated as the sum of length of the thick filament plus twice the length of

the thin filament (plus twice the Z-line width). These calculations however, predicted a shorter length than that observed by Ramsey and Street. Huxley and Peachey (1959, 1961) found the sarcomere striation spacing not to be uniform along the length of stretched frog fibres, with sarcomeres near the ends of the fibres being shorter than those in the middle. During an isometric contraction the shorter sarcomeres near the ends of the fibre could generate more force than the more elongated ones in the middle, resulting in further stretching of the latter. In this way the isometric force developed by the shorter end-sarcomeres and consequently the fibre's F_0, was greater than that expected based on the fibre's average sarcomere length. It was also found that a sarcomere would not shorten, when its length exceeded a critical value of 3.5 μm. Measurements of the lengths of the thick and thin filaments showed that 3.5 μm is the sarcomere length at which filament overlap would be lost, confirming Huxley and Niedergerke's (1954) original hypothesis. At the same time the difficulty of reliable isometric force measurement due to the sarcomere length non-uniformities and the consequent creeping up of force became apparent.

Using gold leaf markers, Gordon *et al* (1966) marked a short segment in each of the isolated frog fibres that they used, within which sarcomere length was uniform. The distance between the two markers was continuously measured during the contraction via a 'spot follower' device and it was maintained constant via a servomotor. In this way they restricted, but not completely eliminated the creep phase of force development. They did not however use the maximal force developed during a tetanus to determine the force-length

relation, as it would be affected by the creep phenomenon. Instead, they used extrapolation to predict the maximal isometric force at the beginning of the tetanus eliminating the effects of creep. Their results showed that there were four main regions in the force-sarcomere length relationship of the frog. A narrow 'plateau region' (sarcomere lengths 2.00-2.25 μm) at which force is optimal. A 'descending limb' was observed at longer sarcomere lengths (2.25-3.65 μm) at which force declines linearly with sarcomere length and reaches zero at that sarcomere length where filament overlap was expected to have just been lost. This was in agreement with the original explanation that Huxley and Niedergerke (1954) attempted to provide to account for Ramsey and Street's results. At sarcomere lengths between 1.67- 2.00 μm, isometric force also declined linearly with the reduction in sarcomere length. An even steeper linear decline was observed at sarcomere lengths shorter than 1.67 μm with the force reaching zero at a sarcomere length equal to 1.27μm. This part of the force-length relationship, at which force declined from its optimal value with sarcomere length reduction is called the 'ascending limb'. The causes of isometric force reduction in the 'ascending limb' may be related to a reduction in active force production and/or to internal forces opposing shortening (for more details see Rassier *et al*, 1999 for review).

The force length relationship reported by Gordon *et al* (1966) holds for frog muscle fibre sarcomeres. Although the length of myosin filaments is remarkably well conserved amongst species, this is not the case with the thin filament lengths and therefore a shift in the force-length relationship would be expected (see Woledge *et al*, 1985; Rassier *et al*, 1999). A human force-

sarcomere length relationship would be expected to be shifted, as actin filaments from human muscle are 0.32 μm longer than in frog muscle (Rassier *et al*, 1999).

2.1.2. Force-length relationship in whole muscles

Rack and Westbury (1969) determined the force-length relationship (as well as the length dependence of force production) in cat soleus whole-muscles, by applying electrical stimulation, in rotation, to different subdivisions of the ventral nerve root supplying the muscles. In such multicellular preparations it is not possible to use the fibre-segment length-clamping approach used by Gordon *et al* (1966). According to Herzog (2000b) determination of the force-length relation in whole muscles can be complicated by factors such as:

a) Non-uniform sarcomere length within fibres

b) Different average sarcomere length between fibres

c) Muscle shortening associated with stretching of the muscle's series elasticity.

Such phenomena may account for the broader plateau and the smoother shape (absence of corners) of the whole soleus muscle force-length relationship compared with the shape of the sarcomere length-force relationship obtained in single length clamped fibre segments by Gordon *et al* (1966). Moreover, muscles inside the body may not operate throughout the entire range of their sarcomere force-length relationship, which may be another reason why most of the 'descending limb' was absent in Rack and Westbury's results. Close (1972) excised whole sartorii muscles from frogs, tying a stainless steel wire on the distal tendon as close to the muscle fibres as possible thereby reducing

series compliance. He reported a force-length relationship similar to that found by Gordon *et al* (1966). Bruce *et al* (1992) calculated the torque that would be exerted in the thumb by isometric contraction of the human adductor pollicis muscle. The calculations were based on measurements of sarcomere lengths, cross sectional area and orientation of different bundles of cadaveric adductor pollicis specimens. They found that the wide range of saromere lengths in the muscle in different positions of the thumb allowed a constant torque production over a wide range of thumb positions, i.e. the plateau of the force-length relationship was broader.

2.1.3. *In vivo* determination of the force-length relationship in humans

It is relatively simple to obtain 'strength curves' that relate the amount of force/torque developed statically at given joint angles. However, determination of i*n vivo* human skeletal muscle force-length relationships is complicated by factors such as controlling the level of muscle activation (voluntary/electrical) (cf. Epstein and Herzog, 1988), action of agonist and/or antagonist muscles (Herzog and ter Keurs, 1988; Maganaris and Baltzopoulos, 2000), stretching of the muscle-tendon complex's series elasticity leading to shortening of the muscle's contractile component (Ichinose *et al*, 1997), muscle architecture (e.g. muscle fibre/fascicle angle with respect with the muscle's line of action) (Kawakami *et al*, 2000; Maganaris and Baltzopoulos, 2000) and finally moment arm changes resulting from muscle contraction and differences in joint configuration (Maganaris and Baltzopoulos, 2000; Rassier *et al*, 1999). Recent advances in technology allow, at least to some extent, some of these factors to be measured and accounted for. Using ultrasonography pennation

angles and tendinous tissue length changes can be estimated (Ichinose *et al*, 1997; Kawakami *et al*, 2000; Maganaris and Baltzopoulos, 2000). Moment arms can also be estimated using magnetic resonance imaging (Maganaris and Baltzopoulos, 2000). Recent studies have estimated the force-length relation of human muscle *in vivo* using voluntary and electrically-evoked contractions. For example, Ichinose *et al* (1997) estimated the force-length relationship for the human vastus lateralis muscle during maximal voluntary contractions at different knee angles and found that its fibres operate in the ascending limb (knee flexion less than 70^0), plateau (70^0 knee flexion) and descending limb (knee flexion greater than 70^0). Maganaris and Sargeant (2001) stimulated electrically two human muscles *in vivo*, the tibialis anterior and the soleus, and found both muscles to operate in the ascending and plateau region of the force-length relationship.

2.1.4. Force-length relationship in sub-maximally activated muscle

When not all the TnC sites in a preparation are occupied by Ca^{2+}, activation is submaximal and the relationship between force and preparation length ('length dependence of force'; see Rassier *et al*, 1999) differs from the force-length relation. In particular, the optimal length for isometric force production increases at submaximal levels of activation compared with the optimal length under full activation (Rack and Westbury, 1969; Endo, 1972; Balnave and Allen, 1996). This is via a leftward shift in the relative force-pCa^{2+} relationship, indicating increased 'Ca^{2+}-sensitivity' as the muscle/muscle fibre length becomes longer (Endo, 1972; Balnave and Allen, 1996). This phenomenon does not seem to be related to changes in the affinity of TnC for

Ca^{2+}, but rather to an increased rate of cross-bridge attachment as a result of increased displacement of cross-bridges from the thick filaments and/or alterations of the cross-bridge attachment/detachment rates due to reduced distance between the thin and thick filaments (Rassier and Herzog, 2000; Rassier *et al*, 1999).

2.2. Force-velocity relationship of shortening muscle

There is a negative relationship between the force a fully active shortening muscle generates and the velocity at which it shortens and *vice versa*, i.e. when the ends of a fully active muscle are completely free to move the muscle shortens with maximal speed. If the ends are opposed to approach one another by a force, the greater the magnitude of that force the lower the shortening velocity. If the opposing force is high enough to completely prevent shortening, the shortening velocity becomes, of course, zero. This relationship between shortening velocity and force is not linear. The non-linear relationship between the force a fully active muscle can exert and the velocity at which it shortens was first recognised by Fenn and Marsh in 1935. Three years later A.V. Hill (1938) described this relationship in frog sartorius muscles using an isometric-release-isotonic contraction protocol. The initial muscle length and amount of muscle shortening during the release were such that most, if not all, of muscle shortening occurred within the plateau region of the force-length relation. The release would take place after the muscle had developed maximal isometric force. Hill described the relationship between the force/load (F) and the 'steady-state' velocity of muscle shortening (V_{CC}) in a simple and convenient way:

$$(F+a)(V_{CC}+b) = \text{constant} = (F_{max}+a)b \qquad (1.1)$$

where a, b are constants equal in magnitude to the force and velocity asymptotes, respectively (see figure 1.1). F_{max} is also a constant representing the maximal isometric force of the muscle preparation. Although some investigators have used variants of Hill's equation to better fit their results (e.g. Allen and Stainsby, 1973; Marsh and Bennett, 1986; Edman, 1988) or used entirely different equations (e.g. Fenn and Marsh, 1935), Hill's original equation still remains the most widely used.

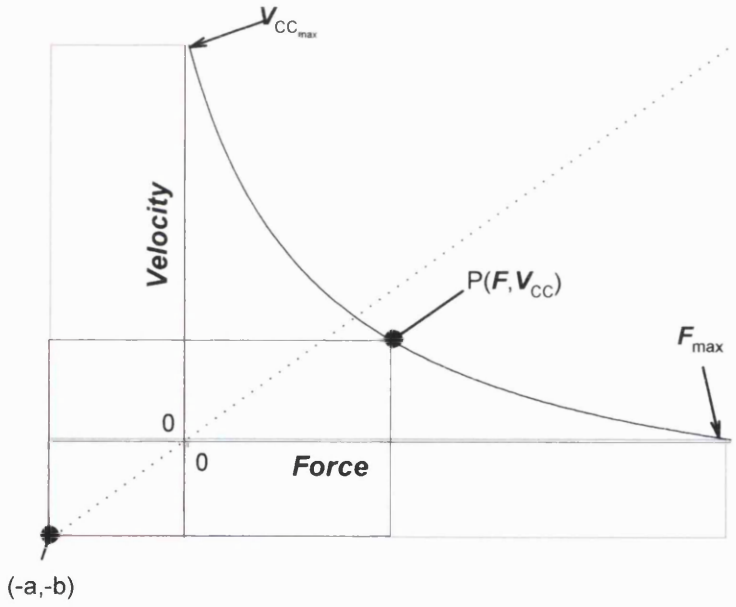

Figure 1.1. Hyperbolic force-velocity relationship (black curve). This curve is part of a rectangular hyperbola with force and velocity asymptotes –a and –b, respectively. The values of these asymptotes with respect to the maximal isometric force and maximal shortening velocity determine the curvature of the relationship. For any point on the curve, the rectangular area bounded by its force co-ordinate plus the force asymptote and its velocity co-ordinate plus the velocity asymptote, is a constant. This is shown by the areas of the rectangles for a point P on the curve (black square), for point (F_{max},0) (blue square) and for point (0,Vcc_{max}) (red square). The hyperbolic force-velocity relationship is symmetric. In this curve, F_{max}=Vcc_{max}=1 and a=b=0.25 and the axis of symmetry is shown as a dotted line.

The force-velocity relationship of a muscle shortening at constant velocity (including zero velocity) within the plateau region of its force-length relation under maximal, steady-state activation conditions can be interpreted in terms of Huxley's cross-bridge theory (Huxley, 1957). When the speed of shortening is zero (isometric contraction), a cross bridge is equally likely to be attached on an actin site within its range of excursion where it can exert a positive force, independently of the location of the actin site within this range. No cross bridge can generate negative force. Also, the probability of a cross bridge being attached is highest when there is no shortening. Thus, under isometric conditions the number of attached cross bridges is maximal with all cross bridges generating positive force. As the speed of shortening increases, the probability of any given cross bridge being attached to actin becomes gradually reduced. This reduction is greater in the cross bridge excursion domain where high positive force can be generated. In addition the probability of shortening 'carrying' an attached cross bridge into a region where it exerts negative force before it has the chance to detach from actin increases. As the speed of shortening increases the probability of an attached cross bridge being carried even further into the negative force excursion domain also increases, thus an attached cross bridge becomes more likely to generate a large negative force. When shortening speed is maximal, the total force generated by cross bridges attached on actin sites where positive force can be generated is exactly balanced by the total force generated by cross bridges that generate negative force. This is why in terms of the cross bridge theory the force exerted by a muscle is zero when it shortens at its maximal speed. Thus, according to the cross bridge theory as shortening speed increases the force drops due to a

decline both in the number of attached cross bridges and in the average force per cross bridge. The former factor is relatively more prominent at low speeds, determining the slope of the force-velocity relationship when the force is near the maximal isometric force. The latter factor is more prominent when shortening speed is high, determining the slope of the relationship when the shortening speed is near the muscles' maximal shortening speed. The overall shape of the force-velocity relationship i.e. its curvature, is determined by the ratio between these two slopes. More information regarding the parameters of the force-velocity curve is given below.

2.2.1. Factors influencing F_{max} (or F_0)

During an isometric contraction, Vcc is zero and the force F becomes equal to the maximal isometric force F_{max}. F_{max} is assumed to be proportional to the number of cross bridges acting in parallel (see Woledge *et al*, 1985). In a fully activated single muscle fibre and at a given fibre length, the number of cross bridges acting in parallel will depend on the fibre cross sectional area and the density of myofilament packing. Although human skinned type I fibres have been reported to produce less force per unit cross sectional area than skinned type II fibres (Stienen *et al*, 1996; Bottinelli *et al*, 1996), the results in the literature are inconsistent and the apparent difference may be due to methodological errors (Schiaffino and Reggiani, 1996).

In a fully active whole muscle the "architecture" of the muscle is also important, that is the way in which the muscle is constructed in 3D space from individual fibres. The correct calculation of the force exerted at the tendons

from these factors is not easy (Van Leeuwen and Spoor, 1992; Epstein and Herzog, 1998). Commonly approximate methods are used such as making 2D approximations of the muscle's structure and ignoring the distortions of the arrangement caused by the constant volume behaviour of the muscle during shortening. For example assuming the simplest possible case where the muscle is represented by a 2D muscle model, the total number of cross bridges acting in parallel will be equal to the sum of the cross bridges acting in parallel in all its fibres. This will be reflected by the physiological cross sectional of the muscle and the amount of extracellular space in the muscle. The amount of isometric force however exerted by the muscle on its point of attachment will also depend on the cosine of the fibres' angle of pennation. The pennation angle in the vastus lateralis muscle was found to increase as a result of heavy resistance training allowing the fibre cross-sectional area and contractile muscle force to increase more (16%) than the muscle's anatomical cross-sectional area and volume(+10%) (Aagaard *et al*, 2001). During efforts performed *in vivo*, the amount of force exerted on a load will also depend on the lever ratio.

F_{max} is sensitive to temperature when temperature is low (Rall and Woledge, 1990; Stienen *et al*, 1996;Bottinelli *et al*, 1996). This is consistent with *in vivo* observations on human muscle. In the human first dorsal interosseus muscle no depression in the maximal voluntary force was observed on cooling from 35 ^{0}C to 25 ^{0}C but a 30% reduction was observed on cooling to 12-15 ^{0}C (Ranatunga *et al*, 1987). Raising the temperature in the triceps surae muscle group by 3.1 ^{0}C (Davies and Young, 1983) or 3.4 ^{0}C (elderly volunteers; Davies and Young,

1985), did not affect tetanic and voluntary tension. Lowering the triceps surae temperature however by 8.4 ^{0}C did produce a fall in tetanic and voluntary tensions (Davies and Young, 1983).

F_{max}, the extrapolated intercept from Hill's equation, and F_0, the observed isometric force, do not necessarily always have the same value. For example Edman *et al* (1976) observed that the force-velocity data of single frog fibres systematically deviated from the hyperbola when force was high (>0.8F_0). Extrapolation of the hyperbola above ~0.78F_{max} overestimated the isometric force of the fibres by an average of 32±6%. More recently Edman (1988) demonstrated a force-velocity relation in frog fibres with two distinct regions, a low/intermediate-force region located in the range of 0-0.78 F_0 and a high-force region between 0.78F_0-F_0. The observations in the high-force region would fall below the hyperbola fitted for the low/intermediate-force observation. Thus, extrapolation of the hyperbolic relationship to forces greater than 0.78F_0 would lead to overestimation of shortening velocity in the high-force region and an overestimation of the maximal isometric force. Edman (1988) devised a modified version of Hill's equation, which operated as a hyperbola in the low/intermediate-force region but included an additional function to account for the deviation observed in the high-force region. He also found that the two curvatures of this double-hyperbolic force-velocity relation were closely related. The explanation for the double hyperbolic shape did not seem to be related to non-uniform contractile behaviour, but it rather appear to reflect contractile behaviour at the sarcomere level.

2.2.2. Factors influencing the maximal shortening velocity

Rearranging Hill's equation (equation (1.1)) an expression for the shortening velocity can be obtained:

$$V_{CC}=[(F_0+a)b/(F+a)]-b$$

When the ends of the preparation are completely free to move (F=0), V_{CC} attains a maximal value (V_{max}, if estimated from Hill's equation; V_0 or V_u, if measured using a slack test (Hill, 1970; Edman, 1979)). A fibre's maximum shortening velocity depends on the number of half-sarcomeres connected in series along the length of the fibre (Woledge *et al*, 1985) and on the rate of cycling of the cross-bridges in these half-sarcomeres.

The rate of cross-bridge turnover and thus the maximum velocity of shortening appears to be primarily determined by the fibre's myosin heavy chain composition (Larsson and Moss, 1993; Stienen *et al*, 1996; Bottinelli *et al*, 1996; Harridge *et al*, 1996). The fibre's myosin light chain composition (see Schiaffino and Reggiani, 1996) and differences in the myofilament lattice spacing (Widrick *et al*, 1999) may also exert a modulatory influence.

The relationship between V_0 and sarcomere length is different to that of the maximal isometric force (Edman, 1979). V_0 is constant at sarcomere lengths between 1.65-2.7 μm, an observation that is consistent with the hypothesis that V_0 is independent of the number of cycling cross-bridges. V_0 drops at lengths shorter than 1.65 μm, probably due to development of passive resistance and

rises at lengths longer than 2.7μm due to the passive compressive tension that is developed at such long lengths (Edman, 1979).

The maximal shortening velocity is greatly influenced by temperature (Bottinelli *et al*, 1996; also see Rall and Woledge, 1990), as the rate of cross-bridge cycling is an enzymatic process reflecting myofibrillar ATPase activity. Investigation of the effect of muscle temperature on V_{max} (and other parameters related to the contractile output) is complicated by temperature gradients existing across the depth of the muscle (e.g. Clarke *et al*, 1958; Gerrits *et al*, 2000). Such gradients are expected to be more pronounced in large, proximal muscles than in small, distal ones such as the first dorsal interosseus and the adductor pollicis muscle. Ranatunga *et al* (1987) found the temperature in the first dorsal interosseus muscle to change rapidly in response to changing skin temperature, with the two temperatures not varying as much as those found in previous studies using larger muscles. Thus, small, distal muscles are more susceptible to changes in environmental temperature. This allows easier manipulation of intramuscular temperature during experiments. De Ruiter and De Haan (2000, 2001) studied the temperature dependence of force-velocity parameters in the human adductor pollicis muscle during isovelocity contractions. The maximal shortening velocity was estimated by fitting Hill's equation to force-velocity observations. Estimates of the Q_{10} value for the V_{max} of the human adductor pollicis muscle were 2.2, 1.6 and 1.6 for the ranges of estimated muscle temperatures of 22.2-25.6, 25.6-31.4 and 31.4-37.1 ^{0}C, respectively (De Ruiter and De Haan, 2000).

Nitric oxide has been found to increase the maximum shortening velocity (Morrison *et al*, 1996; Maréchal and Beckers-Bleukx, 1998) via the cyclic GMP pathway causing a 'slow-to-fast' shift (Maréchal and Beckers-Bleukx, 1998; Maréchal and Gailly, 1999).

It must be noted that V_{max} (obtained from fitting force-velocity data) and V_0 (measured using slack-tests) may be different both in a single fibre (Julian *et al*, 1986) and in a whole muscle (Hill, 1970;Claflin and Faulkner, 1989). Julian *et al* (1986) showed that force-velocity observations in living (intact) frog fibres deviated from Hill's hyperbola at low (as well as at high) loads. The deviation in the low load region (below $0.02F_0$) led to the calculation of a V_{max} value that underestimated the measured maximal shortening velocity. When this deviation was mathematically accounted for, the improved estimate of V_{max} was in good agreement with V_0. In whole muscles, V_{max} is greatly influenced by the heterogeneous fibre composition of the muscle (Hill, 1970; Josephson and Edman, 1988; Claflin and Faulkner, 1989). For example, hypothetical calculations by Hill assuming a normal distribution of V_0 amongst the fibres making up a muscle, showed that the estimated V_{max} was equal to the median value of V_0. This is because at all but the lightest loads, all fibres contribute to the mechanical output of the muscle and therefore extrapolation of the force-velocity curve fitted to such observations would reflect the properties of the whole population of fibres. V_0 however should reflect the maximal shortening velocity of the fastest fibres in the muscle (Josephson and Edman, 1988). Experimental and modelling results by Claflin and Faulkner (1989) showed that the disparity between V_0 and V_{max} is indeed due to the

heterogeneity in the V_0 of the muscle fibres. *In vivo* measurements of V_0 in man are complicated by factors relating to muscle architecture, lever arms and the inertia of the moving limbs and apparatus. There are no convincing *in vivo* measurements of the maximal shortening velocity in human muscle as it is not easy to produce genuine unloaded contractions.

2.2.3. Factors influencing the curvature of the force-velocity relationship

When $V_{CC}=V_{max}$, Hill's equation (equation (1.1)) can be simplified to:

$$V_{max} = F_0 \cdot \frac{b}{a}$$

After re-arrangement of the terms it becomes:

$$\frac{V_{max}}{b} = \frac{F_0}{a} = G$$

These ratios, which are called G here (see Woledge *et al*, 1985) determine the curvature of the force-velocity relation when $0 \leq F \leq F_0$. The value of G is determined by the ratio of the slope of the force-velocity relationship near F_{max} to the slope near V_{max} (see Woledge *et al*, 1985). These two slopes reflect the effect on the force-velocity relationship of the two different processes, which according to Huxley's 1957 cross-bridge model can explain the hyperbolic shape of the force-velocity curve. As mentioned above, according to this model the reason for the decline in force with velocity when velocity is slow, is due to a decline in the number of attached cross bridges. At high velocities however, the decline in force is due to less average force exerted per cross

bridge, as more cross bridges now exert negative force. The value of G is the least temperature sensitive parameter of the force-velocity relationship (Hill, 1970; Woledge *et al*, 1985; Rall and Woledge, 1990). Studies using human skinned fibres have shown that fast type II fibres have smaller values of G (less curved force-velocity relationship) than slow type I fibres, with type IIX fibres having a smaller G than type IIA and IIA-IIX fibres (Bottinelli *et al*, 1996; Widrick *et al*, 1996).

2.2.4. Commonly used methods and relevance to the *in vivo* force-velocity output

The majority of information on the force-velocity properties of shortening muscle have utilised either constant load ('isotonic') (e.g. Fenn and Marsh, 1935; Hill, 1938; Jewell and Wilkie, 1958) or constant velocity ('isovelocity') shortening contractions (e.g. Cecchi *et al*, 1978). Quick-release and afterloaded isotonic contractions have been shown to produce identical force-velocity results (Fenn and Marsh, 1935; Jewell and Wilkie, 1958). Isotonic contractions are performed with the muscle shortening against a constant external load (force). Muscle velocity takes a finite time after the imposition of a fixed force to adjust to a stable value. The force corresponding to the magnitude of the external load and the stable velocity of the preparation provide a single force-velocity observation. The process is repeated for a number of loads in order to obtain a force-velocity relationship. An isovelocity protocol has a muscle preparation shortening at a constant velocity while its force output is measured. Again one force-velocity observation per contraction is obtained. In both of these protocols shortening is allowed only over a limited range in order to

avoid the effects of sarcomere length change (e.g. Granzier *et al*, 1989) and shortening deactivation (e.g. Lännergren, 1978) on the preparation's output. Wilkie (1950) was one of the first researchers to investigate whether voluntary shortening contractions of human muscle also have a hyperbolic force-velocity relationship. In his experiments on the maximum voluntary flexion of the elbow, the set up was designed to provide a constant load to the movement ('isotonic'). It was realised however that the load was not exactly constant due to the inertia of the apparatus and of the forearm. After corrections for the effects of inertia, the resulting force-velocity curves were typical of those obtained *in vitro* from isolated muscle preparations. The force-velocity output of human muscle has also been investigated during constant velocity movements. Cook and McDonagh (1996a) timed the release of the index finger into constant velocity abductions during the rising phase of maximal electrically-evoked tetanic contractions of the first dorsal interosseus (FDI) muscle-tendon complex, such that a constant-force phase was generated in each record. During these constant force phases the series elastic component was not expected to change length and the observed external velocity was therefore attributed to shortening of the FDI muscle. When the constant-force values of each volunteer were plotted against the corresponding constant-velocity values, Cook and McDonagh found the force-velocity relationship of the FDI muscle to be similar to the hyperbolic relationships observed in isolated muscle preparations. More recently (Ichinose et al, 2000) it was shown, using ultrasound imaging, during 'isokinetic' knee extension at two different angular velocities (30 and 150 $^{0}\cdot sec^{-1}$) the muscle fascicle shortening velocity of the vastus lateralis changed throughout the movement. Moreover,

the change in the average muscle fascicle velocity in the vastus lateralis was not in the same proportion to the change in the angular velocity of knee extension. This was attributed mainly to the series elastic properties of the muscle-tendon complex. Thus, real 'isotonicity' and 'isovelocity' conditions at the level of the muscle fibres are very difficult to achieve under *in vivo* conditions.

Even during isometric contractions in which there is no external movement (and hence the external velocity is zero), the muscle fascicles have been shown to shorten, stretching the muscle's series elasticity (Ito *et al*, 1998). Macpherson (1953) using frog sartorius muscles determined their force-velocity (and their series elastic component load-elongation) properties by comparing in each muscle two isometric contractions, one with and another without added series compliance. The force-velocity relationship during such isometric contractions was also found to have a typical hyperbolic shape. The same method of comparing two isometric contractions with and without added compliance was also used by Wilkie (1950) to determine the series elastic properties of the elbow flexors in humans and use this compliance result to make corrections that improved the predictions of the velocity output during his 'isotonic' experiments. Cook and McDonagh (1996a) found the force-velocity relationships of the electrically-stimulated first dorsal interosseus muscle to be similar under isometric and 'isokinetic' conditions.

The force-velocity relationship during voluntary contractions performed *in vivo* has also been shown to depend on the level of muscle activation,

activation here referring to motor unit recruitment (Chow and Darling, 1999). A family of hyperbolic force-velocity curves was obtained for the wrist flexors of human volunteers, each different curve corresponding to a different level of 'activation' and reflecting the force-velocity properties of the currently recruited motor units. These results were not expected to have been affected, at least to any considerable extend, by the muscle group's series elasticity as the wrist flexors have very stiff tendons and the force the muscles produced was too small to cause appreciable tendon elongation.

Force-velocity properties have also been investigated under different levels of activation (Cecchi *et al*, 1978; Curtin *et al*, 1998; De Haan, 1988, 1998) and more complex patterns of the preparation's length change mimicking *in vivo* movement (e.g. Askew and Marsh, 1997, 1998; Curtin *et al*, 1998). Although the findings of such studies are not dealt with in detail in this thesis, the general conclusion is that when certain factors are accounted for (e.g. activation levels, length change of the series elastic component etc) the force-velocity output of muscles can be fitted well, at least in most of its range, by a hyperbolic relationship.

2.3. Mechanical power output of shortening muscle

Mechanical power refers to the rate at which mechanical work is performed. The total amount of work (W_{CC}) performed by a shortening muscle during a contraction can be expressed as the integral of its force output with respect to the distance shortened (X_{CC}):

$$W_{CC} = \int_0^{X_{CC}} F \cdot dX_{CC}$$

Mechanical power, P_{CC} ,or simply power for the purposes of this work, is the rate at which work is performed:

$$\begin{aligned} P_{CC} &= \frac{d}{dT}(W_{CC}) \\ &= \frac{d}{dT}\left(\int_0^{X_{CC}} F \cdot dX_{CC} \right) \\ &= F \cdot \frac{d}{dT}(X_{CC}) \\ &= F \cdot V_{CC} \qquad (1.2) \end{aligned}$$

Equation (1.2) shows that the capability of a shortening muscle to generate power is closely related to its force-velocity properties. For this reason power could be used to describe a muscle's functional performance since it reflects not only how strong a muscle is, but also how fast it contracts and *vice versa*. The power output of a fully active muscle can be calculated by multiplying each velocity observation in its force-velocity curve by the corresponding value of force and *vice versa*. In this way a power-velocity or power-force relationship can be constructed.

These relationships have a maximum at:

$$\frac{d}{dF}(F \cdot V_{CC}) = 0$$

or

$$\frac{d}{dV_{CC}}(F \cdot V_{CC}) = 0$$

As a consequence of the symmetric nature of the hyperbolic force-velocity relationship in a fully active muscle, peak power occurs at the same relative value of the maximum isometric force as of the maximal shortening velocity, *M*, which is determined by the curvature, *G*, in the following way (see Woledge *et al*, 1985 for derivation):

$$M = \frac{\sqrt{1+G} - 1}{G}$$

For a value of *G*=4, which is commonly used in the literature (Epstein and Herzog, 1998), $M \approx 0.31$. According to equation (1.2) the muscle power at that load or velocity is equal to the product of the force and the muscle's shortening velocity and therefore, power, in relative terms, is equal to M^2. For a value of *G*=4, this is approximately 0.1. For a linear force-velocity relationship, the normalised power output is 0.25, i.e. 2.5 times greater than when *G*=4. The maximal muscle power in absolute terms is given by the following equation:

$$P_{CC_{max}} = M^2 \cdot F_{max} \cdot V_{CC_{max}} \quad (1.3)$$

Widrick *et al* (1996) using skinned fibres from human volunteers found that the maximal isometric force per fibre cross sectional area, the maximal

shortening velocity expressed in fibre lengths per second and reciprocal of G, i.e. the value of $\frac{a}{F_{max}}$, were higher in type IIX fibres than in type IIA and in type IIA fibres than in type I fibres. As these differences add up in a geometric manner when the peak power is calculated (see equation (1.3)), it is not surprising that type IIX fibres and type IIA fibres produced ten and five times more power than type I fibres, respectively. The optimal force for power production relative to the fibres' maximal isometric force also decreased from type IIX to type IIA and from type IIA to type I fibres. These observations were similar in fibres coming from both sedentary and endurance trained volunteers. The temperature during their experiments was 15 ^{0}C. These results are in remarkable agreement with those of Bottinelli *et al* (1996) also on human skinned fibres at 12 ^{0}C. Calculations using the mean specific isometric force (or F_{max} per fibre cross sectional area), V_{max} normalised for fibre length and G reported in their paper, show that fibres containing type IIx, type IIa-x, type IIa and type I-IIa myosin heavy chain isoforms produce 11, 7, 5 and 2 times greater peak power than fibres containing the type I isoform. The optimum velocity for peak power production expressed in fibre lengths per second, also decreased in the same order as power, being highest in fibres containing predominantly the type IIx myosin heavy chain isoform and being lowest in fibres containing the type I isoform. It is not known however whether the relationship of peak power, optimal load or shortening velocity that was observed between different fibre types remains the same at physiological temperatures. Bottinelli *et al* (1996) found that the specific tension and maximal shortening velocity of type I fibres showed greater temperature

sensitivity than type II fibres, though this difference was not statistically significant. This is in agreement with Ranatunga's (1984) observations that the maximal shortening velocity and maximum rate of isometric force development of the slow soleus mouse muscle were more temperature sensitive than those of the fast extensor digitorum longus of the same animal. It is most likely however that even under physiological temperatures, fast fibres produce greater peak power and at higher shortening velocities than slow fibres. Evidence coming from carp swimming suggests that different fibre types are recruited during movement in such a way that power output and efficiency of movement is optimised (Rome *et al*, 1988). Thus, fast muscle fibres are recruited during fast, brief swimming during which they shorten at velocities optimal for power generation. On the other hand, slow, more efficient muscle fibres generating relatively less peak power and at slower shortening velocities, are recruited in steady, sustainable, slow swimming during which the fibres' shortening velocity is optimal for peak power generation.

During voluntary movements and locomotion mechanical work done by the muscles is used to change the kinetic energy of limbs and of the centre of mass. The amount of work performed by an actively shortening muscle depends on how much it can shorten and how much force it can generate during shortening. In order to maximise the work output of a shortening muscle during a concentric movement, the muscle has to shorten over a long distance producing a large amount of force. Muscles have finite lengths and the extent to which isolated muscle preparations can shorten while capable of

generating force is constrained by their force-length relationship (see section 2.1). In addition, anatomical constraints may limit the operating range of muscle shortening inside the body (e.g. Burkholder and Lieber, 2001). The amount of force generated by a shortening muscle during a movement critically depends, amongst other things such as extent of activation, deactivation, force-length relation etc., on the speed of shortening. As discussed above, force generation is reduced with the speed of shortening. Under certain circumstances it is desired to maximise the kinetic energy of the limbs or of the centre of mass of the whole body during a single movement, such during jumping for example. This would require that the muscle produce a lot of work before the end of range of movement of the joint be reached. High work output by the muscle during such a movement would result in high limb/body speed and the moving joint reaching the end of its range in a relatively short period of time. However, as a consequence of the force-velocity relationship fast contracting muscle can only generate a small amount of work per unit of time. By introducing elasticity between a muscle and a limb, the performance during such explosive movements can be improved. Early during a contraction, while the kinetic energy of the limb is low, muscle shortening is taken up by both extension of the elasticity and by limb movement. However, as the kinetic energy of the limb increases and the limb moves faster, fast limb displacements can be taken up by both recoiling of the series elasticity and by muscle shortening. That means that while a limb has been accelerated to high velocities series elasticity allows muscle shortening to proceed at slower rates as part of the limb movement can now be taken up by recoiling of the series elasticity. This allows the muscle to produce more force

and hence work during the later stages of the movement. In the absence of elasticity however, the whole of the limb displacement would have to be taken up by muscle shortening alone and the muscle would have to shorten faster and hence generate less force and work.

If during such explosive movements the series elasticity could deliver all its elastic energy to the limb raising the limb's kinetic energy (i.e. if complete recoiling was possible and no energy was lost as heat), the final kinetic energy of the limb would be equal to the total work done by the muscle during shortening. However, there is another feature of the series elasticity that is important during fast movements. Elasticity can store work when stretched by a force, but this work can, by definition, be released instantantaneously when the force falls. Tendinous structures connected in series with muscles and limbs are very good elastic materials (see section 3.2). The rate at which muscles can generate work is constrained by their force-velocity properties but series elasticity can, in principle, generate large amounts of power by releasing the finite amount of its elastic potential energy very fast. Thus, a muscle doing work against its series elasticity can do so relatively slowly, but the stored energy can be released much faster than it was put in it in a similar manner as in a catapult. The limit to how much power is released from the series elasticity depends on how fast the force acting on it drops or, in other words how fast the elasticity is recoiling. Thus, in addition to enabling the muscle to perform a greater amount of work during a fast movement, the series elasticity allows part of this work to be delivered to a limb at higher rates than the muscle alone would be capable of delivering it. It has been shown that during

explosive movements such as jumping certain animals can develop much greater power outputs than their muscles alone could generate (Aerts, 1998; Peplowski and Marsh, 1997; Bennett-Clark, 1975). This 'power amplification' appears to be brought about by mechanisms that enhance 'storage' of mechanical energy generated by the muscle in its series elasticity and quick 'recovery' of this stored elastic energy later on during the contraction. In this way during the later stages of a movement both the muscle and its series elasticity can deliver power to an external load thereby exceeding the delivery of power that the muscle alone could provide. In addition, fast release of energy from the tendon can further enhance this power delivery. Recently, Kurokawa *et al* (2001) using ultrasonography estimated the shortening velocity of fascicles in the gastrocnemius medialis muscle of human volunteers during squat jumps. They combined this information with other kinetic and kinematic data and showed (figure 4 in their paper) that the peak muscle-tendon complex output was greater than the peak fascicle power output (More details about the work by Kurokawa *et al* are given in later sections). However, there are no studies, to my knowledge, that have systematically investigated the extent to which the peak muscle power is amplified during a movement as a function of the load to the muscle-tendon complex.

2.4. Shortening deactivation

Isometric force at a given muscle length is reduced following a period of active shortening compared to the isometric force at the same muscle length if the isometric contraction is not preceded by active shortening. This 'shortening deactivation' phenomenon has been observed in single fibres (e.g. Edman *et al*,

1993) and in whole isolated muscles (e.g. Herzog *et al*, 2000). Shortening deactivation has also been observed *in vivo* during electrically-evoked (De Ruiter *et al*, 1998) and voluntary (Lee *et al*, 1999) contractions of human muscle. Recently Herzog *et al* (2000) varied the amount of mechanical work performed during shortening by cat soleus muscles prior to isometric force development at a given muscle length. The mechanical work was varied by either changing the amount of shortening keeping the force constant or by changing the force levels keeping the amount of shortening constant. In the latter case the force was varied either by changing the shortening speed between different contractions and within the same contraction, or by changing muscle activation between different contractions and within the same contraction. They found that 85% of the variation in isometric force depression could be explained in terms of the work performed in the preceding shortening contraction, independently of how the changes in the work output were brought about. These results by Herzog *et al* (2000) are in agreement with the notion of a stress-induced cross-bridge inhibition in the newly formed actin-myosin overlap zone during active shortening.

3. Passive elements associated with muscle

Passive elements, i.e. structures not utilising chemical energy in order to generate a particular mechanical output, are associated with muscles. Such passive elements can be distinguished into parallel and series elements.

3.1. Parallel passive elements

Parallel passive elements so far identified may include titin molecules found within each half sarcomere, the sarcolemma and the connective tissue sheaths surrounding each single muscle fibre (endomysium), fascicles (perimysium) and the whole muscle (epimysium). The mechanical properties of titin have recently been reviewed by Herzog (2000a). The connective tissue sheaths are thought to be primarily elastic and contribute to passive tension development when a fibre, fascicle or whole muscle is stretched beyond a certain length (for example see Edman, 1979). Most of the passive tension in a whole muscle must be associated with stretching the connective tissue sheaths of the muscle since resting tension in individual fibres increases by a very small amount as the fibres are stretched to relatively long lengths (Hill, 1970). The total force a muscle can produce under *in vivo* or *in vitro* conditions represents the algebraic sum of the active and the passive force. Therefore the passive force-length relationship must be taken into account when calculating the active force production by the muscle (for example see Morgan, 1977; Cook and McDonagh, 1996a).

3.2. Passive elements in series

Morphologically myofilaments, Z-disks, tendons and aponeurosis (i.e. intramuscular tendinous sheets) have been identified as passive elements connected in series with contractile apparatus. In addition, the contractile apparatus itself, the cross bridges, have elastic properties and their compliance makes up part of the total series compliance of the muscle-tendon complex. Because of this, although the cross bridges are 'active' elements, their elastic

properties are briefly discussed in this section. Originally, observations that muscle shortening or elongation is the result of sliding of the myofilaments with respect to each other and not due to changes in their lengths (Huxley and Hanson, 1954; Huxley and Niedergerke, 1954), led to the conclusion that myofilaments were inextensible. More recent evidence however suggests that this is not true and that myofilament compliance does make up a large part of the total sarcomere compliance (e.g. Linari *et al*, 1998; Herzog, 2000a). However, this compliance is usually assumed to be very small compared to the compliance of the tendon and its aponeurosis. For example, using the values from Linari *et al* (1988) obtained from by applying step length changes in isolated frog fibres contracting at the plateau of their force-length relation, the approximate compliance of the thin and thick filament and of the cross bridge was estimated to be ~2, ~1 and ~1 $nm \cdot \mu m^{-1} \cdot T_0^{-1}$ (units are normalised to half sarcomere length and to the maximal isometric force (T_0)). Adding all these values together makes up a total half sarcomere compliance of ~4 $nm \cdot \mu m^{-1} \cdot T_0^{-1}$. The optimal half sarcomere length for tension generation is approximately 1 μm in frog fibres, and therefore at that length under isometric conditions cross bridge and total sarcomere compliance would be ~1 and ~4 $nm \cdot T_0^{-1}$, respectively. Extrapolating this result to human sarcomeres, which have longer actin filaments than frog ones, predicts that the equivalent values would be approximately 30% larger (see Rassier *et al*, 1999) than those for frog half sarcomeres i.e. ~1.3 and ~5.2 $nm \cdot T_0^{-1}$ for the cross bridge and total half sarcomere compliance. The compliance of a tendinous structure would depend on its Young's modulus and dimensions. Taking the human tibialis anterior as an example (e.g. Maganaris and Paul, 1999), tendon strained at ~2.5% by its

muscle's maximal isometric force. For such a tendon, the compliance of 1.3 μm (i.e. length approximately equal to one thin filament) length of tendon would be 0.025·1.3 μm = 32.5 nm at its maximal isometric force. This compliance is more than twenty five times greater than that in the cross bridge and approximately six times greater than the total sarcomeric compliance. Of course the results of these calculations are very rough approximations and the ratios of sarcomeric to tendinous compliance may vary within the same and between different muscle-tendon complexes as a result of different contraction conditions (such as for example differences in filament overlap and activation levels) and also due to dimensional and structural differences. Interestingly, it has recently been shown using ultrasonography that when the human ankle joint is moved passively the tibialis anterior and gastrocnemious tendons take up more than 50% of the total MTC length change, even though the forces experienced by the MTC are low (Herbert *et al*, 2002).

The force (load)-extension tendon properties -or stress-strain properties, when force and extension are normalised for the tendon's cross sectional area and unloaded length respectively - have been investigated both *in vitro* (e.g. Rigby *et al*, 1959; Diamant *et al*, 1972; Ker, 1981; Ker *et al*, 1988) and *in vivo* (e.g. Maganaris and Paul, 1999; 2000a,b; Kubo *et al*, 2000). The load-extension behaviour of a tendon changes irreversibly at strains exceeding a certain limit (Rigby *et al*, 1959) which is approximately 4-5 % (see Herzog and Gáll, 1999) or when a tendon is subjected to prolonged static or repetitive cyclic loading (Wang and Kerr, 1995; Wang *et al*, 1995). At loads and strains lower than those corresponding to the tendons' elastic limits, tendons behave in a

reproducible manner. The tendon stiffness (or Young's modulus when the stiffness is normalised for the tendon cross sectional area and initial length) shows a gradual increase with tendon elongation at strains up to 2-4% (Rigby *et al*, 1959; Ker, 1981; Proske and Morgan, 1987). This region of the load-elongation curve is called the 'toe' region and has been associated with straightening of the waviness of the collagen that is observed when the tendon is slack (Rigby *et al*, 1959; Diamant *et al*, 1972). At even greater strains ranging from 2-3% up to 5-6% however, tendon stiffness remains almost constant (Rigby *et al*, 1959; Ker, 1981; Proske and Morgan, 1987). This region of the tendon load-elongation relationship is referred to as the linear region and it reflects the elastic properties of straightened collagen fibres.

The area under the load-elongation curve for a tendon represents the energy expended to stretch the tendon. When a tendon is allowed to recoil after elongation back to its original resting length, the force (stress) for a given value of elongation from its original length (strain) is less compared to when the tendon is being stretched. The energy recovered from the tendon, i.e. the area under the load-elongation curve during recoiling, is therefore less than the energy expended to stretch it (e.g. Ker, 1981; Lieber *et al*, 1991). However, the difference is very small and it has been estimated that 89-94% of the energy expended to stretch a tendon is recovered during recoiling (see Herzog and Gáll, 1999).

In the past, intramuscular tendon (or aponeurosis) has been incorporated in muscle models as being inextensible (e.g. Woittiez *et al*, 1984). However it is

now known that this is not the case and that aponeurosis have elastic properties (e.g. Lieber *et al*, 1991; Zuurbier *et al*, 1994; Kawakami and Lieber, 2000; Maganaris and Paul, 2000a,b). Interestingly, some studies have shown that aponeurosis undergoes a greater elongation compared to the tendon for the same level of force and therefore being more compliant than the tendon (Lieber *et al*, 1991;Maganaris and Paul, 2000a,b). Extension non-uniformities along the length of the aponeurosis under loading conditions have also been reported, indicating regional differences in aponeurosis compliance and/or non-uniform force distribution along its length (Zuurbier *et al*, 1994; Maganaris and Paul, 2000a,b).

Tendon structure appears to be highly adaptable depending on functional demands (Ker, 1999). Although mechanical tests on mammalian tendon properties have not revealed systematic differences between species or anatomical sites their dimensions can vary considerably depending on the function of the muscle-tendon complex (see Alexander and Ker, 1990). Ker *et al* (1988) measured the mass and length of mammalian muscles and tendons obtained from a wide range of species and from these measurements they estimated their cross sectional areas and the stress in the tendon while subjected to the maximal isometric force of the muscle. They found a wide continuum of stresses ranging between 2-105 MPa, having a skewed frequency distribution with the most commonly occurring value being approximately 13 MPa. This stress is very low compared to the maximal stress a tendon can withstand before it is ruptured (>100 MPa; see Ker, 1999). They suggested a theory according to which tendons are adapted so that the total mass of muscle

and tendon is minimised; they calculated the minimum of this sum to occur when the ratio of muscle-to-tendon cross sectional area is equal to 34. This ratio is found to vary widely but the value of 34 appears to be the most commonly encountered value (see Ker, 1999). This theory applies for muscle-tendon complexes doing positive work and tendons that do not act as energy-saving springs during locomotion. Tendon adaptability has been examined in relation to the function and location of the muscle-tendon complex (Alexander and Ker, 1990). Alexander and Ker (1990) classified muscle-tendon complexes in the limbs of a wide range of mammalian species into three main categories. Type I have long fascicles and relatively short tendons. The muscles have a large volume and are therefore capable of generating and absorbing/degrading large amounts of work. Such muscles are located in the proximal segments of limbs such that the moment of inertia of the limb does not increase as much as if they were located more distally. In addition this location is advantageous during explosive movements such as, for example, jumping where large moments around more proximal limb joints such as the hip have to be generated. Type II muscle-tendon complexes have tendons that are long relatively to the muscle fascicles and are also relatively thick. The long tendons allow muscles located more proximaly (thus keeping limb inertia relatively low) to act on remote joints located distally, such as for example the finger joints moved by muscles located in the forearm. Such muscle-tendon complexes are commonly involved in performance of precise movements. In order for muscle fascicle shortening to be precisely transmitted to the joint, the compliance of the tendon has to be low. As these tendons are long, they are also relatively thick to minimise compliance. Type III muscle-tendon

complexes have tendons that are very long relative to the muscle fascicles and also relatively thin so they become highly stressed. Type III muscle-tendon complexes are involved in locomotion and are designed so that metabolic cost of locomotion is kept relatively low. As locomotion involves stretch-shortening cycles, in the absence of series compliance the length changes would have to be taken up by muscles. In the absence of tendons, joint movements would have to be completely taken up by muscle fascicles length changes. If a compliant tendon is introduced between the muscle and the limb, joint movements are taken up by combined length changes of muscle and tendon and as a result smaller length changes would be required by the muscle fascicles. Alexander and Ker (1990) argue that if the increased metabolic energy expended by the muscle while doing work was assumed to be exactly balanced by the reduction in energy expended while absorbing work, so the energy spent during a stride would be proportional to the time integral of the force, a long and/or fast muscle would spend more metabolic energy than a short and slow one to maintain the same force output. Thus, the length changes of the tendon during locomtion reduces the metabolic cost by allowing for shorter and slower muscle fibres. Again, in order not to add unnecessarily to the inertia of the limb, the muscle is located more proximally than the tendon. The tendons are long, but since a relatively large compliance is required, the tendons are also slender. This results in these tendons becoming highly stressed and hence strained during locomotion. An example of such a muscle-tendon complex is the triceps surae acting as an ankle plantarflexor during running.

4. Summary and aims of this study

The contractile properties of muscle and the elastic properties of tendinous tissue associated with muscle have been studied using a variety of experimental approaches and a considerable amount of knowledge has been produced as a result. However, not much is known about how these contractile and elastic properties interact during active shortening of muscle-tendon complexes against inertial loads to produce the mechanical outputs observed during natural movements. This thesis is part of an investigation on the interaction between contractile, elastic and inertial properties during maximal shortening contractions of muscle-tendon complexes. The experimental work presented in subsequent sections has been performed on human muscle-tendon complexes shortening *in vivo*. The modelling work presented in the following section however, can be applicable to all species.

Modelling muscle-tendon complexes shortening against inertial loads

1. Summary

The theoretical mechanical behaviour of muscle-tendon complexes (MTCs) shortening against inertial loads was investigated. A muscle-tendon complex (MTC) is represented as a Hill model consisting of a contractile component (CC) and a series elastic component (SEC). In the simplest case considered in this section, the relationships between the force in the system and SEC extension, CC velocity and load acceleration are all linear. The instantaneous mechanical behaviour of the CC, SEC and of the load was obtained by numerical integration of a system of differential equations using mathematical software (Mathcad, version 7). Dimensional analysis shows that this behaviour can be predicted by only one dimensionless constant, representing the magnitude of the normalised inertial load. It was also found that the inertial properties of the load, over a wide range of loads, operate as a 'catch' mechanism to amplify the power delivered to the load compared to the maximal power the CC alone could generate. Power amplification by this mechanism has a maximum when the inertial load is approximately equal to one normalised units and it is 1.436 (3 decimal places) times the CC power maximum. Introduction in the model of non-linear CC and SEC properties, and of a gravitational force produces deviations from the original theoretical behaviour. Additional dimensionless constants equal in number to the number of additional degrees of freedom, are required in order to describe the new behaviour. Under the assumptions made in the models presented in this work power amplification never exceeded two times the maximal muscle power.

2. Introduction

A mathematical model is an attempt to represent a real-life phenomenon using mathematics. As with other areas of science, mathematical models have been proposed to improve the understanding and/or make predictions of the mechanical performance of muscle (e.g. Hill, 1938; Huxley, 1957) or of the musculo-skeletal system (e.g. Bobbert and van Soest, 2001).

A muscle-tendon complex can be conveniently represented as a Hill model (Hill, 1938) consisting, in its simplest form, by a contractile component (CC) and a series elastic component (SEC). The advantages and disadvantages of Hill type models have been reviewed (Winters, 1990; Epstein and Herzog, 1998). Most loads overcome by MTCs during maximal concentric contractions performed *in vivo* have an inertial component. Thus, the simplest model for such movements could be a MTC shortening against a purely inertial load.

Although Hill type models shortening against inertial loads have frequently been incorporated in biomechanical studies that model particular tasks, such as jumping (e.g. Bobbert et al, 1986a, b; Hof, 1990), not many studies have attempted to systematically investigate their mechanical behaviour. In such complex models this behaviour is usually obscured by the presence of various additional factors that contribute to the performance of the particular task.

Caldwell (1995) used a Hill model for MTCs shortening against an inertial load in order to investigate the effects of relative muscle fibre-to-tendon length and of tendon elasticity on the mechanical behaviour of the system. Three particular

cases with different fibre-to-tendon length ratio and maximal tendon extensibility range were simulated, while the CC properties and the mass (inertia) of the load remained constant. Each of the three simulated MTCs fell into a different functional category according to a MTC classification proposed by Alexander and Ker in 1990 (see General introduction).

However, a vast range of muscle-tendon-inertial load (MTI) systems occur in nature. Some of the differences are due to differences in size. For example, the smallest MTC in a flea acts on a tiny mass (part of the flea's body) whilst the largest MTC in an elephant acts on a mass many million times larger than that of the flea's body. Some differences are also due to differences in the composition of the components of systems. The slowest muscle of a tortoise compared to the fastest muscle in a mouse or someone trying to accelerate a plastic dumbbell compared to a steel one of the same volume, can serve as examples. Even if the number of parameters used to describe the behaviour of MTI systems is kept relatively low, the wide range of values for each of these parameters would require a vast number of simulations in order to model such a diversity.

This part of the thesis uses simplified MTI system models in order to answer the following questions:

1. Are there any fundamental principles underlying the mechanical behaviour of all MTI systems? If there are, what are they?
2. Can the behaviour of such a wide diversity of MTI systems be generalised and therefore predicted on the basis of these principles or are particular solutions the only option?

At the present time, there are no models that have systematically investigated the mechanical behaviour of MTI systems attempting to answer these questions. The present investigation begins considering the simplest case of linear mechanical properties and linear motion for all the components of the MTI system. The effect of non-linear mechanical properties while motion of all components is linear is considered next. Rotational motion of the load in the absence or presence of a gravitational field are considered last.

3. Formulation of the model

A MTC is represented as a Hill model (Hill, 1938) consisting of a contractile component (CC) and an undamped elastic component connected in series with the CC (SEC). In our work the other end of the SEC is either attached directly to an inertial load (L) or indirectly via a lever system, as shown in figures 2.1 and 2.3 respectively. A gravitational force may also act upon the mass of L (figure 2.4). This section attempts to model the mechanical behaviour of such muscle-tendon-inertia (MTI) systems, starting with the simplest case of direct attachment of the SEC onto L in the absence of gravity and introducing, in a gradual manner, the complexities associated with rotational motion of L and with the presence of a gravitational field.

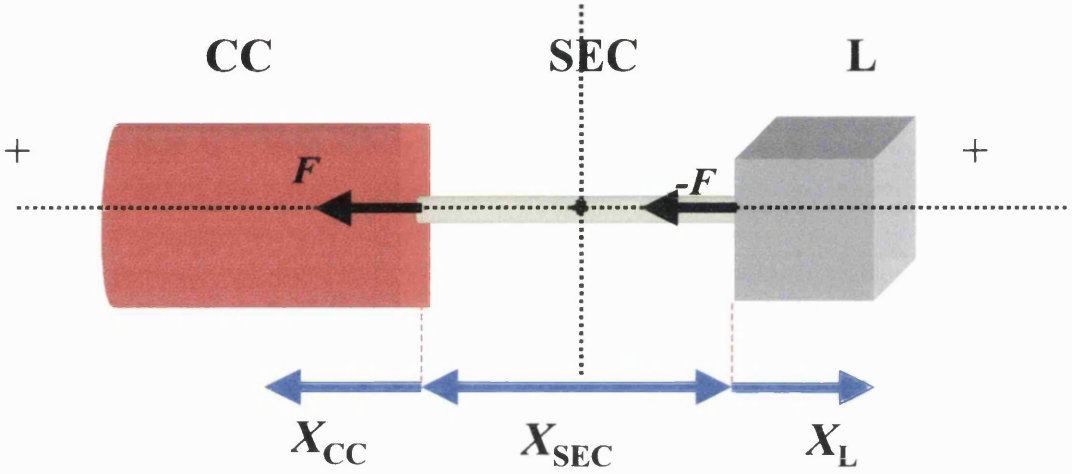

Figure 2.1. Hill model of a muscle-tendon complex consisting of a contractile component (CC) whose right-hand end is connected to one end of a series elastic component (SEC). The other end of the SEC is connected directly onto a mass (L). L has inertia. According to the sign convention in this work, the sense of a vector is positive when it is directed away from the centre of the SEC. Blue arrows show movement of the components with positive sense. Black arrows show how force generated by the CC acts on the nodes of this system.

3.1. MTI system with linear motion

3.1.1. Mechanical implications of series connection

The components of this system, namely CC, SEC and L, are connected in series with respect to one another (Figure 2.1). The sign convention is that movements away from the centre and forces tending to cause such movements are positive. In such a system, the instantaneous magnitude of force (F) is the same in all components (equation (2.1)):

$$F_{CC} = -F_{SEC} = -F_L = F \qquad (2.1)$$

Movements (X) of the individual components however add up (equation 2.2; note the sign convention):

$$X_{SEC} - X_{CC} - X_L = 0 \qquad (2.2)$$

Equations (2.1) and (2.2) describe mathematically the consequences, in terms of mechanics, of the series connection between the three components. Notice that equation (2.1) only contains forces and equation (2.2) only contains movements. However, the relationship between force and movement (or derivatives of movement with respect to time) within each component is unique and different from that of the other two components (see figure 2.1). Modelling the instantaneous mechanical behaviour of the system during a contraction therefore requires that the mechanical behaviour of each component is defined.

3.1.2. Linear equations

3.1.2.1. SEC force-extension relationship

This model assumes a positive linear relationship between SEC extension, X_{SEC}, and the force, F, required to produce that extension. The slack length of the SEC in this model is zero. In addition, at SEC lengths shorter than the resting length, force does not develop. These two conditions are represented mathematically in equation (2.3):

$$\begin{aligned} F &= K \cdot X_{SEC} \qquad \textit{if} \quad X_{SEC} \geq 0 \\ F &= 0 \qquad\qquad\quad \textit{otherwise} \end{aligned} \tag{2.3}$$

K is a constant, representing the slope of the SEC force extension relationship. Figure 2.2 illustrates this relationship graphically.

3.1.2.2. CC force-velocity relationship

The relationship between force and velocity of CC shortening is negative, i.e. shortening velocity drops with force and *vice versa* (Fenn and Marsh, 1935; Hill, 1938). Let us assume for simplicity, that this is also a linear relationship with a Y- and an X-intercept equal to $V_{CC_{\max}}$ and $F_{\max}$, respectively. $V_{CC_{\max}}$ is the maximal shortening velocity that the CC can achieve and $F_{\max}$ is its maximal isometric force. This relationship, for the purposes of this work, is restricted to muscle forces with a positive sense along the direction of shortening, whose magnitude ranges between 0 and $F_{\max}$ and can be represented mathematically in equation (2.4):

$$\frac{d}{dT}(X_{CC}) = V_{CC_{max}} - \frac{V_{CC_{max}}}{F_{max}} \cdot F$$
$$= V_{CC_{max}} \cdot \left(1 - \frac{F}{F_{max}}\right) \qquad (2.4)$$

$\frac{d}{dT}(X_{CC})$ in this work is the rate of CC shortening with respect to time, T, or the CC shortening velocity. Notice that the slope of this line is $-\frac{V_{CC_{max}}}{F_{max}}$. This relationship is displayed graphically in figure 2.2.

3.1.2.3. L force-acceleration relationship

The relationship between the motion of a mass and the force applied on it, is described by Newton's second law (equation (2.5)):

$$\frac{d^2}{dT^2}(X_L) = \frac{F}{M} \qquad (2.5)$$

In this equation $\frac{d^2}{dT^2}(X_L)$ is the second derivative of the displacement of L with respect to time (or the acceleration of L). M is the mass of L, a quantitative measure of its inertia. Notice that this is also an equation for a straight line passing through a zero origin, with a positive slope equal to $\frac{1}{M}$. This relationship is illustrated graphically in figure 2.2.

Inspection of equations (2.3)-(2.5) reveals that in order to determine the relationship between force and movement in all three components of a particular

system, the values of four constants (or parameters), namely K, F_{max}, V_{max} and M, must be specified.

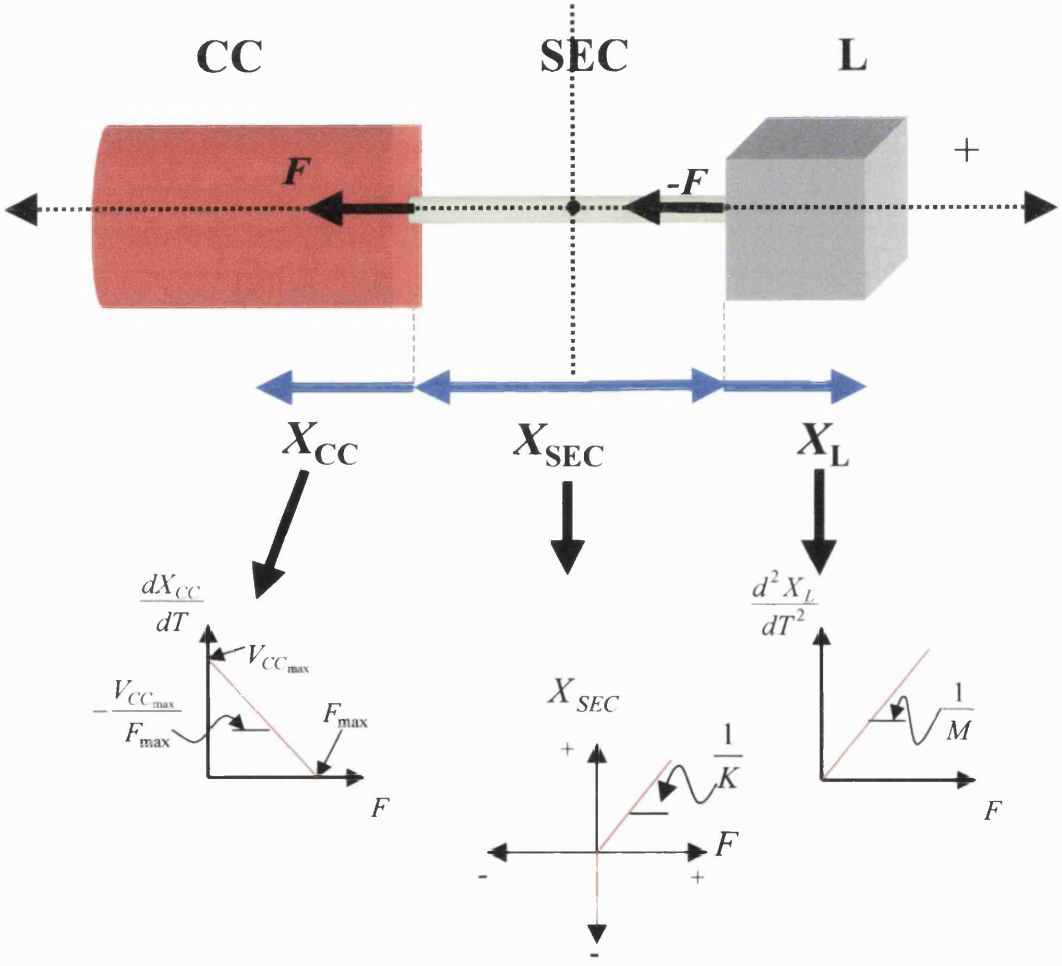

Figure 2.2. Linear relationship between force and movement (or time derivatives of movement) for the CC, SEC and L. Notice how in this simplest form of the model all relationships between force and movement or time derivatives of movement are linear.

3.1.3. Non-linear properties

3.1.3.1. Hyperbolic SEC force-extension relationship

The non-linear force-extension properties of 'passive' elastic tissues in series with the muscle have been commonly modelled using second order polynomial equations (e.g. Kurokawa *et al*, 2001; deGraaf et al, 1987; Bobbert *et al*, 1986) and sometimes 'hybrid' curves with two parts, a non-linear and a linear part (see Winters, 1990). A simplified way of describing the SEC force-extension curve using only one dimensionless shape constant (C) and the force-extension co-ordinates of a single point from the force-extension curve has been suggested by Winters (1990):

$$F_{SEC} = \left(\frac{F_1}{e^C - 1}\right) \cdot \left(e^{\frac{C}{X_{SEC_1}} \cdot X_{SEC}} - 1\right)$$

where F_1 and X_{SEC1} are the co-ordinates of any point on the plot (conveniently F_{max} and X_{SECmax}, respectively). Although this equation uses only the dimensionless constant C to set the shape, C must be different to zero (i.e. there is a discontinuity of the resulting relationship when C=0). In this thesis an alternative way of modelling the SEC force-extension properties is suggested.

The force-extension properties for any given SEC can be expressed in terms of a part of a rectangular hyperbola such that:

$$F = \frac{X_{SEC} \cdot F_{\max}}{\left[1 + H \cdot \left(1 - \frac{X_{SEC}}{X_{SEC\max}}\right)\right] \cdot X_{SEC\max}} \quad if \quad X_{SEC} \geq 0 \tag{2.6}$$

$$F = 0 \quad if \quad X_{SEC} < 0$$

H is a constant controlling the curvature of the force-extension relationship. (For derivation of this equation see appendix 1: Derivation of hyperbolic SEC force-extension equation).

In this thesis H can only be positive or zero as the shape of the relationship for negative values of H would not be compatible with the experimentally observed SEC properties. When H is positive the curvature decreases as H decreases and when H is equal to zero, the force extension relationship becomes linear.

The relationship between this equation when H is zero and the linear equation (equation (2.3)) can be demonstrated as follows:

When H=0,

$$F = \frac{X_{SEC} \cdot F_{\max}}{\left[1 + H \cdot \left(1 - \frac{X_{SEC}}{X_{SEC\max}}\right)\right] \cdot X_{SEC\max}}$$

$$= \frac{X_{SEC}}{X_{SEC\max}} \cdot F_{\max}$$

After rearranging equation (2.3) and solving for K:

$$K = \frac{F}{X_{SEC}}$$

$$= \frac{F_{\max}}{X_{SEC\max}}$$

Therefore the force when H=0, can be expressed as:

$$F = K \cdot X_{SEC}$$

which is the same as equation (2.3).

It is convenient to associate the value of H=0 with no curvature in the SEC force-extension relationship, i.e. with a linear relationship, and with the curvature increasing as the value of H increases. Thus, equation (6) provides a convenient way of expressing the SEC force-extension properties.

3.1.3.2. Hyperbolic CC force-velocity relationship

The most commonly used CC force-velocity relationship is that described by Hill in 1938, which can be expressed in the following convenient form:

$$\frac{d}{dT}(X_{CC}) = V_{CC_{\max}} \cdot \frac{1 - \frac{F}{F_{\max}}}{1 + \frac{F}{F_{\max}} \cdot G} \qquad (2.7)$$

where G is a constant. For derivation see Woledge *et al*, 1985, pp. 49 (appendix 2).

When the value of G is set to zero to remove any curvature from the relationship equation (2.7) becomes:

$$\frac{d}{dT}(X_{CC}) = V_{CC_{\max}} \cdot \left(1 - \frac{F}{F_{\max}}\right)$$

which is identical to equation (2.4) describing a linear force-velocity relationship.

3.1.3.3. CC with an exponential activation time-course

In order to account for the finite amount of time during which cross-bridge activation within the CC rises after the onset of stimulation, an activation parameter (A) was incorporated on equation (2.8):

$$\frac{d}{dT}(X_{CC}) = A \cdot V_{CC_{\max}} \cdot \frac{1 - \frac{F}{F_{\max}}}{1 + \frac{F}{F_{\max}} \cdot G} \qquad (2.8)$$

The activation parameter, A, takes values that range from zero to one and is defined as:

$$\begin{aligned} A &= 1 - e^{-\frac{T}{TC}} \quad if \quad TC > 0 \\ A &= 1 \qquad\qquad if \quad TC = 0 \end{aligned} \qquad (2.9)$$

Thus, if the time constant, TC, is greater than zero A rises from zero to one with an exponential time course as shown on the top line of equation (2.9). If activation were instantaneous the time constant would be zero, but that would not make sense mathematically as the exponent of e on equation (2.9) would have to have zero as denominator. For that purpose, the second line of equation (2.9) specifies that A has

its peak value, which is one, throughout the contraction. As muscle relaxation mechanics is not studied in this work a declining activation time-course is not defined.

It must be noted that in order to describe the non-linear properties of the components of a MTI system in this model the number of the values of constants (or parameters) that must be specified has increased from four (in the previous model with linear relationships) to seven, namely $X_{SEC\max}, H, F_{\max}, V_{CC_{\max}}, G, TC$ and M.

3.2. Rotational motion load

Imagine a muscle-tendon complex acting on an inertial load via a rigid lever system connected to a pulley as shown in figure 2.3. The following assumptions are made for simplicity:

1. The lever system and the string are of negligible mass or the contribution of their mass to the inertia experienced by the muscle-tendon complex has been included in the value of the moment of inertia of L.
2. The short and long lever arm lengths do not change during the contraction
3. The muscle-tendon complex always 'pulls' at right angles relative to the lever system.
4. The string is so thin that wrapping it around the pulley does not alter the length of the lever through which it acts on the pulley.

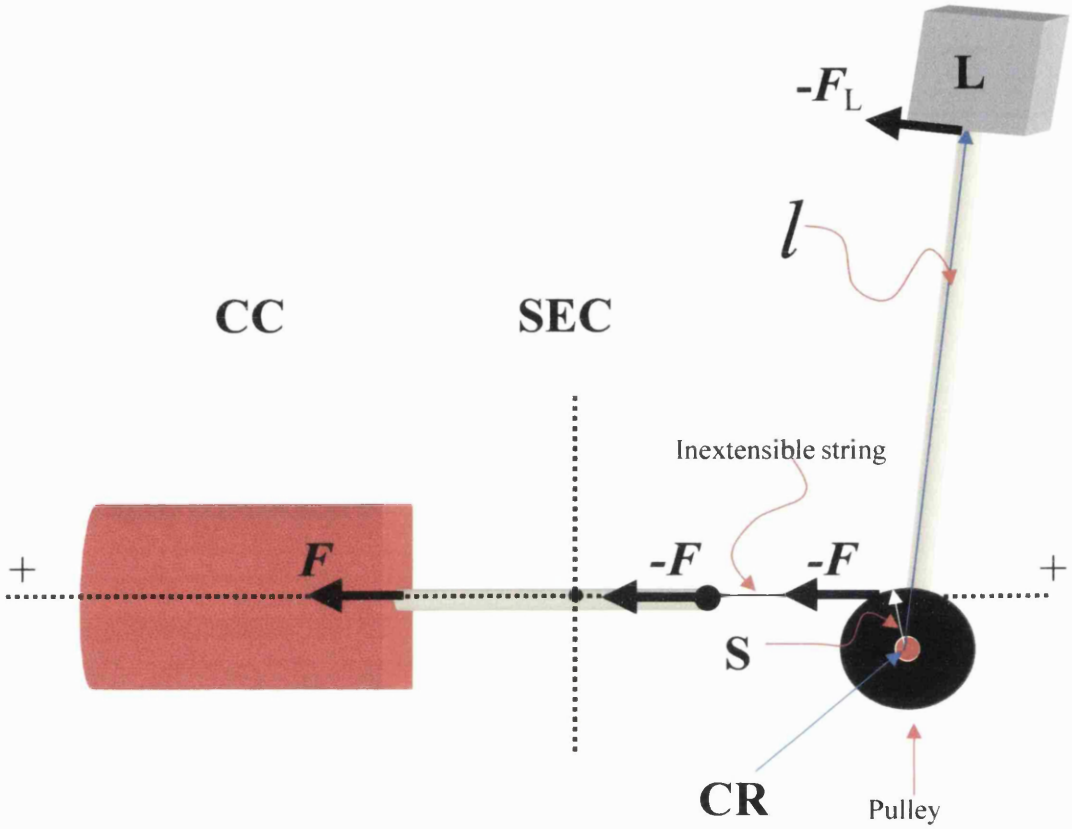

Figure 2.3. Model of MTC with rotational motion load. A muscle-tendon complex represented as a Hill model, acting on a mass, L, via a lever system connected to a pulley. In this model one end of the SEC is connected to the CC and the other to an inextensible string that is wrapped around a pulley, at distance *S* from the centre of rotation of the pulley (CR). Movement of the pulley is constrained so that only rotation around the CR is possible. L is connected to the CR of the pulley via a lever. The distance between L and CR is *l*. As a result of this connection, forces developed by the CC always act tangentially to the movement trajectory of L. Movements and forces here have a positive sense when they are directed away from the centre of the SEC. The black arrows represent how the force generated by the CC acts on the nodes of the system. Torque is positive when it tends to rotate L in an anticlockwise sense.

3.2.1. Mechanical implications of series connection in the rotational load system

Equation (2.1) shows how the forces in the nodes of the system are related. Equation (2.1) has been adapted for the model presented in this section (figure 2.3) (equation (2.10)):

$$F_{CC} = F_{SEC} = -F_{Str} = -F_{Pul} = -F_L \cdot \frac{l}{S} = F \qquad (2.10)$$

Notice that the magnitude of the instantaneous force at all nodes, except the one between the lever and the load, is the same. This is because the force experienced by the load acts at a different distance from the centre of rotation of the lever system compared to the force experienced by all other components. The force acting on the load however is at a constant proportion to the force in the other nodes of the system. This constant proportion depends on the ratio of the two levers in the system, S and l and it is equal to $\frac{S}{l}$. The reciprocal of this ratio (i.e. $\frac{l}{S}$) is called the lever ratio, LR. The force experienced by L is the same as anywhere else in the system only when $l = S$.

As each of these forces is assumed in this model to have a perpendicular direction with respect to the lever, equation (2.10) can be multiplied by S to express these forces in rotational terms:

$$S \cdot F_{CC} = S \cdot F_{SEC} = -S \cdot F_{Str} = -S \cdot F_{Pul} = -F_L \cdot l = S \cdot F \qquad (2.11)$$

Using Tq as a symbol for torque, i.e. the rotational effect of a force on an object when this force is acting at a distance from the centre of rotation of that object, equation (2.11) can be written in an equivalent form (equation (2.12)):

$$Tq_{CC} = Tq_{SEC} = Tq_{Str} = Tq_{Pul} = Tq_L = Tq \qquad (2.12)$$

The sign convention for the torque used in this model is that torque tending to cause anticlockwise rotation of L is positive.

The relationship between the movements of the components can also be described in rotational terms by dividing the linear movement at the nodes of the system with S:

$$\frac{X_{SEC} - X_{CC} - X_L \cdot \frac{S}{l}}{S} = \Theta_{SEC} - \Theta_{CC} - \Theta_L = 0 \quad (2.13)$$

where Θ is displacement expressed in angular terms. The term X_{Str} has been omitted since the string that is wrapped around the pulley is assumed to be inextensible. Thus both X_{Str} and Θ_{Str} are equal to zero.

3.2.2. Expressing the properties of the SEC, CC and L for rotational motion load

3.2.2.1. SEC torque-angular extension relationship

The SEC force-extension properties, for SEC lengths greater than the initial slack SEC length (top line; equation (2.6)), can be converted into rotational terms as follows.

Both sides of equation (2.6) are multiplied by S:

$$S \cdot F = S \cdot \frac{X_{SEC} \cdot F_{max}}{\left[1 + H \cdot \left(1 - \frac{X_{SEC}}{X_{SECmax}}\right)\right] \cdot X_{SECmax}}$$

This expression can be written as:

$$Tq = \frac{\frac{X_{SEC}}{X_{SECmax}} \cdot Tq_{max}}{\left[1 + H \cdot \left(1 - \frac{X_{SEC}}{X_{SECmax}}\right)\right]}$$

where Tq_{max} is the maximal torque around the centre of rotation of the lever system that can be generated by any given MTC. This amount of torque is of course achieved when the CC develops maximal isometric force, F_{max}. Not all terms in this equation however are in rotational form. As the relationship between rotation and angle is:

$$X = S \cdot \Theta$$

the above equation can be written in an equivalent form as:

$$Tq = \frac{\frac{S \cdot \Theta_{SEC}}{S \cdot \Theta_{SECmax}} \cdot Tq_{max}}{\left[1 + H \cdot \left(1 - \frac{S \cdot \Theta_{SEC}}{S \cdot \Theta_{SECmax}}\right)\right]}$$

which can be re-written in the form:

$$Tq = \frac{\Theta_{SEC} \cdot Tq_{\max}}{\left[1 + H \cdot \left(1 - \frac{\Theta_{SEC}}{\Theta_{SEC\max}}\right)\right] \cdot \Theta_{SEC\max}} \qquad (2.14)$$

This equation is of course restricted to positive angular extensions of the SEC. When $\Theta_{SEC} < 0$, $Tq = 0$.

3.2.2.2. CC torque-angular velocity relationship

The force-velocity properties of the CC can also be expressed in rotational terms as a torque-angular velocity relationship due to CC shortening, if the appropriate lever lengths are used to divide displacements and multiply forces. The CC acts at a perpendicular distance S from the CR. Therefore equation (2.7) could be written as:

$$\frac{d}{dT}(\Theta_{CC}) = \frac{1}{S} \cdot V_{CC_{\max}} \cdot \frac{1 - \frac{F}{F_{\max}}}{1 + \frac{F}{F_{\max}} \cdot G}$$

$$= \Omega_{CC_{\max}} \cdot \frac{1 - \frac{F}{F_{\max}}}{1 + \frac{F}{F_{\max}} \cdot G}$$

In this last expression $\Omega_{CC_{max}}$ is the maximal rotational velocity of the lever that the CC alone could produce. This rotational velocity due to the sole action of the CC on the lever can be attained while the CC shortens at its maximal velocity, $V_{CC_{max}}$. Notice however that not all terms in this expression are in rotational form as force is still used instead of torque. Force in equation (2.7) is expressed as a fraction of the maximal isometric force and therefore each of the forces in this fraction can be multiplied by S without altering the result:

$$\frac{d}{dT}(\Theta_{CC}) = \Theta_{CC_{max}} \cdot \frac{1 - \dfrac{S \cdot F}{S \cdot F_{max}}}{1 + \dfrac{S \cdot F}{S \cdot F_{max}} \cdot G}$$

As the relationship between force and torque is of the form $Tq = S \cdot F$ and the expression can therefore be written as:

$$\frac{d}{dT}(\Theta_{CC}) = \Omega_{CC_{max}} \cdot \frac{1 - \dfrac{Tq}{Tq_{max}}}{1 + \dfrac{Tq}{Tq_{max}} \cdot G} \qquad (2.15)$$

CC activation is not assumed to be affected by the presence of the lever system and will therefore not be discussed any further in this section.

3.2.2.3. L torque-angular acceleration relationship

As L is at distance l from the CR the second derivative of its angular displacement, i.e. the angular acceleration of the load, is

$$\frac{d^2}{dT^2}(\Theta_L)=\frac{1}{l}\cdot\frac{F}{M}$$

The tangential force experienced by L is equal to the torque experienced around the centre of rotation of the lever system divided by l:

$$F=-F_L=\frac{Tq}{l}$$

and also:

$$\frac{X_L}{l}=\Theta_L$$

The last two expressions can be substituted into the previous one to obtain:

$$\frac{d^2}{dT^2}(\Theta_L)=\frac{1}{l}\cdot\frac{\left(\frac{Tq}{l}\right)}{M}$$

$$=\frac{1}{l^2}\cdot\frac{Tq}{M}$$

which can be re-written as:

$$\frac{d^2}{dT^2}(\Theta_L)=\frac{Tq}{MI} \qquad (2.16)$$

where $MI = M\cdot l^2$ and it is the moment of inertia due to the mass of L at distance l from the centre of rotation.

Thus, this system can be described by a set of equations identical in form to those used for the system with linear motion of L. The only difference is the inclusion of the short, S and long, l, lever arms. It must be mentioned that the number of constants (parameters) that must be specified in this model in order to describe the properties of a particular system is seven, namely $\Theta_{SEC\max}, H, Tq_{\max}, \Omega_{CC_{\max}}, G, TC$ and MI. This is the same number of constants as for the equivalent model with linear motion of the load. Table 2.1 shows the relationship between the linear and rotational terms used in the model.

Linear	Rotational	Linear to rotational conversion
M	MI	$M \cdot l^2$
X	Θ	$\frac{X}{S}$ or $\frac{X}{l}$
F	Tq	$S \cdot F$ or $l \cdot F$

Table 2.1. Relationship between linear and rotational quantities. Three quantities (mass, length and force) from the linear model (column 1) expressed in rotational terms (moment of inertia, angle and torque; column 2). Column 3 shows how a rotational quantity was obtained from the corresponding linear quantity. The force and movement at the CC and SEC can be expressed in rotational terms using S as the lever arm, whereas the mass of L, its movement and the force it experiences must use l as the lever arm.

3.3. Rotational motion under the influence of gravity

Figure 2.4 shows a constant gravitational force F_G acting on L tangentially to its movement, opposing the force F_L that L experiences due to the shortening contraction of the CC. This model will only be applicable to small movements which do not take the lever significantly away from an orientation which is orthogonal to the gravitational field.

The gravitational force is proportional to the mass of L:

$$F_G = M \cdot g \qquad (2.17)$$

where g is the proportionality constant with units of acceleration.

The same assumptions are made in this model as in the model with rotational motion of the load in the absence of a gravitational force (assumptions 1-4, pp 99).

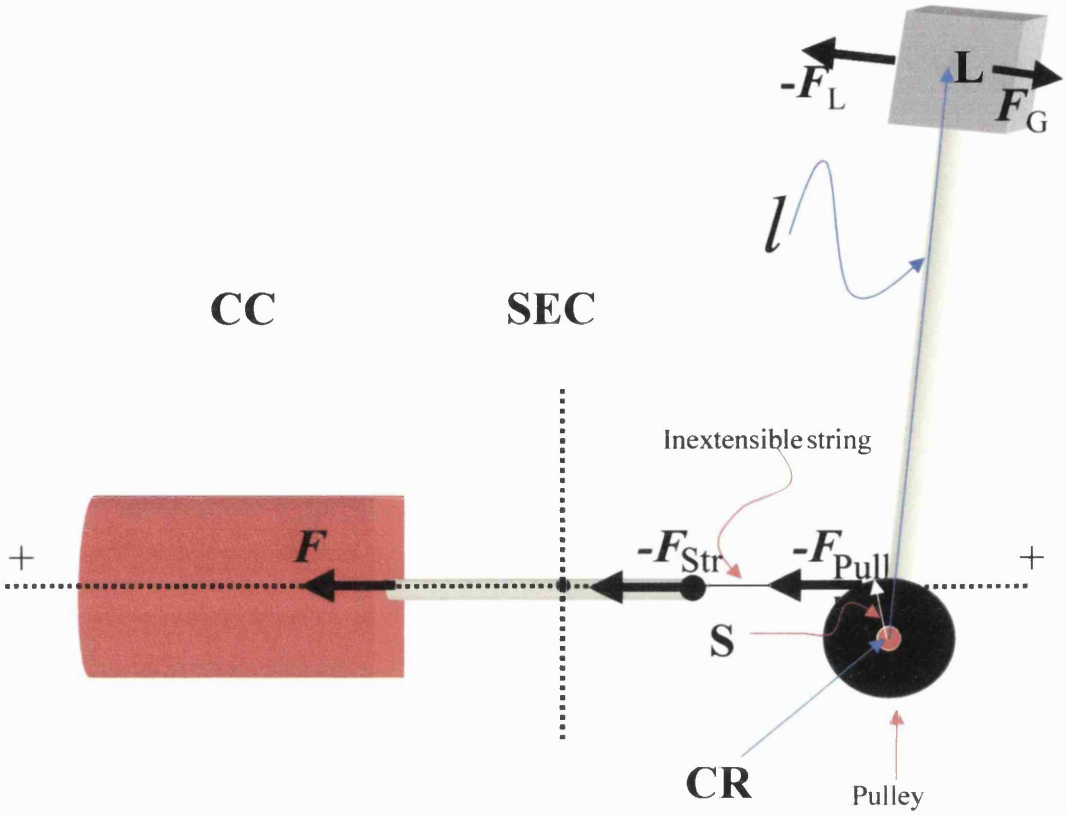

Figure 2.4. Model of a MTC shortening against inertia and gravity. A muscle-tendon complex represented as a Hill model, acting on a mass, L, via a lever system connected to a pulley. A gravitational force F_g, whose direction is tangential to the motion of L also acts upon L. In this model one end of the SEC is connected to the CC and the other to an inextensible string that is wrapped around a pulley, at distance S from the centre of rotation of the pulley (CR). Movement of the pulley is constrained so that only rotation around the CR is possible. L is connected to the CR of the pulley via a lever system. The distance between L and CR is l. As a result of this connection, forces developed by the CC always act perpendicularly on L. Movements and forces here have a positive sense when they are directed away from the centre of the SEC. The black arrows represent how the force generated by the CC and gravity act on the nodes of the system.

3.3.1. Implications of the series connection between the components

In this model, the torque around CR reflects the net torque, i.e. the algebraic sum of the torque due to the shortening contraction of the CC and the torque due to the gravitational force acting on the mass of L:

$$Tq = Tq_{CC} - Tq_G = Tq_{SEC} - Tq_G \qquad (2.18)$$

The negative sign of the torque due to gravity in equation (2.18) is because it tends to cause clockwise acceleration of the load around the CR.

The rotations in the system are related in exactly the same way as shown by equation (2.13) (also shown below):

$$\Theta_{SEC} - \Theta_{CC} - \Theta_L = 0$$

3.3.2. SEC, CC and L properties for rotational load motion under the influence of gravity

The expressions describing the properties of the components of the MTI system are modified in this section to include the effect of the torque due to gravity.

3.3.2.1. Torque and SEC properties

The SEC torque-angular extension relation as described by equation (2.14):

$$Tq_{SEC} = \frac{\Theta_{SEC} \cdot Tq_{\max}}{\left[1 + H \cdot \left(1 - \frac{\Theta_{SEC}}{\Theta_{SEC\max}}\right)\right] \cdot \Theta_{SEC\max}}$$

As $Tq = Tq_{SEC} - Tq_G$ equation (2.18) can be re-written in the form:

$$Tq = \frac{\Theta_{SEC} \cdot Tq_{\max}}{\left[1 + H \cdot \left(1 - \frac{\Theta_{SEC}}{\Theta_{SEC\max}}\right)\right] \cdot \Theta_{SEC\max}} - Tq_G \qquad (2.19)$$

This equation relates the SEC torque-angular extension properties to the torque around the CR.

3.3.2.2. CC torque-angular velocity relationship

The CC torque-angular velocity relationship can be re-written to account for the torque due to gravity following a similar argument as in the case of the SEC torque-angular extension relationship. In equation (2.15) the angular velocity of L that is due to CC shortening is expressed as function of the torque around the CR that is due to the force that the CC generates. In this model however there is an additional force generator, gravity, and equation (2.15) must be re-written in a way that allows distinction between the two components of the torque, that due to the CC and that due to gravity:

$$\frac{d}{dT}(\Theta_{CC}) = \Omega_{CC_{\max}} \cdot \frac{1 - \frac{Tq_{CC}}{Tq_{\max}}}{1 + \frac{Tq_{CC}}{Tq_{\max}} \cdot G}$$

This expression shows that the rotational velocity of L due to CC shortening, depends on the torque that the CC generates (as well as on $\Theta_{CC_{max}}, Tq_{max}$ and G). It would be desired for the purposes of this work to express this velocity relative to the torque around the CR . From equation (2.18):

$$Tq_{CC} = Tq + Tq_G$$

This can be substituted into the above torque-angular velocity expression to obtain:

$$\frac{d\Theta_{CC}}{dT} = \Omega_{CC_{max}} \cdot \frac{1 - \frac{Tq + Tq_G}{Tq_{max}}}{1 + \frac{Tq + Tq_G}{Tq_{max}} \cdot G} \qquad (2.20)$$

3.3.2.3. L torque-angular acceleration relationship

The angular acceleration of the load is given by Newton's second law as the net torque experienced by the load divided by its moment of inertia (equation (2.16)). The net torque experienced by the load is of course the difference of the torque due to activation of the muscle-tendon complex and the torque due to gravity (equation (2.18)). However, a restriction is set so that there is no negative angular acceleration of L (i.e. clockwise around the CR) leading to extension of the muscle-tendon complex at early times during a simulated contraction while the magnitude of the torque due to CC shortening is smaller than the magnitude of the torque due to gravity. This restriction introduces a 'support' for L while L is at its initial position. Equation (2.21) includes this restriction:

$$\frac{d^2}{dT^2}(\Theta_L) = \frac{Tq}{MI} \quad if \quad Tq \geq 0 \quad and \quad X_L > 0$$
$$= 0 \quad otherwise \qquad (2.21)$$

In this model the values of eight constants, namely $Tq_{\max}, \Theta_{SEC_{\max}}, H, Tq_G, \Omega_{CC_{\max}}, G, TC$ and MI, determine the behaviour of a particular system. Therefore inclusion of gravity has introduced one more constant (Tq_G) than when gravity is absent.

As already mentioned in the introduction of this modelling section, the values of these parameters can exhibit an enormously wide variation when comparing different muscle-tendon-load complexes that exist in nature. Investigating the mechanical behaviour of muscle-tendon-inertia systems over a wide enough range to cover the versatility that is observed in nature, an enormous number of simulations would be required. For example, if it were to combine ten values of each of the four parameters of the first model with ten values of each of the other parameters, ten thousand simulations would be required. As one of the goals of this part of work is to investigate whether there are any fundamental principles governing the general mechanical behaviour of muscle-tendon-inertia systems, the large number of combinations might complicate the analysis thereby obscuring the presence of such principles. In order to reduce the number of combinations, dimensional analysis was used and the above equations were normalised as shown in the following section.

4. Dimensional analysis of the MTI models

4.1. Normalising the system with linear motion load

4.1.1. Derivation of normalising factors

In order to remove the effects of dimensions from the mechanical behaviour of the system, appropriate normalising factors were derived from combinations of the four constants, $F_{max}, V_{CC_{max}}, M$ and K. The relationship between dimensioned quantities, dimensionless quantities and normalising factors is:

$$(\text{Dimensionless quantity}) = \frac{(\text{Dimensioned quantity})}{(\text{Normalising factor})}$$

Thus, a dimensionless quantity can be obtained as the ratio of a dimensioned quantity and a normalising factor. The symbols for dimensioned and dimensionless quantities and normalising factors are shown in table 2.2. There are several ways of deriving the normalising factors. A comprehensive way of doing this is as shown below.

Because these models contain only quantities that have dimensions of M (mass), X (length) and T (time), three normalising factors must be chosen. All other required normalising factors can then be derived. The first three described below are the chosen factors in this work.

The constant of choice in this work as a velocity normalising factor is the maximal velocity for CC shortening, such that:

$$v = V_{CC_{\max}} \qquad (2.22)$$

Unit	Dimensioned quantity	Normalising factor	Dimensionless quantity
Mass	$\boldsymbol{M}$	$\boldsymbol{m}$	Ξ
Distance	$\boldsymbol{X}$	$\boldsymbol{x}$	χ
Time	$\boldsymbol{T}$	$\boldsymbol{t}$	τ
Force	$\boldsymbol{F}$	$\boldsymbol{f}$	ϕ
Stiffness	$\boldsymbol{K}$	$\boldsymbol{k}$	κ
Velocity	$\boldsymbol{V}$ **or** $\frac{d}{dT}(X)$	$\boldsymbol{v}$	υ **or** $\frac{d}{d\tau}(\chi)$
Energy	$\boldsymbol{E}$	$\boldsymbol{e}$	ε
Power	$\boldsymbol{P}$	$\boldsymbol{p}$	ρ

Table 2.2. Units and corresponding (dimensioned and dimensionless) quantities and normalising factors.

The constant of choice in this work for normalising force is the maximal isometric force of the CC such that:

$$f = F_{\max} \qquad (2.23)$$

The stiffness normalising factor is the stiffness of the SEC:

$$k = K \quad (2.24)$$

A length normalising factor is obtained by dividing the force normalising factor by the stiffness normalising factor, such that:

$$\begin{aligned} x &= \frac{f}{k} \\ &= \frac{F_{\max}}{K} \\ &= X_{SEC_{\max}} \end{aligned} \quad (2.25)$$

$X_{SEC_{\max}}$ is the maximal extension that the SEC can undergo during a simulated contraction, which of course happens when $F_{\max}$ is applied on it.

A power factor is calculated here as the product of the force and the velocity normalising factors:

$$\begin{aligned} p &= f \cdot v \\ &= F_{\max} \cdot V_{CC_{\max}} \end{aligned} \quad (2.26)$$

The energy normalising factor is obtained from the SEC force-extension relationship as the integral of force with respect to the length change from zero to maximum extension:

$$\begin{aligned} e &= \int_0^x f \cdot dx \\ &= \int_0^x k \cdot \chi_{SEC} \cdot dx \\ &= \frac{k \cdot x^2}{2} = \frac{(k \cdot x) \cdot x}{2} = \frac{f \cdot x}{2} \\ &= \frac{F_{\max} \cdot X_{SEC_{\max}}}{2} \end{aligned} \quad (2.27)$$

Notice that this factor represents the maximal area under the SEC force-extension relationship (equation (2.3)) for a given muscle-tendon complex.

A time normalising factor is defined here as follows:

$$\begin{aligned} t &= \frac{x}{v} \\ &= \frac{\left(\frac{f}{k}\right)}{v} = \frac{f}{k \cdot v} \\ &= \frac{F_{\max}}{K \cdot V_{CC_{\max}}} \end{aligned} \quad (2.28)$$

An expression for mass can be obtained by rearranging equation (2.5), such that the mass is expressed as the ratio of force to acceleration. Using the same approach a mass normalising factor is worked out as follows:

$$m = f \cdot \frac{t^2}{x}$$

$$= f \cdot \frac{\left(\frac{x}{v}\right)^2}{x} = f \cdot \frac{x}{v^2}$$

$$= f \cdot \frac{\left(\frac{f}{k}\right)}{v^2} = \left(\frac{f}{v}\right)^2 \cdot \frac{1}{k}$$

$$= \left(\frac{F_{\max}}{V_{\max}}\right)^2 \cdot \frac{1}{K} \quad (2.29)$$

4.1.2. Normalising the equations that describe the implications of the series connection

Equation (2.1) can be expressed in dimensionless terms by dividing the force in each component by the force normalising factor, f:

$$\frac{F_{CC}}{f} = \frac{-F_{SEC}}{f} = \frac{-F_L}{f} = \frac{F}{f}$$

This is equivalent to:

$$\varphi_{CC} = -\varphi_{SEC} = -\varphi_L = \varphi \qquad (2.30)$$

Equation (2.2) can be expressed in dimensionless terms by dividing the movement in each one of the components by the length normalising factor, x:

$$\frac{X_{SEC} - X_{CC} - X_L}{x} = 0$$

This is equivalent to:

$$\chi_{SEC} - \chi_{CC} - \chi_L = 0 \qquad (2.31)$$

4.1.3. Normalising the linear equations

The normalising factors derived as described are used to normalise the equations governing the behaviour of the system and of its components.

4.1.3.1. Normalising the linear SEC force-extension relationship

The SEC dimensioned force-extension relationship (equation (2.3)) can be expressed in dimensionless terms by dividing both of its sides with the force normalising factor:

$$F \cdot \frac{1}{f} = K \cdot X_{SEC} \cdot \frac{1}{f}$$

It can be seen from equation (2.34) that the force normalising factor could be expressed in terms of the stiffness and length normalising factors as:

$$f = k \cdot x$$

and therefore:

$$F \cdot \frac{1}{f} = K \cdot X_{SEC} \cdot \frac{1}{k \cdot x}$$

Making the appropriate substitutions:

$$F \cdot \frac{1}{F_{\max}} = K \cdot X_{SEC} \cdot \frac{1}{K \cdot X_{SEC\max}}$$

and simplifying:

$$\frac{F}{F_{\max}} = \frac{X_{SEC}}{X_{SEC\max}}$$

This expression can be written using symbols for the dimensionless quantities:

$$\varphi = \chi_{SEC} \qquad (2.32)$$

Notice that when this relationship is expressed in normalised terms, the stiffness constant is unity. Thus, normalisation removes the effects of stiffness from the behaviour of the SEC. This can also be understood by re-writing equation (2.32) as follows:

$$\varphi = \kappa \cdot \chi_{SEC}$$

Here κ is the normalised stiffness. The normalised stiffness while $\chi_{SEC} \geq 0$ is of course:

$$\kappa = \frac{K}{k}$$
$$= \frac{K}{K} = 1$$

Thus, when the stiffness of the elongating SEC is expressed in dimensionless terms, it is equal to one.

Notice that in its dimensionless form, the linear SEC force-extension relationship does not contain any constants. The effect of stiffness as a constant has effectively been removed.

4.1.3.2. Normalising the linear CC force-velocity relationship

In order to obtain a dimensionless expression for CC shortening velocity, the amount of CC shortening and the time scale must be expressed in dimensionless terms. This can be achieved by dividing CC shortening with the length

normalising factor and the time scale by the time normalising factor. In this way equation (2.4) can be re-written as:

$$\frac{d}{d\tau}(\chi_{CC}) = V_{CC_{\max}} \cdot \left(1 - \frac{F}{F_{\max}}\right) \cdot \frac{t}{x}$$

Substituting for t on the right side (RS) of the equation:

$$\frac{d}{d\tau}(\chi_{CC}) = V_{CC_{\max}} \cdot \left(1 - \frac{F}{F_{\max}}\right) \cdot \frac{\left(\frac{x}{v}\right)}{x}$$

$$= V_{CC_{\max}} \cdot \left(1 - \frac{F}{F_{\max}}\right) \cdot \frac{1}{v}$$

Substituting for $v = V_{\max}$ on the RS yields:

$$\frac{d}{d\tau}(\chi_{CC}) = \frac{V_{CC_{\max}}}{V_{CC_{\max}}} \cdot \left(1 - \frac{F}{F_{\max}}\right)$$

which simplifies to:

$$\frac{d}{d\tau}(\chi_{CC}) = 1 - \varphi \qquad (2.33)$$

Notice how in this normalised force-velocity expression the effects of the two constants present in its dimensioned form (equation (2.4)) disappear.

4.1.3.3. Normalising the linear L force-acceleration relationship

Equation (2.5) is an expression for the acceleration of the load. The dimensions of acceleration is (Length)·(Time^{-2}). In order to remove the effect of these dimensions, equation (2.5) must be divided by the length normalising factor and multiplied by the square of the time normalising factor:

$$\frac{d^2}{d\tau^2}(\chi_L)=\frac{F}{M}\cdot\frac{t^2}{x}$$

Substituting t and x with equivalent expressions yields:

$$\frac{d^2}{d\tau^2}(\chi_L)=\frac{F}{M}\cdot\frac{\left(\frac{f}{k\cdot v}\right)^2}{\left(\frac{f}{k}\right)}$$

$$=\frac{F}{M}\cdot\frac{f}{k\cdot v^2}$$

Substituting the normalising factors on the RS with their equivalent constants:

$$\frac{d^2}{dT^2}(\chi_L)=\frac{F}{M}\cdot\frac{F_{\max}}{K\cdot V_{\max_{CC}}{}^2}$$

The RS can be multiplied by $\frac{F_{\max}}{F_{\max}}$ and be rearranged in the following way

without altering the result:

$$\frac{d^2}{dT^2}(\chi_L)=\frac{F}{F_{\max}}\cdot\frac{F_{\max}{}^2}{K\cdot V_{\max_{CC}}{}^2}\cdot\frac{1}{M}$$

In this expression notice that the first fraction on the RS is equivalent to the normalised force, the second fraction is the mass normalising factor (equation (2.29)) and the last fraction is the reciprocal of the mass. Therefore this expression is equivalent to:

$$\frac{d^2}{d\tau^2}(\chi_L)=\frac{\varphi}{\Xi} \qquad (2.34)$$

This equation contains only one dimensionless constant, Ξ, which reflects the normalised magnitude of the mass of the load.

4.1.3.4. Comments

Thus, by normalising the dimensioned expressions that determine the mechanical behaviour of a muscle-tendon-inertia complex in its most simple form, the complexity of this behaviour has been reduced from four degrees of freedom to only one.

This result shows that the normalised mechanical behaviour of MTI systems such as those described in section 1 of this chapter, only depends on the value of the normalised inertia experienced by the muscle-tendon complex, i.e. only on Ξ. Thus the behaviour of all possible systems, whether from an elephant or a flea can be described by a range of perhaps 10 solutions for just this one variable. Dimensionless constants have been found to determine the behaviour of various systems in nature (McMahon and Bonner, 1983). A well known such constant is, for example, Reynolds number, which determines whether, for a given fluid velocity, its flow in a tube is laminar or turbulent.

Dimensioned	Dimensionless
$F_{CC} = -F_{SEC} = -F_L = F$	$\varphi_{CC} = -\varphi_{SEC} = -\varphi_L = \varphi$
$X_{SEC} - X_{CC} - X_L = 0$	$x_{SEC} - x_{CC} - x_L = 0$
$F = k \cdot X_{SEC}$	$\varphi = \chi_{SEC}$
$\frac{d}{dT}(X_{CC}) = V_{CC_{max}} - \frac{V_{CC_{max}}}{F_{max}} \cdot F$ $= V_{CC_{max}} \cdot \left(1 - \frac{F}{F\,max}\right)$	$\frac{d}{d\tau}(\chi_{CC}) = 1 - \varphi$
$\frac{d^2}{dT^2}(X_L) = \frac{F}{M}$	$\frac{d^2}{d\tau^2}(\chi_L) = \frac{\varphi}{\Xi}$

Table 2.3. Summary of the dimensioned and normalised versions of all equations of the MTI system with linear properties. These expressions are valid under the constraints explained in the relevant section.

4.1.4. Normalising non-linear relationships

The non-linear properties of the components of the MTI system does not alter the implications of the series connection between them. The normalised equations (2.30) and (2.31) expressing these implications are also applicable in this section.

4.1.4.1. Normalising the hyperbolic SEC force-extension relationship

Equation (2.6) is an expression for the force developed when the SEC length is changed with respect to its initial length. Therefore, in order to remove the dimensions of force, this expression must be divided by the force normalising factor. Starting with the top line of this equation:

$$F = \frac{\frac{X_{SEC}}{X_{SEC\max}} \cdot F_{\max}}{1 + H \cdot \left(1 - \frac{X_{SEC}}{X_{SEC\max}}\right)} \quad if \quad X_{SEC} \geq 0$$

As $\chi_{SEC} = \frac{X_{SEC}}{X_{SEC\max}}$, substitution in the above equation yields:

$$F = \frac{\chi_{SEC} \cdot F_{\max}}{1 + H \cdot (1 - \chi_{SEC})} \quad if \quad X_{SEC} \geq 0$$

Also, dividing X_{SEC} in the condition set on the right by the positive quantity of $X_{SEC\max}$ leaves the relationship unaltered. Therefore, the above equation can be written as:

$$F = \frac{\chi_{SEC} \cdot F_{\max}}{1 + H \cdot (1 - \chi_{SEC})} \quad if \quad \chi_{SEC} \geq 0$$

Dividing both sides by the force normalising factor f :

$$F \cdot \frac{1}{f} = \frac{\chi_{SEC} \cdot F_{\max}}{1 + H \cdot (1 - \chi_{SEC})} \cdot \frac{1}{f} \quad if \quad \chi_{SEC} \geq 0$$

Substituting $F_{\max}$ for f and re-writing the equation:

$$\frac{F}{F_{\max}} = \frac{\chi_{SEC}}{1 + H \cdot (1 - \chi_{SEC})} \cdot \frac{F_{\max}}{F_{\max}} \quad if \quad \chi_{SEC} \geq 0$$

and normalising:

$$\varphi = \frac{\chi_{SEC}}{[1 + H \cdot (1 - \chi_{SEC})]} \quad if \quad \chi_{SEC} \geq 0$$

The bottom line of equation (2.6) can also be normalised in a similar manner to obtain the complete form of the normalised version of this equation:

$$\begin{aligned} \varphi &= \frac{\chi_{SEC}}{1 + H \cdot (1 - \chi_{SEC})} \quad if \quad \chi_{SEC} \geq 0 \\ \varphi &= 0 \qquad\qquad\qquad\qquad if \quad \chi_{SEC} < 0 \end{aligned} \tag{2.35}$$

In this expression, if the value of H is set to zero, equation (2.35) is transformed into its linear version (equation (2.32)). Also notice how normalisation has reduced the number of constants required to express the hyperbolic SEC force-extension relationship from three in the dimensioned form of this equation (i.e. $X_{SEC_{\max}}$, $F_{\max}$ and H) to only one (dimensionless constant, H).

4.1.4.2. Normalising the hyperbolic CC force-velocity relationship

The hyperbolic CC force-velocity equation is described in absolute terms by equation (2.7). Before normalising, equation (2.7) can be simplified by noticing that the ratio $\frac{F}{F_{\max}}$ in the RS of this equation is the normalised force φ such that equation (2.7) can be re-written as:

$$\frac{d}{dT}(X_{CC}) = V_{CC_{\max}} \cdot \frac{1-\varphi}{1+\varphi \cdot G}$$

The dimensions of the result of this expression is (Length)·(Time)$^{-1}$ and in order to remove these dimensions the expression must be divided by the length normalising factor and multiplied by the time normalising factor:

$$\frac{d}{d\tau}(\chi_{CC}) = V_{CC_{\max}} \cdot \frac{1-\varphi}{1+\varphi \cdot G} \cdot \frac{t}{x}$$

Substituting $\frac{x}{v}$ for t in the RS:

$$\frac{d}{d\tau}(\chi_{CC}) = V_{CC_{\max}} \cdot \frac{1-\varphi}{1+\varphi \cdot G} \cdot \frac{\left(\frac{x}{v}\right)}{x}$$

$$= V_{CC_{\max}} \cdot \frac{1-\varphi}{1+\varphi \cdot G} \cdot \frac{1}{v}$$

As $v = V_{CC_{\max}}$:

$$\frac{d}{d\tau}(\chi_{CC}) = \frac{1-\varphi}{1+\varphi \cdot G} \qquad (2.36)$$

Equation (2.36) is the hyperbolic normalised force-velocity equation for the CC. If the value of G is set to zero, equation (2.36) is transformed into its linear version (equation (2.33)). This dimensionless version of the CC force-velocity relationship only requires the value of one dimensionless constant, G, to be

specified. Its dimensioned version included three constants ($F_{\max}, V_{CC_{\max}}$ and G).

4.1.4.3. Scaling the time course of the CC activation parameter

The exponent in the top line of the activation parameter definition (equation (2.9)) is the absolute time elapsed since the onset of CC activation divided by the activation time constant. Although expressing this time and time constant in dimensionless terms would not alter the result (as the time normalising factors in this ratio ultimately cancel out), when the value of the time constant is specified in this model in which the time scale is dimensionless, the value of TC must also be specified in dimensionless terms. Division of the time scale and of the time constant by the time normalising factor yields a scaled form of equation (2.9):

$$\begin{aligned} A &= 1 - e^{-\frac{\tau}{\tau c}} \quad if \quad \tau c > 0 \\ A &= 1 \qquad\qquad if \quad \tau c = 0 \end{aligned} \tag{2.37}$$

4.1.4.4. Comments

The force-acceleration relationship for the load is linear as it is in the model described in the previous section. Therefore equation (2.34) can also be used in this model. Notice that in its dimensioned form this model requires specification of seven constants ($X_{SEC_{\max}}, H, F_{\max}, V_{CC_{\max}}, G, TC, M$). Normalisation has reduced the number of required constants to four (dimensionless

constants: $H, G, \tau c, \Xi$). A summary of the dimensioned and dimensionless equations in this model is shown in table 2.4.

Dimensioned	Dimensionless
$F_{CC} = -F_{SEC} = -F_L = F$	$\varphi_{CC} = -\varphi_{SEC} = -\varphi_L = \varphi$
$X_{SEC} - X_{CC} - X_L = 0$	$\chi_{SEC} - \chi_{CC} - \chi_L = 0$
$F = \frac{X_{SEC} \cdot F_{\max}}{\left[1 + H \cdot \left(1 - \frac{X_{SEC}}{X_{SEC\max}}\right)\right] \cdot X_{SEC\max}}$	$\varphi = \frac{\chi_{SEC}}{1 + H \cdot (1 - \chi_{SEC})}$
$\frac{d}{dT}(X_{CC}) = A \cdot V_{CC_{\max}} \cdot \frac{1 - \frac{F}{F_{\max}}}{1 + \frac{F}{F_{\max}} \cdot G}$	$\frac{d\chi_{CC}}{d\tau} = A \cdot \frac{1 - \varphi}{1 + \varphi \cdot G}$
$\frac{d^2}{dT^2}(X_L) = \frac{F}{M}$	$\frac{d^2}{d\tau^2}(\chi_L) = \frac{\varphi}{\Xi}$

Table 2.4. Summary of the dimensioned and normalised versions of the equations for the MTI system with linear load motion and non-linear SEC and CC behaviour. The above expressions are valid under the constraints explained in the relevant sections.

4.2. Normalising the system with rotational motion of the inertial load

4.2.1. Purely inertial load

4.2.1.1. Normalising factors

A convenient way for normalising lever arm length, would be to introduce an additional scaling factor, s, such that:

$$s = S \qquad (2.38)$$

where S is the length of the short lever. As already mentioned in section 3.2.1, the length of the long lever l can be expressed relative to the length of the short lever, i.e. the lever length normalising factor s, as a dimensionless lever ratio, LR.

All other rotational scaling factors can be derived from appropriate combinations of s and the linear scaling factors as shown below.

An angular velocity scaling factor, ω, can be defined as a ratio of the linear velocity scaling factor, v and the lever arm scaling factor, s, such that:

$$\omega = \frac{v}{s} = \frac{V_{CC_{max}}}{S} = \Omega_{CC_{max}} \qquad (2.39)$$

A torque normalising factor, tq, can be obtained by multiplying the force scaling factor, f, by the lever arm scaling factor, s:

$$tq = s \cdot f = S \cdot F_{\max} = Tq_{\max} \qquad (2.40)$$

Rotational stiffness, K_{rot}, is the ratio of torque to angular displacement and therefore a rotational stiffness scaling factor, k_{rot}, can be obtained as the ratio of the torque scaling factor and the angular movement scaling factor:

$$k_{rot} = \frac{tq}{\theta} = \frac{Tq_{\max}}{\Theta_{SEC_{\max}}} = \frac{S \cdot F_{\max}}{\frac{X_{SEC_{\max}}}{S}} = \frac{S^2 \cdot F_{\max}}{X_{SEC_{\max}}} = S^2 \cdot k \quad (2.41)$$

An angular movement scaling factor, θ, can be obtained by dividing the length scaling factor from the linear model by the lever arm factor:

$$\theta = \frac{x}{s} = \frac{X_{SEC_{\max}}}{S} = \Theta_{SEC_{\max}} \quad (2.42)$$

A rotational power normalising factor in this model could be found by multiplying the torque and angular velocity normalising factors:

$$p_{rot} = tq \cdot \omega = S \cdot F_{\max} \cdot \frac{V_{CC_{\max}}}{S} = F_{\max} \cdot V_{CC_{\max}} = p \quad (2.43)$$

Therefore, due to the reciprocal effects of a lever system on the force and movement, the product of torque and angular movement or its time derivatives is independent of whether there is a lever or not. This is consistent with the law of conservation of energy as levers cannot generate or dissipate energy. Thus the same power scaling factor, p, is used in this model as in the model with linear motion load.

A rotational scaling factor appropriate for energy, e_{rot}, could be obtained from the SEC torque-angular extension relation as the integral of the torque with respect to the angular extension from zero to maximal extension:

$$e_{rot} = \int_0^{\theta} tq \cdot d\theta = \int_0^{\theta} k_{rot} \cdot \theta \cdot d\theta = \frac{k_{rot} \cdot \theta^2}{2}$$
$$= \frac{k \cdot s^2 \cdot \frac{x^2}{s^2}}{2} = \frac{k \cdot x^2}{2} = e \qquad (2.44)$$

As in the case of power, there is no difference between the linear and rotational models in terms of energy as the lever arms cancel out when rotation and torque are multiplied together.

A time normalising factor could be expressed as the ratio of rotation to angular velocity normalising factors:

$$t_{rot} = \frac{\theta}{\omega} = \frac{\left(\frac{x}{s}\right)}{\left(\frac{v}{s}\right)} = \frac{x}{s} = t \qquad (2.45)$$

which is the same as the time factor for the rotational model.

Finally, a moment of inertia normalising factor, i, can be obtained as follows:

$$i = tq \cdot \frac{t^2}{\theta} = s \cdot f \cdot \frac{\left(\frac{x}{v}\right)^2}{\frac{x}{s}} = s^2 \cdot f \cdot \frac{x}{v^2} =$$
$$s^2 \cdot \frac{1}{k} \cdot \left(\frac{f}{v}\right)^2 = s^2 \cdot m = S^2 \cdot \frac{1}{K} \cdot \left(\frac{F_{max}}{V_{max}}\right)^2 \qquad (2.46)$$

Thus the inertia normalising factor is equal to the product of the mass normalising factor and the square of the lever normalising factor.

4.2.1.2. Normalising the implication of the series connection

The dimension of (Torque) can be removed from equation (2.12) by dividing it with the torque normalising factor:

$$\frac{Tq_{CC}}{tq} = \frac{Tq_{SEC}}{tq} = \frac{Tq_L}{tq} = \frac{Tq}{tq}$$

which can be written in normalised form as:

$$\tau q_{CC} = \tau q_{SEC} = \tau q_L = \tau q \qquad (2.47)$$

In order to normalise the relationship between angular movement of the components, equation (2.13) is divided by $\Theta_{SEC_{max}}$:

$$\frac{\left(\Theta_{SEC} - \Theta_{CC} - \Theta_L\right)}{\Theta_{SEC_{max}}} = 0$$

This expression is equivalent to:

$$\vartheta_{SEC} - \vartheta_{CC} - \vartheta_L = 0 \qquad (2.48)$$

4.2.1.3. Normalising the hyperbolic SEC torque-angular extension relationship

The part of equation (2.14) which describes the torque around the CR in terms of the extension of the SEC beyond its initial length, can be rearranged to:

$$Tq = \frac{\frac{\Theta_{SEC}}{\Theta_{SECmax}} \cdot Tq_{max}}{1 + H \cdot \left(1 - \frac{\Theta_{SEC}}{\Theta_{SECmax}}\right)}$$

Notice that $\Theta_{SEC_{max}}$ is the angular displacement normalising factor θ (equation (2.42)) and therefore the above expression is equivalent to:

$$Tq = \frac{\vartheta_{SEC} \cdot Tq_{\max}}{1 + H \cdot (1 - \vartheta_{SEC})}$$

Dividing both its sides by the torque normalising factor *tq* (i.e. Tq_{max}) yield the following dimensionless expression:

$$\tau q = \frac{\vartheta_{SEC}}{1 + H \cdot (1 - \vartheta_{SEC})}$$

For negative angular displacements of the SEC:

$$\varphi = 0$$

Thus:

$$\begin{aligned} \tau q &= \frac{\vartheta_{SEC}}{1 + H \cdot (1 - \vartheta_{SEC})} \qquad if \quad \vartheta_{SEC} \geq 0 \\ &= 0 \qquad otherwise \end{aligned} \tag{2.49}$$

Equation (2.49) is identical to equation (2.35) which is used for linear load motion as: $\vartheta_{SEC} = \frac{\Theta_{SEC}}{\Theta_{SEC\max}} = \frac{S \cdot X_{SEC}}{S \cdot X_{SEC\max}} = \frac{X_{SEC}}{X_{SEC\max}} = \chi_{SEC}$

4.2.1.4. Normalising the CC torque-angular velocity relationship

Equation (2.15), expressing the angular velocity of the CC with respect to the torque around the CR , can be simplified to:

$$\frac{d}{dT}(\Theta_{CC}) = \Omega_{CC_{\max}} \cdot \frac{1 - \tau q}{1 + \tau q \cdot G}$$

This expression has dimensions of (Angular displacement)·(Time)$^{-1}$ (i.e. (Angular velocity)), which can be removed by dividing both its sides by the angular velocity normalising factor ω to obtain:

$$\frac{d}{d\tau}(\vartheta_{CC}) = \frac{1-\tau q}{1+\tau q \cdot G} \qquad (2.50)$$

Equation (2.50) is identical to equation (2.36) for the model with linear load motion, for $\tau q = \frac{Tq}{Tq_{\max}} = \frac{S \cdot F}{S \cdot F_{\max}} = \frac{F}{F_{\max}} = \varphi$.

4.2.1.5. Normalising the L torque-angular acceleration relationship

Equation (2. 24) is Newton's second law expressed in rotational terms. It has dimensions of (Angular displacement)·(Time)$^{-2}$ and can therefore be normalised by dividing both sides by the angular displacement normalising factor, such that:

$$\frac{d^2}{d\tau^2}(\vartheta_L) = \frac{Tq}{MI} \cdot \frac{t^2}{\theta}$$

Substituting the normalising factors by equivalent expressions yields:

$$\frac{t^2}{\theta} = \frac{\left(\frac{\theta}{\omega}\right)^2}{\theta} = \frac{\theta}{\omega^2} = \frac{tq}{k_{rot} \cdot \omega^2}$$

and therefore the above expression can be written as:

$$\frac{d^2}{d\tau^2}(\vartheta_L) = \frac{Tq}{MI} \cdot \frac{tq}{k_{rot} \cdot \omega^2}$$

Multiplying the right hand side of the above expression by $\frac{tq}{tq}$:

$$\frac{d^2}{d\tau^2}(\vartheta_L) = \frac{Tq}{MI} \cdot \frac{tq^2}{k_{rot} \cdot \omega^2} \cdot \frac{1}{tq}$$

As the inertia normalising factor, *i*, could also be expressed as $\frac{\omega^2 \cdot k_{rot}}{tq^2}$, the above expression can be simplified to:

$$\frac{d^2}{d\tau^2}(\vartheta_L) = \frac{\tau q}{\xi} \qquad (2.51)$$

where ξ is the normalised inertial load. This dimensionless quantity is equivalent to $\Xi \cdot LR^2$.

4.2.1.6. Comments

Inclusion of a lever does not alter the activation properties of the CC and therefore equation (2.37) can also be used in this model. Seven constants are required to specify the dimensioned behaviour in this model ($\Theta_{SEC_{max}}, H, Tq_{max}, \Omega_{max}, G, TC, MI$) and four (dimensionless) constants for its normalised version ($H, G, \tau c, \xi$). Table 2.5 shows the equations of this model in dimensioned and dimensionless form.

Dimensioned	Dimensionless
$Tq_{CC} = Tq_{SEC} = Tq_L = Tq$	$\tau q_{CC} = \tau q_{SEC} = \tau q_L = \tau q$
$\Theta_{SEC} - \Theta_{CC} - \Theta_L = 0$	$\vartheta_{SEC} - \vartheta_{CC} - \vartheta_L = 0$
$Tq = \frac{\Theta_{SEC} \cdot Tq_{\max}}{\left[1 + H \cdot \left(1 - \frac{\Theta_{SEC}}{\Theta_{SEC\max}}\right)\right] \cdot \Theta_{SEC\max}}$	$\tau q = \frac{\vartheta_{SEC}}{1 + H \cdot (1 - \vartheta_{SEC})}$
$\frac{d}{dT}(\Theta_{CC}) = A \cdot \Omega_{CC\max} \cdot \frac{1 - \frac{Tq}{Tq_{\max}}}{1 + \frac{Tq}{Tq_{\max}} \cdot G}$	$\frac{d}{d\tau}(\vartheta_{CC}) = A \cdot \frac{1 - \tau q}{1 + \tau q \cdot G}$
$\frac{d^2}{dT^2}(\Theta_L) = \frac{Tq}{MI}$	$\frac{d^2}{d\tau^2}(\vartheta_L) = \frac{\tau q}{\xi}$

Table 2.5. Summary of the dimensioned and normalised versions of non-linear equations for the model with rotational motion of a purely inertial load. The above expressions are valid under the constraints explained in the relevant sections.

4.2.2. Normalising the inertial-gravitational system

4.2.2.1. Normalising the implications of the series connection

Equation (2.18) can be normalised using a process similar to that followed to obtain equation (2.47) to obtain:

$$\tau q_{CC} - \tau q_G = \tau q_{SEC} - \tau q_G = \tau q_L - \tau q_G = \tau q \quad (2.52)$$

In this work $\tau q_G = \frac{M \cdot g \cdot l}{F_{max} \cdot S}$. Substituting $\gamma = \frac{M \cdot g}{F_{max}}$ in this expression yields $\tau q_G = \gamma \cdot LR$.

Inclusion of a gravitational force does not alter the relationship between the movement in the components and therefore equation (2.48) can also be used in this model.

4.2.2.2. Normalising hyperbolic SEC torque-angular extension relationship in the presence of gravity

Equation (2.19) expresses the torque around the CR as consisting of two components: one coming from the SEC and one coming from gravity. This equation can be simplified to:

$$Tq = \frac{\vartheta_{SEC} \cdot Tq_{max}}{1 + H \cdot (1 - \vartheta_{SEC})} - Tq_G$$

This expression has dimensions of torque and can be normalised by dividing it by the torque normalising factor, tq (i.e. Tq_{max}) to obtain:

$$\tau q = \frac{\vartheta_{SEC}}{1 + H \cdot (1 - \vartheta_{SEC})} - \tau q_G \quad (2.53)$$

From this expression an equivalent normalised expression using linear terms can be obtained:

$$\varphi = \frac{\chi_{SEC}}{1 + H \cdot (1 - \chi_{SEC})} - LR \cdot \gamma$$

4.2.2.3. Normalising CC behaviour in the presence of gravity

Equation (2.20) describing the CC force-velocity relationship in angular terms can be written in a simplified way:

$$\frac{d}{dT}(\Theta_{CC}) = \Omega_{CC_{max}} \cdot \frac{1 - (\tau q + \tau q_G)}{1 + (\tau q + \tau q_G) \cdot G}$$

This expression has dimensions of (Angular displacement)·(Time)$^{-1}$ or (Angular velocity) and can be normalised by dividing both sides by the corresponding normalising factors to obtain:

$$\frac{d}{d\tau}(\vartheta_{CC}) = \frac{1 - (\tau q + \tau q_G)}{1 + (\tau q + \tau q_G) \cdot G} \qquad (2.54)$$

An equivalent expression using dimensionless variables of linear load motion is:

$$\frac{d}{d\tau}(\chi_{CC}) = \frac{1 - (\varphi + LR \cdot \gamma)}{1 + (\varphi + LR \cdot \gamma) \cdot G}$$

4.2.2.4. Normalising the behaviour of L in the presence of gravity

Expression (2.21) relates torque and angular acceleration of L in the presence of a gravitational force. It has dimensions of (Angular displacement).(Time)$^{-2}$ and can therefore be normalised by dividing it by appropriate factors – in a similar way as that used to obtain expression (2.51)- which ultimately yields:

$$\frac{d^2}{d\tau^2}(\vartheta_L) = \frac{\tau q}{\xi} \quad if \quad \tau q \geq 0 \quad and \quad \vartheta_L > 0$$

$$= 0 \qquad otherwise$$

This is the same as expression (2.51). However, due to the presence of a gravitational torque, the normalised torque can be split into two components, one coming from the MTC (either τq_{CC} or τq_{SEC}) and one coming from gravity:

$$\frac{d^2}{d\tau^2}(\vartheta_L) = \frac{\tau q_{CC} - \tau q_G}{\xi} \quad if \quad \tau q \geq 0 \quad and \quad \vartheta_L > 0 \qquad (2.55)$$

$$= 0 \qquad otherwise$$

Expressed in linear terms:

$$\frac{d^2\chi_L}{d\tau^2} = \frac{\varphi_{CC} - LR \cdot \gamma}{\xi} \quad if \quad \varphi \geq 0 \quad and \quad \chi_L > 0$$

$$= 0 \qquad otherwise$$

Notice that in the absence of gravity, i.e. g=0, $\tau q_G = 0$ and expression (2.55) becomes identical to expression (2.51).

4.2.2.5. Comments

In this model, as with previous one, equation (2.37) can be used to describe the time course of CC activation. Inclusion of gravity has incorporated an additional constant to the model, namely τq_G, i.e. the torque due to gravity. However, in the normalised system the values of five constants are required to specify its behaviour $(H, \tau q_G, \tau c, G, \xi)$ compared to eight in its dimensioned version $(Tq_G, \Theta_{SEC_{max}}, H, Tq_{max}, TC, \Omega_{CC_{max}}, G, MI)$. Table 2.6 shows the equations of this model in dimensioned and dimensionless form.

Dimensioned	Dimensionless
$Tq_{CC} - Tq_G = Tq_{SEC} - Tq_G$ $= Tq_L - Tq_G = Tq$	$\tau q_{CC} - \tau q_G = \tau q_{SEC} - \tau q_G$ $= \tau q_L - \tau q_G = \tau q$
$\Theta_{SEC} - \Theta_{CC} - \Theta_L = 0$	$\vartheta_{SEC} - \vartheta_{CC} - \vartheta_L = 0$
$Tq = \frac{\Theta_{SEC} \cdot Tq_{\max}}{\left[1 + H \cdot \left(1 - \frac{\Theta_{SEC}}{\Theta_{SEC\max}}\right)\right] \cdot \Theta_{SEC\max}} - Tq_G$	$\tau q = \frac{\vartheta_{SEC}}{1 + H \cdot (1 - \vartheta_{SEC})} - \tau q_G$
$\frac{d}{dT}(\Theta_{CC}) = A \cdot \Omega_{CC_{\max}} \cdot \frac{1 - \frac{Tq_{CC} - Tq_G}{Tq_{\max}}}{1 + \frac{Tq_{CC} - Tq_G}{Tq_{\max}} \cdot G}$	$\frac{d}{dT}(\vartheta_{CC}) = A \cdot \frac{1 - (\tau q_{CC} - \tau q_G)}{1 + (\tau q_{CC} - \tau q_G) \cdot G}$
$\frac{d^2}{dT^2}(\Theta_L) = \frac{Tq_{CC} - Tq_G}{MI}$	$\frac{d^2}{d\tau^2}(\vartheta_L) = \frac{\tau q_{CC} - \tau q_G}{\xi}$

Table 2.6. Summary of the dimensioned and dimensionless versions of expressions for the model with rotational motion of the load in the presence of gravity. These expressions are valid under the constraints explained in the relevant sections.

5. Numerical solution process

5.1. Initial conditions

Even if the values of the constants required to specify the properties of one of the above models have been chosen, an infinite number of solutions can be obtained for that particular model unless initial conditions are specified. For example, the same MTC would behave differently during each contraction, if the inertial load moved at a different speed at the onset of each of these contractions. As an infinite number of L velocities could be chosen, an infinite number of solutions could be obtained. It is therefore important to define the initial state of the system at the onset of a simulated contraction (τ_0=0). The initial conditions describing this state are the same in all models, i.e. for both linear and rotational motion load and in the absence or presence of a gravitational force. These initial conditions are shown underneath:

1. L is at rest immediately prior to the onset of the contraction, or mathematically expressed:

$$\left[\frac{d}{d\tau}(\chi_L)\right]_0 = 0$$

(The zero subscript denotes the time instant at which contraction starts).

2. L displacement is equal to zero immediately prior to the onset of contraction. The initial value of zero was chosen because any other value would add the unnecessary complication of having to subtract it later on from the load displacement results. Therefore:

$$\chi_{L0} = 0$$

3. The SEC is just slack, so that it is at its resting length where its extension is zero:

$$\chi_{SEC0} = 0$$

Notice that according to the last condition, the initial level of force in the system is also zero, as according to equation (2.32):

$$\varphi_0 = \chi_{SEC_0} = 0$$

5.2. Solving process

With the three initial conditions described in the previous section, the equations on the loop diagram (figure 2.5) below can be solved numerically over pre-set simulation times, in order to determine the time-course of the behaviour for a particular system. A diagram of the solving process is only shown for the simplest one of the MTI models presented in this thesis (linear motion load with linear properties) (figure 2.5). Although the solution process is explained for this simplest model only, more complex models including CC activation and hyperbolic CC force-velocity and SEC force-extension relationships and gravity have been solved in exactly the same way. The explanation given here provides a framework onto which the solving process of the more complex models in this work can be understood.

Firstly, the duration of the simulated contraction is chosen such that the value of $\frac{d}{d\tau}(\chi_{CC})$ attains its final asymptotic value within at least six decimal places. A simulated contraction, which is long enough for this to occur, is called in this thesis a 'complete contraction'. It is recognised that anatomical constraints are important in setting limits to the extent of MTC shortening inside the body. Such constraints were not included in the model in order to focus on the fundamental principles governing

the mechanical output of shortening MTI systems. The potential importance of anatomical constraints in the conclusions drawn in this thesis is discussed in later sections. The number of observations (N) to be generated within the selected duration is then chosen so that the peak force is within at least three decimal places of its peak value for that contraction. The time interval, $\Delta\tau$, between subsequent observations is equal to the selected duration divided by N-1.

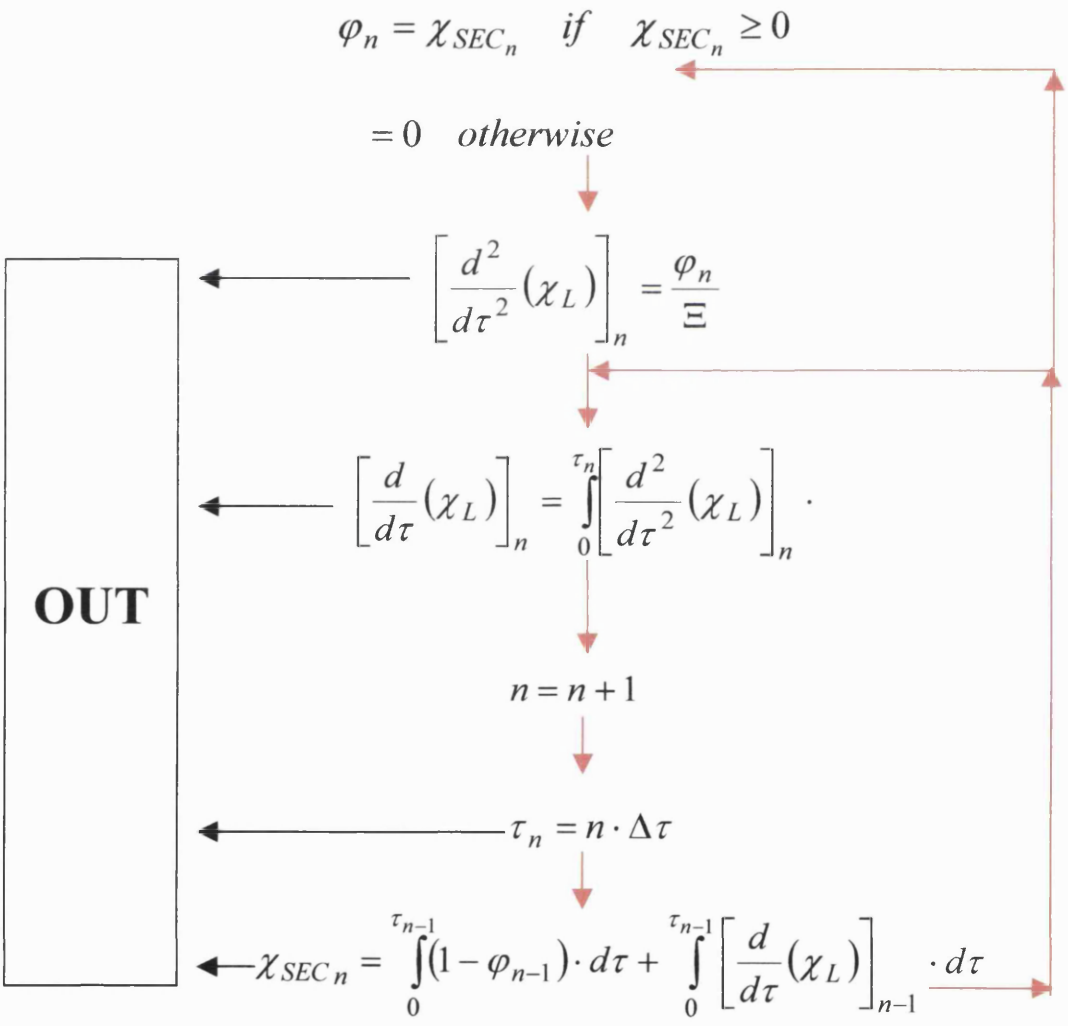

Figure 2.5. Flow diagram of the numerical solution process for the MTI system with linear motion and properties. n is a range variable indicating the order of the terms of the sequence generated by the solving process. n=0,1..,N-1, where N is the total number of terms to be generated for a given duration of simulation. The values of L acceleration and velocity, SEC extension and time are retained (as indicated by the black arrows).

Calculation starts using the values set in the initial conditions at time τ_0=0. According to the third condition SEC extension is zero. The top equation of the loop calculates the magnitude of the dimensionless force from the dimensionless SEC extension (equation (2.32)). As already shown in the initial conditions the initial value of force in the system will be zero. This value of force is then fed into the second equation from the top (equation (2.34)), which calculates the normalised acceleration of L as a function of the dimensionless force and inertia. Notice how the first value obtained from this equation is zero, because the initial force in the system is zero at this time. The third equation from the top represents the dimensionless velocity of L and it is simply the integral of equation (2.34) with respect to time. The first value at that level is also zero because the initial values of force and load velocity are zero. The first results from these three steps in the loop apply for time τ_0=0. Once the values of load acceleration and velocity have been obtained for the onset of the contraction, the extension of the SEC at the next time instant can be calculated. The fourth equation initiates calculation of the next term of the calculated variables. Thus, after the results at τ_0=0 have been obtained, calculation at $\tau_1=\Delta\tau$ starts, as shown by the fifth equation which calculates the new time by adding on the previous time the value of one time interval. The bottom equation in this diagram is a rearranged form of equation (2.31) calculating the new dimensionless SEC length change. In this equation, the dimensionless CC and L movements are obtained by integration of the corresponding velocities with respect to time over the duration of the simulated contraction. Notice that the first result value of this calculation is not going to be zero, but τ length units instead. The new value of the dimensionless SEC length change is then fed back to beginning of the loop to calculate the new dimensionless force in the system. Notice

how the second iteration gives values different to zero for all equations, as a result of starting from a level of force greater than zero. In this iterative manner a pre-set number of points can be generated over the desired simulated contraction duration thereby obtaining the time course of the SEC extension, force, load acceleration and velocity. This process is carried out using the mathematical software mathcad version 7. This process of obtaining the time course of SEC extension, L acceleration and velocity is common for all models, although the number sequences of these variables are generated from equations which are specific to each model.

It was mentioned in a previous paragraph that the duration of each simulated contraction is based on the final value of the CC shortening velocity. As shown above the CC shortening velocity is not calculated in the loop. However, the values of all the dimensionless variables of interest during the time course of the simulated contraction, including the CC shortening velocity, can be calculated from the dimensionless SEC extension and L velocity results. This is achieved as follows:

CC shortening. By inputting the values of χ_L and χ_{SEC} in equations (2.31) and solving for χ_{CC}.

Force in the CC and SEC. From equations (2.32) by inputting the values of χ_{SEC}.

CC shortening velocity. By inputting the CC (or SEC) force values in equations (2.33).

SEC velocity: As the sum of CC and L velocity. (In the rotational models L velocity must be expressed relative to the point of SEC attachment on the lever).

Mechanical work generated by the CC (ε_{CC}). From the force and CC shortening according to equation:

$$\varepsilon_{CC} = \int_0^{\chi_{CC}} \varphi_{CC} \cdot d\chi_{CC} \qquad (2.56)$$

SEC elastic potential energy (ε_{SEC}). From the force and SEC length change according to equation (2.57):

$$\varepsilon_{SEC} = \int_0^{\chi_{SEC}} \varphi_{SEC} \cdot d\chi_{SEC} \qquad (2.57)$$

Kinetic energy of L (ε_L). From the velocity of L according to equation (2.58):

$$\begin{aligned} \varepsilon_L &= \frac{\Xi}{2} \cdot \left(\frac{d}{d\tau}(\chi_L) \right)^2 \\ &= \frac{\xi}{2} \cdot \left(\frac{d}{d\tau}(\vartheta_L) \right)^2 \end{aligned} \qquad (2.58)$$

Power generated by the CC (ρ_{CC}). As the product of force and CC shortening velocity:

$$\rho_{CC} = \varphi_{CC} \cdot \frac{d}{d\tau}(\chi_{CC}) \qquad (2.59)$$

SEC Power (ρ_{SEC}). Product of force and SEC extension velocity:

$$\rho_{SEC} = \varphi_{SEC} \cdot \frac{d}{d\tau}(\chi_{SEC}) \qquad (2.60)$$

Power delivered to L (ρ_L). Product of force and L velocity:

$$\rho_L = \varphi_L \cdot \frac{d}{d\tau}(\chi_L) \qquad (2.61)$$

A similar approach can be used to obtain solutions for the more complex models by using the appropriate equations. All calculated variables are dimensionless. The time course of the mechanical behaviour of the components of MTI systems is presented below in dimensionless, rather than dimensioned, terms as fewer simulations are

required to illustrate this behaviour over a wide range of different systems. It is, however, easy to revert back to the dimensioned system simply by multiplying each variable by the appropriate normalising factor.

6. Numerical results

6.1. Dimensionless time course of mechanical events

6.1.1. Purely inertial load

The dimensionless time-course of movement, velocity, force, mechanical energy and power in dimensionless terms are displayed graphically for all three MTI components (CC, SEC and L) in figures 2.6.A-2.9.A. The time course of normalised force, velocity and power relative to variables other than normalised time is shown in figures 2.6.B-2.9.B. Each figure (2.6-2.9) shows, for comparison purposes, simulation results for a different value of normalised inertial load, Ξ. These results are obtained from the model with linear motion and a purely inertial load (modelling sections 4.1.2, 4.1.3). The effects of $\Xi, H, G, \tau c$ and LR are described in section 6.1.2. for selected values of these parameters. The time course of mechanical events under the influence of gravity is considered separately in section 6.1.3.

As shown in figures (2.6.A-2.10.A) the initial force in the system is zero and therefore CC shortening starts at the maximal shortening velocity. Due to the inertia of L, early during the contraction the CC shortens faster than L can move and as a result the SEC is being stretched. SEC stretching leads to a rise of force in the system causing a reduction in the shortening velocity of the CC but also to acceleration of L towards the CC (thus the negative sign for load velocity). Stretching of the SEC also results in an increase of its elastic potential energy. According to the equations of this model mechanical energy is not dissipated in any way. Thus, part of the mechanical energy generated by the CC is used to

rise the elastic potential energy of the SEC and part of it to increase the kinetic energy of L, such that the sum of SEC and L energies at any instant is equal to the energy generated by the CC. Early during the contraction, while force is rising, the energy delivered to the load is less than the energy generated by the CC, because part of the CC is doing work against the SEC. A consequence of that is that the power output of the CC exceeds the power delivered to L.

As L moves at increasingly higher speeds due to the force in the system, at some time after the start of the contraction, it is going to move at the same speed as the speed of the CC shortening. At that instant the SEC is not stretching because its two ends are moving in the same direction at equal speeds. At that time, the force in the system is at its peak, the CC shortening velocity is at its minimum and all of the CC power output is delivered to the load as the SEC length is not changing.

After that time instant, the load will keep accelerating due to the force in the system, moving faster towards the CC than the speed at which the CC shortens. As a result the SEC will be recoiling and the force in the system will be dropping. As force is reduced the CC velocity starts to rise again according to its force-velocity relationship. Recoiling of the SEC gradually leads to release of its elastic potential energy, which is now being used to raise the kinetic energy of L. That means that the kinetic energy of the load is increased by two sources, i.e. by both the CC and the SEC. As a result the power of L during the falling phase of force in the system exceeds the power that the CC is generating.

Given enough time, the velocity of the load rises to high enough values with respect to the muscle velocity, such that the SEC goes slack and the force in the system drops to zero. At zero force, CC shortening achieves its maximal shortening velocity and L is moving at a constant speed at least as high as the CC maximal shortening velocity. Because the force in the system is zero, no work is done by the muscle, the energy content of the SEC is zero and the kinetic energy of L stays constant. As a result power in all components is also zero.

Figures 2.6.B-2.9.B show the CC (red) and L (blue) force-velocity (graph a), power-force (graph c), power-CC velocity (graph d), and the SEC force-extension trajectories (graph b) for the corresponding simulations presented in figures 2.6.A-2.9.A. It can be seen that the trajectories for the CC and the SEC make up part of the corresponding relationships. The extent to which part of the relationship is utilised depends on the magnitude of the inertial load: The greater the inertial load, the greater the force output and the greater the extent to which a relationship will be utilised. Due to the inertial nature of the load, L trajectories, except for infinitely large Ξ values, will always have a portion which lies below and a portion which lies above the corresponding CC relation. The portion below corresponds to the time interval during the contraction before force reaches its peak value. The portion above corresponds to the time interval after peak force has been reached. The two points of intersection between the CC and L trajectories correspond to the time at which contraction started and the time at which peak force was reached.

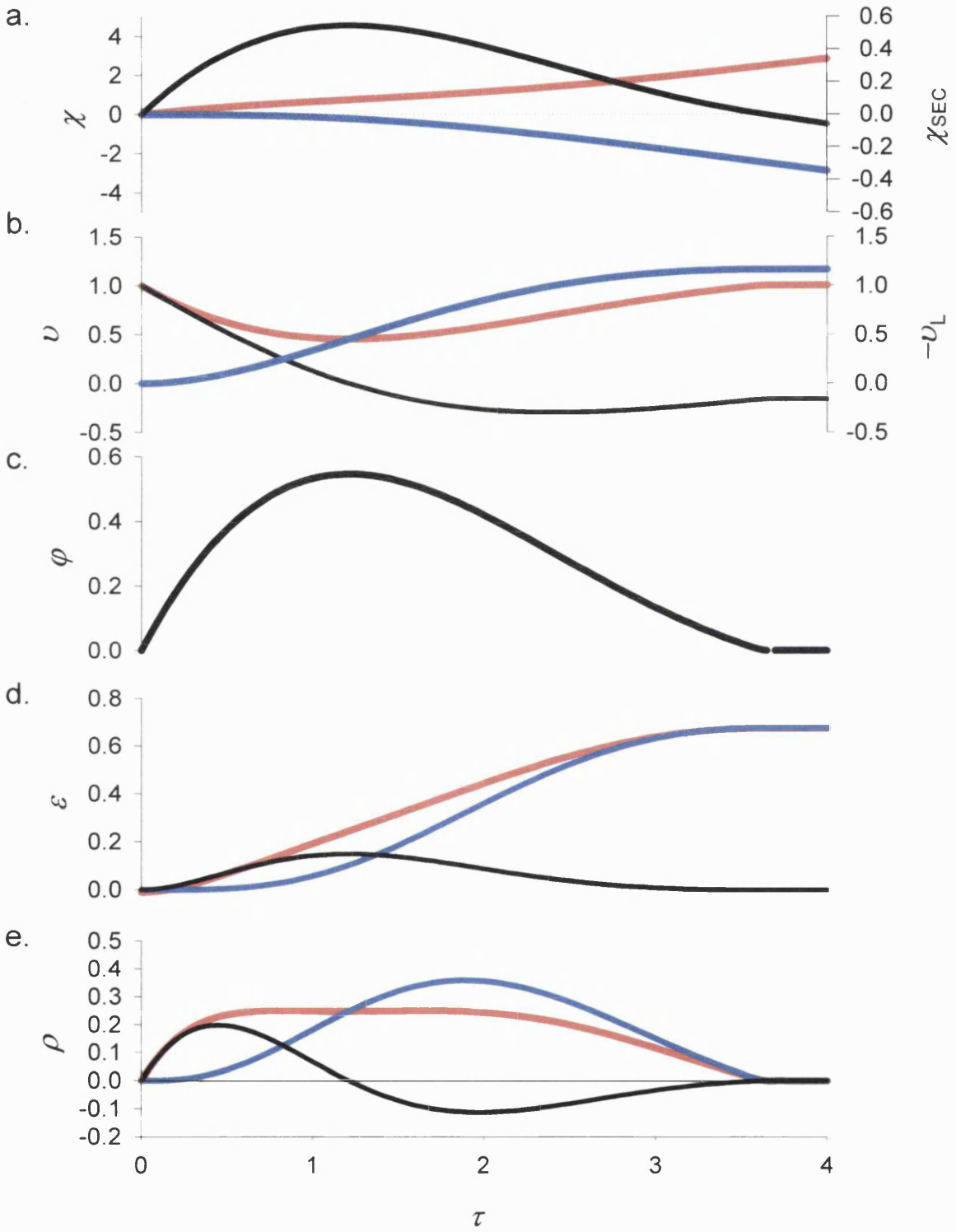

Figure 2.6.A. Time-course of movement (χ; panel a), velocity (υ; panel b), force (φ; panel c), mechanical energy (ε; panel d) and power (ρ; panel e) in the CC (red), SEC (black) and a purely inertial L (blue) during a simulated contraction. $\Xi = 1$.

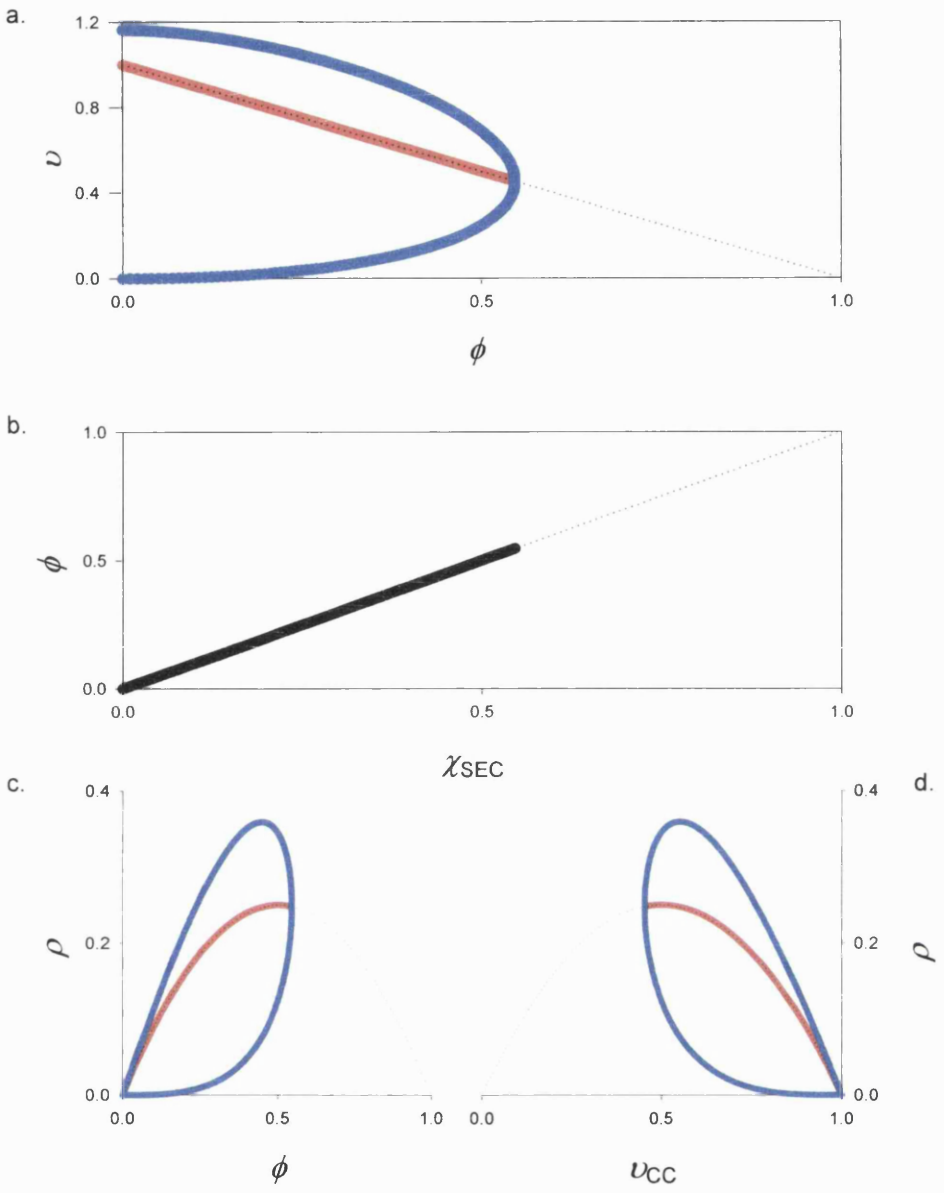

Figure 2.6.B. Results from simulated contraction where $\Xi = 1$. Graph a: L (blue) and CC (red) velocity are plotted against the force. CC force-velocity relationship (black dotted line). Graph b: Force plotted as a function of SEC extension (thick black line); SEC force-extension relationship (thin black line). Graph c: CC (red) and L (blue) power plotted against the force; CC power-force relationship (black line). Graph d: CC (red) and L (blue) power plotted against the CC velocity ; CC power-velocity relationship (black line).

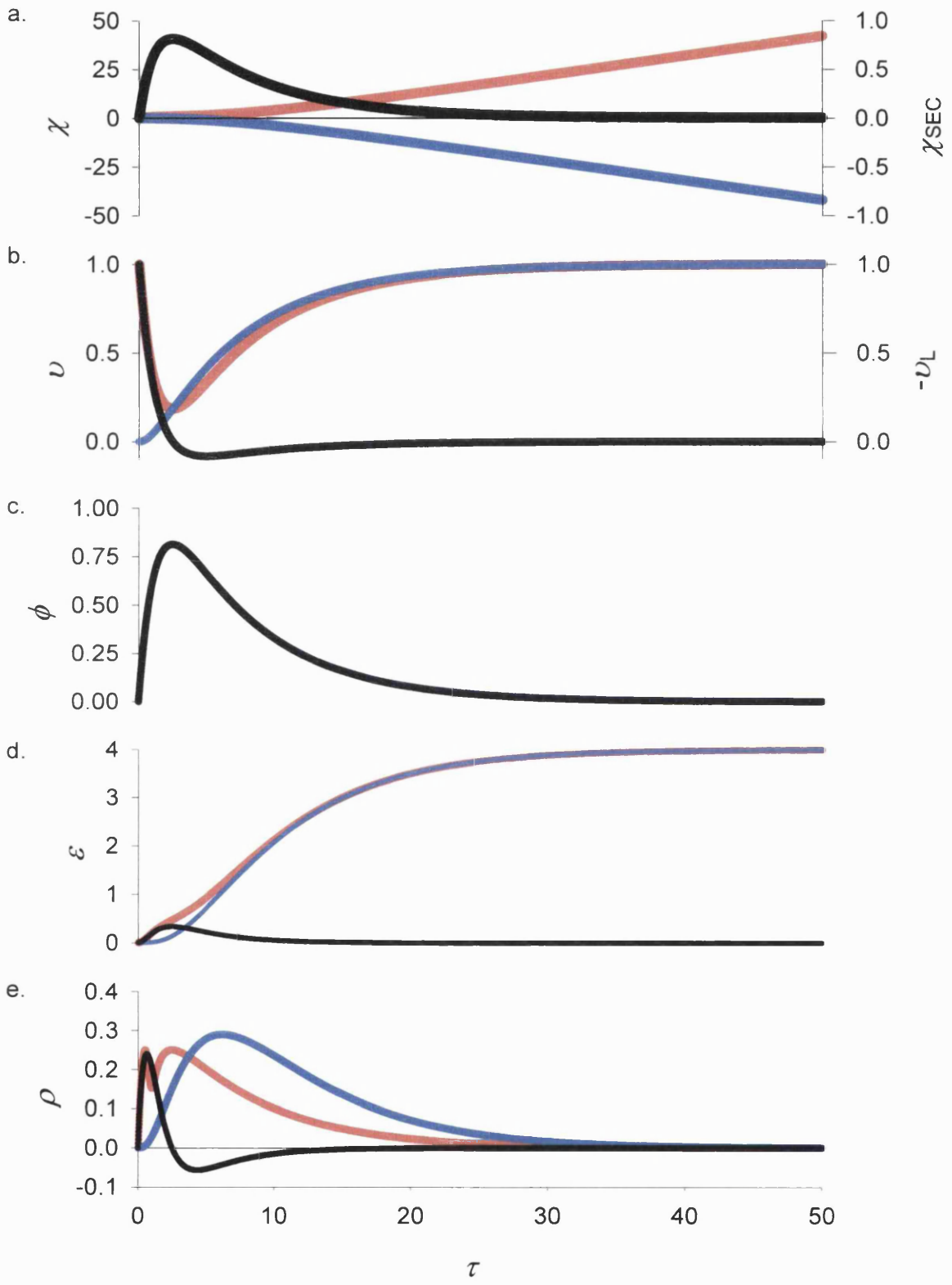

Figure 2.7.A. Time-course of movement (χ; panel a), velocity (υ; panel b), force (φ; panel c), mechanical energy (ε; panel d) and power (ρ; panel e)in the CC (red), SEC (black) and a purely inertial L (blue) during a simulated contraction. $\Xi = 8$.

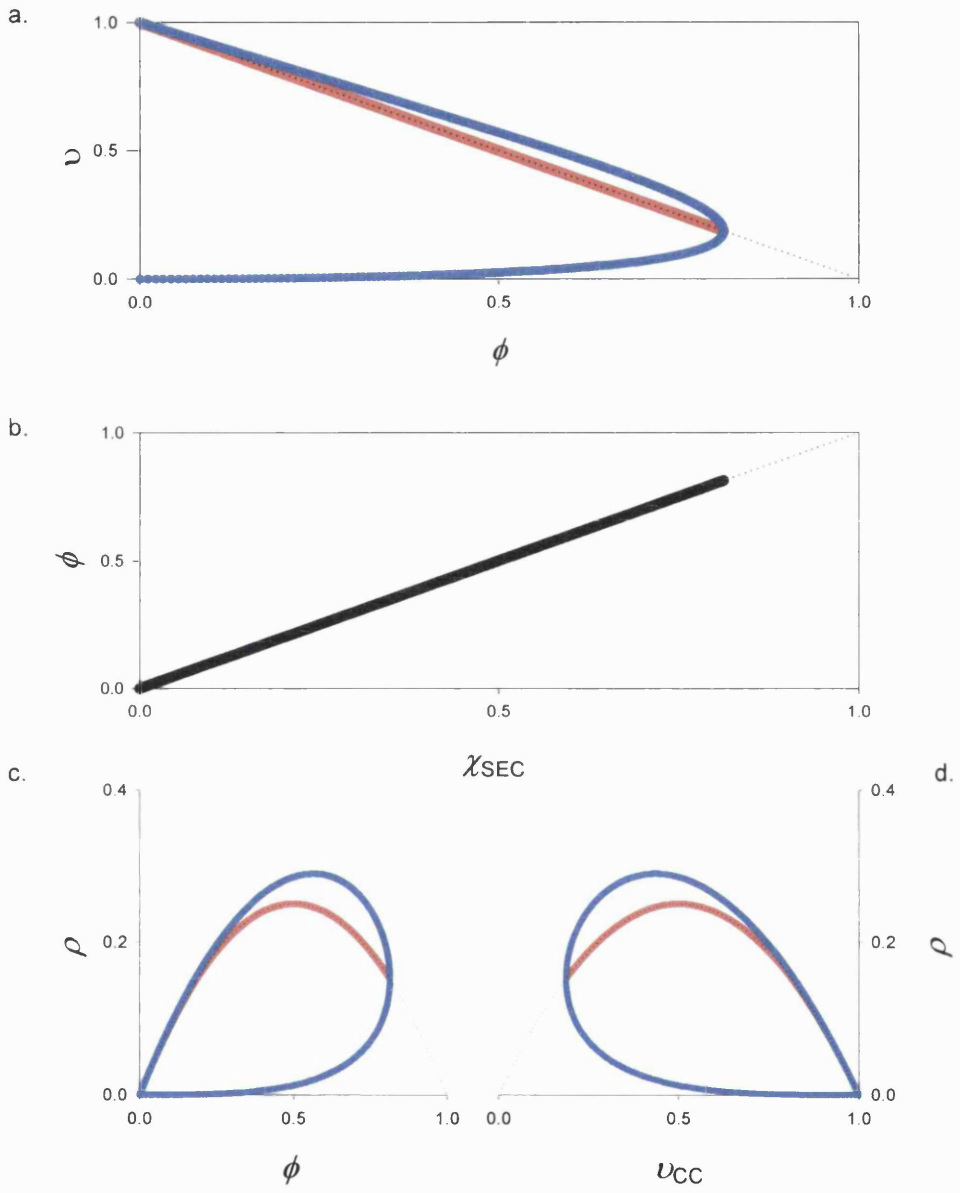

Figure 2.7.B. Results from simulated contraction where $\Xi = 8$. Graph a: L (blue) and CC (red) velocity are plotted against the force. CC force-velocity relationship (black dotted line). Graph b: Force plotted as a function of SEC extension (thick black line); SEC force-extension relationship (thin black line). Graph c: CC (red) and L (blue) power plotted against the force; CC power-force relationship (black line). Graph d: CC (red) and L (blue) power plotted against the CC velocity ; CC power-velocity relationship (black line).

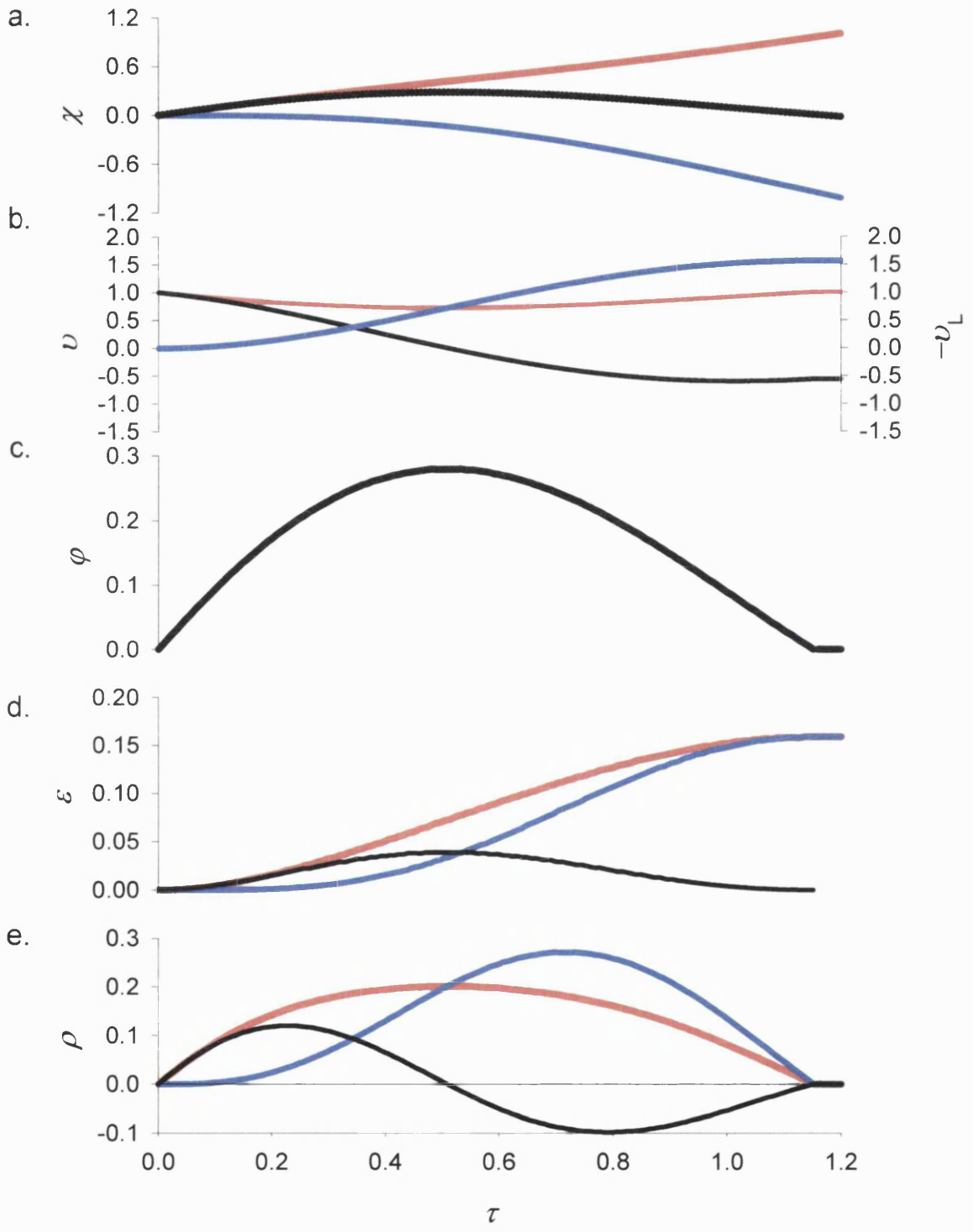

Figure 2.8.A. Time-course of movement (χ; panel a), velocity (υ; panel b), force (φ; panel c), mechanical energy (ε; panel d) and power (ρ; panel e) in the CC (red), SEC (black) and a purely inertial L (blue) during a simulated contraction. The red horizontal line in (e) indicates the maximal CC power (0.25 units). $\Xi = 0.13$.

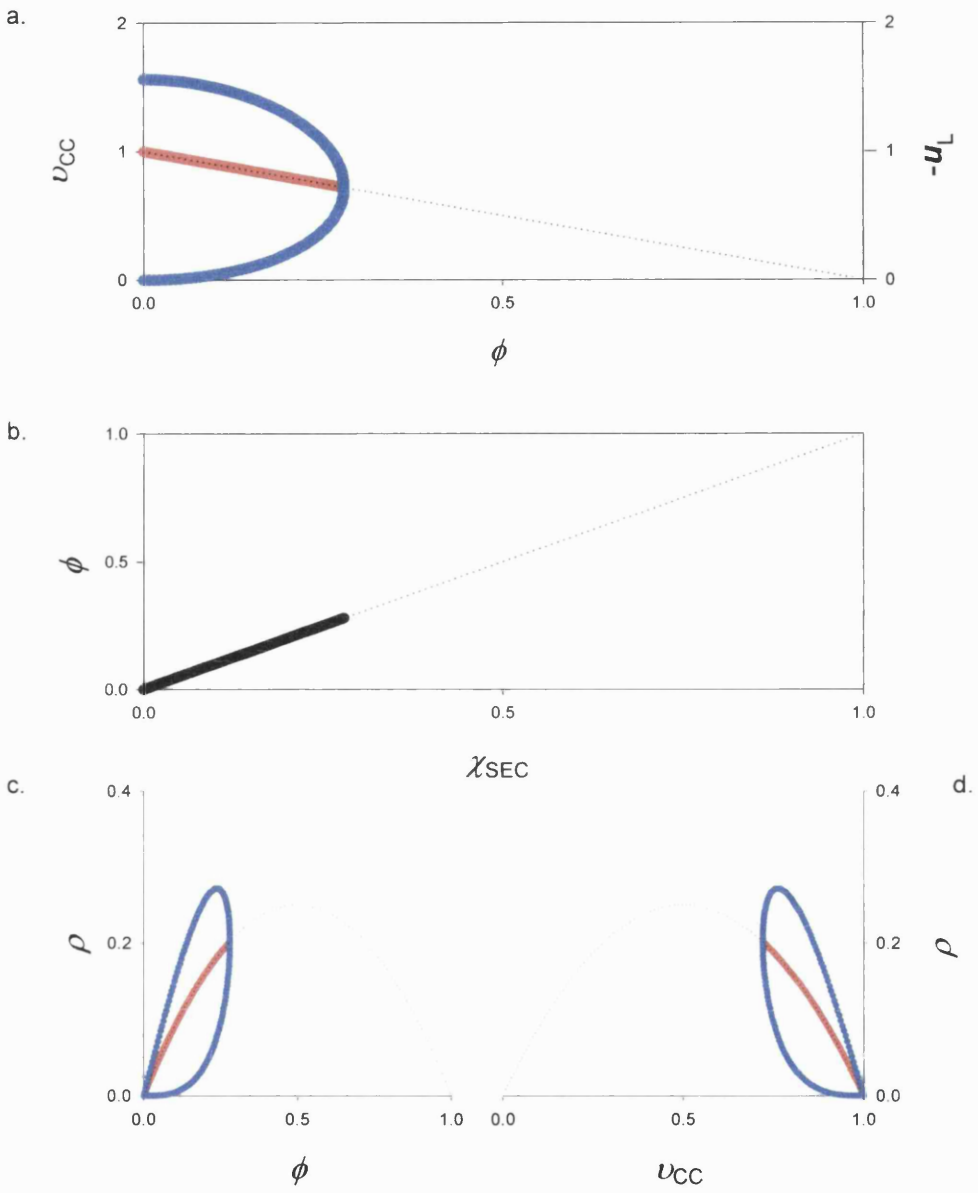

Figure 2.8.B. Results from simulated contraction where $\Xi = 0.13$. Graph a: L (blue) and CC (red) velocity are plotted against the force. CC force-velocity relationship (black dotted line). Graph b: Force plotted as a function of SEC extension (thick black line); SEC force-extension relationship (thin black line). Graph c: CC (red) and L (blue) power plotted against the force; CC power-force relationship (black line). Graph d: CC (red) and L (blue) power plotted against the CC velocity ; CC power-velocity relationship (black line).

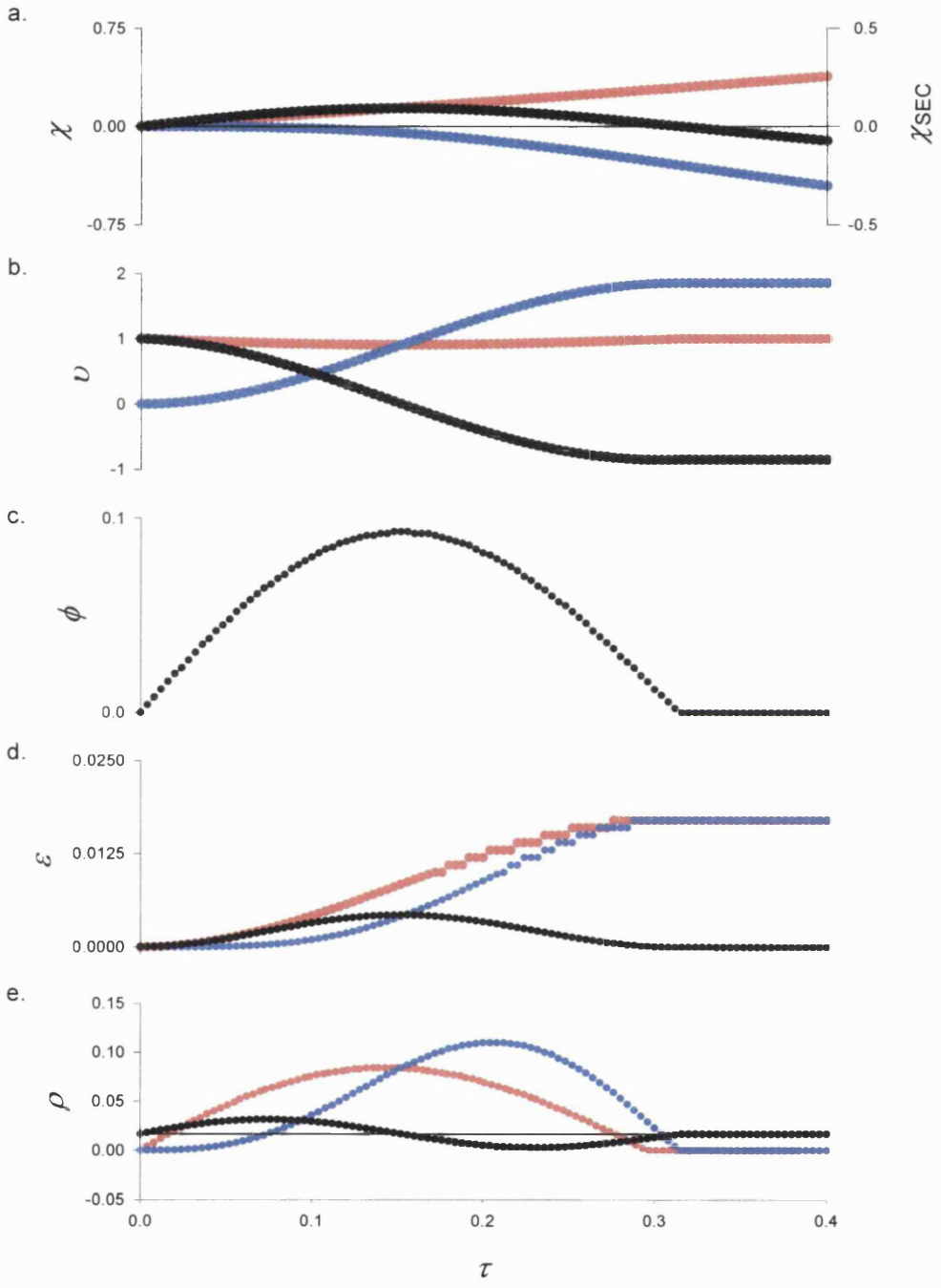

Figure 2.9.A. Time-course of movement (χ; panel a), velocity (υ; panel b), force (φ; panel c), mechanical energy) (ε; panel d) and power (ρ; panel e) in the CC (red), SEC (black) and a purely inertial L (blue) during a simulated contraction. $\Xi = 0.01$.

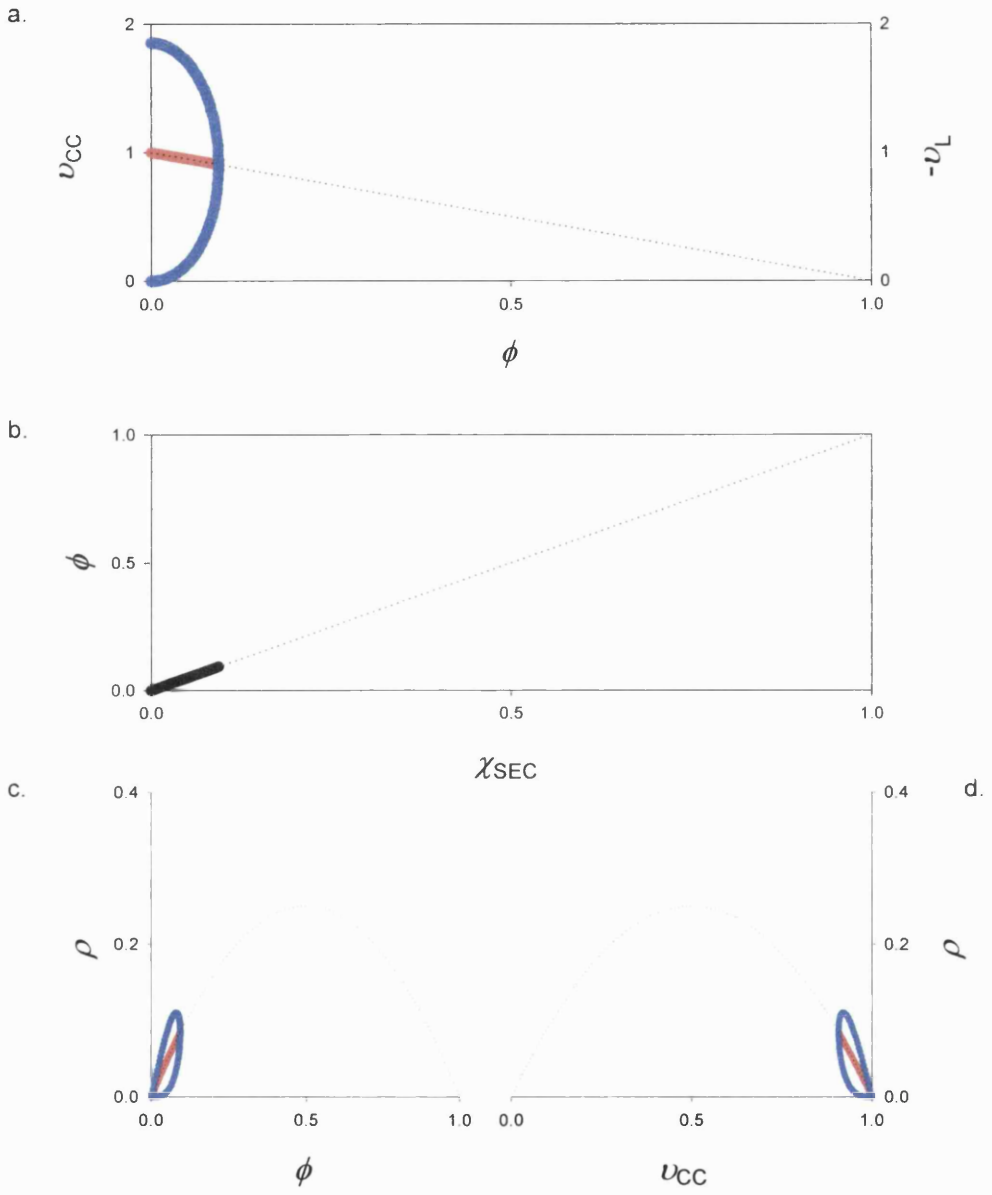

Figure 2.9.B. Results from simulated contraction where $\Xi = 0.01$. Graph a: L (blue) and CC (red) velocity are plotted against the force. CC force-velocity relationship (black dotted line). Graph b: Force plotted as a function of SEC extension (thick black line); SEC force-extension relationship (thin black line). Graph c: CC (red) and L (blue) power plotted against the force; CC power-force relationship (black line). Graph d: CC (red) and L (blue) power plotted against the CC velocity ; CC power-velocity relationship (black line).

6.1.2. Effects of constants

6.1.2.1. Effects of Ξ

It can be visualised from figures 2.6-2.9, that the time course of the mechanical events during a contraction differs for different values of normalised load, Ξ. This is because the slope of the load acceleration-force relationship changes when Ξ changes (Figure 2.10).

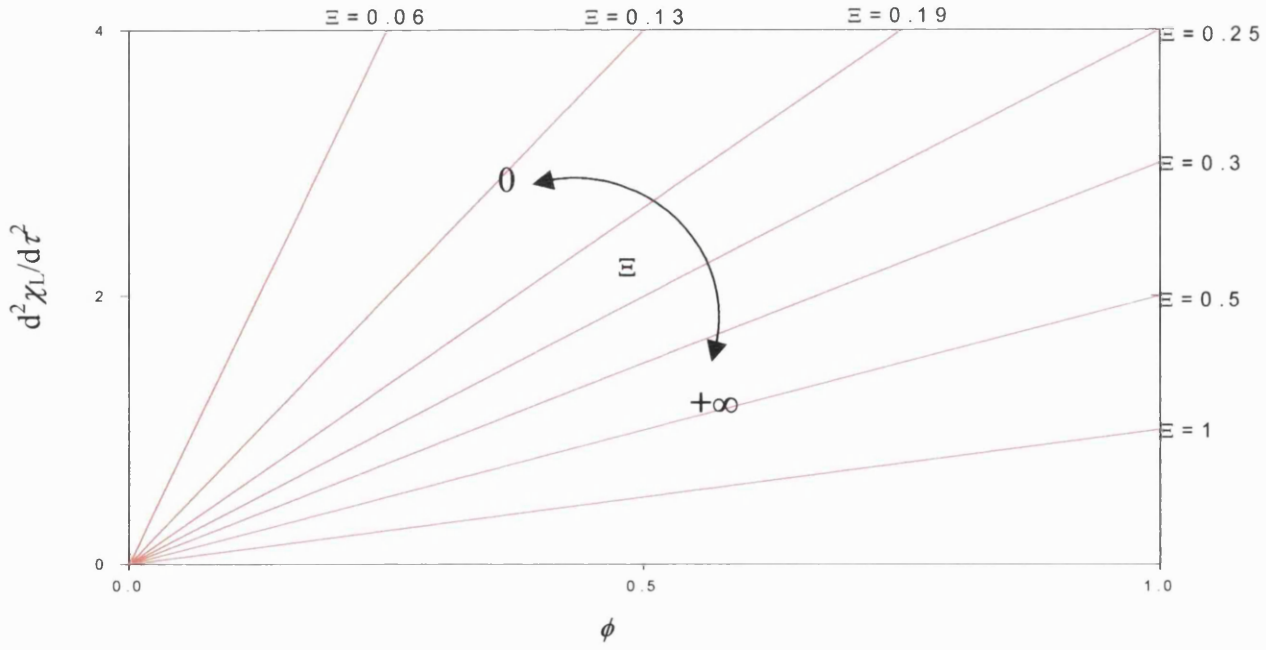

Figure 2.10. Normalised load acceleration-force relationship for different levels of normalised load, Ξ. The slopes of the different lines are Ξ^{-1}. Notice how as Ξ tends to zero, load acceleration for a given force tends to infinity and as Ξ tends to infinity, acceleration for a given force tends to zero.

6.1.2.1.1. Ξ and contraction duration

Given enough time, any force, no matter how small, can accelerate an inertial load, no matter how large its inertia is, to any desired velocity. Recall that a simulated contraction in this thesis is considered to be 'complete' when the CC velocity attains its final asymptotic value within six decimal places. When the load is purely inertial this final value is equal to the maximal CC shortening velocity, $V_{CC_{max}}$. In order for this condition to be satisfied, L must be moving at a velocity at least equal to $V_{CC_{max}}$ at the end of a contraction. Otherwise the CC will be able to 'catch up' with the load and keep the SEC stretched, thereby maintaining a level of force in the system to a value that is greater than zero. This force would prevent attainment of $V_{CC_{max}}$ by the CC. The greater the normalised inertia, Ξ, the longer it takes for a CC with 'fixed' force-velocity generating capabilities to accelerate that inertial load from zero velocity to $V_{CC_{max}}$ in order for contraction to reach 'completion'.

The fact that it takes longer for L to be accelerated to a given velocity as its inertia increases is shown in figure 2.11. The time at which V_{CC} reaches the value of 0.9 is represented on the graph. This is because the value of 1 is approached asymptotically with time and it is thus easier to resolve when a certain proportion of the CC maximal shortening velocity is achieved.

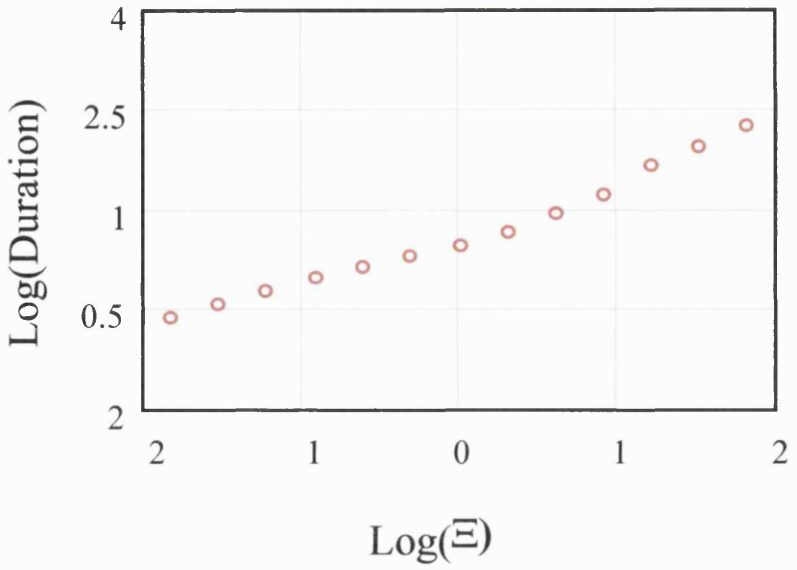

Figure 2.11. Logarithm of normalised time for CC velocity to reach 0.9 plotted as a function of the logarithm of Ξ. Time has a resolution of 10^{-3} normalised time units.

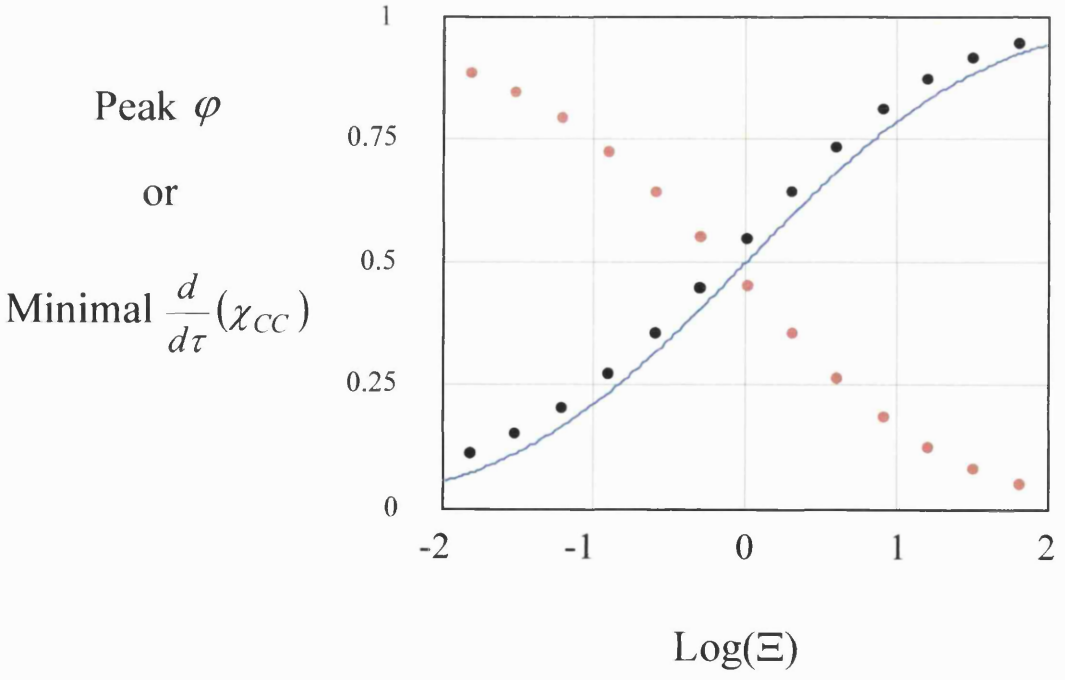

Figure 2.12. Peak normalised force (black points) and minimal CC velocity (red points) plotted as a function of the logarithm of the normalised inertial load 12 ($0.015 \leq \Xi \leq 64$). The blue curve is a cumulative probability function curve containing only two natural constants (see page 150).

6.1.2.1.2. Ξ and peak force

The peak force achieved during a contraction rises with the load as shown in figure 2.12. In the normalised model described in this section, the peak force is equal to the maximal extension of the SEC during a contraction.

SEC extension is equal to the sum of CC and L movement (equation (2.2)). A large inertial load accelerates less compared to a smaller one in response to a given force applied to it for a given period of time. This also means that the larger inertia also moves less than the smaller one during that time. The larger the inertial load, the less L moves and the more the SEC stretches to accommodate the CC length changes. As a result the peak SEC extension and hence the peak force, will be increasing with the load. As Ξ however tends to infinity, the contraction will initially resemble an isometric contraction and the peak SEC extension and force would be close to their maximal value, which is one. Thus the peak force-logarithm of the load curve will be approaching asymptotically the value of one as Ξ tends to infinity. As Ξ tends to zero, acceleration of L to $V_{CC_{max}}$ will be almost instantaneous and therefore SEC extension will be approaching zero.

The shape of the peak force-load curve resembles that of a cumulative frequency distribution function. An attempt was made to fit this curve with a cumulative frequency distribution function containing two natural constants, namely e and π (figure 2.12, blue trace):

$$peak \quad \varphi = \frac{1}{\pi} \cdot \int_{-\infty}^{\log(\Xi)} e^{-\frac{\log(\Xi)^2}{\pi}} \cdot d\Xi$$

The position and shape of this curve can be altered by inclusion of more constants in the above equation, in a similar manner as in a normal distribution curve. No exact match between the two curves could be found when a third constant was included. It can be seen on the graph that there is an asymmetry in the difference between the force-load points and the cumulative frequency function points away from the middle axis. As a result of this asymmetry the difference between the most extreme points in the two curves is less compared to the more central ones. As the exact mathematical description of the relationship appears to be complicated by the involvement of several factors, further investigation was postponed for some later work whose scope is outside that of this thesis.

6.1.2.1.3. Ξ and V_{CC} at peak force

As a result of the relationship between normalised force and velocity (equation (2.33)), the relationship of the CC shortening velocity at the time of peak force (i.e. the minimal CC velocity) and the load is simply a reflection of peak force-load relationship across the axis $\varphi = 0.5$ or $\upsilon_{CC} = 0.5$ (figure 2.12). In other words the red points on this figure are the mirror image of the black points across a horizontal axis through the value of 0.5 units in the vertical axis.

6.1.2.1.4. Ξ and maximal rate of force rise and decline

As the initial level of force in the system is zero, the CC always starts shortening at its maximal shortening velocity. As L has inertia and its initial velocity is zero the initial rate of change of SEC length and hence force is

maximal and equal to one, independently of the magnitude of the load (figure 2.13; red points).

However, the maximal rate of force decline after peak force has been achieved, declines with the load (figure 2.13; blue points). This is due to the fact that larger loads accelerate less compared to smaller loads in response to the same force, as already mentioned above. As a result, the difference between the speed at which the CC shortens and that at which L moves during the SEC recoiling phase of the contraction is smaller, the greater the inertia of the load. As this difference reflects the speed at which the SEC recoils, it also reflects the rate at which force declines in this particular model with a linear SEC force-extension relationship. It can be seen from the graph that as the load tends to zero, the maximal rate of force decline tends to one. As the inertia of the load tends to infinity, the rate tends to zero.

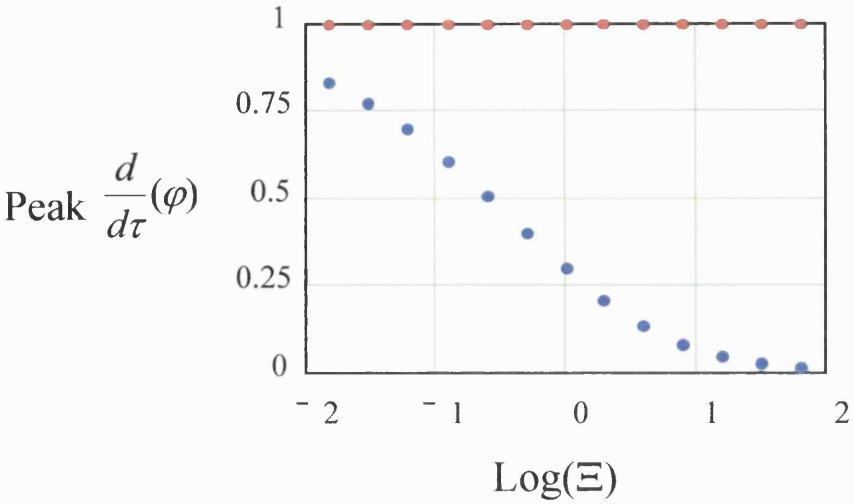

Figure 2.13. Maximal rate of force rise (red) and fall (blue) plotted as functions of the logarithm of the normalised inertial load. The absolute maximal rate values are shown (otherwise the maximal rate of force decline would be plotted on a negative Y-axis scale).

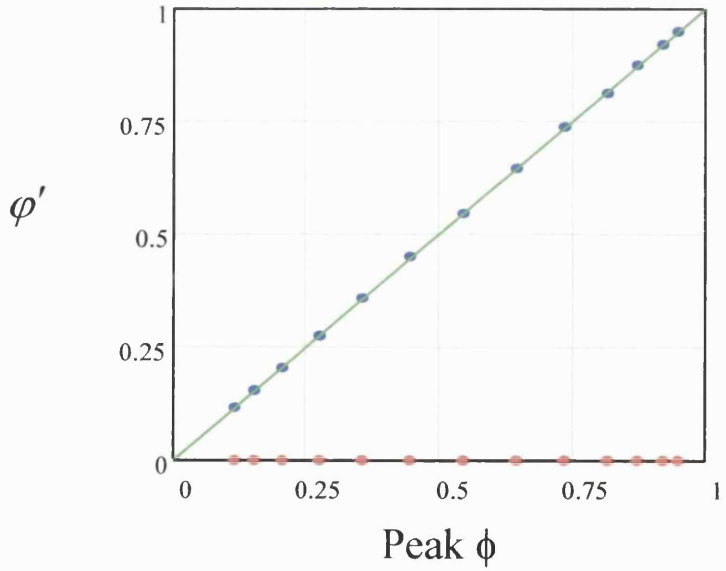

Figure 2.14. Force at maximal rate of force development (red points) and decline (blue points) expressed as proportion of the peak force achieved in that contraction (φ') plotted as a function of that peak force. The line $y = x$ is also plotted (green line).

6.1.2.1.5. Ξ and force at which maximal rates of force rise and decline occur

As explained at the beginning of the previous section, the peak rate of force development always occurs when the force in the system is zero independently of the peak force achieved during the contraction (figure 2.14). A more interesting relationship is that between the force at which the maximal rate of force decline is observed and the peak force. When the force at which the maximal rate of force decline is expressed as a proportion of the peak force achieved in the corresponding contraction (φ'), and this proportion is plotted against the corresponding peak force, a linear relationship arises. The slope of this relationship is equal to one (blue points and green line in figure 2.14). This means that the force at which the maximal rate of force decline occurs is equal to the square of the peak force. In this way the normalised force at which the maximal rate of force decline is occurring can be easily estimated. For example, if the peak force in a contraction is 0.25, the force at which the maximal rate of force decline occurred in that contraction is going to be 0.25 times 0.25, which is equal to 0.0625.

6.1.2.1.6. Ξ and final V_L

Recall that given enough time any purely inertial load, no matter how large, can be accelerated to any desired velocity by a force and that 'completion' of a contraction required L to be accelerated to a speed at least equal to that of $V_{CC_{max}}$ (pp. 148). Also recall that the larger the inertia, the smaller the difference between the speed at which the CC shortens and the speed at which L moves towards the centre of the system (pp. 151). This can be visualised by comparing the figures 2.6-2.9.A and B (previous section) and from in figure

2.15 that shows the maximal final load velocity plotted as a function of the load. As the final velocity of the load corresponds to the load velocity at the time at which CC shortening velocity is equal to one, within six decimal places precision, L velocity may not be exactly equal to its final velocity during each contraction. The difference however between the final L velocities shown here and the actual ones is expected to be very small. When the load is very light, it can be accelerated up to approximately twice the maximal CC shortening velocity (e.g. figure 2.9). As the load tends to infinity the maximal load velocity tends to one, i.e. to the CC maximal shortening velocity.

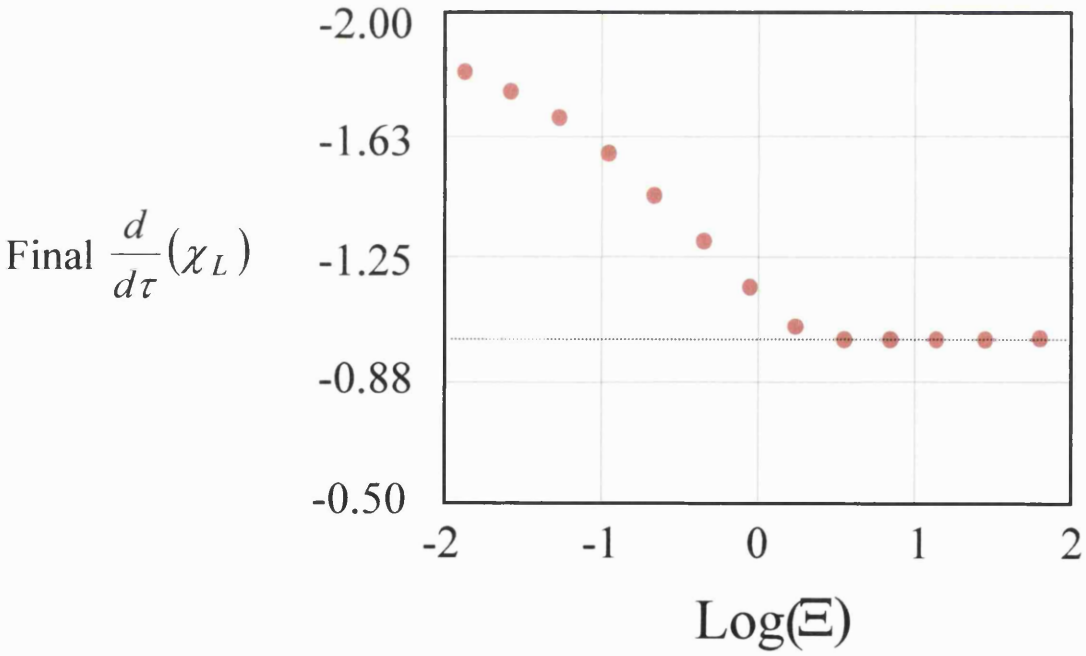

Figure 2.15. Maximal load velocity plotted as a function of the logarithm of the normalised inertial load. Dotted line corresponds to a normalised load velocity of –1. The minus sign indicates motion of the load towards the centre of the SEC. The Y axis is inverted.

6.1.2.1.7. Ξ and maximal ε_{CC} and ε_{L}

The maximal work performed during a contraction by the CC and the kinetic energy of L increase with the load (figure 2.16). As the SEC cannot generate mechanical energy by itself and the force during a contraction rises to a peak and then falls to zero, the kinetic energy of L at the end of the contraction is equal to the total mechanical work generated by the CC (figure 2.16).

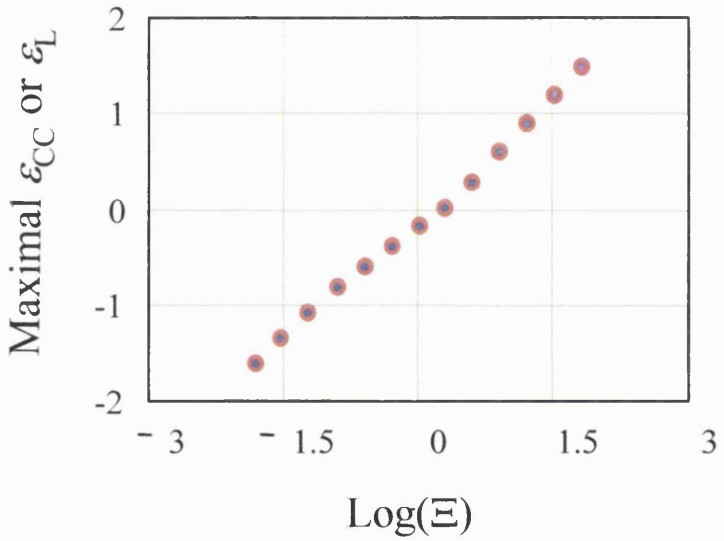

Figure 2.16. Logarithm of the maximal mechanical energy produced by the CC during a contraction (red) or peak kinetic energy of L (blue) during the same contraction plotted as functions of the logarithm of the normalised inertial load.

6.1.2.1.8. Ξ and maximal ε_{SEC}

The part of the SEC force-extension relationship utilised in a contraction differs for different amounts of normalised inertia (graph b; figures 2.6-2.9B). The peak elastic potential energy content of the SEC is the integral of the change in force with respect to the change in SEC length from zero to the maximal elongation achieved in a particular contraction. More simply, it is the maximal area under the SEC force-extension curve that was utilised during a particular

contraction. The greater the load, the greater the peak force and SEC extension and hence the elastic potential energy of the SEC as shown in figure 2.17.

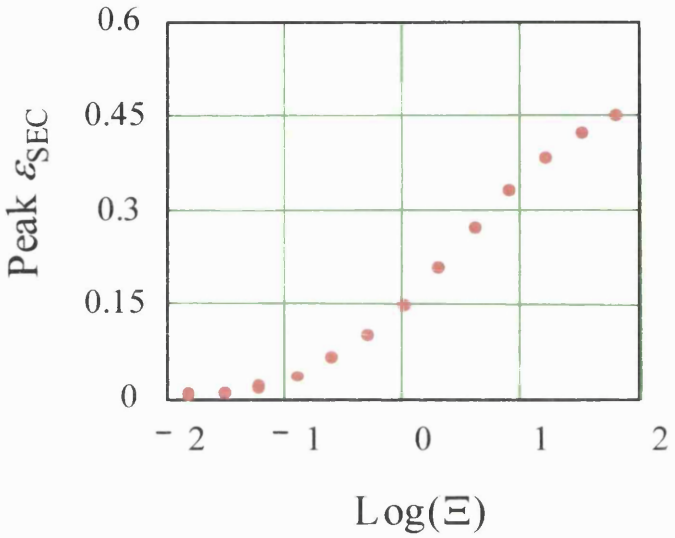

Figure 2.17. Peak elastic potential energy in the SEC plotted as a function of the logarithm of the normalised inertia.

6.1.2.1.9. Ξ and peak ρ_{CC}

In this normalised model there is symmetry in terms of the force-velocity properties of the CC, as the equation:

$$\frac{d}{d\tau}(\chi_{CC}) = 1 - \varphi$$

can also be written as:

$$\varphi = 1 - \frac{d}{d\tau}(\chi_{CC})$$

and both $\frac{d}{d\tau}(\chi_{CC})$ and φ take values that range from 0 to 1. As power can be expressed as the product of force and velocity the following is true:

$$\rho_{CC} = \varphi \cdot \frac{d}{d\tau}(\chi_{CC}) \equiv \varphi \cdot (1-\varphi) = \varphi - \varphi^2$$

Given the symmetry of the force-velocity relationship, the above equation can also be written as:

$$\rho_{CC} = \frac{d}{d\tau}(\chi_{CC}) - \left(\frac{d}{d\tau}(\chi_{CC})\right)^2$$

This is a quadratic equation with a maximum at $\frac{d}{d\varphi}(p_{CC}) = 0$ or $\frac{d}{d\left(\frac{d}{d\tau}(\chi_{CC})\right)}(p_{CC}) = 0$. Taking the first of these two expressions as an example and carrying out the above differentiation which is going to give as the value of the peak power that the CC can generate and force at which it occurs:

$$\frac{d}{d\varphi}\left(\varphi - \varphi^2\right) = 0$$

which after differentiation gives:

$$1 - 2 \cdot \varphi = 0$$

Therefore, the normalised force at which peak power occurs is 0.5. Substituting $\varphi = 0.5$ in the above equation that gives p_{CC} as a function of the normalised force we get:

$$\rho_{CC} = 0.5 - 0.25 = 0.25$$

Therefore, when the normalised force is equal to 0.5, the CC generates its maximal power, which has the value of 0.25. The same result would have been obtained if the expression of power as a function of the CC shortening velocity had been used, with the peak power (0.25 normalised units) occurring at a dimensionless velocity 0.5 units.

Figures 2.6-2.9B (panels c and d) show that when the load is light, the force in the system does not rise as high as 0.5 and nor does the CC shortening velocity drop as low as 0.5. As a result the CC does not generate the maximal power that it is capable of generating during the contraction. On the contrary, when the normalised inertial load is large enough (Ξ is close to one or greater), the force and CC shortening velocity go through the value of 0.5 during the contraction and maximal CC power is achieved transiently (Figure 2.18). Notice the two distinct peaks in the time course of CC power output when the load is sufficiently high (Figures 2.6-2.7 A; panel e). In these examples, maximal CC power is achieved twice during the contraction as the force and CC shortening velocity go through the point (0.5,0.5) in the force-velocity plot twice during the contraction, once while force is rising and once while force is falling.

6.1.2.1.10. Ξ and peak ρ_L

Figures 2.6-2.9A and B show that the peak external power during a complete contraction exceeds the peak power developed by the CC. The way the CC and SEC mechanical outputs combine to deliver to L more power than the CC alone can generate has been described above (see section 6.1.1). The peak power generated by the CC and peak power delivered to L plotted as functions of the logarithm of the normalised inertial load are shown in figure 2.18.

The relationship between the peak power delivered to L and the normalised inertial load has an optimum. At loads larger or smaller, the power delivered to L drops from its optimal value. As explained earlier, when Ξ is large the rate at

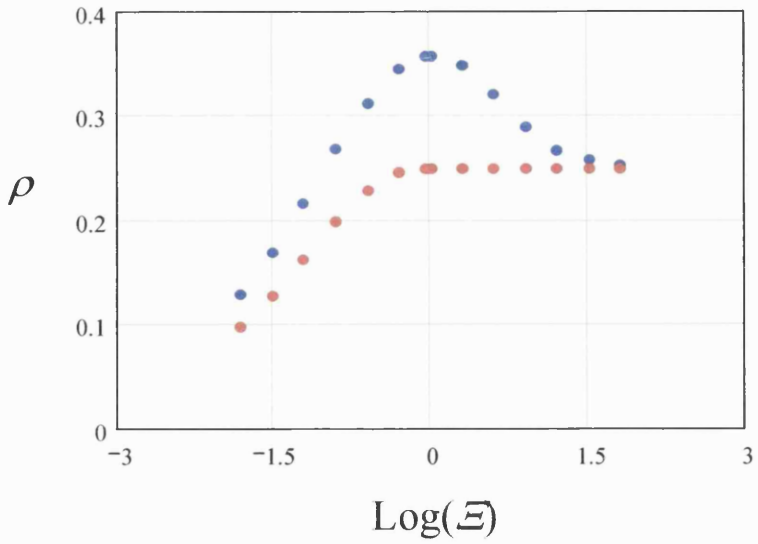

Figure 2.18. Peak CC power (red) and peak power delivered to L (blue) both expressed in normalised terms and plotted as functions of the logarithm of the normalised load, Ξ.

which the SEC recoils diminishes and so does its power delivery to L. Notice that the power generating capability of the CC is at its optimum within this region of large inertial loads. As Ξ tends to infinity the power delivered to L tends to 0.25, i.e. the maximal power that the CC alone can generate.

The situation is slightly more complicated on the other side of the optimum as the normalised load becomes lighter. As the load becomes progressively smaller, the force developed in the system becomes smaller. This results in less elastic potential energy stored in the SEC which can be recovered during the falling force phase of the contraction and also in the CC not reaching the force level required for maximal power production. In this region, as the load tends to zero the power delivered to the load also tends to zero.

6.1.2.1.11. Timing of peak ρ_{CC} and peak ρ_L

Note that the peak power delivered to the load and the peak power output of the CC do not always occur at the same time. When the normalised load is optimal for external power generation ($\Xi = 1$) the time course of ρ_{CC} has two relatively flat peaks (figure 2.19). The peak external power occurs slightly after the end of the second ρ_{CC} peak. When the load is not much greater than 1 normalised units but heavy enough for the force in the system to rise beyond the value of 0.5 which is optimal for power generation by the CC, the lighter the normalised load, the greater the delay for achieving peak power after the peak CC power has been attained (figure 2.19; graphs A and B). As the normalised load becomes progressively heavier, the time course of ρ_{CC} has two distinct peaks and peak power is delivered to L before the second peak is reached (figure 2.19; graph C). At very heavy loads, the peak power delivered to L, is almost equal to the peak CC power (due to the very slow SEC recoil). At such heavy loads, the maximal power of L and that of the second peak of the CC power tend to occur at the same time (figure 2.19; graph D).

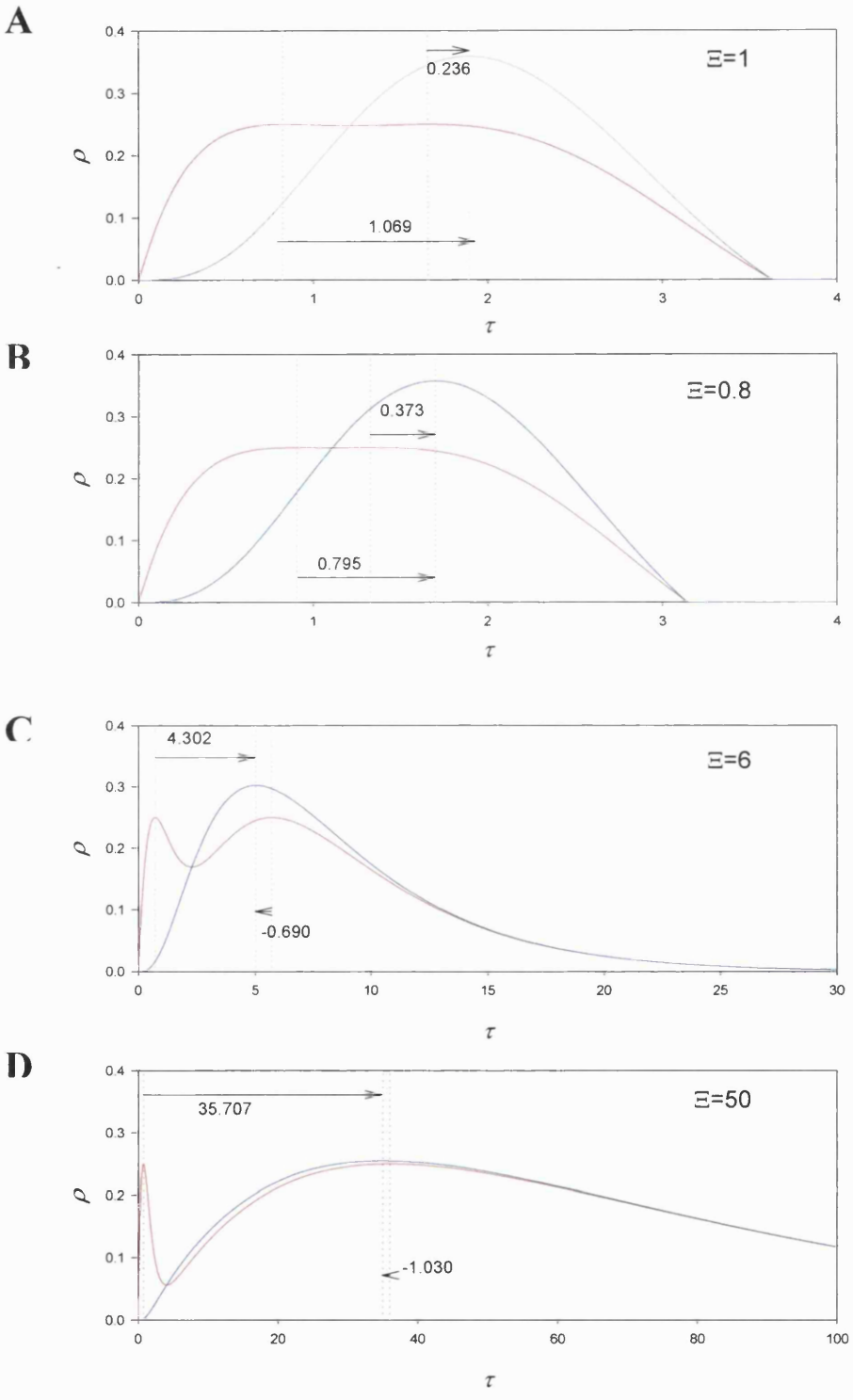

Figure 2.19. Time-course of normalised CC (red) and L (blue) power output for three different normalised loads.

6.1.2.1.12. Ξ and power ratio

As an index of the extent to which the maximal power that the CC alone can generate (i.e. 0.25 in this model) is amplified during a contraction, the power ratio *R* is used:

$$R = \frac{\left(Peak \quad power \quad delivered \quad to \quad L \right)}{\left(Maximal \quad power \quad the \quad CC \quad can \quad generate \right)}$$

In this model where the force-velocity relationship of the CC is assumed to be linear, the power ratio can also be defined as:

$$R = \frac{\left(Peak \quad power \quad delivered \quad to \quad L \right)}{0.25}$$

Another term (less frequently used in this thesis) is the CC power ratio, which is defined as:

$$R_{CC} = \frac{\left(Peak \quad CC \quad power \right)}{\left(Maximal \quad power \quad the \quad CC \quad can \quad generate \right)}$$

or for this model:

$$R_{CC} = \frac{\left(Peak \quad CC \quad power \right)}{0.25}$$

Both these dimensionless quantities are plotted against log(Ξ) in figure 2.20. The *R*-log(Ξ) trace shows the extent to which the maximal power of a muscle inside an animal's body can be amplified due to the presence of its series

elasticity before it appears to the external environment, under the assumptions made in this model. It is obvious from the graph that there is an optimal value. This value is 1.436 (three decimal places) and it occurs when Ξ is approximately equal to one. That means that when the load, as it is sensed by the muscle-tendon complex, is one unit the maximal power that the CC is capable of generating is amplified 1.436 times. As the power ratio is the same whether the model is normalised or expressed in absolute terms, this value represents the upper limit for power amplification no matter what the values of $V_{CC_{max}}$, F_{max}, K and M are. At normalised loads greater or smaller from the optimal value of one, R declines. It approaches the value of one asymptotically as the load tends to infinity, indicating diminished contribution by the SEC. R approaches the value of zero as the normalised load tends to zero, as the power delivering capacity of both the SEC and the CC declines.

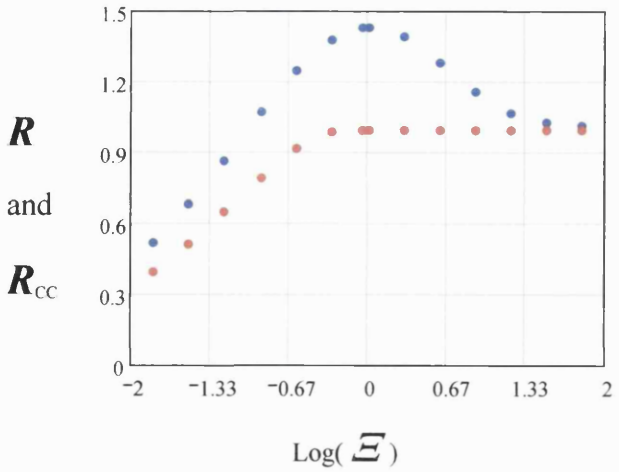

Figure 2.20. Peak power delivered to L (blue) and peak power developed by the CC (red) expressed as fractions of the maximal power that the CC can generate and plotted against the logarithm of the normalised load.

6.1.2.2. Effects of *H*

By changing H in equations (2.6) and (2.35) the curvature of the SEC force-extension relationship increases. This is illustrated in figure 2.21.

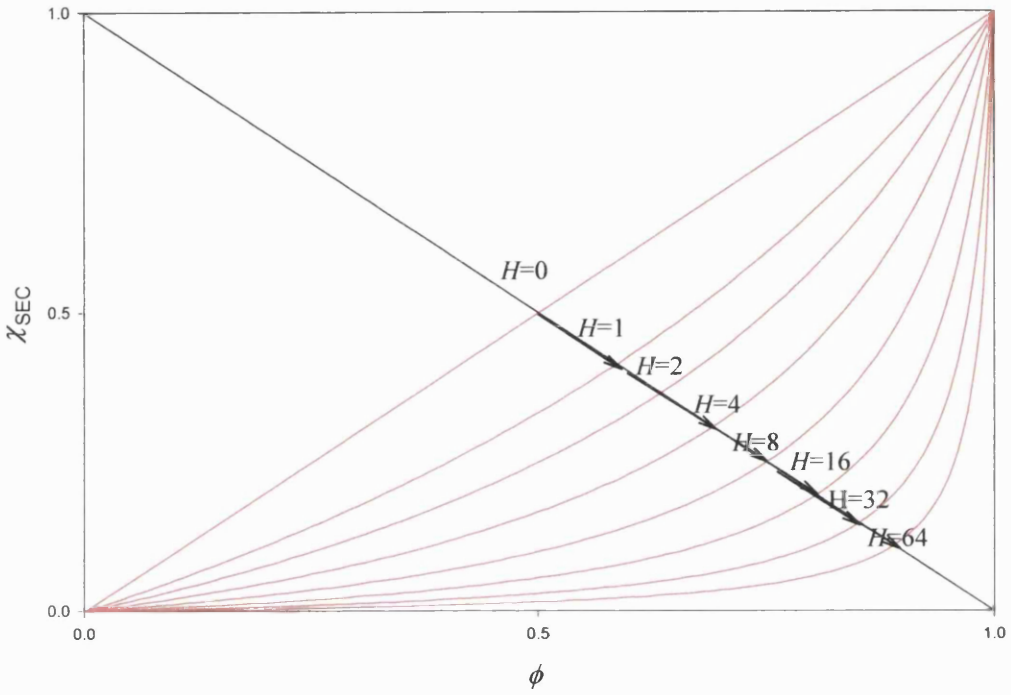

Figure 2.21. Normalised SEC force-extension relationships with different positive values of H. The greater the value of H, the more the curve deviates from a straight line.

The effect of H on the mechanical output of the system is demonstrated by the change in the power ratio-load relationship as shown in figure 2.22. As ***H*** increases, both the peak power ratio and also the load at which it occurs decrease. This effect appears to be due to the reduction in the elastic potential energy that the SEC is capable of storing and releasing during a contraction as the value of ***H*** increases beyond zero. The area under the force-extension curve

represents the capacity for elastic potential energy storage in the SEC. This area declines for greater positive values of ***H*** (figure 2.21).

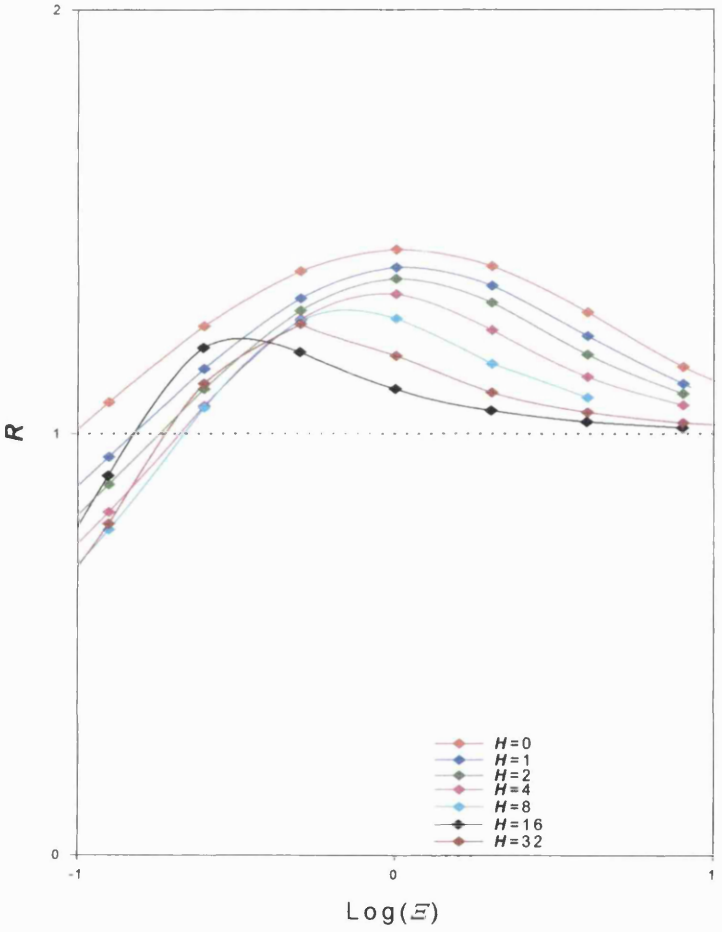

Figure 2.22. Power ratio (***R***) plotted against the logarithm of the normalised inertial load (Ξ) for different values of ***H***. Estimated values of ***H*** for the part of the FDI SEC utilised in the experiments described in the next chapter ranged between 1.068 and 4.755 (table 3.8; pp. 305).

6.1.2.3. Effects of *G*

The greater the value of ***G***, the greater the curvature of the CC force-velocity relationship (figure 2.23) and the smaller the maximal power that the CC is capable of generating. As the maximal power that the CC is capable of generating is the denominator of the power ratio, the power ratio tends to become greater as the positive value of ***G*** increases (figure 2.24). As the CC force-velocity relationship becomes more curved with ***G***, its ability to generate mechanical work decreases. As a result the elastic potential energy that can be stored in the SEC also decreases. This tends to reduce the peak power that is delivered to an external load. However, the reduction in the maximal power that the CC is capable of generating has a relatively greater effect in increasing the value of the power ratio for any given load, than the reduction in the elastic potential energy stored in the SEC has in reducing it. The difference between these two factors is not great and therefore the peak power ratio increases asymptotically from the value of 1.436 at ***G***=0, to 1.473 (3 d.p.) as ***G*** tends to infinity (figure 2.25). This asymptotic value was obtained from simulations using very large values of ***G***. Notice that there is not a sideways shift on the power ratio-load curve as was the case with ***H*** (figure 2.24).

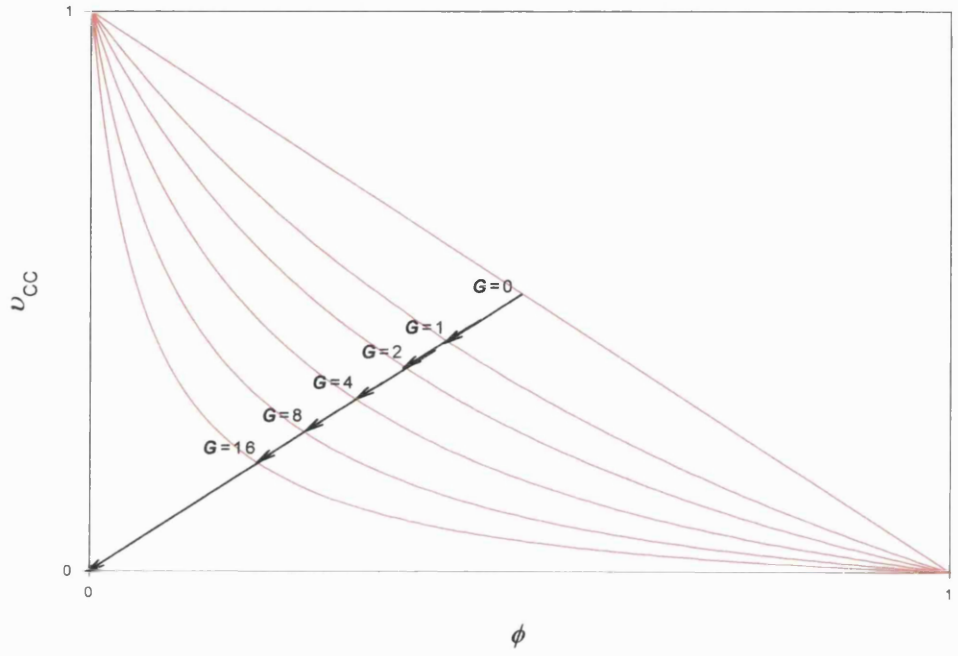

Figure 2.23. Effect of $\boldsymbol{G}$ on the normalised CC force-velocity relationship.

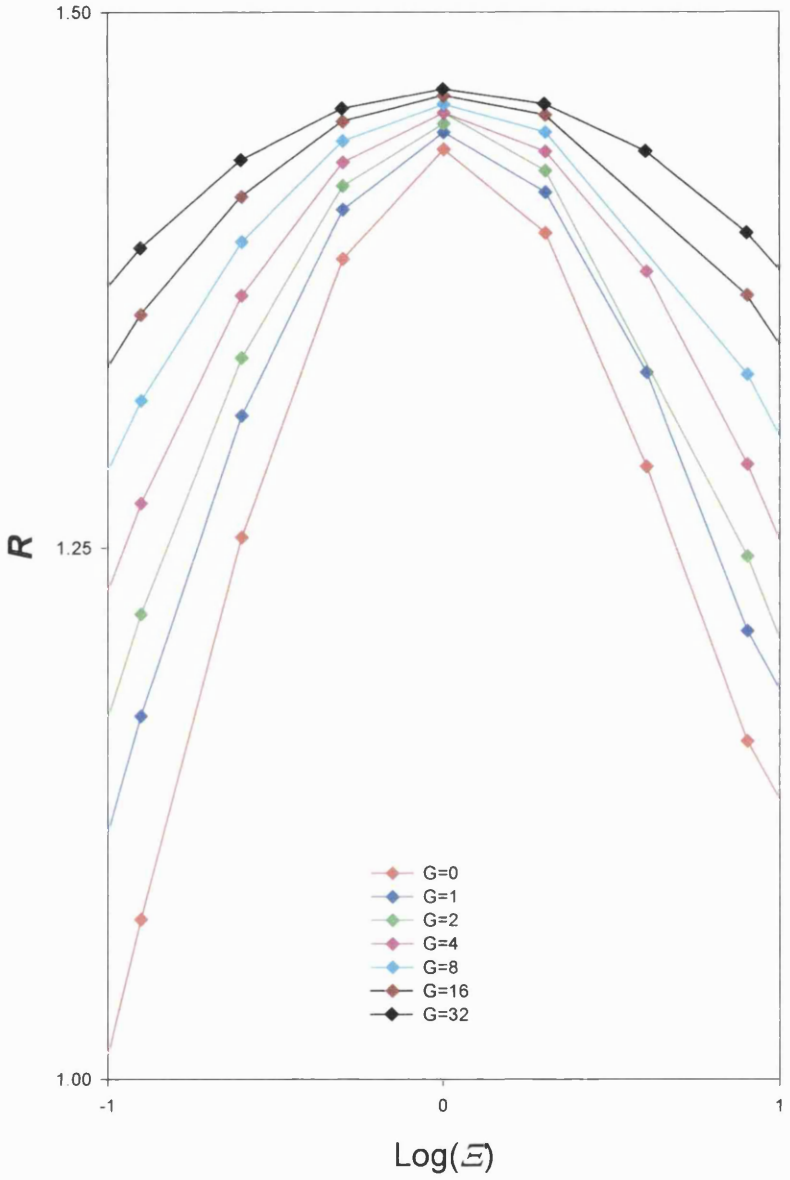

Figure 2.24. Effect of ***G*** on the ***R***-Log(Ξ) relationship. Fitting Hill's equation to the CC torque-velocity relationships of the FDI yielded values ranging from 1.9 to 171.7 (see table 3.10; pp. 312).

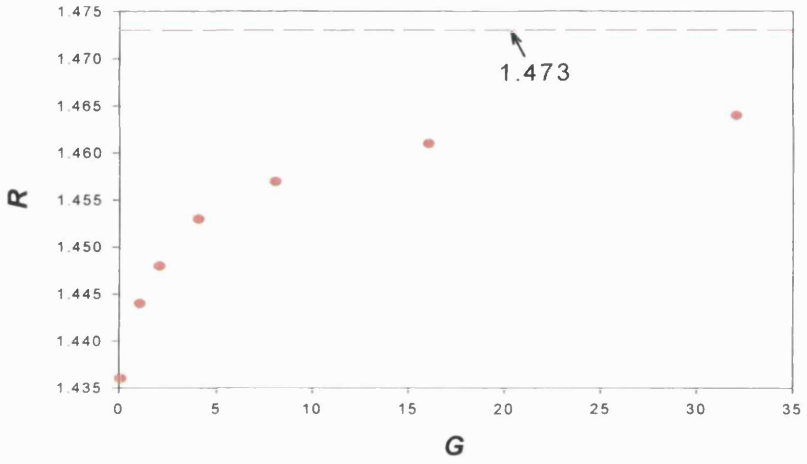

Figure 2.25. Effect of G on the peak power ratio.

6.1.2.4. Effects of τc on the time-course of the CC force-velocity output

The Hill-type hyperbolic CC force-velocity relationship represents the optimal shortening velocity that the CC can achieve as a function of the force that the CC generates. The effect of τc on the force-velocity trajectory of the CC (the path followed during a contraction) is shown in figure 2.26. As τc increases, it takes longer for the CC to reach full activation so that for each level of force there is a sub-optimal shortening velocity. If the duration of a contraction is long enough, while the activation parameter, A, is less than one the CC shortens at sub-optimal velocities and while A is approximately one it shortens at approximately optimal velocities.

The effect of different values of the time constant for activation on the value of the power ratio was not studied in detail in this work.

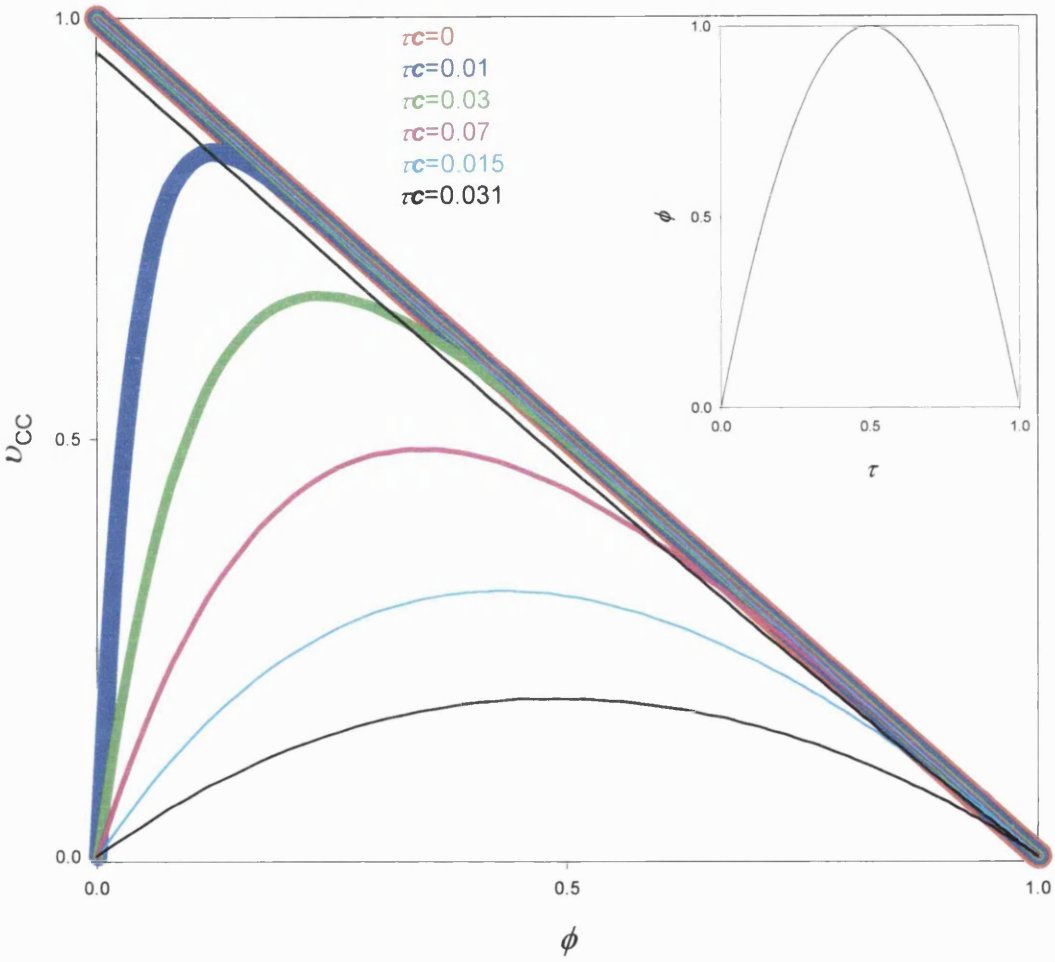

Figure 2.26. Effect of the activation time constant on the normalised CC force-velocity trajectory ($G = 0$). These trajectories start at bottom right and end at top right of the graph. The time constant is short enough to achieve full activation at some time during the contraction in all traces but the black one. The inset shows a hypothetical time-course of force during these contractions.

6.1.3. Inertial-gravitational load

The time course of mechanical events is illustrated for an inertial load ($\xi = 1$) under the influence of a constant gravitational torque ($LR \cdot \gamma$), which is different in each example (figures 2.27-2.30 A and B). The value of all other constants ($H, G, \tau c$) is zero.

At the start of the contraction there is no force in the MTC but the load experiences a constant force due to gravity. This gravitational force is exerted at a normalised distance *LR* from a centre of rotation (CR) generating a clockwise torque. This torque tends to cause a clockwise rotation of L away from its initial position which is prevented by a 'stop' (see conditions in equations (2.21) and (2.52)). Because there is no force in the MTC at the start of the contraction, the CC shortens with maximal speed. As the load is stationary all CC shortening is accommodated by SEC elongation. As a result, the force in the MTC rises and CC shortening velocity slows down. Movement of the load is not possible until the torque around the CR due to the force in the MTC exceeds the constant torque due to gravity. Until that time all the mechanical energy generated by the CC is converted into elastic potential energy in the SEC (this is not immediately obvious in the figures as CC and SEC energy are plotted on different scales). The kinetic energy of the load is, of course, zero. As a result the power in the CC and SEC are equal to each other and the power delivered to the load is zero.

Once the net torque attains an anticlockwise sense, load rotation starts. The angular acceleration of the load is proportional to the net torque around the CR. As the load has inertial properties is takes some time to attain an angular speed

equal and opposite to that due to CC shortening. Until these two speeds are equal and opposite the SEC is being stretched and the force in MTC keeps rising resulting in a rise in the net torque around the CR. The work generated by the CC further increases the SEC elastic potential energy while the rest is used to increase the gravitational potential energy and the kinetic energy of the load (the gravitational potential energy of the load is not shown in figures 2.27-2.30). As the SEC absorbs energy not all power generated by the CC is delivered to L.

At the instant the angular speed of the load due to CC shortening becomes equal and opposite to the angular speed of L, the SEC length does not change. The force in the MTC has reached its peak value and so has the net torque around the CR. The CC shortening velocity is at its minimum. No mechanical energy is absorbed or released by the SEC and therefore all CC energy output is delivered to L. As a result, the power delivered to the load become equal to the power generated by the CC.

Immediately after the instant of peak force in the MTC, L keeps accelerating attaining a higher speed than that of the CC resulting in SEC recoiling. SEC recoiling causes a reduction in the force in the MTC and the net torque around the CR. The elastic potential energy of the SEC is lowering, being converted into potential and kinetic energy of L together with the energy generated by the CC. As a result, the power delivered to L exceeds the power generated by the CC.

At some instant in time SEC recoils to such a length that the net torque around the CR is zero, i.e. the torque due to the MTC force and the torque due to gravity are equal and opposite. At that time load velocity has reached its peak value. However, the CC shortening speed is still lower than the speed of the load resulting in further recoiling and a further drop in the MTC force. This causes the net torque around the CR to attain a clockwise sense. That means that L is now accelerating in the opposite direction and its angular velocity is reduced from its peak value. SEC recoiling and reduction in the MTC-generated torque continue until the dropping speed of L and the rising speed of the CC catch up again with one another other. As the net torque around the CR is still clockwise the load keeps decelerating but the CC now shortens at a greater speed than L, stretching the SEC and causing the force in the MTC to rise. The history of mechanical events described above is repeated but under different initial conditions. The amplitude of the second oscillation of the MTC generated torque about the level of the gravitational torque is much smaller than that of the first oscillation. Such decreasing oscillations in torque (and the resulting velocity and power oscillations) keep occurring during the time course of a simulated contraction. These oscillations eventually become negligible, the net torque around the CR becomes zero and the force in the MTC constant. This constant force in the MTC maintains the SEC stretched to a constant length, now having a constant elastic potential energy. The load has a constant speed and kinetic energy although its gravitational potential energy increases with displacement from its initial position. The work for the increment in the gravitational potential energy of the load is, of course, provided by CC shortening.

If the gravitational torque is too large for the MTC to overcome (figure 2.30), the load does not move and force in the MTC rises the CC maximal isometric force with a concomitant reduction in its shortening velocity. CC shortening is 'buffered' by SEC stretching and all CC generated energy is converted into elastic potential energy. The load has zero kinetic and gravitational potential energy and the power delivered to it is zero.

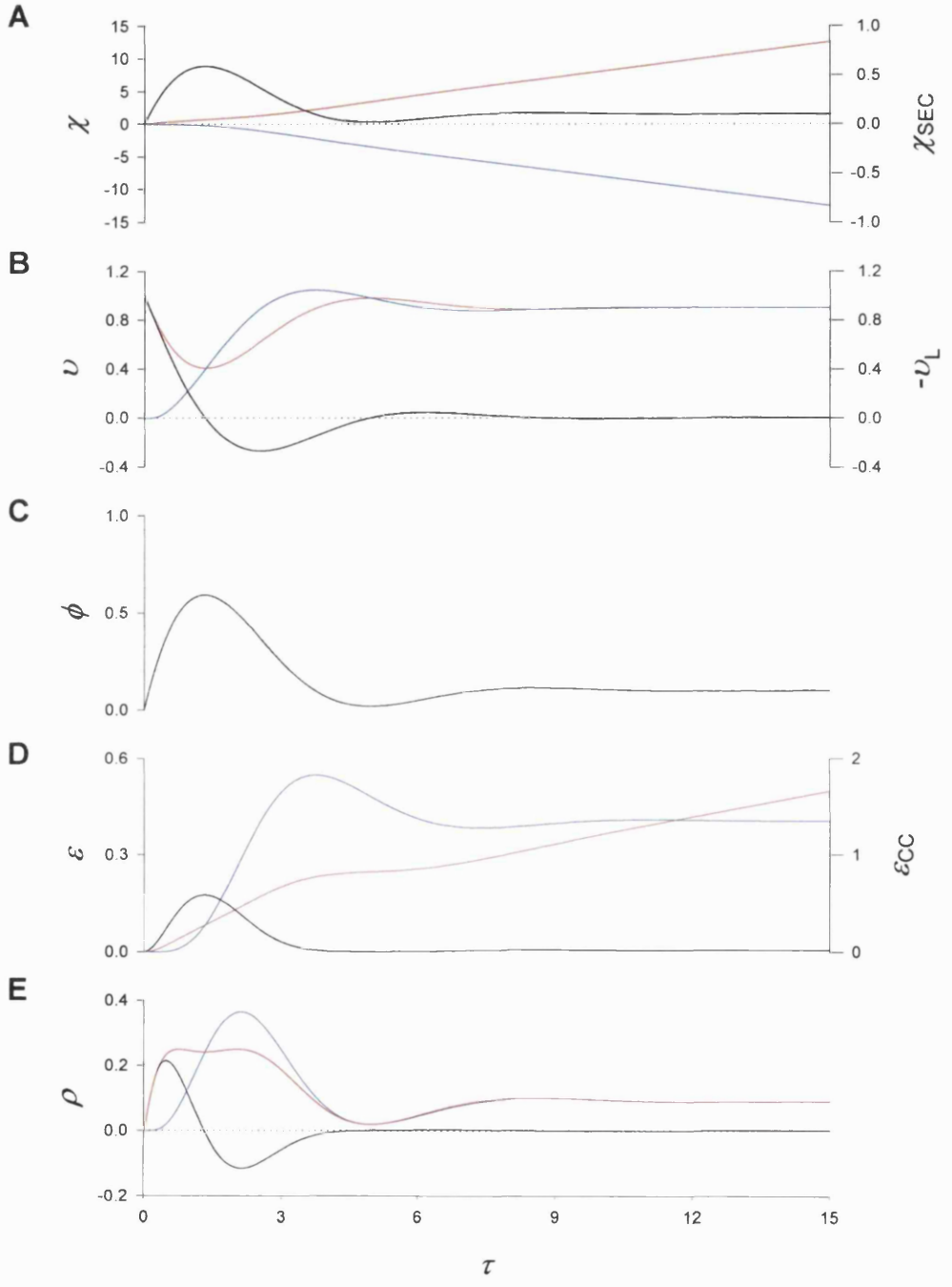

Figure 2.27.A. Time course of movement (A), velocity (B), SEC force (C), mechanical energy (D) and power (E) for the CC (red), SEC (black) and L (blue). $\xi = 1; LR \cdot \gamma = 0.1$.

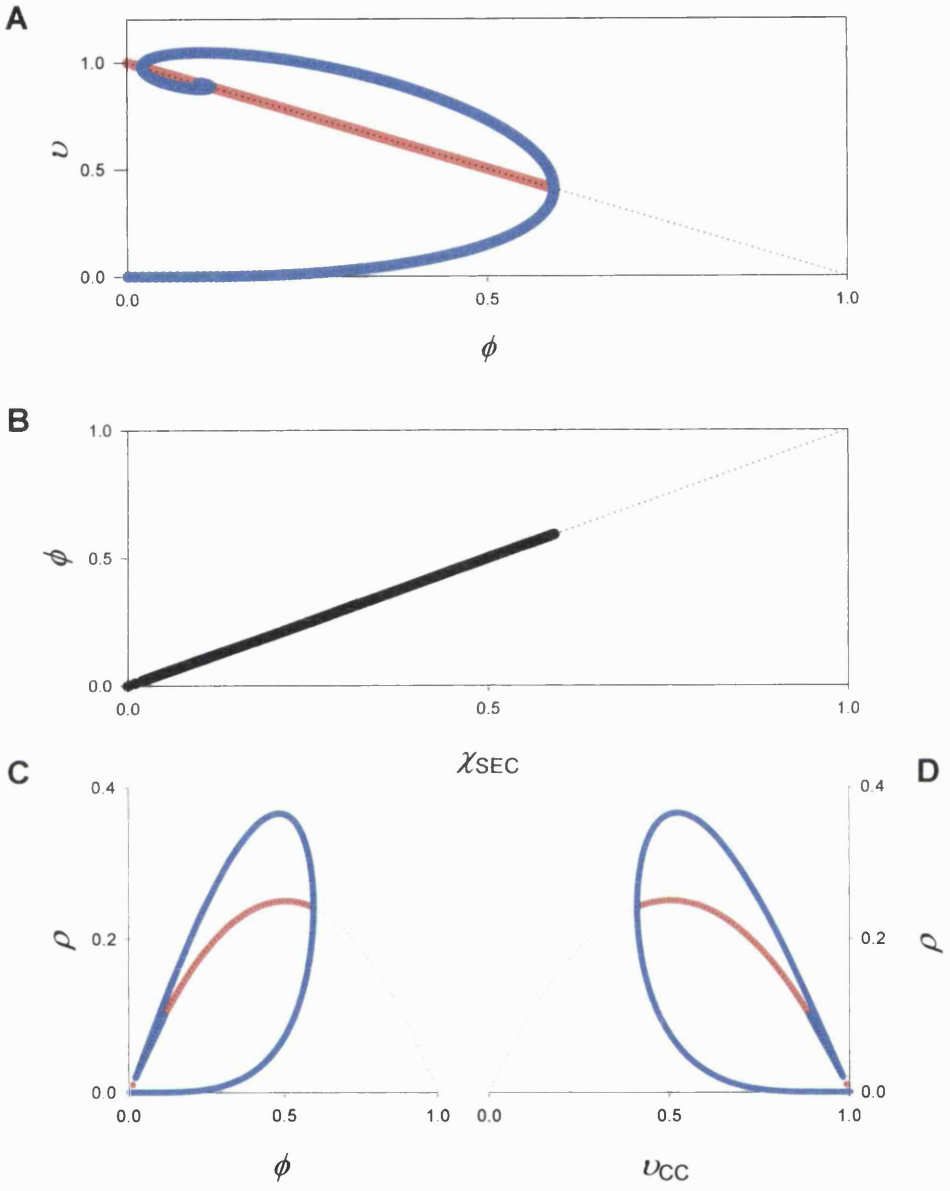

Figure 2.27.B. Time course of the CC (red) and L (blue) force-velocity outputs (A), SEC force-extension output (B), CC and L power-force (C) and power-CC velocity (D) outputs. The broken lines show the complete range for some of these relationships. $\xi = 1; LR \cdot \gamma = 0.1$

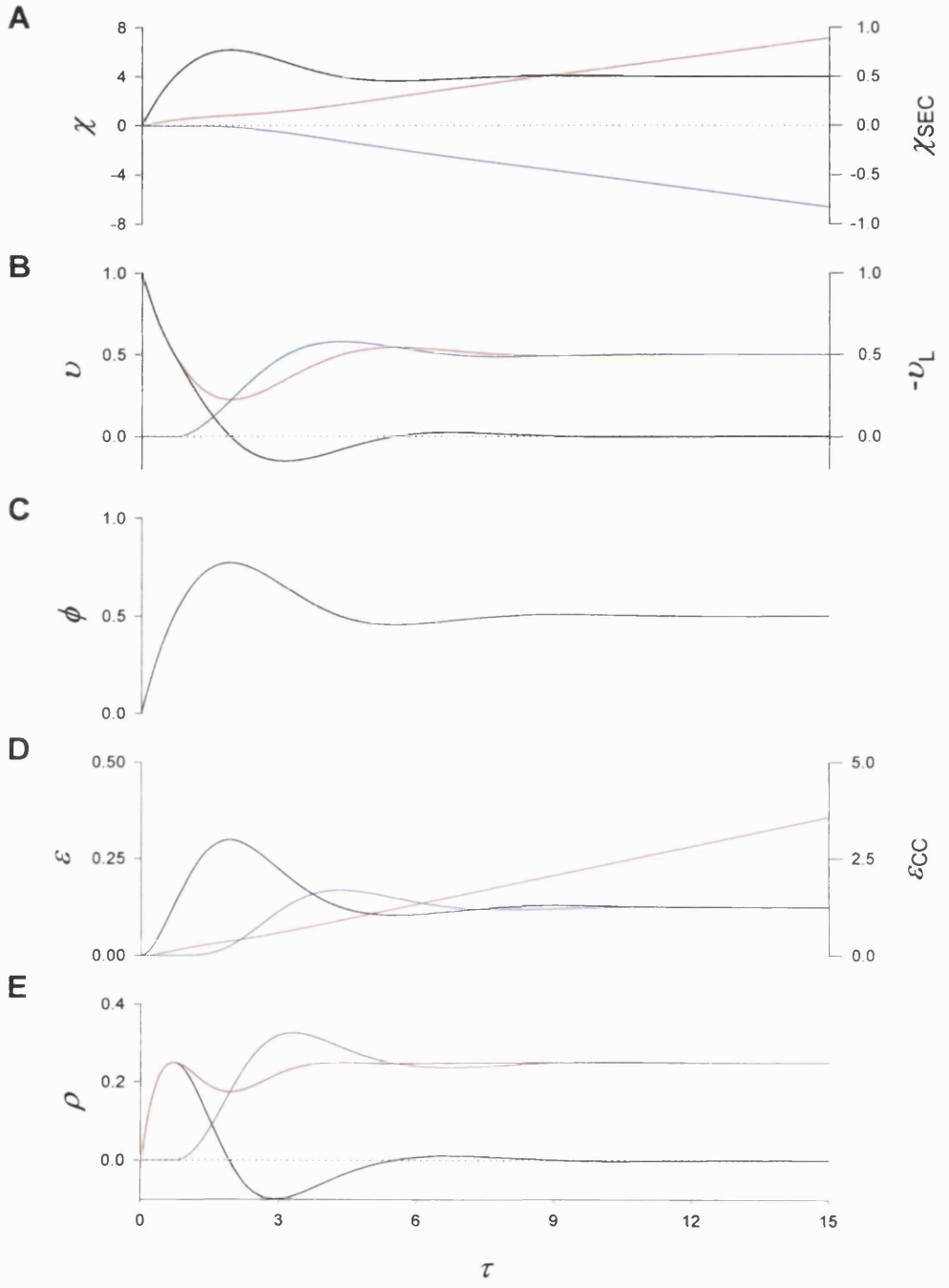

Figure 2.28.A. Time course of movement (A), velocity (B), SEC force (C), mechanical energy (D) and power (E) for the CC (red), SEC (black) and L (blue). $\xi = 1; LR \cdot \gamma = 0.5$.

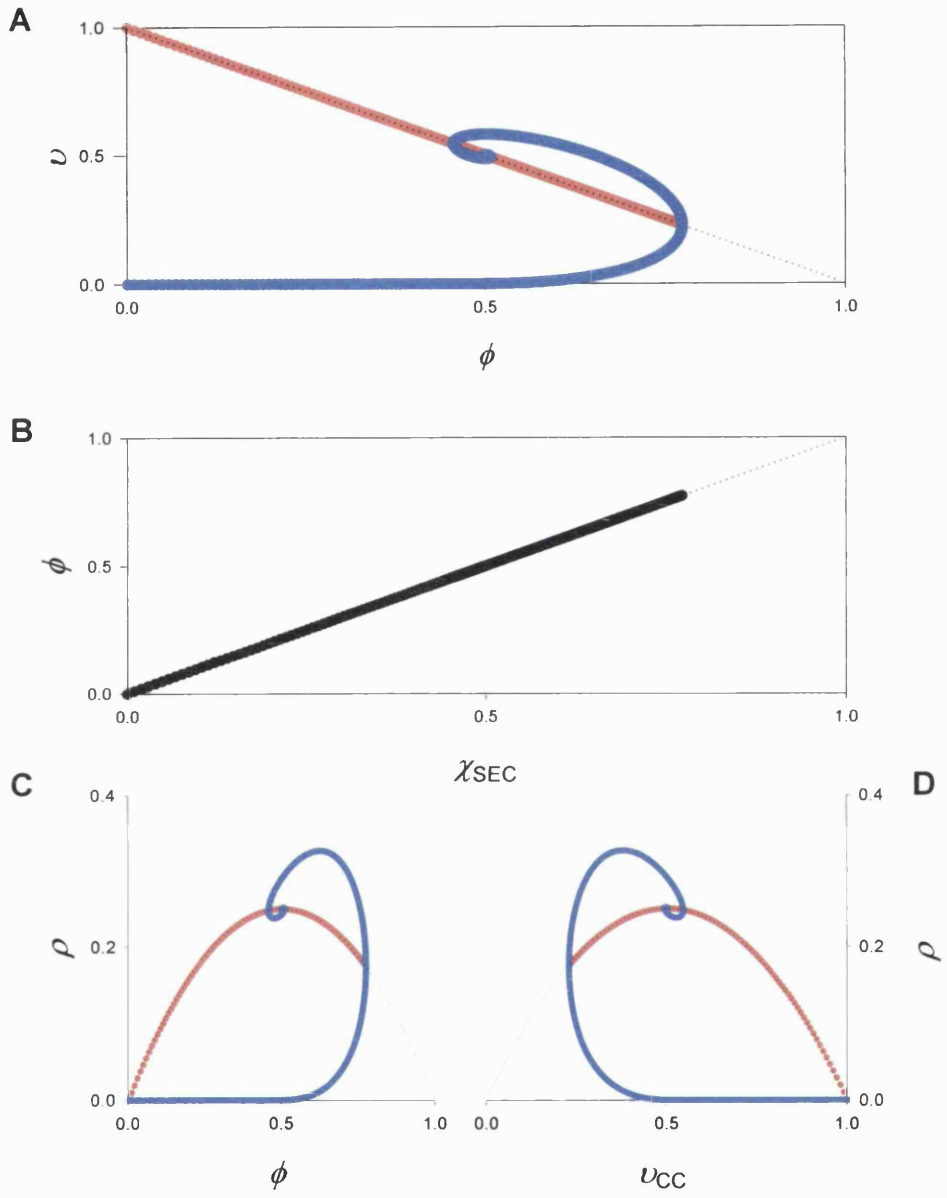

Figure 2.28.B. Time course of the CC (red) and L (blue) force-velocity outputs (A), SEC force-extension output (B), CC and L power-force (C) and power-CC velocity (D) outputs. The broken lines show the complete range for some of these relationships. $\xi = 1; LR \cdot \gamma = 0.5$.

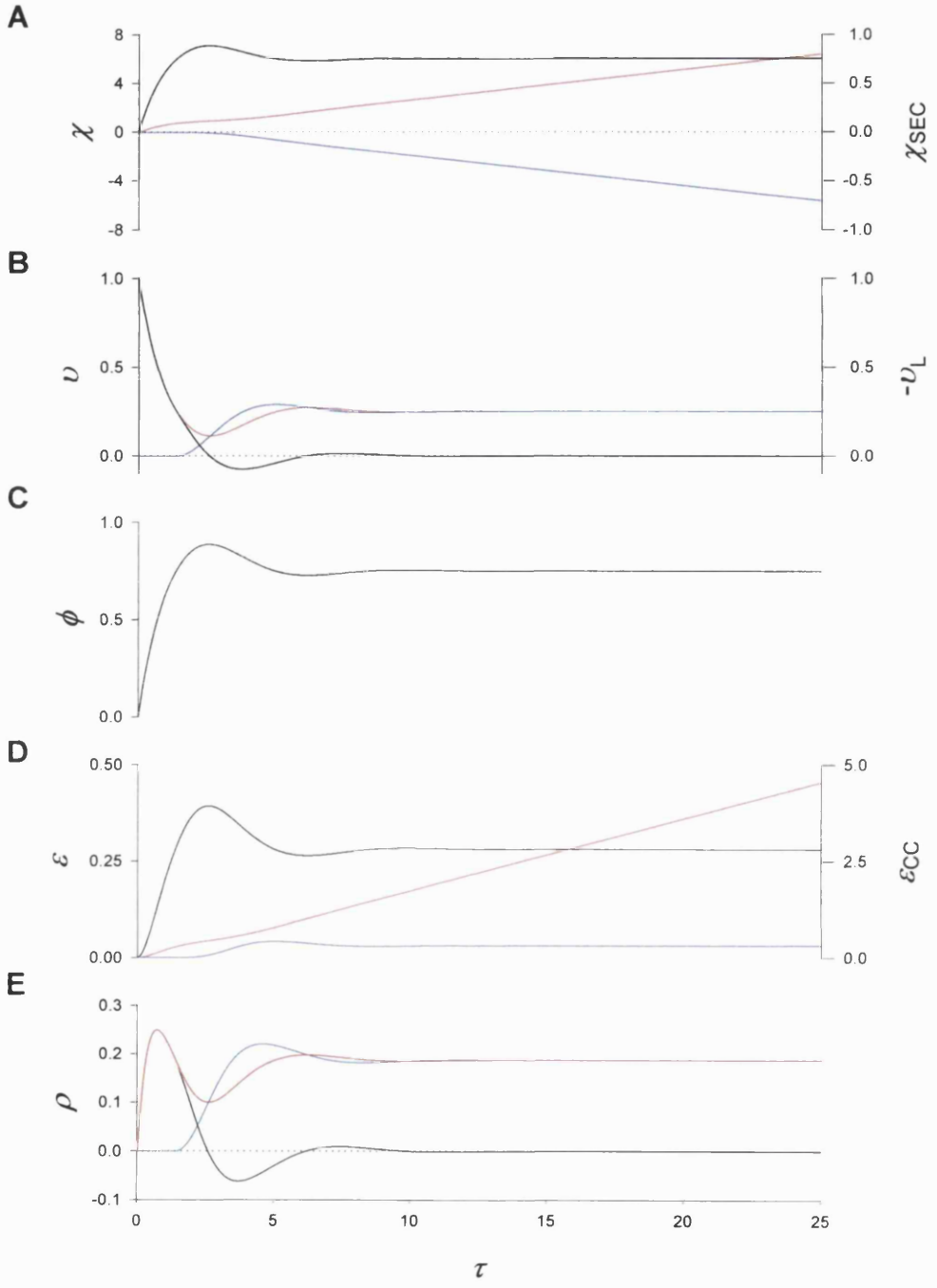

Figure 2.29.A. Time course of movement (A), velocity (B), SEC force (C), mechanical energy (D) and power (E) for the CC (red), SEC (black) and L (blue). $\xi = 1; LR \cdot \gamma = 0.75$.

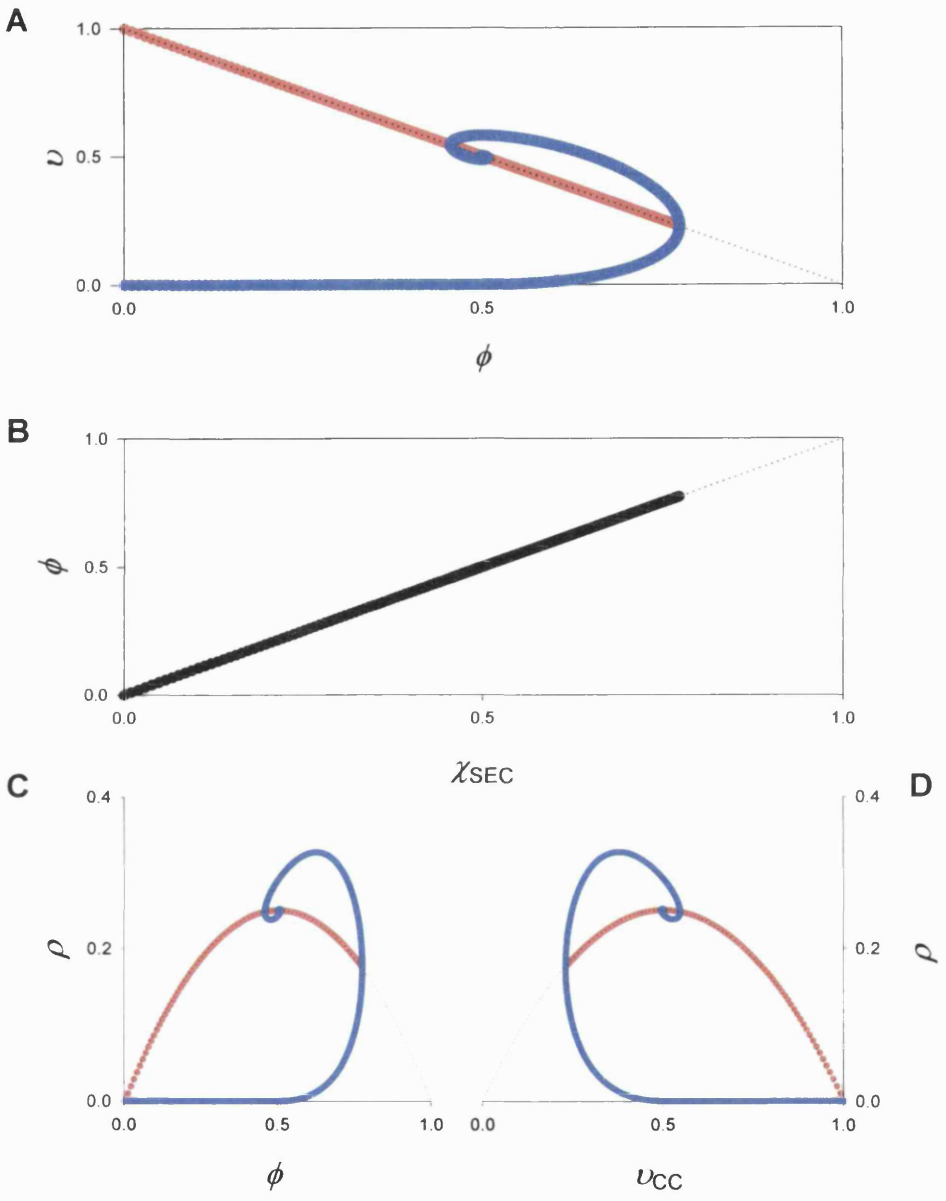

Figure 2.29.B. Time course of the CC (red) and L (blue) force-velocity outputs (A), SEC force-extension output (B), CC and L power-force (C) and power-CC velocity (D) outputs. The broken lines show the complete range for some of these relationships. $\xi = 1; LR \cdot \gamma = 0.75$.

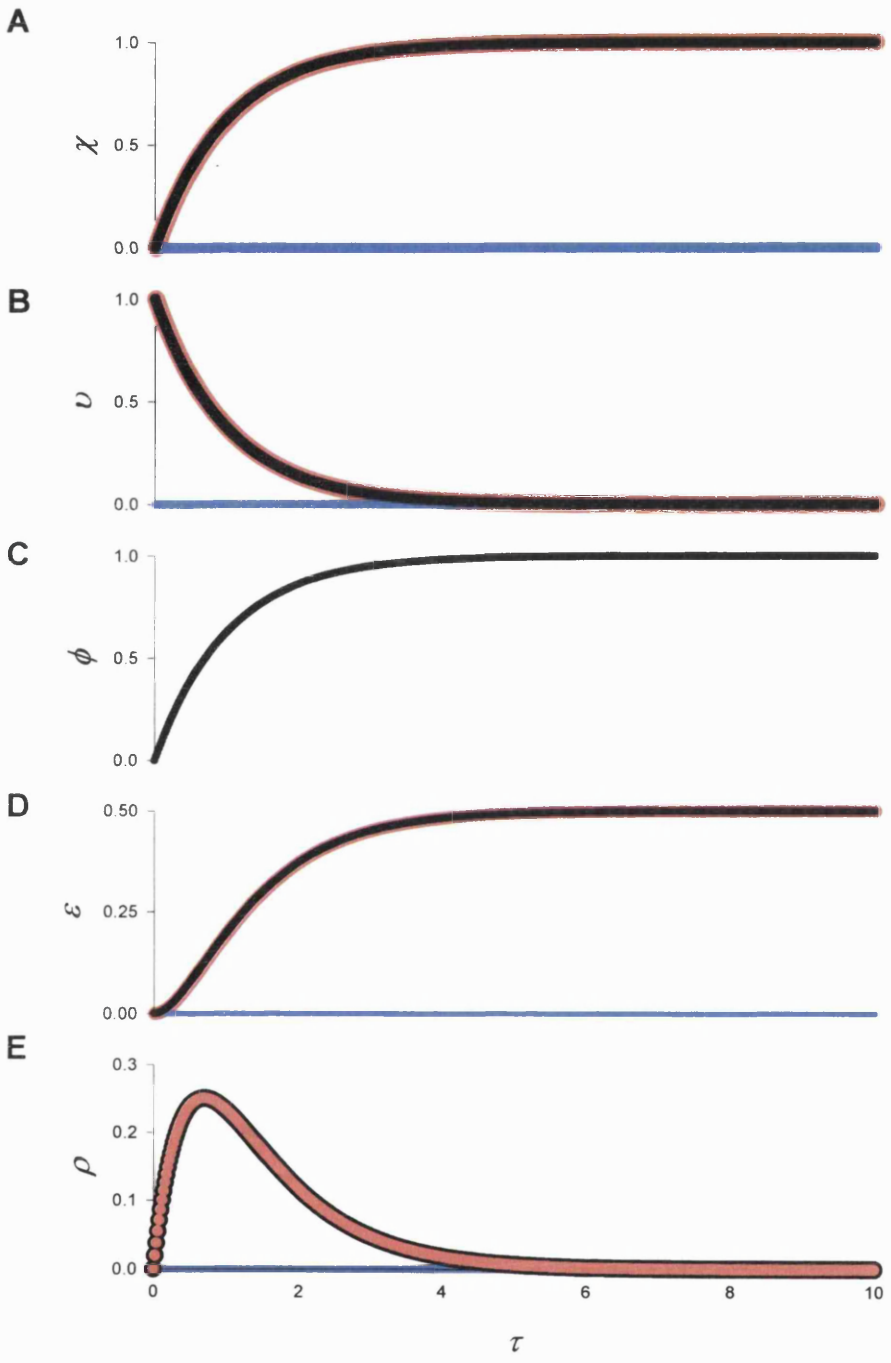

Figure 2.30.A. Time course of movement (A), velocity (B), SEC force (C), mechanical energy (D) and power (E) for the CC (red), SEC (black) and L (blue). $\xi = 1; LR \cdot \gamma = 1$.

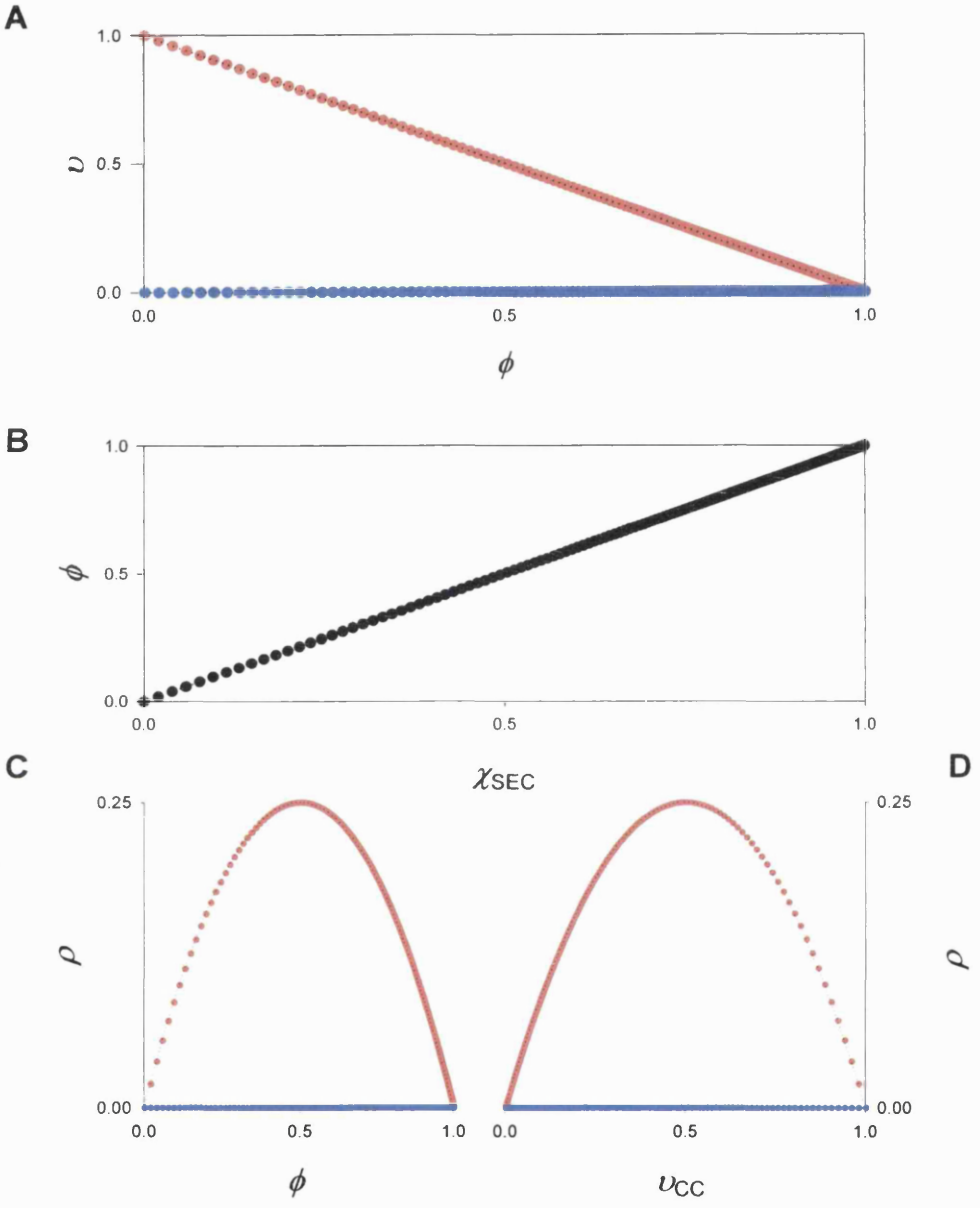

Figure 2.30.B. Time course of the CC (red) and L (blue) force-velocity outputs (A), SEC force-extension output (B), CC and L power-force (C) and power-CC velocity (D) outputs. The broken lines show the complete range for some of these relationships. $\xi = 1; LR \cdot \gamma = 1$.

8.2.1. Effects of a constant gravitational torque ($LR.\gamma$)

According to equations (2.21) and (2.52), acceleration of the load is proportional to the net force acting on it or the net torque around the lever's centre of rotation (CR). The net force on the load (or torque around the CR) is the difference between the force (or torque) due to gravity and that due to the MTC. Moreover, according to the conditions set in these equations the load will not accelerate from its initial position unless the MTC-generated force (or torque) exceeds that due to gravity. The CC has a fixed capacity for force (or torque) generation. In the presence of the gravity only part of this capacity can be utilised to accelerate the load, the rest being used to overcome gravity. As the force (or torque) due to gravity increases, a smaller part of the MTC's force (torque) generating capacity is available to accelerate the load.

The effect of the gravitational force on the behaviour of the system is illustrated in figure 2.31, which shows part of this relationship for three different values of the normalised torque due to gravity, $LR \cdot \gamma$. Only three relationships are illustrated for clarity. Two main observations on the effects of the gravitational torque on this relationship are discussed in this work. Firstly, the peak power ratio of 1.436 (3 decimal places) can be exceeded when gravity is present. Secondly, low inertia-high gravity conditions favour power amplification. This occurs with increasing $\gamma \cdot LR$, up to the value of 0.5. (The behaviour of the system at $\gamma \cdot LR$ values greater than 0.5 has not been studied in as much detail as the memory capacity of the PC used for the simulations was not sufficient to generate the large number of points required. However, observations (not shown

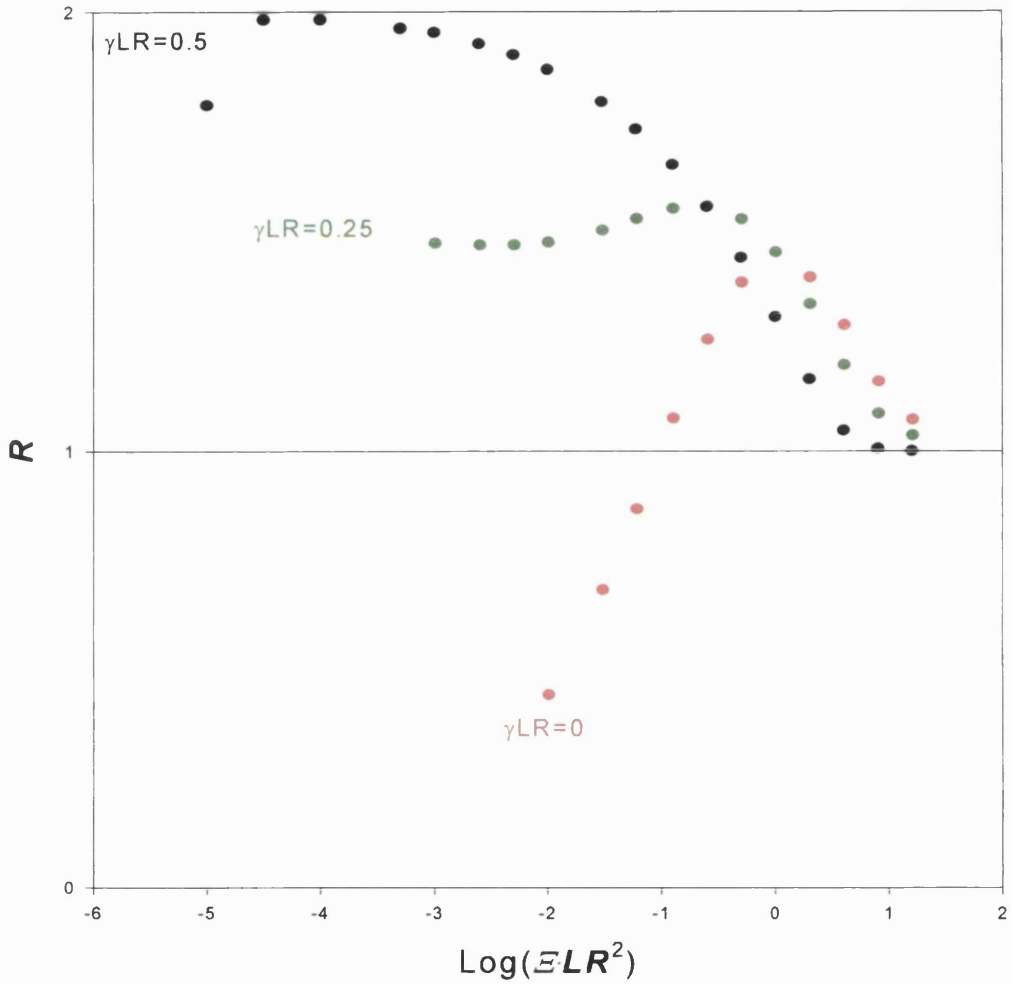

Figure 2.31: Power ratio plotted against the logarithm of the normalised moment of inertia. Each curve corresponds to a different value of normalised gravitational torque.

in figure 2.31) suggest that, the power ratio starts to drop as the $\gamma \cdot LR$ value increases between 0.5 and 1. When $\gamma \cdot LR$ becomes equal to one (or greater) there is movement of the load and no external power is produced, i.e. the power ratio is zero.)

Exceeding the optimal power amplification value of 1.436 by introducing a gravitational force (torque) in the model appears to be due to the greater SEC energy storage and release during a contraction. As explained earlier, when gravity is present L does not move before the torque due to the muscle-tendon complex exceeds the gravitational torque. Thereafter, L accelerates linearly with force. As a result, for the same inertial load, higher forces are generated by the muscle-tendon complex to move a load when gravity is present (Figures 2.32 and 2.33; panel A). As the SEC experiences higher forces it stretches more and stores more elastic potential energy (Figures 2.32 and 2.33; panel B). Although in the presence of gravity there is a lower rate of change of force when power delivery to L reaches its peak (figures 2.32 and 2.33; panel C), the greater storage and release of energy by the SEC appears the main factor responsible for the greater power amplification that is observed at light inertial loads ($\Xi \approx 1$) when gravity is involved.

At lighter inertial loads ($\Xi < 1$), in addition to the greater energy storage and release by the SEC in the presence of gravity, CC power production may achieve its optimal value. This would not be possible in the absence of gravity, as the force in the MTI system would not rise to a level that is optimal for CC power generation.

The combination of these two mechanisms appears to produce a maximum of power amplification, which is approximately two. No value of power ratio was found for this model that is higher than two.

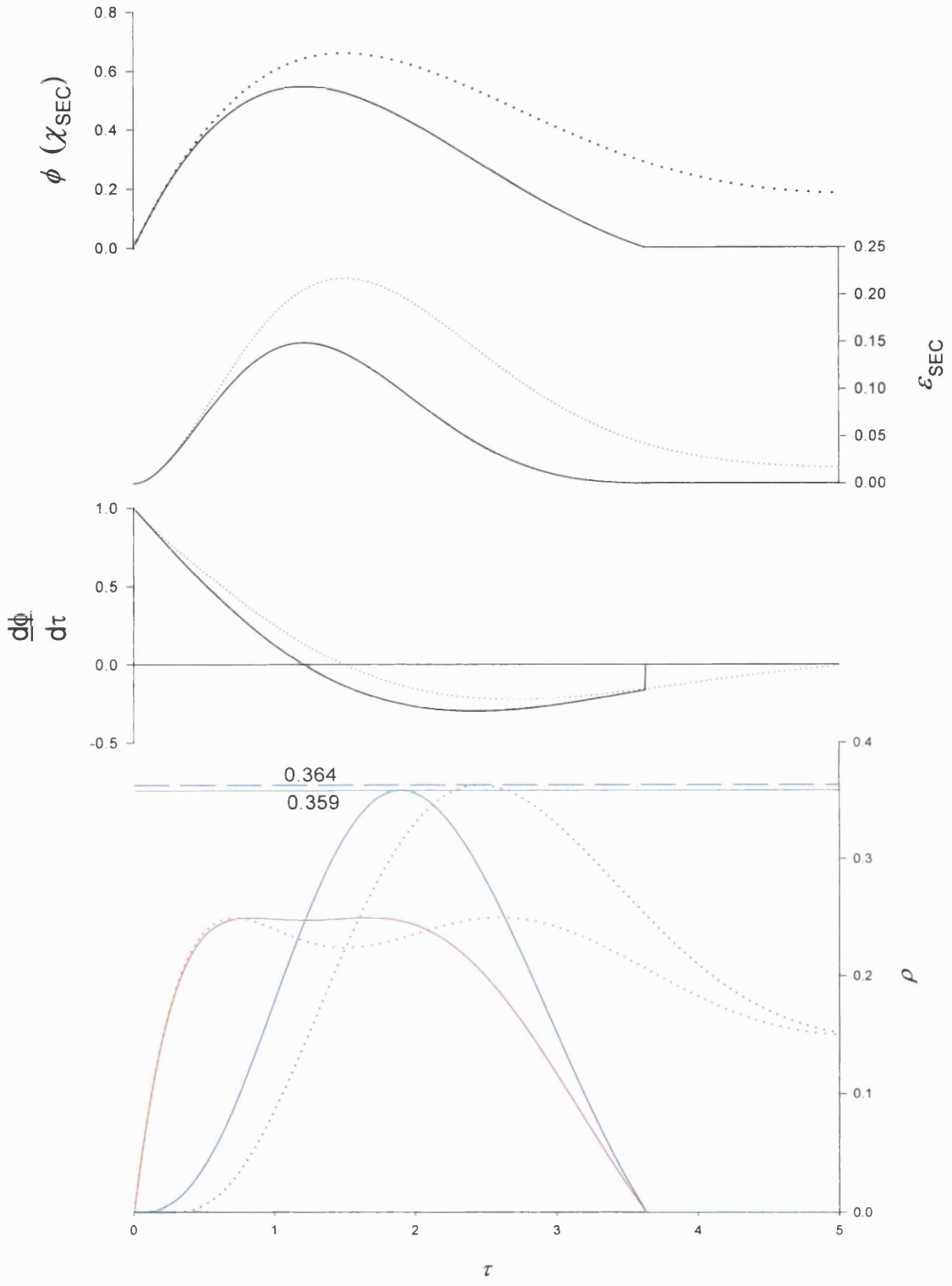

Figure 2.32: Time-course of normalised force (panel A), elastic potential energy in the SEC (panel B), rate of change of normalised force (panel C) and power output of the CC and L (red and blue, respectively; panel D). $\gamma \cdot LR = 0$ (solid line); $\gamma \cdot LR = 0.25$ (dotted line); $\Xi \cdot LR^2 = 1$.

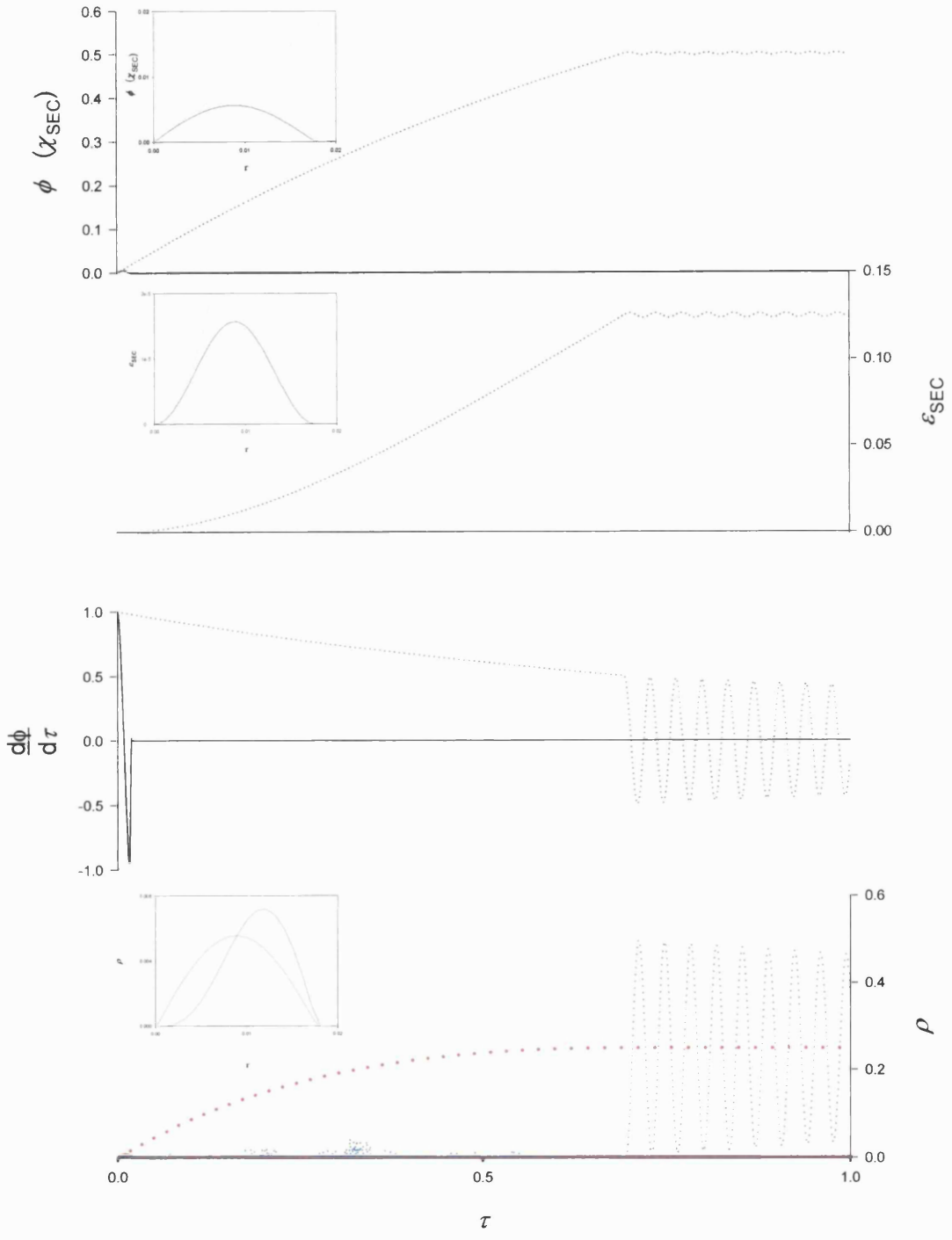

Figure 2.33: Time-course of normalised force (panel A), elastic potential energy in the SEC (panel B), rate of change of normalised force (panel C) and power output of the CC and L (red and blue, respectively; panel D). $\gamma \cdot LR = 0$ (solid line); $\gamma \cdot LR = 0.5$ (dotted line); $\Xi \cdot LR^2 = 10^{-4.5}$.

7. Discussion

The main findings of this section are:

1. The dimensionless mechanical behaviour of any Hill-type MTI system with linear properties (specified in their dimensioned form by four dimensioned constants: F_{max}, V_{max}, K, M), can be predicted on the basis of only one dimensionless constant, Ξ (linear-motion load) or ξ (rotational-motion load), that represents the amount of inertial load 'sensed' by the MTC.

2. The dimensionless behaviour of any Hill-type MTI system with linear properties in a gravitational field (specified by five dimensioned constants: TQ_{max}, Ω_{max}, K_{rot}, MI, g), can be predicted on the basis of two dimensionless constants: the normalised inertial load, ξ, and the normalised torque due to gravity, τq_G.

3. When non-linear properties are attributed to the contractile (CC) and series elastic component (SEC) (specified by the constants G and πc for the CC, and H for the SEC), there are deviations from the behaviour of the system with the linear properties. Under these conditions the dimensionless behaviour depends on the normalised inertia and gravitational torque, as well as on the dimensionless constant producing the non-linear behaviour.

4. When a MTC shortens against an inertial load, the inertial load acts as a 'catch' so that the system can act as a catapult, allowing a greater power to be delivered to the external load than the CC could alone generate. The shape of the relationship between the extent of power amplification and the log of the normalised inertial load resembles that of normal distribution curve with a peak of 1.436 (3 d.p.) when Ξ is approximately 1. Gravity and non-linear

behaviour may alter, to a minor extent, the original shape and the magnitude of power amplification. In the presence of gravity the peak power amplification can exceed that observed when the load is purely inertial, but under no circumstances can the power ratio exceed the value of 2.

Dimensional analysis has been widely used to describe natural phenomena (see for example McMahon and Bonner, 1983) and dimensionless constants determining the behaviour of systems have been identified. A well known example of such a constant is Reynold's number which determines whether flow is laminar or turbulent. The modelling work in this thesis reveals that the dimensionless behaviour of a MTI system with linear properties and in the absence of gravity is also governed by one such constant. This constant, Ξ or ξ depending on whether the load moves along a straight line or whether it rotates respectively, simply represents in dimensionless terms how large a load the MTC 'senses'. This makes sense, when as a result of the normalisation, all MTCs become 'equal' and thereafter their behaviour is determined by the magnitude of the dimensionless load.

The fact that only one such constant determines the behaviour of MTCs with linear properties shortening against purely inertial loads, is in accordance to Buckingham's theorem stating that the number of dimensionless constants required to describe a system is equal to the number of dimensioned constants minus the number of fundamental quantities – such as mass, length and time in this case- that are required to express the properties of the system (see McMahon and Bonner, 1983).

When a gravitational force (F_g) acts on the mass of the load the number of dimensioned constants in the system becomes five but the number of fundamental quantities required to describe the system remain three. Thus, two dimensionless constants (5 minus 3) would be required to describe the dimensionless behaviour of the system. These were found to be ξ and τq_G (rotational-motion load). Again these two constants together determine the magnitude of the load sensed by a MTC in normalised terms.

These observations justify the process of normalising loads to muscle preparations or MTCs relative to the muscle's maximal isometric force, while the force is constant or while the CC velocity is constant. However, when there are accelerations in the system there is also an inertial component of the load which must be expressed as Ξ (or ξ), i.e. relative not only to the muscle's maximal isometric force but also to the muscle's maximal shortening velocity and the stiffness of its series elasticity as for example in equations (2.34) and (2.51). So far, to my knowledge, such a normalisation has not been used in any study.

The effect of non-linear CC and SEC properties produced, as assessed from their effect on the power ratio, small deviations from the original result. It appears that the 'background' shape of the power amplification-load curve is set by the inertial properties of the load. This is also the case in the presence of a gravitational force.

Modelling muscle-tendon complexes shortening against inertial loads

In Caldwell's modelling study (1995) the time course of mechanical events for MTCs shortening against purely inertial loads starting from rest resembles those presented in this thesis. Although the results of his study were expressed in dimensioned terms, the time history of the rise and drop in force accompanied by a drop and rise in CC velocity, the continuous rise in load velocity and the bell-shaped power delivery to the load are present in both his and this study. Three particular cases of MTCs were considered in his study, each having a muscle fibre-to-tendon length and tendon stiffness that differed from the other two (see introduction). For the same total MTC length, increasing the proportion of muscle fibre-to-tendon ratio is equivalent to making the CC faster ($V\text{cc}_{max} \propto$ muscle length) and the SEC stiffer ($k \propto (\text{SEC length})^{-1}$) in this study. The SEC stiffness was also changed by altering the gradients of the SEC force-extension relationships. Thus, it is not surprising that type I MTC which has the most compliant tendon and the slowest muscle, only produces a small force output while type II MTC with the fastest muscle and a stiff tendon produces the highest force output. Type III MTC has as stiff a tendon as the type II MTC but its shortening speed is in between type I and type II and produces an intermediate force response. As a result of these force outputs, the load velocities and power outputs are higher in the order of type II>type III> type I. Other things being equal, a MTI system with higher $V\text{cc}_{max}$ and K will also have a greater value of Ξ and it was shown in section 6.1.2.1.2 (pp. 150) that the higher the value of Ξ, the higher the peak force achieved during a contraction.

In this thesis, the mechanism by which changes are brought about in muscle $V\text{cc}_{max}$ (e.g. changing muscle fibre length or orientation or changing muscle

fibre composition), in SEC stiffness (e.g. by changing the SEC Young's modulus, cross sectional area or resting length) or any other model parameter is not considered. Only the effect of these changes, as reflected in the values of these parameters is considered. Ultimately these values will determine the value of the normalised inertial load in the dimensionless model and hence its dimensionless behaviour. Although the time course of mechanical events has been presented in this work in dimensionless terms, it is easy to revert back to dimensioned behaviour by multiplying the dimensionless result by the appropriate scaling factors on both x and y axes.

The most important parameter of the model determining the behaviour of the MTI system is the dimensionless inertia. This dimensionless constant, as mentioned earlier, section 4.1, is obtained by dividing the actual value of the inertial load by the inertia normalising factor m or i, for linear or rotational motion load respectively. Let us consider the simplest model with a linear motion load, in which the normalised mass is equal to the dimensioned mass, M, divided by the normalising factor, m. In this model the maximal power ratio is obtained when the M/m is approximately equal to one. The curvature of the CC force-velocity relationship does not vary widely in nature (see Woledge *et al*, 1985 for values in various preparations). Moreover, the shape of the SEC force-extension relationship as defined by H does not produce an appreciable shift in the load at which optimal power delivery to the load is achieved at least within the range from 0 to 4 (see fig. 2.22, pp. 166). Values for FDI SEC ranged approximately between 1 and 5 (see table 3.8, pp. 305). Moreover, although the curvature of SEC force-extension relationships has not been expressed as H

before, judging from the stress-strain relationships and Young's moduli from mammalian tendons, H may not vary much beyond values that would cause a dramatic alteration on the original peak power ratio-load relationship. Thus, it is likely that the influence of curved relationships for the CC and SEC, may not cause an appreciable change in the magnitude of the normalised load for optimal power output by the MTC. Thus the value of the normalising factor m can be used as an estimate of the inertia that maximises the power output of the whole MTC. It would be interesting to see what that optimal inertia, m, should be for muscle-tendon complexes performing different functions such as MTCs falling into different categories of Alexander and Ker's classification.

The human quadriceps MTC can be classified as type I, as it has a large muscle volume and a relatively short tendon and it is located in the proximal segment of the lower limb. Using an estimate of maximal shortening speed of ~8 fibre lengths per second (see Epstein and Herzog, 1998; pp. 38) and a fascicle length of ~0.08 m (Kumagai *et al*, 2000), the estimated maximal shortening velocity is ~0.64 $m \cdot s^{-1}$. A maximal isometric torque of ~300 $N \cdot m$ (Aagaard *et al*, 2001) divided by a hypothetical 0.06 m lever arm, yields a 5000 N maximal isometric force. An estimate of the vastus lateralis tendon stiffness could be 50000 N/m representing ~22% of the total stiffness of the quadriceps tendon (Kubo *et al*, 2000); hence total quadriceps tendon stiffness could be 227300 N/m. Combining the above values to form the m of a quadriceps muscle yields a value of approximately 270 kg. This is a large mass, approximately 3-4 fold greater than the total mass of the body. Power amplification greater than one however, can be achieved within a range of inertias ranging approximately from

ten times smaller to ten times larger than the optimum. In this case this range would be approximately 27 to 2700 kg. Another important factor to consider, in addition to the magnitude of the inertial load, is the effect of gravity. For example, if the 70 kg body mass of a person had to be overcome by the action the quadriceps MTC described above, the logarithm of the normalised inertia would be ~ –0.6 and under the influence of earth's gravity the normalised gravitational load (~70kg·g/Fmax) would be ~0.15. The power ratio curve-load in the presence of gravity for such a muscle-tendon complex would be somewhere between the red and green traces of figure 2.31. It can be seen that against an inertial load of this magnitude, the quadriceps MTC would be capable of delivering near optimal power output to the mass of the body. Also, considering the inertia of one lower limb (~5% of total body mass), the normalised gravitational component would be negligible and the normalised inertial load very small (log of normalised inertia ~-3). That means that during knee extension against the inertia of the lower leg alone, power amplification is low but the final velocity of the lower limb would be very high (figure 2.15). Also notice that the work normalising constant ($0.5 \cdot Fmax^2/K$) of this muscle is high (~60 joules), as expected from its architecture. Moreover the time normalising constant is ~34 ms. Thus a large amount of work can be delivered to the load within ~0.1 sec (see power output on figure 2.27.A). Thus, this muscle-tendon complex is expected to deliver high absolute levels of work and power to a large mass or to a mass approximately equal to the body mass in the presence of gravity. It is also capable of accelerating the relatively low mass of the lower limb to high speeds.

The human extensor carpi radialis longus (ECRL), which acts synergically with other muscles to extend and abduct the wrist, could be classified as a type II MTC. An estimate of the maximal isometric force and tendon stiffness for ECRL could be ~32 N and ~7000 N/m (Loren and Lieber, 1995) and assuming a maximal shortening velocity of 5 fibre lengths per second or ~0.64 m/sec, the optimal mass is 0.37 kg. Surprisingly close, one human hand (~0.6% of total mass) of a 70 kg person would be 0.42 kg, very close to the optimal inertia for power amplification. When gravity is involved the normalised gravitational load is ~0.125 and therefore either in the presence or absence of gravity high levels of power can be delivered to the hand (see figures 2.18 and 2.31). The time normalising factor ($Fmax/K{\cdot}VCC_{max}$) of this MTC is relatively short (~7 ms), reflecting the high tendon stiffness relative to the maximal isometric force of the muscle, an important feature of type II MTCs, which are primarily involved in 'precision' movements. The work normalising factor of ECRL however is relatively small (~0.075 Joules), approximately 700 times smaller compared to that of the quadriceps.

A typical type III MTC could be represented by the human triceps surae, which has a thin, long tendon relatively to its muscle and could act as an 'energy-saving spring' in locomotion. Parameter values obtained from the paper by Hof *et al* (2002) (VCC_{max}~0.5 m/s (see paper, figure 4), Fmax=3900 N and K~350000 N/m) yield an optimal mass m~170 kg, i.e. approximately 2-2.5 times the body weight. The mass of the body of a 70 kg person poses a relatively small normalised inertial load (~0.4 units; or approximately –0.4 log units) to the triceps surae MTC, so high final speeds can be achieved while still

in the region of the load-power ratio plot where high power amplifications are achieved. However, when gravity is taken into account the normalised gravitational load due to the body mass becomes ~0.2 units and with an inertial load of –0.4 log units power amplifications are very near their optimum (figure 2.31). The work normalising factor (~20 Joules) for this MTC is about a third of that of the quadriceps. The time normalising factor is approximately ~20 ms. Thus, the triceps surae MTC can deliver large amounts of work to the mass of the body under the influence of gravity within ~0.1 seconds (see power output in figures 2.27-2.28 A). This is very close to the power output contraction time of the quadriceps.

The examples given above are only rough calculations and are not suggested to represent a precise explanation of MTC design according to the model. They show however, how the simple models described in this section may link to the existing understanding of MTC structure and function and how these findings may change the way we think about MTC function.

Marsh and Bennett (1986) used the term power ratio as an index of the curvature of force-velocity curves fitted by a hyperbolic-linear equation. According to their definition, power ratio is the maximum of the power calculated from the force-velocity curve divided by the product of the maximal isometric force and maximal shortening velocity. The term power ratio in this thesis however, is used as a functional index of the performance of a MTI system and has been defined as the peak power delivered to an external load during a contraction divided by the maximal power the CC can generate (also

see section 6.1.2.1.12, pp. 163). This definition is relevant to the following observations about animal movements. It has been estimated that certain animals produce much greater power outputs during the acceleration phase of a jump than can be accounted for by their muscles alone (Aerts, 1998; Peplowski and Marsh, 1997; Bennett-Clark, 1975; Alexander, 1988). In insects very high values of power amplification can be observed during jumping. Locusts during jumping seem capable of amplifying the power of the extensor tibiae (36 mW) more than 20-fold (0.75 W) (Bennett-Clark, 1975). However, the anatomy of locusts hind legs uses a special 'catch' mechanism being specifically designed to amplify power (Bennett-Clark, 1975; Alexander, 1988). In jumping bushbabies, a power amplification of 15 has been suggested (Aerts, 1998). Peplowski and Marsh (1997) suggest that the power during the take off phase of a jump in small frogs exceeds that available from their muscles by at least seven fold, i.e. the power ratio -according to the definition in this thesis- is at least seven. These values greatly exceed the power ratio limits identified in this thesis under the conditions for which the models are valid, indicating the presence of other power amplification mechanisms.

Modelling studies in man (e.g. Bobbert et al, 1986b) have also shown that more power can be delivered externally during a jump than is available from the muscles and more recently using a combination of kinetic, kinematic and ultrasound imaging techniques, from which muscle fascicle shortening could be measured, Kurokawa *et al* (2001) provided more concrete evidence that this is so. Eight subjects performed squat jumps without counter-movement. Their gastrocnemius medialis MTCs developed, on average, during phase II of the

jump (i.e. –100 ms to toe off), a peak power output that was higher, and occurred later in the movement, than the peak power exerted by the muscle fascicles. Although the values for the peak MTC and fascicle power are not reported, it appears from figure 4 of their paper, that the peak power at the triceps surae MTC was approximately 1.5 times greater than the peak fascicle power. If the peak fascicle power is used as an estimate of the maximal muscle power, the power ratio was, on average, approximately 1.5. This value is consistent with the values in the modelling work presented in this section. Also the time course of velocity, force and power in the MTC, CC and SEC during the jump are very similar in shape to those from our modelling work (with the CC velocity having an exponential activation time course).

Several mechanisms have been proposed as power amplifiers, which can use the basic mechanism of storage and release of elastic energy from the SEC.

1. Change in the lever arm of the agonist muscle such that it is shorter at the beginning of the movement and it increases later on ('cum').
2. Contraction of antagonistic muscles early during a movement followed by their relaxation later on
3. Other specialised mechanisms such as the 'catch' mechanism in the locust hind limbs

In this work two more mechanisms are identified:

4. Inertia of the load and
5. Gravity

When a muscle contracts against an inertial load at rest energy can be stored in the SEC early during the contraction while the CC shortens faster than the load

can move. As the load accelerates and starts to move faster than the speed at which the CC is shortening, SEC recoils releasing the stored energy and amplifying the muscle's maximal muscle power. As was shown in the results section, this happens for a wide range of inertial loads but not for very small (less than approximately 0.06 dimensionless units) or large (greater than approximately 100 dimensionless units) inertial loads (see figure 2.20, pp. 164). The upper limit of this mechanism for power amplification is 1.436 times the maximal muscle power. In the animal body, anatomical restraints may prevent the full utilisation of this mechanism, with the inertial load being stopped or hindered before it has been accelerated to the necessary speeds. However, this was probably not the case in the FDI experiments described in the next section, where the peak power output delivered to inertial loads was in good agreement with that predicted by the model, which does not incorporate anatomical constraints.

Gravity may also act as a catch allowing even more energy to be stored in the SEC prior to any external movement is observed. In this way, the SEC is being stretched until enough force (torque) is generated to overcome that due to gravity. Thereafter, any force (torque) in excess of the gravitational force (torque) is used to accelerate the inertia of the load. However, the SEC is now preloaded and under favourable conditions (especially low inertia-high gravity; see results) the power ratio may exceed the optimal value for purely inertial loads (figure 2.31, pp. 186). Nevertheless, even in the most favourable conditions for power amplification when gravity is present no more than twice

the maximal muscle power can be delivered to an external load under the conditions for which the model applies.

During an explosive movement, such as throwing or jumping, the distance covered by a projectile depends on its position, speed and angle of excursion at the moment of take off as well as the acceleration due to gravity. For a given position and gravitational acceleration, vertical and horizontal distances are maximised when the excursion angles are 90^0 and 45^0 with respect to the horizontal, respectively. The speed of the projectile can be maximised by maximising its kinetic energy. Raising the kinetic energy of the projectile requires input of energy from a source. Taking jumping as an example, active muscles convert chemical energy into mechanical work and heat. Some of the mechanical work will be distributed as elastic potential energy in tendons and some as increased kinetic and gravitational potential energy of the animal's centre of mass. The amount of kinetic energy the centre of mass will be limited by the length of an animal's limbs. If the limbs are long, muscles can shorten over a longer distance and therefore generate more work before the end of range of the movement is reached compared to when limbs are short. However, long limbs would be disadvantageous, if a movement had to be produced within a short period of time for survival purposes, as it would take longer to fully flex or extend the joint. Moreover, long limbs would add to the inertial and gravitational load the muscles would have to overcome. Thus, a compromise must be made by optimising limb length such that a large amount of kinetic energy is imparted on the load within a relatively short period of time.

For a given limb length, muscle and inertial load, the determining factor for the kinetic energy that can be imparted on the load is the amount of in series compliance between the muscle and the load. On the grounds of the modelling work presented in this thesis it was shown that the speed and hence the kinetic energy of a purely inertial load, such as for example the mass of an animal's body, is maximal at the end of a contraction. It was also shown (figure 2.15; pp. 155) that as the normalised inertia becomes infinitely small, the final load velocity approaches an asymptotic value equal to twice the maximal shortening velocity of the muscle. On the contrary, as the normalised inertia becomes infinitely large the load can only be accelerated up to the maximal shortening velocity of the muscle. For a given muscle and mass of the load, the value of the normalised inertial load will directly depend on the compliance (1/stiffness) of its series elasticity: if the series elasticity becomes infinitely stiff, the normalised load will also become infinitely large and final load velocities can only reach V_{CCmax}. If the series elasticity becomes infinitely compliant, it can be accelerated as much as two times V_{CCmax}. Intermediate values of stiffness (and hence load), will produce final load velocities between these two extreme values (see figure 2.15). Thus, it appears that when a given muscle shortens against a given inertial load, adding infinite compliance in series between these two components allows the final kinetic energy of the load to be increased four-fold compared to when compliance is not present. However, despite this advantage, high series compliance makes the dimensioned time course of mechanical events slow which, as mentioned above, would be a disadvantage when for example an animal has to complete the jumping movement fast for survival purposes. The same applies when compliance becomes too small, as this will

increase the value of the normalised load. For a given muscle and inertial load, optimal values of compliance minimising the duration of the contraction produce a normalised inertial load between 1 and 4 units. That means that in order to deliver a high amount of kinetic energy to an inertial load within a short amount of time, the rate at which this energy must be delivered is of importance. In agreement with this argument the optimal compliance

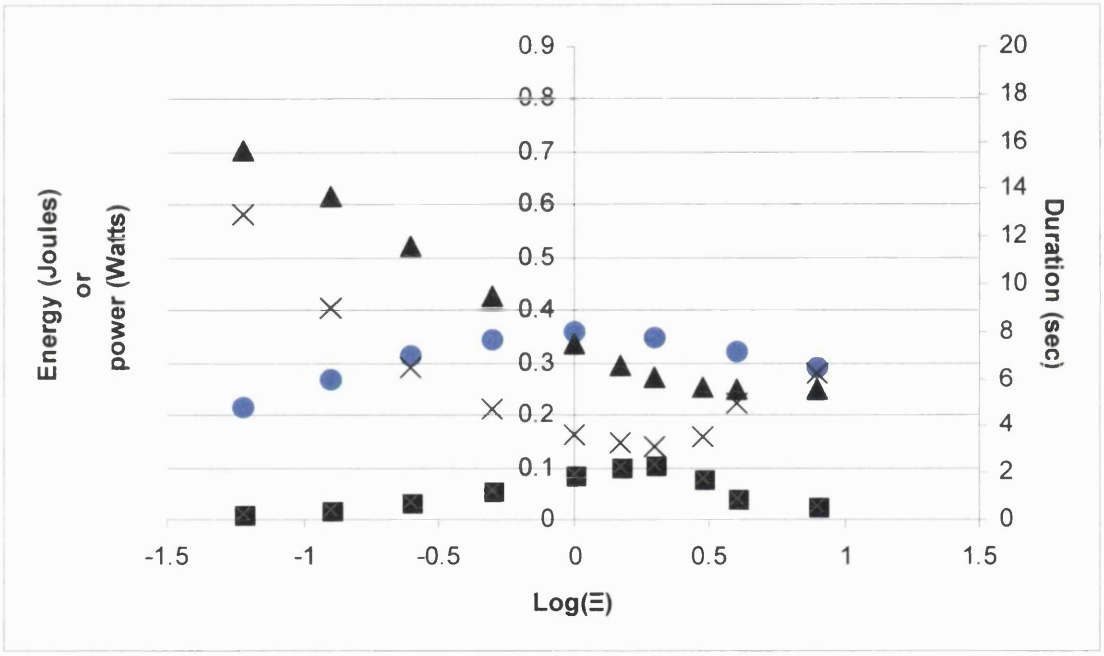

Figure 2.34.Effect of changing the series compliance on movement performance. X-axis: Logarithm of the normalised inertial load. The normalised inertial load was varied by changing the value of the SEC stiffness, while keeping all other parameters constant.Y-axis: Peak power delivery to an inertial load (circles), final kinetic energy of the load (triangles), contraction duration (crosses) and final kinetic energy divided by contraction duration (squares). Contraction duration and final kinetic energy of the load were approximated as the corresponding values after VCC had fallen and increased back up to 0.999VCCmax.These results were obtained from the model with linear CC force-velocity, linear SEC force-extension properties and a purely inertial load.

to maximise kinetic energy while minimising the duration of the contraction also corresponds to that required for the normalised inertial load to be between 1 and 4 units (figure 2.34). This is very close to that producing optimal or near optimal power delivery, reflecting optimal muscle-tendon mechanical interaction.

It was shown in this thesis that the maximal rate at which energy delivered by a muscle to a purely inertial load can be increased by approximately 40% as a result of adding compliance between the muscle and the inertia. In the presence of gravity this increment can reach 100%. Despite these increments, additional mechanisms, such as cams and catches, or movement strategies such as stretch-shortening cycles and optimising coordination of joint action in multijoint movements must operate to explain the even higher power outputs developed by animals during explosive movements such as in jumping bushbabies.

The fact that there are optimal inertial loads relative to the muscle and tendon properties for work and power generation could be taken into consideration, together with the requirements of other functional demands which are not considered in this model, when designing an artificial limb. However, in addition to inertial considerations, performance during a movement involving an artificial limb could be further enhanced by including other mechanisms such as cams for example, which appear to be particularly important during animal movement and could enhance work and power output even further.

The models described in this thesis have limitations and advantages. Only shortening contractions starting with the load at rest are considered. Activation of the CC in the model does not incorporate properties of the central nervous system relevant to recruitment and decruitment of motor units that may occur during a voluntary contraction (see for example Chow and Darling, 1999): the CC in the models is assumed to behave as though it was maximally stimulated. The CC can shorten indefinitely in the model. This is also true for the length

change of the SEC and for the movement of the load. The output of the muscle represents the 'lumped' output of all the fibres it consists of, which in reality will not all have the same length and intrinsic properties as each other. The CC properties have been modelled in terms of a force-velocity relationship and an activation parameter. The output of shortening muscle may also be influenced by its force-length relationship (e.g. Granzier *et al*, 1989; Abbot and Wilkie, 1953) and the time history of the contraction such as shortening deactivation (e.g. Lee *et al*, 1999; Herzog *et al*, 2000). These properties have not been incorporated in the model. The parallel elastic component has also been neglected although in some muscles it may contribute to force development at relatively short lengths (Epstein and Herzog, 1998). The lever system assumes a constant lever ratio, which may not be the case for many movements. Finally, gravity acts always at right angles to the rotating load, which may be a good approximation when a limb starts to move from a horizontal position or nearly horizontal position and the angular displacement it undergoes is only small. Future work could incorporate these complications to imitate more closely muscular contractions in real life.

Very relevant to real life movements is the fact that muscles can only function over a limited range. Due to their force-length relation isolated muscle preparations can only shorten a finite amount before they become incapable of generating force (see general introduction). In addition to this, the range of movement of the joint imposes a constraint to how much a muscle can shorten inside the body. Thus, real muscles can only shorten over a finite distances and therefore the modelling results are not applicable to very large inertial loads in

which the load comes to a halt before contraction has achieved completion as defined in this thesis. Solutions of the model could have been obtained incorporating conditions that limited the amount of the amounts of muscle shortening and load displacement. However, for the purposes of understanding the fundamental principles underlying the mechanical behaviour of MTCs shortening against inertial loads, it was decided not include such an additional constraint. If a constraint had been incorporated to the model such that the load, after it had been displaced by a given distance, reached a halt there would be a large enough normalised inertia for which the duration of a complete contraction would be limited by that distance. Once that distance was reached the total length of the MTC would remain constant and isometric force would develop. However, this force would not cause acceleration of the load from its stationary position, as it would balance exactly with the reaction force exerted by the stop on the load. External work and power would of course be zero.

However, the simplifications mentioned above allowed the fundamental principles underlying the behaviour of such systems to be identified thereby building a foundation from which other more complex models can be understood. Moreover, the predictions made from the models such as the time course of the mechanical output and power amplification seem to agree well with the existing literature.

The following two sections are focused on experimental work using two different human muscle-tendon complexes shortening maximally against inertial loads.

Contractile and elastic behaviour of the human first dorsal interosseus

1. Summary

The output of a muscle (CC) is delivered to an external load via series elastic components (SEC). When an inertial load is rotated by a muscle-tendon complex (MTC), the torque (*Tq*) generated goes through a maximum. This allows points of equal torque on either side of a torque trace to be paired and the corresponding load velocities (ω_L) and torque rates ($\frac{d}{dT}(Tq)$) to be used to calculate the SEC stiffness-torque and the CC torque-velocity relationships. The instantaneous behaviour of the CC and SEC during individual contractions can also be obtained. Six volunteers (n=6) participated in this study. The first dorsal interosseus muscle of the right hand of each volunteer was stimulated percutaneously with maximal voltages at a frequency of 100 Hz to produce index finger abductions against a wide range of purely inertial loads which could rotate around the same axis as that of the second metacarpophalangeal (2^{nd} MCP) joint. The force applied by the finger on the load and the angular velocity of the load were recorded. The torque around the centre of rotation of the 2^{nd} MCP joint was calculated as the product of force and its perpendicular distance from this centre. The torque and angular velocity records were used to separate the contractile and elastic properties of the FDI MTC, determine the instantaneous behaviour of its CC and SEC and calculate the extent to which muscle power is amplified.

2. Introduction

An indispensable part of the modelling process is to assess how well the model describes the situation under consideration by comparing its results with relevant experimental observations. The previous section describes certain possible theoretical behaviours of a muscle-tendon complex MTC shortening against inertial loads (MTI system). This section is based on experimental work on maximal concentric contractions performed *in vivo*.

Despite the fact that during *in vivo* concentric movements agonist MTC(s) would almost always shorten against loads with inertial properties, not many studies have examined MTC mechanics during active shortening against purely inertial loads or loads with large inertial components. Because of the interdependence of muscle force and its shortening velocity (Fenn and Marsh, 1935; Hill, 1938, 1970), most information about the behaviour of human muscle and its series elasticity *in vivo* studies comes from studies in which agonist MTC(s) is(are) loaded either isokinetically (constant angular velocity) or isotonically (constant external load).

During an isokinetic limb movement the agonist MTC, as a whole, may also shorten at a constant speed (provided no considerable changes in its lever arm occur during the movement). Under conditions where inertia may have a considerable effect, corrections may be applied (e.g. Hof, 1997). It was shown however, (Ichinose *et al*, 2000) that during maximal voluntary isokinetic testing at two different velocities of knee extension ($30^0 \cdot sec^{-1}$ and $150^0 \cdot sec^{-1}$) muscle fascicle shortening speed in the vastus lateralis changed throughout the

movement. In addition, while there was a fivefold difference between the two different knee extension velocities, the average shortening speed showed a fourfold change. The authors attributed their observations mainly to the effects of elongation of the tendinous tissue, although other factors such as lever arm changes, fascicle pennation angle, activation and involvement of synergestic muscles could have been involved to some extent. When the fascicle force-velocity observations were obtained at fascicle lengths that were optimal for tension generation, the resulting plot resembled more those obtained from isolated muscle preparations. Cook and McDonagh (1996a) also estimated the force-velocity relationship of the CC for the first dorsal interosseus (FDI) MTC, either from the rising phase of force during isometric tetani using estimates of the stiffness of the FDI SEC (Cook *et al*, 1995) or after timing the isovelocity-release during isometric tetani so as to obtain a force plateau thereby eliminating length changes of the SEC. The resulting CC force-velocity relationships were similar between the two different approaches. The shape of these relationships was typical of those obtained using isolated muscle preparations.

Isotonic experiments, in which the external load is fixed and the speed of movement is measured, also require corrections for the apparatus and limb inertia and for the compliance in series with muscle, in order to estimate the muscle properties (e.g. Wilkie, 1950).

Thus it appears that the behaviour of human MTCs shortening against inertial loads has been somewhat neglected mainly due to the accelerative effects of

force application on the load. Moreover, the interaction between the contractile and elastic properties in a shortening MTC has complicated the interpretation of experimental results. Therefore the aims of the work described in this section were:

a) The development of a method that would allow estimation of the contractile and series elastic properties of a shortening human MTC during contractions performed *in vivo* against inertial loads.

b) Obtaining the instantaneous behaviour of the CC and the SEC during such shortening contractions using the estimated properties from (a).

c) Assess whether and to what extent the maximal CC-generated power is amplified before it is delivered to an inertial load.

The above aims were studied during index finger abductions against inertial loads. Index finger abduction was caused by maximal electrically-evoked shortening contractions of the first dorsal interosseus (FDI) MTC. The small size and superficial position of the FDI muscle are advantageous for maximal activation during percutaneous electrical stimulation. Moreover, the architecture of the FDI muscle has been reported (Cook and McDonagh, 1996a) to be relatively simple, with the majority of the muscle fibres roughly aligned with the tendon (insertion angle to the tendon was less than 5^0 from direct alignment) and with only a small proportion having a different orientation (45^0 insertion angle).

3. Methods

3.1. Volunteers

Five male and one female volunteers (26-44 years; Table 3.1) participated in the experiments using electrically-evoked contractions of the FDI muscle. None of the volunteers reported any neuromuscular or hand-joint disorders. The experiments were approved by the R.N.O.H.T. Ethical Committee.

J.S.	S.P.	A.C.	A.G.	G.O. female	S.H.
30	38	44	29	26	34

Table 3.1. Name initials (top row) and age in years (bottom row) of the volunteers.

3.2. Experimental set-up

The experimental set-up consisted of a purpose-built loading apparatus, transducers for mechanical recordings, an electrical stimulation set-up and a P.C. for data acquisition and processing.

3.2.1. Loading apparatus and transducers

3.2.1.1. Loading apparatus

3.2.1.1.1. Inertia of the apparatus and of the added load

A loading apparatus was designed and manufactured so that the FDI MTC could be loaded with purely inertial loads (figures 3.1 and 3.9). The apparatus consisted of a central aluminium shaft mounted vertically on a frame via two low friction bearings (I.K.O. NAX-1023z). The two bearings were aligned with each other and embedded one at the top platform and the other at the bottom platform of the frame. In this way only rotation of the shaft around its long axis was possible. No other translational or rotational movement of this shaft was possible. Rotation of the shaft around its long axis was prevented during static force measurements by clamping the shaft onto the top platform at the level indicated in figure 3.1.

A small and light aluminium platform could be added onto the shaft near its bottom end. On that platform steel discs of different masses and radii could be attached. Attachment was via pins extending vertically from the base and passing through holes drilled on the steel disks thereby ensuring concurrent rotation of the disks and the shaft. Addition of disks increased the inertial load during shaft rotation.

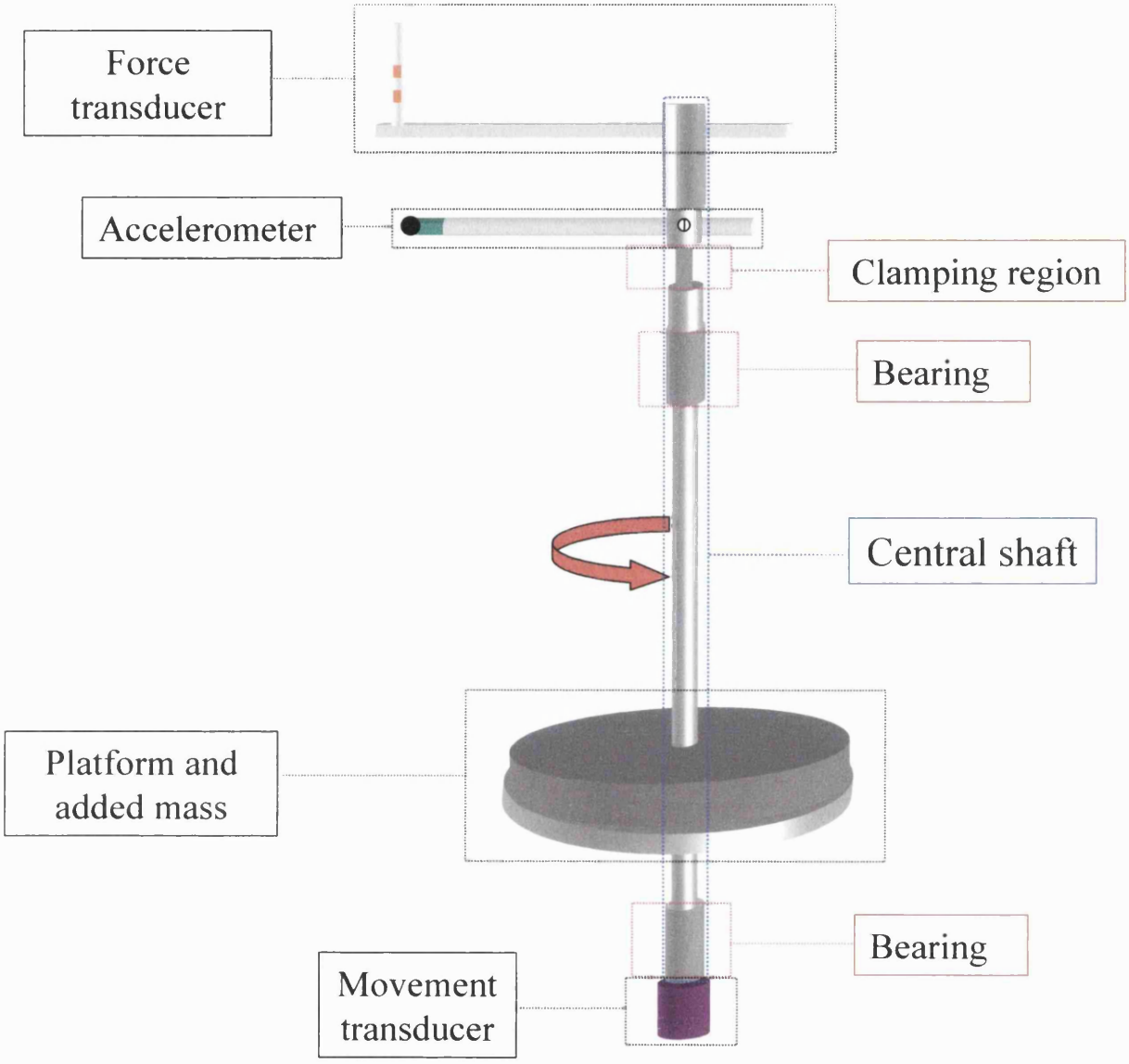

Figure 3.1 Outline of the loading apparatus. See text for description.

The inertia contributed by each added disc (MI_D) during shaft rotation was calculated from its geometrical shape, dimensions and density of the material from which the disks were made according to the following equation (see Low, 1956):

$$MI_D = \frac{\pi \cdot d \cdot h}{2} \cdot \left[R^4 - r^4\right]$$

d is the approximate density of steel, $7.8 \cdot 10^3$ kg·m^{-3} (Kaye and Laby, 1973) ; h is the thickness of the disk, $13 \cdot 10^{-3}$ m; R is the radius of the disc (see table 3.2); r is the radius of the shaft (or of the hollow part of the disk), $12 \cdot 10^{-3}$ m.

R (m)	**0.160**	0.134	0.121	0.113	0.107	0.102	0.098	0.095	0.092	0.895
MI_D (kg·m^2)	0.1004	0.0494	0.0328	0.0250	0.0201	0.0166	0.0141	0.0125	0.0110	0.0098

Table 3.2. Top row: Radius of steel disks (3 decimal places (d.p).). Bottom row: Calculated moment of inertia (4 d.p.) of steel disks around an axis perpendicular to the plane of disk rotation and through its centre.

The total inertia due to disk rotation (MI_{TD}) is the sum of the inertia of all disks attached to the rotating shaft. Moreover, the total inertia during shaft rotation (MI_A; subscript A stands for 'apparatus') is the sum of the inertia of all the structures of the apparatus rotating together with the shaft:

$$MI_A = MI_S + MI_B + MI_{TD}$$

Subscripts S and B denote 'shaft' (and other rotating rods attached to it such as the force transducer) and 'base' (for attachment of steel disks).

3.2.1.1.2. Testing whether the load behaved as a pure inertia

In order to establish that the rotating part of the apparatus indeed behaved as a pure inertial load during contractions, two approaches were used. The first was based on comparison between the recorded torque and angular acceleration traces. The second was based on experimental evaluation of the frictional torque during rotation. The first approach is based on Newton's second law expressed in rotational terms:

$$Tq = MI \cdot \alpha$$

In other words, the angular acceleration (α) of a purely inertial load is proportional to the torque it experiences. The proportionality constant is the moment of inertia of the load. Thus, if the rotating part of the apparatus did behave as a pure inertia, the torque and angular acceleration trace would be identical in shape and only differing by a constant scaling factor equal to that inertia. The angular acceleration traces obtained during contractions were scaled by constant factors to superimpose as well as possible onto the corresponding torque traces (figure 3.2). Such superimposition of traces confirmed that the rotating part of the apparatus behaved as an inertial load.

This method of scaling the angular acceleration trace to match the torque trace was also used to determine MI_S and $MI_S + MI_B$. (It was not possible to use this method to obtain accurate values of MI at higher loads as noise in the accelerometer trace probably due to vibration of the accelerometer rod distorted the records; see figures 3.7 and 3.10 for example). The inertia of the shaft together with the force transducer (i.e. MI_{shaft}) was $1.82 \cdot 10^{-3}$ kg·m^2. When the aluminium base was added to the shaft the moment of inertia (i.e.

$MI_{base} + MI_{base}$) was equal to $2.877 \cdot 10^{-3}$ kg·m^2. Thus the minimal inertia of the apparatus was $1.824 \cdot 10^{-3}$ kg·m^2 and the maximal inertia possible was 0.9062 kg·m^2

According to the second approach, the effect of friction on the rotation of the shaft was determined using the following method. Four infrared light emitting markers were attached on the rotating part of the apparatus, two on the shaft and two on the added steel plates. Torque was then applied to the shaft for a short time in order to accelerate the shaft and the load. After the application of external torque ceased the shaft was allowed to spin freely. During this period of free rotation the position of the markers in 3-D space was measured at 5 msec intervals via a CODA*mpx30* motion analysis system. The friction coefficient, k_f, was then calculated as:

$$k_f = -\frac{MI_A}{2 \cdot \tau}$$

τ is the time constant for the reduction in the kinetic energy of the rotating inertia assuming that no torque other than the frictional torque is acting on the inertia (for details about this method see appendix 3). The values of the frictional coefficient obtained in this way declined linearly with the load within the range of loads used in these experiments (figure 3.3). Assuming this linear relationship holds for the range of loads used in the experiments, the instantaneous value of frictional torque (Tq_f) for all records of index finger abduction was calculated as:

$$Tq_f = k_f \cdot \omega \quad \text{(see appendix 3)}$$

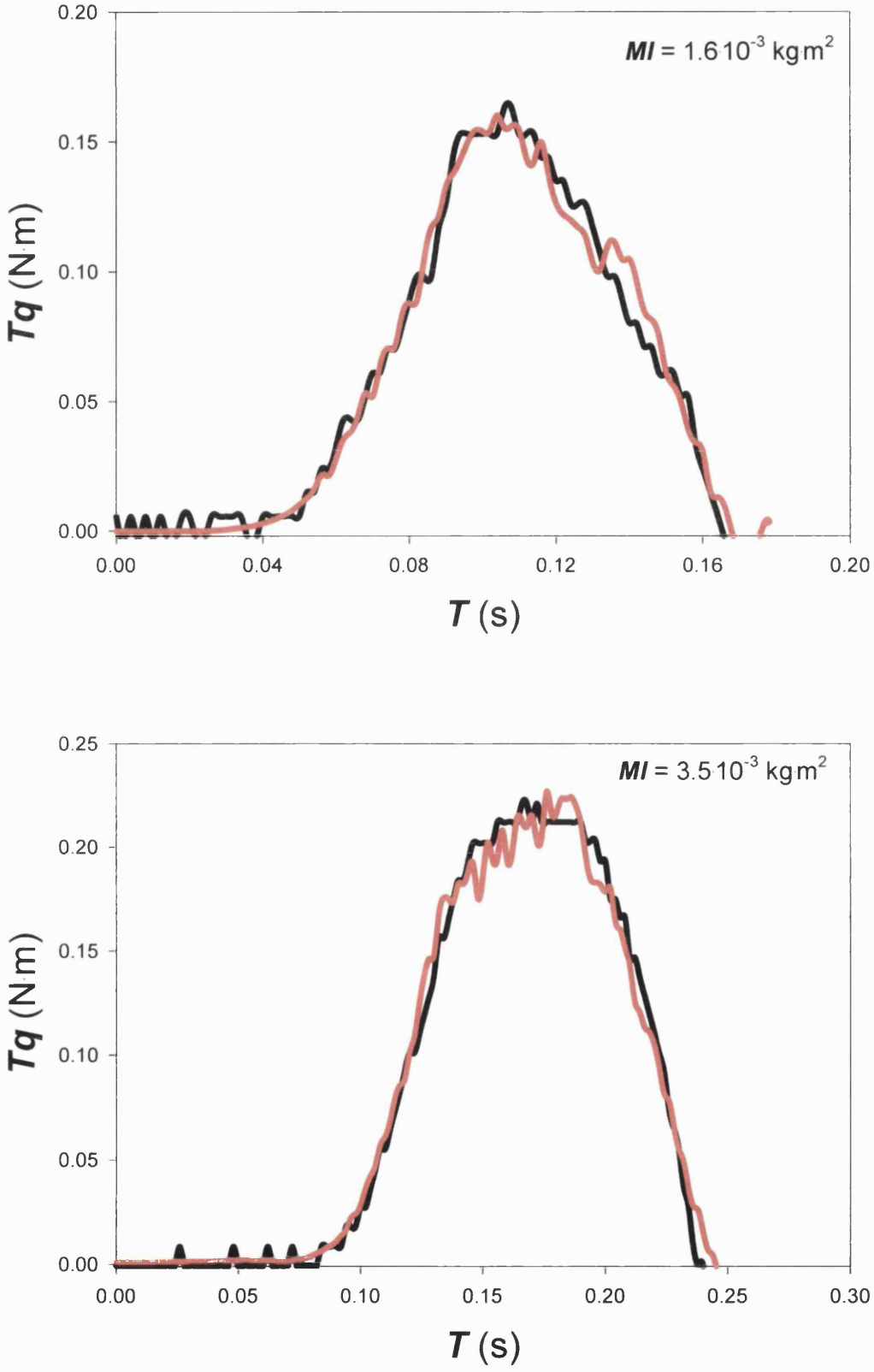

Figure 3.2. Time course of torque (black trace) and angular acceleration (red trace) against two different inertial loads. The angular acceleration trace has been scaled by the corresponding value of the moment of inertia, obtained independently of the accelerometer trace as described below.

for changing the inertia of the rotating part of the apparatus, not all of this range was necessary to utilise during experiments (see section 3.3.2, pp. 243).

This frictional torque was very small in most cases. Parts of records where the frictional torque becomes greater than 1% of the actual recorded torque were not used for analysis.

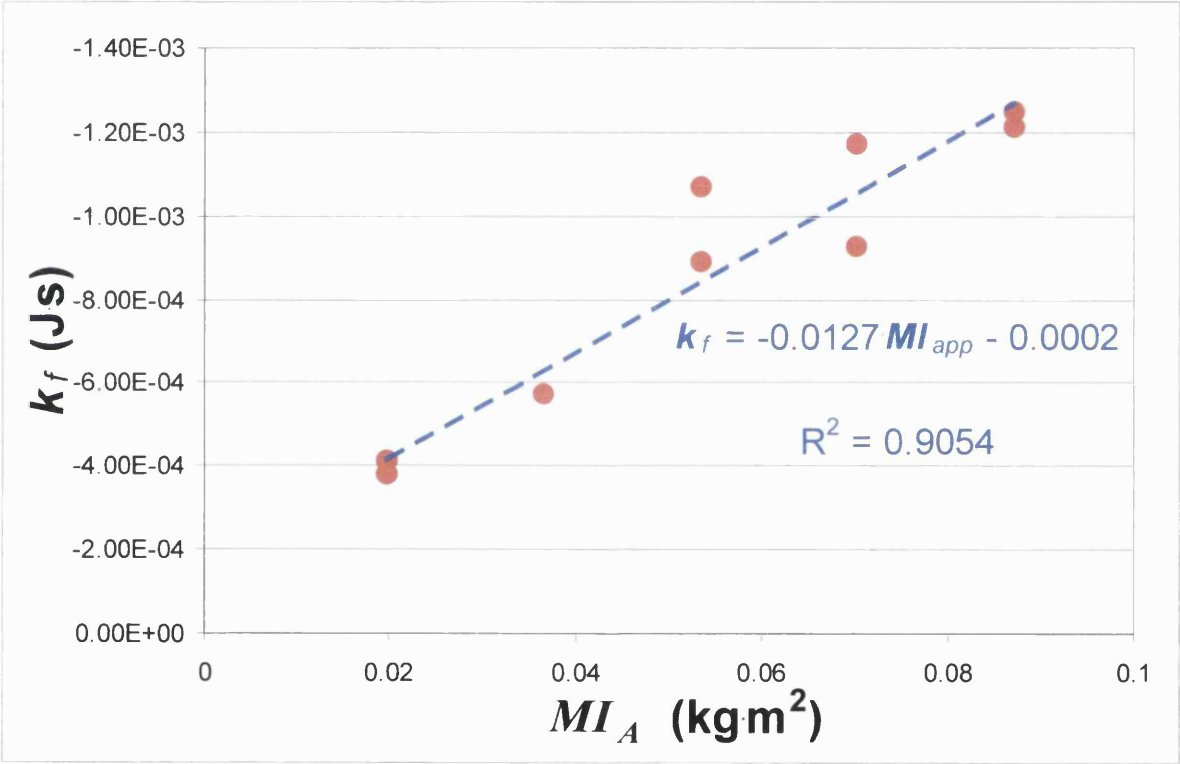

Figure 3.3. Experimental data showing the friction coefficient (k_f) plotted against the moment of inertia of the rotating load (MI_{app}) (red points). The blue broken line shows the best-fit line to these data.

3.2.1.2. Transducers for mechanical recordings

3.2.1.2.1. Force transducer

A force, an acceleration and a movement transducer were attached to the shaft. The force transducer consisted of two aluminium rods connected at right angles with one another (figure 3.4). The longest one of these two rods (FL) was held with two screws (S) into a groove at the top of the shaft (TS) in such a way that the short rod (FS) was projecting upwards. Relaxing the screws (S) allowed sliding of the long rod to a new position before stabilising it again. In this way, the distance of the shorter rod from the centre of rotation of the shaft could be altered. Four foil strain gauges (SG) (5mm, steel; RS 632-168) were attached to the short rod as shown in figures 3.4 and 3.5. The point of application of force (F) during index finger abduction was in the same line as that joining gauges 3 and 4 (figure 3.4 and 3.5). The amplifier (RS AD524AD; Gain: 1000; High cut filter :1000Hz) was receiving current from a ±15 V d.c. power supply. The bridge voltage was 1.5 V.

For a given distance between the top and bottom pairs of strain gauges, when a force is applied on the rod above the top strain gauges, the magnitude of the signal obtained from this particular strain gauge arrangement is sensitive to the force applied on the force transducer rod but not on the position along the length of the rod at which the force is applied. In other words if the same force is applied on different positions along the length of the force transducer rod above the top pair of strain gauges, the signal generated by the force transducer will be the same. This can be understood by looking at the inset in figure 3.4. If a force, F, applied at some distance x, from the top pair of gauges and at distance $x + y$

from the gauges (figure 3.4), the signal is proportional only to the force, F, and the constant distance, y, between the two pairs:

$$[(x+y)\times F]-(x\times F)=y\times F$$

In practical terms this means that if a volunteer applies force at different positions along the length of the force transducer between different efforts, the result will not be affected. This is also true for the same or different volunteers in different experiments. Force application by the index finger on the rod during the experiments was always above the top pair of strain gauges.

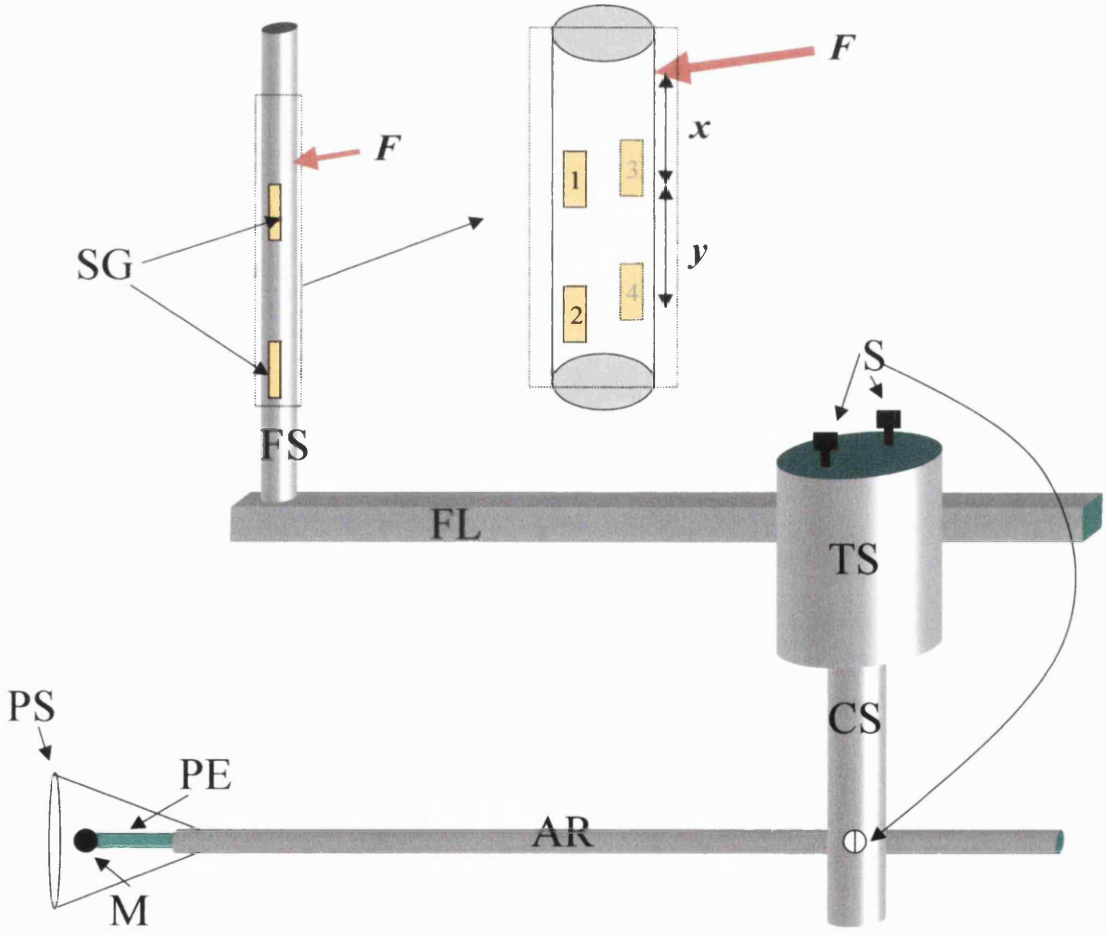

Figure 3.4. Force transducer and accelerometer. *F* = Force. SG =Strain gauge. FS and FL =force transducer short and long rod, respectively. S = screw. TS =Top of shaft. CS =central shaft. AR =Accelerometer rod. PE= piezoelectric element. PS =Plastic shield. M= Added mass. ***x***= Vertical distance between the point of force application on the force transducer and the middle of strain gauges 1 and 3. ***y***= Vertical distance between the top (1 and 3) and bottom set (2 and 4) of strain gauges.

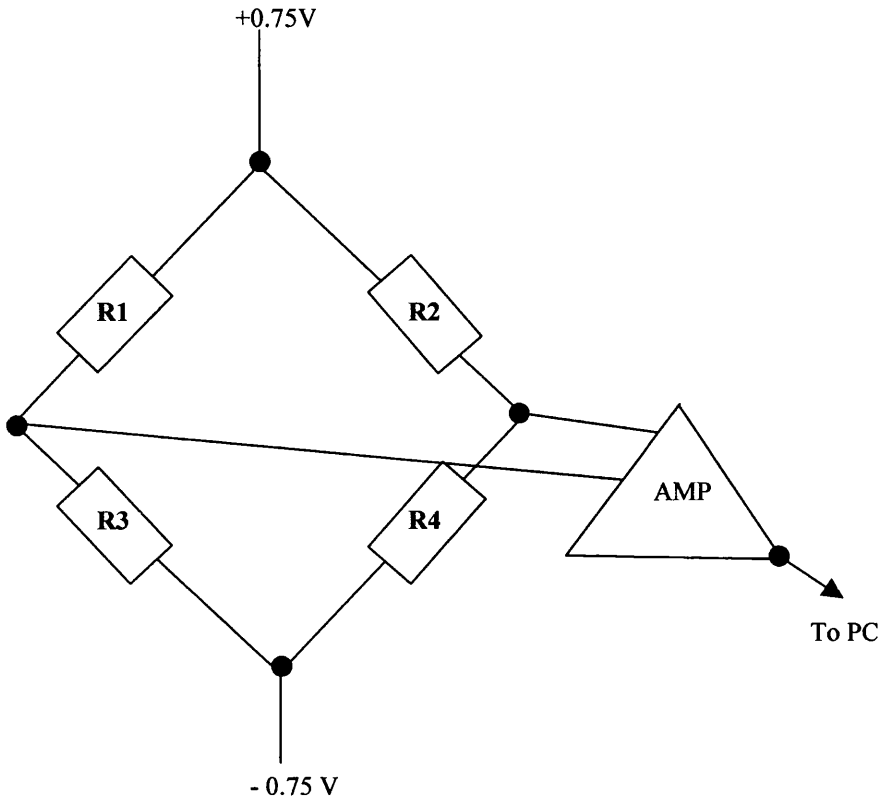

Figure 3.5. Configuration of the strain gauge bridge circuit. Labelling of the strain gauges, shown here as resistors (***R***), is the same as in figure 3.4.

The bare parts of the wires used for connection between the strain gauges and the amplifier were covered with Teflon tape for insulation purposes thereby avoiding sorting of the circuit caused by contact of the wires with the force transducer metal rod.

The force transducer was calibrated by removing it from the apparatus and clamping it with the short rod in a horizontal position. Six separate loads ranging from 0-39.40 N were then added and removed onto the short rod and

the force transducer signal in response to loading and unloading of the rod was recorded. The relationship between the load and the transducer's output was linear with a slope of 30.46 $N \cdot V^{-1}$. An example of a raw signal from the force transducer during finger abduction is shown in figure 3.7.

3.2.1.2.2. Accelerometer

The accelerometer consisted of a piezoelectric bimorph element (RS 285-784) partly inserted in the end of a thin hollow metal tube (figure 3.4). A hole was specifically drilled near the top of the central shaft in order to accommodate the accelerometer rod. The rod was firmly held in that hole by a screw. The part of the piezoelectric element inserted into the tube was firmly held in place by araldite. By adding the piezoelectric element at the end of a rod, the sensitivity to angular acceleration was increased. The length of the rod however was limited by two factors. Firstly, the longer the rod, the greater the amplitude of its vibrations. Secondly, the size of the tabletop frame limited the length of the rod in order to avoid collision between the accelerometer and the pillars of the frame during rotation of the shaft.

To further increase the sensitivity of the element to acceleration a small mass (about 1 g) was added on its tip. As a result of the inertia of this mass, more bending would be caused on the piezoelectric element for a given acceleration. The mass however was kept sufficiently small to avoid damage of the piezoelectric element.

A plastic shield made from an Ependorff pipette was attached to the end of the accelerometer tube in order to protect the piezoelectric element from any kind of contact. The signal from the accelerometer was fed into a high input impedance amplifier, with a parallel condenser across the input (figure 3.6). The accelerometer signal during a contraction was integrated with respect to time to obtain an angular velocity trace. A second angular velocity trace was also obtained by differentiation of the angular displacement trace (see below). The two velocity traces were usually similar in shape when the inertial load was light. At large inertial loads however, the noise in the accelerometer records increased due to vibrations of the accelerometer tube (see figures 3.7, 3.10). Such acceleration signals did not agree well with the movement transducer signal and were not used (see figure 3.10). They were made to overlap by multiplying the velocity trace coming from the accelerometer with a constant value so that the two velocity traces would overlap. This value was then used as the calibration factor for the acceleration signal. An example of a raw accelerometer signal is shown in figure 3.7.

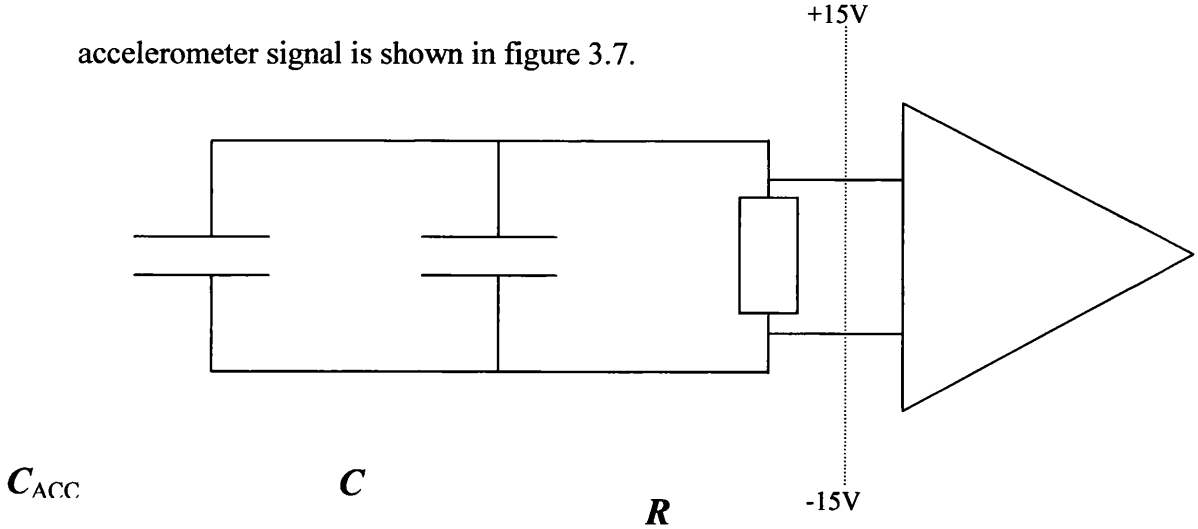

Figure 3.6. Accelerometer circuit. The accelerometer piezoelectric bimorph element is represented as a capacitor (C_{ACC}) whose output is connected to a high-impedance op-amp (RS PMI AMP01 FX9005). A 10 nF capacitor (C) is added in parallel to C_{ACC} to prevent saturation of the amplifier. A 10 MΩ resistor (R) has also been added in parallel to C_{ACC} and C to adjust the time constant of the system and stabilise the input resistance of the amplifier which might otherwise vary from day to day depending on ambient conditions.

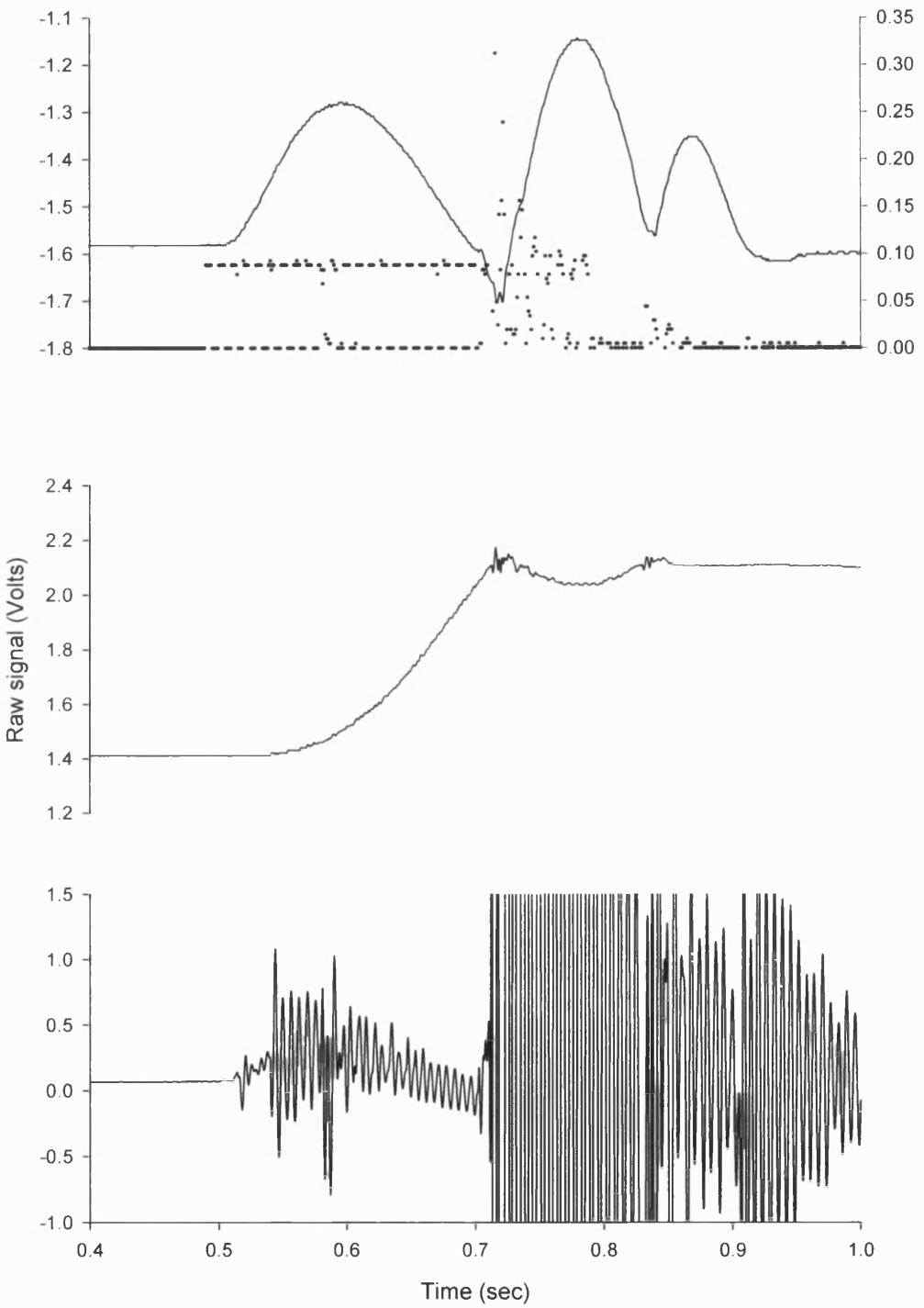

Figure 3.7.Raw signal from transducers. Force transducer signal (left y-axis) and stimulation signals (right y-axis) (top panel), movement transducer (middle panel) and accelerometer signal (bottom panel). Moment of inertia was 0.013 kg·m^2 and lever arm was 0.08 m. Sampling frequency was 1000 Hz. The force applied on the force transducer rod rises and drops as a result of the contraction of the FDI between ~0.5-0.7 sec after acquisition started. Only this part of the record was used for subsequent analysis. A short time after the force has dropped down to its original level and as shaft rotation continues, the shaft hits the stop and bounces back. Force reverses direction until the index finger due to the activity of the FDI, comes in contact with the shaft again and exerts force on it. Because of the noise in the accelerometer signal due to vibrations, its use was limited only to cases were such high noise levels were not present (see text).

3.2.1.2.3. Movement transducer

The shaft of a rotary potentiometer was inserted and firmly held into a hole drilled underneath the bottom end of the shaft. In this way rotation of the shaft caused an equal rotation of the potentiometer shaft. The potentiometer received a voltage supply of approximately 8.2 V. This was done by inserting a 10 KΩ resistor in series with the 12 KΩ resistor of the potentiometer to drop the 15 V supply down to the desired value. The signal from the potentiometer was fed straight to the computer A/D board. The movement transducer was calibrated by rotating the shaft by known small amounts (range: 0-0.524 rad; step size: 0.174 rad) and the signal coming from the movement transducer was recorded. The relationship was linear with a slope 0.733 $rad \cdot V^{-1}$. An example of a raw movement transducer signal is shown in figure 3.7.

3.2.1.3. Hand positioning and stabilisation

3.2.1.3.1. Estimating the position of the centre of rotation of the 2nd MCP joint

In order to ensure that the measured angular displacement was the same as that of the index finger, the centre of rotation (CR) of the second metacarpophalangeal (MCP) joint and of the shaft had to be aligned. The position on the hand of the 2nd MCP-CR was determined in the following manner: The volunteer would place his\her right hand on a sheet of paper resting on a hard but smooth surface. Hand positioning was in the same way as during the experiment. The contour of the hand would then be drawn on the sheet of paper (figure 3.8). He/she would then abduct the index finger against a pen held in a vertical position such that its tip was in contact with the paper. During the abduction the pen was firmly held in the same position with respect

to the finger. As a result of the abduction, the arc of a circle would be drawn on the paper. The process was repeated several times, each time holding the pen in a different position along the volunteer's index finger such that a family of arcs belonging to concentric circles of different radii was obtained (figure 3.8). The sheet of paper with the hand contour and the arcs would then be overlapped by a transparency onto which many concentric circles were drawn. The position of the transparency was then adjusted such that arcs drawn during abduction would be superimposed as well as possible by arcs of the circles in the transparency. The agreement between the arcs resulting from abducting the finger and the arcs of the concentric circles in the transparency, indicate that no considerable translation or gliding took place in the joint during abduction. The position of the 2^{nd} MCP-CR on the hand drawing was the taken to be the same as the position of the CR of the concentric circles in the transparency. A mark was made on the hand drawing to indicate this position (figure 3.8). The contour of the hand was then removed with scissors from the sheet of paper and stuck on the table top of the apparatus, with the 2^{nd} MCP-CR mark directly above the shaft's CR. Assuming no movement of the 2^{nd} MCP-CR during a contraction, the angular displacement during abduction would be the same as that measured from the displacement of the shaft. Furthermore, the distance of the force transducer short rod from the shaft's CR would be the same as the lever through which the load acts on the 2^{nd} MCP joint.

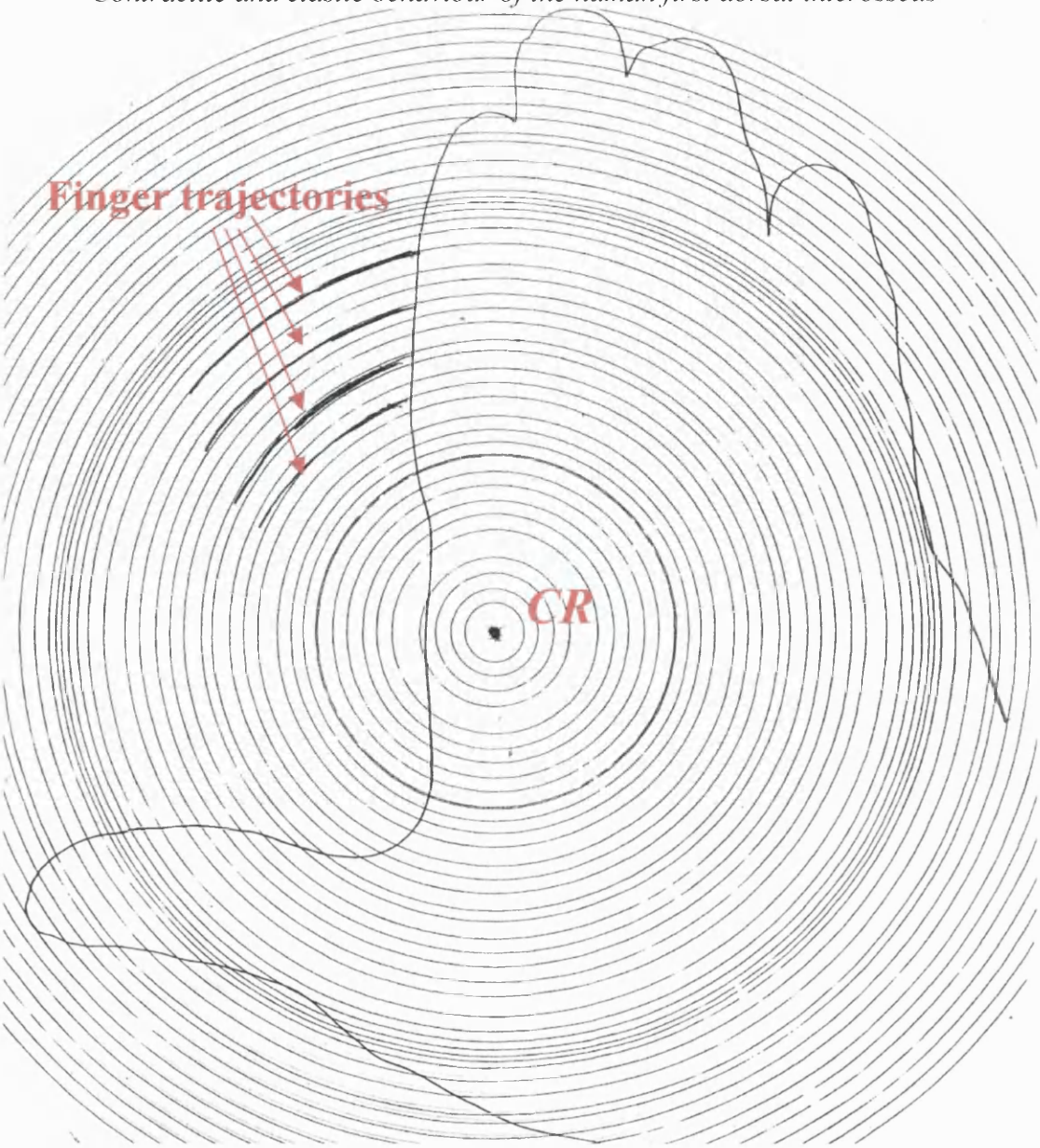

Figure 3.8. Estimating the position of the centre of rotation of the 2nd MCP joint. Contour of a volunteer's (AG) hand. The finger trajectory during abduction is shown as bold dark arcs by the index finger. The centre of concentric circles superimposed on these arcs is taken to represent the centre of rotation (CR) of the index finger during abduction.

3.2.1.3.2. Stabilising the hand

The tabletop of the apparatus was designed to provide a sturdy support for the hand during the experiments while minimising involvement of MTCs other than the FDI during index finger abduction. This was achieved by stabilising the forearm, hand and all fingers other than the index finger. Forearm stabilisation was near the wrist via a Velcro strap that held the forearm tight against the tabletop (FS in figure 3.9). The whole of the hand, except the fingers, was also pushed down against the tabletop using an adjustable perspex block (HS in figure 3.9). The surface of the perspex block in contact with the hand was coated with foam such that sufficient pressure to stabilise the hand could be applied with minimal discomfort. The pressure would be released if necessary during resting periods of the experiment to reduce discomfort arising from prolonged application of pressure and allow restoration of normal blood flow to the hand. As part of the FDI MTC originates from the 1st and 2nd metacarpal and only the amount of index finger rotation was used to indicate movement due to shortening of the FDI MTC, the thumb had be stabilised during the experiment. The thumb was kept in a relatively stretched position that was maintained throughout the experiment and was the same between different experiments for the same volunteer. Stretching of the thumb was via a Velcro strap that could be pulled into different positions via a rigid thin chain (TS in figure 3.9). The broad range of abduction angles in the active torque-angle relation within which maximal or near maximal static torque can be generated (see later section) indicates that the FDI muscle was near its optimal length for isometric force production. If that was not the case, a steeper decline in the ability to generate torque statically could have been observed with increasing the abduction angle

(thus shortening the FDI muscle). The middle, ring and little fingers were separated from the index finger with a metal stop between the index and the middle fingers (S in figure 3.9). The volunteer was also asked to try to consciously minimise possible involvement of MTCs other than the FDI during the experiment by sitting in an upright position and only focusing on index finger abduction.

Part of the force transducer short rod extended upward through a groove made on the tabletop surface (G in figure 3.9). The groove had the shape of the arc of a circle to allow for angular displacement of the force transducer rod. The length of the groove allowed for greater angular displacements than those used during the experiments and its width was sufficiently great to allow adjustment of the position of the long force transducer rod that was necessary due to the different hand sizes between the volunteers.

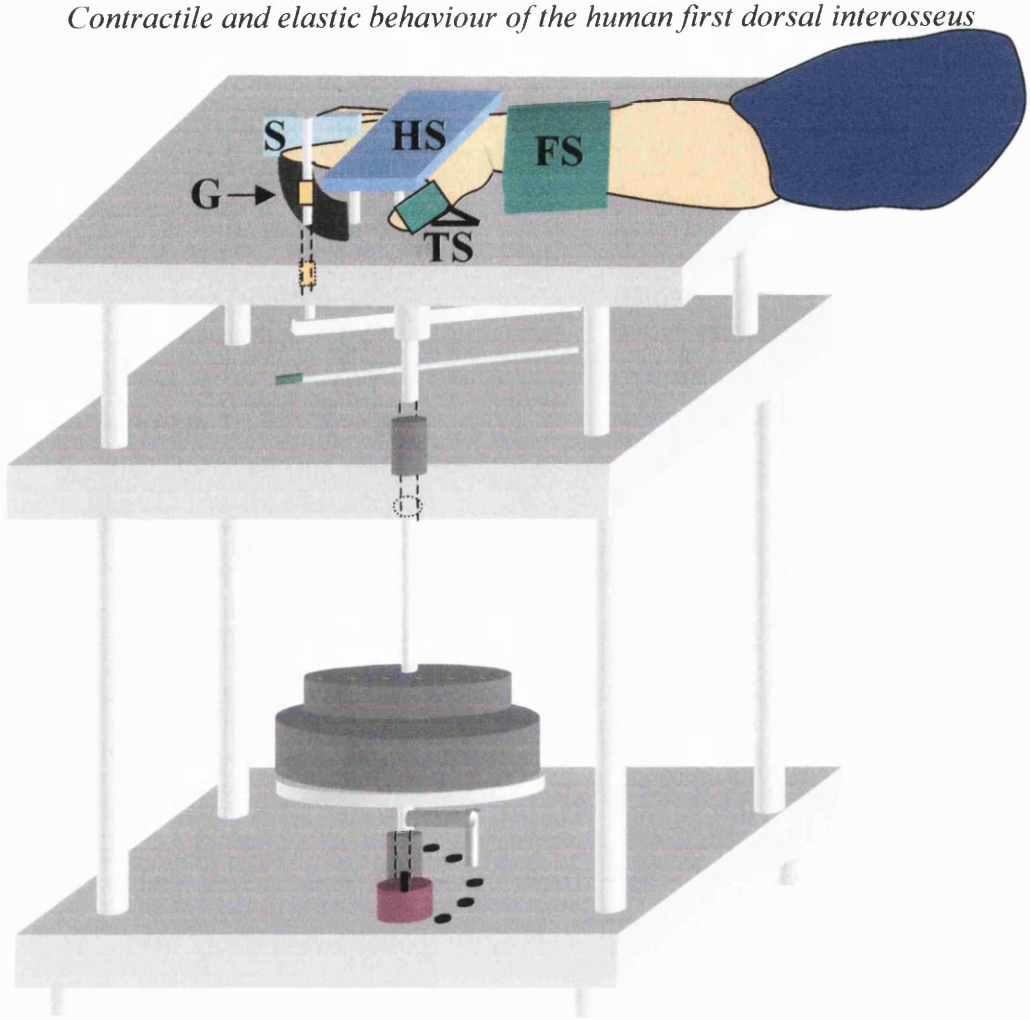

Figure 3.9. Loading apparatus and hand positioning on tabletop. Forearm stabilising strap (FS), hand stabilising block (HS), finger stop (S), thumb stop (TS) and force transducer groove (G).

3.2.2. Electrical stimulation

The skin over the FDI MTC was cleaned with cotton wool soaked in ethanol and two self adhesive disposable electrodes (Blue Sensor N-10-A, 25; circular surface: 10mm diameter) were attached on the hand such that the cathode (-) was near the tip of the angle formed by the first and second metacarpal bones and the anode (+) near the myotendinous junction of the distal part of the FDI MTC. The electrodes were further secured by PVC tape.

The stimulator (Devices, type 3072) produced rectangular pulses of 50 and 100 μsec pulse widths. The pulse train duration and stimulation frequency of the stimulator were controlled by a digital timer (Digitimer D4030). The stimulation frequency was always kept to 100 Hz. The duration of the stimulation was adjusted according to whether the contraction was static or dynamic. The stimulation duration for isometric contractions was always 500 msec. This duration was sufficient for achieving an isometric force plateau. The duration for dynamic contractions was varied according to the time required to overcome the different amounts of inertial resistance. In order to achieve that, the stimulation waveform was recorded together with the force transducer signal to ensure continuous stimulation throughout each push. Whenever that was not the case the duration of the stimulation would be increased accordingly. An example of a raw signal coming from the stimulator is shown in figure 3.7.

In order to achieve maximal activation of the stimulated part of the FDI muscle, maximal voltages were used during the experiments. The voltage of the maximal stimulus and the pulse width were determined prior to each experiment

by applying stimulation trains (500 msec; 100 Hz; pulse width: 50 μsec) every one minute and simultaneously recording the static torque around the 2nd MCP joint at a given index finger abduction angle. The stimulation voltage was increased between subsequent stimulations in steps of 10-20 V until no further increase in the static torque was observed. If this static torque plateau was not reached with stimuli up 190 V, the pulse width was increased to 100 μsec and the process was repeated until a torque plateau was reached. The lowest stimulation voltage and pulse width at which no increment in the torque was observed were subsequently used during the dynamic contractions. The average maximal electrically-evoked torque achieved for different volunteers in the dynamic experiments ranged between 60-103% of the corresponding average maximal voluntary torque.

3.2.3. Data acquisition and processing

The analogue signals coming from the force transducer, accelerometer, movement transducer and the stimulator were collected for 2 sec by a PC at a frequency (f) of 500 Hz in all volunteers except AG (f =1000 Hz) and converted into digital via an A-D converter (12 bit, Keithley DAS-802). The fastest mechanical outputs during index finger abduction were between 10-15 Hz (see figure 3.2 for example). Thus, the sampling frequencies used here were well above the minimal required sampling frequencies (~20-30 Hz) to observe this fundamental frequency and allow higher "harmonics", up to at least 10 times the fundamental frequency, to be observed also. The noise content of the records and its effect on the results is discussed in a later section. The software

used for data acquisition and part of the processing was Keithley TESTPOINT 3.3 and MathCad 7.

3.2.3.1. Calculation of a time scale

A time scale was created for each contraction. If r is a range variable representing the order number for each data point in a record, time (T) was calculated as:

$$T_r = r \cdot \Delta T \quad (r = 0,1,2,..,N-1)$$

where N is the number of points collected during the two second period.

The first one hundred points in the torque, movement and acceleration traces, while the FDI MTC was not activated, were averaged and subtracted from the corresponding records to obtain a zero baseline. After this, each record was truncated to include only the time period while the FDI muscle was being stimulated. The time scale was therefore recalculated in the same manner as describes above for the selected part of each record, such that zero time would correspond to the onset of electrical stimulation.

3.2.3.2. Calculation of torque

A short recording period preceded the start of stimulation so that the average of the first 100 points coming from the force transducer could be subtracted from the whole record in order to obtain a baseline that is equal to zero. The torque around the 2nd MCP joint, $Tq\,(N \cdot m)$, was calculated as the product of that force and the distance of the CR from the centre of the force transducer short rod; this distance was measured in each experiment.

3.2.3.3. Angular acceleration of the load

The signal coming from the accelerometer was recorded and processed as described in section 3.2.1.2.

3.2.3.4. Angular displacement of the load

The signal coming from the movement transducer was also corrected in a similar manner as the force trace to obtain a baseline equal to zero. The corrected trace was then multiplied by the angular displacement calibration factor (0.733 rad·V^{-1}) to obtain the angular displacement of the load, Θ_L (rad).

3.2.3.5. Recording the stimulation

The signal coming from the stimulator was also recorded. After the end of each contraction, the calculated torque, angular displacement and stimulation traces were graphically displayed on the computer screen to ensure that electrical stimulation lasted throughout the time while torque and angular acceleration were greater than zero. This ensured that the recorded mechanical outputs were produced by an activated and not by a relaxing muscle.

The traces of Tq, Θ_L and the stimulation trace were saved together as text files for subsequent processing using Mathcad 7.

3.2.3.6. Calculation of the inertia of the load from torque and movement records

The moment of inertia of the rotating part of the apparatus was estimated from the torque and angular displacement traces. As $Tq = MI_A \cdot \frac{d^2}{dT^2}(\Theta_L)$, Θ_L can be obtained as $\Theta_L = \frac{1}{MI_A} \cdot \int_0^T \int_0^T Tq \cdot dT$. Re-arranging this expression $MI_A = \frac{\int_0^T \int_0^T Tq \cdot dT}{\Theta_L}$. The quantity at the top of the fraction can be obtained from double integration of the torque output with respect to time. Integrating once yields the area under the torque time curve. Integration to obtain the area under the torque-time curve, i.e. the impulse or its equivalent the angular momentum, was obtained using the 'rectangle' rule. Angular momentum is the product of the moment of inertia times the angular load velocity. Second integration using the same method yielded the area under the momentum-time curve, which is equivalent to the moment of inertia times the angular displacement of the load. By dividing the mean angular displacement value for the each record by the corresponding mean value of the area under the impulse-time curve, the value of the moment of inertia for the particular contraction was obtained. Rather than quoting the moment of inertia values calculated from the dimensions and material density of the parts of the apparatus (section 3.2.1.1.1, pp. 215) the moment of inertia during each effort was calculated separately for each contraction as described in this section.

The moment of inertia overcome by shortening of the FDI MTC is equal to the sum of the inertia offered by the apparatus plus the inertia of the index finger around the 2nd MCP joint. In order to assess whether an accurate estimation of the inertia of the finger was worthwhile, a maximal finger-inertia value was calculated assuming a perfectly cylindrical finger of length equal to the longest finger of the volunteers ($L = 0.101$ m), a diameter equal to the width of the widest index finger ($D = 0.029$ m) and a density equal to the density of cortical (compact) bone (d=2.0·10^3 kg·m^{-3}; Nigg and Herzog, 1999; Snyder *et al*, 1981). The moment of inertia for this model index finger was calculated as:

$$\frac{1}{4}\cdot\pi\cdot d\cdot L\cdot\left(\frac{D}{2}\right)^4 \approx 7\cdot10^{-6}\ \text{kg·m}^2$$

This value is $\frac{1.8\cdot10^{-3}}{7\cdot10^{-6}} \approx 257$ times smaller than the smallest inertia due to the apparatus that the FDI had to overcome. Because of its small magnitude this quantity was considered negligible and was therefore not taken into account.

3.2.3.7. Torque rate calclation

For dynamic contractions, the torque rate ($\frac{d}{dT}(Tq)$) at a given time was calculated as the slope of the best fit regression line through the torque point at that time and also five points immediately before and after that time, i.e. using a smoothing factor of 5. Thus, the torque rate calculation started from the fifth point of each acquisition (r=4) and ended five points before the last point (r=N-6). For static contractions, the torque rate at a given time used a smoothing factor of 10.

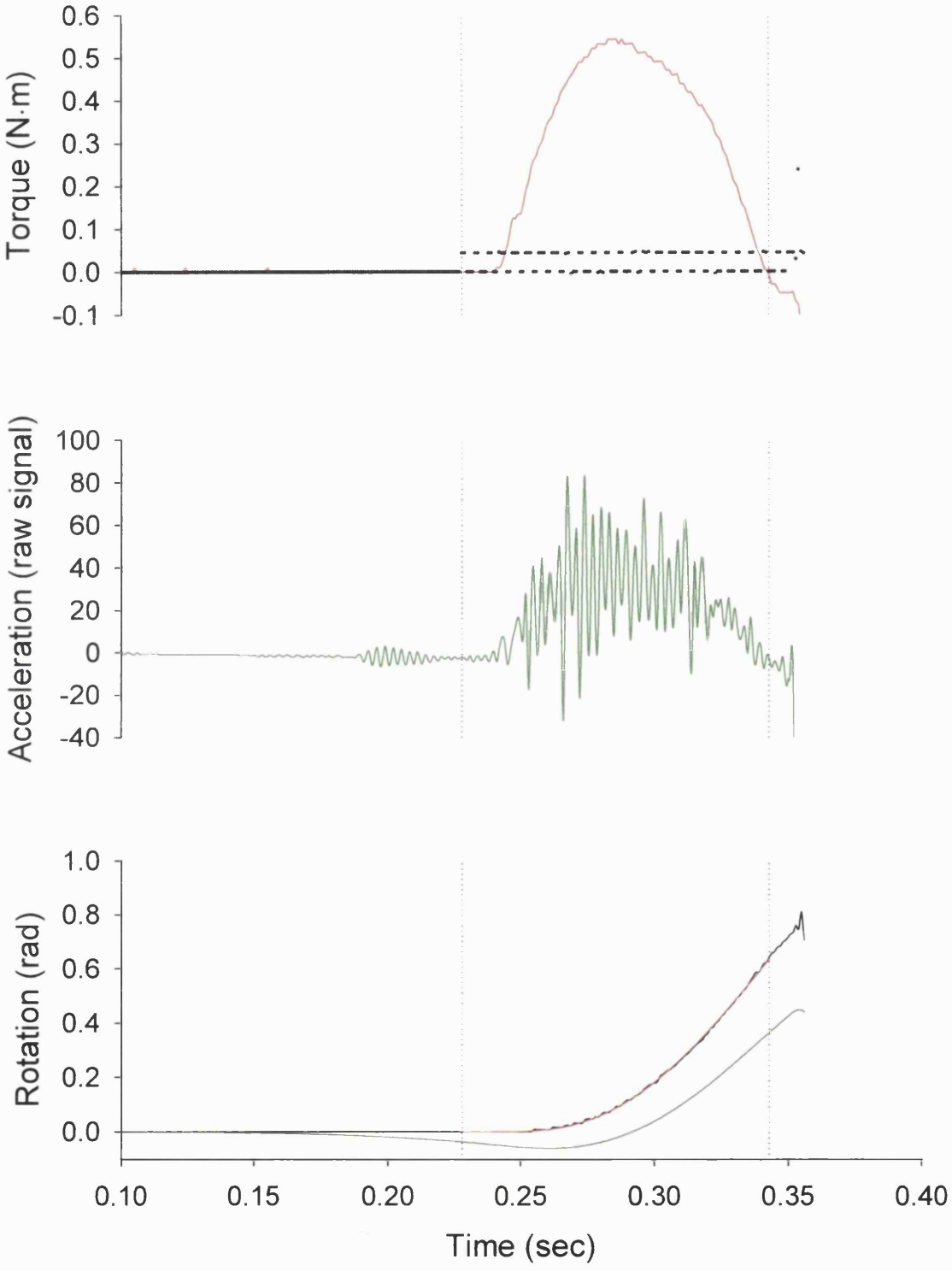

Figure 3.10. Agreement between transducer signals. Top panel: Torque output (red) and stimulation signal (black). Middle panel: Raw accelerometer signal (middle panel). Bottom panel: Rotation measured by the movement transducer (black) and calculated by double integration of acceleration (green) and torque (red) and appropriate scaling. The time scale is with respect to the time of the start of data acquisition. Vertical lines indicate the part of the original acquisition that was used for further processing. Moment of inertia was 0.012 $kg \cdot m^2$.

3.2.3.7. Calculation of the angular load velocity

The angular velocity of the load (Ω_L) was calculated as the area under the torque-time trace using the 'rectangle rule' divided by the moment of inertia of the external load (see methods for calculation of moment of inertia). Using the rectangle rule was expected to cause a leftward time shift in the resulting curve but this shift would only be by a fraction of ΔT and this effect was therefore treated as negligible. Although this method for calculating velocity is not often encountered, it was preferred to differentiating the angular displacement trace with respect to time in order to avoid noise resulting from the differentiation process. Moreover, the integrating acceleration records with respect to time was avoided as they often contained noise that appeared to be due to vibration of the thin metal accelerometer tube. This is evident in the raw accelerometer signal shown in figures 3.7 and 3.10. Double integrating acceleration records from contractions against inertial loads and applying appropriate scaling to match the result with the measured rotation did not result in very good agreement. This is illustrated in figure 3.10.

3.2.3.8. Calculation of the power delivered to the load

The power delivered to the load (P_L) was calculated as the product of the torque and the corresponding angular velocity.

3.3. Experimental protocol

3.3.1. Static torque measurements

3.3.1.1. Electrically evoked

Static torque-angle plots of the index finger FDI MTC were obtained during maximal electrically evoked contractions. The torque around the 2nd MCP joint was measured in four different abduction angles, within the range of movement of the joint. The first angle was zero radians (i.e. no abduction). The fourth angle was the greatest abduction angle possible to achieve voluntarily by the subject and the other two were intermediate between the first and fourth angles (approximately one third and two thirds of the abduction range, for the second and third angle respectively). The second angle was serving as a fatigue control angle and measurements at this angle were repeated after every two other contractions. All other angles were tested twice during the experiment. At least one minute rest intervals were allowed between subsequent contractions to minimise fatigue. The order of the abduction angle at which static torque was measured was the following:

$$2^{nd} \rightarrow 3^{rd} \rightarrow 1^{st} \rightarrow 2^{nd} \rightarrow 4^{th} \rightarrow 3^{rd} \rightarrow 2^{nd} \rightarrow 1^{st} \rightarrow 4^{th} \rightarrow 2^{nd}$$

3.3.1.2. Passive

Passive torque was also measured in either three or four different angles within the full abduction range. Passive measurements were performed by placing the finger on the other side of the force transducer compared to the 'active' torque experiments. The experimenter would then rotate the force transducer long rod and thus the index finger of the volunteer to the desired angle. Data acquisition started about 2 sec after reaching the set angle, and while data was recorded the

experimenter quickly moved the force transducer away from the volunteer's finger back to the corresponding no-abduction angle, causing the torque to drop. An example of a torque and angular displacement trace obtained in this way is shown in figure 3.12. The passive torque for that index finger angle would be the difference between the torque while the finger was held in the abducted position and the torque registered after the finger had lost contact with the force transducer. The corresponding angle was determined from the angular displacement trace obtained as the force transducer was moved from the abduction angle at which the torque was measured to the no-abduction position. A correction was applied to that angle to take account of the thickness of the volunteer's finger and the radius of the force transducer force rod.

3.3.2. Dynamic contraction experiments

Maximal electrically evoked shortening contractions of the FDI MTC are considered in this study. The features of the maximal stimulus (voltage and pulse width) were determined at the beginning of the experiment and in the same way as described in section 3.2.2. The inertial load during index finger abduction was varied over a wide range (approximately 280-fold) (table 3.3).

MI_A (10^{-3}·kg·m^2)	1.8	2.9	12.7	15.3	19.5	27.8	52.2	103.2	203.6	304.0	404.3	504.7

Table 3.3. Inertial loads in the order used in the experiments. Although the inertial load was calculated during each contraction as described in section 3.2.3.6, this brief summary of the inertial loads has been calculated as described in section 3.2.1.1.1.

In designing the format of the experiment several factors were taken into account. The total duration of the experiment was kept to no longer than an hour for the convenience of the volunteers. Within this hour maximal contractions were performed against twelve loads. Two contractions were performed against each load so that sufficient time for recovery between contractions was allowed during the one hour of the experiment. The recovery time between dynamic contractions was at least sixty seconds.

In order to test whether the recovery period was sufficiently long to prevent fatigue, a maximal static torque measurement at a 'control' abduction angle was obtained every three loads throughout the experiment and was compared with the result of the same measurement obtained just prior to the dynamic experiment. Due to the greater torque-time integral in a static contraction compared to a dynamic contraction, a two-minute resting period was allowed after the static efforts. Results from the control contractions are shown in figure 3.19. (Also see later sections regarding adjustment for variations in the control static torque).

In most of these experiments the electrical stimulation probably did not reach all of the FDI muscle, even when maximal as defined above. Therefore in order to assess the relative volume of the FDI muscle that was activated during electrically evoked contractions, a maximal voluntary contraction was performed at the start of the experiment and the peak static torque obtained via electrical stimulation was compared to the peak static torque obtained voluntarily. Each volunteer repeated the experiment at least twice, each session performed on a different day. However, for

each volunteer, analysis was carried out on results coming from the session in which electrical stimulation elicited the highest static torque.

4. Results and analysis

4.1. Static torque-angle relationship for the FDI MTC

4.1.1. Measurements

Figure 3.11 shows a typical torque record of a static (or isometric) contraction in response to electrical stimulation of the FDI muscle. Figure 3.12 shows a record representative of those used for measurement of passive torque and of the corresponding index finger abduction angle.

4.1.2. Static torque-angle plots

The peak values of passive torque and electrically evoked ('active') torque together with the corresponding abduction angles were used to construct the passive and active static torque-angle plots that are shown in figures 3.13.A and 3.13.B.

Analysis of the dynamic data usually took place in the 0-0.3 rad range (see section 4.3, pp. 292). The 0.3 rad angle limit is marked on the graphs of figure 3.13.A and 3.13.B to help visualise the magnitude of passive torque relative to the active torque within the angle range the dynamic results apply. The graphs also include the best-fit line to the passive data generated by an exponential equation of the form:

$$Tq_{PAS} = C_1 \cdot \left(e^{\frac{\Theta}{C_2}} - 1 \right) \quad (3.1)$$

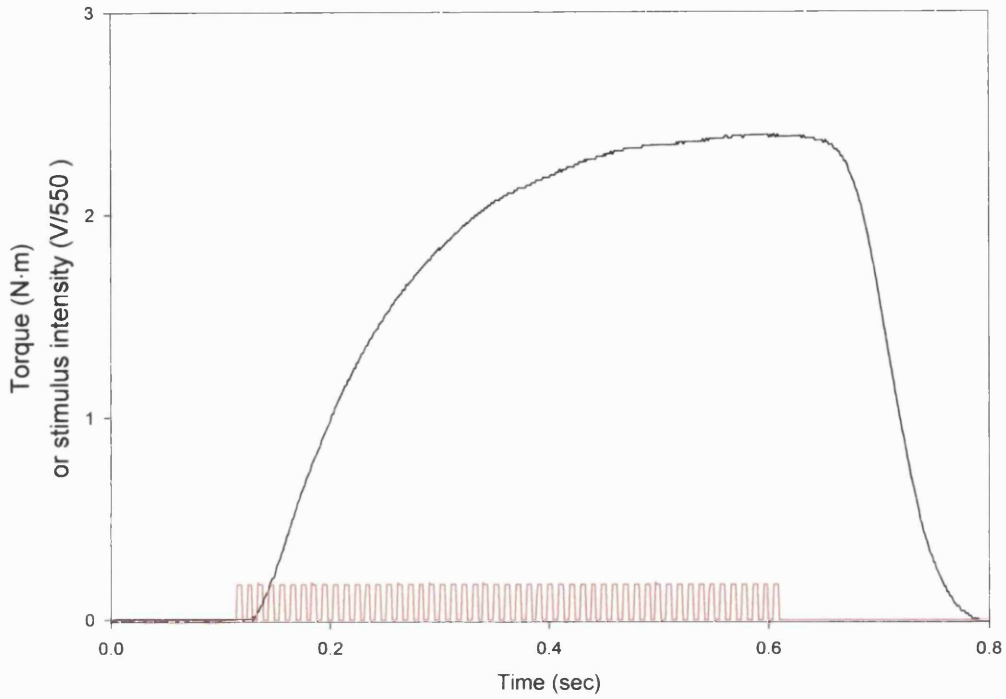

Figure 3.11. Static torque (black trace) and corresponding electrical stimulation record (red). The peak torque achieved in this contraction was 2.395 N·m.

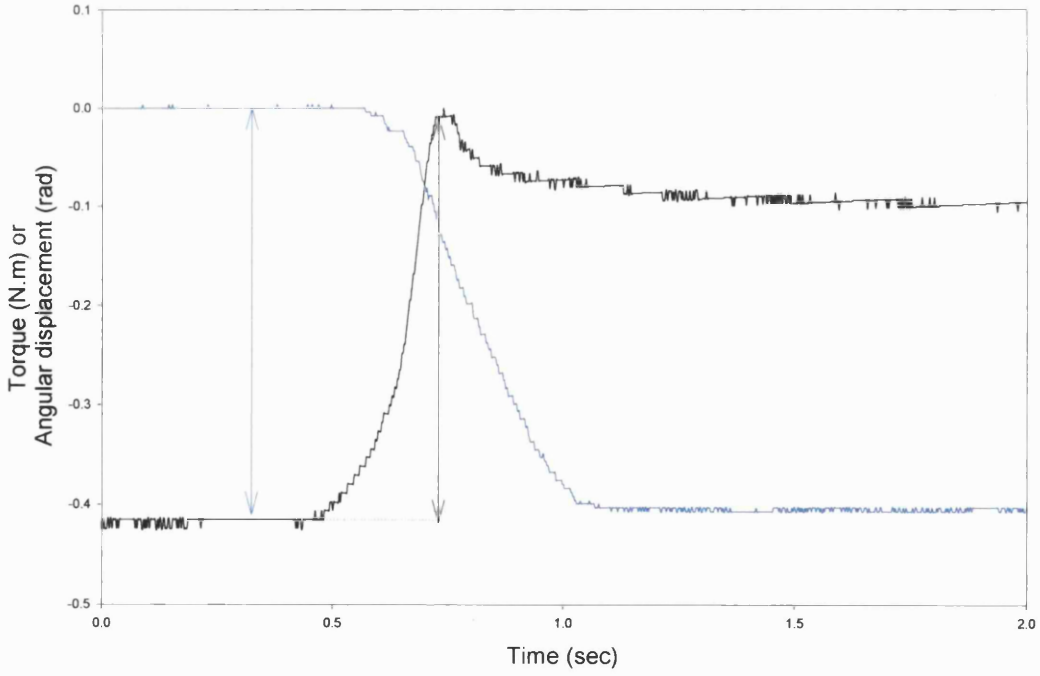

Figure 3.12. Passive torque (black trace) and angular displacement (blue trace) records. Zero torque is at the top of this graph and negative sign indicates clockwise sense. The magnitude of the passive torque and of the index finger abduction angle at which the torque was measured are shown by the corresponding arrows. The passive torque temporarily reaches zero while the force transducer and the index finger are not in contact and then increases again as the finger catches up again with the transducer.

where Tq_{PAS} is the passive torque, Θ is the angle at which Tq_{PAS} is measured and C_1 and C_2 are constants that provide the best fit to the passive torque-angle observations.

The values of these two constants were determined using Mathcad 7 and are shown for each volunteer in table 3.4. Equation (3.1) along with the values of C_1 and C_2 can be used to obtain an estimate of the passive torque that has to be overcome by the FDI MTC at any angle within the range of abductions used in the experiments.

Volunteer	JS	SP	AC	AG	GO	SH
C_1	$2.526 \cdot 10^{-3}$	$1.144 \cdot 10^{-7}$	$2.156 \cdot 10^{-8}$	$3.393 \cdot 10^{-4}$	$8.095 \cdot 10^{-4}$	1.545
C_2	0.280	0.062	0.056	0.166	0.214	11.924

Table 3.4. Values for C_1 and C_2 of equation (3.1).

Calculation of the active torque around the 2nd MCP joint uses the force registered by the force transducer. However, if passive torque was considerable, part of the electrically-evoked muscle force would be used to overcome the passive torque and part would be registered by the force transducer. This would lead to an underestimation of the actual active torque generated by the FDI-MTC. Therefore, before creating active torque-angle plots for the FDI-MTC it was assessed whether the passive torque was considerable compared to the externally recorded active torque. As the active torque-angle relationship is only of interest in this work because of possible effects on the mechanical output during dynamic contractions, the above assessment only took place within the

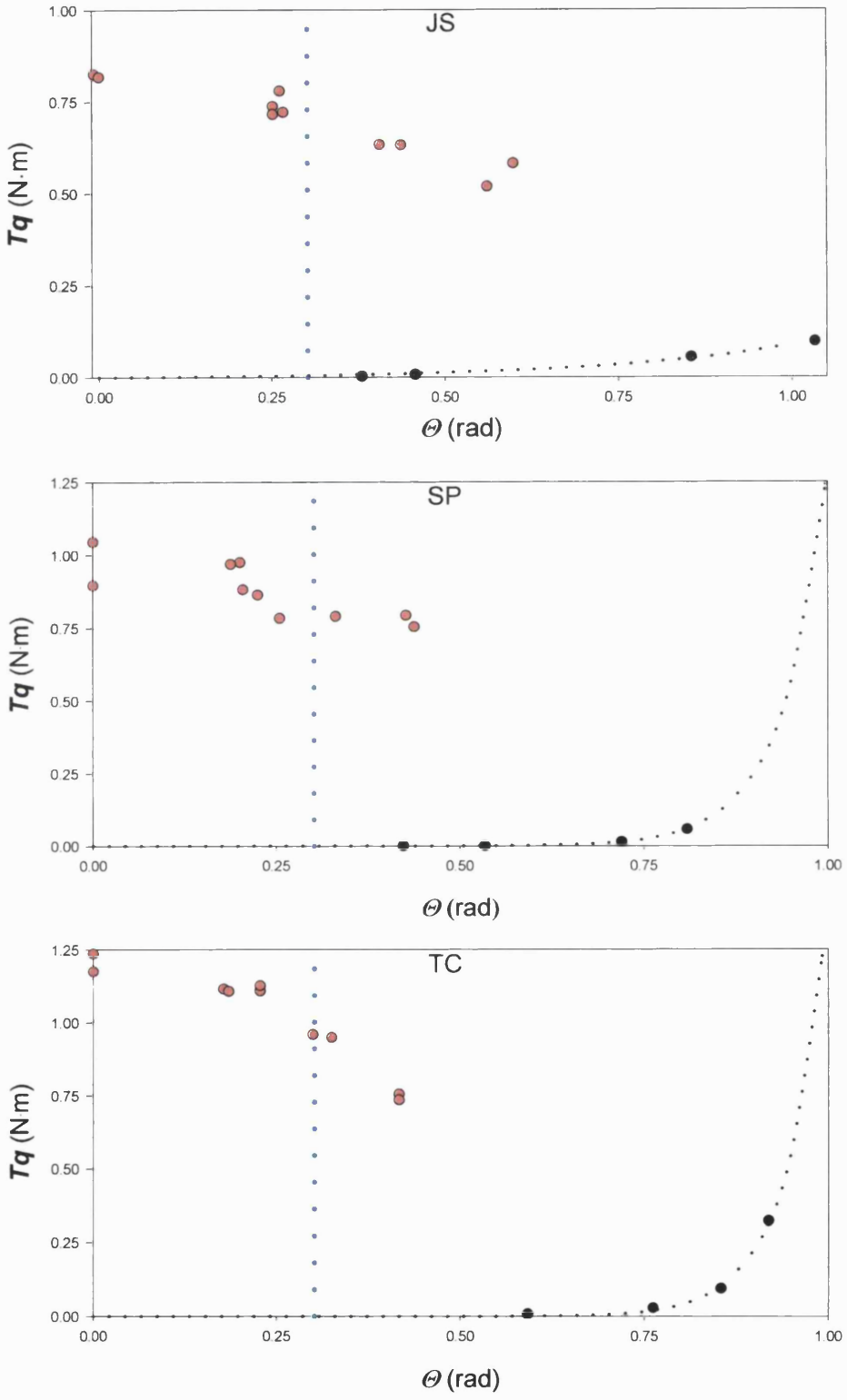

Figure 3.13.A. Active (red circles) and passive (blue circles) torque-angle relation for three volunteers. Best-fit line to the passive data (black dotted) generated by an arbitrarily chosen exponential function (see text). The blue dotted vertical line indicates 0.3 radians.

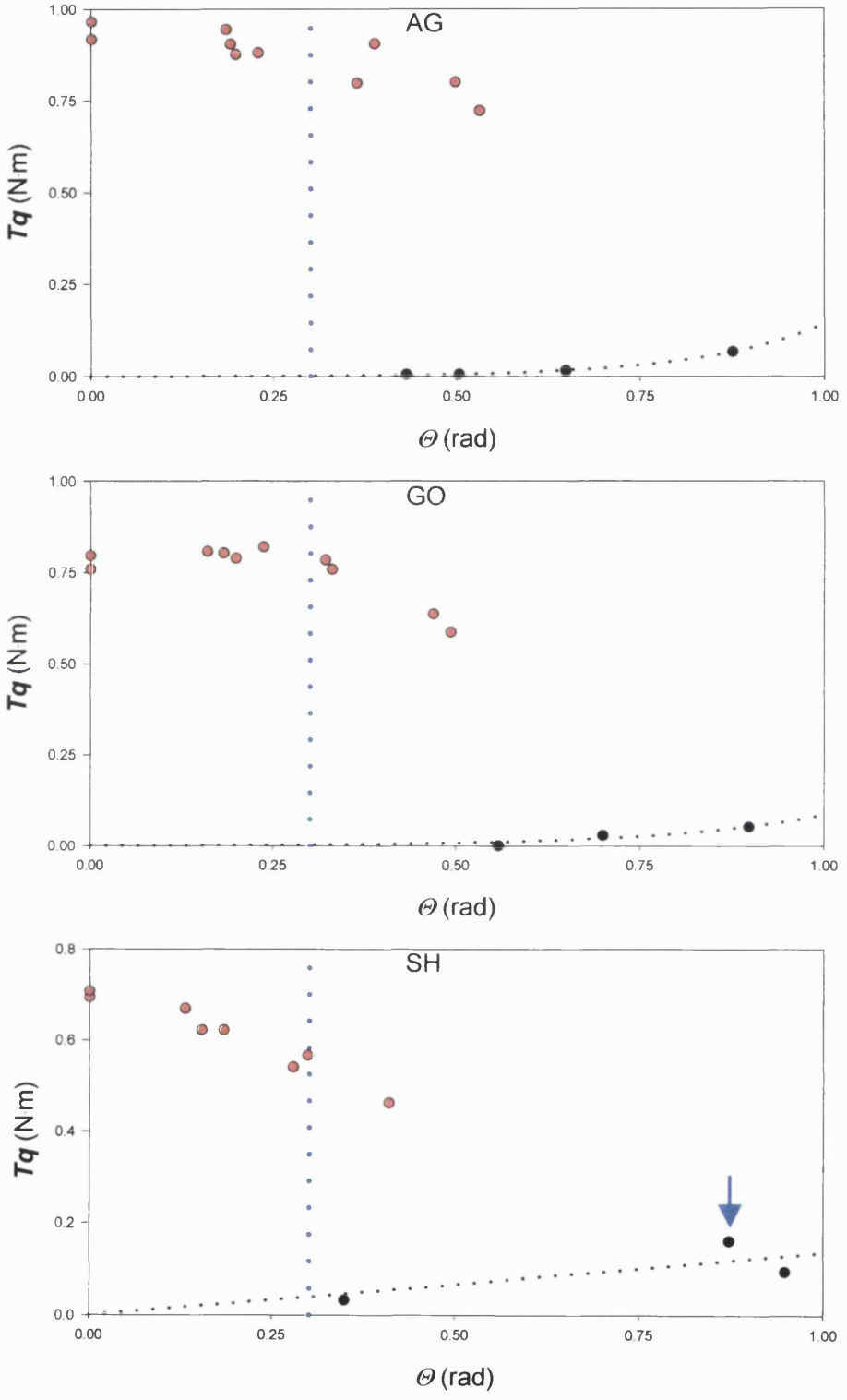

Figure 3.13.B. Active (red circles) and passive (blue circles) torque-angle relation for three volunteers. Best-fit line to the passive data (black dotted) generated by an arbitrarily chosen exponential function (see text). The blue dotted vertical line indicates 0.3 radians.

angle range (~0.3 rad) the index finger moved through during the dynamic contractions. The limits of FDI MTC excursion during shortening due to the anatomy of the joint did not seem to reduce the magnitude of the peak power attained during contractions against the range of loads used in this study (see later sections).

4.1.3. Is passive torque considerable?

The passive torque was very small, for all volunteers except SH, compared to the active torque achieved within the abduction angle range for which the dynamic results were obtained (figures 3.13). In the only exception (SH), the passive torque-angle relation is almost linear within the abduction range of interest. This is probably due to one observation, (indicated by the blue arrow on the graph in figure 3.13.B), of a higher than expected torque. It is unlikely that the torque at that angle would be greater than the torque at a greater angle. This greater torque might have been due to the volunteer not being completely relaxed during this measurement and generating some active torque in addition to the actual passive torque. Thus, the passive torque was not included in the calculation of the normalised torque-angle curves for all volunteers, including volunteer SH.

4.1.4. Adjustment for changes in the control active torque

As mentioned in section 3.3.1.1 active torque control measurements at a given angle were repeated every after two contractions in order to test whether force production deteriorated with time throughout the experiment. Figures 3.14.A and B show the peak static torque achieved in each contraction plotted against

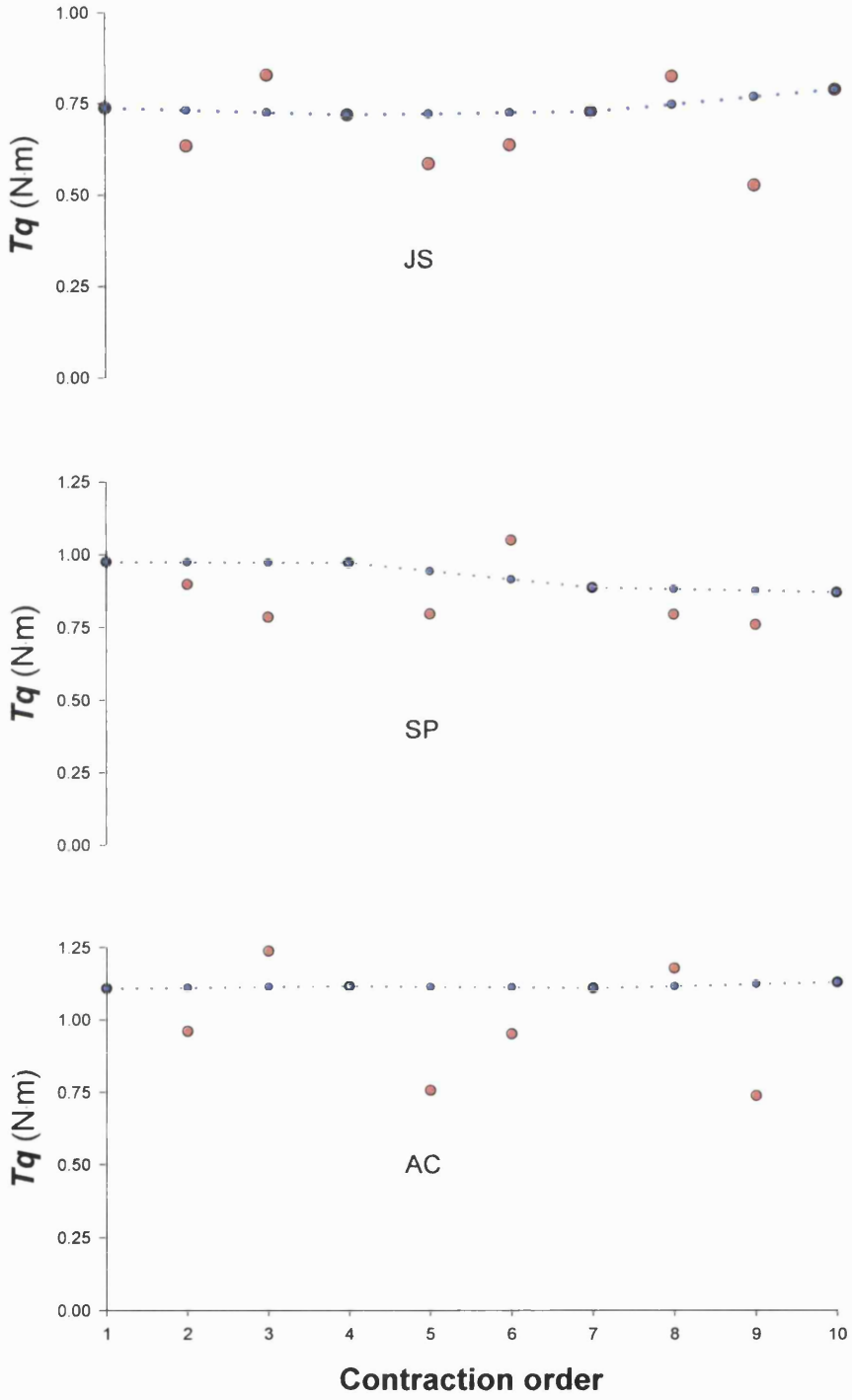

Figure 3.14.A. Peak active torque observations from static contractions plotted in the order at which the contractions were performed (red circles). Interpolated static torque at the control angle (blue line and points).

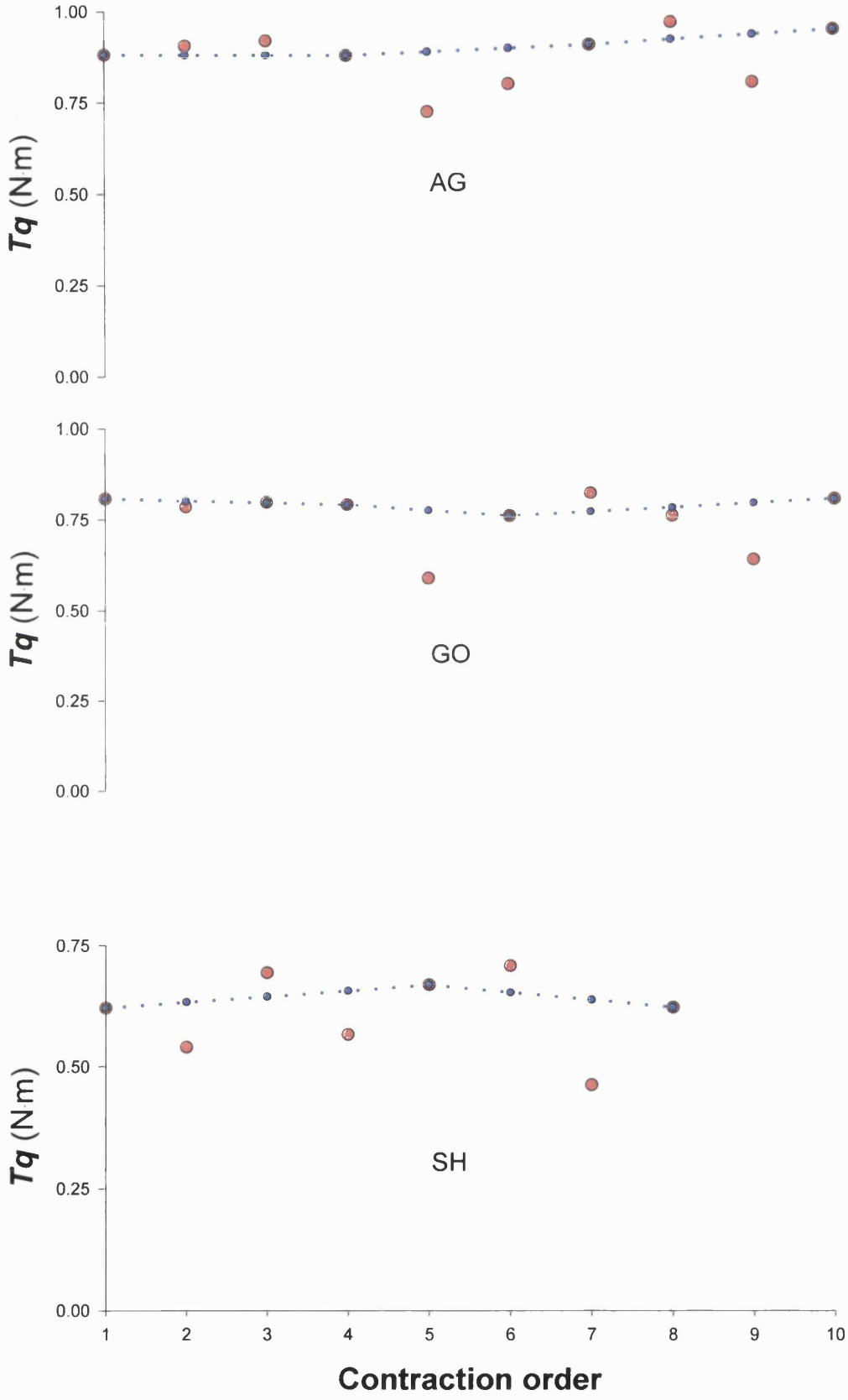

Figure 3.14.B. Peak active torque observations from static contractions plotted in the order in which the contractions were performed (red circles). Interpolated static torque at

the order number of the contraction. The 'active' static torque in the control position often varied during an experiment (figures 3.14.A and B). As the abduction angle was the same in the control measurements, the change in the control static torque during the experiment reflects the influence of factors other than the abduction angle (e.g. fatigue) on the ability to generate torque. Assuming that the peak static torque recorded in the control position would change linearly with the number of contractions between subsequent control recordings, linear interpolation between the control values was used to estimate the expected control values at any time during the experiment. If abduction angle was the only factor accounting for the differences in static torque, all measured (and interpolated) control values in an experiment would be the same. That means that the lines connecting these values in figure 3.12 would be straight horizontal lines. Such horizontal lines can be achieved by dividing each control value by itself, yielding a constant control value equal to one normalised unit throughout each experiment. Thus, correcting for the influence of factors other than abduction angle would require that each measured value be divided by the corresponding (measured or interpolated) control value. The result of the interpolation was therefore used to normalise the actual peak static torque values by dividing them with the corresponding interpolated control values, thereby accounting for the observed variation in the control torque.

4.1.5. Fatigue-corrected torque-angle relationships

The normalised torque values obtained as described in the previous section (4.1.4) were plotted against the corresponding index finger abduction angles (figure 3.15). Four of the volunteers gave interpolated torque-angle plots that

were similar to one another (Figure 3.15; middle graph). It was therefore decided to describe their normalised torque-angle relationships as one (not separately). The interpolated torque-angle plots for the other two volunteers were different from that for the four volunteers but they were similar to each other (Figure 3.15; bottom graph). These two plots were also used together to describe one interpolated torque-angle relationship for these two volunteers. Thus, instead of describing six distinct torque-angle relationships, only two were necessary to describe the whole set of results. The difference between the two groups in terms of their torque-angle plots was the angle range: the angle range was narrower in the second group.

Each of the data for each group was fitted with a second order polynomial curves of the form:

$$Tq = P_1 \cdot \Theta_L^{\,2} + P_2 \cdot \Theta_L + P_3 \quad (3.2)$$

where P_1, P_2 and P_3 are constants (values in table 3.5 and figure 3.15).

VOLUNTEER	JS; SP; AG; GO	AC; SH
P_1	-0.7078	-2.1784
P_2	-0.925	-0.0399
P_3	1.0453	1.0788

Table 3.5. Polynomial coefficients for the curves fitted to the fatigue-corrected static peak torque-angle data.

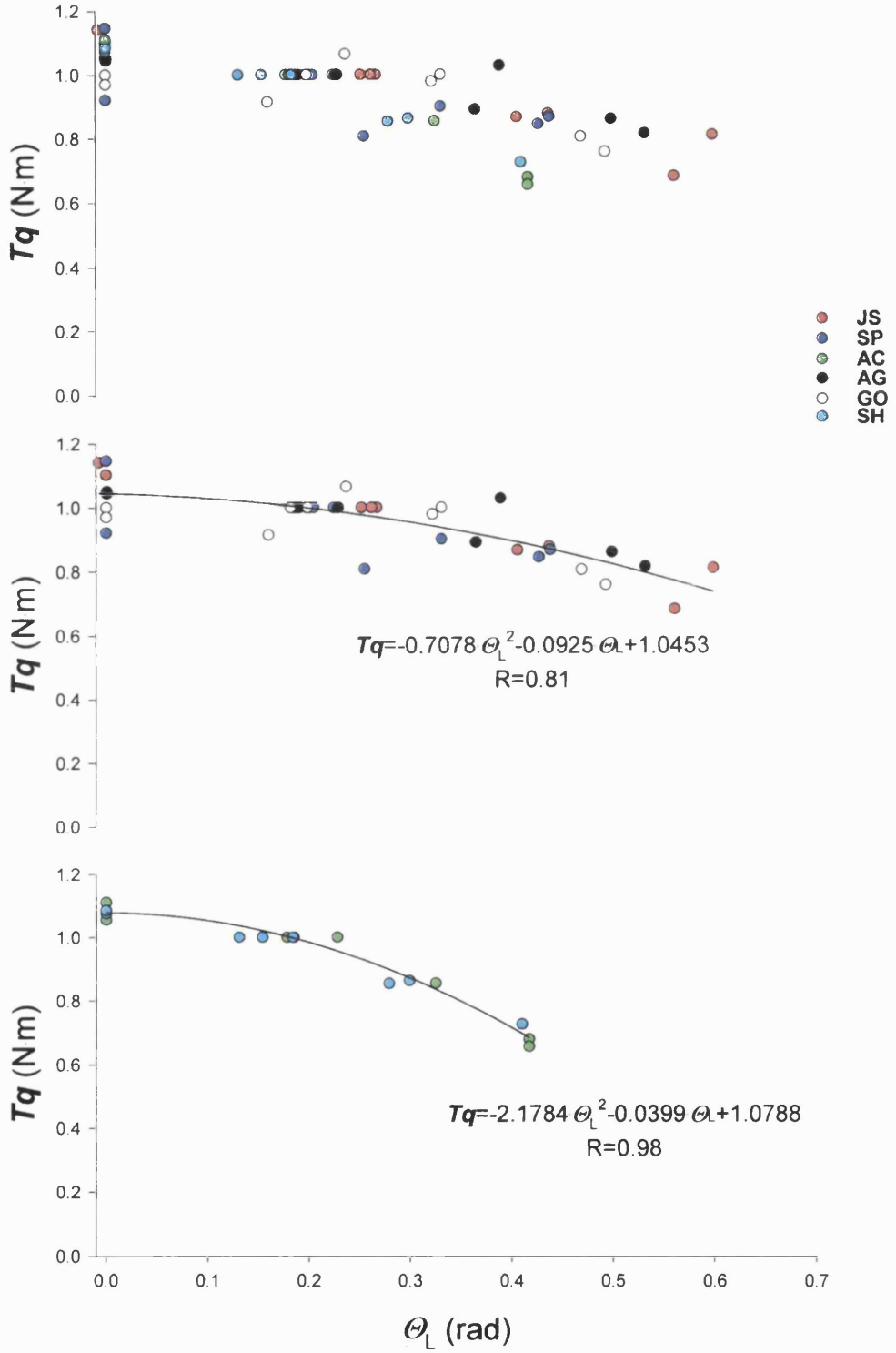

Figure 3.15. Fatigue-corrected torque-angle relationships. Top graph: Interpolated static torque-angle plot for all volunteers. Middle graph: Interpolated static torque-angle plots from four of the volunteers and best-fit second order polynomial curve. Bottom graph: Interpolated static torque-angle relationships from two of the volunteers and best-fit second order polynomial curve. Each volunteer is represented by a different colour.

Within the range of observed abduction angles, the optimum force appears from the fitted equations to be at the smallest angle, which corresponds to the longest muscle length. In two subjects the angle can increase to 0.4 rad before the torque has dropped by approximately 35 %. In the other four subjects the torque drops by approximately 30% as a result of increasing in the angle by 0.6 rad. Thus, the static torque-angle relationship for the two subjects is steeper than that of the other four.

4.1.6. Summary of section 4.1

Measurements of peak active and passive torque were obtained at different index finger abduction angles in each of the six volunteers. Within the range of abduction angles relevant to dynamic efforts, passive torque was negligible

4.2. Shortening contractions against inertia

4.2.1. Estimating mechanical properties of CC and SEC

Kinetic variables associated with the motion of load, as those described in this section will be collectively termed 'external' kinetic variables in the rest of this work. Such variables may include for example, the acceleration, velocity and power delivered to the load. 'External' kinetic variables can readily be recorded or calculated. In contrast, 'internal' variables such as for example the shortening velocity of the contractile component (CC) cannot be recorded directly from measurements performed on the load. Internal variables are associated with the mechanical properties and the kinetic output of the CC and of the series elastic component (SEC), i.e. the components of the MTC. This section discusses a method that was developed as part of this work for estimating these 'internal' mechanical properties and outputs during contractions performed against inertial loads.

A common characteristic of all torque traces of the FDI MTC during shortening contractions against inertial loads is that they are 'bell-shaped' (figure 3.16.A). Moreover, the angular speed of the inertial load increases throughout the contraction (figure 3.16.B). The shape of the torque-time and load velocity-time traces were in accordance to the modelling work presented in the modelling section 6.1.1 (pp. 136), modelling work by others (e.g. Caldwell, 1995) and experimental observations on explosive movements with large inertial components (e.g. Kurokawa *et al*, 2001). The method for estimating the properties and the instantaneous mechanical behaviour of the CC and SEC

during a contraction in this work is based on making use of such 'bell'-shaped torque records and of the corresponding angular velocity records.

4.2.1.1. Assumptions

This method is based on two assumptions:

Assumption A. The angular velocity of the CC depends on :

1. The torque exerted

and in addition, it may or may not depend on:

2. The level of activation.

3. The angle of the MCP joint

4. Fatigue/potentiation of the CC

A single function of these four parameters can describe the velocity of shortening as a function of relative torque where relative torque is a function of torque, activation, MCP joint angle and number of preceding contractions. The influence of activation, angle and history of preceding contractions are relatively small compared to the large torque variations. How these influences are taken into account is shown in section 4.2.1.2, pp. 261.

Assumption B. The extension, in angular terms, of the series elastic component (SEC) only depends on the torque that it experiences.

Based on these two assumptions it is expected that there would only be one value of angular velocity due to CC shortening for a given value of torque, when an adjustment has been made to account for CC activation torque-angle relation and fatigue/potentiation. Likewise, there would be only one value of

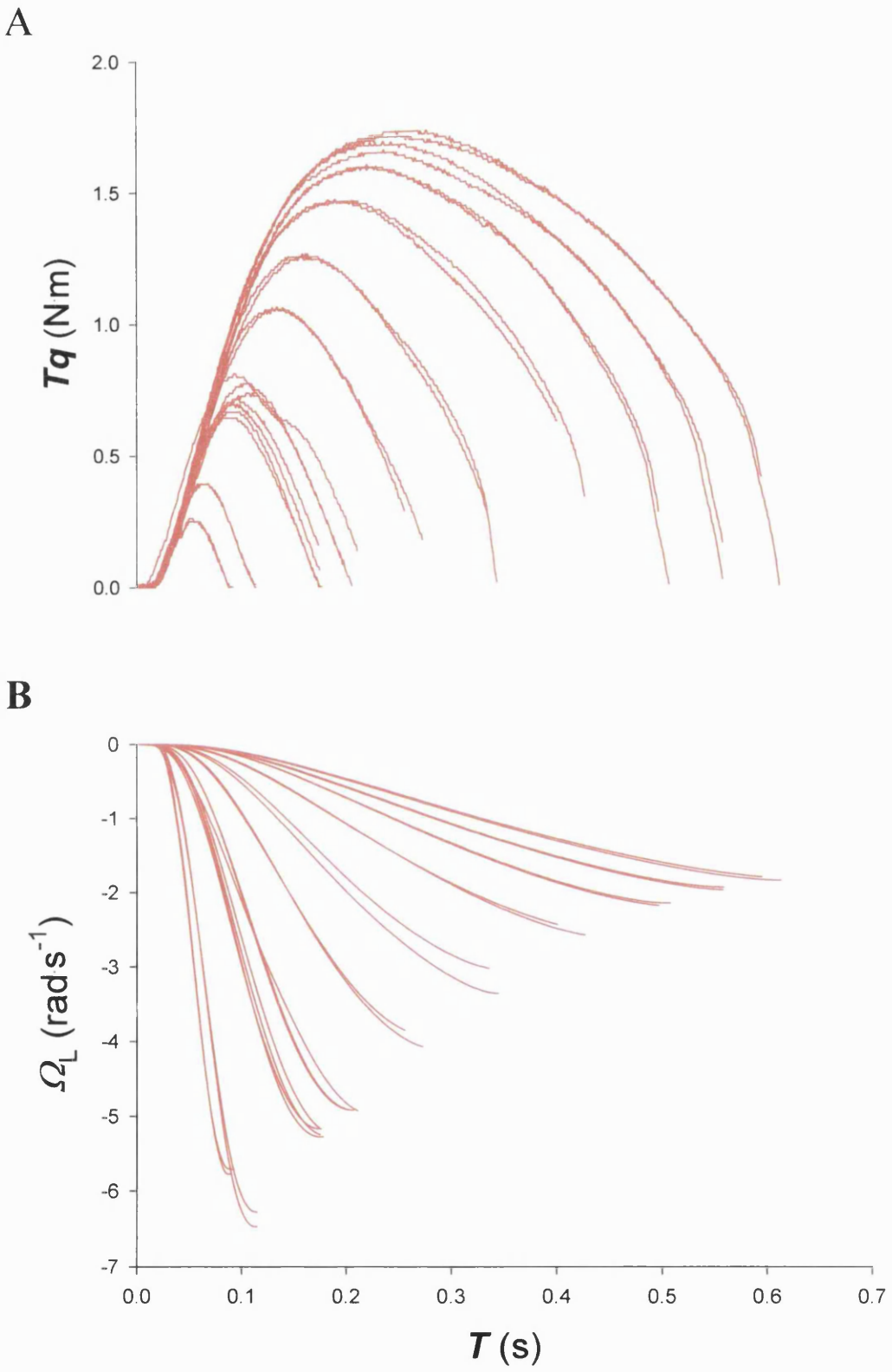

Figure 3.16. Grouped results from an experiment showing the time course of torque around the MCP joint (panel A) and angular velocity of the inertial load (panel B) during electrically evoked contractions. Each different trace corresponds to a different contraction. A wide range of inertial loads was used (see methods).

angular SEC extension for a given value of torque, and this value would be independent of the level of CC activation and torque-angle relation. The SEC rotational stiffness, i.e. the slope of its torque- angular extension curve, is also expected to be a function of the SEC angular extension. Thus, for any given value of torque only one value of rotational stiffness exists. In other words, for a fully active MTC shortening at the plateau of its torque-angle relationship, both the rotational CC shortening velocity and the rotational stiffness of the SEC would be functions of the recorded torque around the joint. However, no other assumptions are made at this point regarding the nature (shape) of these relationships.

As discussed above, CC velocity may be assumed to be a function of one or more of four factors. Adjustments can be made to take into account of these factors. These adjustments are discussed in the following section.

4.2.1.2. Adjusting for CC activation, torque-angle relation and the effect of preceding contractions

4.2.1.2.1. Adjustment for activation

Activation in this part of the work means the number of cross bridges in the CC capable of interacting with actin to produce shortening and/or generate force, relative to the maximal number of cross bridges that could be interacting with actin under the conditions of the particular contraction. In this thesis the level of activation (A) is considered only while the muscle is being stimulated and it is assumed to be a function of the time elapsed (T) since the onset of stimulation according to the following equation:

$$A = \begin{cases} 1 - e^{-\frac{(T - T_{LAT})}{TC}}, & if \quad TC > 0 \\ 1, & if \quad TC = 0 \end{cases}$$

T_{LAT} is an adjustable latent period, usually of the order of 10^{-2} sec, to account for the electromechanical delay between the delivery of an electrical stimulus to the CC and acto-myosin interaction. The activation parameter is not used for times less than T_{LAT}. TC is the time constant for the rise of activation and it only takes positive values or zero. The value of the TC for each volunteer will be estimated in an iterative manner and in relation to the goodness of fit of the SEC stiffness-torque results (see section 4.2.2.2.2, pp. 270). The units of time used in this work are seconds.

Activation takes values ranging between zero and one. Zero indicates no activation, i.e. no cross bridges capable of attachment to actin. One indicates full activation, i.e. a maximal number of cross bridges is interacting with actin.

The experimentally recorded torque was divided by the activation parameter to obtain a torque value relative to the activation level. This relative torque is for use in comparing force with speed of shortening. It is assumed that when the muscle is not fully active its velocity of shortening will depend on the relative torque rather than the actual torque. This relative torque is higher than the observed torque while activation is less than maximal, with a greater effect early during the contraction (figure 3.17). This effect is more prominent in brief, low-torque records coming from light inertial loads (figure 3.17).

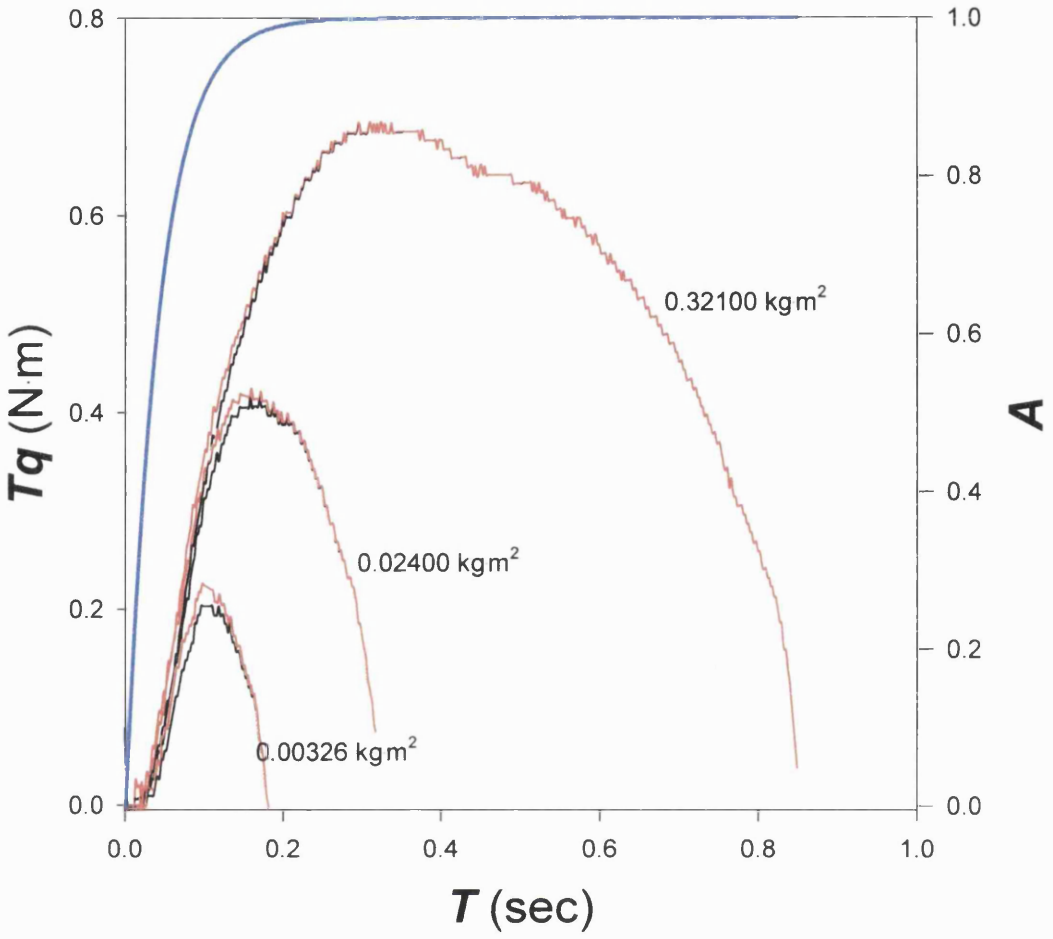

Figure 3.17. Recorded torque (black), torque normalised for CC activation (red) and activation (blue) traces for three different inertial loads. Results from volunteer AC.

4.2.1.2.2. Adjustment for the torque-angle relationship

It was shown earlier that the maximal static torque generated by a fully active, non-fatigued part of the FDI MTC is a function of the abduction angle of the index finger (section 4.1.5, pp. 254). During a dynamic contraction, the index finger rotates and goes through abduction angles of different 'potential' for maximal static torque development. The relationship between maximal static torque and abduction angle has already been described in terms of second order polynomial functions whose coefficients have been estimated (section 4.1.5). Thus, the maximal static torque that could be developed by the FDI MTC at each of the angles the index finger moves through during a dynamic contraction can be calculated. The result can be expressed relative to the peak maximal, fatigue-corrected static torque so that its maximal value is equal to one. This normalised variable is termed 'static torque potential', tq_P, in this thesis (figure 3.18). When $tq_P = 1$ during a dynamic contraction, the FDI MTC generates torque under optimal torque-angle conditions. When however $tq_P < 1$, less torque is produced than it would, if the finger was at optimal abduction angles. By dividing the dynamic torque observations by the corresponding values of tq_P, the relative torque at these angles becomes greater than the actual torque. This corresponds to the torque trace that would have been obtained, if the FDI MTC had been shortening at the plateau of its torque-angle relation (figure 3.18).

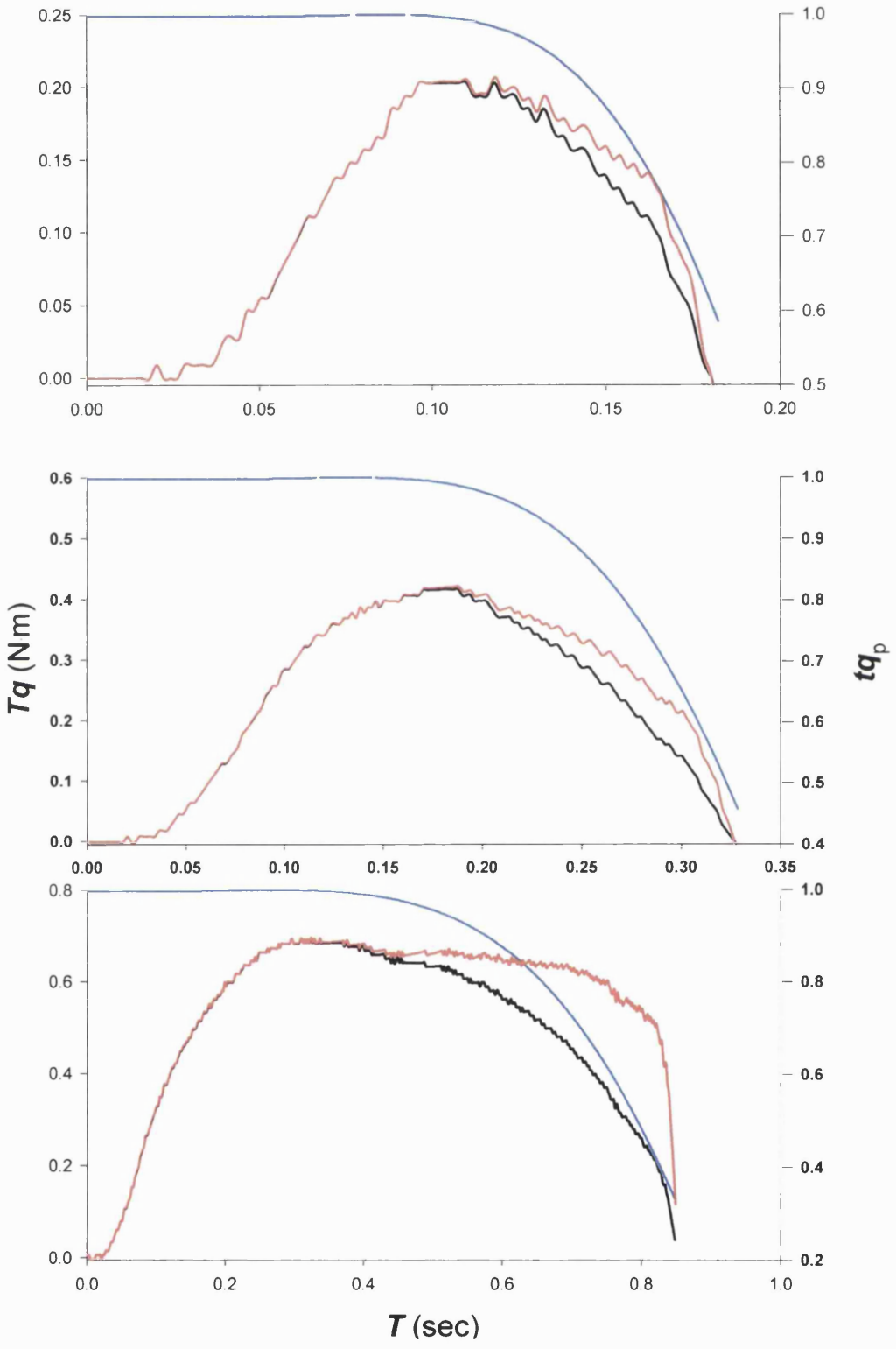

Figure 3.18. Time course of torque (black), static torque potential (blue) and torque corrected for the torque-angle relationship (red) for three different inertial loads (Top graph: 0.0033 kg·m^2 ; Middle graph: 0.0230 kg·m^2; Bottom graph: 0.3210 kg·m^2).

4.2.1.2.3. Adjustment for effects of preceding contractions

Control records of maximal static torque were obtained at the beginning and at the end of each dynamic experiment, as well as after completion of contractions against three different inertial loads (i.e., after every six dynamic contractions; see methods section 3.3.2, pp. 243). The peak static torque achieved from each control contraction was expressed relative to the peak static torque value that was obtained at the start of the experiment. These values of relative peak static torque, tq_H, served as an index of whether the performance of the CC changed with time during the experiment. The relative peak static torque values were plotted in the order they were performed during the experiment against the corresponding numbers of contraction (figure 3.19). In order to adjust the torque records for possible changes in the contractile performance each dynamic torque record was divided by the corresponding relative torque value calculated by using linear interpolation between the contraction number-relative static torque observations.

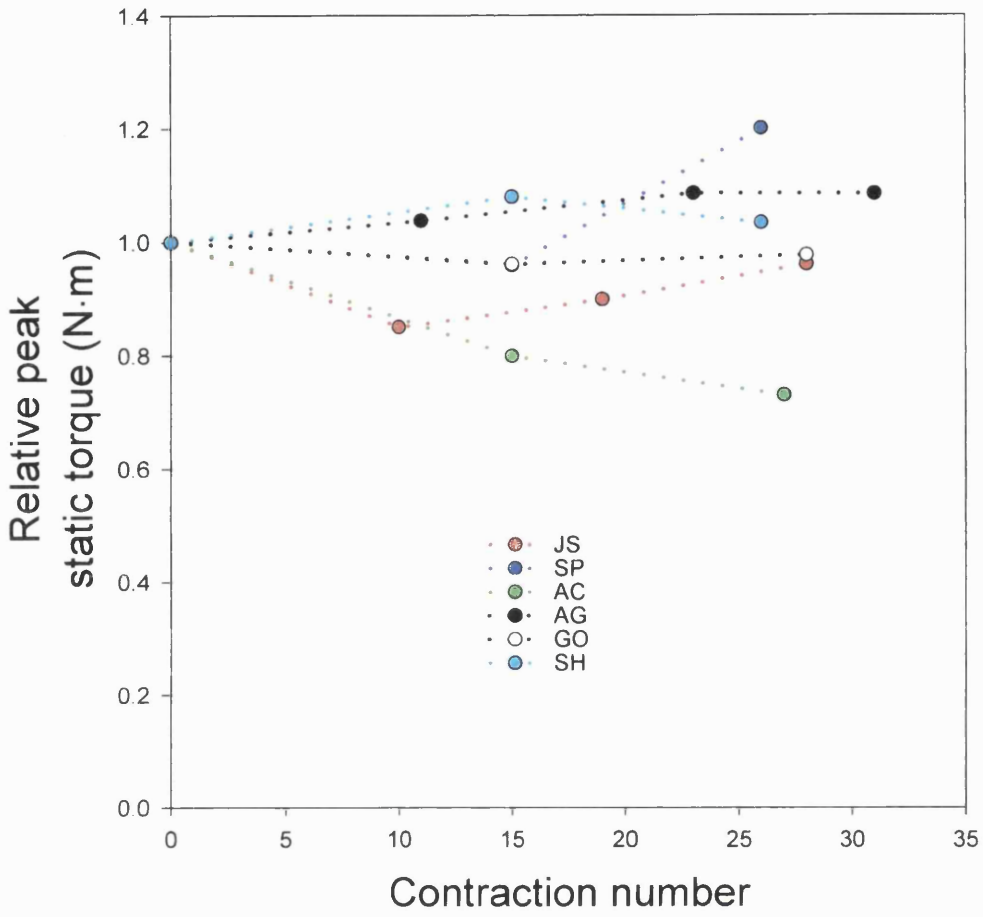

Figure 3.19. Relative peak static torque from control contractions during the dynamic experiments plotted against the corresponding contraction number.

4.2.1.2.4. Summary of sections 4.2.1.2.1-3

So far section 4.2.1.1 has presented possible ways in which the recorded torque during maximal electrically-evoked shortening contractions can be adjusted to take account for the time course of CC activation (4.2.1.2.1), the torque-angle relation (4.2.1.2.2) and the effects of preceding contractions on MTC performance (4.2.1.2.3). The adjusted torque records could be regarded as those that would have been generated by a fully active muscle, shortening at the plateau of its torque-angle relationship and without being affected by fatigue or potentiation.

4.2.1.2.5. Possible cases under study

As discussed above, CC velocity may be assumed to be a function of one or more out of four factors (section 4.2.1.1), whereas SEC stiffness is assumed to only depend on the torque. This can produce a number of possibilities with regard to the underlying assumptions when analysing the data. For example, in the simplest case, both CC shortening velocity and SEC stiffness can be assumed to be functions of the torque around the 2^{nd} MCP joint only. In the most complex case, CC shortening velocity can be assumed to be a function of all the four factors mentioned above (while SEC stiffness is assumed to be a function of the torque only). Cases of intermediate complexity can also be considered, if CC shortening velocity is assumed to be a function of two or three of the aforementioned factors. In this section a choice is made regarding to which ones of the possibilities will be considered. Four possibilities were considered:

i) The CC is fully active; the dynamic performance of the MTC is not affected by its torque-angle relation; torque generation is not affected by the history of preceding contractions. In this case $Tq_N = Tq$, where Tq_N stands for normalised torque, i.e. it is the torque that would be generated if the CC became fully active instantaneously and shortened at the plateau of its torque angle relationship without being affected by preceding contractions.

ii) The CC is fully active and its ability to generate torque remains unaltered throughout the experiment. However, the dynamic performance of the MTC is affected by its torque-angle relation and therefore the torque is adjusted to take account of this, such that $Tq_N = \frac{Tq}{tq_P}$.

iii) The CC is fully active but its the dynamic performance of the MTC is influenced both by its static torque-angle properties and the history of preceding contractions, such that $Tq_N = \frac{Tq}{tq_F \cdot tq_P}$.

iv) The torque traces are generated by a CC whose activation is not maximal at least for part of the contraction such that $Tq_N = \frac{Tq}{A}$.

4.2.1.2.6. Summary of section 4.2.1.2.

Torque and load velocity observations can be used (see following section) to obtain a possible solution for the contractile and series elastic properties of a muscle-tendon complex shortening against inertial loads. Estimating these properties is based on two assumptions: one regarding the factors, in addition to the torque, which may or may not be involved in determining the CC shortening velocity, and the other assumption stating that the SEC stiffness is a function of the torque around the moving joint

(section 4.2.1.1). Only four versions of the first assumption are considered in this work (section 4.2.1.2.5). Ways in which these assumptions are incorporated into the analysis by normalising the torque records using appropriate parameter values are discussed in sections 4.2.1.2.1-4.2.1.2.3. The following section describes how the elastic and contractile properties can be calculated on the basis of the four assumptions.

4.2.1.3. 'Torque-pairing' method of analysis

4.2.1.3.1. Simplest case

According to the assumptions made in section 4.2.1.1 (pp. 259), the angular velocity of the index finger due to CC shortening, Ω_{CC}, is a function of Tq_N. The rotational stiffness of the SEC, $K_{rot\,SEC}$, is a function of the actual torque, Tq. The description of the method for obtaining the 'internal' mechanical properties and outputs begins by first considering the simplest case where $Tq_N = Tq$ (4.2.1.2.5. (i)). As the torque traces are bell-shaped, values of torque such as the values at points ***a*** and ***b*** on figure 3.20, occur twice along the record. Two equations can be written for each pair of equal torques relating the velocities, in angular terms, of the CC, SEC and L; one equation for point ***a*** and one for point ***b***:

$$\Omega_{CCa} = \Omega_{La} + \Omega_{SECa} \quad (3.3)$$

$$\Omega_{CCb} = \Omega_{Lb} + \Omega_{SECb} \quad (3.4)$$

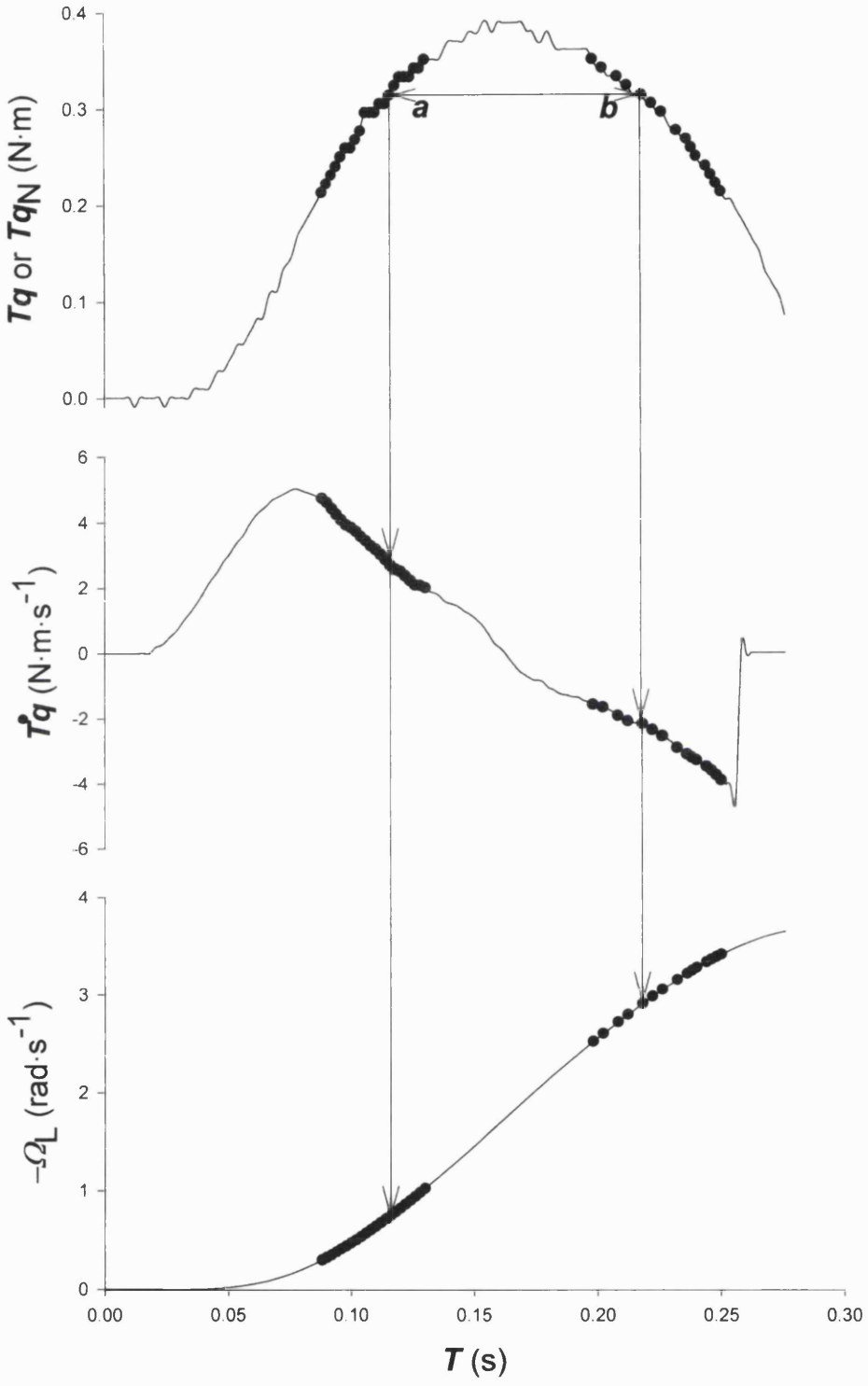

Figure 3.20. Time course of torque (top trace), torque rate (middle trace) and angular velocity of the inertial load (bottom trace) during a contraction. Selected pairs of equal torque (such as points ***a*** and ***b***) and corresponding torque rate and load velocity points (black points) are shown. Notice that points corresponding to very low and very high values of torque have been excluded. The angular displacement limit for this selection was $\Theta_L < 0.32$ radians. For torque-pairing exclusion criteria see section 4.2.1.2.3.

Ω_L and $\frac{d}{dT}(Tq)$ at points ***a*** and ***b*** can be obtained from the torque and angular velocity record. There are also two unknown quantities, namely Ω_{CC} and K_{rot}. Thus, there are two equations with two unknowns for these two points, that can be solved simultaneously to obtain the common value of K_{rot}:

$$K_{rot} = \frac{\left[\frac{d}{dT}(Tq)\right]_a - \left[\frac{d}{dT}(Tq)\right]_b}{\Omega_{L_b} - \Omega_{L_a}} \quad (3.10)$$

In each experiment, contractions are usually performed against twelve different inertial loads (pp. 243) producing a wide range of different mechanical outputs (for example figure 3.16, pp. 260). Thus, despite certain torque pairs being excluded from the analysis (see section 4.2.1.2.3.), a large number of pairs is selected for each volunteer allowing determination of the rotational stiffness over a wide range of torque values (section 4.3, pp. 290).

The stiffness-torque plots have a sigmoidal appearance (see section 4.3.1.). The sigmoidal change in stiffness with the load (or torque) is in accordance with the expected change in the slope of a typical SEC force-extension relationship (Hill, 1970; Rigby *et al*, 1959; Maganaris and Paul, 1999, 2000b). The slope of the force-extension curve gradually rises with extension until it reaches an almost constant value. The equation describing this sigmoidal stiffness-torque relationship contains three parameters and it is of the form:

$$K_{rot} = \frac{A_1}{1 + e^{\frac{A_2 - Tq}{A_3}}} \quad (3.11)$$

where A_0, A_1, A_2 and A_3 are all constants. A_1 is a scaling determining the limit of this function. A_2 is the value of the torque at which the stiffness is half its limit value. A_3 alters the gradient of the curve. The values of these three constants are determined by an iterative process using the in-built mathcad function GENFIT. Initially guess values are assigned on these constants and GENFIT calculates new values that produce a better fit to the stiffness-torque plot. The process is repeated until the last and previous estimate converge within six decimal places.

Once the values of the three constants have been determined, the value of K_{rot} for any given value of Tq can be calculated. This allows determination of the instantaneous Ω_{CC} during each contraction from the torque output according to equation (3.12):

$$\Omega_{CC} = \Omega_L + \frac{1}{\left(\frac{A_1}{1+e^{\frac{A_2-Tq}{A_3}}}\right)} \cdot \frac{d}{dT}(Tq) \quad (3.12)$$

Notice how in this equation, the value of K_{rot} has been replaced with the equivalent equation predicting the value of K_{rot} for any given value of Tq within the torque range recorded from the experiment. In this way a CC torque-velocity relationship can be obtained over the range of torque values and angular displacement values for which the stiffness-torque relationship holds.

It must be noted that the estimated K_{rot} values include not only the stiffness of connective tissue in series with the CC ($K_{rot\,SEC}$), but also the stiffness of the force transducer rod ($K_{rot\,FT}$):

$$K_{rot} = \frac{K_{rot\,SEC} \cdot K_{rot\,FT}}{K_{rot\,SEC} + K_{rot\,FT}} \quad (3.13)$$

This inclusion of the force transducer stiffness is appropriate when calculating the CC torque-velocity properties, as the CC was 'sensing' this composite stiffness during the contractions, rather than the stiffness of the SEC alone. The value of $K_{rot\,FT}$, i.e. the stiffness of the short rod cantilever system was calculated as:

$$K_{rot\,FT} = \frac{3 \cdot E \cdot I \cdot LA^2}{L^3}$$

where E is the elastic modulus for aluminium (70.3 $GN \cdot m^{-2}$; Kaye and Laby, 1973); I is the calculated moment area of the force transducer short rod around its long axis ($6.362 \cdot 10^{-11}$ m^4); LA is the perpendicular distance through which force typically acts around the centre of rotation of the short rod (typically 0.06 m); L is the distance from the free end at which force is applied (approximately 0.09 m). Substituting these values in the above expressions yields $K_{rot\,FT} = 66.3$ N·m. This stiffness is taken into account after calculation of the CC torque-velocity properties by solving equation (3.13) for $K_{rot\,SEC}$:

$$K_{rot\,SEC} = \frac{K_{rot\,FT} \cdot K_{rot}}{K_{rot\,FT} - K_{rot}} \quad (3.14)$$

The stiffness-torque result is plotted again, now using $K_{rot\,SEC}$ instead of K_{rot} and a new relationship (new values for the three parameters) is now established,

reflecting the properties of the elastic tissue in series with the CC, independently of the elastic properties of the force-transducer rod.

To summarise, the first part of this section has shown how based on two simple assumptions made in section 4.2.1.1 and 4.2.1.2.5 (case (i), pp. 269), it is possible to estimate:

a) the total and SEC rotational stiffness-torque relationship

b) the CC torque-velocity relationship

for the simplest case where $Tq_N = Tq$.

4.2.1.3.2. Other cases

This section considers the situation in which $Tq_N \neq Tq$. Tq_N is calculated depending on the assumptions made ((ii)-(iv), pp. 269). An initial value is assigned for TC, if case (iv) (section 4.2.1.2.5) is considered. Following calculation of Tq_N, pairs of equal Tq_N are selected from each Tq_N record using the same selection criteria (section 4.2.1.3.3.) as for the Tq records (figure 3.21). According to the assumptions made in section 4.2.1.1, Ω_{CC} is dependent upon Tq_N and K_{rot} is dependent upon Tq. For two points ***a*** and ***b*** of equal Tq_N therefore, Ω_{CC} will be expected to be the same. K_{rot} however may be different as the value of Tq at point ***a*** may be different to the value of Tq at ***b*** (figure 3.22). Equations (3.6) and (3.7) therefore relate the angular velocities of the components of the muscle-tendon-inertial load system for points ***a*** and ***b*** and are rewritten below:

$$\Omega_{CCa} = \Omega_{La} + \frac{1}{K_{rota}} \cdot \left[\frac{d}{dT}(Tq)\right]_a$$

$$\Omega_{CCb} = \Omega_{Lb} + \frac{1}{K_{rotb}} \cdot \left[\frac{d}{dT}(Tq)\right]_b$$

Introducing a ratio of the stiffness for any pair of torque values such that:

$$Z = \frac{K_{rota}}{K_{rotb}} \quad (3.15)$$

and re-arranging equation (3.15) one stiffness value can be expressed in terms of the other and the value of the value of this ratio:

$$K_{rota} = Z \cdot K_{rotb}$$

equations (3.6) and (3.7) can now be written as:

$$\Omega_{CC} = \Omega_{La} + \frac{1}{Z \cdot K_{rotb}} \cdot \frac{d}{dT}(Tq) \quad (3.16)$$

$$\Omega_{CC} = \Omega_{Lb} + \frac{1}{K_{rotb}} \cdot \frac{d}{dT}(Tq) \quad (3.17)$$

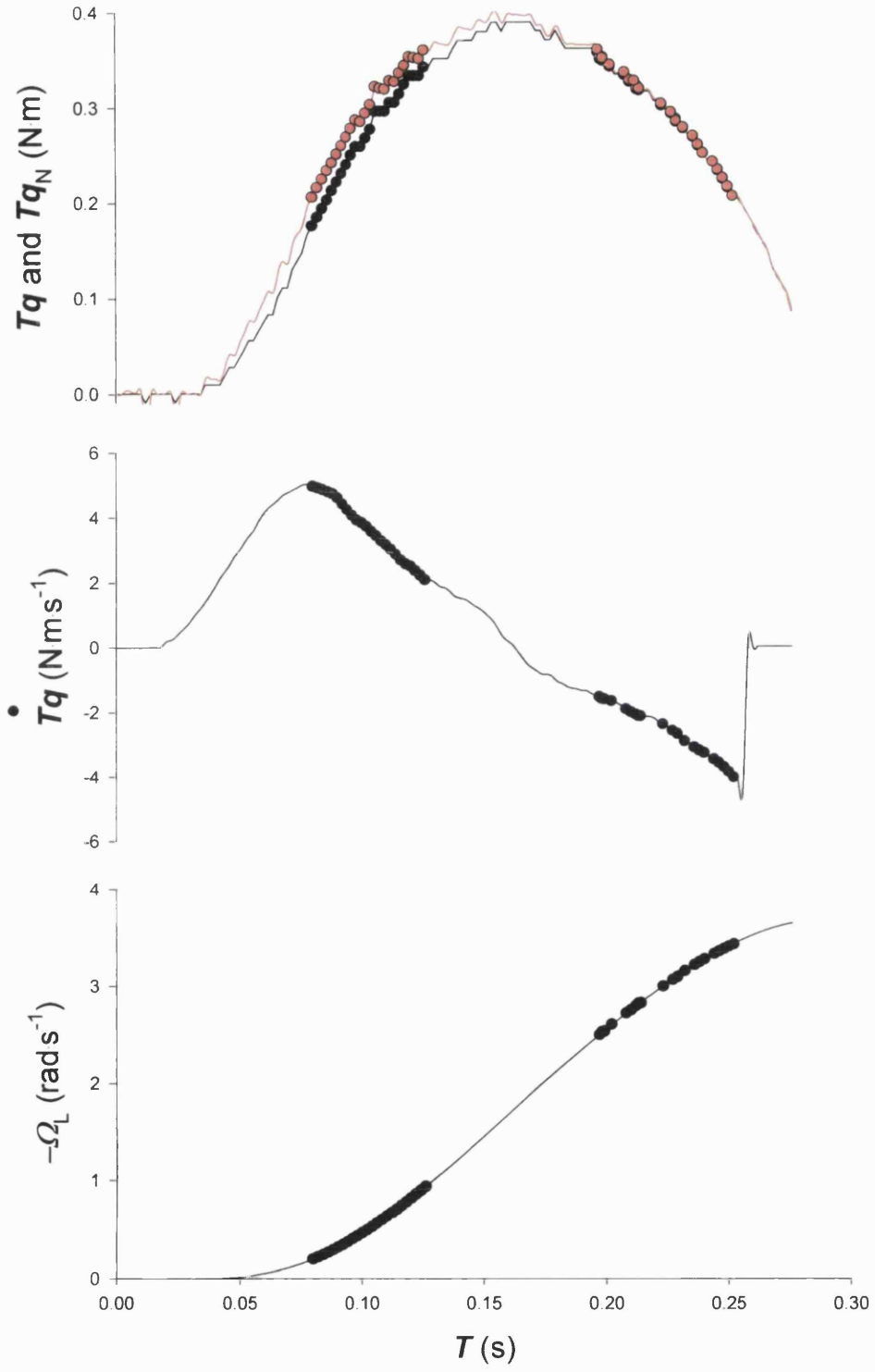

Figure 3.21. Top graph: Torque (black trace) and normalised torque (red trace). While the rate of change of torque (bottom graph: black trace) is positive, all values of normalised torque between 30-90% of its peak value are selected (red points). The corresponding points while the torque rate is negative are also selected (red points), but only until Θ_L reaches a limiting value (0.32 radians here). The corresponding points of torque (black points) are also found. Middle graph: Torque rate (black trace) and points at times of equal normalised torque (black points). Bottom graph: Load velocity (black trace) and matching points (black points)

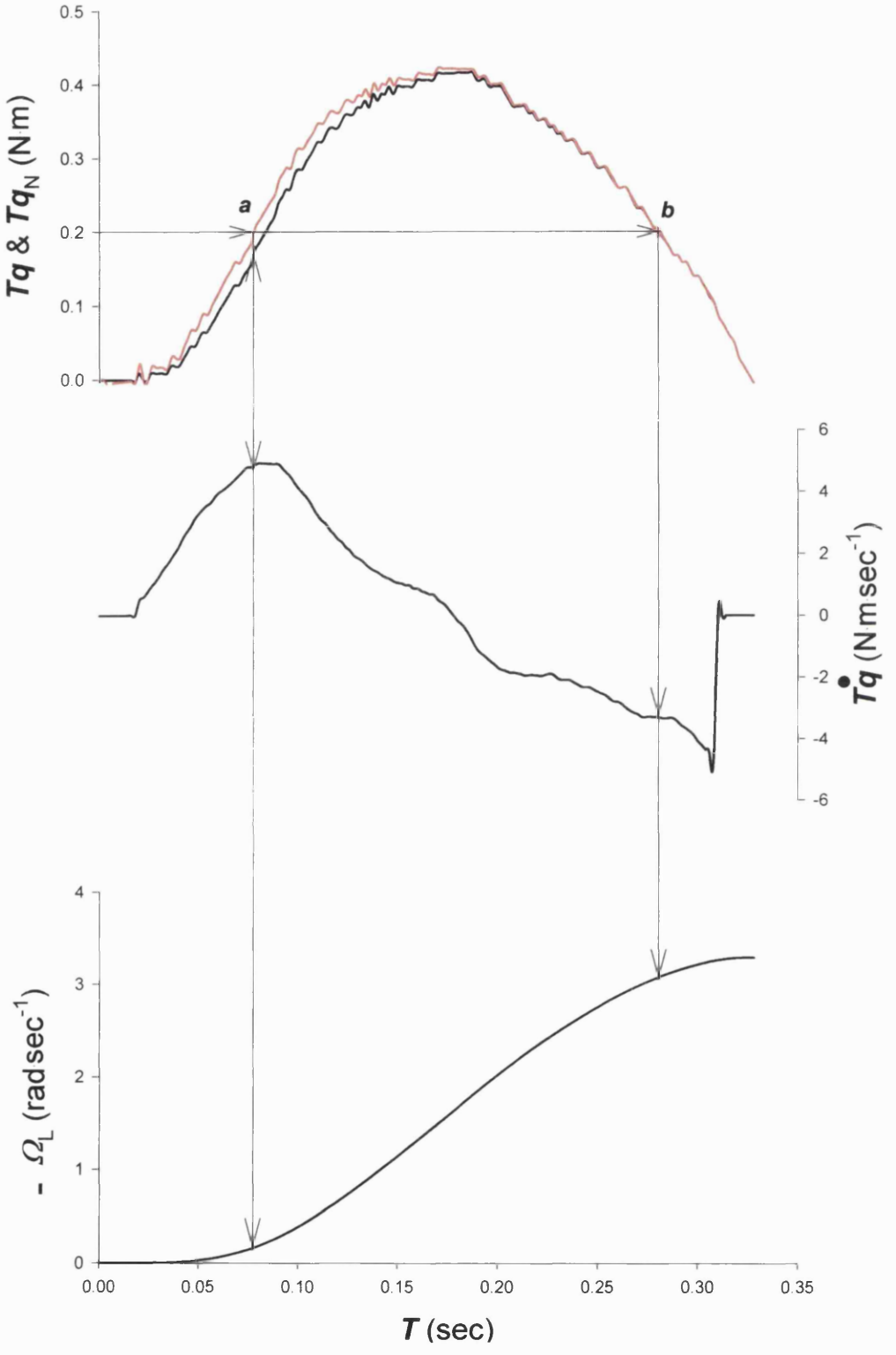

Figure 3.22. Top graph: Time course of torque (black trace) and normalised torque (red trace). Middle graph: Rate of change of torque. Bottom graph: Angular velocity of the load. An example of points of equal normalised torque (a and b) and the corresponding values of torque, torque rate and angular load velocity are also shown. Notice how the value of recorded torque at ***a*** is lower than the torque value at ***b***.

The numerical value $K_{rot\,b}$ however cannot be found unless the numerical value of Z is known. The rotational stiffness however, can be found for any given value of torque using equation (3.11). Thus, by combining equations (3.11) and (3.15) the stiffness ratio Z can be expressed as:

$$Z = \frac{\left(\dfrac{A_1}{1+e^{\frac{A_2 - Tq_A}{A_3}}}\right)}{\left(\dfrac{A_1}{1+e^{\frac{A_2 - Tq_B}{A_3}}}\right)} = \frac{1+e^{\frac{A_2 - Tq_B}{A_3}}}{1+e^{\frac{A_2 - Tq_A}{A_3}}} \qquad (3.18)$$

Recall that initially 'guess' values are assigned for the constants of equation (3.11) and an initial value of Z for a particular pair of torque points is calculated by equation (3.18). Once the value of Z is known, $K_{rot\,b}$ is calculated by simultaneously solving equations (3.16) and (3.17). The value for $K_{rot\,a}$ can then be calculated using equation (3.15). In this way, initial values of Z, $K_{rot\,b}$ and $K_{rot\,a}$ are calculated. This process is repeated for all the selected points of equal Tq_N from one experiment to generate an initial stiffness-torque plot. New values for the three constants of equation (3.11) can be obtained providing the best fit three-parameter sigmoidal curve through the calculated stiffness-torque plot. These new values provide a better fit to the stiffness-torque plot than the previous ones. Using these 'improved' parameter values, new values of Z, $K_{rot\,b}$ and $K_{rot\,a}$ are calculated and the process described above is repeated until convergence between the previous and current values of A_1, A_2 and A_3 is obtained within six decimal places. If case (iv) (section 4.2.1.1.5, pp. 269) is considered, this process is repeated for different values of the time constant TC

until the *TC* value that generates the best goodness of fit of the sigmoidal curve through the stiffness–torque plot is found.

The goodness of fit of the sigmoidal curve generated by equation (3.11) is assessed by the value of the coefficient of variation of the data about the line of best fit i.e. the ratio:

$$CV = \frac{\sqrt{SSE}}{\overline{K}_{rot}} \quad (3.19)$$

Recall that at this stage the calculated stiffness includes the effects of the force transducer stiffness. Using this result, the value of Ω_{CC} is calculated by equation (3.12) for any given value of torque. In order to obtain an SEC stiffness-torque plot, equation (3.14) must be used on the total stiffness-torque result.

Although the method of analysis used when $Tq_N = Tq$ was described first as an introduction to the more complex situation where $Tq_N \neq Tq$, the former is just a special case where $Z = 1$ throughout the contraction.

To summarise, when $Tq_N \neq Tq$ then the term Z is introduced in the analysis, denoting the ratio between the stiffness at selected points of equal Tq_N. Using an iterative process, better estimates of Z and of the stiffness-torque relationship are obtained. If CC activation is assumed to be an exponential function of time, the value of TC is changed systematically to the TC value that minimise the CV. This analysis yields:

a) The stiffness-torque relationship

b) The CC torque-angular velocity relationship.

c) The time course for CC activation, if case (iv) (section 4.2.1.2.5, pp. 169) is considered.

4.2.1.3.3. Torque pair selection

Not all pairs of equal torque values in a torque record are utilised when calculating the contractile and elastic properties of the FDI MTC. Results arising from matching torque values near the peak of a record, where the torque rate approaches the value of zero, are more sensitive to noise. An upper torque-limit for analysis was arbitrarily set to 90% of the peak (normalised) torque achieved in each contraction. Thus, results were not obtained, while the normalised torque exceeded 90% of the peak value achieved in each contraction.

While the normalised torque is less than or equal to 90% of its peak value, it is desired to make use of as many torque-pairs as possible. The top graph of figure one shows two stiffness-torque plots, one using torque-pairs within 0-0.6 radians of angular load displacement whereas the other carries out the calculation in the 0-0.4 radians range. Consider the latter plot first in which the calculation is carried out within the 0-0.4 radians range. The result in this plot was fitted by a sigmoidal relationship, which was then used to calculate the CC torque-velocity relationship. When this calculation is performed within the range of validity of the stiffness-torque relationship, i.e. within the range of

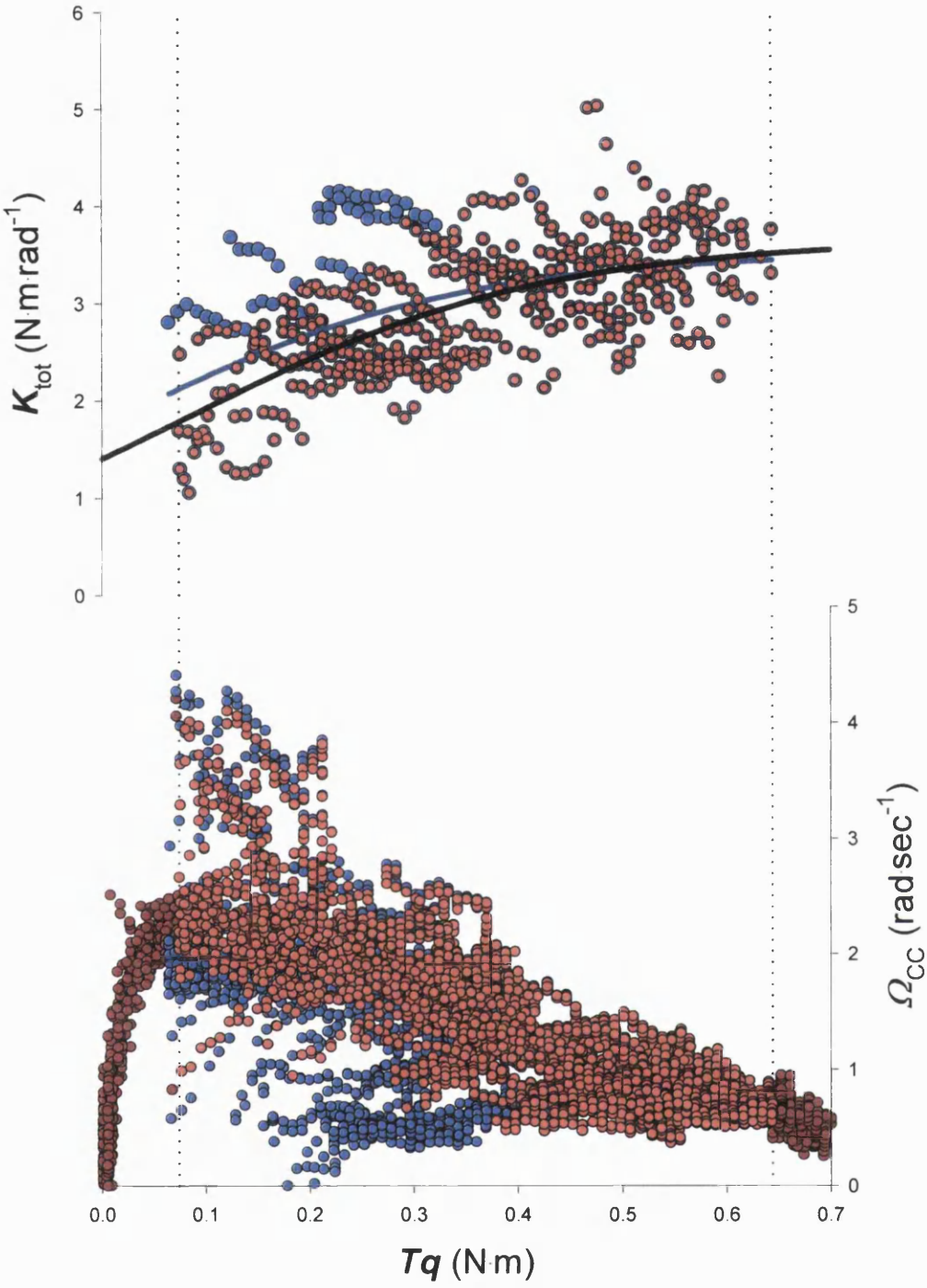

Figure 3.23. Calculated elastic and contractile properties using different restrictions. Top graph: Calculated total stiffness plotted against torque and best-fit sigmoidal curves using an angular displacement limit of 0.4 rad (red points and black curve) and 0.6 rad (blue points and dark blue curve). The vertical dotted lines mark the range of validity of the former curve. Bottom graph: Calculated CC velocity-normalised torque curves within the range of validity of the corresponding stiffness-torque curve (red and blue points) and using extrapolation (dark red points) with an angular displacement limit between 0-0.4 rad (red and dark red points) and between 0-0.6 rad (blue points). Matching-torque procedure was carried out over the 10-90% of peak-torque range. These results come from one volunteer (AC).

torque-values used in the stiffness-torque plot, the red torque-velocity points are generated. Extrapolation of stiffness-torque relationship outside this validity range, also gives rise to the dark red torque-velocity points. In this example, the points generated by extrapolation at high torque values lay in a smooth continuation with the other points. However, extrapolation to low torque values creates a region in the torque-velocity plot in which the resulting points lie below what would be expected to be a smooth continuation of the hyperbolic curve. Assuming that a fully active CC would generate a hyperbolic torque-velocity relationship, three possibilities exist:

a) Extrapolation of the stiffness-torque relationship to low torque values is incorrect and more low-torque points are required in order to establish its shape in the low-torque region.

b) If the extrapolated stiffness-torque relationship is correct, as the low-torque points in the torque-velocity curve also correspond to early contraction times, the activation of the CC is incomplete with regards to its maximal shortening velocity early in the contraction. According to the shape of the plot in the low-torque region, activation would rise from the start of the contraction to reach its maximal value by the time the low-torque points join the main part (red area) of the torque-velocity plot.

c) The low-torque region of the CC torque-velocity curve is partly due to incomplete activation and partly due to incorrect stiffness-torque relationship in the low-torque region.

Thus, extrapolation of the stiffness-torque relationship beyond its range of validity, especially in the low torque region, produces ambiguous results. As a

conclusion, both the stiffness-torque and the CC torque-velocity relationships are more likely to represent the real state of the muscle when considered within the range of torque values for which there are stiffness-torque observations.

The upper limit of the validity range for the stiffness-torque (and the CC torque-velocity) relationship is set to be 90% of the peak torque achieved during the dynamic experiment. The lower limit is set by the angular displacement of the load. The stiffness-torque plot in figure 3.23 with torque values selected from a wider range of angular displacements has more points than the one using a narrower range. These extra points alter the shape of the stiffness-torque relationship compared to when fewer points are used. The question arises as to which one of the two stiffness-torque relationships is more reliable. The corresponding CC torque-velocity plots calculated within the range of validity of each stiffness-torque relationship also differ from one another. The major difference between the two torque-velocity plots is that points deviate from the core of the plot in a downward direction (e.g. in the region torque is approximately 0.25 and the velocity is 0.5 in figure 3.23) when a wider range of angular load displacement is used. This could be due to difference in the active state of the CC as a result of extensive shortening (shortening deactivation; De Ruiter *et al*, 1998; Lee *et al*, 1999; Herzog *et al*, 2000) resulting in lower contraction velocities for a given torque production or lower torque production for a given contraction velocity. It has been shown that the adductor pollicis, a muscle of the hand, can show a force deficit of up to 37% following isokinetic concentric contractions (De Ruiter *et al*, 1998). If however the CC deactivates with shortening, the assumption made that the active state of the CC is the same

when torque is the same is not valid, if the CC has shortened considerably between the times the torque rises and drops to a given value. In addition, the torque-angle relationship shows a steeper decline with the abduction angle at large angles than at smaller ones. Thus, although at small abduction angles the torque is almost constant, at larger abduction angles the torque may be considerably lower. This could influence the result when matching torque points coming from small abduction angles with ones coming from large angles. The effect would be consistent with a decline of the calculated CC velocity from the velocity expected from a fully active muscle shortening at the plateau of its torque-angle relation. It is not known exactly to what extent shortening deactivation and the torque-angle relation contribute to the observed decline in the CC shortening velocity, but this decline appears to be effectively removed from torque-velocity plots when an angular load displacement upper limit is set for the torque-matching procedure. Moreover, accounting for the torque-angle relation, did not improve the result (see later sections). Thus, as the CC properties are altered beyond a certain amount of angular load displacement, the stiffness-torque relationship would be more valid when angular displacement does not exceed that limit and the CC torque-velocity relationship would better reflect the properties of the fully active muscle.

To summarise, the matching-torque procedure is applied within a range of (normalised) torque values whose:

a) Upper limit is equal to 90% of the peak (normalised) torque

b) Lower torque limit is set by the angular displacement beyond which the CC appears to deactivate.

The stiffness-torque and CC force-velocity relationships are considered mainly within this range.

Following the observation that the 'active state' of the CC may be a function of the shortening that it undergoes, it would be reasonable to assume that, within the range of validity for the analysis, the smaller the amount of CC shortening that has occurred between two instants at which the torque is the same, the more similar the active state of the CC would be at these two instants. By pairing torque values over a narrow range in each torque record such that the temporal separation of these paired values is kept relatively short, the deactivating effect of CC shortening could be kept relatively small. Figure 3.24 can be used to compare the difference in the result obtained from the same data set, when torque pairs are obtained from a large part of the record (10-90% of the peak torque) and when obtained from a smaller part of the record near its peak (75-90% of the peak torque). When using large parts of records more values are obtained compared to when using shorter parts. These extra values increase the variability in the plot especially at lower torque values which when paired on a torque record show a longer temporal separation compared to the higher torque values nearer its peak. As the result obtained from such points may be influenced relatively more by shortening deactivation, the plot resulting from pairing fewer torque values nearer to the peak of each record may be more valid.

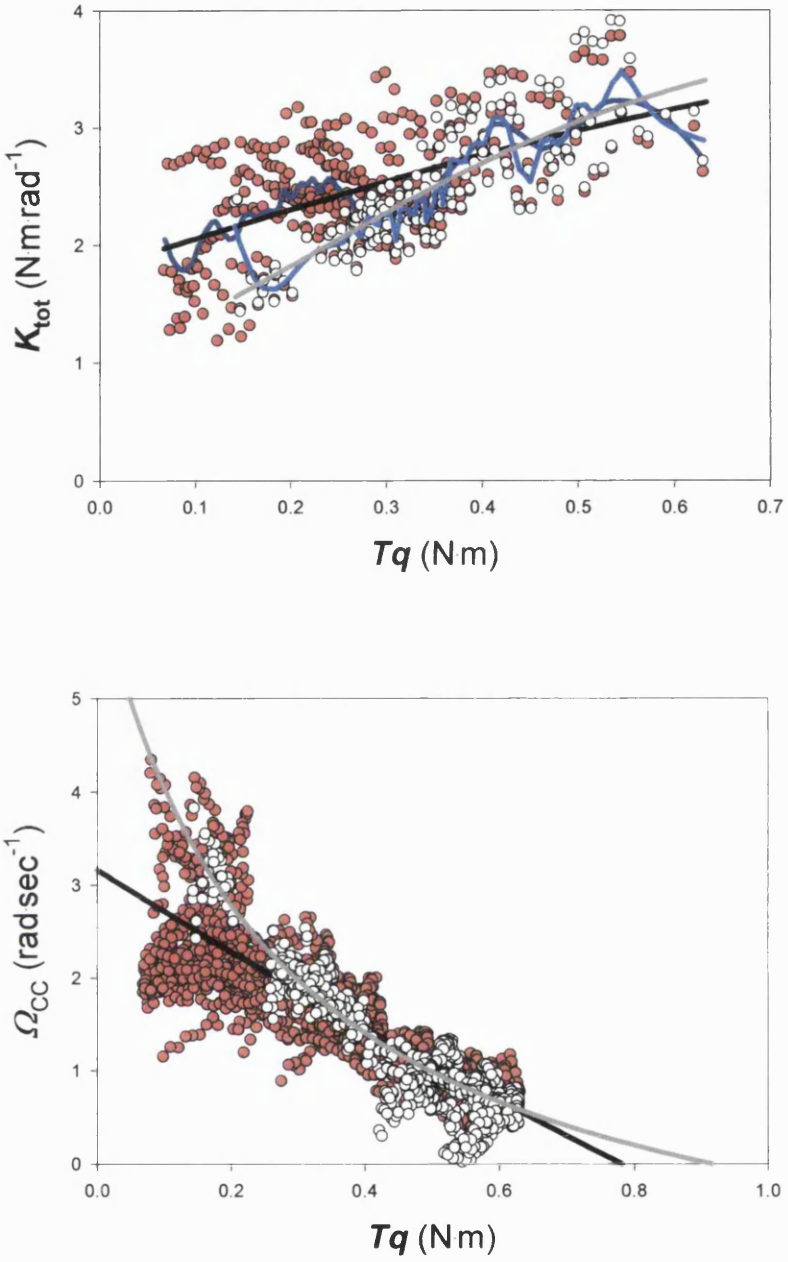

Figure 3.24. Effect of further restriction in torque range on the calculated elastic and contractile properties. Top graph: Stiffness-torque relationship using torque-pairs within 10-90% of peak torque (red points) and 75-90% of peak torque (white points). Fitted curves using interpolation and best-fit sigmoidal curves (10-90%: dark blue and black, respectively; 75-90%: blue and dark grey, respectively) are also shown. Bottom graph: CC torque-velocity plots and best-fit rectangular hyperbolas when torque pairs are obtained within the 10-90% of peak torque (red points and black curve, respectively) and within the 75-90% of peak torque, respectively. The fitted curves have been extrapolated for visual clarity. Results from one volunteer (AC).

When calculating the CC torque-velocity relationship the best-fit sigmoidal curves are used as representing the total stiffness-torque relationship. Another alternative could be to use interpolated curves. As shown however in the top graph of figure two for both plots, both the interpolated and the sigmoidal curves show a similar pattern. Moreover, the sigmoidal curves provide a convenient means of describing the relationship between stiffness and torque using only three parameters.

The CC torque-velocity plots calculated using a wide and a narrower torque-range for pairing and the corresponding stiffness-torque relationships are also different from one another. The plot obtained from the narrower range is more curved than the one obtained from the wider torque range. As already discussed, the relationship arising from pairing torque values in the narrow range near the peak of the torque records would be expected to be less influenced by shortening deactivation and therefore be more valid.

Using this procedure improved the quality of the result obtained for certain volunteers, but as good or better a result was obtained for the other volunteers when using a wider range of torque values (see table 3.6 for ranges). The range of torque values that gave the best result was used in each case and these results are presented in the following section.

To summarise, the effect of possible shortening deactivation on the calculation of the contractile and elastic properties of the FDI MTC could be minimised by pairing torque values within a relatively narrow range near the peak of the

record. Pairing equal torque values occurring relatively close in time, could minimise the influence of differences in the state of activation of the CC may have on the results.

4.3. SEC elastic properties

4.3.1. SEC stiffness-torque relationship

4.3.1.1. No adjustment for the torque-angle relation, effect of previous contractions on static torque or activation

Total stiffness-torque values were calculated for pairs of torque values selected using the criteria described previously (section 4.2.1.3.3). The relationship between the stiffness of the SEC (see definition on page 274) and the torque for the six volunteers was calculated from the total stiffness-torque by applying a correction for the force transducer compliance (section 4.2.1.3.1). The result is shown in figure 3.25 and table 3.6.

The range of stiffness and torque values and the shapes of the SEC stiffness-torque plots shown in figure 3.25 differ between volunteers. Normalised stiffness-torque relationships expressed in terms of the maximal static torque are less variable (figure 3.26).

In the rest of this chapter, when results for all volunteers are plotted together in one graph, each individual volunteer's results can be identified by the following colour code: JS red; SP blue; AC green; AG black; GO pink; SH cyan.

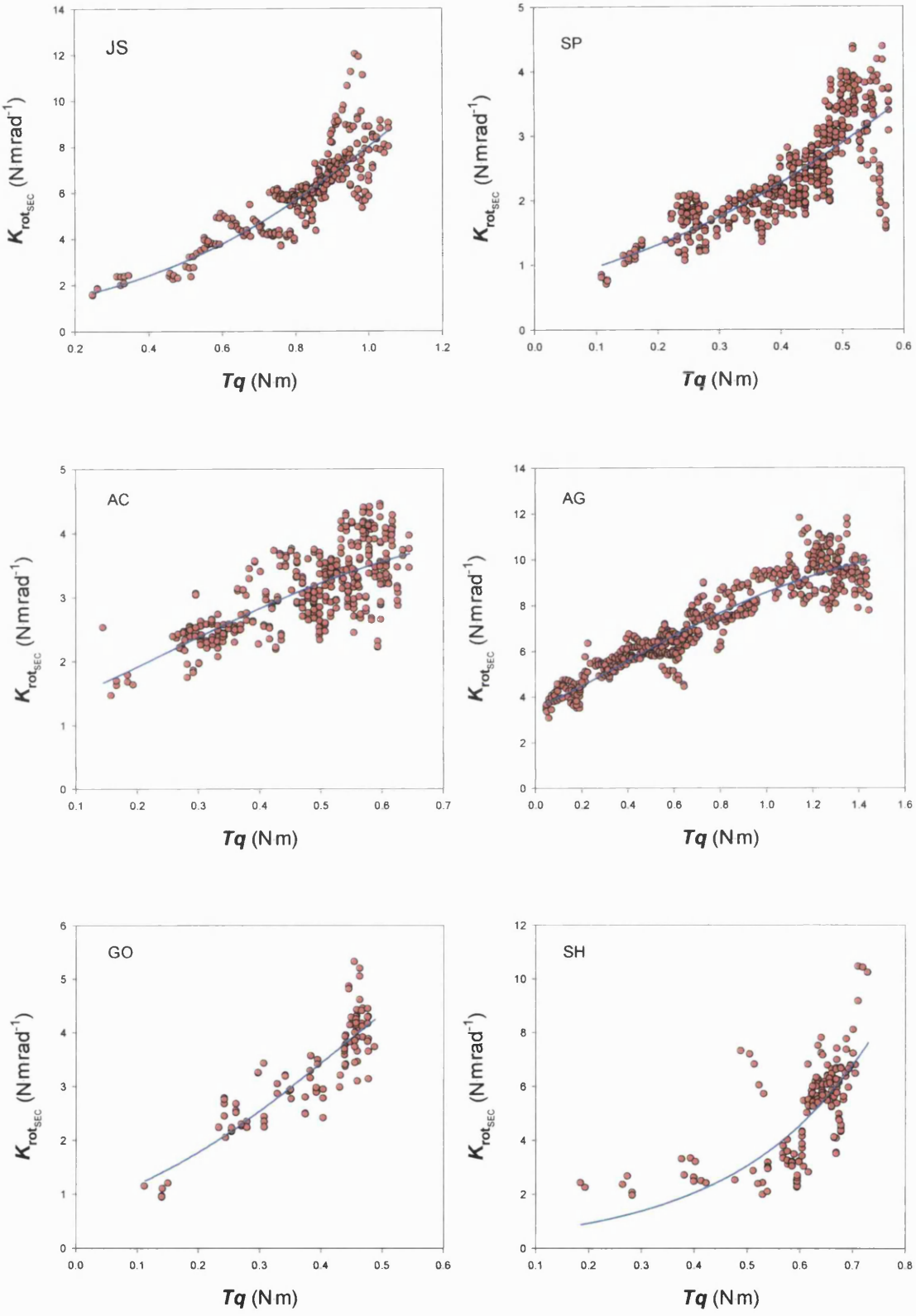

Figure 3.25. SEC stiffness-torque plots (red circles) and best-fit three-parameter sigmoidal curves (blue curves) for the six volunteers. The calculation of these results was made assuming no influence of the torque-angle relation and of the history of previous contractions. See table 3.6 for details.

Subject	No of Records	Torque range (xTq_{PEAK})		Max(θ_L) (rad)	No of Points	CV	CC	A_1 (N·m·rad^{-1})	A_2 (N.m)	A_3 (N.m)
		Min	Max							
JS	23	0.75	0.90	0.27	534	0.170	0.848	19.136	1.120	0.374
SP	25	0.75	0.90	0.35	914	0.193	0.808	8.412	0.687	0.290
AC	25	0.75	0.90	0.30	736	0.140	0.725	4.400	0.260	0.236
AG	18	0.10	0.90	0.30	1076	0.097	0.931	11.263	0.405	0.509
GO	25	0.85	0.90	0.23	214	0.138	0.882	7.349	0.424	0.198
SH	20	0.80	0.90	0.20	314	0.262	0.701	593.440 (NC)	1.824 (NC)	0.252 (NC)

Table 3.6. Information regarding the calculation of the SEC stiffness-torque relationship, assuming no influence of CC activation, torque-angle relation and of preceding contractions. Volunteers' name initials; number of records analysed, range of torque values for the pairing procedure expressed as proportion of peak torque achieved in each record; upper angular displacement limit; stiffness-torque points obtained from the analysis; CV is the coefficient of variation of the stiffness i.e. the square root of stiffness residual variance expressed as a proportion of the mean stiffness; CC is correlation coefficient for the fitted sigmoidal curve and parameters of the sigmoidal relationship. NC indicates that more iterations were required to obtain convergence to a solution within the desired error limit, although the values for the coefficient of variation and the correlation coefficient had stabilised within 3 d.p.

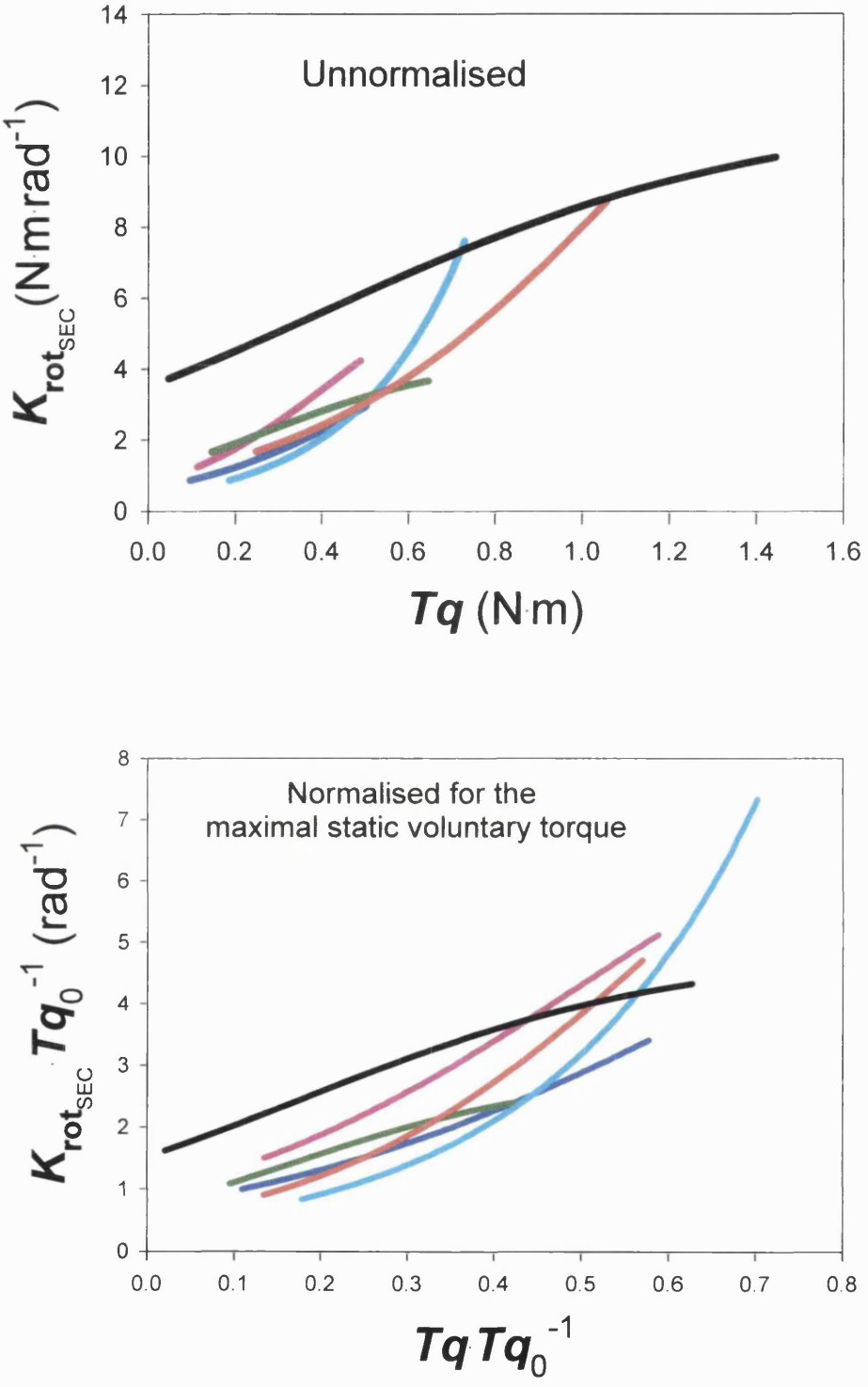

Figure 3.26. SEC stiffness-torque fitted curves for all volunteers before (top graph) and after normalisation for the corresponding maximal voluntary static torque achieved during each experiment (bottom graph). Also notice the different scales. Red: JS; Blue: SP; Green: AC; Black: AG; Pink: GO; Cyan: SH.

4.3.1.2. Torque adjustment for the torque-angle relation and the effects of preceding contractions

If the CC torque generation during dynamic contractions is assumed to be influenced by the maximal static torque-angle relationship, the dynamic torque should be adjusted to take account of that as described earlier (section 4.2.1.2.2, pp. 264 and 4.2.1.2.5, pp. 268). Moreover, when the maximum static torque at the control angle changes by more than 10% during the experiment compared to the initial value, an additional adjustment is also made to account for this change (sections 4.2.1.2.3, pp. 266 and 4.2.1.2.5, pp. 268). The latter adjustment was only necessary in two out of the six volunteers (see table 3.7). The resulting SEC stiffness-torque relationships are shown in figure 3.27. Information regarding the stiffness-torque relationship after adjustment for the static torque-angle relation and the effect of preceding contractions is shown in table 3.7.

The fitted SEC stiffness-torque curves are shown in figure 3.28. Normalising for the maximal voluntary static torque reduces the variation observed before normalising (figure 3.28). This is consistent with the SEC being adapted to the ability of the CC to generate force.

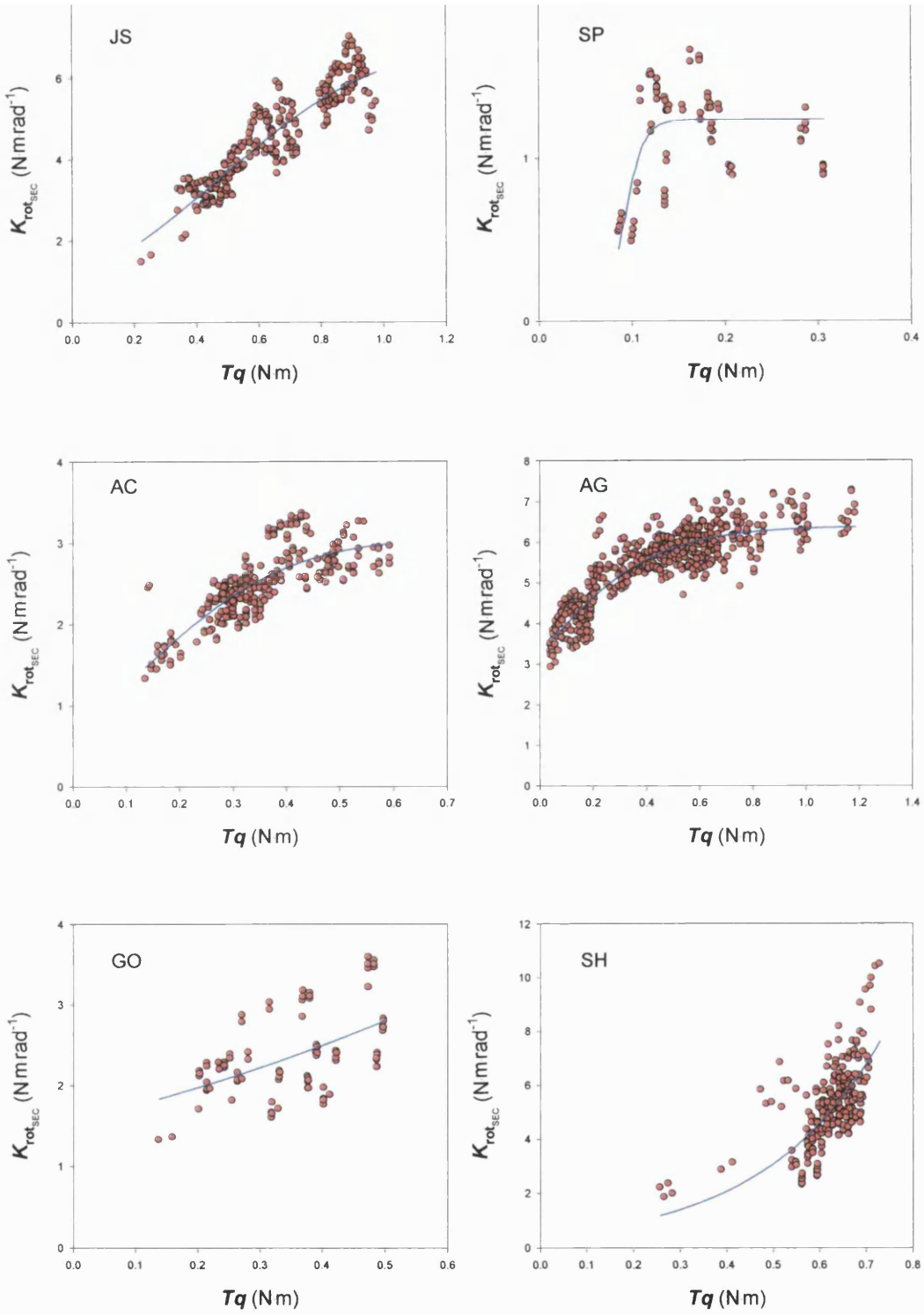

Figure 3.27. SEC stiffness-torque plots (red points) and best-fit sigmoidal curves (blue) after adjustment for the static torque-angle relationship and effects of preceding contractions. See table 3.7 for details.

Subject	Records	Torque range (xTq_{PEAK})		Max(Θ_L) (rad)	Points	CV	CC	A_0 ($N{\cdot}m{\cdot}rad^{-1}$)	A_1 (N.m)	A_2 (N.m)
		Min	Max							
JS*	12	0.1	0.90	0.40	276	0.101	0.912	7.130	0.477	0.271
SP	7	0.75	0.90	0.35	82	0.206	0.658	1.234	0.090	0.010
AC*	19	0.75	0.90	0.30	264	0.104	0.796	3.097	0.147	0.131
AG	16	0.10	0.90	0.30	540	0.079	0.875	6.393	-0.010	0.213
GO	11	0.85	0.90	0.23	88	0.176	0.525	45.910	2.721	0.813
SH	11	0.80	0.90	0.20	262	0.215	0.664	593.440 (NC)	1.824 (NC)	0.252 (NC)

Table 3.7. Volunteers' name initials, number of records analysed, range of torque values for the pairing procedure expressed as proportion of peak torque achieved in each record; upper angular displacement limit; stiffness-torque points obtained from the analysis; stiffness coefficient of variation (CV); correlation coefficient (CC) for the fitted sigmoidal curve and parameters of the sigmoidal relationship. NC indicates that more iterations were required to obtain convergence to a solution within the desired error limit, although the values for the variance and the correlation coefficient had stabilised within 3 d.p.* result includes adjustment for maximal static torque generation.

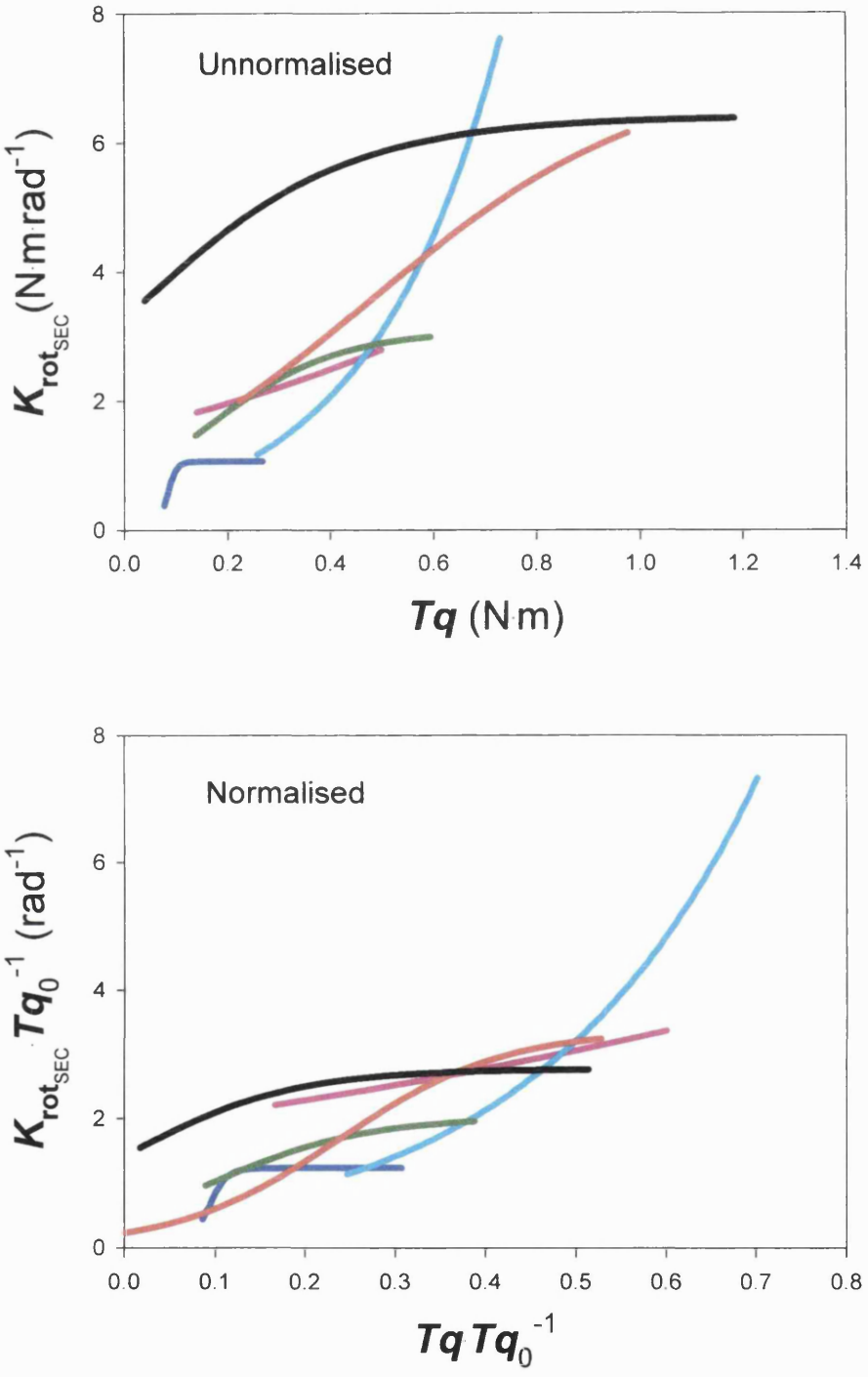

Figure 3.28. Best-fit SEC stiffness-torque curves after adjustment for the static torque-angle relation and change in maximal static voluntary torque generation during the experiment. The top graph shows the best-fit sigmoidal curves for all volunteers. The bottom graph shows these curves normalised for the corresponding maximal voluntary static torques.

4.3.1.3. Torque adjustment for CC activation

When an exponentially rising time course of CC activation was assumed (sections 4.2.1.2.1, pp. 261 and 4.2.1.2.5, pp. 268) a multitude of equally well fitting solutions could be found in many cases, i.e. the solution became indeterminate.

4.3.1.4. Which model?

Figure 3.29 shows a comparison for each volunteer of the SEC stiffness-torque curves that were obtained with and without adjustment for the torque-angle relationship and the effects of preceding contractions. In all but one case (volunteer SH) there are differences in the resulting relationships. The difference appears to be smaller on the left side of the relationship where the torque is lower, compared to the right side (higher torque portion) of the relationship. When no adjustment has been made, higher stiffness is obtained on the right side of these relationships.

When comparing the coefficient of variation and the correlation coefficient between the two methods for each subject, none of the two methods appears to be consistently better than the other (see tables 3.6 and 3.7). However, when no adjustments are made, more records can be analysed and a greater number of stiffness-torque points is generated. Because of this and for the sake of simplicity, the results presented in later parts of this thesis are obtained using no adjustments in the torque records. It is accepted that this may lead to some overestimate of the stiffness of the SEC at high torques.

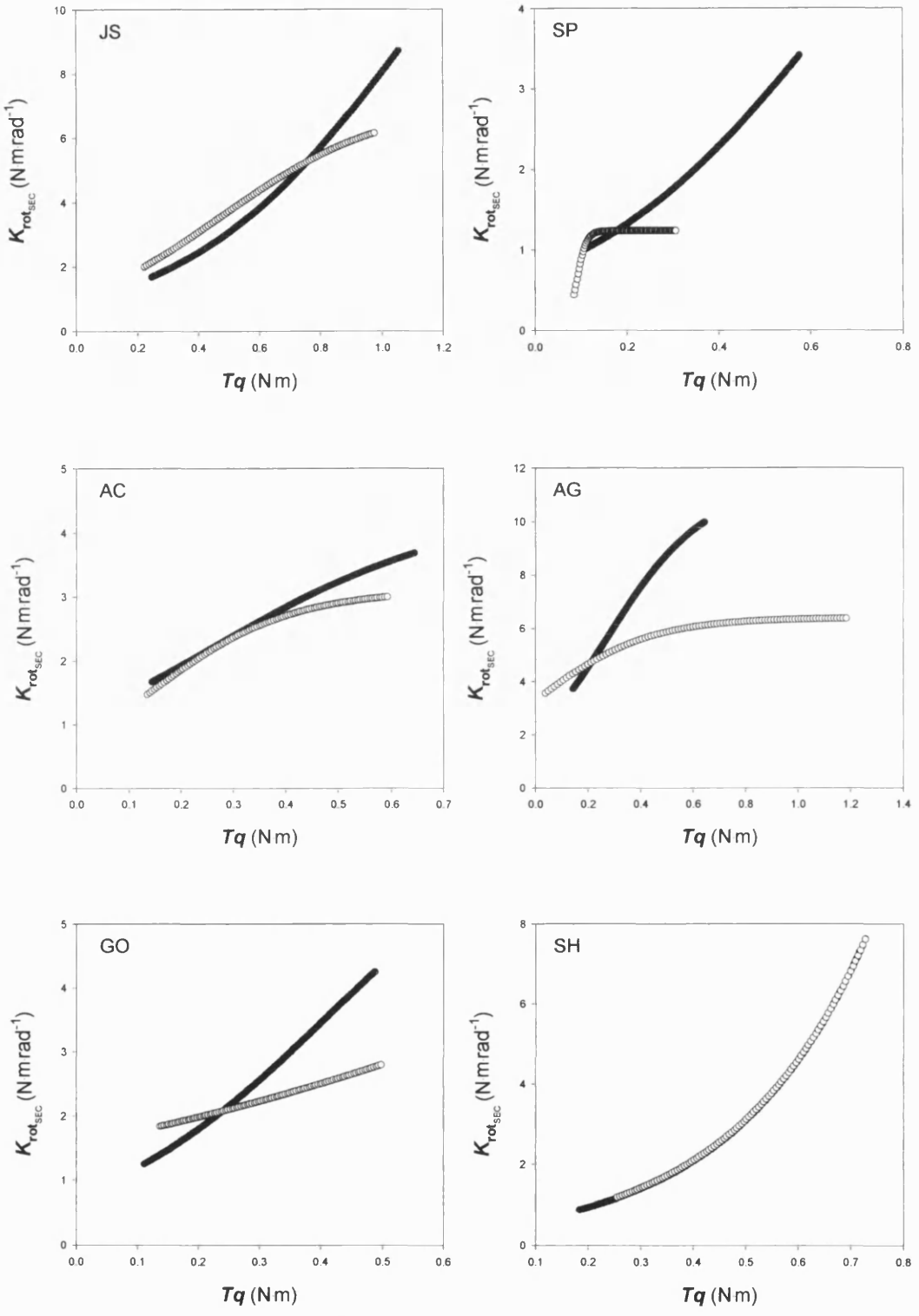

Figure 3.29. Best-fit SEC stiffness-torque curves with and without adjustment for the torque-angle relationship and effect of preceding contractions (open and closed circles, respectively) for each volunteer.

4.3.2. SEC torque-angular extension curves

The area under the compliance-torque curve represents SEC extension (in rotational terms), within the torque range for which compliance is known. As compliance is the reciprocal of stiffness, compliance torque curves could easily be generated for each volunteer from his/her SEC stiffness-torque results. In order to obtain the area under such curves, the torque domain was split into 5 –8 intervals of equal size, each interval containing a number of torque-compliance points. The torque and compliance values within each torque interval were averaged to obtain a 'grouped-average' compliance-torque curve, that is a curve based on the averages of the data grouped in this way. The torque interval size was chosen so that the averaged data would adequately reflect the overall shape of the curve, which was presumed to be monotonic. The torque-extension curves for all volunteers were calculated using numerical integration of their grouped-average interpolated compliance with respect to the torque. The SEC angular extension ($\Delta\Theta_{SEC}$) is expressed with regard to the extension at the minimum grouped average torque value for each volunteer. Figure 3.30 shows these curves.

As the origin of $\Delta\Theta_{SEC}$-axis is reflects the SEC extension corresponding to the first torque value in the plot and the amount of this extension is unknown, a torque value that is common between all the curves could be used as reference point for the SEC torque-extension curves. Figure 3.31 shows the SEC torque-extension curves translated to the left along the $\Delta\Theta_{SEC}$-axis so they all intersect at a given torque value. As a result of this translation $\Delta\Theta_{SEC}$ becomes negative at the left of the point of intersection. With the graphs in this form it is also

easier to visually compare the curves. Similarly with the stiffness-torque curves, the variation observed between the SEC torque-extension curves is reduced when expressing torque relative to each volunteer's maximal static torque.

The SEC torque-extension curve for each subject is fitted by a rectangular hyperbola (figure 3.32) of the form:

$$Tq = \frac{\Delta\theta_{SEC} + \Delta\theta_T}{1 + (1 - \Delta\theta_{SEC} - \Delta\theta_T) \cdot H} \cdot Tq_{\max}$$

where $\Delta\theta_{SEC}$ is the amount of SEC extension expressed relative to the extension the SEC undergoes from its resting length when the maximal static torque is applied on it ($\Delta\theta_0$). $\Delta\theta_T$ is a 'translation' parameter, also expressed in relative terms, representing the amount of extension the SEC has undergone beyond its resting length as a result of applying the minimal torque in each torque-extension curve. The values of the parameters for all fitted hyperbolas are shown in table 3.8.

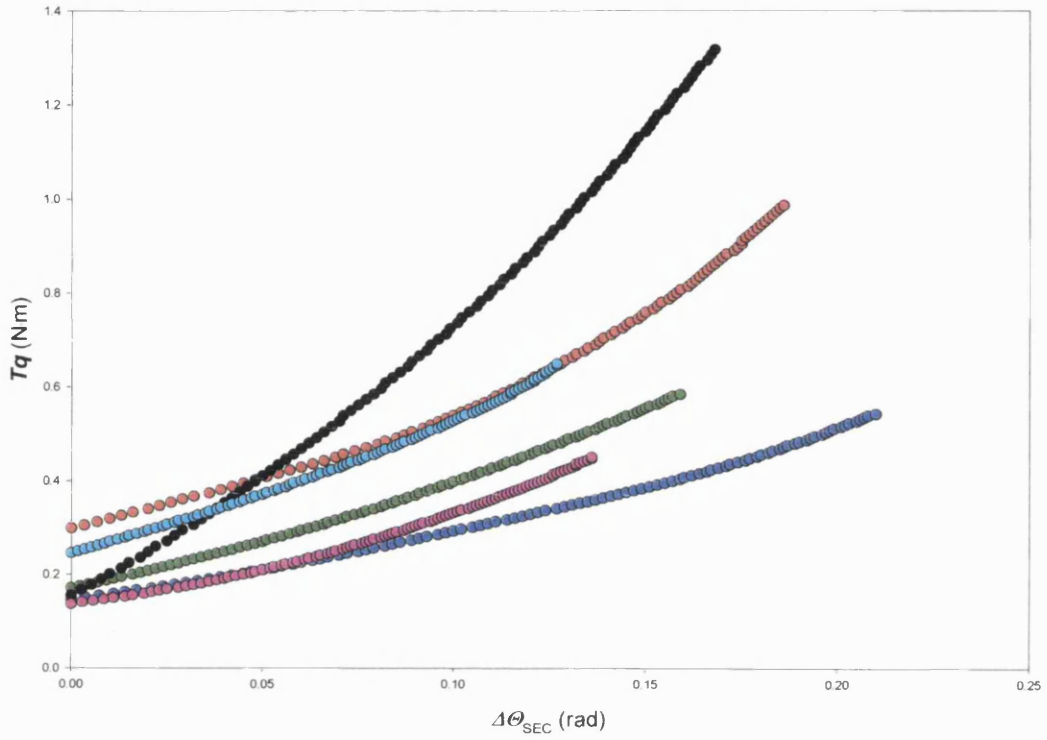

Figure 3.30. SEC torque-angular extension curves for all subjects.

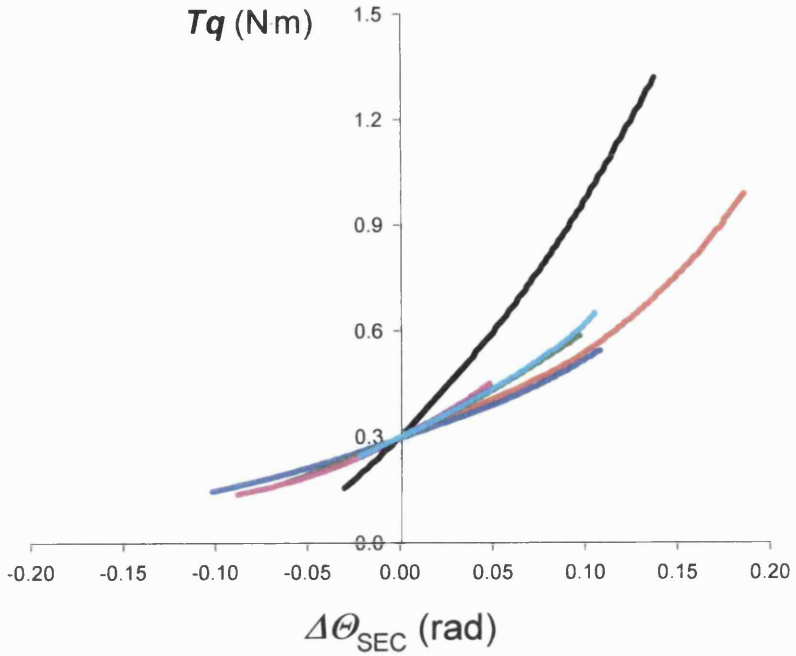

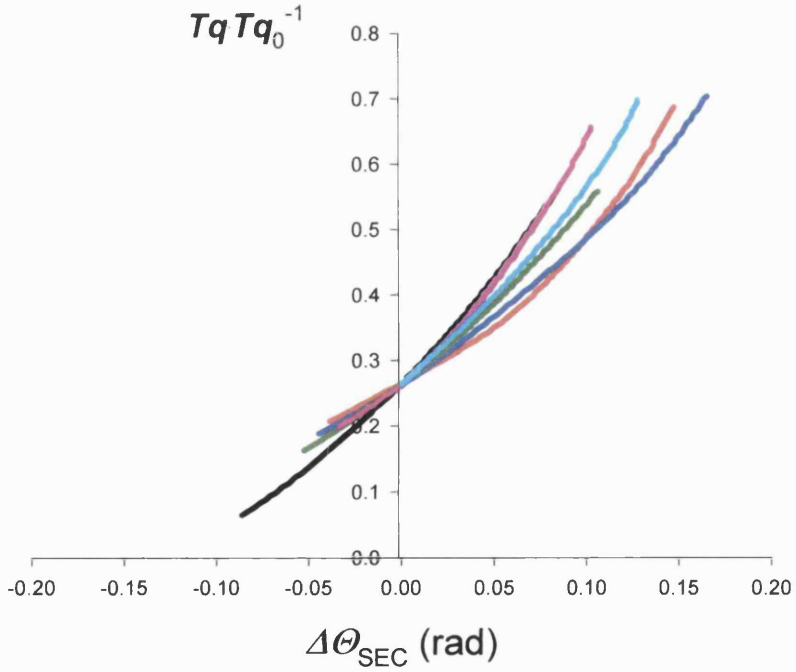

Figure 3.31. SEC torque-extension curves shifted along the $\Delta\Theta_{SEC}$-axis to intersect at approximately 0.3 N·m (top graph) and 0.27 normalised torque units (bottom graph). Notice how expressing the torque relative to each volunteer's maximal static torque in the bottom graph reduces the variation observed between volunteers in the top graph.

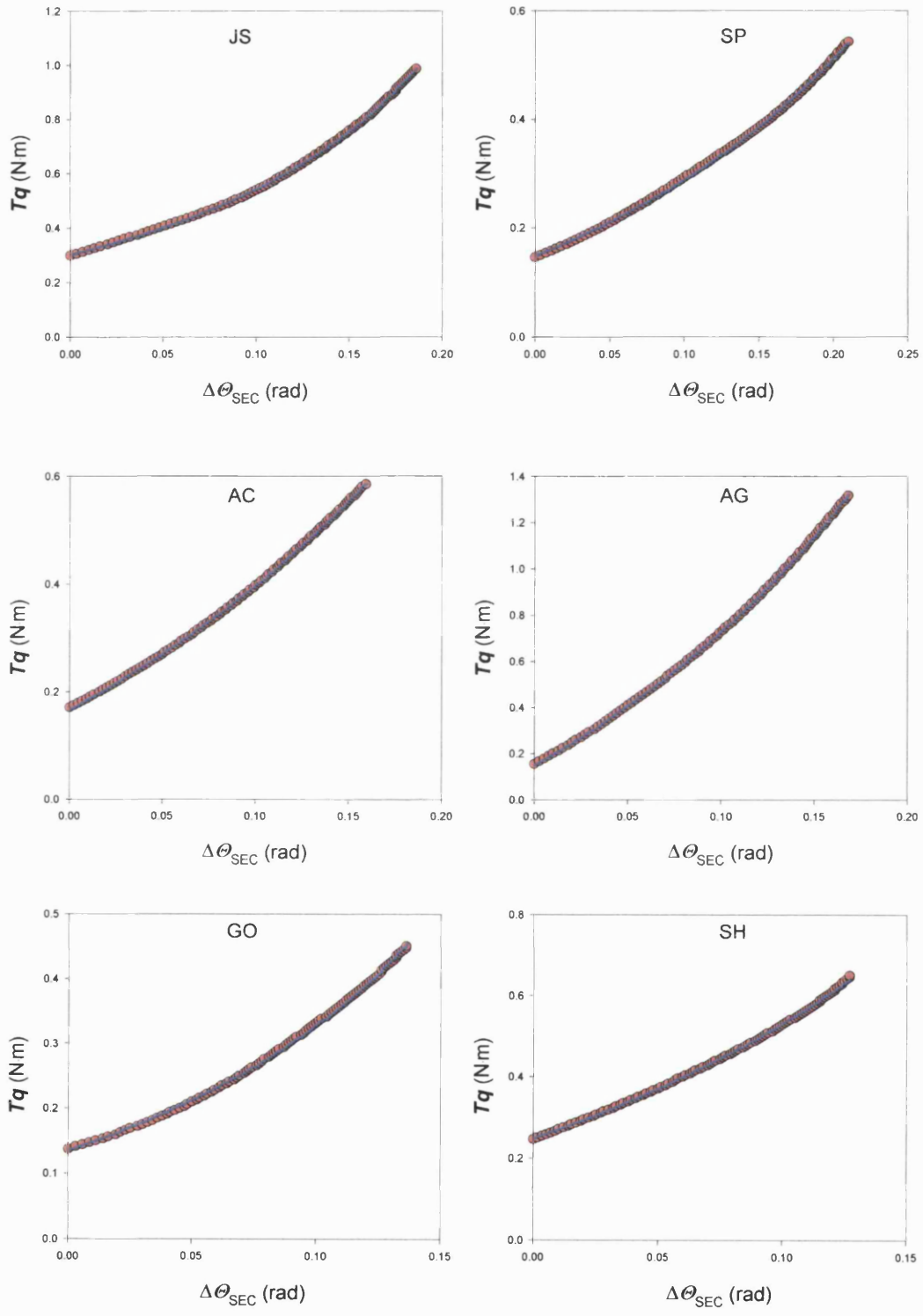

Figure 3.32. SEC force extension curves (red circles) and fitted hyperbolic curves (blue lines). See table 3.8 for details.

Volunteer	H	$\Delta\Theta$ (rad)	$\Delta\Theta_0$ (rad)	SSE (N·m)
JS	4.755	0.349	0.577	$5.954 \cdot 10^{-4}$
SP	1.616	0.169	0.441	$5.228 \cdot 10^{-4}$
AC	1.131	0.103	0.359	$1.335 \cdot 10^{-4}$
AG	1.068	0.034	0.281	$2.355 \cdot 10^{-4}$
GO	2.619	0.158	0.336	$5.492 \cdot 10^{-4}$
SH	1.373	0.157	0.339	$5.089 \cdot 10^{-4}$

Table 3.8. Curvature (H), translation ($\Delta\Theta$) and maximal extension ($\Delta\Theta_0$) parameters for the best-fit rectangular hyperbola to the SEC torque-angular extension curve. SSE is the sum of the squares of the errors.

4.4. Contractile properties

4.4.1. CC torque-velocity relationship

4.4.1.1. Estimation from dynamic contractions against inertial loads

Using the stiffness-torque relationship for the total stiffness in series with the CC of the FDI MTC, the CC torque-velocity relationship was calculated as described in section 4.2.1.3.1 (pp. 270). This calculation has been made for all points that satisfy these criteria:

- The torque is within the range of torques for which the stiffness is determined
- The angular displacement is less than a set value. This value is same as that used to restrict the data point pairing in the determination of the stiffness (section 4.2.1.3.3, pp. 282).
- The torque is higher than 10 % of the maximum torque in that same record.

The results are shown in figure 3.33 and table 3.9.

The purpose of this analysis is to obtain a 'model-independent' assessment of the success (correlation coefficient) of the force-velocity curves obtained by this method. (In the following paragraph the term frequency will be applied to velocity vs torque data as though the torque axis represented time). The frequency components of the calculated CC torque-velocity relationships can be obtained using Fourier analysis. The overall shape of the curves will be due to relatively low-frequency components and high frequency components could be regarded as 'noise', increasing the scatter of velocity values at any given level of torque. The noise in the CC toque-velocity relation was assessed by a fast Fourier analysis of the velocity points after sorting in order of torque. The total

area under the power spectrum curve is equal to the total variance of the CC velocity measurements, i.e. sum of velocity variance reflecting the CC behaviour and velocity variance due to other factors. The power spectrum (see example in fig 3.34) becomes flat after the first 10-40 points and the area of the power at "frequencies" below this level is equal to the 'explained' variance. This means that the variation in velocity with torque within this range of the power spectrum is 'explained' (or is due to) the mechanical behaviour of the CC. The larger the explained variance relative to the total variance, the more the relationship is expected to represent the behaviour of the CC.The square root of the ratio of the explained to total variance is equal to the correlation coefficient, r^2. The value of r for each set of CC velocities is shown in table 3.9. The high values of the correlation coefficients suggest that the effect of noise on the torque-velocity relationship is small.

The grouped-average curves provide a better visual impression of the shape of the relationship than when all torque-velocity points are included (figure 3.35) partly because the points overlap each other when all are plotted, and therefore cannot be weighted visually. The black lines are fitted curves using a modified version of Hill' s equation:

$$\Omega_{CC} = \Omega_{\max} \cdot \frac{1 - \frac{Tq}{Tq_{\max}}}{1 + \frac{Tq}{Tq_{\max}} \cdot G} \cdot \left(1 - e^{-\frac{Tq}{C}}\right)$$

Ω_{max} represents the maximal shortening velocity of the fully active CC; Tq_{max} is 1.2 times the maximal static torque achieved in the experiment (Edman *et al*, 1976); G controls the curvature of the curve; C is an exponential torque

constant to account for the lower than expected velocities sometimes observed when the torque is low (see AG in figure 3.33). Three degrees of freedom were allowed for curve fitting, such that Ω_{max}, G and C could be adjusted to minimise the SSE, while Tq_{max} was kept to its set value. The curve fitting results are shown in table 3.10. Visually the fitted curves seem to provide a reasonable description of the experimental data. However most of the grouped data points are more than two standard errors away from the corresponding fitted value, as indicated by the stars in figure 3.35. Therefore the deviations of the grouped-mean points from the fitted ones are not very likely to be due to chance and may represent the behaviour of the CC.

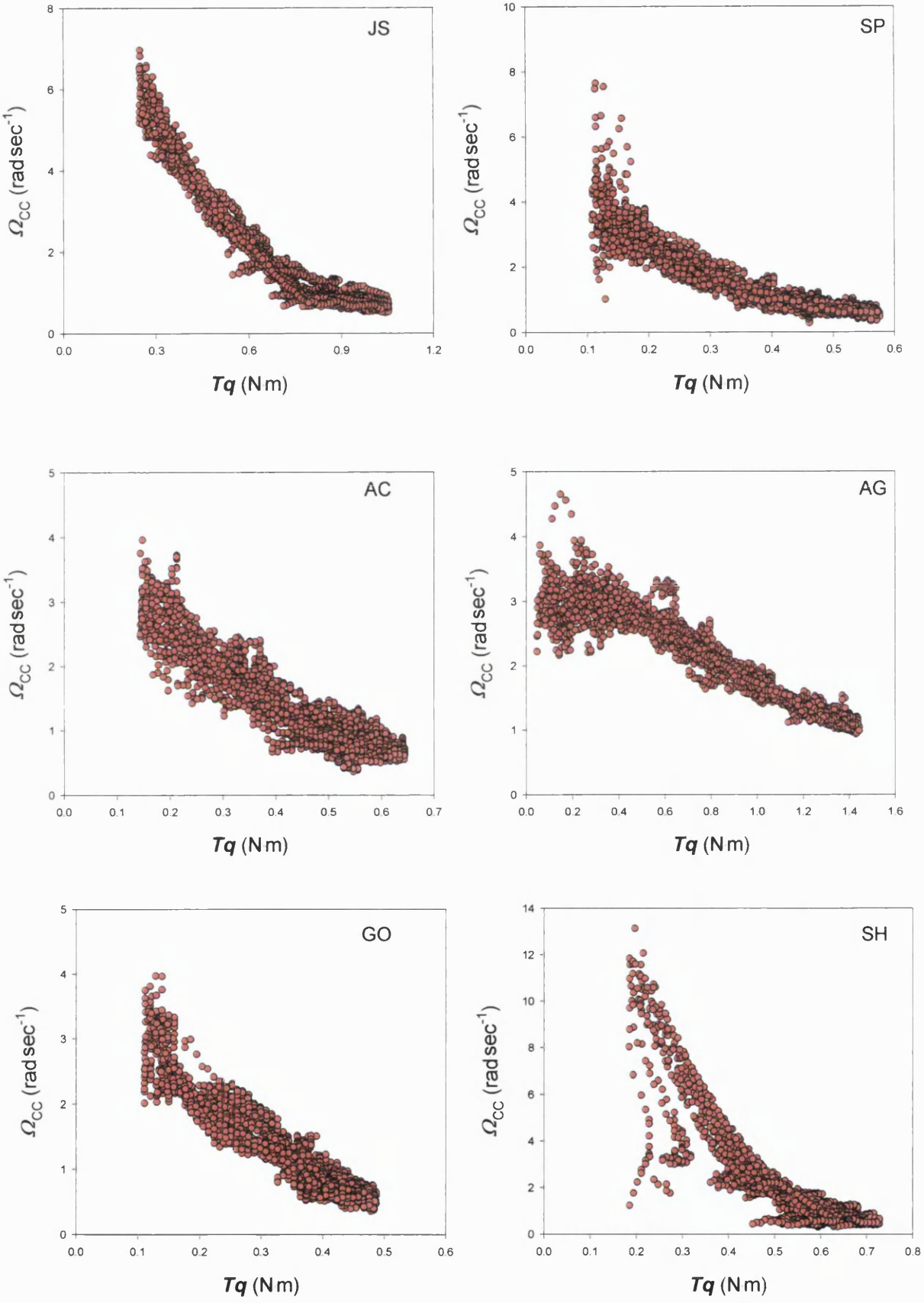

Figure 3.33. CC torque-velocity plots for all volunteers. See table 3.9 for details.

Volunteer	No. of records	Lower ***Tq*** limit (N·m)	Upper ***Tq*** limit (N·m)	Angular limit (rad)	No. of points	*r*
JS	23	0.247	1.054	0.27	2268	0.978
SP	24	0.108	0.576	0.35	3535	0.921
AC	25	0.144	0.644	0.30	3014	0.932
AG	18	0.047	1.444	0.30	2833	0.951
GO	24	0.112	0.483	0.23	2851	0.951
SH	23	0.184	0.728	0.20	1987	0.908

Table 3.9. Information regarding the calculation of the CC torque-velocity plots. Number of records analysed, torque range and angular displacement upper limit, number of points and correlation coefficient (*r*) for the CC torque-velocity relationship of each volunteer.

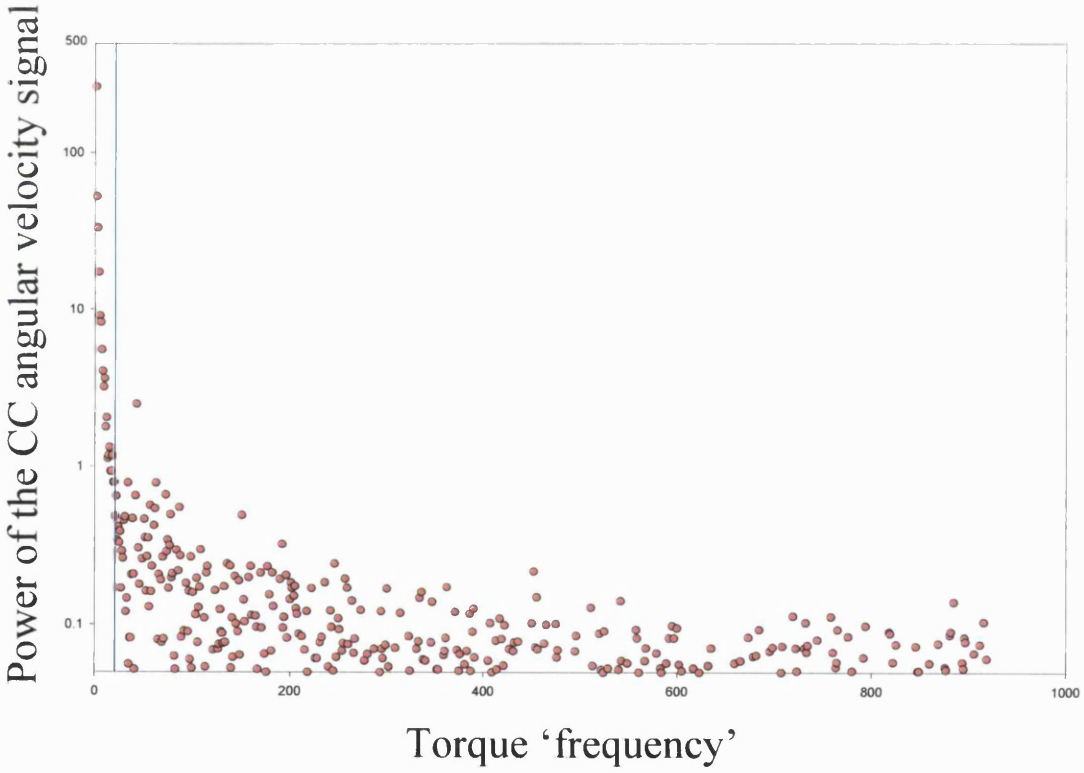

Figure 3.34. Power spectrum for a CC torque-velocity relationship.

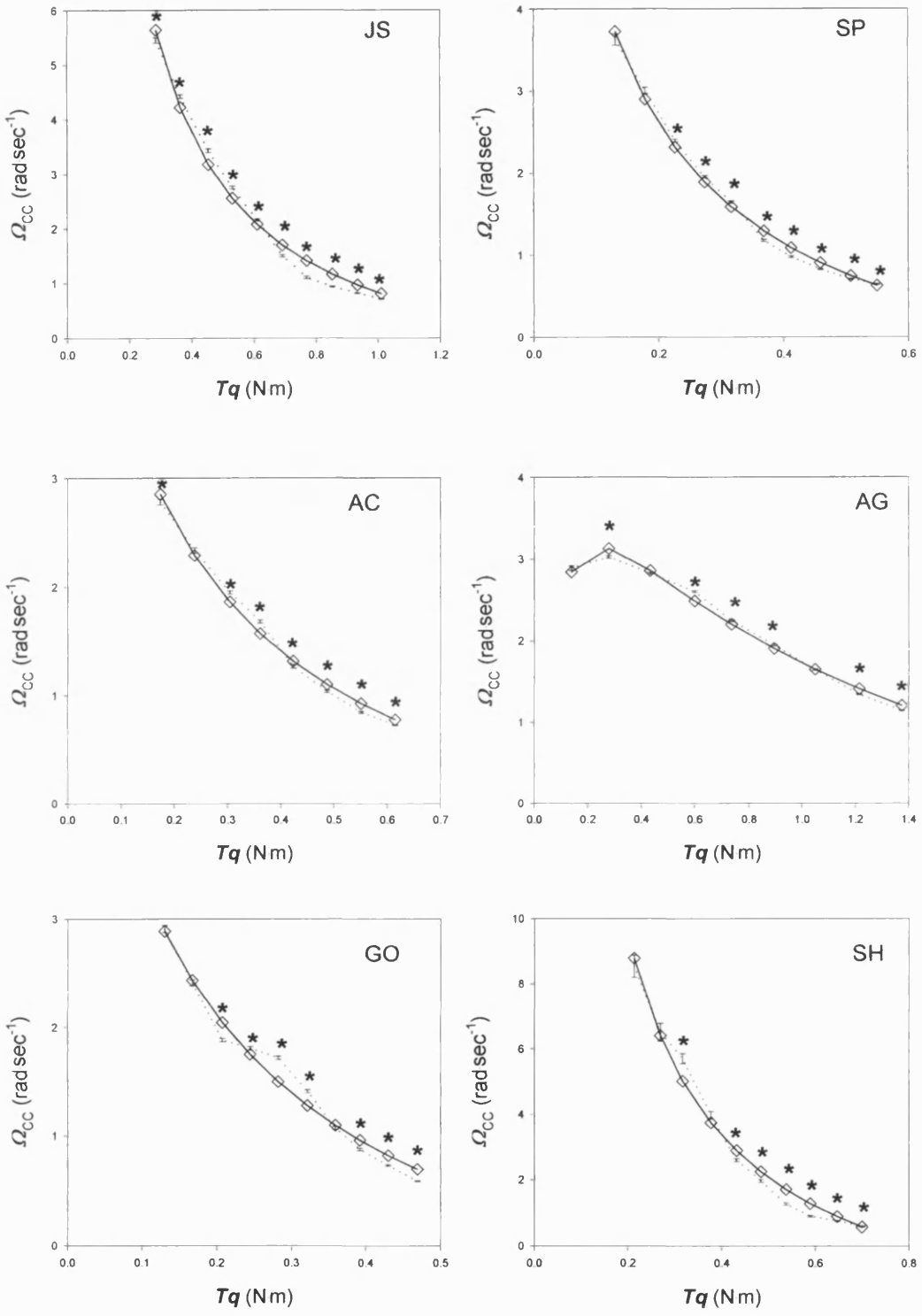

Figure 3.35. Grouped-average CC torque-velocity curve (line and standard error bars) and best-fit modified hyperbolic curve (line and diamonds). * indicates a difference of more than two SE between the average CC velocity and corresponding fitted point. See table 3.10 for details.

Volunteer	Hypothetical Tq_{max} (N·m)	Ω_{CCmax} (rad·sec^{-1})	G	C (N·m)	SSE
JS	1.725	198.609	171.719	-	0.401
SP	0.926	10.048	9.295	-	0.070
AC	1.258	6.207	6.321	-	0.043
AG	2.872	4.406	1.902	0.103	0.039
GO	0.824	6.012	4.787	-	0.124
SH	1.118	173.479	52.832	-	1.123

Table 3.10. Fitting parameters and SSE for the modified Hill's equation to the grouped-average CC torque-velocity curves for all volunteers.

4.4.1.2. Obtaining CC torque-velocity observations independently of elastic properties

It can be seen from equations (3.6) and (3.7) that when $\frac{d}{dt}(Tq)=0$, $\Omega_{CC}=\Omega_L$. $\frac{dTq}{dt}$ is equal to zero at the peak of the torque record and therefore at that time it is expected that the angular velocity of the load and of the CC are the same. In this way CC torque-velocity observations can also be collected from the values of peak dynamic torque and the corresponding load velocities (figure 3.36; green points).

4.4.1.3. Estimating CC torque-velocity during static contractions

CC torque-velocity observations were also collected for static contractions by dividing torque rate values with the corresponding value of total stiffness in series with CC such that:

$$\Omega_{CC}=\frac{1}{K_{rot_{TOT}}}\cdot\frac{d}{dt}(Tq)$$

This equation is the same as equations (3.6) and (3.7) but the velocity of the load, V_L has been neglected from this equation as it is equal to zero during static contractions. The CC torque-velocity points resulting from this approach are shown in blue colour in figure 3.36.

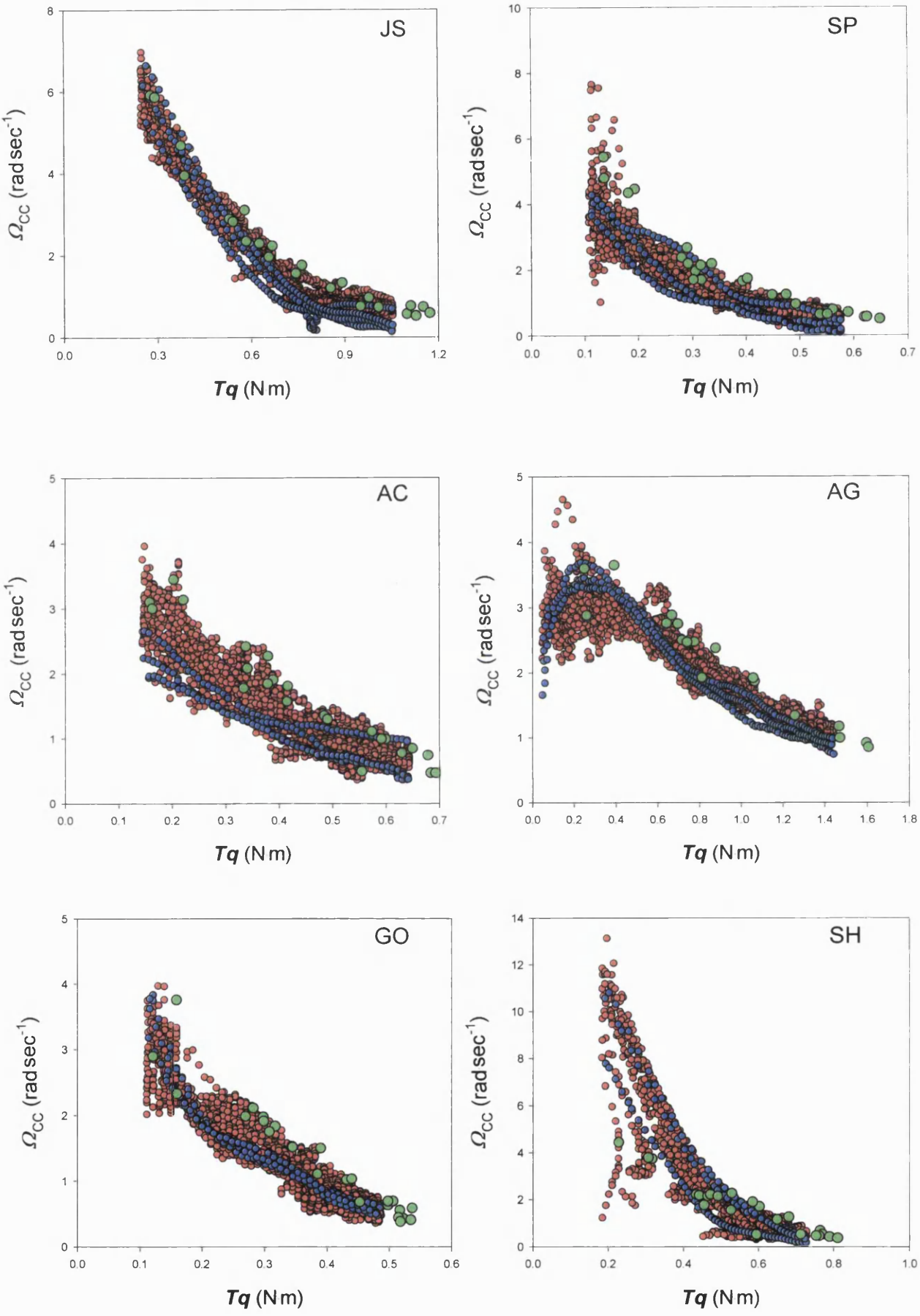

Figure 3.36. CC torque-velocity plots obtained using the calculated stiffness-torque relationship from dynamic (red) and static records (blue). Peak dynamic torque values and corresponding velocities are also plotted (green).

4.4.1.4. Comparison between the three different approaches

The question arises whether the results generated using the three different approaches shown in the figure belong to the same population of CC torque-velocity properties. The null hypothesis is that each method on average yields the same result.

CC torque-velocity observations arising from the latter two methods were compared to those obtained using the 'bell-shaped' torque-pairing method. First a "local estimate" formula was used to draw a smooth line through all the data (see figure 3.37). Interpolation can be used on the local estimate to obtain the mean CC velocity from the torque pairing method for any torque value within the range of torque values of this data set ($\Omega_{CC_{INT}}$). The variance, *V*, of the "local population" of CC velocity observations was then calculated as the local estimate of the squares of the differences between Ω_{CC} and $\Omega_{CC_{INT}}$ (see inset in figure 3.35). The standard deviation, *sd*, of Ω_{CC} at any given torque was calculated as the square root of the corresponding variance:

$$sd = \sqrt{V}$$

Upper and lower 95% confidence limits were calculated as:

$$Limit = V_{CC_{INT}} \pm 1.96 \cdot sd$$

These confidence limits are shown in figure 3.37.

The difference between the velocity values obtained for static contractions ($\Omega_{CC_{static}}$) or at the time of peak torque during dynamic contractions

($\Omega_{CC_{peakTq}}$) and $\Omega_{CC_{INT}}$ at the corresponding torque value was expressed as a proportion of sd, i.e. as a z-score,:

$$z = \frac{\Omega_{CC_{static}} - \Omega_{CC_{INT}}}{sd}$$

or

$$z = \frac{\Omega_{CC_{peakTq}} - \Omega_{CC_{INT}}}{sd}$$

This means that each observation is a sample drawn from a population with unit standard deviation of which the mean is zero, if the null hypothesis is correct. This z-score was calculated for each point within the range of torque values of the 'matching torque' method. A t score was then calculated for the two populations of CC velocity values within the torque range of the CC torque-velocity relationship:

$$t = \bar{z} \cdot \sqrt{n-1}$$

where $\bar{z}$ is the mean z-score for the data set and n is the number of $\Omega_{CC_{peakTq}}$ observations or the number of $\Omega_{CC_{static}}$ contractions for each volunteer (treating isometric contractions as independent of one another). The results are shown in table 3.11.

According to the results shown in table 3.11, the null hypothesis is accepted in the 5% significance level such that the CC torque-velocity relationship arising from dynamic contractions against inertial loads is not different the from the CC torque-velocity relationship arising from static contractions.

Although there were no significant differences for any one volunteer between the CC torque-velocity data arising from dynamic and static contractions, when all CC torque-velocity data arising from static contractions were treated collectively by obtaining a mean *z*-score for all volunteers and a *t*-score (t=-5.752) for all static contractions (n=19), the CC velocities obtained from static contractions were found to be significantly different ($p<0.01$) to those arising from dynamic contractions. The velocities arising from static contractions were lower on average than the mean velocities obtained during dynamic contractions.

Moreover, the null hypothesis that CC torque-velocity relationship arising from dynamic contractions against inertial loads is not different from the CC torque-velocity relationship arising from torque-velocity observations at the time of peak torque, is rejected in all but one subject (SH) in favour of the alternative hypothesis ($p<0.01$). The velocities obtained at the time of peak torque are higher on average than those arising from the 'matching torque' method.

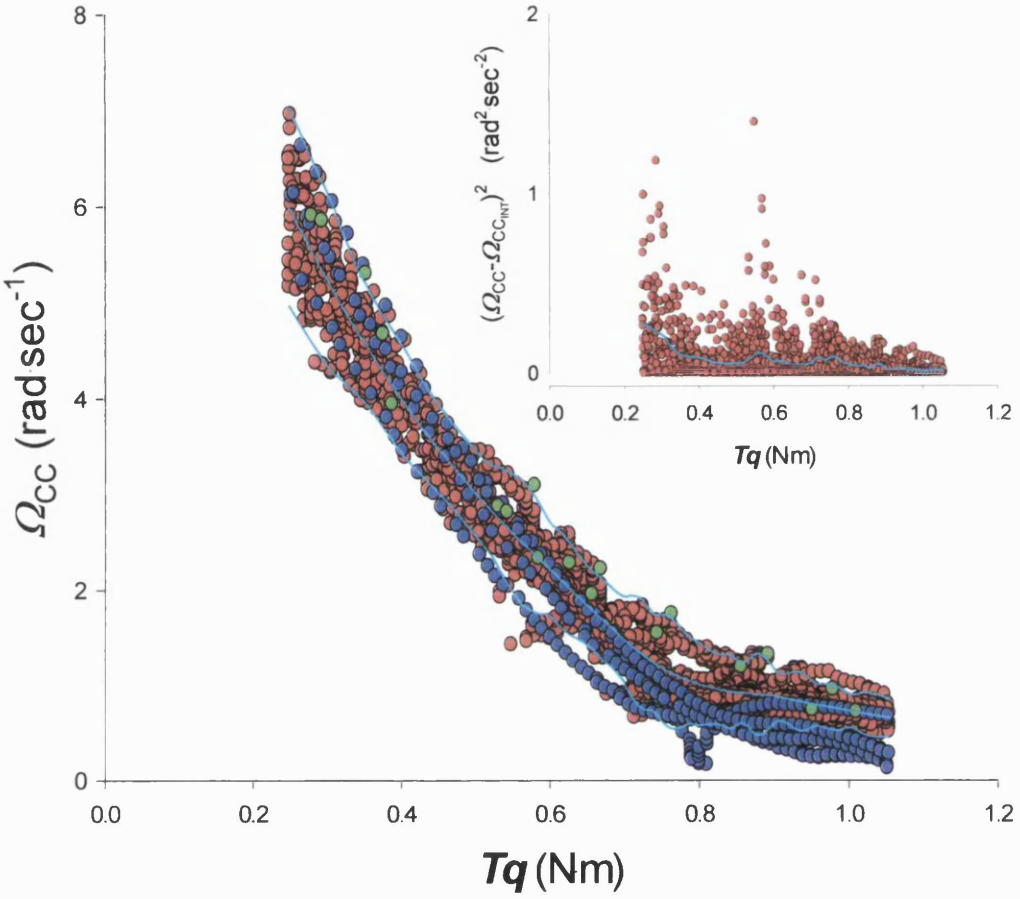

Figure 3.37. CC torque-velocity plots for volunteer JS from dynamic (red points) and static contractions (blue points) and from torque-load velocity observations at the time of peak torque during dynamic contractions (green). Cyan curves show the interpolated mean (middle) based on a "local estimate"of the points and the interpolated upper and lower 95% confidence limits for the Ω_{CC} obtained from dynamic contractions (red points). Inset: Square of the difference between the interpolated and actual value of Ω_{CC} (red points). A "local estimate" interpolation through these points gives an estimate of the variance of the corresponding CC torque-velocity observations (cyan curve).

Volunteer	Isometric vs. Dynamic		Peak vs. Dynamic	
	d.f.	t-score	d.f.	t- score
JS	3	-3.146	18	4.912**
SP	2	-2.986	19	8.571**
AC	2	-1.828	18	5.416**
AG	2	-1.388	13	6.577**
GO	2	-0.588	15	6.296**
SH	2	-0.691	16	1.185

Table 3.11. Comparison for each subject between CC torque-velocity data sets arising from different methods. The degrees of freedom (d.f.) and the t-scores are shown for each volunteer. Note that d.f. has been taken as number of contractions-1 rather than the number of data points-1; this is because of the obvious correlation between nearby data points within the same contraction. Significant differences are indicated by * ($p<0.05$) or ($p<0.01$) ** .

4.5. Sources of experimental variation

4.5.1. Effects of noise

The effect of noise present in the torque traces on the variability observed in the calculated SEC stiffness-torque and CC angular velocity-torque results was assessed as follows.

4.5.1.1. Identifying noise sources and characteristics

The source of the noise in the torque records was investigated by obtaining records on an oscilloscope of the signals coming from:

a) the strain gauge amplifier short-circuited,

b) the amplifier connected to the strain gauges but with bridge supply removed,

c) the force transducer signal with bridge supply connected,

d) as in c, but with the hand resting against the force transducer rod (to test for possible vibrations due to movement in the hand and finger)

e) as in d, with 'dummy' electrical stimulation (voltage, 180 V; frequency, 100 Hz; pulse width, 50 μsec; duration 900 msec) while the FDI was insulated,

f) as in d, during a voluntary contraction against a light load thus producing rapid movements.

During these measurements all other transducers were turned on, as in the actual experiments. In order to capture the characteristics of the noise, records were obtained at a sampling frequency of 2 kHz, as it was noticed from torque traces such as those shown in figure 3.2, that the range of frequencies in the noise oscillations could be approximately 100 - 200 Hz. An example of such a recording is shown in the top panel of figure 3.38.

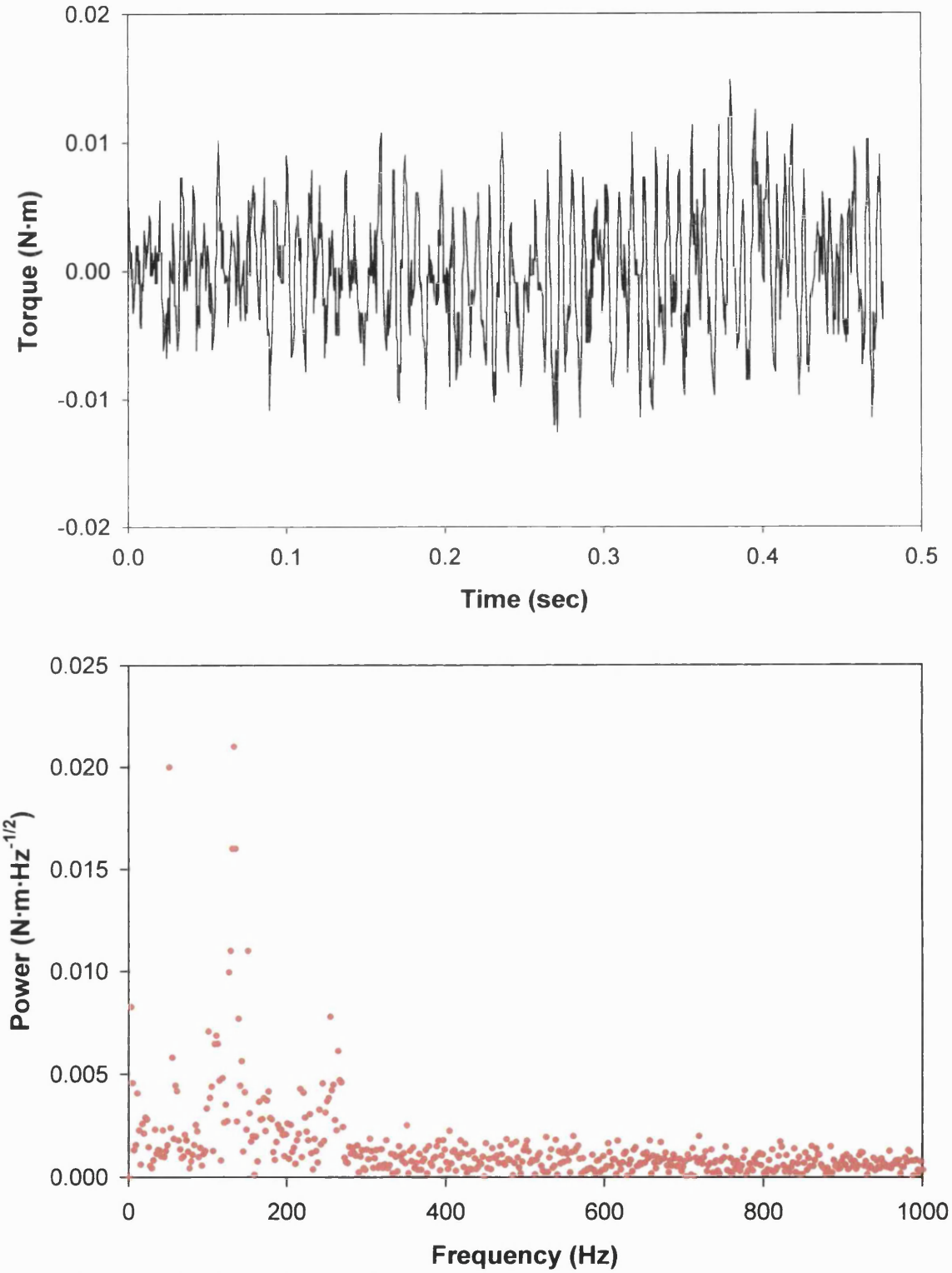

Figure 3.38. Noise characteristics.Top panel: Record of the strain gauge signal with the bridge supply removed and translated vertically to have a zero baseline. The r.m.s. of this record was $2.67 \cdot 10^{-3}$ N·m. Bottom panel: Power spectrum of the frequency components of the above trace. This trace contains one thousand points.

The noise in such records was assessed as the root-mean-square (r.m.s.) value of the oscillations. In order to be consistent with the torque dimensions of the force transducer signals presented in the thesis, the dimensions of the calculated r.m.s. values were also converted from volts into Newton-meters, via multiplication by the force calibration factor (30.46 $N \cdot V^{-1}$; pp. 222) and a lever arm of 0.06 m which was commonly used in the experiments. The r.m.s. values obtained for the first five conditions ((a)-(e); pp. 320) were: $2.86 \cdot 10^{-3}$ (a), $4.67 \cdot 10^{-3}$ (b), $2.74 \cdot 10^{-3}$ (c), $2.64 \cdot 10^{-3}$ (d) and $2.87 \cdot 10^{-3}$ N·m (e). These results are similar for conditions (a) and (c)-(e). There is more noise coming from the strain gauge bridge circuit alone (condition (b)), but the excess noise disappears when the strain gauge circuit is connected to the power source, probably due to grounding effects. The r.m.s. value of the noise in all these conditions is relatively low. However, as a result of a voluntary push against a light inertial load (condition (f)), after the force-transducer rod had lost touch with the index finger, the r.m.s. value could be as high as $55 \cdot 10^{-3}$ N·m. This noise is most likely to be due to mechanical vibration of the rotating components. Although not as much noise is observed while abducting the index finger against the force transducer, some vibration of the apparatus' rotating components, could also be present during the index finger abductions. In typical experiments (see pp. 220) the amplitude noise on the torque records is about $5 \cdot 10^{-3}$ N·m (rms~$3.5 \cdot 10^{-3}$ N.m), not much greater than the electrical noise. Thus the origin of the noise in the experiments is mainly electrical.

The frequency components of the records were obtained using Fast Fourier Transform analysis (for example see bottom panel in figure 3.38).

4.5.1.2. Sensitivity analysis

Computer simulation results for the torque, angular load displacement and velocity were obtained for a range of normalised inertial loads (fig. 3.55, pp. 363) similar to those calculated from the experimental results (nine loads ranging from 0.01-100 ξ units). The dimensionless properties of the SEC and CC (model equations (2.35) and (2.36), respectively; pp. 112-115) were specified by setting the values of the parameters $\boldsymbol{H}$ ($\boldsymbol{H}$=2.094) and $\boldsymbol{G}$ ($\boldsymbol{G}$=5.576). These values were calculated as the average corresponding values obtained from fitting experimental results ($\boldsymbol{H}$ from table 3.8, pp. 305; $\boldsymbol{G}$ from table 3.10 on pp. 312, excluding JS and SH). Data points were generated at a frequency of 500 Hz for 2 sec, which were the sampling frequency and duration of experimental records. The results obtained were expressed in a dimensioned form by multiplying the torque, angular load velocity and displacement by the corresponding normalising factors (1.2 N·m; 6.7 rad·sec^{-1}; 0.4 rad, respectively). These normalising factors were obtained from averaging experimental results or estimates arising from these results. These torque and angular velocity traces are shown in figure 3.39.

Computer simulation noise traces having the noise features described in the previous section were obtained via a MathCad 2001 in-build random number generator. The simulated noise traces' duration and sampling frequency were 2 sec at 500 Hz, which were the sampling time and frequency in almost all experiments. The mean, standard deviation (or r.m.s.) and the cut-off frequency of the noise were 0 N·m, $4.43 \cdot 10^{-3}$ N·m and 250 Hz, respectively (see features of the noise in previous section).

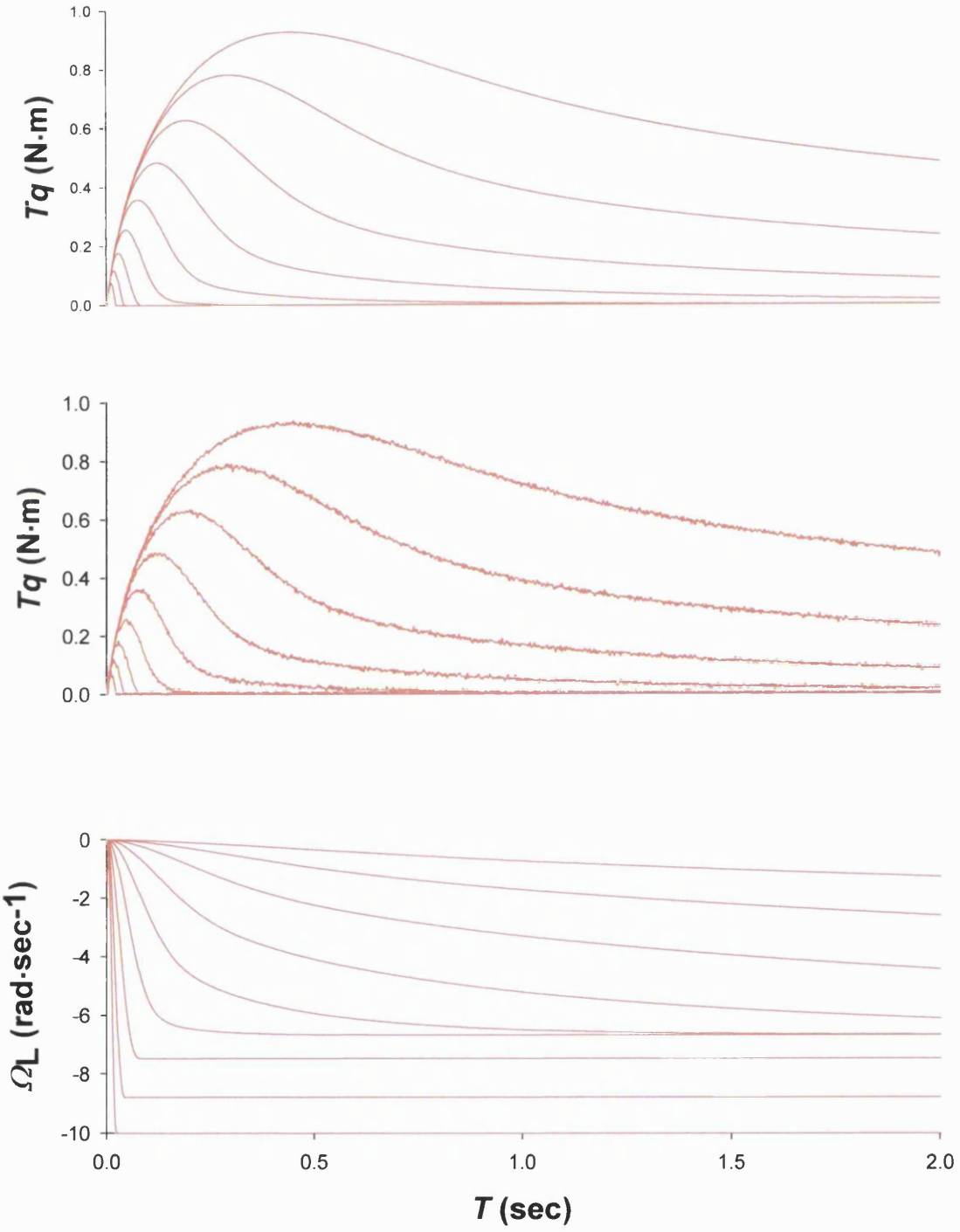

Figure 3.39. The top graph and middle graphs show model simulations of the time course of torque output, without and with noise. The bottom graph shows the corresponding angular velocity time courses. Records were truncated to include the first two seconds of a contraction. Each trace contains 1000 points.

Thirty different simulated noise traces were superimposed to the model-generated torque traces (figure 3.39; compare with figure 3.16, pp. 260). Torque-pairing analysis (section 4.2.1.3.1; pp. 270-275) was carried out in the presence and absence of noise.

The restrictions imposed in this analysis were:

a) Most torque records were analysed in the range of 10-90% of their peak value to obtain the SEC stiffness-torque relationship. Some records in which the hypothetical load was large, the torque at the end of the two-second contraction was a greater proportion than 10% of the peak value and the analysis begun at that level of torque.

b) The CC angular velocity - torque relationship was obtained for the full range of torque values in the records and then truncated to include data points within the range of torque values for which the SEC stiffness-torque relationship is valid.

No angular displacement restriction was included in this analysis, as the model does not include the effects of shortening deactivation or anatomical restrictions.

The SEC stiffness-torque relationship arising from assigning values to the parameters ($H, Tq_{\max}, \Theta_{SEC_{\max}}$) of the model (equation 2.14) and the result of the torque-paired analysis using torque records without noise is shown in the top graph of figure 3.40.

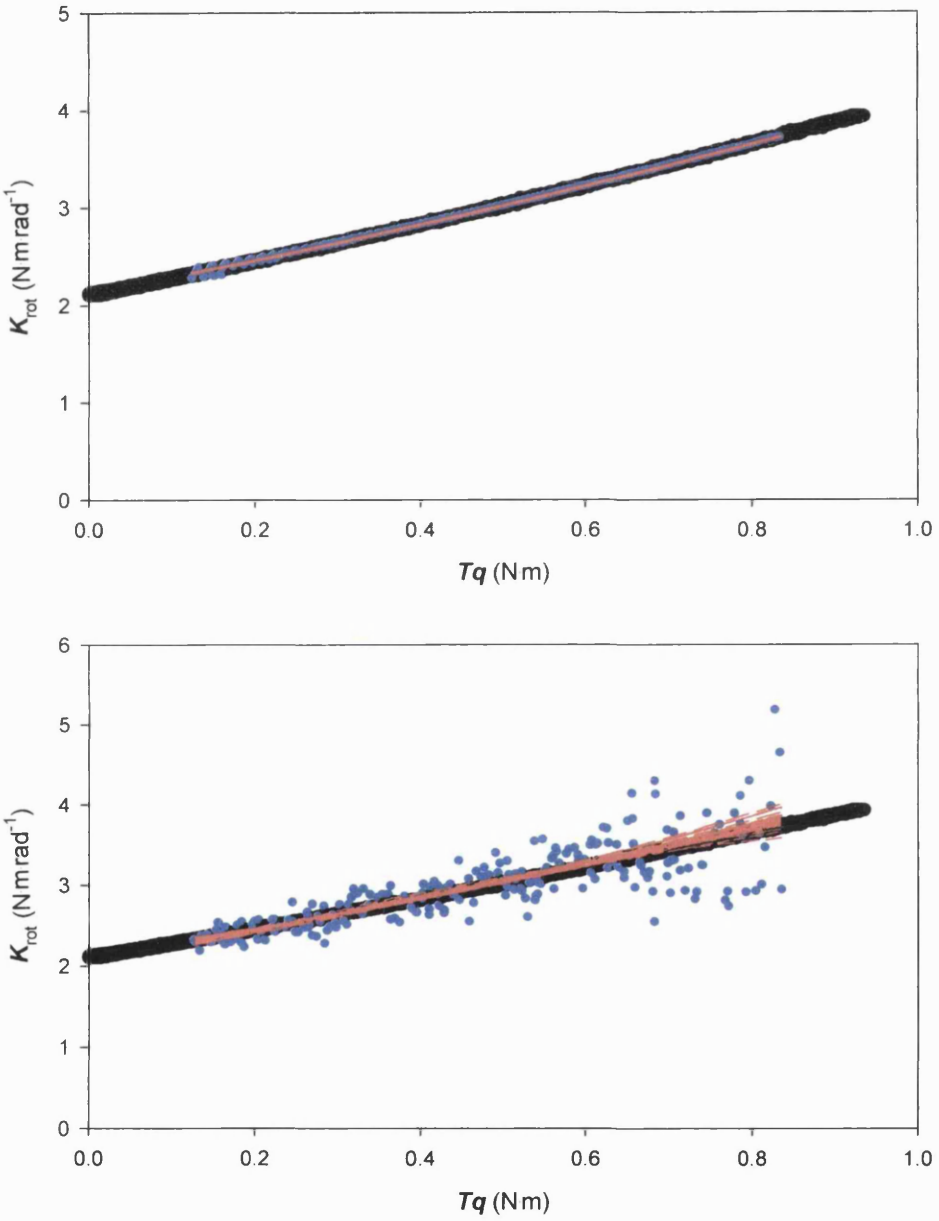

Figure 3.40. Model SEC stiffness-torque relationship (black points) and fitted sigmoidal curves to the stiffness-torque points generated from the torque pairing analysis (red curves). Top panel: Torque traces did not contain noise. Stiffness-torque points generated via torque-pairing analysis are shown (2773 points; blue). Bottom panel: Noise was added to the torque-traces. All thirty fitted

curves and an example of a record of calculated stiffness-torque points (451 points; blue) are shown.

It becomes apparent that the torque-pairing method only introduces a very small amount of scatter in the calculated stiffness-torque points (figure 3.40, top panel, blue points) compared to the modelled relationship (figure 3.40, black points). The coefficient of variation for the calculated stiffness-torque points was $3.71 \cdot 10^{-3}$. Reasons for this variation could be due to:

a) The torque rate calculation due to smoothing and

b) Linear interpolation between consecutive torque points in the descending part of the record to find matched values for the torque observations on the ascending part.

The accuracy of the torque rate calculation and of the linear interpolation would be greater in records against large loads as there would be more points on each record for a given sampling frequency and duration compared to when the loads are small and the time-course of torque output is relatively short. This is consistent with the larger deviations observed when torque is low.

The fitted sigmoidal curve to those points is in excellent agreement with the modelled SEC stiffness-torque curve (figure 3.40, top panel). The coefficient of variation is about 45 times smaller compared to the average variation in the SEC stiffness-torque relationships arising from experimental records (see table 3.6, pp. 292).

In the presence of noise the variability in the calculated stiffness-torque points increases compared to when noise is absent. The median of the coefficient of

variation for the thirty relationships was $91.9 \cdot 10^{-3}$ with range of $43.1 \cdot 10^{-3}$ units. This variability is about 1.5-2.5 times smaller than the average variability observed in the experimentally derived relationships (see table 3.6, pp. 292). The thirty fitted stiffness-torque curves arising from adding noise to the torque records are shown on the bottom panel of figure 3.40. These curves are in good agreement with the modelled SEC stiffness-torque relationship for most of the range of validity of the relationship. Larger deviations from the modelled relationship are observed at the 'high-torque end' of the calculated curves. This could be due to the fact that these stiffness points arise from torque points nearer the peak of records corresponding to large simulated inertial loads. Under these conditions the corresponding torque rates are relatively low and noise can have a relatively greater effect in the difference between matched torque-rate points (see equation 3.10; pp. 272). Most of these deviations appear to overestimate the stiffness at high values of torque.

In the absence of noise, the variability in the CC angular velocity-torque relationship (figure 3.41) was small (coefficient of variation = $2.554 \cdot 10^{-3}$). Adding noise increased the variability further (median value of coefficient of variation = $26.2 \cdot 10^{-3}$; range $105 \cdot 10^{-3}$). Thus, the CC angular velocity-torque result shows less variability than the SEC stiffness-torque result. The calculated CC angular velocity-torque relationships both in the absence and in presence of noise in the torque records were in good agreement with the modelled relationship. Calculated values of the parameters of the CC angular velocity-torque relationship (G, Tqmax, ΩCCmax) are in good agreement with the pre-set model values whether there is noise or not (Table 3.12). Thus, the torque

pairing method of analysis does not seem to introduce significant errors in the calculation. In addition, the presence of noise with features typical to those observed in the experimental records can only partly explain the variability of the properties calculated from experimental results.

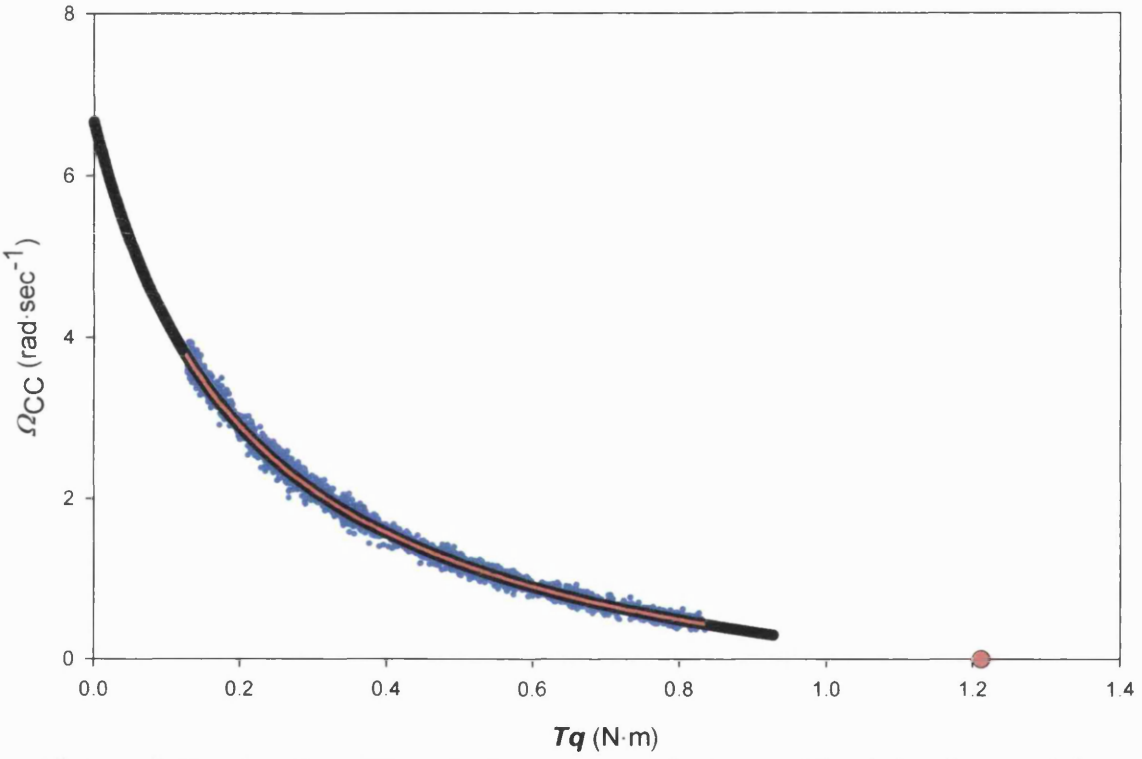

Figure 3.41. Angular CC velocity-torque trajectory utilised in the model simulations with (blue; one example) and without added noise (black points). The curves fitted to thirty such trajectories in the presence of different noise time courses are also shown (red curves). The model maximal isometric torque is also shown (red filled circle).

	ΩCCmax (rad·sec^{-1})	Tqmax (N·m)	G
Model	6.668	1.212	5.576
Calculated (no added noise)	6.680	1.216	5.613
Calculated (noise added; r.m.s.= 4.43·10^{-3} N·m)			
Median	6.668	1.212	5.576
Range	0.050	0.011	0.108
Calculated (increased noise added; r.m.s.= 0.011N·m)			
Median	6.668	1.212	5.576
Range	0.084	0.020	0.191

Table 3.12. Noise effects on estimated values of the CC angular velocity-torque relationship. Values are given in 3 d.p.

In order to assess the sensitivity of the result to even greater noise levels, another ten simulations were run with the noise r.m.s. value increased by 2.5-fold with respect those described earlier (i.e. r.m.s.=$11 \cdot 10^{-3}$ N·m compared to $4.43 \cdot 10^{-3}$ N·m). An example of simulated torque time courses during contractions against the same nine different inertial loads that were used in the previous simulations is shown in figure 3.42.

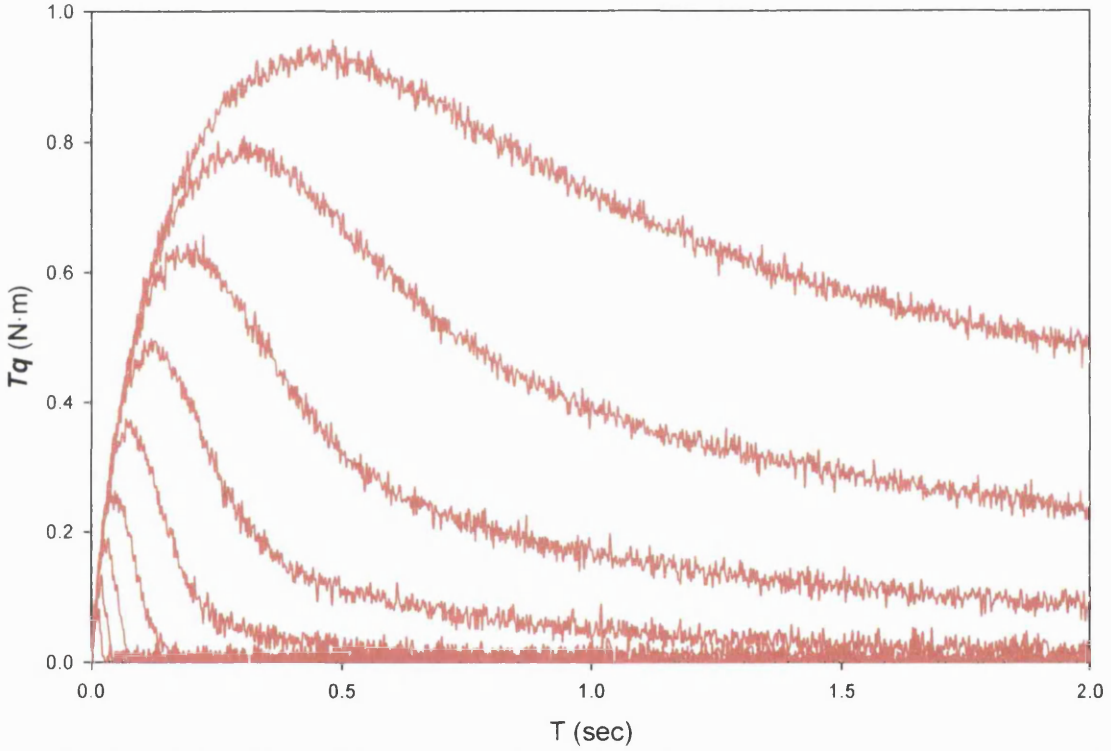

Figure 3.42. Simulated time course of torque output against nine loads of different inertia with noise levels with a mean amplitude of $11 \cdot 10^{-3}$ N·m.

The increased noise level further increased the variability in the SEC stiffness-torque relationship with respect to the lower noise levels (coefficient of variation median = $240 \cdot 10^{-3}$; range=$51.2 \cdot 10^{-3}$) (figure 3.43). This variability is 30-60% greater to the average variability observed in the stiffness-torque relationship that was calculated from experimental results (table 3.6). The variability in the CC angular velocity-torque result also increased (coefficient of variation median

=0.065; range=0.289), but not as much as the variability of the stiffness-torque result (figure 3.44). The parameters of the CC angular velocity-relationship were calculated reasonably accurately (Table 3.12).

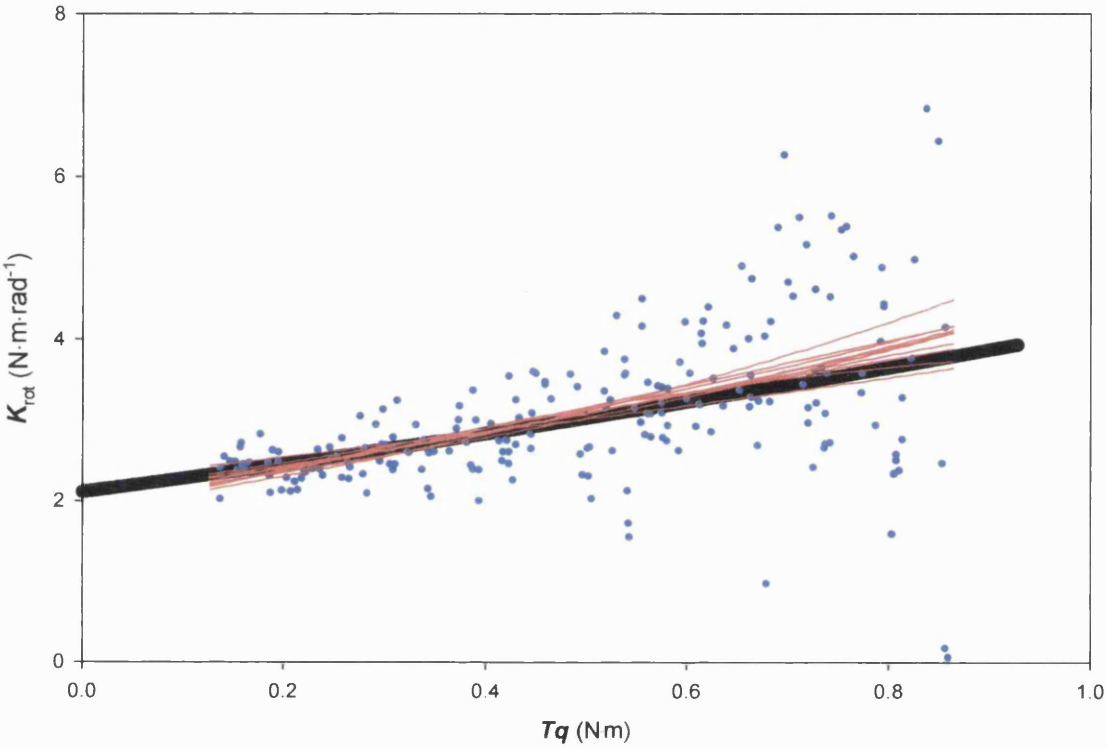

Figure 3.43. Simulated stiffness-torque trajectory in the absence of noise (black), stiffness-torque result for one simulation in the presence of noise (r.m.s.=11·10^{-3} N·m; blue points) and ten fitted sigmoidal curves to such results (red).

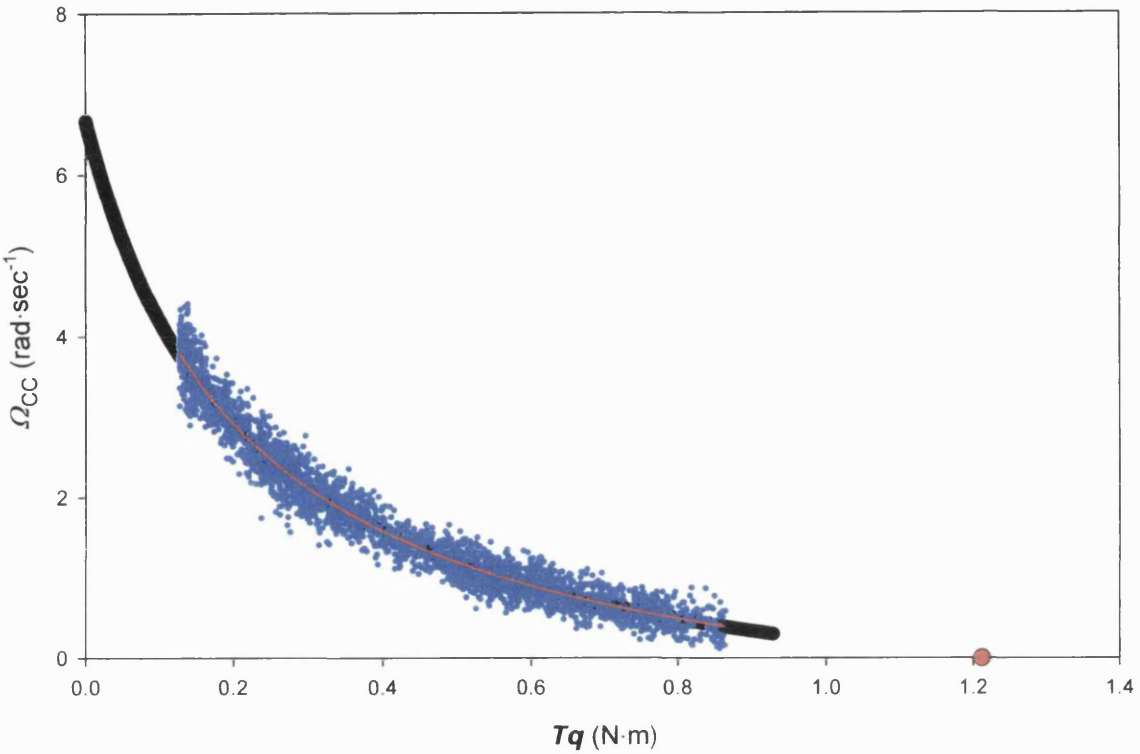

Figure 3.44. Simulated CC trajectory in the absence of noise (black), calculated CC angular velocity-torque result in the presence of noise (one simulation; noise r.m.s.=0.011 N·m) (blue points) and ten curves fitted to such results (red). The maximal isometric torque is also shown (red circle).

These results suggest that variation in the SEC stiffness-torque results observed in these simulations arises mainly from the noise in the records (and to a much smaller extent from the method of calculation). The sigmoidal curves fitted to such results do reflect the SEC stiffness-torque and the CC angular velocity-torque relationships in the absence of noise. In the presence of noise, the variability increases and the fitted curves deviate to some extent from the actual SEC stiffness-torque relationship. Despite the variability introduced by the noise (and the torque-pairing method), the CC angular velocity-torque relationship is less affected by the noise than the SEC stiffness-torque relationship, and its

parameters can be calculated with good accuracy. These conclusions were valid up to noise levels well beyond those observed in the torque records obtained experimentally.

Only part of the variability observed in the SEC and CC relationships calculated from experimental results can be accounted for by the levels of noise present in the torque records. Therefore, additional sources must be responsible for the observed variation, especially for the CC angular velocity-torque relationship, whose calculation is less sensitive to noise than that of the SEC stiffness-torque relationship.

4.5.2. Discussion on other possible sources of within-subject experimental variation

Observing CC angular velocity-torque trajectories each calculated from individual contractions, such as those shown in figure 3.45, reveals that for the same contraction (a) the CC angular velocity may not be exactly the same for the same value of torque as originally assumed and (b) that the shapes of these trajectories may not be monotonic. In addition, these trajectories do not show perfect overlap between different contractions (c). Finally, the variation between individual trajectories is smaller in contractions against large loads compared to contractions against low loads (d).

The larger discrepancies observed within individual contractions may have been due to uncertainty in the shape of the SEC stiffness-torque relationship at

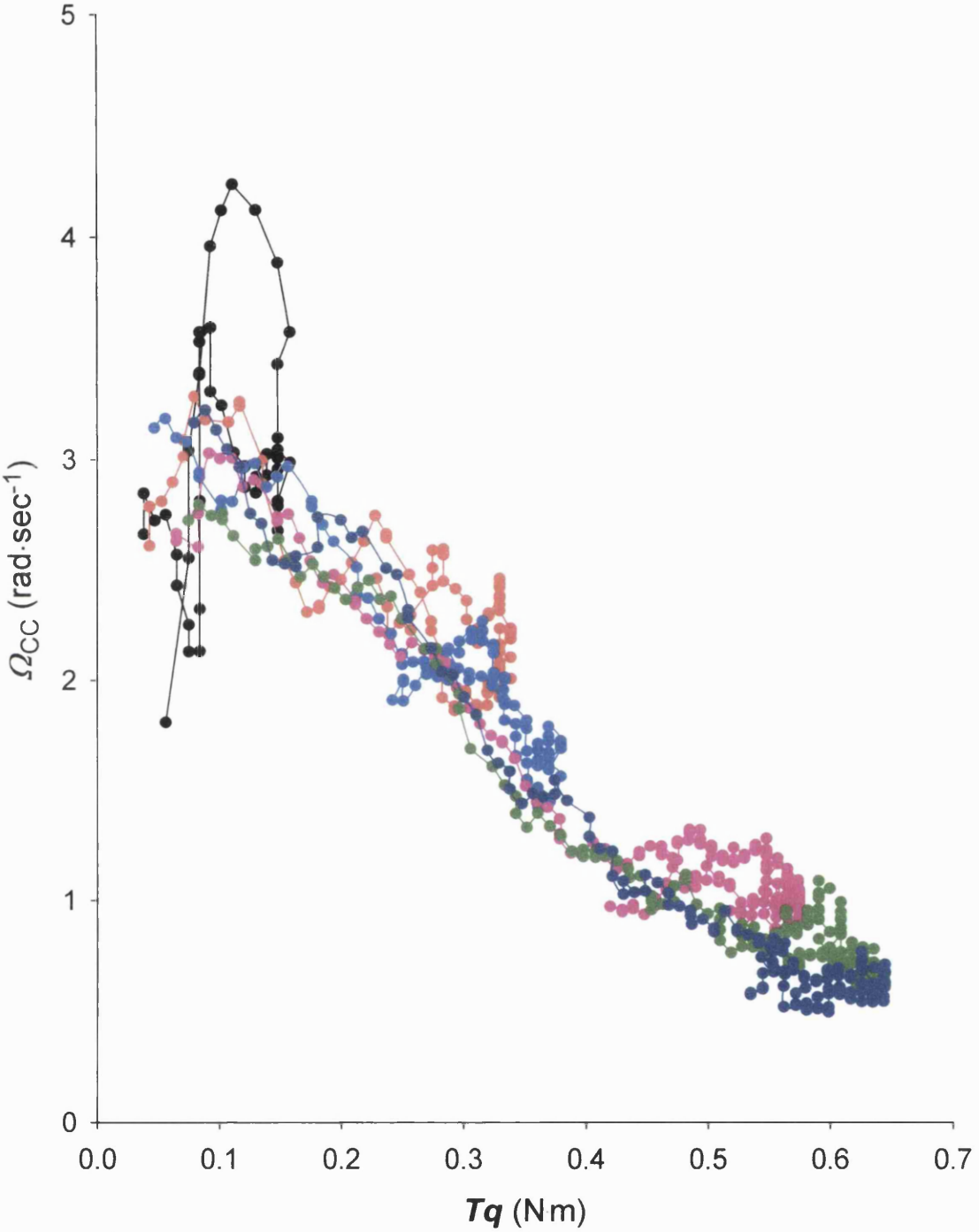

Figure 3.45. CC angular velocity-torque trajectories (volunteer AC). Every fifth contraction is shown for visual clarity. Five trajectories are superimposed.

relatively low torque values as there are relatively few such values in this region and therefore the fitting procedure in this region may be influenced from the more 'dense' areas of the plot at higher torques. Physiological factors such as variable activation may also be responsible. The influence of the torque-angle relationship for the FDI may be only small, as appropriate adjustment did not reduce the variability of the stiffness-torque result (see table 3.7). Shortening deactivation is expected to be relatively small for low loads and measures were taken to minimise its influence in all contractions (see 'Torque pair selection'). Another possibility may be changing of the FDI lever arm with the abduction angle. If that were true, the SEC stiffness-torque relationship and the CC force-velocity relationship would be out of phase with the SEC rotational stiffness-torque relationship and the CC torque-angular velocity relationship, respectively. An *et al* (1983) calculated the moment arms of tendons acting on the index finger at different joint angles. These calculations were based on measurements of tendon excursions. The calculated FDI moment arm was found to decrease with the abduction angle, in a more or less linear manner as shown in figure 4 in their paper. Based on this result, the torque output at any given angle for three out of the six volunteers (JS, AC, AG) was divided by the corresponding lever arm to express torque as force at the tendon. The angular load velocity at any given angle was also multiplied by that lever arm to obtain the (linear) shortening velocity of the MTC. Linear SEC stiffness-force and CC velocity-force relationships were obtained. However, the variability of the linear relationships did not show improvement (see figure 3.46 as an example). Tendon hysteresis is another property that was not taken into account. However, it would be expected that energy loss in the tendon as heat would be higher in

contractions against larger loads where the tendon is more stretched and it remains stretched for longer periods of time, whereas the most variable results were obtained from contractions against light inertial loads. Another potential reason for the discrepancies might have been movement of the hand and/or the thumb. If contraction of the FDI was moving the index finger and the thumb at the same time but only the movement of the FDI was recorded the results the

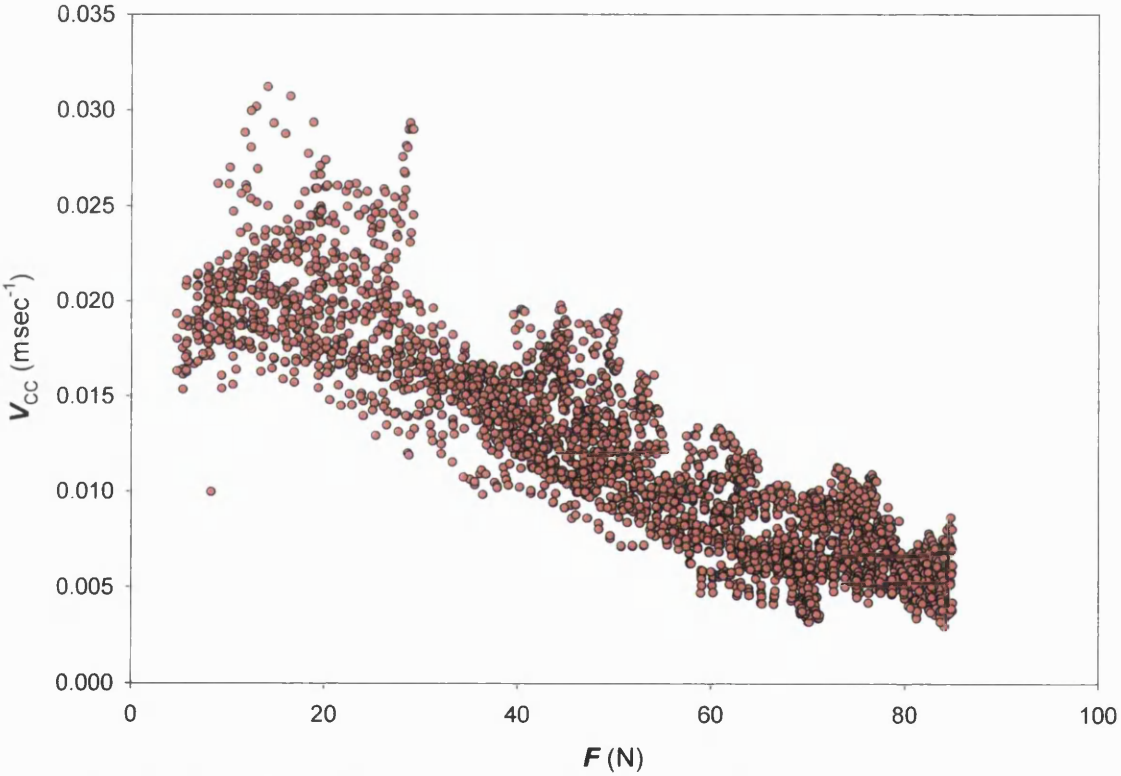

Figure 3.46. CC shortening velocity-force relationship for volunteer AC. Hypothetical lever arm was 8mm at 0^0 abduction and decreased linearly with abduction angle at a rate of 0.08mm/deg.

calculation of the series compliance and shortening velocity would have been affected. Measures had been taken to minimise such movements. However, it is not impossible that such movements might have occurred. Antagonist muscle

co-activation, through spread of the stimulus or voluntary contractions of the subjects in response to the uncomfortable feeling produced by the electrical stimulation, may have also been possible. It is not known whether and to what extend antagonist muscle co-activation was present. Despite the possible methodological factors that might have been responsible, at least in part, for the observed variation as discussed above, the remaining of the observed variability, may reflect the physiological variation in the muscle and tendon properties. For example, the muscle may not follow exactly the same force-velocity trajectory in all contractions. Perhaps the time history of the mechanical output is more important than generally assumed. As already shown, the correlation coefficient for the CC angular velocity-torque relationships is high (see table 3.9,pp. 310), indicating a strong dependence of CC angular velocity on torque, as expected from the force-velocity properties of a muscle. The effects of noise on the torque records on this variability have been examined. However, future work is needed to clarify how much of the observed variation is due to muscle behaviour and how much come from the other sources mentioned above.

4.5.3. Within-subject variation in elastic and contractile properties on different days

The intra-subject variability in the calculated SEC torque-angular extension and CC angular velocity-torque relationships was investigated by comparing results arising from two different experimental sessions in five out of the six volunteers. The torque and angular displacement restrictions where kept as closely matched between each subject's two sets of data as possible. These restrictions are shown in table 3.13.

Subject	Torque range (fraction of peak torque)		Angular load displacement (rad)	
	Set A	Set B	Set A	Set B
JS	0.1-0.9	0.1-0.9	0.35	0.30
AC	0.1-0.9	0.1-0.9	0.25	0.30
AG	0.1-0.9	0.1-0.9	0.30	0.30
GO	0.1-0.9	0.1-0.9	0.30	0.30
SH	0.8-0.9	0.8-0.9	0.20	0.20

Table 3.13. Restrictions in calculating SEC properties. The torque range column shows the range of torque values that were used from each record relative to the peak torque achieved on that record. The angular load displacement column shows the maximal load displacement for which the records were analysed.

The SEC torque-angular extension relationship was calculated as described previously (section 4.3.2., pp. 300). The results are displayed in figure 3.47.

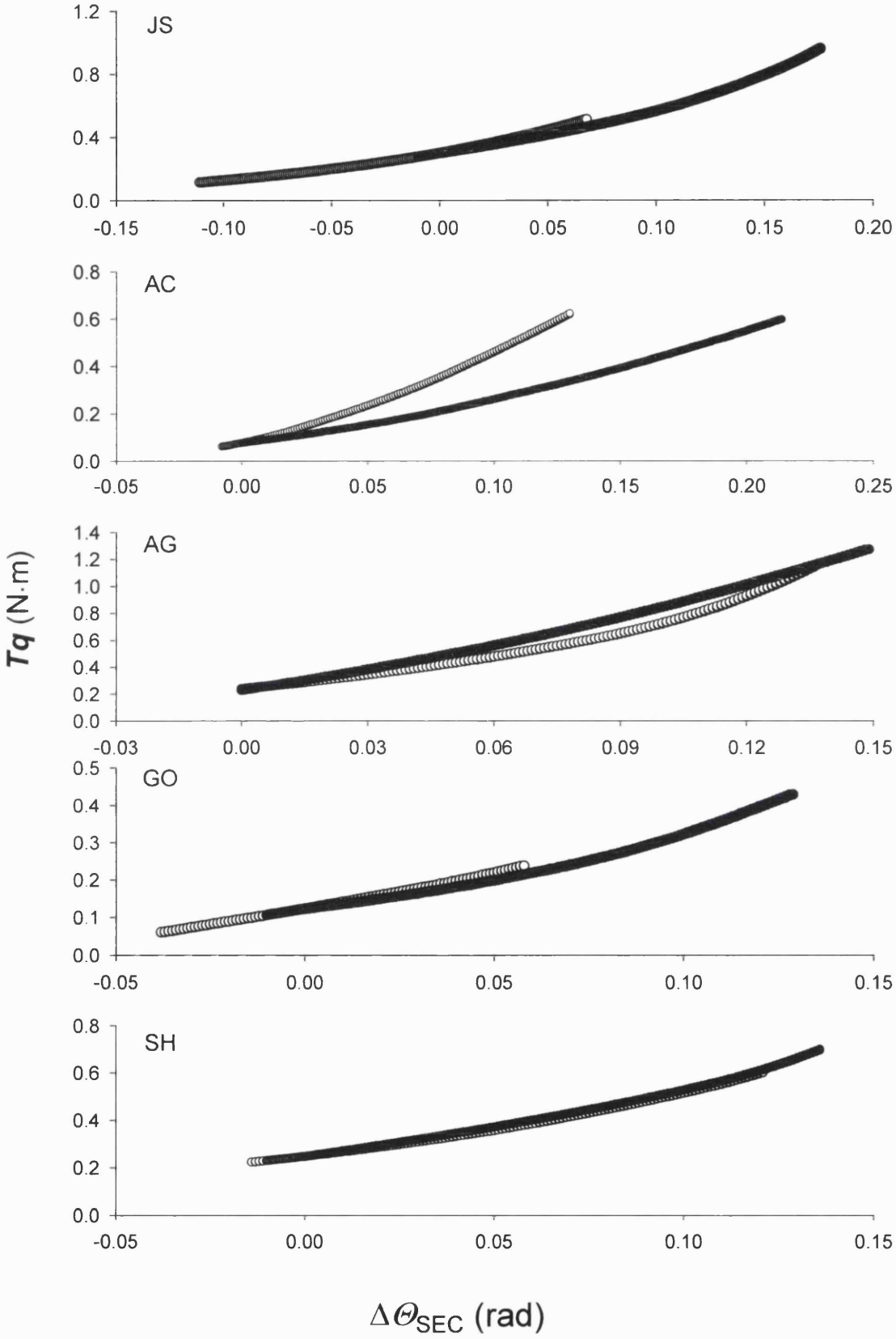

Figure 3.47. SEC angular extension-torque curves from two different experimental sessions for five volunteers. One of the two curves in each set has been translated along the $\Delta\Theta_{SEC}$-axis to intersect the other curve at its minimal torque value, thus providing a continuum of torque values between the two results.

In four out of five volunteers the two SEC torque-extension relationships are similar. The torque-range over which SEC extension has been calculated shows considerable, if not complete, overlap in three cases (AC, AG, GO). In two out of these three volunteers there is a good agreement in terms of SEC extension, too. Less complete overlap in the range of torque values has been achieved in two cases (JS, SH). This was due to differences in the electrical stimulation of the FDI muscle such that lower torque was produced in one session compared to the other. Nevertheless, the SEC torque-extension curves in the later two volunteers show a good agreement within the area of torque overlap, as well as a relatively smooth continuum of SEC extension values in non-overlapping torque regions.

In volunteer AC the two relationships are different. Despite the similar torque range, there is less SEC extension for the same values of torque (open circles) on one day, compared to the other day (closed circles). It is not possible to know the exact reason for this difference but it could be speculated that either the same part SEC was utilised but its rotational stiffness was altered, or different parts of the SEC were utilised between the two experiments. If the former was the case, the rotational stiffness of the SEC could have been altered between the two sessions by a change in its linear stiffness and/or a change in the lever arm through which it acts on the joint. A 40% reduction in the lever arm required to bring about the observed differences, via for example differences in muscle swelling, is difficult to reconcile. However, it is not impossible that such differences might have played a small part. A two-fold change in the linear stiffness of the same SEC, as that observed between the two sessions, would not be very likely in terms of tendon adaptation due to mechanical loading within the two-day period between the two sessions in this particular volunteer. However, if

tendon temperature was greater in the second session (closed circles on figure 3.47) compared the first session (open circles), the linear stiffness of the SEC could have been lower in the first session compared to the second. It has been shown that while the rat-tail tendon strain is constant and after stress-relaxation has reached its limiting value, increasing the temperature from approximately 18^0C to approximately 30^0C reduces the tension in the tendon to approximately 50% of its value at 18^0C (Rigby et al, 1959). This effect was reversible. Moreover, Ettema and Huijing (1994) found the component of the rat gastrocnemius medialis muscle-tendon complex compliance that was independent of the muscle force and hence expected to originate to large extend from tendon, to increase by 15% when temperature was increased from 27 ^{0}C to 37 ^{0}C. However, Magnusson et al (2000) showed that passive energy absorption did not change in the human hamstring MTC as a result of elevated muscle temperature following exercise. It has recently been shown that during passive length changes in other human MTCs (tibialis anterior and gastrocnemius) tendon elasticity can account for a considerable component of the total MTC elasticity (Herbert et al, 2002). Thus, assuming that elevated muscle temperature in the study by Magnusson et al (2000) also translates to elevation in the tendon temperature, it is possible that temperature differences might have not been very important in explaining the marked differences in the SEC stiffness observed between the two sessions. As the tendon temperature was not monitored either directly or indirectly in our experiments, the above discussion is only speculative. If different parts of the FDI MTC had been utilised between the two experiments, there could be more possibilities in explaining the observed differences as these two parts could have had different linear stiffness (even if temperature was the same), act through different lever arms on the joint and in addition the above effects could be further altered through differences in temperature.

Nevertheless, it is not easy to understand why such a difference is present in only one volunteer.

The above discussion points to certain measures that could be applied in future experiments facilitate interpretation of the results. Firstly, electrical stimulation of the FDI muscle could be better standardised by taking particular care to attach the stimulating electrodes as precisely as possible on the same area of the skin above the FDI. This would improve the possibility that the same part of the FDI SEC is utilised in different experiments. Secondly, FDI MTC temperature could be controlled by immersion of the hand in a water tank of the desired temperature for some time before the start of the experiment. During the experiments an infusion bag circulated with water at a given temperature could be placed over the volunteer's lower arm (e.g. De Ruiter and De Haan, 2001) or the skin of the FDI muscle (e.g. Ranatunga *et al*, 1987) and the FDI temperature could be assessed by using the linear relationship between skin and intramuscular temperature described by Ranatunga *et al* (1987) for the FDI muscle.

The CC angular velocity-torque results are shown in figure 3.48. When the normalised torque is relatively high (i.e. above approximately 0.5 units), the calculated torque-velocity relationships show considerable overlap. However, when the normalised torque is relatively low (i.e. below 0.5 units) then calculated relationships show considerable deviation. In all volunteers but GO, the two sessions were only separated by a few days interval (2-7 days) and thus considerable fibre type composition changes were not expected to occur. In volunteer GO, the there was a

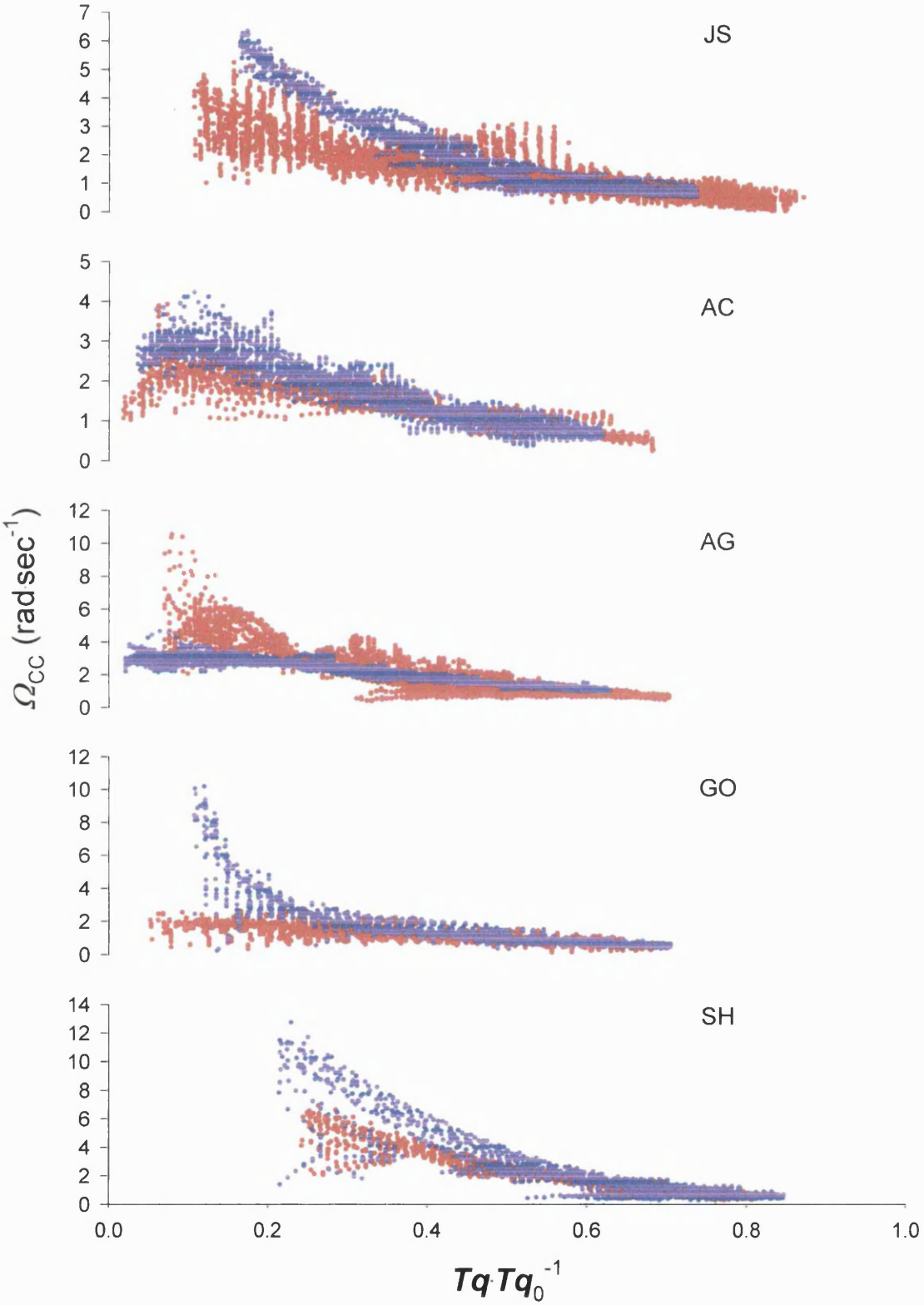

Figure 3.48. CC torque-angular velocity relationships arising from two different experimental sessions. The torque scale is normalised for the maximal electrically-evoked torque achieved before the start of the dynamic contractions.

longer interval between the two sessions (approximately 8 months), so fibre type composition changes could have been more likely. Interestingly, GO shows the most pronounced deviation of shortening velocity at the low torque region. Another possibility is that more fast fibres were recruited in one session compared to the other. In general, a greater maximal static torque could be generated in session B (blue, figure 3.48) than in A (red, figure 3.48) probably indicating a greater proportion of the total population of fibres had been recruited in session B. It is therefore likely that more fast fibres, which would be expected to have a higher activation threshold during electrical stimulation, were recruited in session B. This would be consistent with most of the plots in figure 3.48 showing higher velocities in session B. Another important factor could have been differences in the FDI temperature. As mentioned above, muscle temperature was not controlled in this study. It has been shown that parameters of the in vivo force-velocity relationship, such as Vmax and G, of the electrically activated human adductor pollicis muscle, which is another muscle of the hand, are sensitive to differences in temperature (De Ruiter and De Haan, 2000, 2001). For example, it was shown that the Q10 values for the Vmax within the calculated muscle temperature ranges (^{0}C) of 31.4-37.1, 25.6-31.4 and 22.2-25.6 were 1.2, 2.1 and 3.8, respectively. Thus, FDI muscle temperature differences between the two sessions would be expected to affect its shortening speed. Finally, two parts of a muscle with identical contractile properties acting on the joint through different lever arms would be expected to produce different angular velocity-torque relationships. Thus, the part of the muscle with the longer lever arm would produce more torque but slower angular speeds than the part with the shorter lever arm. However, in most volunteers except AG, both higher torque and speed was observed in one session than the other. Thus, it appears that control of muscle temperature and taking particular

care to standardise electrical muscle activation could prove useful in future experiments in explaining and/or minimising variation.

4.5.4. Reproducibility of results arising from the torque-paring method

Although muscle temperature, activation and possibly other factors could have been different, at least to some extent, between the two different sessions of each volunteer, the variation of these factors and hence their influence in the estimated SEC and CC properties, would be expected to be smaller within the same experimental session. Therefore, if the observed variation in these properties arises from not standardising for such factors between different sessions but not from the torque-pairing analysis method, the differences in the SEC and CC properties would be smaller if they were estimated from records obtained within the same session. Typically, two contractions against the same inertial load were performed in each experiment. This allows the hypothesis stated above regarding the reproducibility of the torque-pairing method to be tested by splitting the records from each session into two sets, so that each set contains only one torque and angular displacement record against the same inertial load.

Records against the same inertial load within a session were separated in a random manner using an in-build Mathcad 2001 random number generator. Each one of such two records was incorporated into one of two record-sets such that only one record against the same inertial load was included in each set. The two sets of records were then analysed to obtain two SEC angular extension-torque relationships and CC torque-angular velocity relationships, calculated independently from one another but

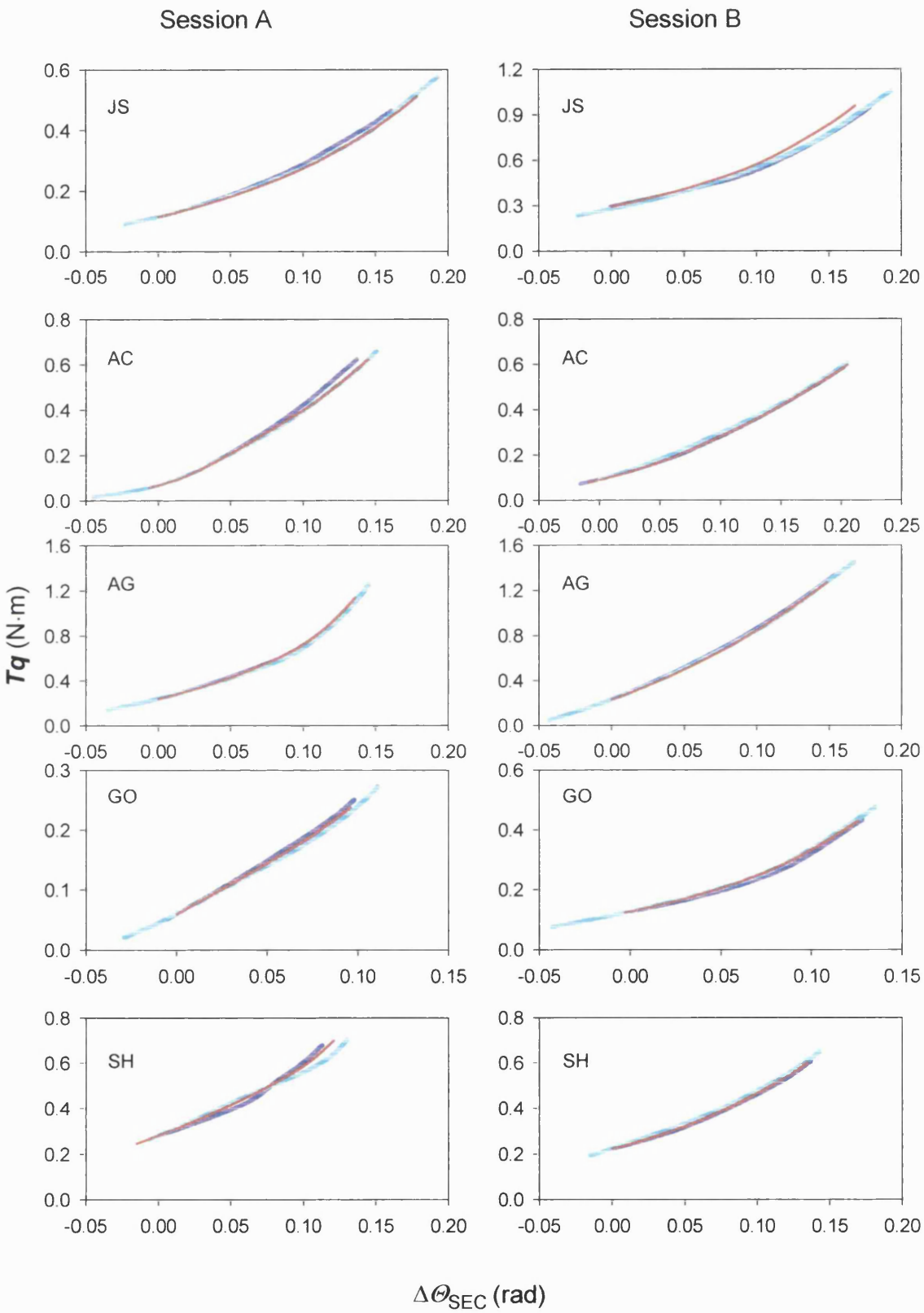

Figure 3.49. Within session reproducibility of SEC $\Delta\Theta$-Tq relationship. Each plot represents one experiment. Red curve is obtained using all torque and angular displacement traces, whereas the blue and cyan curves were obtained by using one of the two sets of records, each containing only one contraction against a given inertial load (for details see text).

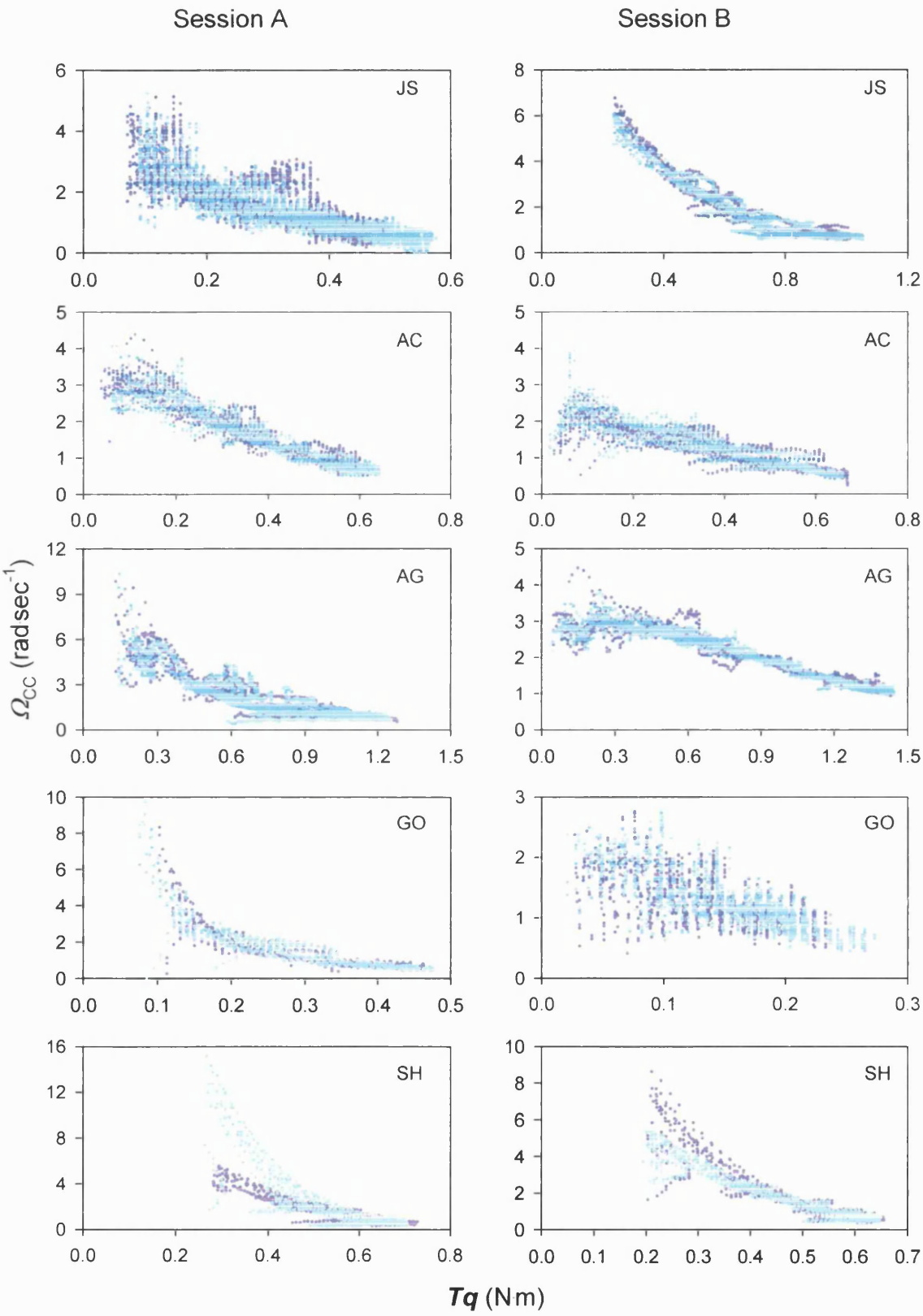

Figure 3.50. Within session reproducibility of CC Tq-ΩCC relationship. Each plot represents one experiment. The two relationships in each plot were obtained by using one of the two sets of records, each containing only one contraction against a given inertial load (for details see text).

using the same restrictions as used for the corresponding session (see table 3.13). The results are shown in figures 3.49 and 3.50.

There is a very good agreement between the two independently calculated relationships, as well as between these relationships and the original result obtained from using all the records in one session, for all volunteers except SH. The CC angular velocity at low torques appears different, especially for session A. Possible sources of such variation have already be discussed (see Sensitivity analysis section). However, in general the torque-pairing analysis method generates reproducible results provided the conditions under which torque and angular displacement records are obtained are similar.

In conclusion, the variability in SEC and CC properties observed between volunteers arises not only from absolute differences between these properties but also from differences in the experimental conditions. In order to compare these properties between volunteers measures are required for standardising experimental conditions such as muscle activation and temperature. This however does not reduce the value of the method as the estimated properties reflect the properties present in each particular experiment.

4.6. Instantaneous behaviour of the CC, SEC and L

4.6.1. Calculations

Once the stiffness-torque relationship is determined, the instantaneous behaviour of the CC and SEC can be calculated, within the torque and angular constraints for which this relationship is known.

The instantaneous value of SEC extension beyond its length at the start of the calculation (Θ_{SEC}) is calculated as the integral of the SEC compliance (reciprocal of stiffness) with respect to the torque using the trapezoidal rule:

$$\Theta_{SEC_0} = 0, \quad \Theta_{SEC_r} = \Theta_{SEC_{r-1}} + \frac{1}{2} \cdot \left(\frac{1}{K_{rot_{SEC\,r-1}}} + \frac{1}{K_{rot_{SEC\,r}}} \right) \cdot (Tq_r - Tq_{r-1})$$

where Tq is the instantaneous value of the torque and K_{rotSEC} is the value of the SEC stiffness corresponding to this value of torque and r is range variable such that r=1,2,..,N-1 where N is equal to the number of ***Tq*** values.

The instantaneous value of CC shortening (Θ_{CC}) from its resting length was calculated using the total stiffness-torque relationship:

$$\Theta_{CC} = \Theta_{rot} + \Theta_L$$

where Θ_{rot} and Θ_L are the instantaneous values of angular displacement of the load and of the total elasticity in series with the CC (SEC plus force transducer). Θ_{rot} was calculated in exactly the same way as Θ_{SEC} except using the value of the K_{rotTOT} instead of K_{rotSEC}.

The instantaneous value of SEC velocity (Ω_{SEC}) was calculated as:

$$\Omega_{SEC} = \frac{1}{K_{rot_{SEC}}} \cdot \frac{d}{dT}(Tq)$$

where $\frac{d}{dT}(Tq)$ is the rate of change of torque and K_{rotSEC} is the SEC stiffness corresponding to the torque value at that instant.

The calculation of the CC velocity was as described in section 4.2.1.3.1., pp. 270.

The instantaneous mechanical power in the SEC (P_{SEC}) was calculated as:

$$P_{SEC} = Tq \cdot \Omega_{SEC}$$

The instantaneous mechanical power generated by the CC (P_{CC}) was calculated as:

$$P_{CC} = Tq \cdot \Omega_{CC}$$

4.6.2. Instantaneous behaviour

4.6.2.1. Dynamic contractions

Examples of instantaneous mechanical behaviour during dynamic contractions against inertial loads are shown in figures 3.36-3.38 (A-C).

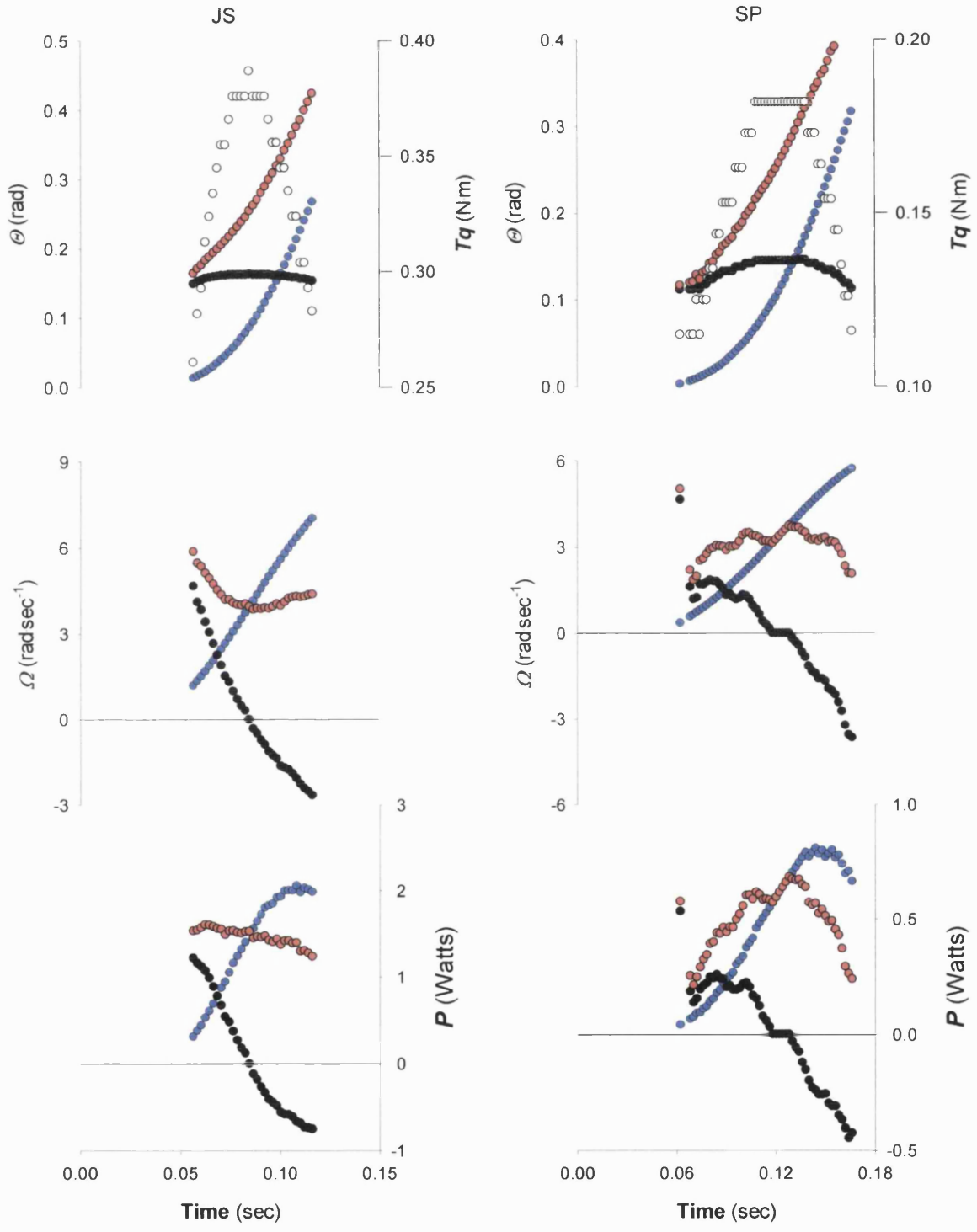

Figure 3.51.A. Instantaneous length change and torque (top graph), angular velocity (middle graph) and power (bottom graph) for the CC (red), SEC (black) and L (blue) for volunteers JS and SP during contractions against light inertial loads ($3.530 \cdot 10^{-3}$ kg·m^2 and $2.871 \cdot 10^{-3}$ kg·m^2 respectively). Torque is shown as open circles.

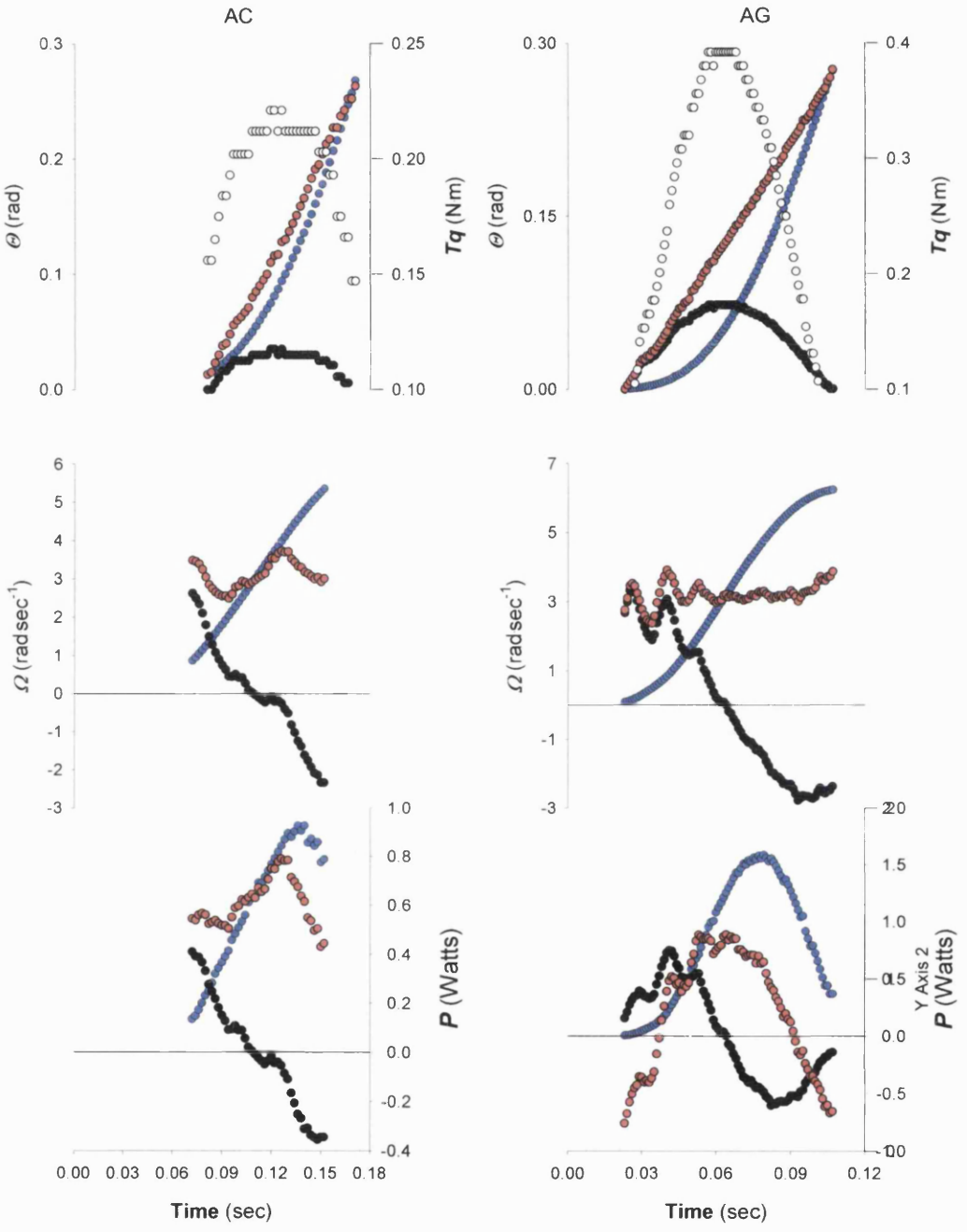

Figure 3.51.B. Instantaneous length change and torque (top graph), angular velocity (middle graph) and power (bottom graph) for the CC (red), SEC (black) and L (blue) for volunteers AC and AG during contractions against light inertial loads ($3.516 \cdot 10^{-3}$ kg·m^2 and $3.529 \cdot 10^{-3}$ kg·m^2 respectively). Torque is shown as open circles.

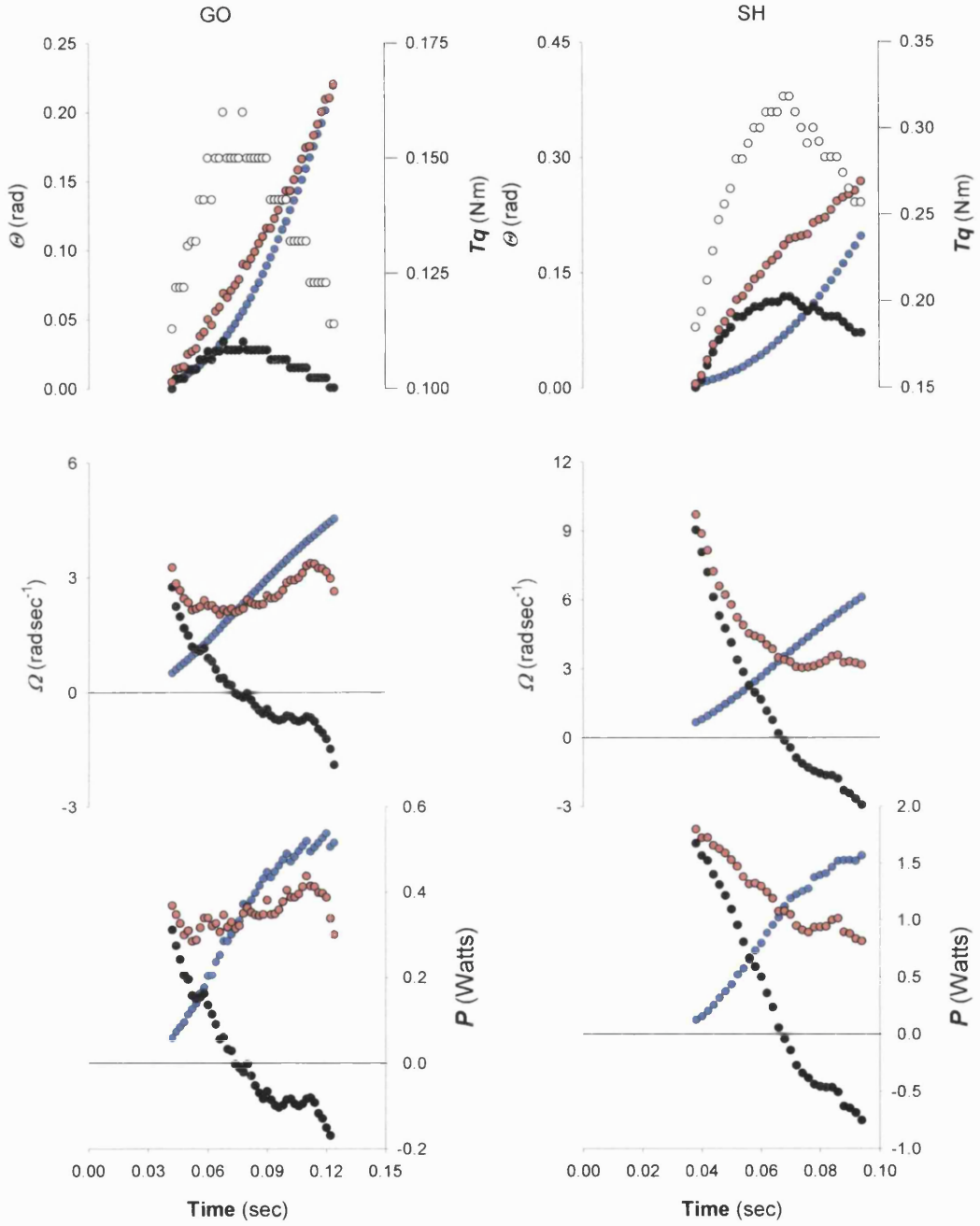

Figure 3.51. C. Instantaneous length change and torque (top graph), angular velocity (middle graph) and power (bottom graph) for the CC (red), SEC (black) and L (blue) for volunteers JS and SP during contractions against light inertial loads ($2.815 \cdot 10^{-3}$ kg·m^2 and $2.871 \cdot 10^{-3}$ kg·m^2 respectively). Torque is shown as open circles.

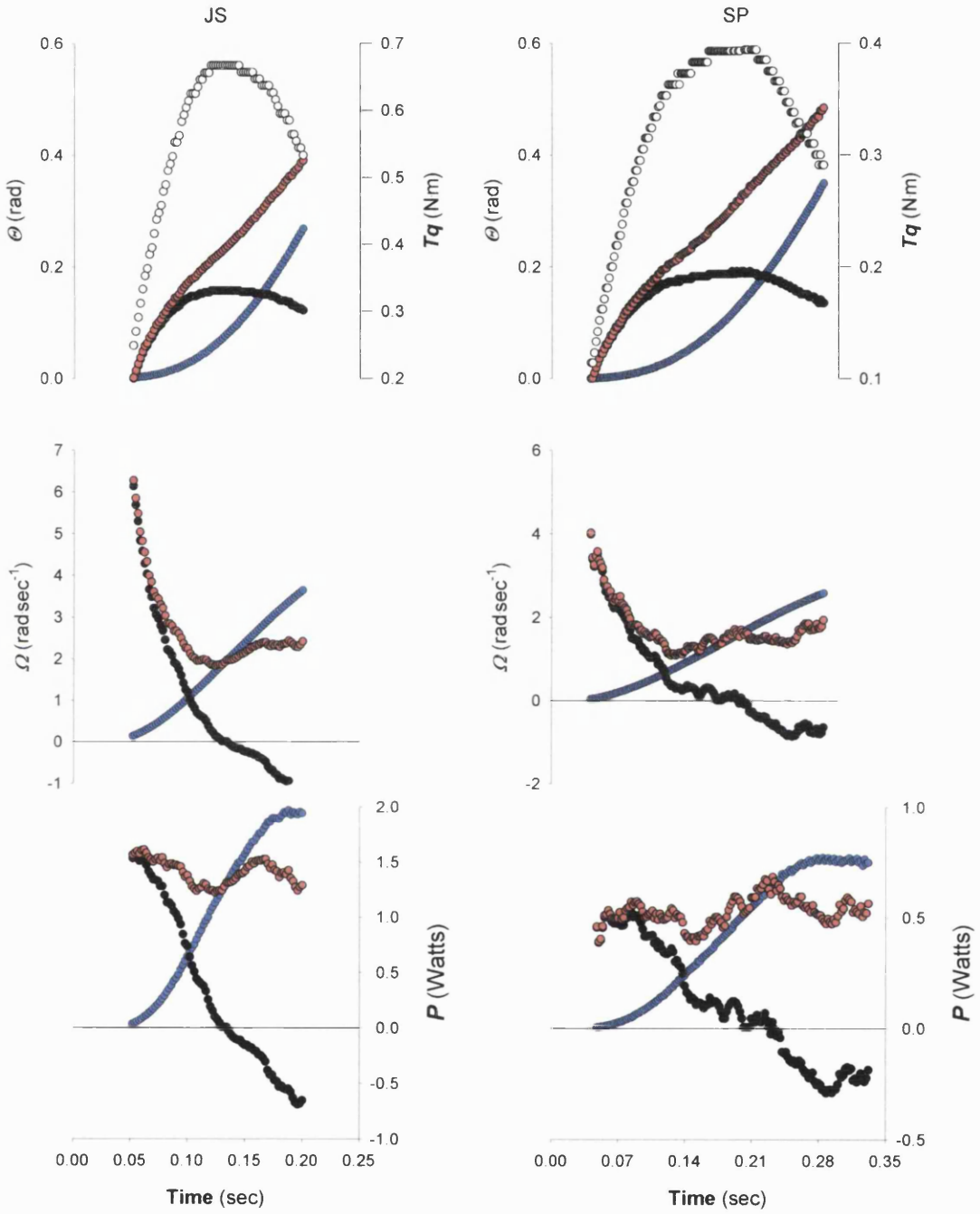

Figure 3.52.A. Instantaneous length change and torque (top graph), angular velocity (middle graph) and power (bottom graph) for the CC (red), SEC (black) and L (blue) for volunteers JS and SP during contractions against 'moderate' inertial loads (0.024 $kg{\cdot}m^2$ and 0.037 $kg{\cdot}m^2$ respectively). Torque is shown as open circles.

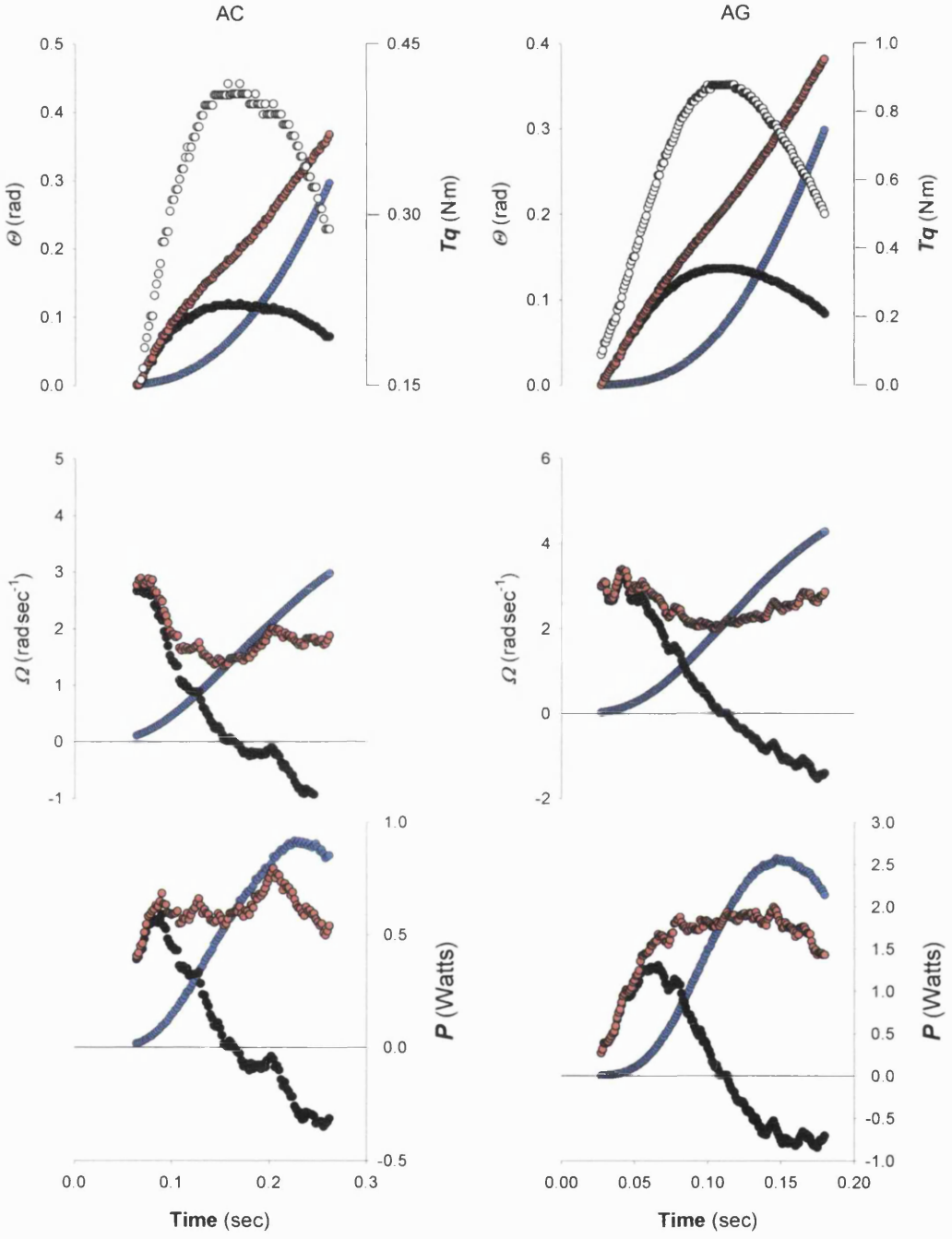

Figure 3.52.B. Instantaneous length change and torque (top graph), angular velocity (middle graph) and power (bottom graph) for the CC (red), SEC (black) and L (blue) for volunteers AC and AG during contractions against 'moderate' inertial loads (0.024 kg·m^2 for both volunteers). Torque is shown as open circles.

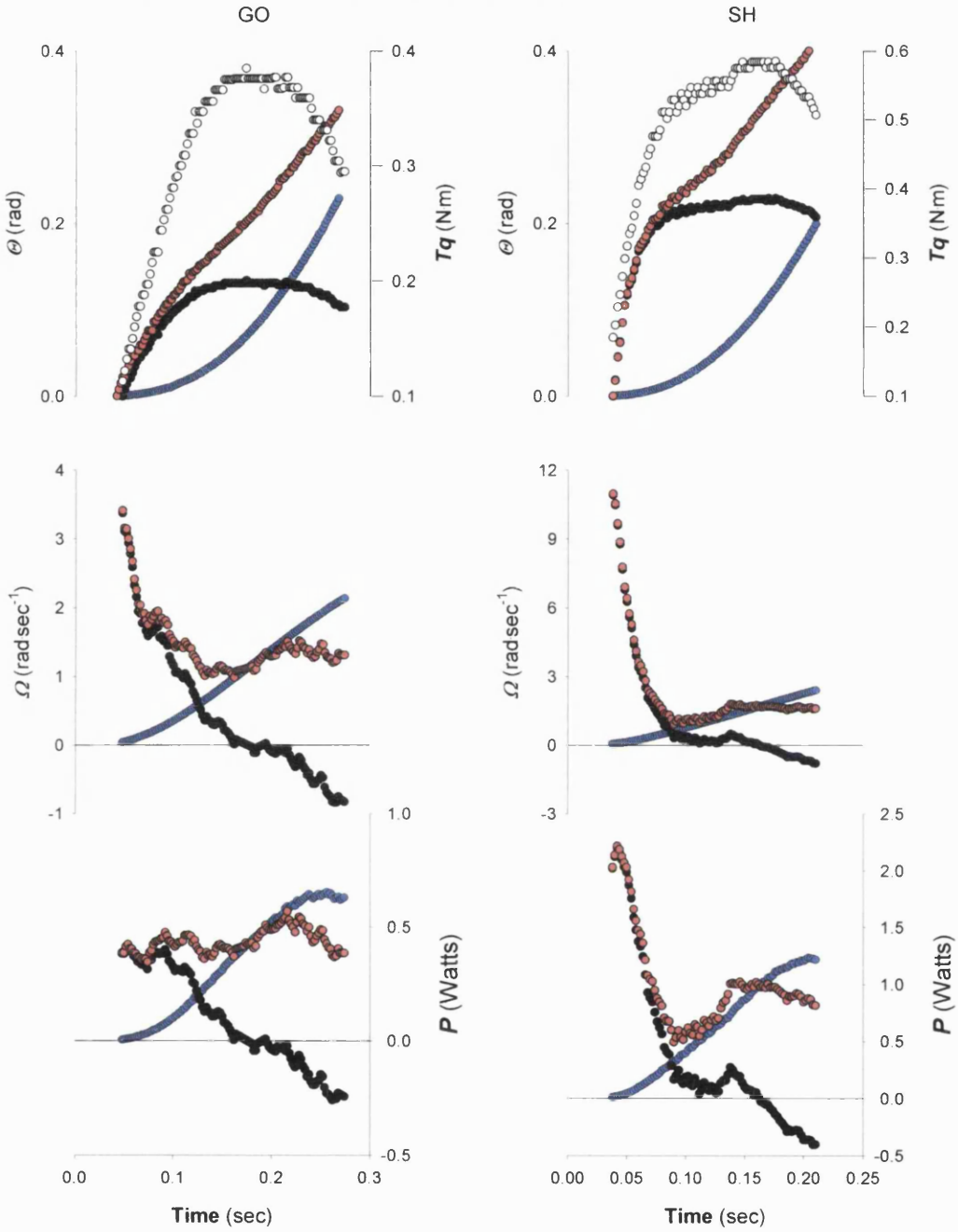

Figure 3.52.C. Instantaneous length change and torque (top graph), angular velocity (middle graph) and power (bottom graph) for the CC (red), SEC (black) and L (blue) for volunteers GO and SH during contractions against 'moderate' inertial loads (0.034 kg·m^2 and 0.037 kg·m^2 respectively). Torque is shown as open circles.

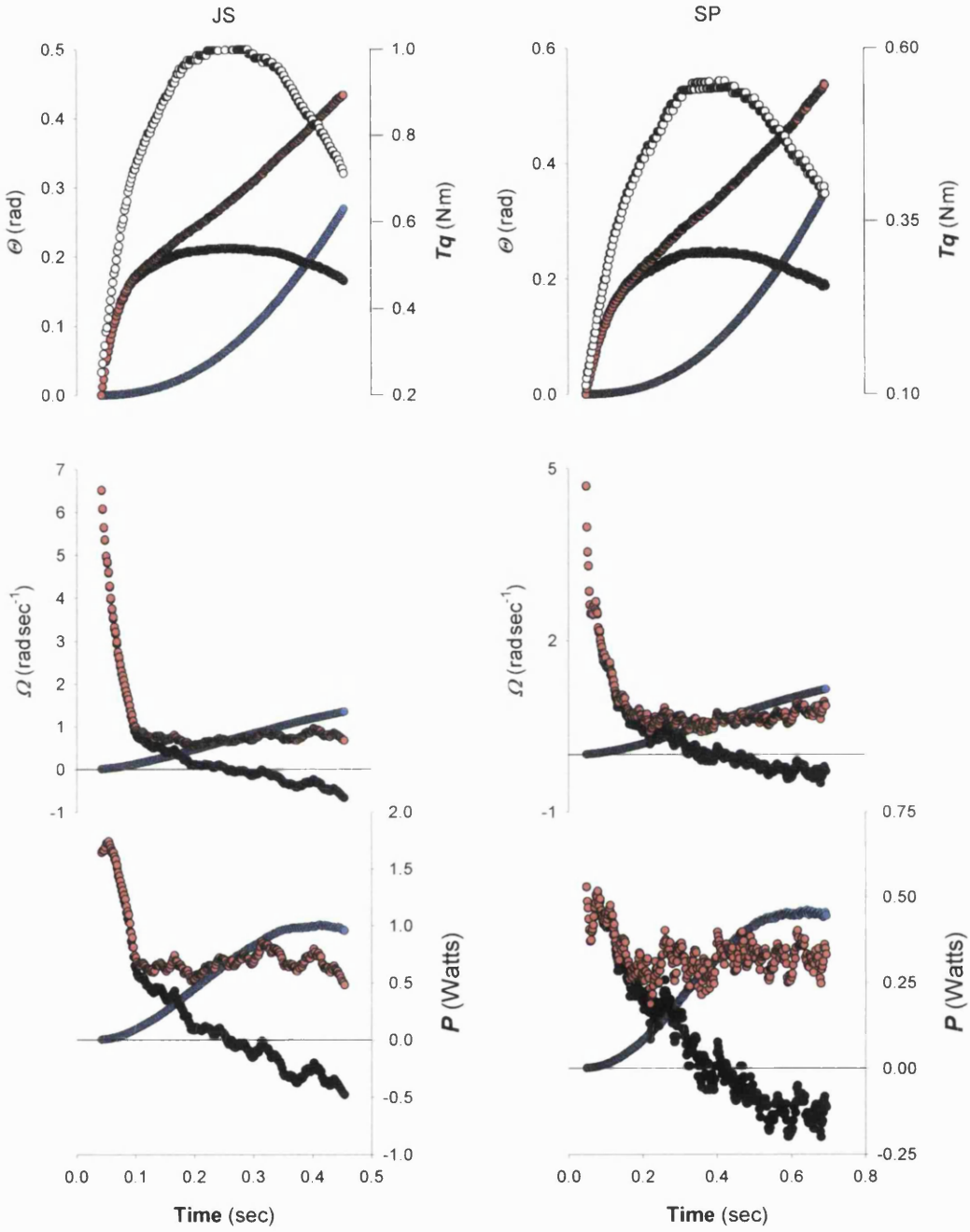

Figure 3.53. A. Instantaneous length change and torque (top graph), angular velocity (middle graph) and power (bottom graph) for the CC (red), SEC (black) and L (blue) for volunteers JS and SP during contractions against 'heavy' inertial loads (0.265 kg·m^2 and 0.037 kg·m^2 respectively). Torque is shown as open circles.

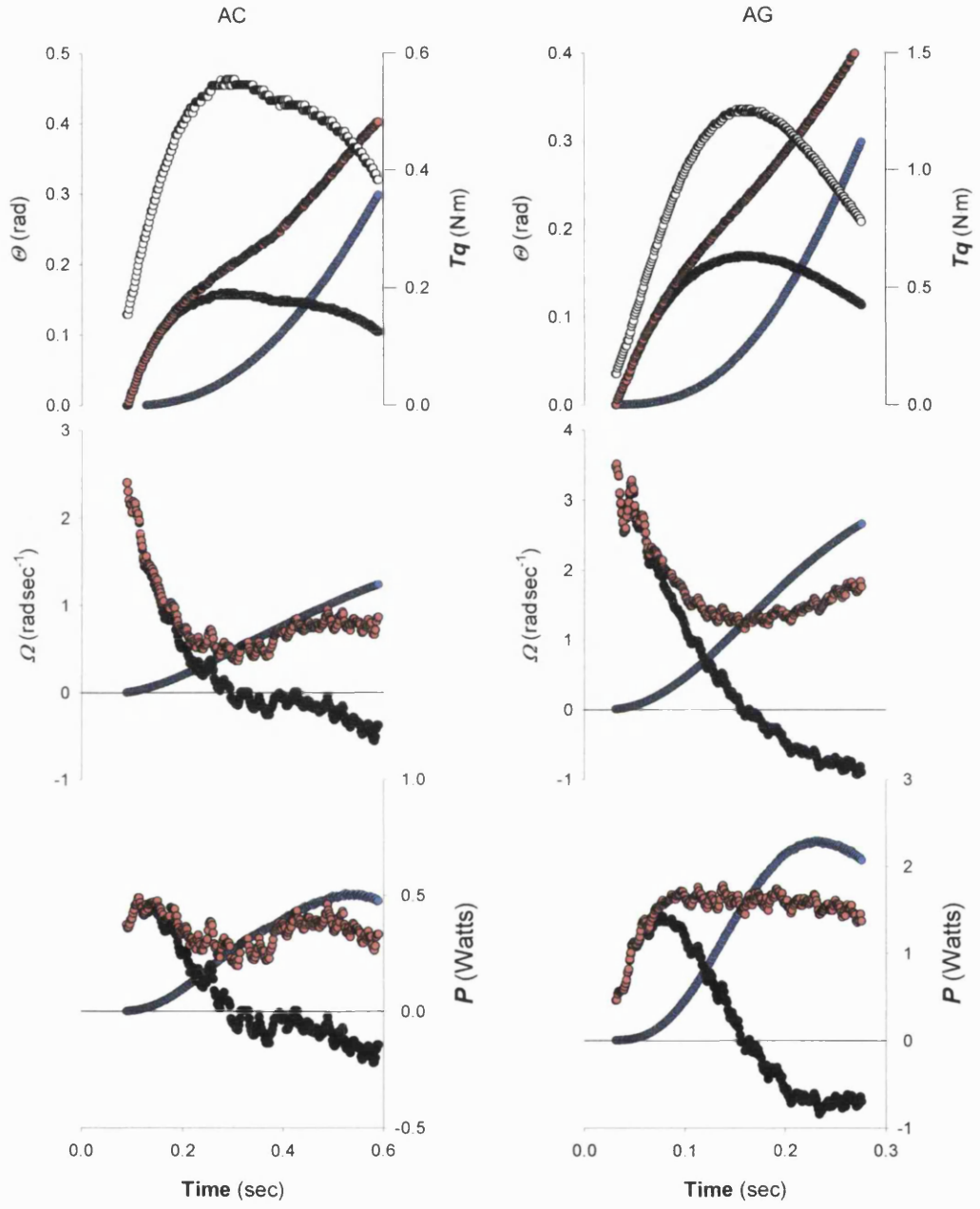

Figure 3.53.B. Instantaneous length change and torque (top graph), angular velocity (middle graph) and power (bottom graph) for the CC (red), SEC (black) and L (blue) for volunteers AC and AG during contractions against 'heavy' inertial loads (0.188 kg·m^2 and 0.089 kg·m^2 respectively). Torque is shown as open circles.

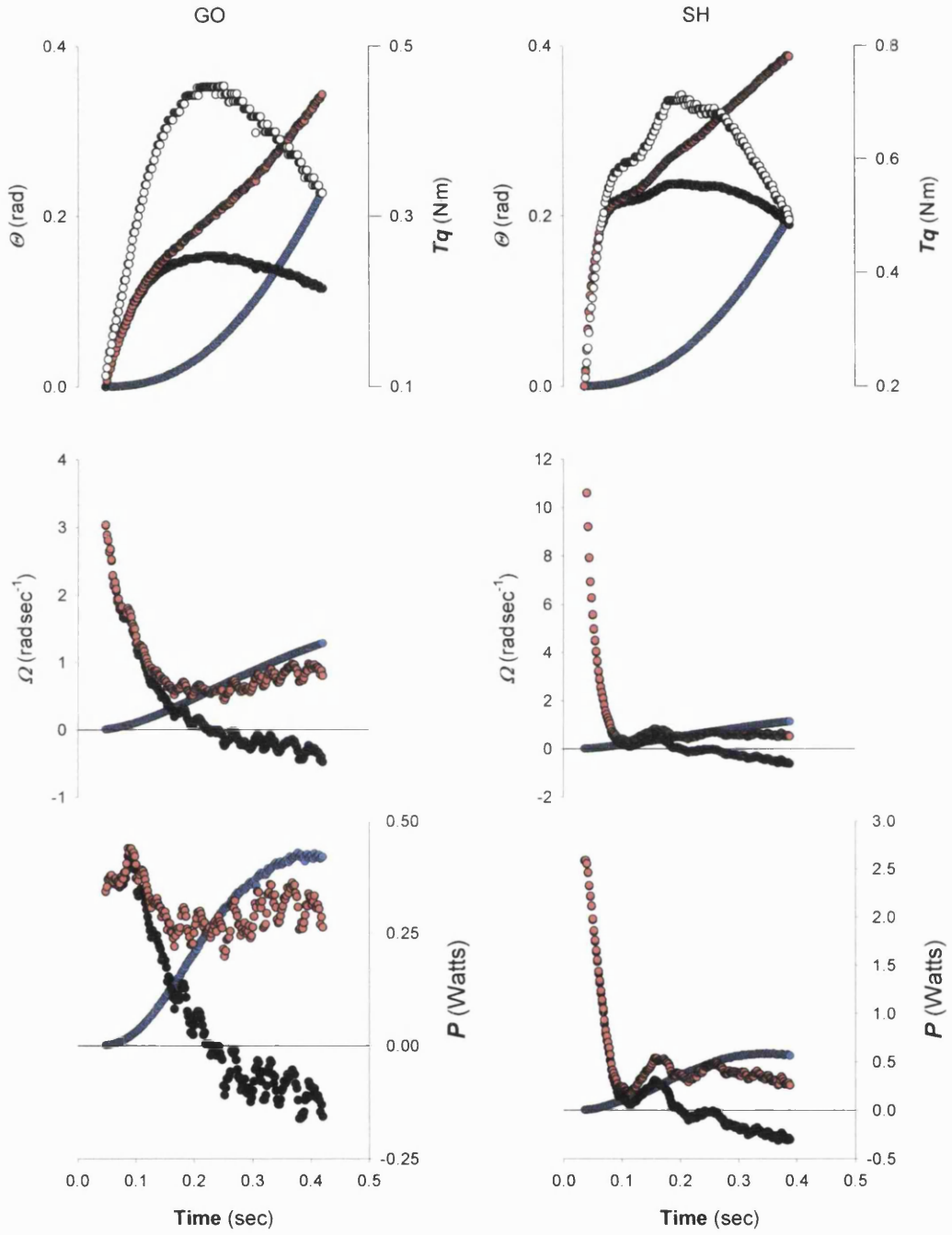

Figure 3.53.C. Instantaneous length change and torque (top graph), angular velocity (middle graph) and power (bottom graph) for the CC (red), SEC (black) and L (blue) for volunteers GO and SH during contractions against 'heavy' inertial loads (0.109 kg·m^2 and 0.188 kg·m^2 respectively). Torque is shown as open circles.

The records shown above show the time-history of mechanical events for part of the contraction and not the whole of it, due to the torque and angular constrains in the calculation. Notice that the time scale differs between contractions depending on the magnitude of the inertial load. The scale of the mechanical parameters may also be different. However, in general, it seems clear from these results that, early during the contraction the CC is shortening (top graph) faster than the load can move due to its inertia (middle graph), the leading to elongation of the series elasticity and a rise in torque (top graph). Also the power generated by the CC is partly delivered to load and partly to the SEC (bottom graph) and the series compliance of the transducer. As a result of the torque in the system, the load accelerates continuously during the contraction, while during the rising phase of torque the CC velocity is falling as expected from the CC torque-velocity relationship (middle graph). At a certain time instant the load and CC velocities become equal (middle graph). At that time instant the series compliance is not changing length and the torque reaches its peak value (top graph). After that instant the load velocity keeps rising exceeding the CC velocity (middle graph) leading to recoiling of the series elasticity and a drop in the torque (top graph). As a result the CC velocity starts to rise again along its torque-velocity relationship (middle graph). During the late part of the contraction while torque is falling and the load velocity exceeds the CC velocity, power is delivered to the load not only by the CC but also by the series elasticity resulting in higher power delivery to the load than the CC alone could deliver. These results are consistent with the modelling work in this thesis (see figures 2.6-2.9 A).

4.6.2.2. Static contractions

The mechanical output of the CC and SEC was also calculated for static contractions. A typical result is shown in figure 3.54. The torque in the system rises as the elasticity in series with CC stretches (figure 3.54 only shows the extension of the SEC and not of the total elasticity) (top graph; figure 3.54). As the torque rises, the shortening velocity of the CC drops (middle graph; figure 3.54). The power generated by the CC reaches its peak value early during the contraction while the torque is relatively low and it then drops as the torque exceeds its optimal value for power generation (bottom graph, figure 3.54).

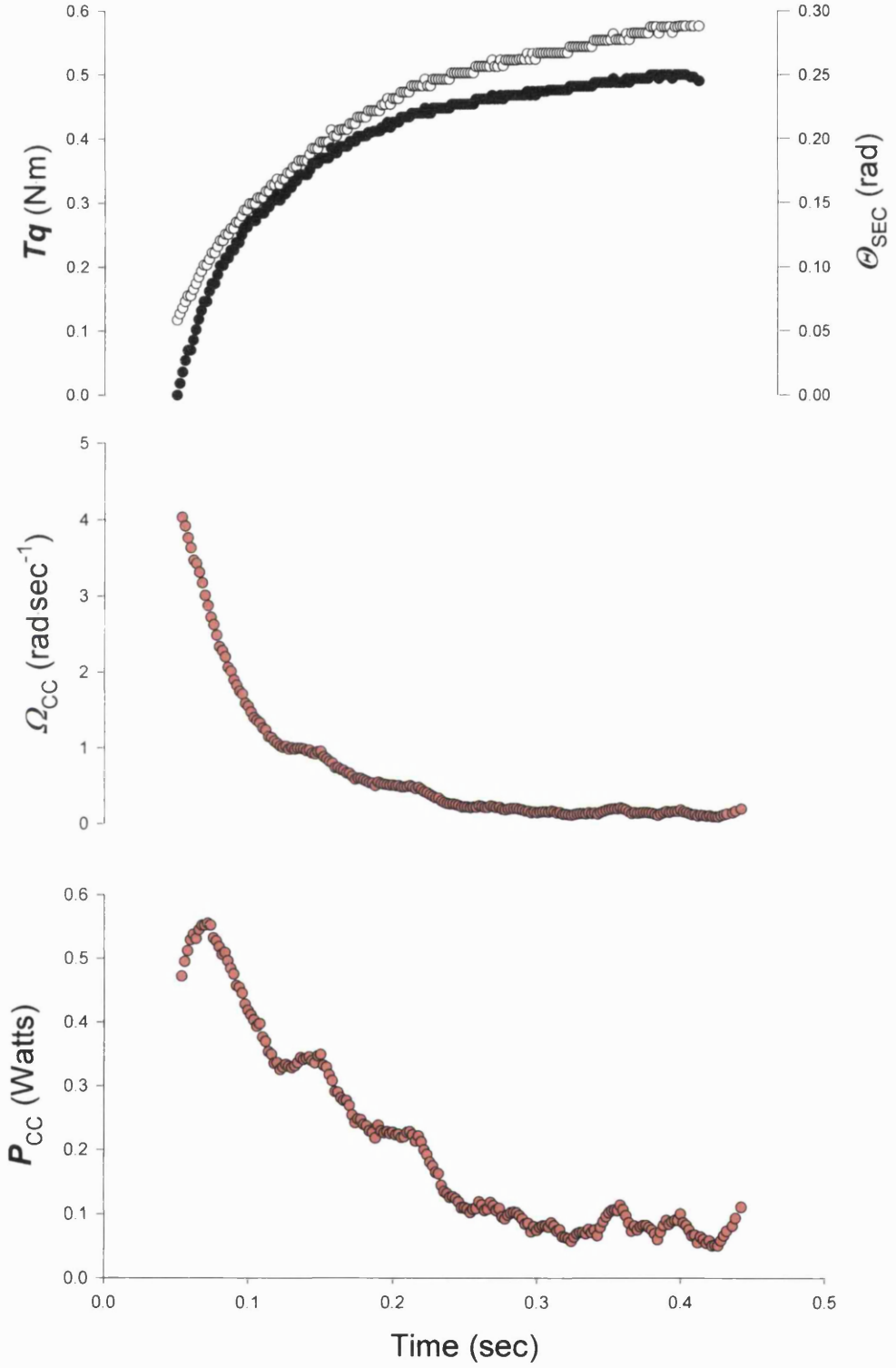

Figure 3.54. Time course of torque (open circles) and SEC extension (closed circles) (top graph), CC velocity (middle graph) and CC power generation (bottom graph) during a static contraction. Result from volunteer SP .

4.7. Series elastic and contractile properties interaction: Power amplification

4.7.1. Normalised load

The modelling work in this thesis has shown that the dimensionless mechanical output of a muscle-tendon-inertial load system mainly depends on the magnitude of the normalised load, Ξ (linear motion) or ξ (rotational motion). The normalised load in rotational terms is defined as:

$$\xi = \left(\frac{\Omega_{CC_{max}}}{Tq_0} \right)^2 \cdot K_{rot_{TOT}} \cdot MI$$

The values of MI and Tq_0 are known. Imagining the total elasticity in series with the CC to have a linear torque-extension relationship with origin at (0,0) and upper limit at (X_{SECmax}, Tq_0), $K_{rot_{TOT}}$ has been calculated as the slope of this straight line. Of course the SEC torque-extension properties shown in section 4.3 were not linear, but their deviation from this straight line can easily be expressed in terms of the constant H (see section 4.3.2, pp. 300). As an estimate of the maximal CC shortening velocity, $\Omega_{CC_{max}}$, the values given in table 3.10 can be used as an estimate for the $\Omega_{CC_{max}}$ of volunteers SP,AC,AG,GO. The $\Omega_{CC_{max}}$ for the other two volunteers (JS and SH) given in this table is too high to accept. The $\Omega_{CC_{max}}$ for these two volunteers was estimated using linear extrapolation from the first two points of the grouped-average CC torque-velocity relationship back to zero torque. In this way, despite the limitations of

using estimated values for the parameters $K_{rot_{TOT}}$ and $\Omega_{CC_{max}}$, an estimate of ξ could obtained. Table 3.14 shows the values for some of the parameters.

Volunteer	JS	SP	AC	AG	GO	SH
Tq_0 (N·m)	1.437	0.772	1.048	2.394	0.687	0.931
$\Omega_{CC_{max}}$ (rad·sec^{-1})	9.216	10.048	6.207	4.406	6.012	16.258
$K_{rot_{TOT}}$ (N·m)	2.401	1.705	2.797	7.547	1.983	2.646

Table 3.14. Values for some of the parameters in ξ (3 d.p.).

4.7.2. Power amplification and normalised load

It was shown in previous sections (modelling sections: 6.1.1 and 6.1.2.1.12.; FDI section 4.6.2.1) that as a result of the presence of elasticity between the CC and L, more power can be delivered to the load during the falling phase of torque than the CC alone could generate. The power ratio, R, is used in this thesis to quantify the extent of this power 'amplification'. R is defined as the ratio of the peak power delivered to an maximal power the CC alone can generate ($P_{CC_{max}}$).

$P_{L_{peak}}$ was obtained as the peak value of the product of the torque and load velocity during each contraction. CC power was calculated for each volunteer from his/her torque-velocity relationship as the product of the torque and corresponding CC angular velocity. In this way CC torque-power plots were created and clusters of data points were used to obtain grouped average values.

The peak value in these plots was used as an estimate of the maximal power the CC could generate. The results are shown in table 3.15. The maximal value of CC power for each volunteer was then used to divide the peak power delivered to the load in each contraction.

Volunteer	JS	SP	AC	AG	GO	SH
$P_{CC_{max}}$ (Watts)	1.612	0.546	0.617	1.747	0.494	1.897

Table 3.15. Estimated $P_{CC_{max}}$ for each volunteer (3 d.p.).

Plots of R against the logarithm of ξ are shown in figure 3.40. The majority of the values of R are above 1 indicating greater power delivery to the load than the CC alone could deliver. Although few values are between 1.5 and 2, most of them are between 1 and 1.5 .

This appears to be a similar feature for all volunteers except volunteer SH whose $\boldsymbol{R}$ values are well below the value of 1. This is due to the high $P_{CC_{max}}$ of this volunteer (Table 3.15) which tends to bring the values of R down and due to the skewed shape of his power-torque relationship, which peaks at low torques (see figure 3.51-3.53C). As a result of the latter, $P_{CC_{max}}$ would be achieved early or late during the contraction while the torque is low so that during peak power delivery to the load P_{CC} has dropped by a considerable amount (see figures 3.36-3.38.C). Thus, the power delivered to the load, which is the sum of CC plus the power in the series elasticity, never reaches values as high as

$P_{CC_{max}}$ at the time of peak delivery. Moreover, it is very likely that the high power output at low torque values is an artefact caused by miscalculation of the SEC stiffness in that torque region (see figure 3.25). Calculation of a lower stiffness would lead to overestimation of the CC shortening velocity and hence power output at low torque values.

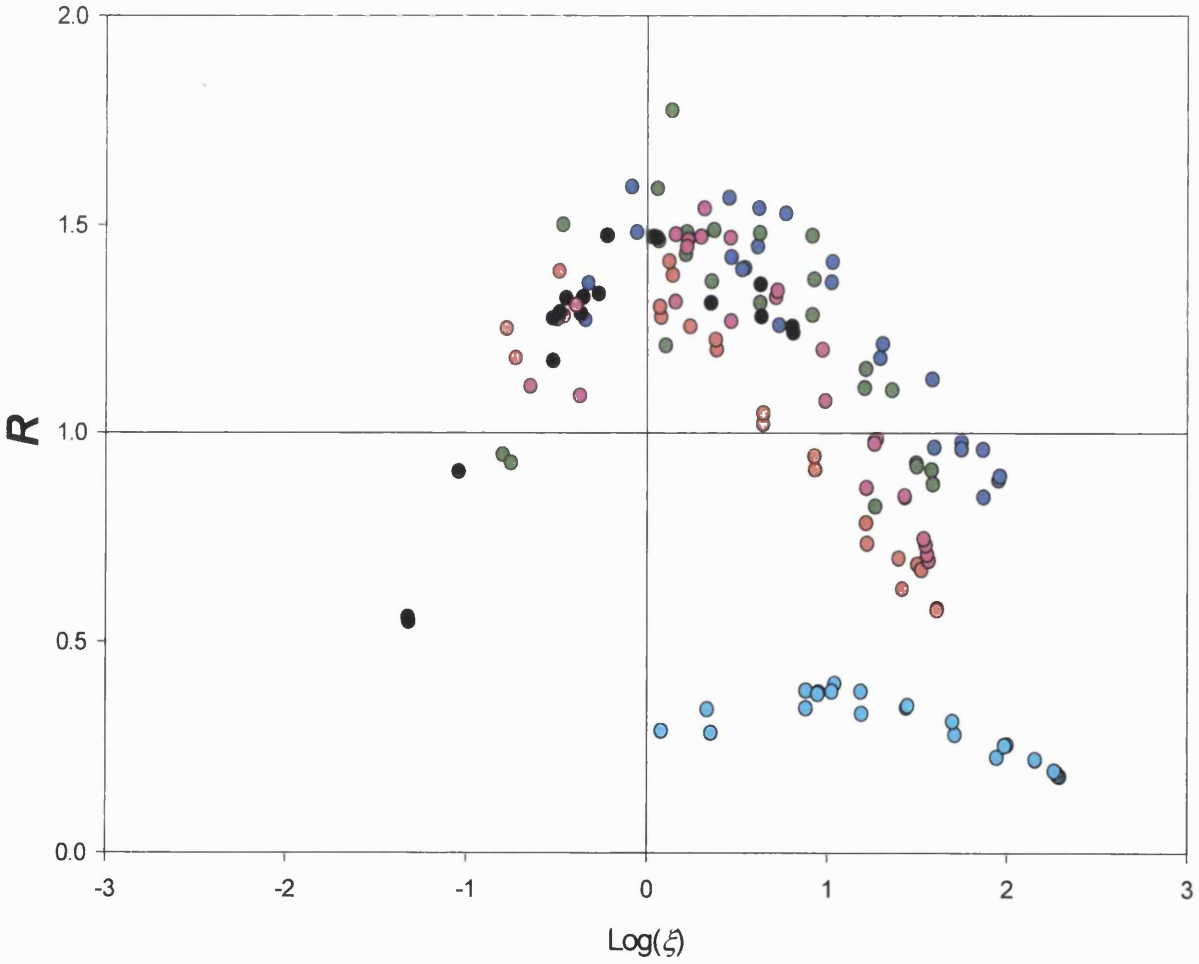

Figure 3.55. Power ratio plotted against the logarithm of the normalised load for each volunteer (red:JS; blue:SP; green:AC; black:AG; pink:GO; cyan:SH).

The general appearance of the power ratio-logarithm of inertial load plot (figure 3.55) is bell-shaped, with the highest R values in the centre corresponding to a ξ value of approximately 1. The bell-shape is a feature of all the individual records. This is also the case for the position of the peak except the record of volunteer SH whose R- ξ relationship is shifted to the right. This appears to be due to the high $\Omega_{CC_{max}}$ relative to Tq_0 leading to a high $\left(\frac{\Omega_{CC_{max}}}{Tq_0}\right)^2$ value of approximately 305 resulting in greater ξ values than for any other volunteer. The very high value of $\Omega_{CC_{max}}$ for this volunteer is perhaps due overestimation of the CC shortening velocity at low torque values and due to the fact linear extrapolation was used in order to obtain an estimate of $\Omega_{CC_{max}}$.

R drops from its peak value at ξ equal to approximately 1, at higher and lower values of ξ. The few R values that are below 1 on the left side of the peak occur as the normalised load becomes approximately ten times smaller than its optimal value. On the right side of the peak it appears that R values below 1 occur as the normalised load becomes 10 to100-fold larger than its optimal value (with the exception of volunteer SH). Thus, power amplification appears to be the case for these volunteers (except SH) over a wide range of normalised loads (from 0.1 to 10-100 units).

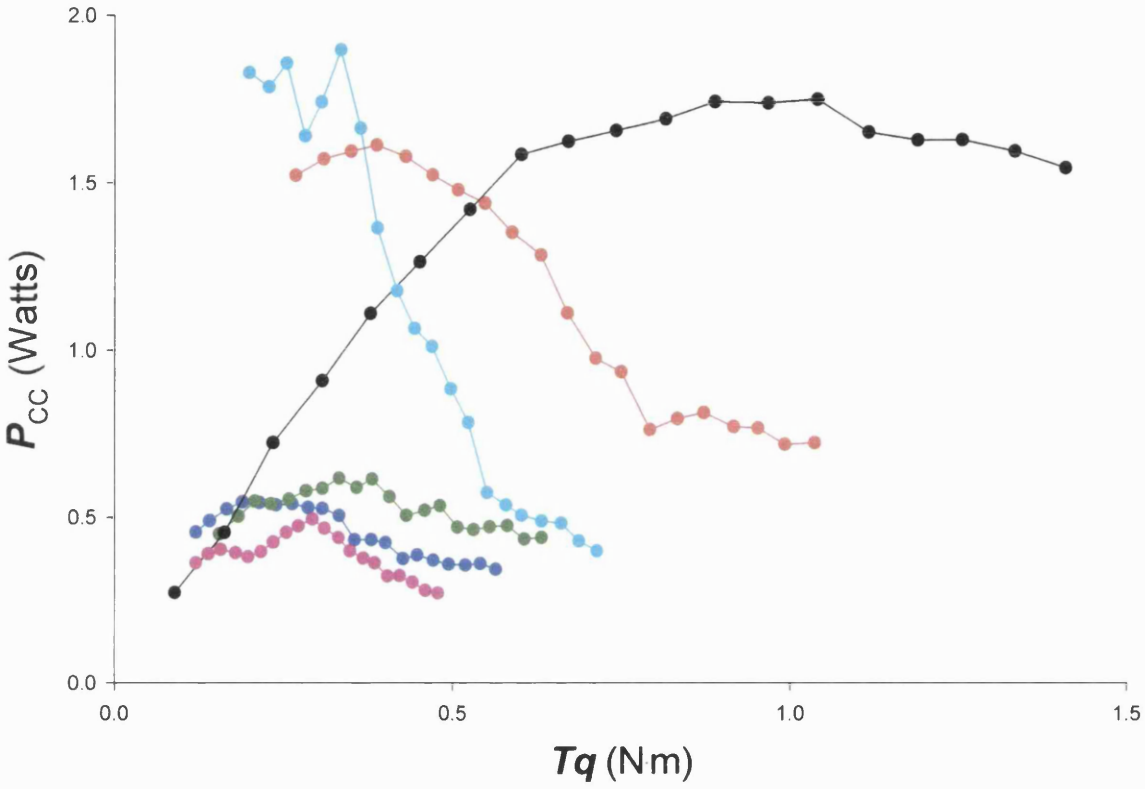

Figure 3.56. CC power-torque grouped average relationships for each volunteer (JS-red, SP-blue, AC-green, AG-black, GO-pink, SH-cyan).

4.8. Model versus experimentally obtained results

4.8.1. Time course of mechanical output

In order to assess whether experimental and modelling results are in agreement, torque records from one volunteer (JS) were fitted with simulated torque outputs generated by a model with linear CC force-velocity and linear SEC force-extension relationship (modelling section 4.2.1). Three constants must be specified to compare an experimental record that is dimensioned, with a dimensionless prediction from this simplest model. One constant is specified by the maximal static torque achieved in the experiment (1.437 N·m) which was used to normalise the experimentally recorded torque. The other two constants were determined using a simple fitting procedure to optimise the values of the dimensionless inertia and of the time scaling factor so as to minimise the sum of the squares of the errors between the modelled and the experimental result. Nine torque traces corresponding to different inertial loads were fitted thus determining the above two constants for each record. Actual and fitted time courses are shown in figure 3.57. The time scale was normalised by dividing the actual time with the corresponding time scaling factor obtained from the fitting procedure (see table 3.16).

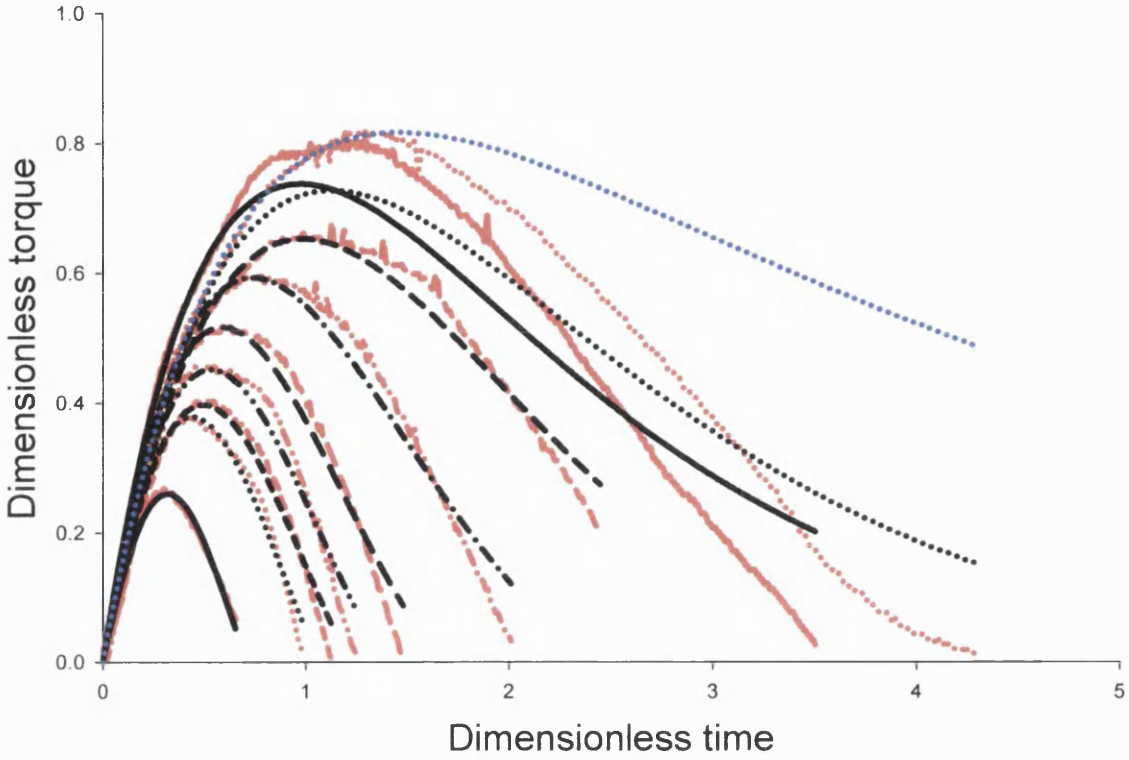

Figure 3.57.Experimental (red) and model-predicted (black) normalised torque time courses for contractions made by one volunteer against nine different inertial loads. The torque output against the largest inertia has been fitted by two simulation curves: one generated to fit the whole output (black) and one to fit the ascending part only (blue).

Actual and fitting parameters as well as the r^2 value are shown in table 3.16. In this table the actual and normalised moments of inertia have been expressed relative to the corresponding values for the contraction in which the highest peak power was achieved during the experiment. This makes it easier to compare whether increasing the actual inertia results in proportional increases of the normalised moment of inertia. The values of t are approximately constant across the range of loads but the relation between the relative actual and modelled inertial loads changes systematically with the size of the load. This trend is reduced when the load is large, if only the ascending part of the record is used in the curve fitting. This is illustrated by the blue curve figure 3.57 and the last line of table 3.16.

MI/MI_{OPT}	Ξ/Ξ_{OPT}	t (sec)	r^2
0.263	0.313	7.890	0.994
0.889	0.870	8.411	0.991
1.000	1.000	8.185	0.989
1.838	1.493	8.580	0.980
3.315	2.362	8.969	0.987
6.440	4.020	8.871	0.986
12.570	6.154	8.319	0.989
25.240	11.770	9.336	0.955
30.880	10.830	8.559	0.949
30.877	24.792	8.553	0.977

Table 3.15. Parameters related to fitting experimental torque records with model simulations. MI/MI_{OPT} is the ratio of the actual moment of inertia in the corresponding contraction and the inertia at which peak external power was maximal (0.013 $kg{\cdot}m^2$); Ξ/Ξ_{OPT} is the optimised dimensionless inertia relative to the value for the record in which peak power generation was maximum in this experiment (0.345 units); t is the normalising time factor in seconds and SSE is the sum of the squares of the differences between experimental and model curves in units of Newton-meters all squared. The last line in this table shows the result of fitting only the ascending part of the torque output of the largest load (previous row; blue curve in figure ..).

The first thing to notice is that a simple model, using only three degrees of freedom (Tq_0, Ξ, t) provides a relatively good description of the magnitude and shape of actual torque outputs. This description is more accurate when the load is relatively light (~0.9-13 X MI_{OPT}). However, the fit is less good when larger loads are considered (figure 3.57). This suggests that the main features of the mechanical output at relatively light loads are determined mainly by the magnitude of the normalised inertial load, as described in the modelling section. This magnitude of course is dependent on the parameters of the linear CC and SEC properties.

Additional factors are required to accurately model torque outputs against relatively large inertial loads (e.g. >25x MI_{OPT}). Larger torques were predicted by the model at late times than those actually observed. This is illustrated by comparison of the blue curve with the corresponding experimental result in figure 3.57 and by the value of the r^2 in table 3.16.When fitting is optimised only for the rising phase of the torque output, a much greater torque output is predicted during the falling phase (blue curve). When fitting the whole output is optimised, the simulated result balances the higher torque predicted at late times with lower torque values at earlier times (figure 3.57). Factors not included in the model such as changing lever arms, the CC isometric force-length relationship, CC shortening deactivation and hysterisis of the SEC may become more important during contractions against large inertial loads in which the range of finger abduction may be larger, more muscle shortening and work is performed and the tendon stretches more and remains under tension longer. It could also be that, to some extent, the CC and SEC properties are more closely approximated by linear relationships when the CC force-velocity and SEC force-extension trajectories are relatively short, as expected during contractions against light inertias. However, the curvature of these relationships may have a greater influence when larger trajectories are utilised, such as when the inertial load is large.

Thus, a precise modelling approach would probably require taking into account a number of additional factors such as muscle activation, force-length relation, curved force-velocity relationship, shortening deactivation, tendon curved force-

extension relationship and hysteresis, joint levers etc. However, given the complexity associated with precise prediction of the output during joint movements arising from these factors, it is very encouraging that such a simple model using only three degrees of freedom provides a reasonable fit as illustrated in figure 3.57.

The agreement between modelling results and results arising from experimental observations was further considered by superimposing such results for one volunteer (GO). Results from three contractions are shown (figures 3.58.A-C), each contraction performed against a different inertial load. The choice of loads in these three contractions covers almost the whole spectrum of loads used in this experiment; it includes one contraction against a light, one against a moderate and one against a large inertial load. The values of three parameters, namely $\boldsymbol{Tq}_0$, $\boldsymbol{\Omega}_{Ccmax}$ and $\boldsymbol{K}_{rotTOT}$ that were obtained from experimental results (see table 3.14 for values) were used to normalise the experimentally obtained outputs, in the same way as described in the modelling section 4.1. Briefly, the torque output was normalised by dividing it with $\boldsymbol{Tq}_0$; rotation was divided by $\boldsymbol{Tq}_0 \cdot \boldsymbol{K}_{rotTOT}^{-1}$; rotational velocity was divided by $\boldsymbol{\Omega}_{Ccmax}$; power was divided by $\boldsymbol{Tq}_0 \cdot \boldsymbol{\Omega}_{Ccmax}$; time was divided by $\boldsymbol{Tq}_0 \cdot \boldsymbol{\Omega}_{Ccmax}^{-1} \cdot \boldsymbol{K}_{rotTOT}^{-1}$. Numerical solutions were obtained for this dimensionless output using a model of an FTI system with curved SEC force-extension and CC force-velocity relationships. Values for the corresponding curvatures $\boldsymbol{H}$ and $\boldsymbol{G}$ were those obtained for volunteer GO from experimental results for the results (see tables 3.8 and 3.10, pp.305 & 312, respectively). The values of these constants were slightly

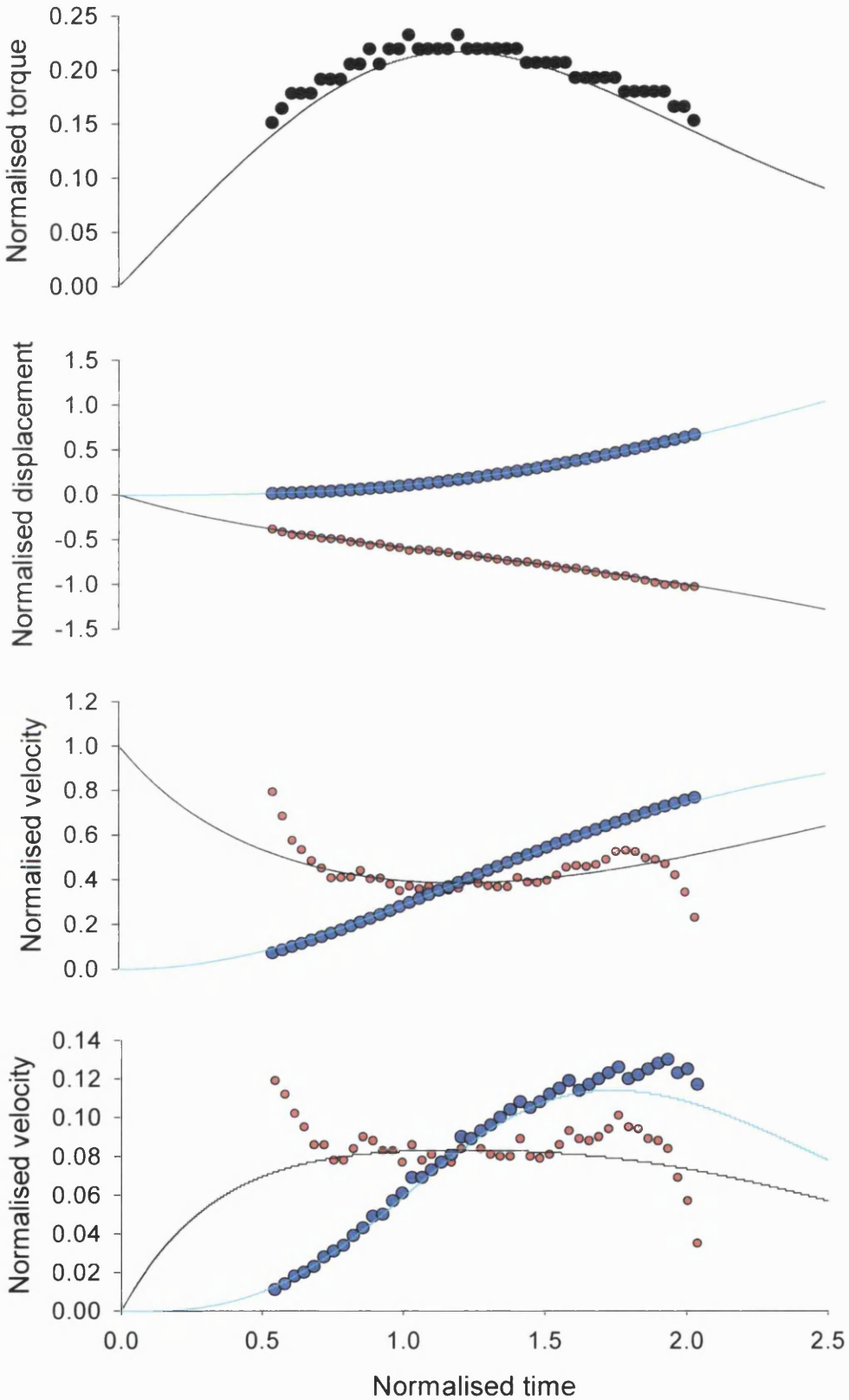

Figure 3.58.A. Experimentally obtained time course of mechanical output and model simulation results for volunteer GO. Inertial load was $2.815\,10^{-3}$ kg m^2. Ξ=0.216. Points come from experimentally obtained results (red: CC; blue: L; black: whole MTI). Curves come from model simulations (black: muscle; cyan: L).

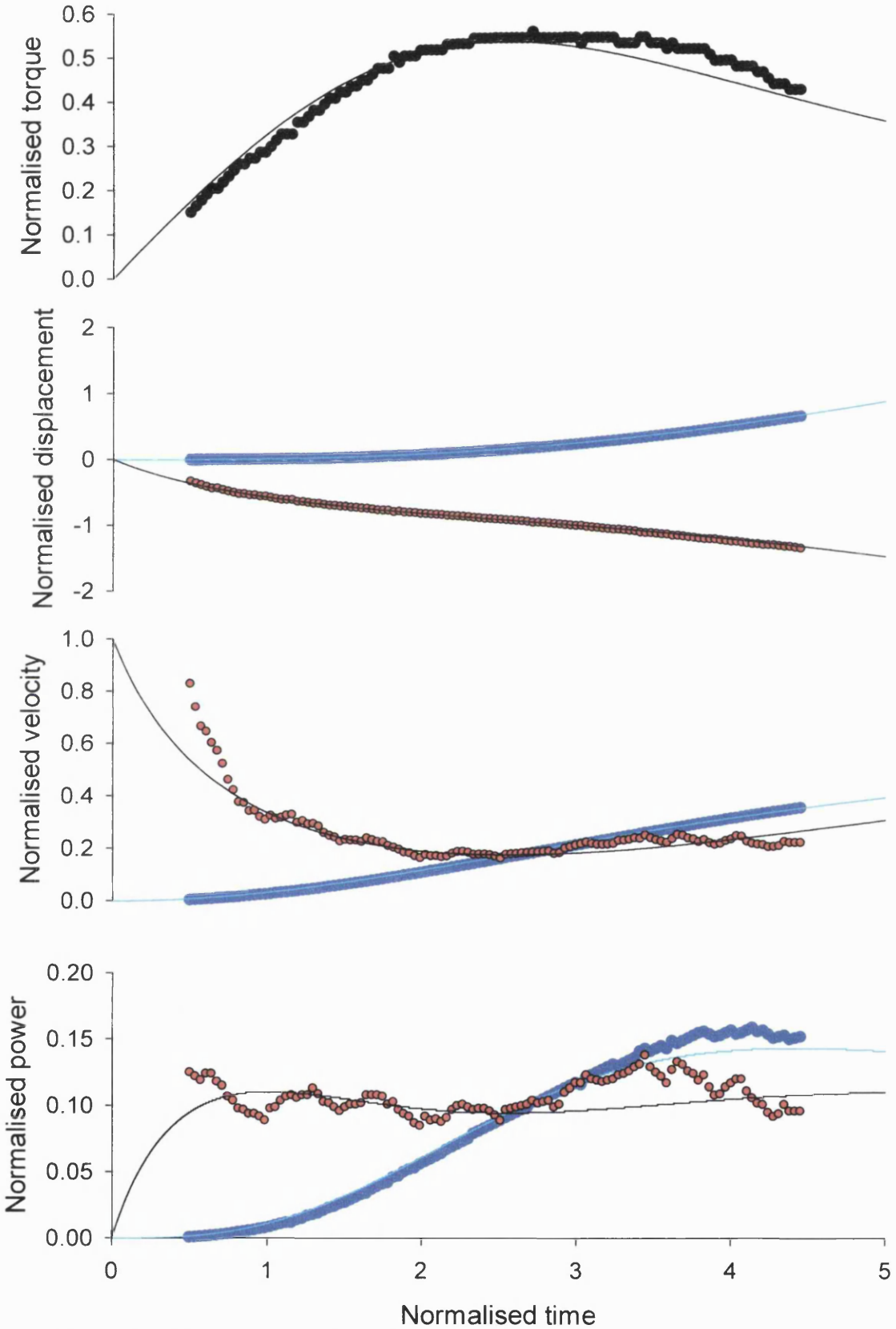

Figure 3.58.B.Experimentally obtained time course of mechanical output and model simulation results for volunteer GO. Inertial load was 0.034 kg·m^2. Ξ=5.199. Points represent experimentally obtained results (red: CC; blue: L; black: whole MTI). Curves represent from model simulations (black: muscle; cyan: L).

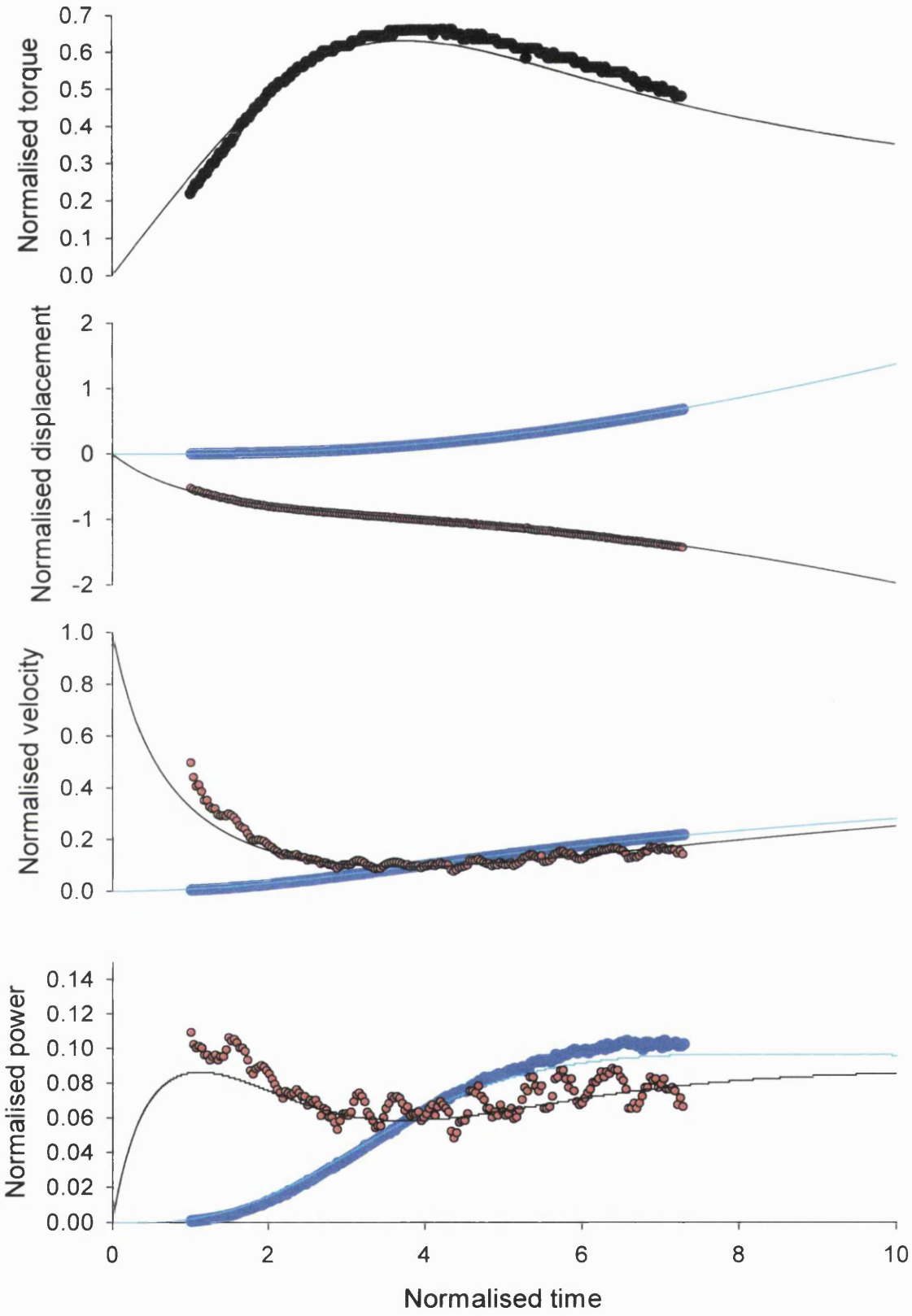

Figure 3.58.C. Experimentally obtained time course of mechanical output and model simulation results for volunteer GO. Inertial load was 0.109 $kg \cdot m^2$. Ξ=16.563. Points represent experimentally obtained results (red: CC; blue: L; black: whole MTI). Curves represent results from model simulations (black: muscle; cyan: L).

modified (G=3.037; H=1.619) to obtain a better fit for the experimentally obtained results shown in figure 3.58.B.CC shortening has been translated due to the uncertainty of knowing the SEC extension at the first value of torque. The translations for the three contractions shown in figures 3.58.A-C were carried out by subtracting 0.375, 0.325 and 0.4 dimensionless displacement units from the corresponding experimentally derived CC shortening outputs.

The agreement between the model and the experimentally obtained results appears to be good. Within the torque limits set by the torque-pairing analysis, the experimentally obtained torque, rotation, rotational velocity and power are accurately predicted by a simple model specified only by a CC force-velocity, a SEC force-extension relationship and a L force-acceleration relationship. The same is true for CC rotation, angular velocity and power output derived from experimental results. Within the torque limits considered here, when the torque is relatively low the angular velocity (and hence power) due to CC shortening appears greater than predicted by the model. This is probably due to lack of information about the exact shape of the SEC stiffness-torque relationships at low values of torque. Thus, the effects of activation, CC force-length relation, deactivation, SEC hysteresis, anatomical constraints etc. do not appear to be very important in determining the output of the muscle-tendon complex within most of the range of torques the torque-pairing analysis is valid. This range of torque values covers the greatest portion of the contractions including the part of maximal power delivery by the MTC to the load. Thus, although the CC and SEC properties not included in the model may be involved in the early or late times of the contraction and accurate modelling of the MTI output at such times

may require their inclusion in the model, these properties are not very influential for the majority of the time the FDI MTC is shortening against an inertial load. The determining factors appear to be the shape of the three relationships included in the model. Anatomical constraints do not seem to prevent maximal energy transfer from the MTC to the load as maximal peak power output appears to be achieved in all contractions, whether against a small or a large inertial load. If joint anatomy had restricted the range of movement considerably and the externally recorded torque dropped because the end of movement had been reached before optimal CC and SEC interaction was possible, the power output recorded during the experiments would not reach maximal levels as indicated by comparison between modelling results (which do not incorporate such an anatomical constraint) and recorded results.

4.8.2. Power amplification

The general shape, position of peak R and values of power amplification are not far from the predictions of the modelling work in this thesis as shown in figure 3.59. The power ratio-logarithm of normalised inertial load is expressed as grouped average values for all volunteers except SH due to the peculiarities in his record. For all other volunteers the mean value of H and G (calculation of mean G did not include the unusually high value for JS) and a range of ξ values were used to run a dimensionless model simulation. The resulting curve is also shown in figure 3.59 for comparison. In the central region of the plot ($-0.5 \leq \log(\xi) \leq 0.5$) the three-parameter (H, G, ξ) model curve provides a reasonable description of the data. Outside this range the deviation of the points obtained from experimental observations from the predicted values becomes

larger. The experimental result also includes negative values at large loads that are not expected according to the modelling result.

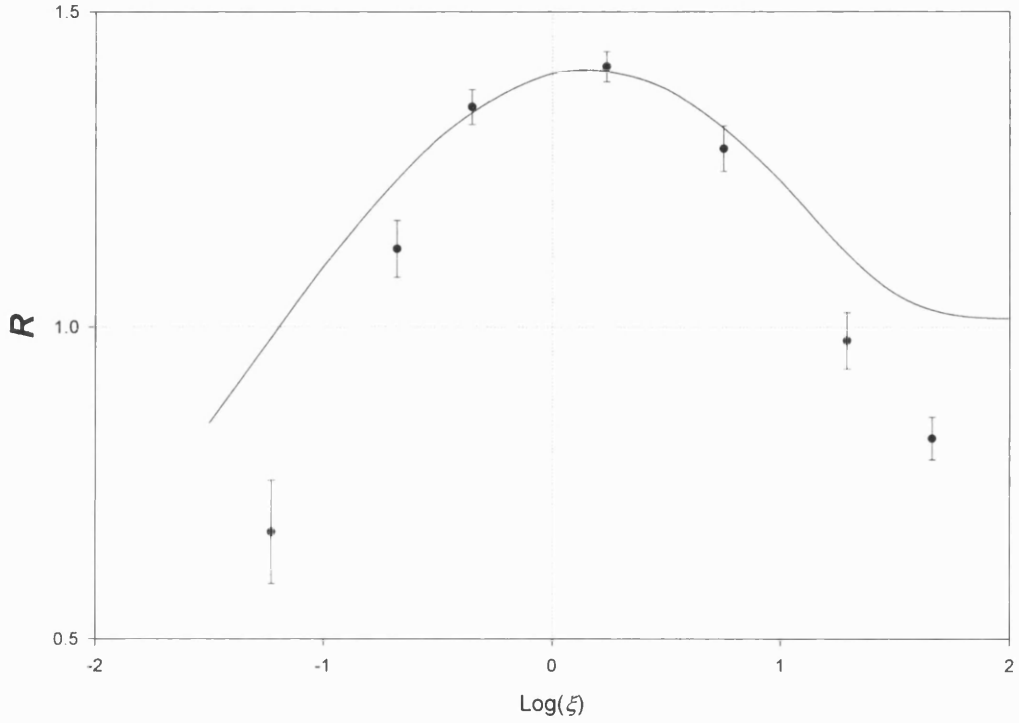

Figure 3.59. Grouped average power ratio (±SE) plotted against the logarithm of normalised inertial load (closed points) for all volunteers except SH and model prediction (black curve; H=2.238; G=5.57625).

5. Discussion

5.1. Main findings

The main findings from this section are:

1. A possible solution for the FDI CC velocity - torque and SEC stiffness-torque relationships can be found for electrically-evoked shortening contractions of the FDI MTC against purely inertial loads for each volunteer. This means that these relationships can be used to give a self consistent description of the experimental records.

2. Based on the estimated elastic and contractile properties, the time course of the CC and SEC mechanical outputs during individual contractions can be calculated and compared to the output of the MTC as a whole.

3. Power amplification was found to occur in all but one of the volunteers.

5.2. SEC elastic properties

The mechanical properties for the FDI CC and SEC have been studied in detail by Cook and McDonagh (Cook *et al*, 1995; Cook and McDonagh, 1995, 1996a, 1996b). They used Morgan's method (Morgan, 1977) to separate the total MTC stiffness during electrically-evoked contractions into muscle and tendon stiffness. The measurements took place in the region of 30-100% of the maximal isometric force, assuming tendon stiffness is constant within this range. They report a range of tendon stiffness for all volunteers ranging from 87.0 to 179.5 $N{\cdot}mm^{-1}$ with a mean of 157.4 $N{\cdot}mm^{-1}$ (Cook *et al*, 1995; Cook and McDonagh, 1996b). To validate the result they also estimated the stiffness from a cadaveric FDI tendon specimen by measuring its dimensions and

assuming a value for its Young's modulus and found the stiffness to be 149 $N \cdot mm^{-1}$, very close to the values obtained *in vivo*.

In our work the SEC stiffness of the FDI MTC has not been assumed to be a constant, but a function of the torque generated by the FDI around the 2nd metacarpophalangeal joint. This is reflected in the SEC stiffness-torque records (see section 4.3). These records are fitted well by three-parameter sigmoidal curves. This is in accordance with the expected relationship, if the slope of a typical SEC force-extension curve from an animal (see Rigby *et al*, 1959; Hill, 1970; Alexander, 1988) or human (Loren and Lieber, 1995; Ito *et al*, 1998; Kubo *et al*, 2000; Maganaris and Paul, 1999, 2000b), is plotted against the force, within the tissue's elastic limits. At low forces the stiffness is low and it progressively increases with force to reach a constant value at high forces. However, several *in vivo* studies performed in humans using imaging techniques have shown elastic structures in series with the muscle fascicles to operate within the 'toe' region (i.e. increasing stiffness region) of their force-extension relationship for forces up to their maximal voluntary (Ito *et al*, 1998; Kubo *et al*, 2000) or electrically-evoked (Maganaris and Paul, 1999, 2000b) isometric force. In the present study, the electrically-evoked static torque was, in most cases, lower than the maximal voluntarily torque and therefore the increase in stiffness with torque that was observed is in agreement with the studies on human tendons mentioned above.

Both the stiffness-torque relationships presented in this thesis and the constant stiffness values reported by Cook and McDonagh have been estimated on the

basis of assumptions. Unless direct measurements are performed, it is not possible to know how valid these results are. The highest stiffness values from the fitted stiffness-torque curves from all volunteers appear to range between 3.5-10 $N.m.rad^{-1}$. Assuming a reasonable average lever arm of 0.01 m, a rough estimate of linear stiffness would range between 35-100 $kN{\cdot}m^{-1}$ (or $N{\cdot}mm^{-1}$). Given the methodological differences mentioned above, this estimate is not far from the values reported by Cook and McDonagh.

Usually the SEC stiffness-force relationship is calculated from the tissue's force-extension properties. In this work the opposite has been done. The SEC torque-angular extension relationship for each volunteer has been calculated from the corresponding fitted SEC stiffness-torque. The resulting SEC torque-extension curves closely resemble those obtained from animals (e.g. Rigby *et al*, 1959; Hill, 1970; Alexander, 1988) and humans (Loren and Lieber, 1995; Ito *et al*, 1998; Kubo *et al*, 2000; Maganaris and Paul, 1999, 2000b). These curves were fitted very well by rectangular hyperbola equations whose curvature is determined only by constant one constant, H (see section 4.3.2, pp. 305) as suggested in the modelling section 3.1.3.1, pp. 81.

5.3. CC force-velocity output

The force-velocity relationship of the FDI muscle has also been studied by Cook and McDonagh (1996a) during electrically-evoked contractions. The difficulty associated with determining CC shortening velocity due to length changes in the SEC was dealt with using two different methods:

1. The CC velocity was obtained by dividing the rate of rise of isometric force by the stiffness of the FDI SEC, which was estimated from SEC force-extension curves that were obtained using Morgan's method.
2. Length changes of the SEC were minimised by timing the start of isokinetic index finger abductions relative to the time at which stimulation begun so that a constant force would be applied by the finger to the apparatus. That would mean that the SEC would not change length and the velocity of the finger would reflect that of the muscle alone.

Both approaches yielded similar Hill-type force-velocity curves with a V_{max} of 200-250 $mm \cdot s^{-1}$ at the actuator (~4.5 times smaller at the MTC i.e. 44-56 $mm \cdot s^{-1}$).

In this work the FDI CC torque-angular velocity relationship was estimated:

1. For dynamic contractions against inertial loads using the estimated (total) stiffness-torque relationship (result in section 4.4.1.1, pp. 306).
2. For static contractions using the estimated (total) stiffness-torque relationship (section 4.4.1.3, pp. 313)
3. From the peak torque and the angular load velocity at peak torque (section 4.4.1.2, pp. 313)

The three different methods produced CC torque-velocity relationships showing the expected trend: the CC shortening velocity declined with the rise in torque. The points generated from each one of the methods are close to the points generated from the other two methods as shown in figure 3.36 (section 4.4.1.4, pp. 315).

The CC torque-angular velocity relationship was similar for static and dynamic contractions for each volunteer when using the estimated stiffness-torque relationship (i.e. for methods 1 and 2 above). However, when these results were treated collectively for all volunteers, the CC velocity during static contractions was found to be lower than during dynamic contractions. It is reasonable to assume that stimulation of the FDI muscle was the same during dynamic and static contractions. The static torque-angle relationships for the FDI MTC of the volunteers suggest that the FDI CC operates in the ascending limb of its force-length relationship and that during index finger abduction its ability to generate force (and torque) declines with the abduction angle. Although most CC grouped average torque-angular velocity points from dynamic contractions were found to deviate from those describing the best-fit rectangular hyperbola, the general trend was similar for both curves. For a FDI CC with a Hill-type force-velocity relationship the expected decline in isometric force with the abduction angle would reduce its shortening velocity for a given value of force as the CC length would be reduced with abduction. Static contractions took place at a zero radians abduction angle and on the basis of the above argument higher CC velocities would be expected during isometric contractions than during dynamic contractions. However, the opposite was observed and therefore the CC force-length relation is unlikely to be the cause of the discrepancy. The deactivation of the muscle observed as a result of its active shortening has recently been shown to be a function of the work done by the muscle-tendon complex (e.g. Herzog *et al*, 2000). During static contractions the FDI MTC as a whole does not produce any mechanical work. However, if during the static contractions considered in this study the FDI CC performed more mechanical work than it

did during the dynamic contractions, the discrepancy mentioned above could be partly accounted for. Calculations of the work done by the CC (not shown in this thesis) for randomly selected records revealed that, as would be expected, the mechanical work during dynamic contractions was at least as much or greater than during static contractions. As not all dynamic and static contractions were analysed for the work done by the CC, it is not possible to completely exclude shortening deactivation as a possible cause, at least in part. Although a physiological mechanism accounting for this difference was not discovered there is a possible methodological cause. A smoothing factor is used in the calculation of the torque rate from each time-torque record (also see next paragraph). The smoothing factor used to calculate the torque rate for static contractions (linear fit in a running window of 21, 2 msec intervals) was greater than for dynamic (11 intervals) contractions. This difference would result in calculating relatively lower CC velocities for static contractions, which is the most likely explanation of the observed difference (also see below).

Although the CC velocities at the time of peak torque are very close to those calculated using the torque pairing method (see section 4.4.1.4, pp. 315), they were found to be, on average, significantly higher than the corresponding average values estimated from the torque-pairing method. When using the torque-pairing method, the CC velocity was calculated as the sum of the load velocity and the velocity of all the compliance in series with the CC. The instantaneous velocity of the series compliance was calculated as the ratio of the torque rate and the stiffness estimated for the value of torque at that instant. The CC torque-velocity points obtained at the time of peak torque were based on the

fact that the torque rate at that time is zero and therefore the velocity of the load and of the CC are equal. However, the calculated torque rate at the time of peak torque is not exactly zero but it frequently has a small negative value. This is due to smoothing in the torque record in order to reduce the noise resulting from the process of differentiating the torque record with respect to time (for more details in torque rate calculation see section 3.2.3.7, pp. 239). At the time of peak torque the torque rate was calculated as the slope of the regression line through the torque-time plot including the peak torque value as well as the five points occurring immediately before and immediately after that time. Commonly the points on the 'descending' part have more of an effect in determining the slope of the regression line such that it attains small negative values. In this way the velocity of the total series compliance at the time of peak torque has a negative value (i.e. the series compliance is shortening) which, when added to the velocity of the load, reduces the calculated value of the CC velocity.

Thus there is a trend in the way the estimated CC velocities deviate from one another. The more smoothing is used to calculate the torque rate, the lower the estimated CC velocities. Therefore, calculation of the CC shortening velocity using the first two methods is sensitive to how accurately the torque rate has been determined. Thus, care must be taken to obtain the value of the torque rate as accurately as possible by eliminating sources of noise in the torque measurements and using a high sampling frequency. Use of a transducer sensitive to rate of change of torque, rather than obtaining rate of change by differentiation of the torque signal might be beneficial. Although statistically

significant, in absolute terms the differences between the CC torque-velocity points obtained from the different methods are not very large and considerable overlap exists (see figure 3.36, pp. 314).

Similarly to the stiffness-torque relationship, the CC torque-velocity relationship does not include very early points while the torque is very low. Thus, it was not possible to obtain an accurate estimate of the maximal shortening velocity. For comparison purposes however, a rough estimate of the maximal shortening velocity could be obtained for four of the volunteers from the fitted hyperbolic curves to the grouped average torque-velocity data obtained using the torque-pairing method. Most of these velocities ranged approximately from 4 to 10 $rad \cdot sec^{-1}$ in this thesis (tables 3.10 and 3.14). Using a reasonable hypothetical value of lever arm of 0.01 m (10 mm), a range of linear maximal shortening velocity of 0.04-0.1 $m \cdot sec^{-1}$ (40-100 $mm \cdot s^{-1}$) can be obtained. The range of these estimates is greater than that for the values suggested by Cook and McDonagh (1996a) (44-56 $mm \cdot sec^{-1}$). However, the latter values fall within the 'low-end' of the range of rough estimates made in this work.

5.4. Time course of mechanical events

The estimated SEC and CC properties were used to obtain information about the time course of mechanical events in the MTC during contractions. The results are strikingly similar to time history of mechanical events predicted by the model. Faster CC shortening compared to load movement results in SEC extension and a rise in torque. During this phase more power is produced by the

CC than is delivered to the load resulting the excess power being delivered to the SEC (and to the elasticity of the force transducer rod). At the instant of same speed between the CC and the load the torque reaches its peak value. Thereafter the situation reverses with the load moving faster than the load, the SEC recoiling and the torque dropping. The work done on the SEC during the rising phase of torque is now recovered fast adding to the power delivered on the load by the CC. During this phase the peak power delivered to the load exceeds the peak power generated by the CC during the contraction.

It must be noted however that results of SEC and CC instantaneous behaviour are not available for early and late contraction times. This is because the analysis is restricted to times where the effects of muscle activation, shortening deactivation (and possibly of anatomical constraints) would be minimised (see section 4.2.1.2.3, pp. 282). As a result it is not possible to know from observations of the calculated time courses what the maximal shortening velocity of the CC is or what proportion of it was reached at the end of the contraction.

5.5. Power output

An estimate of the inertial load relative to each volunteer's contractile and elastic properties was obtained as described in section 4.7.1, pp. 363. To our knowledge, this is the first time an inertial load to a MTC has been expressed relative to its contractile and elastic properties. Despite the uncertainty concerning the exact value of the maximal shortening velocity, when the power ratio is plotted against the estimates of normalised inertia, a pattern very similar

to this observed in a model (using three dimensionless constants: ξ, H and G) appears (figure 3.59, pp. 379). An exception is the result of volunteer SH which has been discussed in the results section; the following discussion concerns only the results of the other five volunteers. A power ratio greater than one was observed over an approximately 100-fold range of normalised inertial loads. Beyond this range the power delivered to the load was smaller than the maximal CC power. According to the model, one of the reasons for the decline in power at very light inertial loads is that the muscle does not develop its maximal power. Comparison between the estimated maximal CC power (table 3.15) and that achieved during contraction against relatively light loads (figures 3.51.A-C) shows that the muscle did indeed generate maximal power during the contraction. However, there are only few points obtained from experimental observations in this low inertia region and more points might be necessary to establish the actual relationship between normalised load and power amplification. The reduction of the value of the power ratio below one at large normalised inertial loads cannot be accounted for by any of the models of MTC shortening against purely inertial loads presented in this thesis. Inspection of figures 3.53.A-C reveals that on most occasions the timing between maximal CC power and maximal power delivery to the load may not be optimal (compare with figures 3.52.A-C). At relatively heavy normalised loads the optimal torque for maximal CC power development may occur early during the contraction but near the time of peak power delivery to the load the torque may be still higher than optimal (figure 3.53.A and C; volunteers JS, SP, GO). Another reason could be that maximal CC power generation may not be achieved at all during some contractions (possibly volunteer AC; figure 3.53.B).

The modelling work in this thesis has shown (pp. 161) that as the normalised inertial load increases peak power delivery to the load is expected to occur earlier than the second peak of the CC power up to its maximal value. In the model movement of the components of the MTC may continue for an infinitely long amount of time. Moreover, the model does not include CC shortening deactivation properties. In reality however, both of these two factors may contribute to the lower than expected power ratio at large loads. Evidence for shortening deactivation prevented torque-pairing analysis beyond a certain value of angular load displacement for each volunteer. As a result of shortening deactivation power generation by the CC would decline at later times during the contraction and as a result maximal CC power might not be attained for a second time during the contraction nearer the time of peak power delivery to the load thereby reducing the amount of power delivered to the load. Moreover, even if shortening deactivation was not a factor, the movement has to stop due to the joint's anatomical constraints. That might mean that a large load might come to a stop before it has been delivered the maximal amount of power that it could have been delivered, if motion could continue for infinitely long periods. However, the reduction of the power ratio at large inertial loads as a result of deactivation and of the joint's anatomical constraints was not confirmed when modelling results not incorporating these features yielded good agreement with experimental observations (section 4.8.1, pp. 369). Perhaps, the maximal power output was overestimated as a result of not knowing the exact shape of the stiffness-torque relationship at low values of torque, leading underestimation of SEC stiffness in that region. This would cause calculation of higher CC shortening velocities and hence power at low torque values, which could cause

an overestimation of the maximal CC power. This would lead to an underestimation of the calculated power ratio.

5.6. Limitations and advantages

The limitations of the methods used in the section may be summarised as follows:

1. Accurate determination of the torque rate is important when estimating the contractile and elastic properties of a MTC.
2. The stiffness-torque and CC torque-velocity relationships are not known for early or late times during the contraction while the torque is low. This does not allow for accurate determination of the CC maximal shortening velocity and as well as the total amount of movement, and other variables based on this knowledge, of the CC and the SEC.
3. The moment arm of the tendon was not known. Applying a correction based on the results by An *et al* (1983) to express the recorded torque and angular load velocity as MTC force and shortening velocity in three out of six volunteers did not improve the variability in the calculated SEC and CC properties (see section 4.5.2, pp. 333). It is not known exactly how much the lever arm of the FDI may have changed during abductions and therefore the results. Some of this effect may have been eliminated when adjusting for the torque-angle relation (section 4.3.1.2, pp.294). However, for reasons explained in section 4.3.1.4 it was decided to focus on the results of arising from the simplest method of analysis.

Despite these limitations this method has advantages:

1. A possible solution can be found for the elastic and contractile properties of a MTC and the CC and SEC outputs during individual contractions can be obtained, during shortening contractions against inertial loads.
2. It is inexpensive and quick. The above information can be obtained from torque and a movement records, using a simple inertial loading device.
3. It is not invasive.

5.7. Future directions

In this section the CC and SEC properties have been obtained using an analytical approach. Although this approach yielded interesting results more information could have been yielded, if modelling was also applied. Such a combination might have produce for example a better estimate for the CC shortening velocity. Future work could combine both approaches.

Future work could also include validation of the method by comparing the results arising from this method with more direct measurements of the CC and SEC outputs. Such direct measurement could be obtained for example using the optic fibre technique to measure the force in the tendon and ultrasonography could be used to observe the movement in the muscle fascicles. Imaging techniques could also provide information regarding possible lever arm changes during index finger abduction that could then be used to apply corrections, if necessary and also convert the results from rotational linear units.

Contractile and elastic behaviour of the human triceps surae muscle-tendon complex

1. Summary

When a muscle (CC) shortens against a load, the length of its series elastic component (SEC) may be changing. Therefore the movement of the load represents the algebraic sum of CC shortening and SEC length change. A method was suggested in the previous section of this thesis allowing estimation of the contractile and elastic properties of a muscle-tendon complex (MTC) and the instantaneous mechanical output of the CC and of the SEC. A preliminary experiment is now described which attempts to apply the same method to the triceps surae MTC. One volunteer performed single maximal voluntary standing ankle plantar-flexions (heel-rises) against a range of inertial-gravitational loads. The ground reaction force and its centre of pressure during each heel-rise were obtained using a force platform. The position of anatomical landmarks on the foot and shank were obtained via a motion analysis system (CODA mpx30). Kinetic analysis was performed in the saggital plane. The force in the Achilles tendon and the velocity of the triceps surae (TS) MTC were calculated. From these an estimate was obtained of the contractile and elastic properties of the TS MTC and of the extent to which muscle generated power was delivered to an external load.

2. Introduction

In the previous section, experimental observations were collected from electrically evoked contractions of the first dorsal interosseus (FDI) muscle tendon complex (MTC) against purely inertial loads. A method was developed which provided possible solutions for the contractile and elastic properties of the FDI MTC which could then be used to calculate its instantaneous mechanical output during individual contractions. This made evident a 'catapult' mechanism whereby the maximal muscle-generated power could be amplified by the SEC and the inertial properties of the load.

The advantages of using the FDI MTC were discussed in the previous section. The aim of this section is to extend the experimental observations to more functional movements performed voluntarily.

3. METHODS

3.1. Volunteers

None of the volunteers for this experiment suffered from an injury or disorder that could have affected their performance during the experiments. This study was approved by the local ethical committee (RNOHT). The results of only one of these volunteers (male; age 29 years) is considered in this thesis.

3.2. Movement under study

The volunteers were asked to perform single, straight-legged, maximal, voluntary standing plantarflexions against their own body mass and weight as well as against added inertial and gravitational loads. Maximal in this context means attempting to deliver the highest power possible to the load. The details of the experimental protocol are given in section 3.4. Standing ankle plantarflexions were chosen to study because they frequently occur in everyday activities (e.g. walking) or sporting activities (e.g. running). Moreover the mechanical properties of the triceps surae MTC have been studied by other investigators and it would be interesting to compare the results of this study to those already existing in the literature.

3.3. Experimental set-up

The experimental set-up consisted of a loading apparatus, a force plate, a CODA *mpx30* motion analysis system and a P.C. for data acquisition and processing.

3.3.1. Loading apparatus

The purpose of the loading apparatus was to add inertial and gravitational resistance to each volunteer's own body mass and weight. The loading apparatus consisted of scaffold assembly with a rigid and a rotating part (figure 4.1). The rigid part was firmly attached to a pillar. The rotating part was connected through a collar onto the rigid part such that it could freely rotate in the saggital plane.

The volunteer applied force on the rotating frame through his shoulders via wide, padded surfaces attached on the frame approximately 1.87 m from its centre of rotation. In fact, the part of the rotating frame extending from the centre of rotation towards the volunteer accounted for most of its length. This minimised the change in the load experienced by the volunteer in the vertical direction as the lever rotated around its pivot point. For example starting with the rotating part horizontal, for a vertical displacement at the shoulder pads of 0.1 m, the change in the angle would be equal to the $\arcsin\left(\frac{0.1}{1.87}\right) = 0.054$ rad (3.065 degrees). As the vertical component of the force applied by the load through the pads on the volunteer's shoulders would change with the cosine of

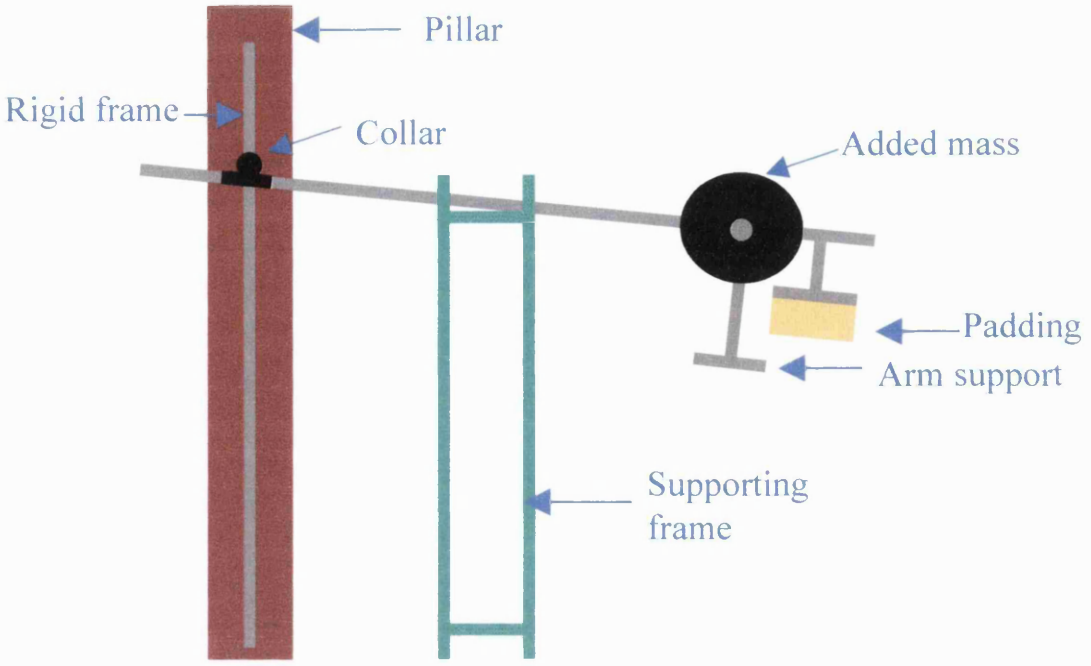

Figure 4.1. Outline of the loading apparatus.

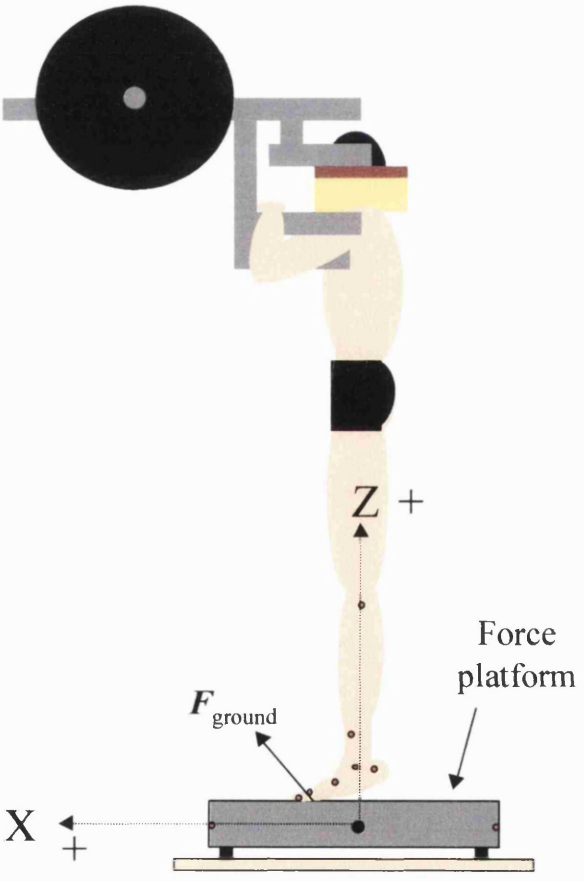

Figure 4.2. Positioning of the volunteer on the heel rise rig. During a heel rise the volunteer experiences a ground reaction force (F_{ground}) from the force platform. The axis (X and Y axis) and sign convention for forces and movements are also shown. Red dots represent markers attached on the volunteer.

this angle, the force would become 0.999 (3 d.p.) of the original force at the uppermost position in the above example, i.e. the change in the force would be negligible. The height of the rotating part could be adjusted to the volunteer's height by sliding its collar up or down along the rigid part, so that prior to the effort the rotating part was almost horizontal.

The load on the rotating frame was increased by adding on to it disks of different masses, ranging from 5-20 kg. These disks were secured on the frame via collars at a distance approximately 1.68 m from the frame's rotation centre. This added mass was not added directly above the point of application of force by the volunteer on the frame for safety purposes, but was kept relatively close to that point to minimise the ratio between the force coming from the load and the force generated by the volunteer (1.000 :0.898).

Another frame was used to support the rotating part during the rest periods between contractions at a height that would be convenient for the volunteer to slide under and lift the rotating part on his\her shoulders to an almost horizontal position before each contraction.

3.3.2. Force platform

The ankle plantarflexions were performed against different loads with the volunteer standing on Kistler type force platform (Rolls Royce). This force platform was used to measure the position and magnitude of the ground reaction force during the movement (see results and analysis section 4.1). Because the

movement was primarily performed in the saggital plane, the force and its position were recorded in the saggital plane only.

Calibration of the force plate was performed separately on the vertical (Z-) and horizontal (X-) axis. The calibration factor (250.0 $N \cdot V^{-1}$) and the time constant (1.0 sec) was the same for both sets of piezoelectric elements. The force plate and amplifier respond to the steady application of force with an exponentially decaying output signal with a time constant of 1.0 sec. The records were therefore deconvoluted to correct for this decay by adding at each instant after a convenient baseline point (1) the record minus the baseline value and (2) its integral above the baseline divided by the time constant.

3.3.1. Motion analysis system

The motion analysis system used was CODA mpx30 (Charnwood Dynamics). This system has a scanner unit which detects infrared light pulses coming from Coda markers, which are small light emitting diodes powered from small, rechargeable power packs. Detection is via three cameras rigidly attached in the scanner unit. The angular resolution of each camera is approximately 0.03 mrad resulting in a vertical and horizontal resolution of about 0.1 mm at 3 meters distance of a marker from the unit. The scanner unit is pre-calibrated by the manufacturers to detect the position of the markers in a 3D co-ordinate system, which is fixed with relation to the unit. The nominal origin of the co-ordinate system however, can be set to any desired point. (For more information see: Coda *mpx30* User Manual, Charnwood Dynamics, 1995).

Coda markers were positioned with medical double sided tape on certain anatomical landmarks on the volunteer's foot and leg as well as on the force platform. The anatomical landmarks were:

1. proximal phalanx of fifth toe
2. distal end of the firth metatarsal
3. cuboid
4. lateral malleolus
5. calcaneous (near the point of attachment of the Achilles tendon)
6. fibula
7. head of fibula

The two markers on the force platform were attached on its horizontal boundaries in the middle of the platform's thickness.

3.4. Experimental protocol

Once the markers were attached, the volunteer would perform three maximal voluntary ankle plantarflexions against each load. Each contraction was separated from the next by at least one minute of rest to minimise fatigue. Typically six to eight different loads were used in each experiment and eighteen to twenty four contractions were performed. The first load was against the volunteer's own body mass and weight. The second load was the volunteer's own body mass and weight plus those of the rotating frame. The load on the rotating part was subsequently increased by adding disks (section 3.3.1, pp. 397) in steps of 10 kg. Typically, the largest load in an experiment would be obtained by adding 40 to 60 kg on the frame.

3.5. Data acquisition

The analogue signals coming from the force plate and those coming from the motion analysis system were collected for 10 s by a separate PC in each case. Acquisition was synchronised between the two P.C.s such that starting force data acquisition would automatically trigger acquisition of movement data.. Acquisition frequency was 100 Hz for both force and movement data. The analogue signals were converted into digital via A-D converters. The software used for force data acquisition was TESTPOINT (version 3.3) and for movement data was provided by CODA. The force and movement data were stored as text files for later processing.

4. Results and analysis

4.1. Calculation of the ground reaction force

The baseline-corrected and deconvoluted force signals from all the piezoelectric elements responding to vertical (Z-) forces were added together, multiplied by the calibration factor to obtain the vertical force exerted on the force plate and by –1 to obtain the vertical component of the ground reaction force (F_Z). Similarly the horizontal (X-) component of the ground reaction force (F_X) was calculated in exactly the same manner using the corrected signals from the piezoelectric elements responding to horizontal forces. Assuming that the lateral (Y-) component of this force had negligible contribution to the performance of the movement compared to the other two and that most of the triceps surae MTC's mechanical output is used in the saggital plane, the total ground reaction force was calculated as:

$$F = \sqrt{F_Z{}^2 + F_X{}^2}$$

An example of the time course of the ground reaction force and of its components during a heel rise is shown in figure 4.3.

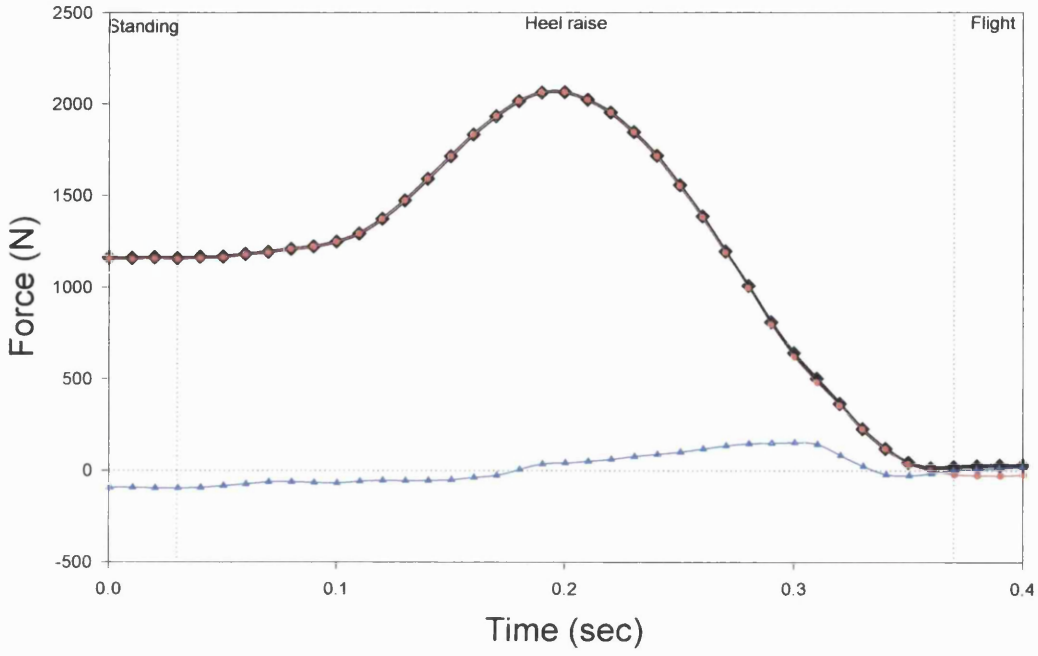

Figure 4.3. Time course of the ground reaction force (black line and diamonds) and of its vertical (red line and circles) and horizontal component (blue line and triangles) during a 'heel rise'. Three phases of the plot are shown (a) the force is almost constant during standing prior to the heel rise, (b) the force rises and drops while overcoming inertia and gravity during the heel rise, (c) the force is zero as both feet are not in contact with the force platform during this flight phase. Not all records had a flight phase.

4.2. Calculation of the position of the point of application of pressure on the force platform

The position of the point of application of force on the X-axis of the force platform (p_X) relative to the centre of the platform was calculated as:

$$p_X = \frac{-Cal}{F_Z} \cdot \left[\frac{FPL}{2} \cdot \left(f_{Z_1} + f_{Z_2} - f_{Z_3} - f_{Z_4} \right) + \frac{FPH}{2} \cdot \left(f_{X_{14}} + f_{X_{23}} \right) \right]$$

where *Cal* is the calibration factor (250 $N \cdot V^{-1}$), *FPL* is the horizontal length of the platform (0.23 m), *FPH* is the vertical distance from the piezoelectric elements to the top surface of the platform (0.06 m), *f* represents the corrected force outputs from the piezoelectric elements, which are identified with subscripts.

The vertical position of the ground reaction force acting on the volunteer's body (p_Z) was expressed relative to the surface of the force platform and it was a constant during the heel rise (p_Z=0). Thus, the position of the force in the sagittal plane was expressed relative to the centre of top surface of the force platform.

4.3. Alignment between CODA mpx30 and the force platform

The position of the force plate and of the CODA mpx30 scanner unit prior to the experiment only showed a negligible misalignment with one another (1.882 degrees) in the transverse, which was therefore ignored. A correction was

applied on the movement data such that they had the same origin with the force data. An example of a 'butterfly' force record and the movement of a marker are shown in figure 4.4.

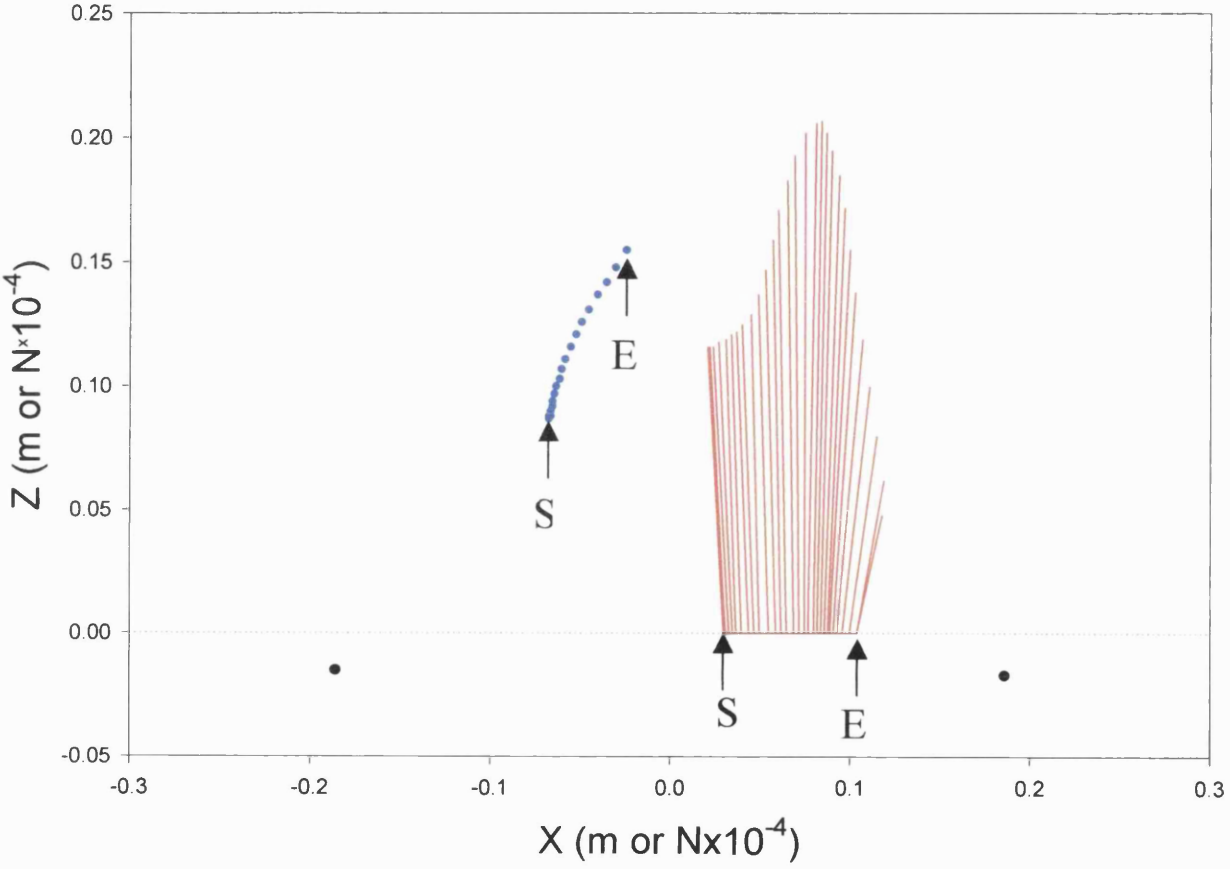

Figure 4.4. 'Butterfly' diagram (red) showing the ground reaction force vector (in N scaled by a factor of 10^{-4}) in the saggital plane. The position of the ankle marker (blue dots), the force platform boundaries in the X-axis (black dots) and the level of its upper surface (dotted line) are also shown. Arrows labelled as S and E indicate the beginning and the end of the heel rise.

4.4. Calculation of the torque around the ankle joint

The torque in the Y-axis around the centre of rotation of the foot, i.e. the torque tending to cause rotation of the foot in the sagittal plane, can be obtained as the product of the ground reaction force vector and its perpendicular distance from this centre. Therefore, in order to calculate the torque around the centre of rotation of the ankle joint due to the ground reaction force, the ground reaction force and its position as well as the position of the centre of rotation of the ankle joint must be known. The first two were calculated as described in the previous section. The following section describes how the position of the centre of rotation of the foot was calculated.

In order to estimate the centre of rotation of the foot during each heel rise, them movement of markers attached on the foot relative to the lower leg was examined. The marker position and the ground reaction force were transformed by embedding an axis system on a lower leg segment defined by the two markers attached on the fibula, with the lower one of these markers serving as the new origin. In this way the movement of the markers attached on the cuboid and on the distal end of the fifth metatarsal was observed (figure 4.5). During part of the heel rise the position of each of these two markers lies near the arc of a circle. The best fit circle on these points was obtained such that the sum of the square of the errors was minimised. The distance between the centres of the two circles ranged between 0.006 and 0.014 m. The mean value for the centre of the two best fit circles was used as an estimate of the position of the centre of foot rotation during the heel rise.

The points deviating from the circle represent early points during the movement. This deviation might have been due to some gliding within the ankle joint. This estimate of the position for the centre of foot rotation was used, together with the ground reaction force, to calculate the torque around the joint.

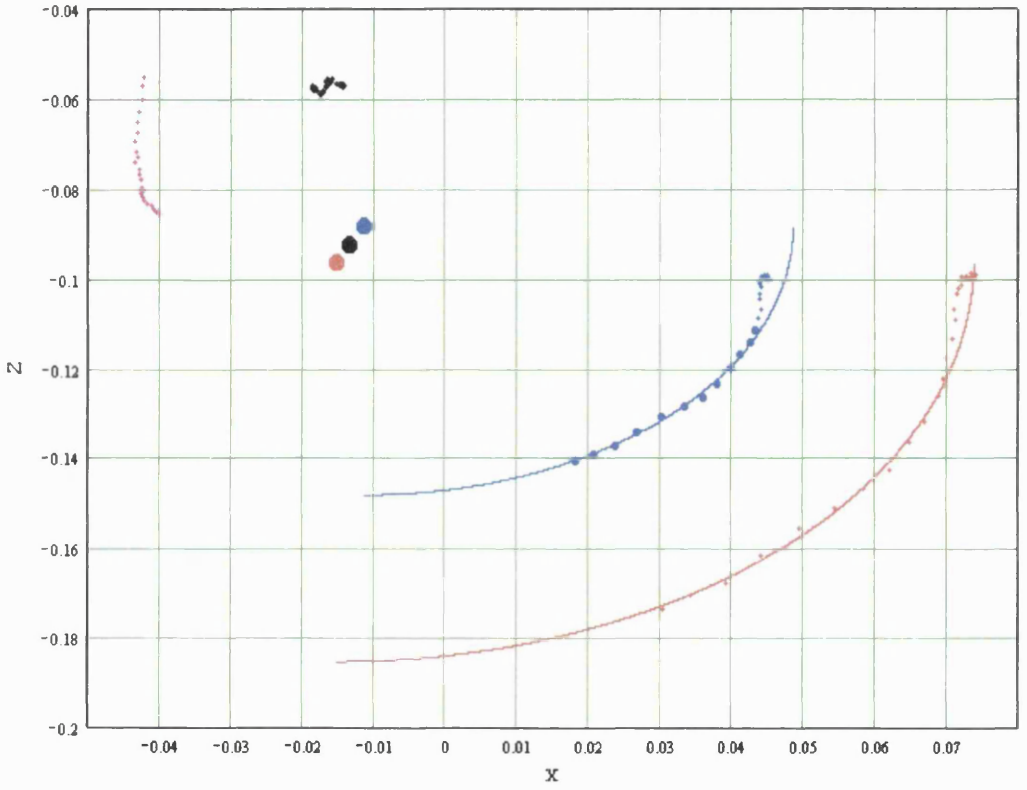

Figure 4.5. Estimating the centre of rotation of the ankle joint from marker movement. Position of the markers on the cuboid (blue dotted trace), metatarsal (red dotted trace), ankle (black dotted trace; top left) and heel (pink dotted trace; top left) during a rise, after transformation of the data. The circular arcs (blue and red arcs), the corresponding centres (blue and red dots) of the fitted circles and the mean position of the centres (black dot) are also shown. (Note that because of the scales used the arc does not appear circular in this plot). The points of the cuboid marker position fitted by the circles are shown as bold blue points. In this graph Z and X (both in m) denote the vertical and horizontal direction respectively, of the transformed data. The distance between the two centres was $8.71 \cdot 10^{-3}$ m. The SSE for the parts of the movement fitted was $4.149 \cdot 10^{-6}$ and $7.927 \cdot 10^{-6}$ for the cuboid and the metatarsal marker respectively. Notice that the heel marker (pink trace) moves with respect to the estimated foot rotation centre (large black dot) but not along the arc of a circle, indicating that estimated torque was not directly proportional to the force in the tendon. Note that although the calculated position of the centre of rotation (black dot) appears fixed in this plot, it actually translated with respect to the floor during the heel rise.

Care was taken during attachment of the heel marker on the calcaneous to palpate the heel so that the marker would be attached as close to the insertion of the Achilles tendon on the calcaneous as possible. Thus, the position of the heel marker was used as an estimate of the insertion of the triceps surae MTC to the calcaneous. The position of the heel marker during a heel rise is shown in figure 4.5. It was apparent from observations on records similar to that shown in figure 4.5 that the distance of the heel marker from the estimated rotation centre changed significantly during the movement. That means that the calculated torque around the centre of rotation of the foot was not directly proportional to the force in the MTC.

An estimate of the force in the MTC was obtained by dividing the torque by the horizontal distance between the foot rotation centre and the position of the heel marker. This distance changes during a heel rise, initially more and less during the later stages of the movement, as evidenced from figure 4.5. This estimate is based on the assumption that the majority of the force in the MTC would have a direction that is parallel to the lower leg segment defined as above. Notice that part of the force record is bell-shaped (figure 4.6) and therefore appropriate for the match-torque (or force) procedure described in the first dorsal interosseus section 4.2.1.

The movement of the MTC in the direction of the force (D_L) was estimated from the vertical displacement of the heel marker (i.e. parallel to the lower leg segment). The instantaneous shortening velocity of the MTC (V_L) was obtained as the slope of the best fit regression line through the displacement-time point at

that instant and three to four points before and after that instant. Such a velocity trace is displayed in figure 4.6.

4.5. Force pairing

It can be seen in figure 4.6 that the part of the force and linear velocity records are similar in shape to the torque and angular velocity records and therefore the method used in the first dorsal interosseus section 4.2.1 for calculation of internal parameters can also be applied on these records. As these are voluntary contractions and muscle activation is controlled by the CNS, force pairing assumes that the activation level is the same when force is the same. It is also assumed that the tricep surae length-tension relation and the history of previous contractions did not significantly affect its performance. These simplifying assumptions are critically discussed in the discussion section.

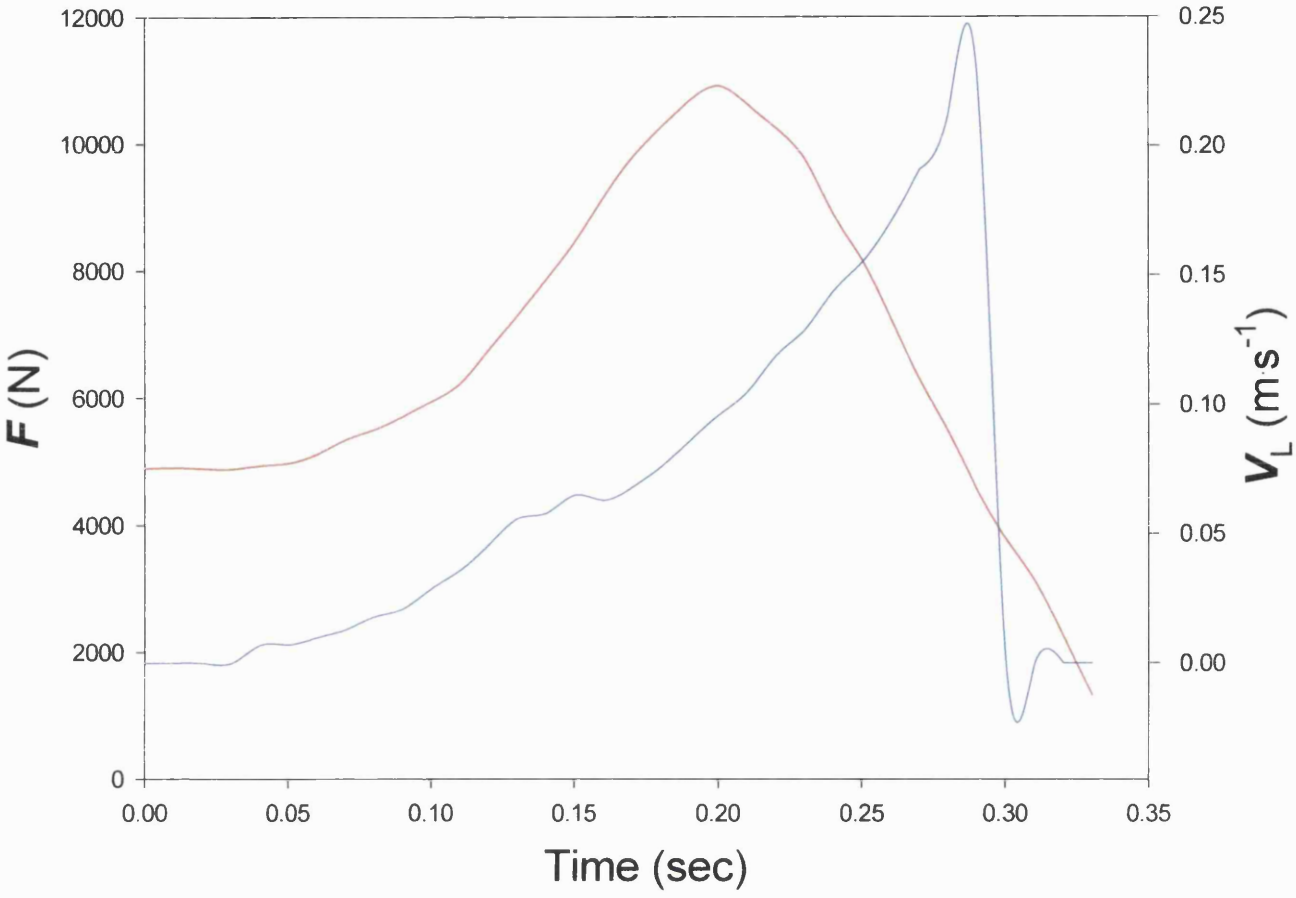

Figure 4.6. MTC force (red) and velocity (blue) during a heel rise. The direction of this force and velocity is parallel to the lower leg segment.

4.6. SEC properties

4.6.1. Force-stiffness relationship

The stiffness of the triceps surae SEC for both legs in parallel was calculated as described in the FDI section 4.2.1.3.1 (pp. 282). There seems to be a positive relationship between the stiffness and the force in the muscle-tendon complex (figure 4.7). At first sight it appears from the scatter plot as though the relationship between the two variables may be linear. However, extrapolation of a regression line through these points to low forces would intersect the force axis at a high value of positive force and the stiffness-axis at a negative value. Neither of these would make sense in physiological terms. When the stiffness and torque observations are expressed as grouped averages, the force-stiffness relationship appears to be sigmoidal. A best-fit three-parameter sigmoidal curve is shown in figure 4.7. The values of its parameters of the curve and values for its goodness of fit are shown in the legend of figure 4.7.

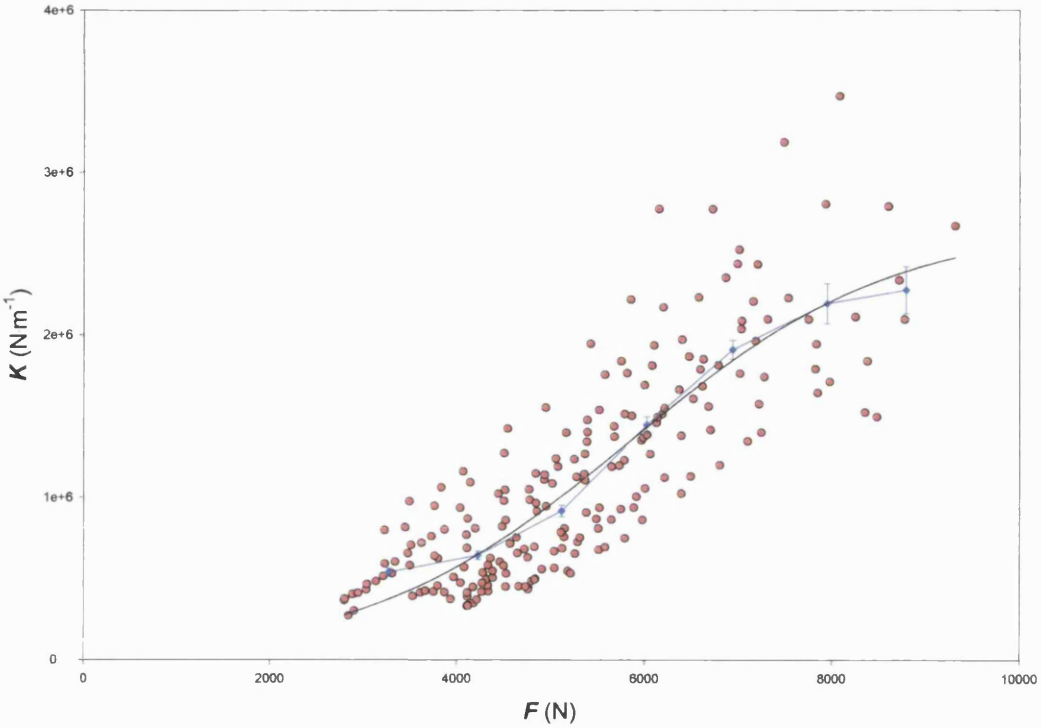

Figure 4.7. Stiffness for triceps surae SEC of both legs (***K***) plotted against force (***F***) (red points). This plot is also shown as grouped average values (blue line) including SE bars. A best-fit three parameter sigmoidal (A_0=2.689.106, A1=5.838.103, A2=1.410.103; r=0.836; CV=0.321).

4.6.2. Force-extension relationship

The force-extension relationship for the triceps surae SEC for both legs of the volunteer was calculated from the grouped average stiffness-torque relationship as the area of the SEC compliance (reciprocal of stiffness) with respect to the force using the trapezoidal rule. The result is shown in figure 4.8.

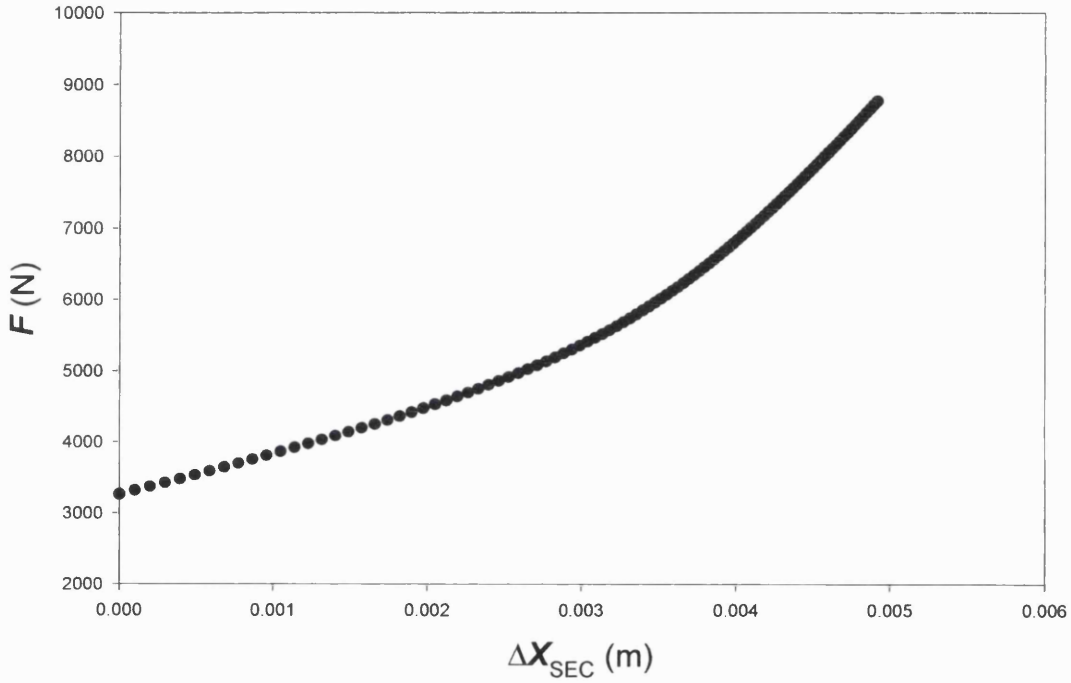

Figure 4.8. SEC force-extension relationship for both triceps surae of the volunteer. Linear interpolation has been used in order to generate more points than in the grouped average stiffness-torque relationship from which this plot was generated.

4.7. CC force-velocity output

The fitted force-stiffness relationship was used to calculate the force-velocity output for the CC in the way described in FDI section 4.2.1.3.1 (pp. 270). The CC velocity is lower when the force is low and rises to almost a plateau at high forces (figure 4.9). This plateau value appears to be at approximately 0.08 $m \cdot s^{-1}$ at forces higher than 6 kN for both legs.

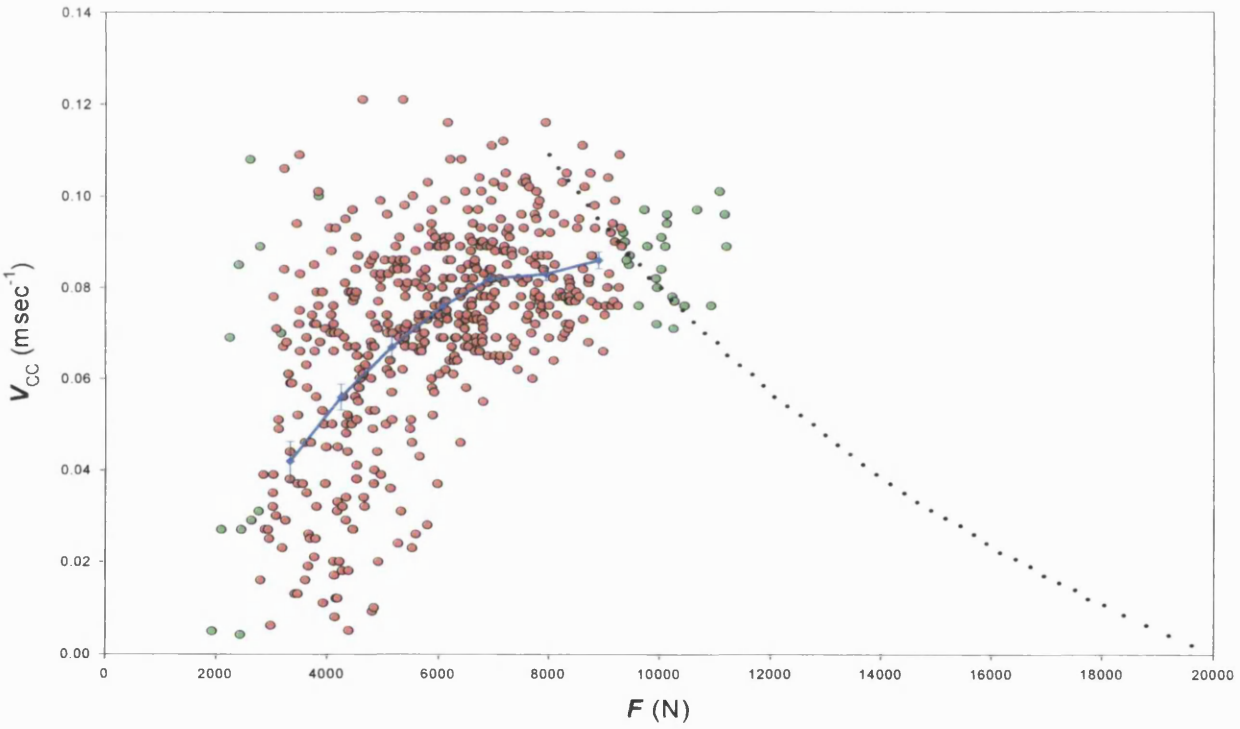

Figure 4.9. Force-velocity output calculated within and outside the range of torques for which the force-stiffness relationship is known (red and green points, respectively). The former plot is also shown in grouped average form (blue points and line). A hypothetical force-velocity curve of a fully active CC is also shown (Fmax=20 kN; Vmax=0.4 m.s-1; G=4) (black dotted line).

The time course of the CC force-velocity relationship from a number of individual contractions is shown in figure.. In general, while the force is rising during the contraction, the CC velocity rises steeply with the force initially and not so steeply while the force is approaching its peak value. This part of the relationships will be referred to in this section as the 'ascending limb'. While the force is dropping ('descending limb') from its peak value the velocity may not follow the same 'path' as during the ascending limb. The velocity may increase even more before it starts dropping back down again with the descending limb being higher than the ascending limb throughout the contraction. Alternatively, the descending limb may have lower values than the ascending limb either throughout the contraction or early after the force starts to drop but later attain values higher than in the ascending limb. It appears as though the activation pattern during voluntary contractions may be of importance for the differences observed between the two limbs of the curve.

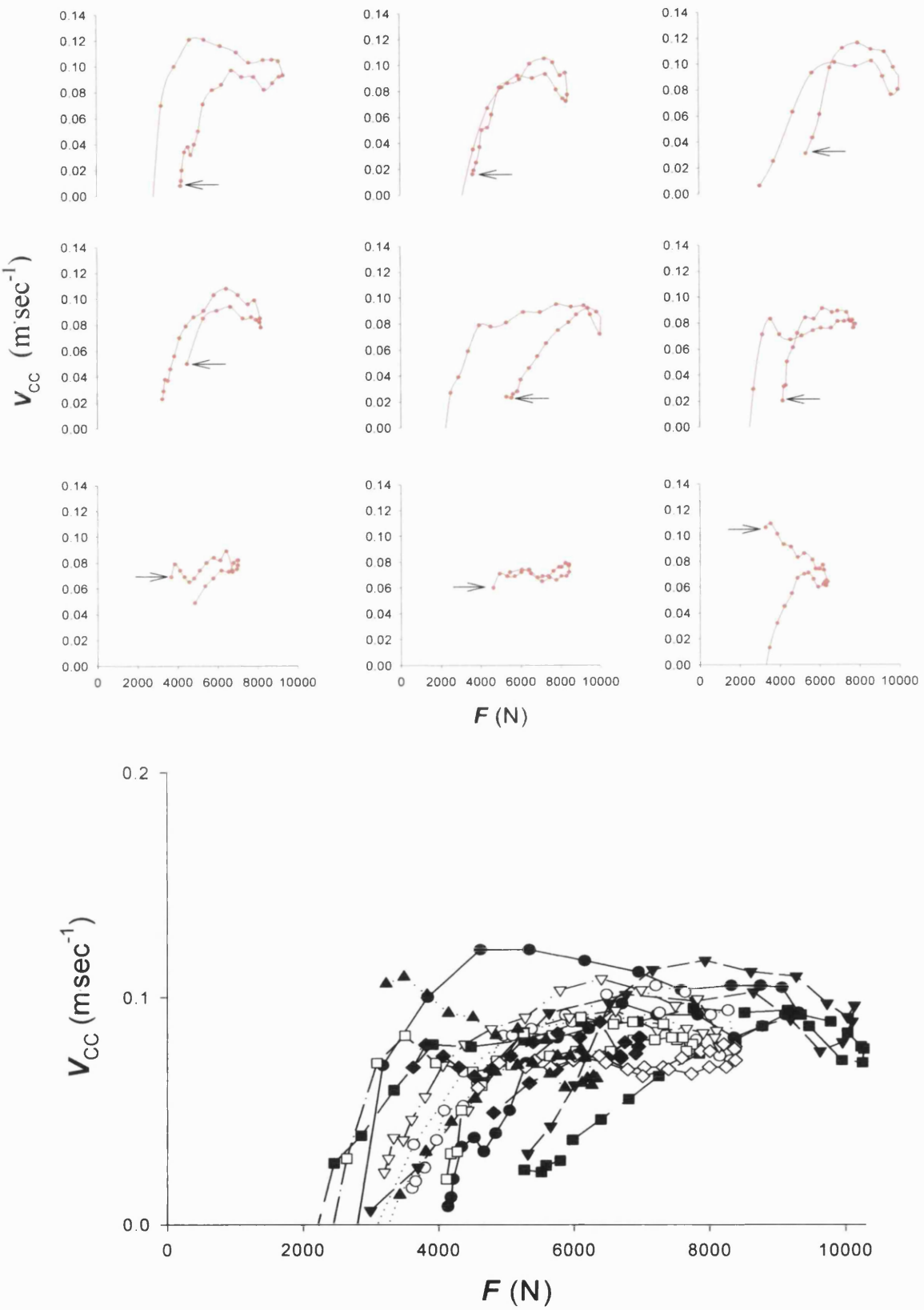

Figure 4.10 Time-course of the force-velocity output from nine contractions shown separately (red curves) and combined (bottom plot). Arrows indicate the starting end of the curve. The load added to the volunteer increases from left to right and from top to bottom for the red curves. Negative velocity values arise from late points during the contraction (not shown for the red curves). These results have been calculated for the whole range of forces achieved in the corresponding contractions, which may take values outside the range of validity of the force-stiffness relationship.

4.8. Power amplification

The instantaneous power output of the CC during a contraction can be calculated as the product of its force and velocity at any instant. Figure 4.11 shows the time course of power output for the CC and for the load (i.e. the product of the MTC force and velocity). Because the CC force-velocity relationship of the triceps surae MTC was calculated only over a limited range of force values (see figure 4.9), there was no attempt to estimate the optimal power that the CC can generate. It was possible however to calculate the ratio of the peak power delivered to the load to the peak power generated by the CC *during each contraction.* This ratio differs to the power ratio as defined in the modelling section 6.1.2.1.12 (pp. 163) as the power delivered to the load is now expressed relative to the maximal performance of the CC during each contraction and not relative to the optimal CC performance. Nevertheless, it does provide an estimate of how much more external power was obtained relative to how much power the CC put in. The distribution of these ratios for the twenty contractions performed this experiment was approximately normal with a mean of 1.104 (3 d.p.) and a standard deviation of 0.083 (3 d.p.). Thus, according to the calculations the volunteer could deliver to the external world, on average and over the range of loads considered in the particular experiment, approximately 12% more power than his muscle alone generated.

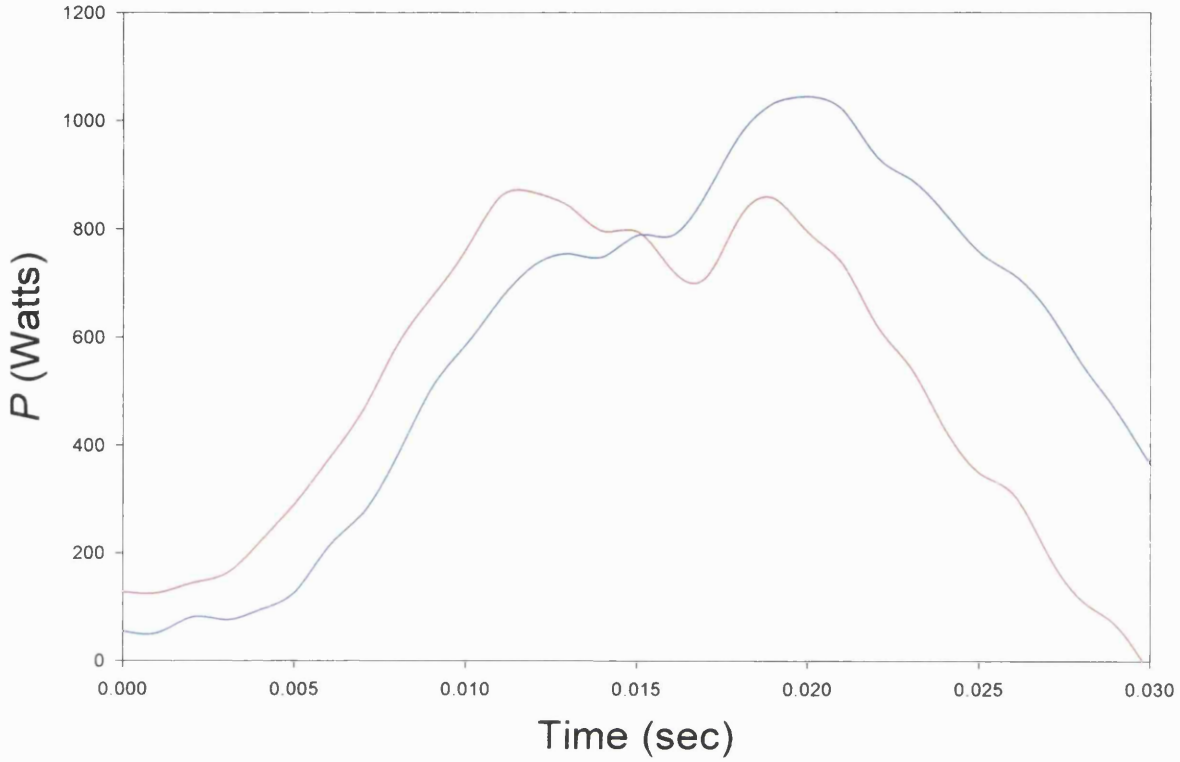

Figure 4.11. Time course of power output for the CC (red) and the load (blue). Notice how the power generated by the CC exceeds the power delivered to the load during the early half of the contraction and how the situation reverses in the later half. The ratio of peak external to peak CC power for this contraction was 1.205 (3 d.p.).

5. Discussion

The force-pairing method has been applied to maximal voluntary standing ankle plantarflexion to obtain estimates of:

1. The elastic properties of the triceps surae SEC
2. The CC force-velocity properties of the triceps surae CC
3. The extent to which the peak power developed by the triceps surae MTC exceeds the peak power developed by the triceps surae CC during each contraction.

5.1. Elastic properties

5.1.1. Stiffness-force relationship

5.1.1.1. Shape of the relationship

The grouped average triceps surae SEC stiffness-force relationship has a sigmoidal shape which is in agreement with the result obtained for the FDI SEC. Maganaris and Paul (1999) stimulated the tibialis anterior (TA) muscle in human volunteers under static conditions while recording force development via a dynamometer, tendon origin displacement and cross sectional area via real-time ultrasonography and tendon length and moment arm via magnetic resonance imaging. The TA tendon stiffness-force relationship showed a similar pattern to the result found in this work: in that the stiffness increased with force, more steeply at low forces and less steeply at higher forces. Ito *et al* (1998), using similar methodology as that of Maganaris & Paul (1999), also found a similar shape of stiffness-force relationship for the tendon of the tibialis anterior MTC. The same group (Kubo, Kanehisa, Kawakami, Fukunaga, 2000)

estimated the compliance-force relationship of the human vastus lateralis and medial gastrocnemius tendon structures *in vivo*. Both tendinous structures showed very similar behaviour in that their compliance decreased with force from 10% to 40-50% of the maximal voluntary force and thereafter became almost constant in the range of 50-100% of the maximal voluntary force. As compliance is the reciprocal of stiffness, the results from these studies are also consistent with the shape of the stiffness-force relationship reported in our work.

5.1.1. 2. Range of stiffness-force values

In this thesis the grouped average stiffness was found to increase with tendon force from approximately $5.4 \cdot 10^5$ to $2.3.10^6$ $N \cdot m^{-1}$. The corresponding tendon forces were $3.3 \cdot 10^3$ and $8.8 \cdot 10^3$ N. As these values reflect the combined result for both legs, it would be reasonable to assume that the stiffness and the force for one SEC would range between $2.7 \cdot 10^5$-$1.2 \cdot 10^6$ $N \cdot m^{-1}$ and 1.7-$4.4 \cdot 10^3$ N (i.e. half the reported values).

5.1.1.2.1. Force range

Calculation of the maximal voluntary tendon force during static contraction of the ankle plantar flexors from data reported by Kubo *et al* (2000) yields average values of approximately $2.6 \cdot 10^3$ N for sprinters and $2.7 \cdot 10^3$ N for controls. Calculations based on results by Kurokawa *et al* (2001) estimate that during a squat jump, the force in the tendon of the triceps surae is approximately $2.8 \cdot 10^3$ N on average. These results are in agreement with studies in which Achilles tendon force has been measured invasively during squat jumps using implanted

buckle transducers, showing a tendon force of approximately $2.2 \cdot 10^3$ N (Fukashiro *et al*, 1995). However, Fukashiro *et al* (1995) found the peak force in the Achilles tendon to be approximately $3.8 \cdot 10^3$ N during repetitive submaximal hopping on the spot. In another study using an implanted buckle transducer, the force in the Achilles tendon could range approximately from $5 \cdot 10^3$ to $9 \cdot 10^3$ N during running (Komi, 1990). Hopping and running include phases during which the triceps surae will be active while lengthening. This would be expected to produce bigger forces than the other activities.

Although the triceps surae tendon force values during static maximal voluntary contractions and during squat jumps reported in the literature are within the range of the tendon forces for which the grouped average stiffness-force relationship has been calculated, they are considerably lower (by about 30 %) than the maximal grouped average force reported in this thesis. One possibility for the high tendon forces in the present work might be that the Achilles tendon lever arm has been underestimated resulting in overestimation of the tendon force. Another possibility might be that the triceps surae muscle group is not maximally recruited under the conditions present during isometric force testing in the study by Kubo *et al* . Moreover, during a squat jump the knee extensors may produce appreciable upward acceleration of the body mass and as a result the triceps surae may not develop as much force as they would have had, had they been the only agonist muscle group. Triceps surae muscle recruitment during a heel-rise is possibly somewhere in between that occurring under isometric conditions or squat jumps and that occurring during hopping and running. Finally, part of the difference between the forces reported in this work

compared to those reported in the literature may be due to the possibility that the volunteer in the present study was stronger than the ones in the other studies.

5.1.1.2.2. Stiffness range

In the study by Kubo *et al* (2000) the calculated compliance of the medial gastrocnemius tendon became almost constant when force production exceeded 40-50% of the maximal voluntary isometric force. This compliance was on average $4.53 \cdot 10^{-5}$ $m \cdot N^{-1}$ for sprinters and $4.12 \cdot 10^{-5}$ $m \cdot N^{-1}$ for control subjects. The stiffness for the two groups would have therefore been $2.21 \cdot 10^{4}$ and $2.43 \cdot 10^{4}$ $N.m^{-1}$ respectively. This stiffness (or compliance) corresponds to the portion of the tendon that would be stretched only by the medial gastrocnemius muscle and the cross sectional area of this portion was assumed by Kubo *et al* to be 18% of the total cross sectional area of the tendon. Therefore, in order to obtain the stiffness for the whole tendon the stiffness values calculated above must be divided by 0.18. This yields values of $1.23 \cdot 10^{5}$ $N \cdot m^{-1}$ and $1.35 \cdot 10^{5}$ $N \cdot m^{-1}$ for the two groups.

Another calculation was performed using the data of Kurokawa *et al* (2001) by drawing a tangent by eye to the highest value of the force-extension curve for the medial gastrocnemius tendon. By measuring the slope of this tangent and by applying a correction to obtain the stiffness for the whole triceps surae tendon a value of approximately $2.5 \cdot 10^{5}$ $N \cdot m^{-1}$ was calculated. Both these values of stiffness obtained from the literature are lower and outside the range of grouped average stiffness reported in this thesis ($2.7 \cdot 10^{5}$-$1.2 \cdot 10^{6}$ $N \cdot m^{-1}$). As mentioned earlier, one possibility might be underestimation of the lever arm in the present

study which could result in overestimating stiffness. However, the difference might have been partly due to a stiffer tendon of the volunteer participating in this study and partly due to the greater tendon force achieved. Another possibility is some error introduced by the assumptions of the force-pairing method (see later discussion).

5.1.2. SEC force-extension relationship

The SEC force-extension curve calculated from the grouped average stiffness-force relationship was of the expected shape with the force rising with extension of the SEC, slowly initially and more steeply at high forces, until it becomes almost linear (see Loren and Lieber, 1995; Maganaris and Paul, 1999; Kubo *et al*, 2000; Kurokawa *et al*, 2001). In our study it is not possible to know by how much the triceps surae SEC had extended at forces before the minimum for which the stiffness-torque relationship has been calculated. However, the maximal elongation achieved within the range of forces attained in this study was $5 \cdot 10^{-3}$ m. The relatively short SEC extension observed in this study could be due to the fact that the tendon was already stretched to a high stiffness region of its stiffness-force relationship, such that a small increment in length would cause a large increment in force. Of course calculation of the SEC force-elongation properties are subject to the same methodological errors as the stiffness calculation, such as underestimation of the lever arm or error introduced by the assumptions of the force-pairing method.

5.2. CC force-velocity output

5.2.1. Shape of the force-velocity relationship

The contractile component force-velocity relationship of human muscle has been studied using skinned fibre preparations (e.g. Widrick *et al*, 1996, 1999). Human skinned fibre experiments have been performed only at a lower temperature than that encountered in the body (e.g. 15 ^{0}C; Widrick *et al*, 1996, 1999), since the fibres are not stable at 37 ^{0}C. It has been shown for several species of animals that the force velocity curves of skinned and of live fibres may be different; both preparations have a hyperbolic relationship, but it is more curved in the skinned fibres, that is they are not capable of producing such high power output as the live fibres (Ferenczi *et al*, 1984; Curtin and Woledge, 1988). In line with this the Widrick *et al* results (1996, 1999), showing a hyperbolic relation with a curvature (G) between 8 and 60 , is in accord with the best studies of human muscle in-vivo, which have taken care to separate the CC behaviour from that of the SEC (Wilkie, 1950, Cook and McDonagh, 1996a) ; these studies give curvatures (G) of 2 and 5.

.

The force-velocity plot for the tricep surae CC did not have a typical hyperbolic shape (figure 4.9, pp. 379). Instead, velocity increased with force until almost a plateau was reached. This observation would be consistent with the hypothesis that muscle maximal shortening velocity, $V_{CC_{max}}$, rises with muscle activation.

The statistical nature of the force-velocity relation in whole muscle was demonstrated by Hill (1970) in which the output in a muscle model containing

fibres of different intrinsic speeds reflected the mean output of all the fibres. This conclusion has also been confirmed experimentally (e.g. Josephson and Edman, 1988). Thus, the force-velocity relation arising from a muscle activated using maximal electrical stimuli so that all the activated fibres contract at the same time, would reflect the mean output of all the activated fibres.

During voluntary contractions however, motor units are probably recruited according to the size-principle with small slow motor units recruited at low force levels and fast large motor units at higher force levels (see general introduction). This would be equivalent to changing the muscle properties from a weaker and slower muscle to a stronger and faster one as the force level rises. Chow and Darling (1999) manipulated wrist flexor muscles' activation during 'isotonic' flexions of the wrist by allowing each volunteer to develop a certain proportion of his\her maximal isometric force before the wrist was released to move concentrically against a constant external load. The authors did not expect considerable contribution to the total movement by the SEC as the wrist flexors are small muscles not capable of generating large forces to cause appreciable stretching of their very stiff (~10^5 $N{\cdot}m^{-1}$) tendons. They found that $V_{CC_{max}}$ decreased as 'activation' decreased and they attributed this behaviour to the contractile properties of the different motor unit types recruited at the different 'activation' levels.

The tricep surae muscle group in humans contains a mixture of slow and fast fibres (e.g. Harridge *et al*, 1995; Gollnick *et al*, 1974; Edgerton *et al*, 1975). During a heel-rise the force in the Achilles tendon was found to rise and drop.

The instantaneous force-velocity relationship of the muscle would be determined by the number and intrinsic properties of the active fibres at any instant. Therefore at high forces a greater total number of motor units and a greater number of faster motor units can be recruited. This means that the muscle at a relatively high level of force would behave like a stronger and faster muscle compared to when the force is lower. Such an explanation would be consistent with the rise in the velocity with force that was observed in this work (figure 4.9).

When the tendon force exceeded 6000-7000 N the calculated velocity of the contractile component became almost constant. One possible interpretation of the force-velocity plateau might be that the motor units recruited within this range of force have fibres with similar intrinsic speeds of shortening. Possibly all or the majority of the tricep surae motor unit pool had been recruited within this force range. It has been shown that during 'ballistic' contractions the motor unit recruitment threshold may drop (Desmedt and Godaux, 1977, 1978). Assuming a lowering of the recruitment threshold for the tricep surae motor units during the maximal heel-rise efforts to be similar to that found for the tibialis anterior during 'ballistic' contractions, i.e. approximately 0.3 times the recruitment threshold (Desmedt and Godaux, 1977, 1978), it seems possible for a CC capable of generating $20 \cdot 10^3$ N or less for both legs (or $10 \cdot 10^3$ N per leg) to be fully active within this force range. It is unlikely that the volunteer in this study would have been able to develop more force than $20 \cdot 10^3$ N in his tendons as this would correspond to him lifting a weight between 500-600 kg on the balls of his feet (assuming from the data a 3:1-4:1 ratio between the load and

tendon lever arm). It is therefore reasonable to assume that all or the majority of the motor units were active at the plateau of the force-velocity relationship. Thus, the plateau may represent a small part of the force-velocity relationship of the fully active ticeps surae CC. Part of such a hypothetical force-velocity relationship is shown in figure 4.9.

It has been shown that during a squat-jump the fascicle angle in the medial gastrocnemius muscle changed on average from approximately 17.5 degrees to approximately 37 degrees (Kurokawa *et al*, 2001). As the fascicle angle increased during the squat-jump, the value of the cosine decreased causing a drop in the proportion of the actual force and increase in the movement transmitted from the fascicles to the tendon. It is likely that the fascicle angle in the gastrocnemius of the volunteer in this study also increased during the heel rise in a similar manner such that the proportion of the actual fascicle force transmitted to the tendon changed from 95% to 79%, while the movement (or velocity) transmitted increased proportionally. This would cause a leftwards and upwards move of the force velocity curve during the contraction. This is not what is observed, and so cannot explain the deviations from the hyperbolic behaviour.

Some excellent biomechanical studies, using experimental results together with models, have attempted to explain the 'externally' recorded mechanical output during movements to the mechanical output of the triceps surae muscles and tendons (e.g. Bobbert *et al*, 1986; De Graaf *et al*, 1987; Bobbert and van Ingen Schenau, 1990). In such studies, the muscle models have hyperbolic force-

velocity properties modified to include possible length-force effects. However, the results of the present study indicate that a whole muscle's force-velocity output during a voluntary movement may be very different from a typical Hill hyperbola, as the CC shortening velocity may be rising to a plateau with the rise in muscle force. It would be interesting to see how well the output of muscle models with such force-velocity relationships might fit experimental observations. It would be essential in such modelling to include a time course of muscle activation to generate the observed force-velocity plot.

In the force-velocity plot reported in this thesis the CC grouped average velocity ranged between approximately 0.044 $m{\cdot}s^{-1}$ and 0.086 $m{\cdot}s^{-1}$. Kurokawa *et al* (2001) using ultrasonography and cinematography to obtain a more direct picture of the kinematic behaviour of medial gastrocnemius fascicles in eight volunteers during squat jumps found fascicle velocity to range on average between 0 and approximately 0.15 $m{\cdot}s^{-1}$. As these were fascicle velocities, in order to obtain the corresponding velocity at the tendon these values must be divided by the cosine of the fascicle angle. At the time the peak velocity was recorded the fascicle angle was approximately 30 degrees, and therefore the fascicle velocity at the tendon ranged between 0 and 0.17 $m{\cdot}s^{-1}$. The maximal value of CC shortening velocity reported in this study is approximately half of that reported in the study of Kurokawa *et al* (2001). Considerable overlap exists in the CC shortening velocities between the two studies. The higher CC velocities reported in the study of Kurokawa *et al* might have been due to the lower force developed in the tricep surae MTC of their volunteers compared to the force values reported in this study. For example, at the time of the peak

fascicle velocity the force in the tendinous structures for both legs in the Kurokawa *et al* study can be calculated to be approximately $4.5 \cdot 10^3$ N. The electromyographic activity of the medial gastrocnemius muscle had more or less reached its plateau value at approximately 50 ms before the peak fascicle velocity was attained. The delay between onset of electromyographic activity and mechanical response in human muscle tendon complex has been shown to be approximately 50 ms (Cavanagh and Komi, 1979). Thus, muscle activation might have reached its plateau value at that time. If the same proportion of the motor unit pool is assumed to active in the two studies (possibly the whole pool), it can be seen that extrapolation of the hypothetical force-velocity curve the CC shortening velocity corresponding to $4.5 \cdot 10^3$ N force would be much closer to the value of 0.17 $m \cdot s^{-1}$.

5.2.2. Estimated time-history of the force-velocity output during individual 'heel-rises'

The time history of the force velocity relationship during individual contractions is shown in figure 4.10. It is evident from these time courses that the CC shortening velocity is different while force is rising compared to while is falling. This contrasts with the original assumption onto which the torque-pairing method is based, according to which the shortening velocity of the CC is the same when force is the same.

Possible reasons for the observed discrepancy may include the force-length relationship of the tricep surae muscle, different number of active motor units on opposite sides of the force trace and relaxing muscle fibres on the descending

limb of the force. Tendon hysterisis (e.g. Ker, 1981; Lieber *et al*, 1991) could also be a factor. However, if the relatively poor vascularity and hence limited capacity for heat exchange of the tendon is taken into consideration, not much mechanical energy dissipation as heat would be expected in the human tricep surae tendon, otherwise severe tendon damage would occur during long distance running.

The error introduced in the results by the assumptions of the force pairing method is not known. However, if during a contraction the CC shortening velocity at a given value of force while force is rising is higher than the CC velocity at the same value of force while force is falling, the calculated value of the stiffness will be overestimated. If the opposite is true for the CC velocities in the matched points, the calculated stiffness will be underestimated. In fact the latter pattern appears to be more common and so the stiffness values reported here are probably lower than the true values.

5.3. Power output and amplification

The time history of power output was similar in the majority of contractions with that predicted by the model and that shown for the FDI MTC (see the example in figure 4.11, pp. 4.19): the muscle power was exceeding the power delivered to the load during the rising phase of force while the reverse happened while force was falling. Only in two contractions was the power delivered to the load slightly less than the peak power the muscle had generated. However, even in those two contractions more power was being delivered to the load while the force was falling than while it was rising. This pattern of power output

generation by the contractile component and power delivery to the load was also observed in the study by Kurokawa *et al* (2001).

Calculations using approximate values from figure 4 in the study by Kurokawa *et al* (2001) show that the peak triceps surae muscle power was on average slightly more than 700 Watts and the peak triceps surae MTC peak power output was slightly less than 1500 Watts. These values are not much different to the muscle and MTC values attained in this study (e.g. figure 4.11,pp.4.19).

It was not as straightforward to calculate the magnitude of load in normalised terms for the heel-rise or to obtain the maximal muscle power that the CC could generate, in order to plot a power ratio-normalised load plot. However, it was found that the power delivered to the load during the heel rise could exceed the peak power the muscle could generate during a heel rise by approximately 10% on average. The reason why a smaller power amplification was observed during heel rises than during index finger abduction may include the magnitude of the load and the motor unit recruitment pattern (i.e. not all motor units active from the onset of contraction).

The ratio of the peak MTC to peak muscle power (as calculated for the whole triceps surae MTC from the data presented) in the study by Kurokawa *et al* (2001) was relatively high (~2). However, this ratio comes from squat jumps rather than straight-legged jumps. During phase I of a squat jump (-350—100 ms before toe off) the total gastrocnemius medialis MTC length remained unchanged while the muscle fascicles shortened stretching the tendinous tissues

and increasing their elastic potential energy. During straight-legged jumps not as much time may be available for the triceps surae SEC to be stretched before MTC shortening starts. It would be interesting to model the power amplification limits of such movements involving two joints and two MTC units. Nevertheless, the power amplification value of two is not far from the prediction of the simple model in this thesis in which a single MTC shortens against an inertial and gravitational load.

5.4. Limitations and advantages of the methods

It appears from the above discussion that the assumption that the velocity of the contractile component is the same when force in the MTC is the same may not be as valid for voluntary contractions as it is for electrically evoked contractions. However, it is very likely that tendon stiffness is the same when tendon force is the same. It was also shown for the FDI muscle that the method proposed here for calculating the elastic and contractile properties of a MTC is sensitive to the values of the torque rate and this also applies in the heel-rise experiments. However, despite the error introduced by the assumptions the results reported here are in general agreement with results reported in the literature from studies using more direct methods for estimating elastic and contractile properties. Moreover, the simplicity of the method proposed here is an advantage compared to other methods using a more direct approach in determining the contractile and elastic properties of human muscle tendon complexes.

5.5. Future directions

Even more information could have been obtained from the current data, if modelling of muscle and tendon properties had been combined together with the analytical approach described here and this deserves attention in the future. Future work could also include measurement of the force-length relation of the tricep surae muscle as well as measurements of the electromyographic activity of the muscle. Using this extra information an estimate of the activity level of the muscle could be made for each moment during the recording and this could be taken into account in the analysis using the force pairing method. The current method could also be validated against methods providing more direct information about the contractile and elastic properties (e.g. direct tendon force measurements, ultrasonography for fascicle angle and displacement, MRI scans for lever arm determination).

Thesis summary and conclusions

A muscle-tendon-inertial load system represented as a Hill model, consisting of a CC with a linear force velocity relationship and a SEC with a linear force-extension relationship, displays a predictable dimensionless behaviour determined only by one dimensionless constant representing the magnitude of the normalised inertial load. Introducing a gravitational force and non-linear CC and SEC properties produces deviations from the original behaviour of the system. Additional dimensionless constants equal in number to the number of added degrees of freedom introduced in the model are required to describe these deviations. Over a wide range, the inertial properties of the load and gravity act as a 'catch' mechanism allowing mechanical energy generated by the CC to be stored in the SEC and quickly released at a later time during a contraction, thereby delivering more power to the load than the CC alone could generate. This power amplification has limits such that under no conditions of shortening contractions against inertia either in the presence or in the absence of gravity, can more than twice the maximal CC power be delivered to the load.

The *in vivo* mechanical output of the human first dorsal interosseus muscle-tendon complex has been recorded while shortening actively against inertial loads; and that of the tricep surae against inertial-gravitational loads. Using a Hill model as a framework the recorded outputs have been analysed and a possible solution has been suggested to describe the series elastic and contractile properties of each of muscle-tendon complex. These properties can be used to obtain the instantaneous 'lumped' output of the contractile and elastic components during individual contractions. Power amplification-as defined in each of the two experiments- was evident in both muscle-tendon complexes.

The contractile component force-velocity output appeared to be different between the two movements. This difference was attributed mainly to the fact that the FDI muscle was electrically stimulated, whereas the TS muscle was activated voluntarily. Voluntary activation complicated the analysis, as the velocity output for a given level of force was found not to be exactly the same during the contraction while force was rising as it was while force was dropping. This difference may have introduced some error (mainly underestimation) in the TS-SEC stiffness calculation. The torque-velocity output of the FDI did not show such complications and the FDI-CC torque-velocity relationship was determined over a wide range of torque outputs. Future use of the force(torque)-pairing method in voluntary contractions must include appropriate assumptions or observations of the time course of motor unit recruitment.

The method for separating the contractile and elastic properties requires accurate determination of the torque (or force) rate. The underlying assumptions of the method are simple but, as mentioned above, additional assumptions may be required to obtain accurate information under certain conditions, such as when CC shortening deactivation is present or while motor unit recruitment/decruitment is occurring during voluntary contractions. The analytical approach used in this thesis to obtain the results could also be complemented with a modelling approach. Future work could focus on validating the results of the method proposed here against results obtained from more direct methods of determining the kinetic output of the muscle and its series elasticity.

References

Aagaard P., Andersen J., Dyhre-Poulsen P., Leffers A.M., Wagner A., Magnusson S., Halkjaer-Kristensen J., Simonsen E. (2001): A mechanism for increased contractile strength of human pennate muscle in response to strength training: changes in muscle architecture. *J. Physiol.*, **534**, 613-623.

Abbott B.C. and Wilkie D.R. (1953): The relation between velocity of shortening and the tension-length curve of skeletal muscle. *J. Physiol.*, **120**: 214-223.

Aerts P. (1998): Vertical jumping in *Galago senegalensis*: the quest for an obligate mechanical power amplifier. *Phil. Trans. R. Soc. Lond. B.*, **353**: 1607-1620.

Allen P.D. and Stainsby W.N. (1973): A 5 parameter curve: The best fit for the force:velocity relationship of in situ dog skeletal muscle. *Physiologist*, **16,** 252.

Alexander R.M.N. (1988): Elastic mechanisms in animal movement. Cambridge University Press.

Alexander R.M. and Ker R.F. (1990): Architecture of leg muscles. In *Multiple Muscle Systems: Biomechanics and Movement Organisation*, Chapter 36, pp. 568-577. Winters J.M. and Woo S.L.-Y. (eds), Springer-Verlag.

Allen P.D. and Stainsby W.N. (1973): A 5 parameter curve: The best fit for the force:velocity relationship of in situ dog skeletal muscle. *Physiologist*, **16,** 252.

An K.N., Ueba Y., Chao E.Y., Cooney W.P. and Linscheid (1983): Tendon excursion and moment arm of index finger muscles. *J. Biomech.*, **16,** 419-425.

Askew G.N. and Marsh R.L. (1997): The effects of length trajectory on the mechanical power output of mouse skeletal muscles. *J. Exp. Biol.*, **200,** 3119-3131.

Askew G.N. and Marsh R.L. (1998): Optimal shortening velocity (V/V_{max}) of skeletal muscle during contractions: Length-force effects and velocity dependent activation and deactivation. *J. Exp. Biol.*, **201,** 1527-1540.

Balnave C.D. and Allen D.G. (1996): The effect of muscle length on intracellular calcium and force in single fibres from mouse skeletal muscle. *J. Physiol.*, **492,** 705-713.

Bennett-Clark H.C. (1975): The energetics of the jump of the locust *Schistocerca gregaria*. *J. Exp. Biol*, **63**: 53-83.

Bennet M.B., Ker R.F., Dimery N.J. and Alexander R.McN. (1986): Mechanical properties of various mammalian tendons. *J. Zool., Lond.*, **209,** 537-548.

Bergström J. (1962): Muscle electrolytes in man. Scand. J. Clin. Lab. Invest., Suppl. **68**:1-110

Blix M.(1895): Die länge und die spannung des muskels. Dritte abhandlung. *Skand. Arch. Physiol.*, **5,** 150-172; Vierte abhandlung, *Scand.Arch.Physiol.*, **5,** 173-206. Quoted by Gordon *et al*, 1966a.

Bobbert M.F., Huijing P.A. and van Ingen Schenau G.J. (1986a): A model of the human triceps surae muscle-tendon complex applied to jumping. *J. Biomech.*, **19** (11): 887-889.

Bobbert M.F., Huijing P.A. and van Ingen Schenau G.J. (1986b): An estimation of power output and work done by the human triceps surae muscle-tendon complex in jumping. *J. Biomech.*, **19** (11): 899-906.

Bobbert M.F. and van Ingen Schenau G.J. (1990): Isokinetic plantar flexion: Experimental results and model calculations. *J. Biomech.*, **23** (2): 105-119.

Bobbet M.F. and van Soest A.J. ''Noek'' (2001): Why do people jump the way they do? *Exrc. Sport Sci. Rev.*, 29 (3): 95-102.

Bottinelli R., Canepari M., Pellegrino M.A. and Reggiani C. (1996): Force-velocity properties of human skeletal muscle fibres: myosin heavy chain isoform and temperature dependence. *J. Physiol.*, **495,** 573-586.

Bruce S.A., Johnson S., Phillips S.K. and Woledge R.C. (1992): Prediction of the length-force relation of adductor pollicis muscle from its internal structure. In Third Vienna Muscle Symposium. Freilinger G. and Deutinger M. (ed.), pp. 61-64, Blackwell-MZV, Vienna.

Burkholder T.J. and Lieber R.L. (2001): Sarcomere length operating range of vertebrate muscles during movement. J. Exp. Biol., **204,** 1529-1536.

Caldwell G.E. (1995): Tendon elasticity and relative length: Effects on the Hill two-component muscle model. *J. Appl. Biomech.*, **11**: 1-24.

Cavanagh P.R. and Komi P.V. (1979): Electromechanical delay in human skeletal muscle under concentric and eccentric contractions. *Eur. J. Appl. Occup. Physiol.*, **42** (3):159-163.

Cecchi G., Colomo F. and Lombardi V. (1978): Force-velocity relation in normal and nitrate-treated frog single muscle fibres during rise of tension in an isometric tetanus. *J. Physiol.*, **285,** 257-273.

Chow J.W. and Darling W.G. (1999): The maximum shortening velocity of muscle should be scaled with activation. *J. Appl. Physiol.*, **86,** 1025-1999.

Claflin D.R., Faulkner J.A. (1989): The force-velocity relationship at high shortening velocities in the soleus muscle of the rat. *J. Physiol.*, **411,** 627-637.

Clarke R.S.J., Hellon R.F. and Lind A.R. (1958): The duration of sustained contractions of the human forearm at different muscle temperatures. *J. Physiol.*, **143,** 454-473.

Close R.I. (1972): The relations between sarcomere length and characteristics of isometric twitch contractions of frog sartorius muscle. *J. Physiol.*, **220,** 745-762.

Cook C.S., Santello M. and McDonagh M.J.N. (1995): An *in vivo* measurement of muscle stiffness in man. *J. Physiol.*, **483**: 86 *P*.

Cook C.S. and McDonagh M.J.N. (1995): Force responses to controlled stretches of electrically stimulated human muscle-tendon complex. *Exp. Physiol.*, **80**: 477-490

Cook C.S. and McDonagh M.J.N. (1996a): Force responses to constant-velocity shortening of electrically stimulated human muscle-tendon complex. *J. Appl. Physiol.*, **81** (1): 384-392.

Cook C.S. and McDonagh M.J.N. (1996b): Measurement of muscle and tendon stiffness in man. *Eur. J. Appl. Physiol.*, **72**: 380-382.

Curtin N.A., Gardner-Medwin A.R. and Woledge R.C. (1998): Predictions of the time course of force and power output by dogfish white muscle fibres during brief tetani. *J. Exp. Biol.*, 201: 103-114.

Curtin N.A. and Woledge R.C. (1988): Power output and force-velocity relationship of live fibres from white myotomal muscle of the dogfish, *scyliorhinus canicula. J. Exp. Biol.*, **140**: 187-197.

Davies C.T. and Young K. (1983): Effect of temperature on the contractile properties and muscle power of triceps surae in humans. *J. Appl. Physiol.*, **55**:191-195.

Davies C.T. and Young K. (1985): Effect of heating on the contractile properties of triceps surae and maximal power output during jumping in elderly men. *Gerontology*, **31** (1): 1-5.

De Ruiter C.J. and De Haan A. (2000): Temperature effect on the force/velocity relationship of the fresh and fatigued human adductor pollicis muscle. *Pflügers Arch.-Eur. J. Physiol.*, **440,** 163-170.

De Ruiter C.J. and De Haan A. (2001): Similar effects of cooling and fatigue on eccentric and concentric force-velocity relationships in human muscle. *J. Appl. Physiol.*, **90,** 2109-2116.

de Graaf J.B., Bobbert M.F., Tetterloo W.E. and van Ingen Schenau G.J. (1987): Mechanical output about the ankle in countermovement jumps and jumps with extended knee. *Human Mov.Sci.*, **6**: 333-347.

De Haan A. (1988): Comparison of force-velocity characteristics obtained using twitches and tetani from *in situ* rat skeletal muscles. *Q. J. Exp. Physiol.*, **73,** 131-133.

De Haan A. (1998): The influence of stimulation frequency on force-velocity characteristics of *in situ* rat medial gastrocnemious muscle. *Exp. Physiol.*, **83,** 77-84.

De Ruiter C.J. and De Haan A. (2000): Temperature effect on the force/velocity relationship of the fresh and fatigued human adductor pollicis muscle. *Pflügers Arch.-Eur. J. Physiol.*, **440**: 163-170.

De Ruiter C.J. and De Haan A. (2001): Similar effects of cooling and fatigue on eccentric and concentric force-velocity relationships in human muscle. *J. Appl. Physiol.*, **90** (6): 2109-2116.

De Ruiter C.J., De Haan A., Jones D.A. and Sargeant A.J. (1998): Shortening-induced force depression in human adductor pollicis muscle. *J. Physiol.*,**507**, 583-591.

Desmedt J.E. and Godaux E. (1977): Ballistic contractions man: Characteristic recruitment pattern of single motor units of the tibialis anterior muscle. *J. Physiol.*, **264,** 673-693.

Desmedt J.E. and Godaux E. (1978): Ballistic contractions in fast or slow human muscles: Discharge patterns of single motor units. *J. Physiol.*, **285,** 185-196.

Diamant J., Keller A., Baer E., Litt M. and Arridge G.C. (1972): Collagen: ultrastructure and its relation to mechanical properties as a function of ageing. *Proc. R. Soc. Lond. B.*, **180,** 293-315.

Edgerton V.R., Smith J.L. and Simpson D.R. (1975): Muscle fibre type populations of human leg muscles. *Histochem. J.*, **7**: 259-266.

Edman K.A.P. (1979): The velocity of unloaded shortening and its relation to sarcomere length and isometric force in vertebrate muscle fibres. *J. Physiol.*, **291,** 143-159.

Edman K.A.P. (1988): Double-hyperbolic force-velocity relation in frog muscle fibres. *J. Physiol.*, **404,** 301-321.

Edman K.A.P., Caputo C. and Lou F. (1993): Depression of tetanic force induced by loaded shortening of frog muscle fibres. *J. Physiol.*, **466**, 535-552.

Edman K.A.P., Mulieri L.A. and Scubon-Mulieri B. (1976): Non-hyperbolic force velocity relationship in single muscle fibres. *Acta Physiol. Scand.*, **98,** 143-156.

Endo M. (1972): Stretch-induced increase in activation of skinned muscle fibres by calcium. *Nature (New Biology)*, **237,** 211-213.

Epstein M. and Herzog W. (1998): *Theoritical models of skeletal muscle.* Herzog W. and Epstein M. (ed). Wiley, Chichester.

Ettema G.J. and Huijing P.A. (1994): Skeletal muscle stiffness in static and dynamic contractions. *J. Biomech.*, 27 (11): 1361-1368.

Faulkner J.A., Jones D.A., Round J.M. and Edwards R.H.T. (1980): Dynamics of energetic processes in human muscle. In: Exercise Bioenergetics and Gas Exchange, P.Cerretelli and B.J. Whipp (eds.), New York: Elsevier, 1980, p.81-90.

Fenn W.O. and Marsh B.S. (1935): Muscular force at different speeds of shortening. *J. Physiol.*, **85,** 277-297.

Ferenczi M.A., Goldman Y.E. and Simmons R.M. (1984): The dependence of force and shortening velocity on substrate concentration in skinned muscle fibres from *Rana Temporaria. J. Physiol.*, **350**: 519-543.

Fukashiro S, Komi PV, Jarvinen M, Miyashita M. (1995): In vivo Achilles tendon loading during jumping in humans. *Eur. J. Appl. Physiol. Occup. Physiol.*, **71** (5): 453-458.

Gerrits H.L., De Haan A., Hopman M.T.E., Var Der Woude L.H.V. and Sargeant A.J. (2000): Influence of muscle temperature on the contractile properties of the quadriceps muscle in humans with spinal cord injury. *Clin. Sci.*, **98,** 31-38.

Gollnick P.D., Sjödin B., Karlsson J., Jansson E. and Saltin B. (1974): Human soleus muscle: A comparison of fibre composition and enzyme activities with other leg muscles. *Pflügers Arch.*, **348**: 247-255.

Gordon A.M., Huxley A.F. and Julian F.J. (1966a): Tension development in highly stretched vertebrate muscle fibres. *J. Physiol.*, **184,** 143-169.

Gordon A.M., Huxley A.F. and Julian F.J. (1966b): The variation in tension with sarcomere length in vertebrate muscle fibres. *J. Physiol.*, **184,** 170-192.

Granzier H.L.M., Burns D.H. and Pollack G.H. (1989): Sarcomere length dependence of the force-velocity relation in single frog muscle fibres. *Biophys. J.*, **55,** 499-507.

Harridge S.D.R., Bottinelli R., Canepari M., Pellegrino M.A., Reggiani C., Esbjörnsson M. and Saltin B. (1996): Whole-muscle and single fibre contractile properties and myosin heavy chain isoforms in humans. *Pflügers Arch.-Eur. J. Physiol.*, **432,** 913-920.

Harridge, S.D.R., White M.J., Carrington C.A., Goodman M., Cumins P. (1995): Electrically evoked torque-velocity characteristics and isomyosin composition of the triceps surae in young and elderly men. *Acta Physiol. Scand.*, **15**:469-477.

Heidenhain R.(1864): *Mechanische Leistung, Wärmeentwicklung und Stoffumsatz bei der Muskelthätigkeit*. P.93. Leipzig Breitkopf und Hartel. Quoted by Gordon *et al*, 1966a.

Herbert R.D., Moseley A.M., Butler J.E. and Gandevia S.C. (2002): Change in length of relaxed fascicles and tendons with knee and ankle movement in humans. *J. Physiol.*, **539,** 637-645.

Herzog W. (2000a): Cellular and molecular muscle mechanics. In: *Skeletal muscle mechanics. From mechanics to function.* Herzog (ed). Wiley, Chichester, pp. 33-52.

Herzog W. (2000b): Considerations on *in vivo* muscle function. In: *Skeletal muscle mechanics. From mechanics to function.* Herzog (ed). Wiley, Chichester, pp. 259-266.

Herzog W. and Gál (1999): Tendon. In: Biomechanics of the musculo-skeletal system, pp. 127-147. Nigg B.M. and Herzog W. (ed), Wiley, Chichester.

Herzog W., Leonard T.R. and Wu J.Z. (2000): The relationship between force depression following shortening and mechanical work in skeletal muscle. *J. Biomech.*, **33**:659-668.

Herzog W. and ter Keurs H.E.D.J. (1988): A method for the determination of the force-length relation of selected in-vivo human skeletal muscle *Pflügers Arch.*, **411,** 637-641.

Hill A.V. (1938): The heat of shortening and the dynamic constants of muscle. *Proc. R. Soc. London B,* **126,**136-195.

Hill A.V. (1970): *First and last experiments in muscle mechanics.* Cambridge University Press, Cambridge.

Hof A.L. (1997): Correcting for limb inertia and compliance in fast ergometers. J. Biomech. **30**(3):295-297.

Hof A.L.(1990): Effects of muscle elasticity in walking and running. In *Multiple Muscle Systems: Biomechanics and Movement Organisation*, Chapter 38, pp. 591-607. Winters J.M. and Woo S.L.-Y. (eds), Springer-Verlag.

Hof A.L., Van Zandwijk J.P. and Bobbert M.F. (2002): Mechanics of human triceps surae muscle in walking, running and jumping. *Acta Physiol. Scand.*, **174**, 17-30.

Huxley A.F. (1957): Muscle structure and theories of contraction. *Prog. Biophys. Biophys. Chem.*, **7**: 255-318.

Huxley A.F. and Niedergerke R. (1954): Structural changes in muscle during contraction. Interference microscopy of living fibres. *Nature*, **173,** 971-973.

Huxley A.F. and Peachey L.D. (1959): The maximum length for contraction in striated muscle. *J. Physiol.*, **146,** 55*P*-56*P*.

Huxley A.F. and Peachey L.D. (1961): The maximum length for contraction in vertebrate striated muscle. *J. Physiol.*, **161,** 150-165.

Huxley A.F. and Simmons R.M. (1971): Proposed mechanism of force generation in striated muscle. *Nature*, **233,** 533-538.

Huxley H. and Hanson J. (1954): Changes in the cross-striations of muscle during contraction and stretch and their structural interpretation. *Nature*, **173,** 973-976.

Ichinose Y., Kawakami Y., Ito M. and Fukunaga T. (1997): Estimation of active force-length characteristics of human vastus lateralis muscle. *Acta Anat.*, **159,** 78-83.

Ichinose Y., Kawakami Y., Ito M., Kanehisa H. and Fukunaga T. (2000): In vivo estimation of contraction velocity of human vastus lateralis muscle during 'isokinetic' action. *J. Appl. Physiol.*, **88**: 851-856.

Ito M., Kawakami Y., Ichinose Y., Fukashiro S. and Fukunaga T. (1998): Nonisometric behaviour of fascicles during isometric contractions of a human muscle. *J. Appl. Physiol.*, **85** (4): 1230-1235.

Jewell and Wilkie D.R. (1958): An analysis of the mechanical components in frog's striated muscle. *J. Physiol.*, **143,** 515-540.

Josephson R.K. and Edman K.A.P. (1988): The consequences of fibre heterogeneity on the force-velocity relation of skeletal muscle. *Acta Physiol. Scand.*, **132,** 341-352.

Julian F.J., Rome L.C., Stephenson D.G., Striz S. (1986): The maximum speed of shortening in living and skinned frog muscle fibres. *J. Physiol.*, **370,** 181-19

Kawakami Y., Kumagai K., Huijing P.A., Hijikata T. And Fukunaga T. (2000): The length-force characteristics of human gastrocnemious and soleus muscles *in vivo*. In: *Skeletal muscle mechanics. From mechanics to function.* Herzog (ed). Wiley, Chchester, pp. 327-341.

Kawakami Y. and Lieber R.L. (2000): Interaction between series compliance and sarcomere kinetics determines internal sarcomere shortening during fixed-end contraction. *J. Biomech.*, **33,** 1249-1255.

Kaye G.W.C. and Laby T.H. (1973): Tables of physical and chemical constants and some mathematical functions. Longman Group Limited, London, 14th edition.

Ker R.F. (1981): Dynamic tensile properties of the plantaris tendon of sheep (*ovis aries*). *J. Exp. Biol.*, **93**: 283-302.

Ker R.F. (1999): The design of soft collagenous load-bearing tissues. *J. Exp. Biol.*, **202**: 3315-3324.

Ker R.F., Alexander R,McN. and Bennett M.B. (1988): Why are mammalian muscles so thick? *J. Zool., Lond.,* **216,** 309-324.

Kerr, R.F. (1981): Dynamic tensile properties of sheep plantaris tendon (*Ovis aries*). *J. Exp. Biol.*, **93,** 283-302.

Ker R.F. (1999): The design of soft collagenous load-bearing tissues. *J. Exp. Biol.*, **202**, 3315-3324.

Ker R.F., Alexander R.McN. and Bennett (1988): Why are mammalian tendons so thick? *J. Zool. Lond.*, **216,** 309-324.

Komi P.V. (1990): Relevance of *in vivo* force measurements to human biomechanics. *J. Biomech.*, **23,** 23-34.

Kubo K., Kanehisa H., Kawakami Y. and Fukunaga T. (2000): Elasticity of tendon structures of the lower limbs in sprinters. *Acta Physiol. Scand.*, **168,** 327-335.

Kumagai K., Abe T., Brechue W.F., Ryushi T., Takano S., Mizuno M. (2000): Sprint performance is related to muscle fascicle length in male 100-m sprinters. *J. Appl. Physiol.*, **88**(3): 811- 816

Kurokawa S., Fukunaga T. and Fukashiro S. (2001): Behaviour of fascicles and tendinous structures of human gastrocnemious during vertical jumping. *J. Appl. Physiol.*, **90** (4): 1349-1358.

Lännergren J. (1978): The force-velocity relation of isolated twitch and slow muscle fibres of *xenopus laevis*. *J. Physiol.*, **283,** 501-521.

Larsson L.D. and Moss R.L. (1993): Maximum velocity of shortening in relation to myosin isoform composition in single fibres from human skeletal muscle. *J. Physiol.*, **472,** 595-614.

Lee H.-D., Suter E. and Herzog W. (1999): Force depression in human quadriceps femoris following voluntary shortening contractions. *J. Appl. Physiol.*, **87** (5): 1651-1655.

Lieber R.L., Leonard M.E., Brown C.G. and Trestik C.L. (1991): Frog semitendinosis tendon load-strain and stress-strain properties during passive loading. *Am. J. Physiol.*, **261,** C86-C92.

Linari M, Dobbie I, Reconditi M, Koubassova N, Irving M, Piazzesi G, Lombardi V.: The stiffness of skeletal muscle in isometric contraction and rigor: the fraction of myosin heads bound to actin. *Biophys. J.,* **74,** 2459-2473.

Loren, G.J. and Lieber R. (1995): Tendon biomechanical properties enhance human wrist muscle specialisation. *J. Biomech.*, 28(7): 791-797.

Low B.B. (1956): Mathematics. Longmans, Green and Co., London.

Macpherson L. (1953): A method for determining the force-velocity relation of muscle from two isometric contractions. *J. Physiol.*, **122,** 172-177.

Maganaris C.N. and Baltzopoulos V. (2000): *In vivo* mechanics of maximum isometric muscle contraction in man: Implications for modelling-based estimates of muscle specific tension. In: *Skeletal muscle mechanics. From mechanics to function.* Herzog (ed). Wiley, Chchester, pp. 267-287.

Maganaris C.N. and Paul J.P. (1999): *In vivo* human tendon mechanical properties. *J. Physiol.*, **521,** 307-313.

Maganaris C.N. and Paul J.P. (2000a): Load-elongation characteristics of in vivo human tendon and aponeurosis. *J. Exp. Biol.*, **203,** 751-756.

Maganaris C.N. and Paul J.P. (2000b): In vivo human tendinous tissue stretch upon maximum force generation. *J. Biomech.*, **33,** 1453-1459.

Maganaris C.N. and Sargeant A.J. (2001): Force-length characteristics of in vivo human skeletal muscle. *J. Physiol.*, **531*P***: 157*P*.

Magnusson S.P., Aagaard P., Larsson B. and Kjaer M. (2000): Passive energy absorption by human muscle-tendon unit is unaffected by increase in intramuscular temperature. *J. Appl. Physiol.*, **88**(4):1215-20.

Maréchal G. and Beckers-Bleukx G. (1998): Effect of nitric oxide on the maximal velocity of shortening of a mouse skeletal muscle. *Pflügers Arch.*, **436,** 906-913.

Maréchal G. and Gailly P. (1999): Effects of nitric oxide on the contraction of skeletal muscle. *Cell. Mol. Life Sci.*, **55,** 1088-1102.

Marsh R.L. and Bennett (1986): Thermal dependence of contractile properties of skeletal muscle from the lizard *Sceloporus occidentalis* with comments on methods for fitting and comparing force-velocity curves. *J. Exp. Biol.*, **126**: 63-77.

McMahon T.A. and Bonner J.T. (1983): On size and life. Scientific American Library Books, Inc., USA.

Morgan D.L. (1977): Separation of active and passive components of short-range stiffness of muscle. *Am. J. Physiol.*, **232,** C45-C49.

Morrison R.J., Miller CC 3rd and Reid M.B. (1996): Nitric oxide effects on shortening velocity and power production in the rat diaphragm. *J. Appl. Physiol.*, **80,** 1065-1069.

Nigg B.M., Herzog W. (1999): Biomechanics of the musculo-skeletal system. 2nd edition,Wiley, Chichester.

Peplowski M.M. and Marsh R.L. (1997): Work and power output in the hindlimb muscles of cuban tree frogs *osteopilus septentrionalis* during jumping. *J. Exp. Biol.*, **200**:2861-2870.

Proske U. and Morgan D.L. (1987): Tendon stiffness: methods of measurement and significance for the control of movement. A review. *J. Biomech.*, **20,** 75-82.

Rack P.M.H. and Westbury D.R. (1969): The effects of length and stimulus rate on tension in the isometric cat soleus muscle. *J. Physiol.*, **204,** 443-460.

Rall J.A. and Woledge R.C. (1990): Influence of temperature on mechanics and energetics of muscle contraction. *Am. J. Physiol.*, **259,** R197-R203.

Ramsey R.W. and Street S.F. (1940): The isometric length-tension diagram of isolated skeletal muscle fibres of the frog. *J. Cell. Comp. Physiol.,* **15,** 11-34.

Ranatunga K.W. (1984): The force-velocity relation of rat fast- and slow-twitch muscles examined at different temperatures. *J. Physiol.*, **351,** 517-529.

Ranatunga K.W., Sharpe B. and Turnbull B. (1987): Contractions of a human skeletal muscle at different temperatures. *J. Physiol.*, **390**: 383-395.

Rassier D.E. and Herzog W. (2000): Length dependence of force production and Ca^{2+} sensitivity in skeletal muscle. In: *Skeletal muscle mechanics. From mechanics to function.* Herzog (ed). Wiley, Chchester, pp. 71-86.

Rassier D.E., MacIntosh B.R. and Herzog W. (1999): Length dependence of active force production in skeletal muscle. *J. Appl. Physiol.*, **86,** 1445-1457.

Rigby, B.J., Hirai N., Spkes J.D. and Eyring H. (1959): The mechanical properties of the rat tail tendon. *J. Gen. Physiol.*, **43,** 265-283.

Rome L.C., Funke R.P., Alexander R.McN., Lutz G., Aldridge H., Scott F. And Freadman M. (1988): Why animals have different fibre types. *Nature*, **335,** 824-827.

Schiaffino S. and Reggiani C. (1996): Molecular diversity of myofibrilar proteins: Gene regulation and functional significance. *Physiol. Rev.*, **76,** 371-423.

Snyder W.S., Nasset E.S., Karhausen L.R., Howells G.P., Tipton I.H. (1981): Report on the task group on reference man. ICRP No.23. Pergamon Press, Oxford.

Silver F.H., Christiansen D.L., Snowhill P.B. and Chen Y. (2000): Role of storage on changes in the mechanical properties of tendon and self-assembled collagen fibres. *Connect. Tissue Res.*, **41**(2):155-164.

Stienen G.J.M., Kiers J.L., Bottinelli R. and Reggiani C. (1996): Myofibrillar ATPase activity in skinned human skeletal muscle fibres: fibre type and temperature dependence. *J. Physiol.*, **493,** 299-307.

Van Leeuwen J.L. and Spoor C.W. (1992): Modelling mechanically stable muscle architectures. *Philos. Trans. R. Soc. Lond. B. Biol. Sci.*, **336,** 275-292.

Wang X.T. and Ker R.F. (1995): Creep rupture of wallaby tail tendons. *J.Exp.Biol.*, **198**, 831-845.

Wang X.T., Ker R.F. and Alexander R.McN. (1995): Fatigue rupture of wallaby tail tendons. *J.Exp.Biol.*, **198**, 847-852.

Widrick J.J., Knuth S.T., Norenberg K.M., Romatowski J.G., Bain J.L.W., Riley D.A., Karhanek M., Trappe S.W., Trappe T.A., Costill D.L. and Fitts R.H. (1999): Effect of a 17 day spaceflight on contractile properties of human soleus muscle fibres. *J. Physiol.*, **516,** 915-930.

Widrick J.J., Trappe S.W., Costill D.L. and Fitts R.H. (1996): Force-velocity and force-power properties of single fibres from elite master runners and sedentary men. *Am. J. Physiol.*, **271,** C676-C683.

Wilkie D.R. (1950): The relation between force and velocity in human muscle. *J. Physiol.*, **110**: 249-280.

Winters J.M. (1990): Hill-based muscle models: A systems engineering perspective. In: Multiple Muscle Systems: Biomechanics and Movement Organization. J.M. Winters and S.L.-Y. Woo (eds), Springer-Verlag.

Woittiez R.D., Huijing P.A., Boom H.B.K. and Rozendal R.H. (1984): A three-dimensional muscle model: a quantified relation between form and function of skeletal muscle. *J. Morphol.*, **182,** 95-113.

Woledge, R.C., Curtin N.A. and Homsher E. (1985): Energetic aspects of muscle contraction. Academic Press, London.

Zuurbier C.J., Everard A.J., van der Wees P. And Huijing P.A. (1994): Length-force characteristics of the aponeurosis in the passive and active muscle condition and in the isolated condition. *J. Biomech.*, **27,** 445-453.

Appendices

1. Derivation of a hyperbolic SEC force-extension equation

A rectangular hyperbola is a hyperbola whose asymptotes are at right angles with one another. When these asymptotes are rotated by 45^0 to coincide with the X and Y axes the equation that describes the hyperbola is of the form:

$$y \cdot x = c \quad (1)$$

In this equation, x and y are the co-ordinates of any point lying on the curve and c is a constant equal to one half of the square of the distance of the vertex of the hyperbola from the origin. Such a curve is illustrated underneath. In this figure the X and Y axis are also the asymptotes.

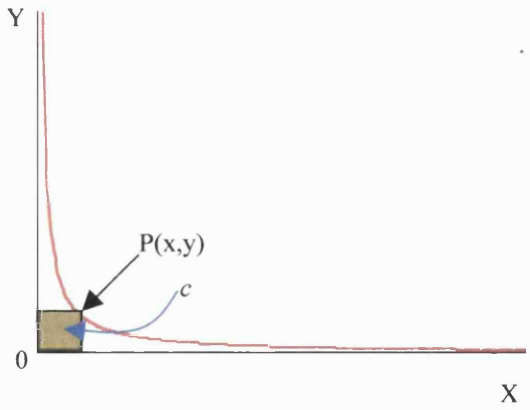

According to the sign convention used in this thesis, SEC extension has a positive sign. A SEC force-extension relationship can be thought of as part of a hyperbola as the one shown in the figure in the next page. A small part of the rotated rectangular hyperbola is selected and used to represent the force extension properties of the SEC. The bottom graph shows that selected part of the top curve expanded, rotated anticlockwise by 90^0 and with the axis labelled

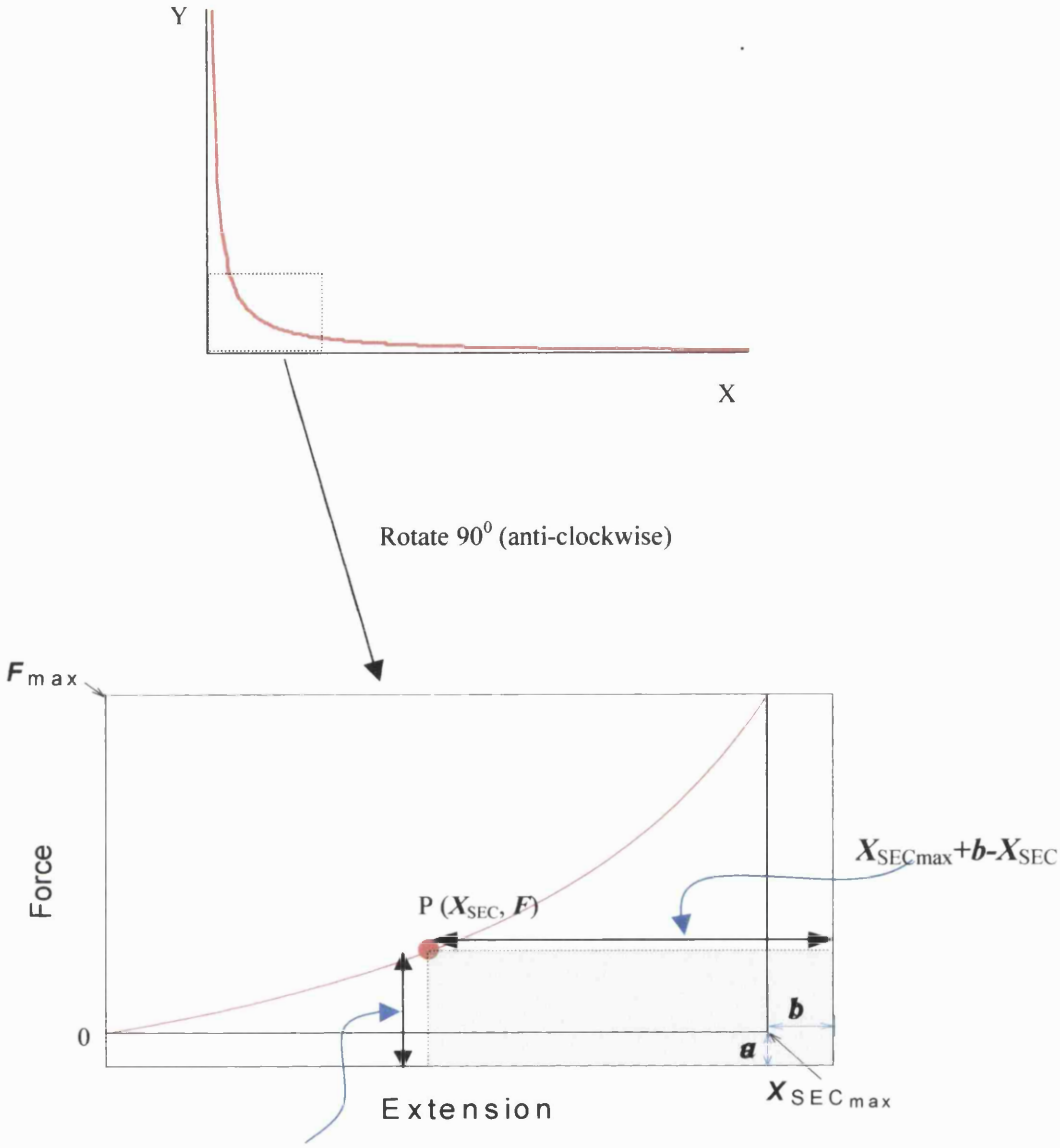

to resemble the familiar SEC force-extension curves. Notice that as a result of the anticlockwise 90^0 rotation the X-axis of the selected part of the hyperbola now becomes the Y-axis and is labelled force. Also, the Y-axis of the selected part of the hyperbola now becomes the X-axis of the force-extension curve and is labelled as extension. According to equation (1) that describes a rectangular

hyperbola, the product of the co-ordinates x and y of any point on such a curve is equal to c, which is a constant. This product gives the area of a rectangle with a diagonal through points (0,0) and (x,y). As a result of the 90^0 anticlockwise rotation and the scaling, for each point P on the force-extension curve with co-ordinates (X_{SEC}, F), it is the area of a rectangle with a height equal to $F + a$ and a width equal to $X_{SEC_{\max}} + b - X_{SEC}$ that stays constant. This area is shown by the shaded area under the SEC force-extension curve above. According to equation (1), the product of the values of its two co-ordinates, which is equal to the area bounded by the dotted lines and parts of the surrounding frame (shaded area), is the same as the product of the co-ordinates of any other point lying on this curve. A convenient way of writing an equation for the SEC force-extension curve shown above is:

$$(F + a) \cdot (X_{SEC_{\max}} + b - X_{SEC}) = (F_{\max} + a) \cdot b \quad (2)$$

The right side of the equation shows the product of a particular point on the curve, which is when force and extension are maximal. The right and left sides of the equation are equal by definition. Notice the similarity of equation (2) with Hill's 1938 force-velocity equation.

In order to derive an expression for force as a function of SEC extension the following process is followed. Dividing both sides by $F_{\max} \cdot X_{SEC_{\max}}$ the above equation can be written as:

$$\frac{(F + a)}{F_{\max}} \cdot \frac{(X_{SEC_{\max}} + b - X_{SEC})}{X_{SEC_{\max}}} = \frac{(F_{\max} + a)}{F_{\max}} \cdot \frac{b}{X_{SEC_{\max}}}$$

This equation can be written in normalised (dimensionless) form as:

$$\left(\varphi+\frac{a}{F_{\max}}\right)\cdot\left(1+\frac{b}{X_{SEC_{\max}}}-\chi_{SEC}\right)=\left(1+\frac{a}{F_{\max}}\right)\cdot\frac{b}{X_{SEC_{\max}}} \quad (3)$$

In this equation φ is the normalised force and χ is the normalised extension.

When $\varphi = 0$, $\chi_{SEC} = 0$ and we can therefore write:

$$\frac{a}{F_{\max}}\cdot\left(1+\frac{b}{X_{SEC_{\max}}}\right)=\left(1+\frac{a}{F_{\max}}\right)\cdot\frac{b}{X_{SEC_{\max}}}$$

Expanding both sides:

$$\frac{a}{F_{\max}}+\frac{a}{F_{\max}}\cdot\frac{b}{X_{SEC_{\max}}}=\frac{b}{X_{SEC_{\max}}}+\frac{a}{F_{\max}}\cdot\frac{b}{X_{SEC_{\max}}}$$

Simplifying:

$$\frac{a}{F_{\max}}=\frac{b}{X_{SEC_{\max}}}$$

Using the symbol H to represent the reciprocal of these two equal ratios and substituting into equation 2:

$$\left(\varphi+\frac{1}{H}\right)\cdot\left(1+\frac{1}{H}-\chi_{SEC}\right)=\left(1+\frac{1}{H}\right)\cdot\frac{1}{H} \quad (4)$$

Expanding:

$$\varphi+\frac{\varphi}{H}-\varphi\cdot\chi_{SEC}+\frac{1}{H}+\frac{1}{H^2}-\frac{\chi_{SEC}}{H}=\frac{1}{H}+\frac{1}{H^2}$$

Simplifying:

$$\varphi+\frac{\varphi}{H}-\varphi\cdot\chi_{SEC}-\frac{\chi_{SEC}}{H}=0$$

Rearranging:

$$\varphi+\frac{\varphi}{H}-\varphi\cdot\chi_{SEC}=\frac{\chi_{SEC}}{H}$$

Factorising the left side:

$$\left(1+\frac{1}{H}-\chi_{SEC}\right)\cdot\varphi=\frac{\chi_{SEC}}{H}$$

Rearranging:

$$\varphi=\frac{\chi_{SEC}}{H\cdot\left(1+\frac{1}{H}-\chi_{SEC}\right)}$$

This last expression can also be written as:

$$\varphi=\frac{\chi_{SEC}}{1+H\cdot(1-\chi_{SEC})}$$

This is an expression giving the normalised force as a function of the normalised extension and the constant *H*. *H* determines the curvature of the force-extension relationship. An expression of the normalised extension can of course be obtained: equation (4) is solved for extension instead of force (equation 5):

$$\chi_{SEC}=\frac{f\cdot(H+1)}{f\cdot H+1} \quad (4)$$

In order to move back into the dimensioned properties, equation (4) must be multiplied by $F_{\max}$ and equation (5) by $X_{SEC_{\max}}$.

2. Table 2.I from Woledge *et al*, 1985 (pp. 49)

TABLE 2.I

Some properties of Hill's equation

Hill's equation, giving the relation between force P and velocity V, is generally written as

$$(P + a)(V + b) = (P_0 + a)b \tag{T-1}$$

where P_0 is the force exerted when $V = 0$ and a and b are constants having the dimensions of force and velocity, respectively. It can be seen that the equation is a rectangular hyperbola with asymptotes at $-a$ and $-b$.

The velocity at $P = 0$ is termed V_{max}. Making these substitutions in Eq. (T-1):

$$a(V_{max} + b) = (P_0 + a)b$$

$$aV_{max} + ab = P_0 b + ab$$

$$aV_{max} = P_0 b$$

$$V_{max}/b = P_0/a \tag{T-2}$$

This ratio is a dimensionless constant. It is sometimes convenient to write Hill's equation in a form in which all terms are dimensionless, that is, as the relation between P/P_0 and V/V_{max}. This is achieved by dividing Eq. (T-1) by $P_0 V_{max}$, which gives

$$(P/P_0 + a/P_0)(V/V_{max} + b/V_{max}) = (1 + a/P_0)b/V_{max}$$

Writing P' for P/P_0, V' for V/V_{max}, and G for P_0/a [$= V_{max}/b$, see Eq. (T-2) above]

$$(P' + 1/G)(V' + 1/G) = (1 + 1/G)(1/G)$$

$$P'V' + P'/G + V'/G = 1/G$$

$$P'(V' + 1/G) = (1 - V')(1/G)$$

$$P' = (1 - V')/(1 + V'G) \tag{T-3}$$

$$V' = (1 - P')/(1 + P'G) \tag{T-4}$$

In this dimensionless form the equation is symmetrical, as is shown by comparison of Eqs. (T-3) and (T-4). Both asymptotes are equal to $-1/G$. The maximum power output (force × velocity) occurs when $P' = V'$ and is, in dimensionless terms, $P'V'$. Writing M for the value of P' at which force is equal to V'

$$M = (1 - M)/(1 + MG)$$

$$GM^2 + 2M - 1 = 0$$

Solving for M gives

$$M = [\sqrt{(1 + G)} - 1]/G \tag{T-5}$$

and the normalized maximum power output (M^2) is

$$M^2 = (2 + G - 2\sqrt{(1 + G)})/G^2 \tag{T-6}$$

The power output is of course $M^2 \cdot P_0 \cdot V_{max}$, which would be in milliwatts if P_0 is in newtons and V_{max} is in millimeters per second.

From Eqs. (T-5) and (T-6) it is clear that the value of the maximum power output (M^2) and the force (and velocity, M) at which maximum power is produced both depend on the curvature ($G = P_0/a$) of the force-velocity curve.

3. Method for estimating the friction coefficient of a decelerating rotating object

The torque due to friction, Tq_f, is proportional to the angular velocity, ω, of the rotating object:

$$Tq_f = k_f \cdot \omega$$

k_f is the proportionality constant or the friction coefficient.

The rate of decline in the kinetic energy, KE, of the freely rotating object is:

$$\frac{d}{dt}(KE) = Tq_f \cdot \omega$$

This expression is of course equivalent to:

$$\frac{d}{dt}(KE) = k_f \cdot \omega^2$$

As

$$KE = \frac{MI \cdot \omega^2}{2}$$

rearranging yields:

$$\omega^2 = \frac{2 \cdot KE}{MI}$$

and therefore the rate of change of KE can be written as:

$$\frac{d}{dt}(KE) = k_f \cdot \left(\frac{2 \cdot KE}{MI}\right) \qquad (1)$$

In the absence of any torque to the rotating object other than a frictional torque, its KE may decline exponentially as:

$$KE = KE_0 \cdot e^{-\frac{t}{\tau}}$$

where KE_0 is the peak value of KE, t is the time and τ is the time constant having the same units as t.

Differentiating the last expression yields:

$$\frac{d}{dt}(KE) = -\frac{KE_0}{\tau} \cdot e^{-\frac{t}{\tau}}$$

which is equivalent to:

$$\frac{d}{dt}(KE) = -\frac{KE}{\tau} \qquad (2)$$

Equating expressions (1) and (2):

$$k_f \cdot \left(\frac{2 \cdot KE}{MI}\right) = -\frac{KE}{\tau}$$

Solving the last expression for k_f yields:

$$k_f = -\frac{MI}{2 \cdot \tau}$$

Thus in order to estimate the value of the friction coefficient two quantities must be known: MI and τ.

MI of the inertial load was calculated and measured as described in the methods. τ was estimated by fitting an exponential curve on the angular velocity trace of the rotating load. This trace was obtained via the motion analysis system CODA*mpx30*.

4. Abstract publications

1. A. Galantis , S.D.R. Harridge and R.C. Woledge (2000): Using kinetic data to separate the contractile and elastic properties of the human triceps surae muscle-tendon complex. J. Physiol., **523. *P.***, 236 *P.* For correct version of figure 1 see erratum in *J. Physiol.*, **531. *P.***, 16S, 2001.
2. A. Galantis , S.D.R. Harridge and R.C. Woledge (2001): Separating the elastic and contractile properties of a muscle-tendon complex using the human first dorsal interosseous. *J. Physiol.*, **528.P.**, 51-52*P.*
3. A. Galantis , S.D.R. Harridge and R.C. Woledge (2001): Properties of the first dorsal interosseous muscle-tendon complex during electrically evoked contractions. *J. Physiol.*, **531.P.**, 39 *P.*
4. A. Galantis and R.C. Woledge (2002): The theoretical limits to the power output of a muscle tendon complex with inertial and gravitational loads. *Comp. Biochem. Physiol.*, **132**: S72.

(Bush *et al.* 1997). These computer controlled 'prod' stimuli occurred at the start of any of the 250 ms quadrants in the metronome cycle in a pseudo-random sequence. The four simultaneous EMG signals (2 surface and 2 intramuscular) were filtered (10 Hz to 1 kHz) and sampled at 2·5 kHz with a CED-1401 interface and Spike2 software. They were rectified and averaged offline, over 20–30 cycles for each stimulus-aligned quadrant, and integral values for each reflex response were then computed.

In most cases peaks in the EMGs representing reflex responses to the prod stimuli were modulated with respect to the phase of the cycle, independently of the on-going background activity. The degree and pattern of modulation differed between the surface and intramuscular electrodes, and the ratio of the reflex response to background EMG activity was generally larger in the latter. These results suggest that the different motor unit populations evidently represented by the intramuscular and surface recordings are modulated in different ways by the CNS.

Bush, B.M.H., Butler, D., Redmond, N.M., Westphely, H., Whitlock, T. & Bateman, A. (1997). *J. Physiol.* **504.P**, 63*P*.

De Luca, C.J. (1997). *J. Appl. Biomech.* **13**, 135–163.

Doemges, F. & Rack, P.M.H. (1992). *J. Physiol.* **447**, 563–573.

Xia, R. & Bush, B.M.H. (1996). *J. Physiol.* **497.P**, 108*P*.

Using kinetic data to separate the contractile and elastic properties of the human triceps surae muscle–tendon complex

A. Galantis, S.D.R. Harridge* and R.C. Woledge

*University College London Institute of Human Performance, RNOHT, Brockley Hill, Stanmore HA7 4PL and *Department of Physiology, Royal Free and University College Medical School, Rowland Hill Street, London, UK*

During movement the power generated by the contractile component (CC) of a muscle is applied to the external load via series elastic components (SEC). Because the elasticity can store and release energy the instantaneous mechanical power output of the CC (P_{CC}) may be different from the externally recorded power (P_{EXT}).

A fully active muscle acting on an inertial load through a spring generates a force which passes through a maximum. This characteristic can be used to determine the relative contribution to the power output of both muscle and elasticity. Choosing two time points at which the force is equal and comparing the velocity of the load at these time points allows the determination of the compliance of SEC, the velocity of CC and thus P_{CC}.

Figure 1 shows an example in which an inertial and gravitational load is provided to the triceps surae of a male subject by his body mass. In this example the subject performed a maximum jump with straight legs whilst on a force platform from which the ground reaction force could be measured. In addition, a motion analysis system (CODA mpx30) was used to follow the position of markers placed on the foot and lower leg. The angular velocity of the foot (ω) was calculated from the movement data. The torque (T) was given as the product of the ground reaction force (represented as a vector in the saggital plane) and its distance from the centre of rotation of the foot. These observations were made with the approval of the local Ethical Committee.

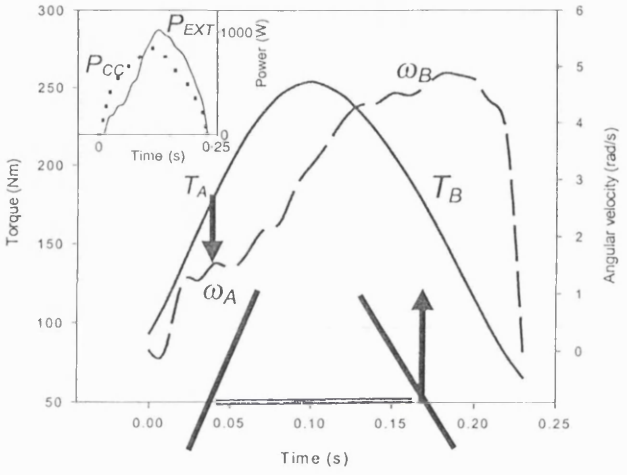

Figure 1. Time course of T (continuous curve) and ω (dashed curve). A line has been drawn joining two arbitrary chosen points (T_A and T_B) of equal T. Vertical lines show the corresponding angular velocities. The slopes of the tangents to T_A and T_B are equal to the corresponding rates of change of T ($\dot{T}$). Inset shows the external power (continuous curve) and calculated muscle power (dotted curve).

The assumptions made in the calculation of P_{CC} are that both ω_{CC} and the torsional stiffness of the SEC (k) are the same for any points of equal T, such as T_A and T_B in Figure 1.

$$k = \frac{\dot{T}_B - \dot{T}_A}{\omega_A - \omega_B}, \tag{1}$$

$$\omega_{CC} = \frac{\omega_B \dot{T}_A - \omega_A \dot{T}_B}{\dot{T}_A - \dot{T}_B}, \tag{2}$$

$$P_{CC} = T\omega_{CC}. \tag{3}$$

This method allows a link between *in vivo* observations and the properties of muscle tendon complexes (MTCs) inside the body. It could therefore be used for studying the functional compliance of the MTC, the differential contribution of the CC and SEC to the mechanical power output and the dynamic properties of an MTC, from external observations of simple movements.

S.H. is a Wellcome Trust Fellow.

ERRATUM

Journal of Physiology (2000) **523.P**, 236*P*

Using kinetic data to separate the contractile and elastic properties of the human triceps surae muscle–tendon complex

A. Galantis, S.D.R. Harridge* and R.C. Woledge

*University College London Institute of Human Performance, RNOHT, Brockley Hill, Stanmore HA7 4PL and *Department of Physiology, Royal Free and University College Medical School, Rowland Hill Street, London, UK*

The correct version of Figure 1 should have appeared as follows:

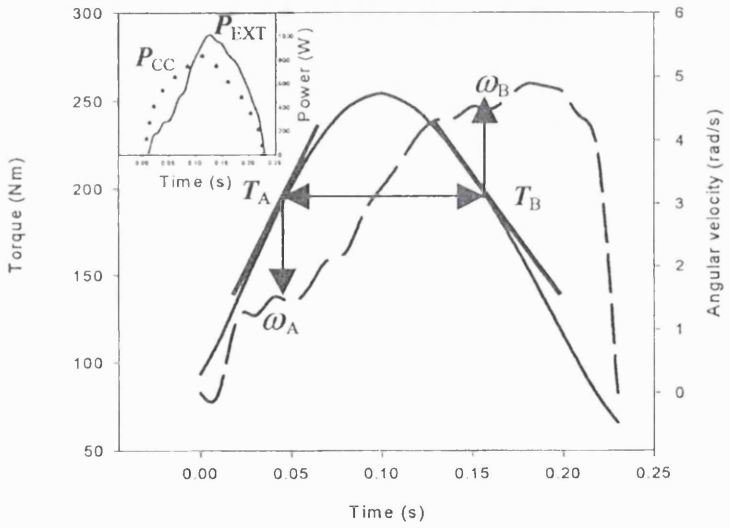

Figure 1. Time course of T (continuous curve) and ω (dashed curve). A line has been drawn joining two arbitrarily chosen points (T_A and T_B) of equal T. Vertical lines show the corresponding angular velocities. The slopes of the tangents to T_A and T_B are equal to the corresponding rates of change of T ($\dot{T}$). Inset shows the external power (continuous curve) and calculated muscle power (dotted curve).

affect rowing efficiency or economy. Although non-significant relationships were observed between $\dot{V}_{O_2,max}$ and GE or EC, further longitudinal studies need to be conducted before a measurable link between training and efficiency can be discounted.

Brouwer, E. (1957). *Acta. Physiol. Pharmacol. Neerl.* **6**, 795–802.
Horowitz, J.F., Sidossis, L.S. & Coyle, E.F. (1994). *Int. J. Sports Med.* **15**, 152–157.

The effect of 6 weeks of sprint training on the growth hormone response to repeated maximal cycle ergometer exercise

K.A. Stokes, M.E. Nevill, P.W. Cherry, G.M. Hall* and H.K.A. Lakomy

*Department of Physical Education, Sports Science and Recreation Management, Loughborough University, Leicestershire LE11 3TU and *St George's Hospital Medical School, University of London, London SW17 0RE, UK*

A single 30 s cycle ergometer sprint produces a distinct increase in serum growth hormone (hGH) concentration with levels remaining elevated for at least 60 min post-exercise (Stokes *et al.* 1999). Nevill *et al.* (1996) studied the metabolic and hormonal responses to a single 30 s treadmill sprint in sprint- and endurance-trained individuals. It was found that sprint-trained individuals had a larger hGH response to sprinting than endurance-trained individuals. The aim of this study was to examine the effect of 6 weeks of a prescribed sprint-training programme on the hGH response to cycle ergometer sprinting. After ethical approval was obtained, sixteen male subjects were assigned to a training (TR) group ($n = 8$) or a control (CON) group ($n = 8$). Each subject completed two main trials consisting of two all-out 30 s efforts separated by 60 min of passive recovery on two occasions, once before and once following a 6 week training period. Blood samples were taken in a seated position via a venous cannula at rest, post-warm-up and 5, 10, 20, 30, 40 and 60 min after each sprint. During the 6 week training period, the TR group completed three supervised sprint-training sessions per week in addition to their normal activity. Control subjects continued with their normal activity. Data were analysed using a three- or four-way ANOVA with repeated measures over time.

Peak (PPO) and mean (MPO) power output increased by 6% and 5%, respectively, in the TR group over the training period (mean ± S.E.M. = 1385 ± 56 to 1468 ± 51 W, $P < 0{\cdot}05$ and 665 ± 27 to 696 ± 21 W, $P < 0{\cdot}05$). Blood lactate concentration and blood pH did not change over the training period but plasma ammonia concentration was lower in the TR group after training (202·6 ± 15·9 to 165·1 ± 9·9 μmol l^{-1}, $P < 0{\cdot}05$) with no change in the CON group. Highest measured mean serum hGH concentration was lower in all subjects in the TR group after training, resulting in a mean decrease of more than 40% (20·5 ± 6·2 to 11·6 ± 5·0 mU l^{-1}, $P < 0{\cdot}05$). There was no pattern of change in serum hGH concentration in the CON group. No differences were found between the pre- and post-training serum cortisol concentrations. This study has shown that a short period of sprint training results in a smaller hGH response to repeated maximal cycle ergometer sprinting. Therefore the larger hGH response to sprinting previously seen in sprint-trained compared with endurance-trained athletes does not appear to be due to sprint-training *per se*.

Nevill, M.E., Holmyard, D.J., Hall, G.M., Allsop, P., van Oosterhout, A., Burrin, J.M. & Nevill, A.M. (1996). *Eur. J. Appl. Physiol.* **72**, 460–467.
Stokes, K.A., Nevill, M.E., Hall, G.M., Lakomy, H.K.A. & Cherry, P.W. (1999). *J. Physiol.* **515**, 75P.

Separating the contractile from the elastic properties of a muscle–tendon complex using the human first dorsal interosseous

A. Galantis, S.D.R. Harridge* and R.C. Woledge

*UCL Institute of Human Performance, RNOHT, Brockley Hill, Stanmore, Middlesex HA7 4PL and *Department of Physiology, Royal Free and University College Medical School, Rowland Hill Street, London NW3 2PF, UK*

The power delivered to an external load (P_{EXT}) by a muscle–tendon complex is the sum of the power generated by its contractile component (CC) and that of its series elastic component (SEC). Mathematical analysis shows that when the external load is purely inertial, P_{EXT} can exceed the maximum possible value of P_{CC} by up to 45%; this is termed power amplification.

The first dorsal interosseous muscle of a male volunteer (age 30 years) was stimulated supramaximally at a frequency of 100 Hz using percutaneous electrodes (Blue Sensor N-10-A), while an inertial load, constrained to rotate around the same axis as the second metacarpophalngeal joint, opposed index-finger abduction. The force exerted on the load by the finger was measured and the torque calculated as the product of this force and its distance from the centre of rotation of the joint. The acceleration and the angular position of the load were also recorded. Records were made with a wide range of inertial loads. These observations were made with the approval of the local ethical committee.

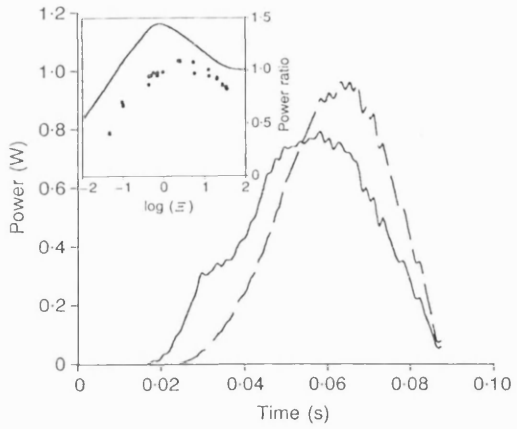

Figure 1. Time course of P_{CC} (continuous line) and P_{EXT} (dashed line) during a contraction. The inset shows the relationship for one subject between the power ratio and the logarithm of the normalized inertial load (Ξ). The dotted line in the inset is the theoretical prediction of the power ratio.

Galantis *et al.* (2000) suggested a method to find P_{CC} and P_{SEC} during contractions performed against inertial loads. That method assumed that the activation of the muscle was instantaneous, and is here improved by assuming a more realistic time course for activation. The joint angle–torque relationship is also taken into account. Analysis produces a stress–strain relationship for the SEC and a force–velocity relation for the CC. Using the stress–strain curve, P_{CC} and P_{SEC} can be calculated. As an index of power amplification we used a ratio calculated as the peak P_{EXT} divided by the maximum power that the CC is capable of generating.

The data show an optimal value of normalized inertial load for power amplification (inset to Fig. 1). These results are consistent with our modelling work. However, the power ratio does not exceed 1·1, well below the theoretical value of 1·45, perhaps because the model assumes instantaneous activation.

Galantis, A., Harridge, S.D.R. & Woledge, R.C. (2000). *J. Physiol.* **523.P**, 236*P*.

We thank Tony Christopher and Phil Oliver for technical assistance. A.G. has an MRC studentship and S.H. is a Wellcome Trust Fellow.

The effects of aerobic and anaerobic capacity on the H- and T-reflexes

R. Ozmerdivenli and S. Bulut

Firat University, Department of Physical Education, Department of Neurology, School of Medicine, Elazig, Turkey

The evaluation of distal segment leg reflexes using classical electrophysiological methods for nerve conduction velocities is not reliable. Local ethical committee approval was obtained for this study on students. In this study, the effects of regular exercise on H-reflex and T-reflex amplitude and latency was investigated. H-reflex and T-reflex amplitude and latency values of trained subjects with anticipated high aerobic capacity (test group 1, 10 football and 10 volleyball players) and sprinters with high anaerobic capacity (test group 2, 18 athletes) who had been regularly exercising for 8·73 ± 4·45 years (mean ± S.E.M.) and twenty students (control group) who had not regularly exercised were measured. The H-reflex amplitude and latency values of test group 1, group 2 and the control group were 3·71 ± 1·6 mV and 27·98 ± 2·16 ms ($n = 20$); 3·31 ± 1·3 mV and 26·35 ± 6·24 ms ($n = 18$); and 6·83 ± 2·23 mV and 27·69 ± 2·0 ms ($n = 20$), respectively. The amplitude of the H-reflex was significantly higher in the control group ($P < 0·05$, Mann–Whitney U test), but no difference between the test groups 1 and 2 ($P > 0·05$). The T-reflex amplitude and latency values of test group 1, group 2 and control groups were 3·78 ± 1·99 mV and 32·08 ± 2·04 ms; 3·20 ± 1·3 mV and 31·58 ± 3·33 ms; and 4·31 ± 1·43 mV and 31·52 ± 2·27 ms, respectively. Only test group 2 values were significantly lower than control ($P < 0·05$). There was no significant difference between the test group 1 and 2 players with respect to H- and T-reflex amplitude and latency.

In conclusion, the H-reflex amplitude recorded from trained muscle was significantly low and this could be due to a lower number of motor neurones stimulated by type Ia fibres. The T-reflex amplitude was lower in sprinters with anticipated high anaerobic capacity compared with endurance-trained subjects with anticipated higher aerobic capacity. Therefore, the level of exercise should be considered as an influencing parameter when evaluating the amplitude of H- and T-reflexes.

0·832 ± 0·033, compared with 0·950 ± 0·064 in Pla ($P < 0·05$, Student's paired t test).

This significantly greater acceleration in heart rate upon voluntary muscle contraction in the Dz group implies that GABAergic suppression of cardiac vagal outflow is in part responsible for contraction-induced tachycardia in man.

Al-Ani, M., Robins, K., Al-Khalidi, A.H., Vaile, J., Townend, J. & Coote, J.H. (1997). *Clin. Sci.* **92**, 175–180.

Farmer, M.R., Vaile, J.C., Osman, F., Ross, H.F., Townend, J.N. & Coote, J.H. (1998*a*). *Clin. Sci.* **95**, 241–248.

Farmer, M.R., Vaile, J.C., Osman, F., Townend, J.N. & Coote, J.H. (1998*b*). *J. Physiol.* **513.P**, 82–83*P*.

M.R.F. was supported by a British Heart Foundation PhD studentship.

Properties of the human 1st dorsal interosseous muscle–tendon complex during electrically evoked contractions

A. Galantis, S.D.R. Harridge* and R.C. Woledge

*UCL Institute of Human Performance, RNOHT, Brockley Hill, Stanmore, Middlesex HA7 4PL and *Department of Physiology, Royal Free and University College Medical School, Rowland Hill Street, London NW3 2PF, UK*

Active shortening of the contractile component (CC) of a muscle–tendon complex (MTC) against an inertial load (L) results in length changes in its series elastic component (SEC). The instantaneous displacement of L is therefore not the same as the instantaneous amount of CC shortening. Recoiling of the SEC during such contractions may result in a greater delivery of power to L by the whole MTC than the CC alone could deliver (power amplification). The aim of this study was to determine the contractile and elastic properties of the human 1st dorsal interosseous (FDI) MTC and the power amplification during electrically evoked contractions under inertial loading conditions.

The FDI of four male and one female volunteer (aged 26–44 years; $n = 5$) were supramaximally stimulated at a frequency of 100 Hz, to contract against a wide range of L whose axis of rotation was the same as that of the second metacarpophalangeal joint. The force exerted by the finger on L, the angular displacement and acceleration of L were recorded. The torque around the joint was calculated as the product of the measured force and its distance from the centre of rotation of the joint. These observations were made with the written, informed consent of the subjects and the approval of the local Ethical Committee.

Using the method described by Galantis *et al.* (2000) that takes into account a hypothetical CC activation time course and the maximal static torque–angle relationship, we determined the force–velocity properties of the of the CC, the mean maximum CC shortening velocity (ω_{max}), the maximum stiffness of the SEC (k_{rot}) and the power amplification ratio (R). R is calculated by dividing the peak power that is delivered to L during a contraction by the maximum power that the CC is capable of generating.

The mean values for k_{rot}, ω_{max} and R were 5·03 Nm rad^{-1} (3·13–7·95), 10·54 rad s^{-1} (4·20–22·91), and 1·16 (0·81–1·35), respectively. Using an approximate moment arm of 7 mm (An *et al.* 1983), the peak stiffness of the FDI SEC, expressed in linear terms, averages 110 N mm^{-1}. This compares to 141 N mm^{-1} reported by Cook & McDonagh (1996*a*) from isometric-lengthening contractions. The lowest ω_{max} values reported here are in general agreement with those reported by Cook & McDonagh (1996*b*) obtained from isovelocity contractions. R is lower than our theoretical prediction of 1·45, probably due to anatomical constraints.

An, K.N., Ueba, Y., Chao, E.Y., Cooney, W.P. & Linscheid, R.L. (1983). *J. Biomech.* **16**, 419–425.

Cook, C. & McDonagh, M. (1996*a*). *Eur. J. Appl. Physiol.* **72**, 380–382

Cook, C. & McDonagh, M. (1996*b*). *J. Appl. Physiol.* **81**, 384–392.

Galantis, A., Harridge, S.D.R. & Woledge, R.C. (2000). *J. Physiol.* **528.P**, 51*P*.

A.G. has an MRC studentship and S.D.R.H. is a Wellcome Trust Research Fellow.

Myofibrillar protein synthesis (MPS) and the activity of p70s6 kinase in human skeletal muscle: the effects of contractile activity and essential amino acids (EAA)

M.J. Rennie, H.S. Hundal, K. Peyrollier, D.J. Cuthbertson, K. Smith, G. Leese* and P.W. Watt

*Department of Anatomy & Physiology, University of Dundee, Dundee DD1 4HN and *Department of Medicine, Ninewells Hospital, Dundee DD1 9SY, UK*

Intense contractile activity plus the availability of increased concentrations of amino acids stimulates muscle protein synthesis to a greater extent than amino acids or contractile activity alone. The regulatory mechanisms involved, particularly possible changes in elements of the signal pathway controlling the translational processes, are not understood. We hypothesized that the stimulation would involve increases in the activity of ribosomal p70 s6 kinase,

muscle was loaded to a force of 8 kN and video motion analysis was used to measure deformation. At 8 kN, the stored energy was 50–57 J and tendon strains were 10%. This is similar to that recorded in other energy storage tendons at peak strain.

Bicep forces were calculated during a trot from shoulder joint moment and limb force using forceplate and motion analysis. The biceps moment arm was determined by radiography. Seventy percent of the shoulder moment was attributed to the biceps. At 85% of stance (when the heel leaves the ground), the peak extensor moment on the shoulder joint was 1600 Nm, producing a peak biceps force of 4.2 kN. The energy stored in the biceps at a force of 4.2 kN is 18 J. If the entire shoulder moment was provided by the biceps, this would rise to 6 kN and 32 J. This is a significant proportion of the energy required to protract the limb.

A9.4–The theoretical limits to the power output of a muscle tendon complex with inertial and gravitational loads

A. Galantis and R.C. Woledge, University College London

A muscle and tendon acting on an inertial load can deliver to the load a power greater than could be generated by the muscle alone. This is because energy stored by the muscle in the tendon early in the contraction, when the load is moving slowly, is delivered to the load at a later stage when the load is moving faster and adds to the work generated at that time by the muscle. We term this 'power amplification'. The question we address in this presentation is how much power amplification can be produced by this mechanism. We consider systems in which the muscle is characterised by its force–velocity curve, either linear or curved; the tendon is characterised by its force–extension curve, which may also be linear or non-linear, and where the load is either a pure inertia or a mass subject also to gravitational loading. The methods we have used are dimensional analysis, standard analytical methods to solve the linear cases, and numerical integration for the more complicated (non-linear) examples. In the absence of gravitational loading, the maximum power available is approximately 1.4 times the power output of the muscle alone. With added gravitational loading, this can increase to almost twice the muscle power. The linearity of the force–velocity curve and force–extension curves have only a minor influence on these conclusions. It seems that only cams or catches can further increase the power amplification.

A9.5–Novel muscle activation patterns in the escape response of *Polypterus senegalus*

E.D. Tytell and G.V. Lauder, Organismal and Evolutionary Biology, Harvard University

The kinematics and muscle activity patterns of escape responses in the bichir, *Polypterus senegalus*, were analyzed using high speed video and electromyography (EMG). Five fish were filmed at 250 Hz while recording white muscle activity at five sites on both sides of the body. Body wave speed and center of mass velocity, acceleration, and curvature were calculated from digitized outlines. Six EMG variables per channel were also calculated to characterize the motor pattern. In contrast to previous studies, which observed mostly uniform escape responses, *P. senegalus* shows a wide range of patterns, from very strong responses, in which the head often touched the tail, to very weak responses, with corresponding variation in the length and magnitude of muscle activity. Unlike the classical pattern for escape response muscle activity, strong activity was observed on both the ipsilateral and contralateral sides during Stage I; contralateral activity, however, was significantly weaker and shorter in duration than ipsilateral activity. While simultaneous, bilateral muscle activation, such as we observed in *P. senegalus*, has been hypothesized to increase body stiffness and bending wave speed, we detected no correlation between bilateral activity and wave speed. Escape responses almost always had Stage II contralateral muscle activity, although it was often limited to the two most anterior electrodes.

A9.6–Viscosity rules the wake? Generation, decay and aging of animal generated vortex wakes

E.J. Stamhuis, University of Groningen

Animals transfer momentum to the water when producing thrust. The momentum can be recognized in jets of water, moving away from the animal. Depending on the size of the animal and the induced flow velocities (and hence, the Reynolds number), the vorticity accompanying the jet stays attached or is shed as single or even as series of individually recognizable vortex rings. The results from flow studies conducted in our lab show that the wake structure and the decaying process of wakes changes with increasing Reynolds number (*Re*). The process of decay of animal generated vortex wakes has hardly been addressed experimentally so far, despite the high ecological importance of wake lifetime with respect to the traceability of a swimming animal by predators and/or conspecifics. Recently, we conducted a series of experiments in which vortex rings were produced artificially over a wide *Re* range. Several parameters of the vortex rings derived from PIV analysis were followed